© 2013 by Jorge Luis Garzón Torres. All rights reserved.

THREE-DIMENSIONAL NUMERICAL ANALYSIS OF REFLECTIVE CRACKS IN AIRFIELD PAVEMENTS

BY

JORGE LUIS GARZÓN TORRES

DISSERTATION

Submitted in partial fulfillment of the requirements
for the degree of Doctor of Philosophy in Civil and Environmental Engineering
in the Graduate College of the
University of Illinois at Urbana-Champaign, 2013

Urbana, Illinois

Doctoral Committee:

Associate Professor C. Armando Duarte, Chair and Director of Research
Professor William G. Buttlar, Co-chair and Co-director of Research
Professor Emeritus Harry H. Hilton
Dr. David Brill, FAA Airport Technology R&D Branch
Dr. Patrick O'Hara, Wright-Patterson Air Force Base

Abstract

Hot mix asphalt (HMA) is used as the primary overlying material of concrete pavements during rehabilitation because of its inexpensive nature when compared to most Portland cement concrete (PCC) rehabilitation/reconstruction alternatives. In airfield pavements for example, a common technique is to place a HMA concrete overlay on top of an existing deteriorated PCC, since the initial cost is low and the placement process is fast. This restores smoothness, structure and water-proofing benefits to existing pavement. However, due to the majority of the PCC pavements being in average to poor condition, many HMA overlays are exposed to extreme movements (both vertical and horizontal). The combination of associated load and environmentally induced movements creates complex stresses and strains in the vicinity of expansion joints and cracks in the PCC, thus dramatically reducing the life of the HMA overlay, typically in the form of reflective cracking. Reflective cracking is a fatigue cracking distress, which is initiated at the bottom of the HMA overlay and propagates through its thickness and the surface. It can reduce the life expectancy of the overlay because it leads to roughness, raveling, and moisture infiltration.

The analysis of reflective cracking involves all modes of fracturing i.e., Mode *I* (opening), Mode *II* (shearing), and Mode *III* (tearing) [61] and thus 3-D models are required. The need for true 3-D modeling of reflective cracking complicates the development of computational models using standard finite element methods. Furthermore, the nature of the linear viscoelastic material (asphalt) makes the crack analysis time dependent. The Generalized or eXtended Finite Element Method (*G/XFEM*) [10, 12, 41, 108, 109, 119, 163] adds flexibility to the FEM while retaining its attractive features. In this study, the computation of the time-dependent energy release rate $\mathcal{G}(t)$ along 3-D crack fronts is done by applying the elastic-viscoelastic correspondence principle to the

associated GFEM elastic solution. The inversion from the Laplace domain to the physical domain is done numerically using the Fourier series method.

In this proposed linear viscoelastic GFEM, adaptive surface triangulations are utilized to explicitly represent complex 3-D crack surfaces. Computational geometry algorithms are used to track the evolution of the crack front and the crack surface representation based on GFEM solutions. This methodology allows us to investigate the behavior of complex 3-D reflective crack surfaces accounting for the viscoelastic behavior of the material while keeping the computational cost and implementation complexity comparable to the case of linear elastic materials. Numerical experiments of long crack growth (crack surface significantly increases from its initial size) and coalescence of multiple crack surfaces demonstrate that the method is robust and is able to perform complex 3-D crack growth simulations. As such, it provides support for the development of mechanistic based design procedures for airfield overlays that are tolerant to reflective cracking.

To my beloved Parents Gonzalo, Beatriz, Michael and Amella.

Acknowledgments

First and foremost, I would like to thank The Lord our Father for giving me wisdom and guidance throughout my life. Thy will be done, always.

I would like to express my sincere gratitude to my advisors, Prof. Armando Duarte and Prof. William Buttlar. This work would not have been possible if it weren't for these two research experts that have taught me so much about their fields of expertise. A great combination of Computational Mechanics and Pavements. Also, I would like to thank them for their support guidance and encouragement through all these years. I am also grateful for the resolute financial support that they have provided me through research assistantships. Special thanks to the Federal Aviation Administration that has supported our project since the beginning.

I also would like to thank my committee members Prof. Harry Hilton, Dr. David Brill and Dr. Patrick O'hara, for the many insightful discussions and suggestions. I thank all members of our research group Varun Gupta, Julia Plews, Piyush Gupta and Phillipe Alves for helping with the proofreading and editing of this document. I wish you all the best finalizing your degrees.

I would like to express the deepest appreciation to the most important people in my life, my family. My hard-working parents that have always given everything to provide unconditional love and care to my brothers and me. Chalito and Bachita I love you with all my heart. You have been a living example for us. I would have not made it this far without your constant encouraging sweet words and advises. To my hermanitos David and Jose for taking care and defending me countless times while kids. Despite the distance, we would remain best friends and sharing brothers. I would also like to thank to my grandparents Jorge, Rigoberto, Ines, in heaven and my grandmother Sarita for their love and blessings. I'm deeply grateful to my American Shade family. You have truly

made me feel like one of your own. Dad Michael and Mom Mel I love you so much. I will be always grateful for opening your arms, home and hearts and letting me be a Shade. Also, I would like to thank my brothers Bryan, Brad, Scott and my sisters Shay, Alexis, Molly and Casey. You guys are Turkey! Specially Bryan, thanks bro so much for being so generous to me. You are a true hermano and as I said it on your wedding, you won't ever get rid of me. I also want to thank Grandpa Tom and Grandma Carlene for your help, love and support. Many thanks for teaching me to fish and always filling my plate with such culinary treats. To my aunt Janet and cousin Lisseth for giving the first push in the transition to the U.S. Thanks for your love and sharing your homes with me. Family, your love and support has motivated me to move forward and try my best everyday.

I also thank my friends for providing support friendship and laughter. To my closer friends Pato and Tibi and other members of the Atletico San Viernes soccer squad. I would like to thank to my Champaign friends Vaca, Perry, Cachorro, Compadrito, Vivi, Tati, Patrick, Anaso, Bere, Santi, Noland, Pequi, Chino, David, Camilo, Angie, Pepe and many others (too many to list here but you know who you are!). To Gentleman, Marseille and Colombian soccer team members and friends, thank you for sharing many games, goals and victories.

Table of Contents

List of Tables

List of Figures

Chapter 1

Introduction

1.1 Motivation

Reflective cracking (RC) is one of the primary forms of distress in Hot Mixed Asphalt (HMA) overlays of flexible and rigid pavements. It accelerates the deterioration of the overlay and the underlying pavement because of the penetration of water and foreign debris (spalling) into these cracks. As consequence it reduces significantly the service life of the pavement and in case of airfields, advanced spalling can also significantly increase Foreign Object Damage (FOD) potential. The basic mechanism causing reflective cracking is strain concentration in the overlay due to movement in the underlaying pavement in the vicinity of joints and cracks. This movement may be induced by bending or shearing action resulting from gear loads or temperature changes. Factors that influence reflective cracking are: traffic volume, daily and seasonal temperature variations, pavement structure, HMA mixture properties and the degree of load transfer at joints among others.

In airfield pavements for example, in order restore the smoothness, structure capacity, and waterproofing benefits of any existing deteriorated Portland Cement Concrete (PCC) pavement, a common practice for rehabilitation consists in placing an asphalt concrete (AC) overlay on top of the deteriorated pavement. In contrast to other rehabilitation techniques, the use of asphalt overlays constitutes low initial cost and a fast process since the existing pavement serves as a foundation for the new pavement. However, in many instances the lifespan of the new overlay greatly depends on the emergence of reflective cracks underneath it, that may later propagate to the surface and/or channel through the overlay.

In the United States significant amount of resources is being invested to reduce reflective cracking in airfields and highways. The commonly used rehabilitation methods include increasing overlay thickness, crack-and-seat, break and seat, saw-and-seal in overlay above existing joints, and the use of crack arrester granular layer or interlayer systems [34]. The Illinois Department of Transportation (IDOT), for example, spends approximately two million dollars annually on reflective cracking control treatments [23]. Some of them consist on commercially available engineering fabrics, fabricated interlayer membranes and asphalt-rubber membrane interlayers. Buttlar et al. [23] evaluated the cost-effectiveness of the IDOT reflective cracking control system. The study was limited to projects constructed originally as rigid pavements and subsequently rehabilitated with bituminous overlays and a nonwoven polypropylene paving fabric. The performance of the projects across Illinois indicated an increase in life spans by 1.1 and 3.6 years for paving fabric strip (over existing cracks) and area applications (over the entire pavement), respectively. The analysis indicated that the control system was marginally cost-effective in Illinois.

The Arizona Department of Transportation (ADOT) studied the use of an Asphalt-Rubber mix (AR) in conjunction with a HMA overlay on a relatively thin and very badly cracked concrete pavement that was in need of reconstruction. It was reported that the AR overlay performed beyond its expectations and after nine years of service the overlay was still nearly crack-free. The benefits represented about eighteen million dollars in construction savings [102]. Other mitigation techniques for reflective cracking in Arizona include commercial paving fabrics and stress absorbing membrane interlayers.

The California Department of Transportation (Caltrans) evaluated the use of geotextiles and the increase of HMA thickness overlays to minimize reflective cracking. Researchers showed that 4.8 inches of overlay is required to reduce reflective cracking for 10 years [133]. Also, they evaluated the use of glassgrid and pavement reinforcing fabrics. Glassgrid is composed of fiber glass strands coated with an elastometric polymer.

None of the techniques used, in the mentioned states and others, provide an ideal solution to prevent reflective cracking [24, 101]. For example, the increase of the overlay thickness is only

applicable for overlays thinner than nine inches [71] and may not decrease thermal stresses significantly, while it may decrease traffic induced stresses [81]. Interlayer systems have been effective in reducing the occurrence of reflective cracking. However, some applications showed little or even no success on retarding reflective cracking. This could be due to the lack of understanding about the interlayer system mechanism in reducing reflective cracking and/or inappropriate interlayer system installation [133].

Even though there are many field practices available to reduce reflective cracking, an accurate life prediction and a successful design to prevent it, lies in the ability to understand and account for all reflective cracking mechanisms. The remaining of this Chapter presents an overview of the definition of reflective cracking, a summary of the available reflective cracking models, a brief review of fracture models in finite elements and outlines the main contributions of this study.

1.2 Reflective Cracking and Available Models

Reflective cracking can be defined as the emergence of cracks on a resurfacing or overlay above a existing deteriorated pavement. This phenomenon is known with this name because of the nature to mirror the cracks and joints of the underlaying pavement before its rehabilitation. Their cause is the movement of the underlaying pavements in the vicinity of joints or cracks due to the combination of bending and shearing action resulting from gear loads and daily and seasonal temperature changes, as illustrated in Figure 1.1. The existing joints or cracks affect reflective cracking because they lead to stress concentrations at the bottom of the overlay which lead to crack initiation and growth. If the new overlay is bonded to the distressed layer, cracks in the existing pavement almost always propagate to the surface within one to five years. Sometimes even as early as few months has been reported [31].

There are generally three common modes of failure associated with reflective cracking, assuming the crack front its parallel to the pavement surface as shown in Figure 1.2: i) Horizontal movement (Mode I) of slab, which is usually associated to temperature. It causes tensile and

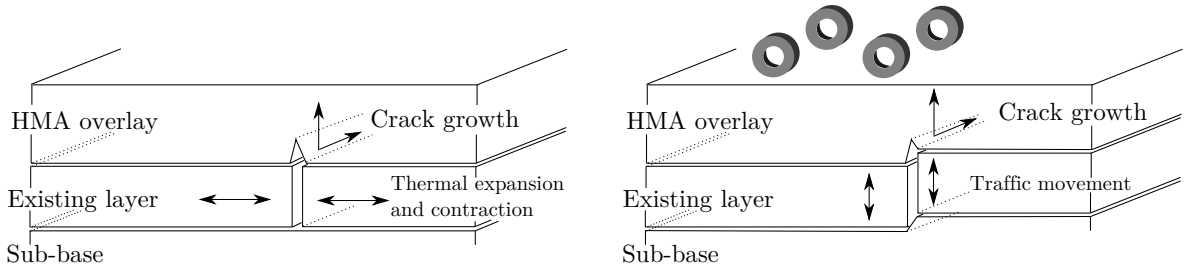

(a) Thermally induced fatigue (b) Traffic induced fatigue

Figure 1.1: *Movements in underlying pavement layers that contribute to reflective cracking.*

bending stresses to develop in the overlay. ii) Vertical Movement (Mode *II*) at the joint or crack area primarily induced by gear loads. It creates shear and tensile stresses within the overlay. iii) Parallel Movement (Mode *III*) of the slab which is not common, however, it may occur if the slab is structurally unstable with minimal frictional resistance.

If the crack front is perpendicular to the pavement surface the vertical movement becomes a Mode *III* while the parallel movement would correspond to a Mode *II*. As it will be shown in this dissertation, the geometry of the crack front varies constantly and it becomes parallel to the pavement surface only at its final stages of propagation. Therefore, these mentioned modes of failure may be present at all times because they are not only influenced by the loads affecting the pavement but also by the geometry of the reflective crack.

In addition, crack initiation and propagation is also influenced by the existing pavement structure and conditions, HMA mixture properties, the degree of load transfer at joints and cracks, RC countermeasures (e.g., reinforcing, interlayer) and others. In order to successfully model reflective cracking all mechanism and influencing factors should be considered. The following section presents a brief overview of available RC models.

1.2.1 Reflective Cracking Models

Many studies have been conducted to study reflective cracking on asphalt overlays over existing pavements. Also, many models have been developed to analyze or predict RC and in general, they can be categorized as:

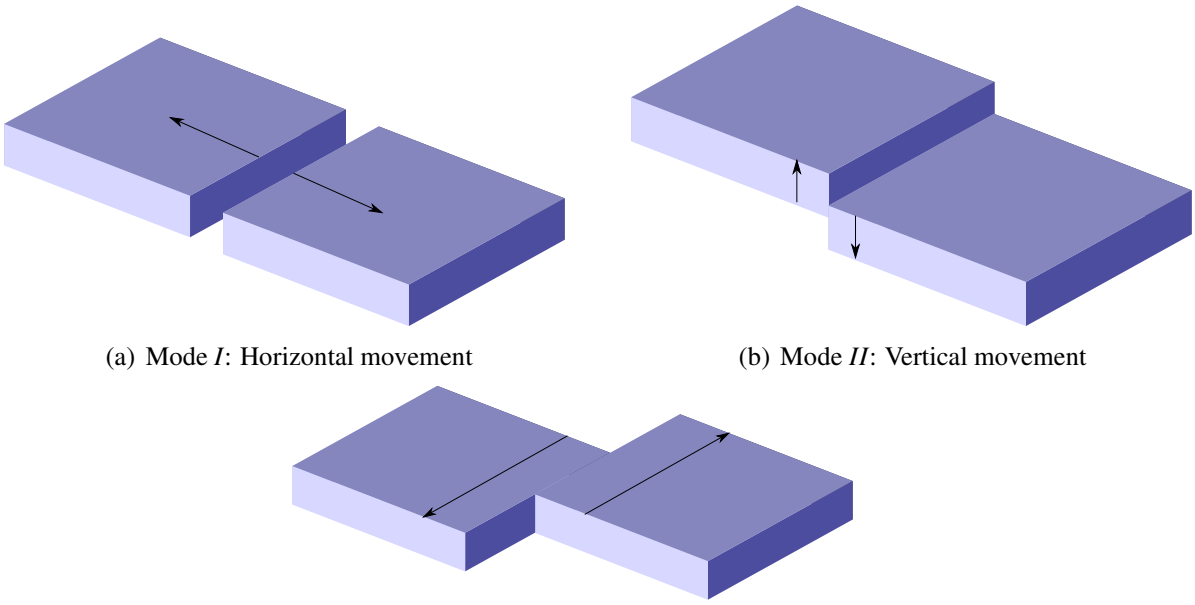

(a) Mode *I*: Horizontal movement

(b) Mode *II*: Vertical movement

(c) Mode *III*: Parallel movement

Figure 1.2: *Mechanisms of reflective cracking.*

- **Empirical models**

  They consist of empirical equations that relate several variables such as existing pavement conditions (e.g. thickness, age), environment, and traffic loading to the amount of reflective cracking. They are based mainly in field observations and laboratory testing. The main drawback of these models is that they are pure simplistic regression equations and they may not include all necessary factors that have a significant impact on reflective cracking. Furthermore, in field crack surveys, the behavior of reflective cracking in its early stages of crack initiation and propagation cannot be examined explicitly, since reflective cracking cannot be observed until it reaches the HMA overlay surface.

- **Extended multi-layer linear elastic model**

  Multi-layer linear elastic theory has been widely used in the asphalt pavement analysis and design. In fact, the pavement response model in the current Mechanistic-Empirical Pavement Design Guide (MEPDG) is based on multi-layer linear elastic theory. This theory assumes an axi-symmetrical geometry; homogeneous, isotropic linear elastic material

properties; and all layers extend to infinity in the horizontal plane. These assumptions can not be fully satisfied when analyzing an asphalt overlay over cracked pavement. Thus, the multi-layer linear elastic theory is not suitable to analyze reflective cracking.

- **Equilibrium equations based models**

  This procedure is based on a simple mechanistic approach in which equilibrium equations are used to estimate the stress and strain in an asphalt overlay. Moreover, this procedure has been implemented in the form of computer programs and charts for practical overlay design. Some assumptions made in this procedure include: linear elastic material properties; temperature variations are uniformly distributed in concrete slab; concrete movement is continuous with slab length; movement of layer is constant through its thickness; and material properties are homogeneous. This procedure has been developed by the Federal Highway Administration (FHWA) and later by the Arkansas State Highway and Transportation Department.

- **Finite element and traditional fatigue equation model**

  This model consists in the use of finite element techniques to examine the state of stress/strain. These state levels can then be used with standard fatigue analysis for prediction of asphalt overlay life. Linear 2-D finite element procedures have been used in [58, 111], linear 3-D finite element [58] and nonlinear 3-D finite element [88].

  The Federal Aviation Administration (FAA) developed a software called The Federal Aviation Administration Rigid and Flexible Iterative Elastic Layered Design (FAARFIELD) to perform airport pavement thickness designs. For the case of rigid pavements and overlays, the procedure combines a 3-D finite element analysis of the rigid pavement system with a performance/failure model based on full-scale traffic tests [20].

- **Finite element and fracture mechanics model**

The fracture mechanics approach has been widely used in predicting pavement cracking since Majidzadeh [104] introduced fracture mechanics concepts into the field of pavements. The occurrence of reflection cracking is a crack propagation process caused by a combination of three modes of loading. Thus, the fact that the mechanisms of reflective cracking (bending, shearing and thermal stresses) discussed previously, can be exactly modeled by fracture Modes *I*, *II* and *III* makes the fracture mechanics approach the best option for modeling RC. This model has been chosen for this study and more details are presented in the next section.

- **Crack band theory based model**

  In this approach, a single discrete crack is replaced by infinitely many parallel cracks of infinitely small opening continuously distributed (smeared) over the finite element. Also, the effect of this smeared cracking can be modeled by reducing the material modulus in the direction normal to the cracks after the peak strength of the material has been reached. Joseph et al. [80] developed a 2-D finite element model to analyze the effect of various treatments on retarding low-temperature reflective cracking. No crack propagation has been attempted in asphalt overlays using the crack band model.

- **Cohesive cracking/zone model (CZM)**

  In this technique the crack length is divided into two separate regions, a traction free length and a cohesive part. In the cohesive part, a crack opening resisting traction exists and there is stress transfer between faces. This is done by introducing closure stresses near the crack tip in the model. The stress transfer capability of the cohesive part follows a descending path, from full transfer capability (when the cohesive crack faces just begin to depart) down to zero transfer capability as the displacement between the two cohesive crack faces reach a critical opening. Outside the process zone, the material properties are governed by the undamaged state.

Song et al. [159] used a bilinear cohesive zone model in conjunction with a viscoelastic bulk material to investigate fracture behavior of asphalt concrete. They were able to simulate crack propagation by inserting cohesive elements over an area of interest. Kim et al. [86] investigated the low-temperature fracture behavior of a rehabilitated airport pavement using also a bilinear CZM in a 2-D FEM. They were able to predict progressive crack behavior of asphalt pavements under critical temperature and aircraft loading conditions.

Although this model is a useful tool for investigating the fracture behavior of pavements it suffers from some disadvantages: the crack path during propagation is mesh dependent, numerical non-convergence becomes pronounced when cohesive elements are inserted over large areas and only 2-D simulations have been reported.

- **Non-local continuum damage mechanics base model**

  Continuum damage mechanics describes the heterogeneous micro-processes involved during the straining of materials and structures at the micro-scale. The ultimate state of local continuum damage mechanics corresponds generally to macroscopic crack initiation upon which it becomes a crack propagation problem and should be considered in the framework of fracture mechanics. If this is used to describe crack propagation, spurious mesh dependency may come into play. This mesh-dependency can be avoided by introducing non-local damage mechanics. This has been accomplished by numerous formulations but the most successful is the implicit gradient formulation, which is recommended since it is much easier to implement in FEM codes. A comprehensive, state-of-the-research review of non-local formulation can be found in [15].

- **Discrete fracture model**

  This model is based on the discrete element method (DEM) which is a numerical method for computing the motion of a large number of particles of micro-scale size and above. Kim et al. [87] developed a heterogeneous fracture approach for modeling asphalt

concrete that is composed of solid inclusions and a viscous matrix. They used a energy-based bilinear cohesive zone model to account for crack initiation and propagation. The drawback of this method is the large amount of elements needed in the simulation which makes simulations costly.

1.2.2 Fatigue testing in Asphalt Pavements

One of the main forms of distress in flexible pavement is fatigue cracking in the bituminous layer [21, 25, 35, 172]. Therefore, most mechanistic flexible pavement design procedures incorporates a fatigue criterion determined from tests with repeated loading. It is believed that cracking in pavements initiates at the bottom of the layer and propagates to the surface as one or more longitudinal or transverse cracks [25]. Jiminez [79] developed fatigue testing machines capable of testing plate specimens and road samples. Results of this type of test tend to be presented in terms of the number of cycles to failure [125]. Typically, repeated load direct tension or beam type tests are used to simulate the bending stress that occurs at the base of the pavement. Jacobs et al. [75] investigated crack growth in a range of asphalt mixtures using notched specimens and testing them in a controlled displacement environment. The authors measured the crack length and the crack mouth opening during dynamic direct tension compression tests. Also, they calculated stress intensity factors (SIFs) using a FEM program to predict fatigue life using the Paris Law [123]. They concluded there is a relationship between the Paris Law constants that depend on temperature and the asphalt mixture.

Collop et al. [35] investigated the use of the compact tension test to assess resistance to crack propagation for bituminous materials. Using digital photographs, the authors measured the crack length and used linear elastic fracture mechanics principles (LEFM) to computed Mode I SIF. Also, they used Paris Law to model the rate of crack propagation. They concluded that results show good correlation between the stiffness modulus of the asphalt mixture and the predicted number of load cycles to failure. Yongqi et al. [182] investigated crack initiation and propagation by performing fatigue tests on asphalt slabs. The authors also used a three-dimensional FEM to

evaluate SIFs and Paris Law to compute propagation fatigue life.

Carpenter et al. [172] have confirmed the existence of a Fatigue Endurance Limit (FEL) for hot mixed asphalt (HMA). Below this limit, HMA does not accumulate damage, meaning that the pavement can resist an infinite number of load cycles. The authors collected fatigue data on a binder mixture that was tested for an extended period from 5 to 48 million load repetitions at very low strain levels. Shen et al. [154] developed a energy based model that can take into account the healing effect due to the rest periods between loads. Also, it can estimate the strain level that produces the FEL.

In short, fatigue testing on asphalt mixtures is an undergoing topic that is important in pavement design procedures. In this dissertation, we aim to simulate crack propagation on asphalt pavements under repeated loading to quantify the number of cycles to failure. As it can be seen in this section, this is commonly done in practice. The term *Fatigue Life* used in this document is the same term used by the pavement research community to define the number of load cycles a pavement can withstand before failure.

1.3 Finite Element and Fracture Mechanics Model

The finite element method (FEM) is a numerical analysis technique used by engineers, scientists, and mathematicians to obtain approximate solutions to partial differential equations (PDE). These differential equations describe a wide variety of physical and non-physical problems. Physical problems include solids, fluids, soils, heat, electromagnetism, dynamics, etc. The basic premise of the FEM method states that a complicated domain can be sub-divided (discretized) into a finite number of smaller regions (elements) in which the differential equations are approximately solved. The behavior of the entire problem is determined by assembling the set of equations of each element. Elements are connected at specific points, called nodes, and the assembly process requires that the solution be continuous along common boundaries of adjacent elements. FEM has become the basic method of choice for solving equilibrium boundary value problems governed

by elliptic partial differential equations, because of its ability to handle complicated geometries. Finite elements are based on an associated minimization principle which, can be used to characterize the unique solution to a positive definite boundary value problem. Restricting the minimizing functional to an appropriately chosen finite-dimensional subspace of functions reduces it to a finite-dimensional minimization problem. As a result, it can be solved by numerical linear algebra. When properly formulated, the resulting finite-dimensional minimization problem has a solution that well approximates the true minimizer. For a boundary value problem governed by a second order differential equation for example, an effective choice of finite-dimensional subspace is to use piecewise continuous functions. Details on FEM can be found in [54].

Fracture mechanics is the field of mechanics concerned with the study of cracked bodies subjected to stresses and strains. It uses methods of analytical solid mechanics to calculate the driving energy on a crack and also the material's resistance to fracture. The crack propagation process is caused by a combination of the three modes of loading, as illustrated in Figure 1.3. Mode *I* is known as opening mode and results from loads applied normal to the crack plane. Mode *II* or in-plane mode results from in-plane shear loading. Finally, Mode *III* or out-of plane mode results from out-of plane shear loading.

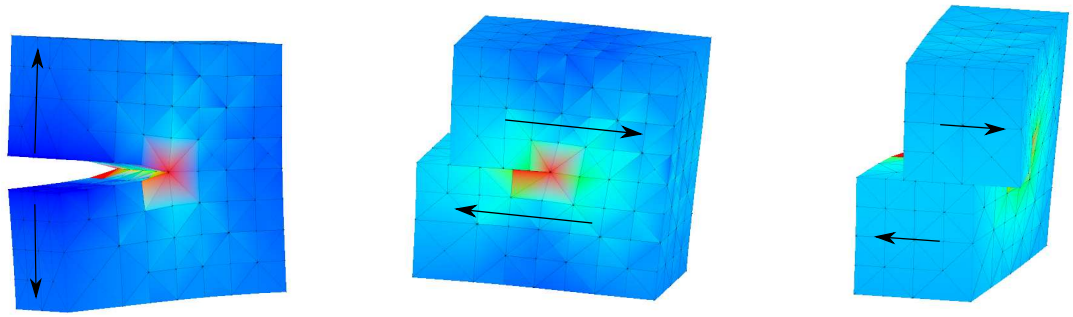

(a) Mode *I* (b) Mode *II* (c) Mode *III*

Figure 1.3: *Three modes of fracture.*

A simplified overlay design model was proposed by Al-Qadi and his associates [51]. It is used to predict the service life of rehabilitated flexible pavement structures against reflective cracking. The model is based on linear elastic fracture mechanics principles and it accounts for crack initia-

tion and stable crack grow stages. The crack initiation phase is described using a traditional fatigue law developed by the Belgium Road Research Center [22], and the crack propagation phase is described using Paris law [123]. Calculations of the stress intensity factors is determined based on the J-integral using 3-D commercial FEM software ABAQUS [2]. In order to investigate the crack initiation and propagation phases dynamic 3-D models were developed for different location of the cracks. Although the above analysis is capable of effectively evaluating the overlay service life against reflective cracking, it is very time consuming and viscoelastic effects are not considered.

There are very capable FEM commercial softwares such as ABAQUS and ANSYS [7] to simulate fracture problems. However, the complexity of these FEM programs and consequently the time-consuming user training process often prevent pavement engineers from using them. Therefore, other FEM tools have been developed specifically for pavement analysis. For example, CRACKTIP is a 2-D FEM software that is able to model a single vertical crack in the asphalt concrete layer using a crack tip element. It was developed for thermal cracking analysis and propagation by Lytton et al. [30] at the Texas Transportation Institute in 1976. However, it is know to all that, the difference between true 3-D nature and 2-D plane strain conditions of a cracked body and loading, leads to an overestimation. Another pavement FEM software is named CAPA (Computer Aided Pavement Analysis) and it was developed at the Delft University of Technology [141, 142]. The CAPA program has some special functions that were created to specifically study reflective cracking, such as: special elements for simulating interface and interlayer, automatic FE re-meshing to simulate crack propagation, and special crack front elements to capture the crack tip singularity among others. Currently this software does 2-D and 3-D fracture simulations and is a good option for reflective cracking analysis and prediction. However, its 3-D character demands high computational time and memory.

A method that improves the calculation speed is known as Semi-Analytical (SA) FEM. This method can transform a 3-D pavement analysis problem into an equivalent 2-D model, at a small computational effort [70]. Thus, a specific pavement crack propagation analysis tool, SA-CrackPro, was developed based on this simplification. Due to the reduction in dimensional analysis, SA-

CrackPro models have less number of degrees of freedom (Dofs) and therefore a matrix with a narrower bandwidth compared to 3-D FEM programs. This reduction is only possible by assuming that the 3-D FEM model has a reflective crack that cuts the entire pavement trough its thickness. This implies that the crack front is always parallel to the pavement surface, which is not a realistic assumption.

In general, the analysis of fracture problems with the FEM requires extremely refined meshes and special elements at the crack front in order to capture the existing singularity. In crack propagation problems, these elements have to be re-meshed at each crack increment, which often makes the simulation and the associated SIFs computation tedious. Even if this task is done automatically, with a re-meshing algorithm, it is computational intensive and it consumes a significant part of the simulation time.

Modeling pavements (e.g. airfield) in 3-D to study reflective cracking is difficult and computationally expensive since the area of interest is orders of magnitude smaller than the domain of the problem. A representative model of an airfield pavement can easily have several meters of length, while the size of the reflective crack is of the order of millimeters. After high refinement close to the crack front, required by the FEM, the element size is thousands of times smaller than the typical pavement model size. As a consequence, the simulation model becomes extremely expensive in terms of computational time and memory and sometimes ill conditioned. Structural problems involving multiple spatial scales of interest like this one are commonly solved using a global-local or sub-modeling procedure [36, 54, 115]. This approach is known to be sensitive to the quality of boundary conditions used in the local domains. Accurate local solutions require the use of sufficiently large local domains. However, the optimal size of the local domain is in general problem dependent.

To overcome the above mentioned difficulties of simulating RC in 3-D, this study proposes a model based on the Generalized Finite Element Method (GFEM). The GFEM [9, 10, 41, 119, 161] is an instance of the so-called partition of unity method which has its origins in the works of Babuška *et al.* [10, 12, 106] and Duarte and Oden [39, 45–47, 119]. The extended FEM

(*XFEM*) [16, 108] and several other methods proposed in recent years can also be formulated as special cases of the partition of unity method. Recent reviews of G/XFEM can be found in [17, 59]. The partition of unity in the GFEM is provided by low order Lagrangian finite element shape functions. These functions are combined with local function approximation spaces built around a-priori knowledge about the solution of a given problem. These functions provide more accurate and robust simulations than the polynomial functions traditionally used in the standard FEM while relaxing some meshing requirements of the FEM. An example of this class of GFEM based on analytically derived local spaces is the GFEM for polycrystals proposed in [157]. In this GFEM, discretization of polycrystalline micro-structures requires only a simple background mesh on which the polycrystalline topology is superimposed.

Pereira et al. [128] used a high-order GFEM for non-planar 3-D crack surfaces. He applied discontinuous p-hierarchical enrichment functions automatically around crack fronts and demonstrated that the GFEM is able to model a crack arbitrarily located within a finite element mesh. Therefore, this method allows fully automated fracture analysis using an existing finite element discretization without cracks. The representation preserves continuity of the crack surface while being able to represent non-planar, non-smooth, crack surfaces inside of elements of any size. His numerical simulations using the GFEM with linear elastic material properties showed high convergence rates of extracted stress intensity factors (SIFs) along non-planar curved crack fronts. For crack propagation Pereira et al. [130], used the face offsetting method (FOM) [78] to track the evolution of complex 3-D crack fronts. At each crack growth step he applied the GFEM and to obtain high-order approximations on locally refined meshes which were automatically created in complex 3-D domains. Section 4.2 summarizes the main ingredients of GFEM and its use in fracture mechanics.

In many classes of problems – like those involving two-scale phenomena or material nonlinearities – local approximation spaces used in the GFEM/*XFEM* are, in general, not amenable to analytical derivation. To overcome this limitation, basis functions for these spaces are defined from the numerical solution of boundary-value problems. Chapter 5 summarizes the so-called

Generalized Finite Element with global-local enrichments ($GFEM^{g\text{-}1}$). In this method, basis functions are numerically defined using concepts from the classical global-local finite element method [54, 69, 115, 180] and a multi-scale decomposition of the solution of a boundary or initial value problem is performed. The coarse scale component of the solution is approximated by discretizations defined on coarse finite element meshes. The fine-scale component is, in turn, approximated by the solution of local problems defined in neighborhoods of regions exhibiting multi-scale effects such as in the neighborhood of micro-cracks. Boundary conditions for the local problems are provided by the available solution at a crack growth step. The methodology enables accurate modeling of, e.g., 3-D propagating cracks on meshes with elements that are orders of magnitude larger than those required by the FEM. The coarse-scale mesh remains unchanged during the simulation. This, combined with the hierarchical nature of GFEM shape functions, leads to significant computational savings when compared with a Direct Numerical Simulation (DNS) approach [131]. An issue with a DNS approach based on available methods is the ill-conditioning of the resulting system of equations [13] due to the extremely large ratio between element sizes in the FEM mesh. One workaround for this issue is to perform the computations using high-precision 128-bit floating-point arithmetic [155]. However, few compilers or software libraries can handle high-precision arithmetic, and those that do so are extremely slow – often 50 to 100 times slower than conventional 64-bit floating-point arithmetic [155].

A related method aimed at modeling interactions among multiple static cracks is the multi-scale method of Loehnert and Belytschko [100]. Other related methods for two-dimensional static cracks include the spider-XFEM [26] and the reduced basis enrichment for the XFEM [27] of Chahine et al.; the method of Menk and Bordas for fracture of bi-material systems [107]; the harmonic enrichment functions of Mousavi et al. [112] for two-dimensional branched cracks.

1.4 Main Contributions

The main objective in this study is to develop a methodology to simulate reflective cracking in 3-D using linear viscoleastic (LV) material properties. This includes the study and numerical simulation of static and propagating cracks in LV, using GFEM and $GFEM^{g\text{-}l}$. The main contributions of this work are:

- Formulation and implementation of a 3-D viscoelastic constitutive model in the GFEM code (ISET).
- Implementation of an algorithm for 3-D static crack simulations using LV material properties. A representative time-dependent energy release rate (ERR) $\mathcal{G}(t)$ is computed along 3-D crack fronts by applying the elastic-viscoelastic correspondence principle to the associated GFEM elastic solution. This crack front parameter can accurately describe the fracture behavior.
- Implementation of the numerical inversion from the Laplace domain to the physical domain using the Fourier series method. Other methods are also studied, but Fourier series proves to be the most robust for the ERR type of function.
- Two-Scale simulation of cracks in LV using the $GFEM^{g\text{-}l}$. It includes an analysis of $GFEM^{g\text{-}l}$ parameters such as local domain and enrichment zone size.
- Development of computational geometry algorithms to track the evolution of the crack front and the crack surface representation based on GFEM solutions. This includes large crack propagation, coalescence of multiple cracks and the interaction between the crack front and the domain boundary.
- Implementation of an algorithm for fatigue crack growth in linear viscoelasticity based on GFEM solutions. Different propagation criteria are studied to accurately predict crack growth magnitude and direction.

- Simulation of reflective cracking in airfield pavements for live prediction. Numerical models are created and solve using all the presented techniques to better understand the behavior of reflective cracking in airfield pavements.

1.5 Dissertation Outline

The remainder of the present dissertation is outlined as follows:

- Chapter 2 presents a review of 3-D linear viscoelasticity, response functions, its transforms, correspondence principle and a nonlinear implementation in a GFEM code.
- Chapter 3 describes the theory for solving static cracks in linear viscoelasticity using the correspondence principle.
- Chapter 4 gives an overview of GFEM, enrichment functions for fracture problems, and numerical examples of static cracks in 3-D with linear viscoelastic material properties. Additionally a reflective cracking example on airfield pavement is solved.
- Chapter 5 presents an overview of *GFEM*$^{\text{g-l}}$, verification examples, RC simulation using *GFEM*$^{\text{g-l}}$ and parameters analysis.
- Chapter 6 describes briefly the methods to represent cracks in partition of unit methods (e.g. GFEM), presents improvements for explicit crack evolution and crack coalescence.
- Chapter 7 presents fatigue crack growth in linear viscoelasticity and its criteria.
- Chapter 8 A reflective cracking problem with multiple cracks is simulated using all techniques and algorithms presented in this dissertation.
- Chapter 9 summarizes the main findings of this study.
- Appendix A presents a three-dimensional formulation of the Contour Integral method (CIM) and the Cut-off Function Method (CFM) for the extraction of stress intensity factors.

Chapter 2

Linear Viscoelasticity

Even though most materials behave elastically under small stress and are described by Hooke's law, there are some that in addition to the elastic behavior exhibit viscous characteristics. The relationship between stress and strain for these type of materials depends on time and are called viscoelastic materials.

The experimental study of these type of materials is much more complicated that those time independent materials, because time can not be kept constant, or be eliminated during an experiment. Commonly the stiffness and strength of a material is illustrated by a stress strain curve, which can be obtained by applying a constant rate of strain to a bar of the material. If the material is linear elastic, the curve is a straight line with a slope proportional to the elastic modulus. On the other hand, if the material is linear viscoelastic, the relationship is given by a surface which is dependent on time and history (see Figure 2.1).

Some common phenomena for viscoelastic materials are known as creep and relaxation. Creep is the increment of strain with time when stresses are held constant. Relaxation is the decrease of stresses with time when strain is held constant. Materials that show a viscoelastic behavior are synthetic polymers, wood, human tissue, asphalt concrete and metals at hight temperatures, among others.

Since the behavior of this type of material is time dependent, it must be expressed by a constitutive equation that includes time as a variable in addition to the stress and strain variables. Various mathematical tools are used in the development of these constitutive equations since mathematics is an indispensable tool to formulate and solve problems with precision. It is important to keep in mind that these mathematical equations only represent a mathematical model which is used to

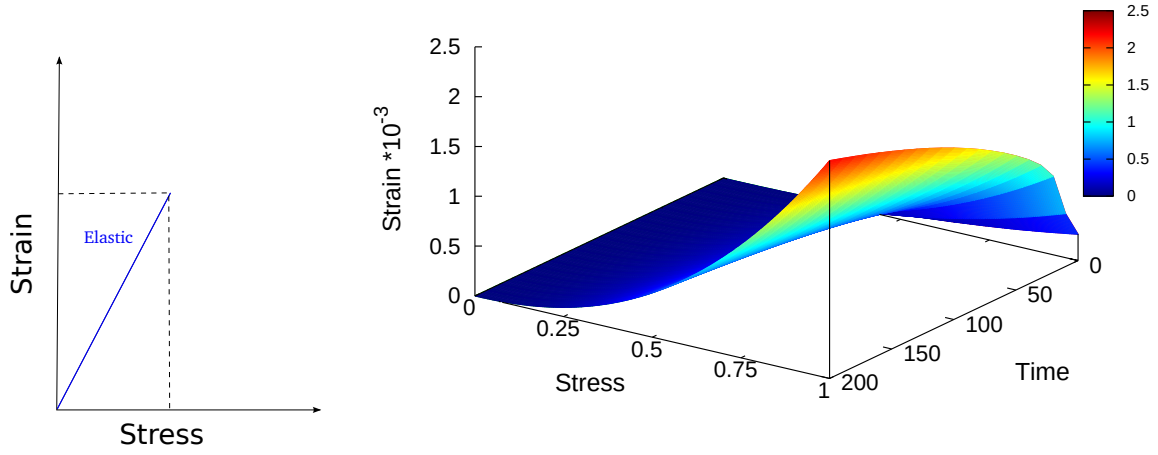

(a) Linear Elasticity (b) Linear Viscoelasticity

Figure 2.1: *Strain-Stress plots for deformation in linear elasticity and viscoelasticity.*

approximate a physical system in reality. Part of the analysis requires the evaluation of these approximations [67]. The viscoelastic functions used in the constitutive equations are obtained by experimentation.

The constitutive relation used in this study corresponds to linear viscoelastic materials. The author has found different ways to dervive the cosntitutive equations for linear viscoelasticity. Some can be found in references [56, 57, 89, 94]. The derivation in this document is mainly based on reference [67].

For isotropic materials it is convenient to separate the strains and stresses into deviatoric (change in shape) and volumetric (change in volume) parts. Materials may obey different and unrelated stress-strain laws for each of the two type of deformations. The mean stress $\sigma = \frac{1}{3}\sigma_{ii}$ and mean strain $\varepsilon = \frac{1}{3}\varepsilon_{ii}$ are measures of the pressure and volume change in the material, respectively. The changes in shape can be obtained by excluding the previous from the total stress and

strain tensors.

$$S_{ij} = \sigma_{ij} - \delta_{ij}\,\sigma \tag{2.1}$$

$$E_{ij} = \varepsilon_{ij} - \delta_{ij}\,\varepsilon \tag{2.2}$$

For now, concentrated only on the components related to the change in volume. Imagine a stress input and a related strain output in an homogeneous, isotropic linear viscoelastic body. Use the principle of superposition for the linear systems and neglect any effects due to thermal expansion. At a time t' in the past relative to t, take an increment in time dt' which in turn gives an increment $d\sigma(t') = (\partial\sigma/\partial t')\,dt'$. This is proportional to the increment $d\varepsilon(t') = (\partial\varepsilon/\partial t')\,dt'$ at time t', (see Figure 2.2).

$$d\sigma(t') \sim d\varepsilon(t') \tag{2.3}$$

Take any function $\psi^v(t-t')$ that relates them exactly.

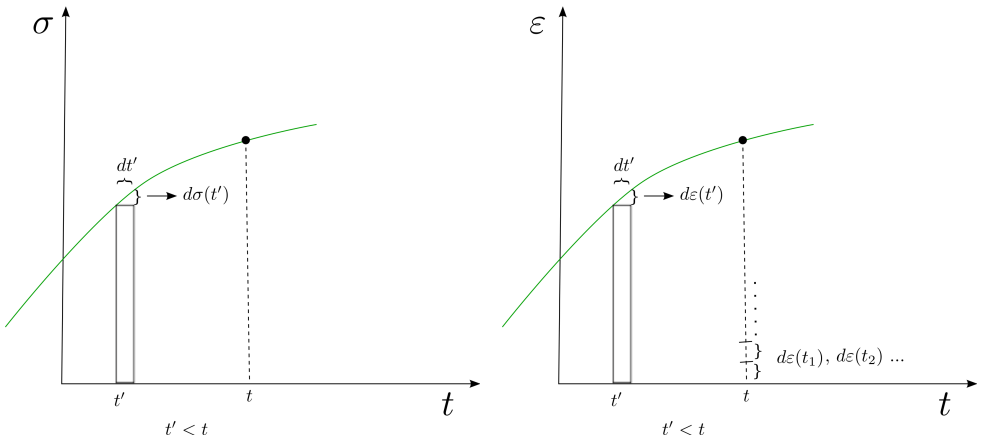

(a) Input (b) Output

Figure 2.2: *Example of a Stress-Strain relation for a viscoelastic body.*

$$\frac{\partial\varepsilon(t')}{\partial t'} = \psi^v(t-t')\frac{\partial\sigma(t')}{\partial t'} \tag{2.4}$$

This is true for all t' between $0 < t$. In Section 2.1 more details about this function are provided.

The total strain at time t is the sum of all past contributions, therefore, integrate the previous equation from $-\infty$ up to time t:

$$\int_{-\infty}^{t} \frac{\partial \varepsilon(t')}{\partial t'} dt' = \int_{-\infty}^{t} \psi^{v}(t-t') \frac{\partial \sigma(t')}{\partial t'} dt' \tag{2.5}$$

$$\varepsilon(t) - \varepsilon(-\infty) = \int_{-\infty}^{t} \psi^{v}(t-t') \frac{\partial \sigma(t')}{\partial t'} dt' \tag{2.6}$$

Assume that no strains are present at $t = -\infty$ and therefore $\varepsilon(-\infty) = 0$.

Finally we obtain what is know as the Boltzmann superposition integral, which expresses a convolution.

$$\varepsilon(t) = \int_{-\infty}^{t} \psi^{v}(t-t') \frac{\partial \sigma(t')}{\partial t'} dt' \tag{2.7}$$

In a similar way if the role of stress and strain are interchanged and the analysis done above is repeated ,a complementary relation is found. Assuming $\sigma(-\infty) = 0$:

$$\sigma(t) = \int_{-\infty}^{t} \phi^{v}(t-t') \frac{\partial \varepsilon(t')}{\partial t'} dt' \tag{2.8}$$

The corresponding deviatoric components of the stress-strain relations are:

$$S_{ij}(t) = 2 \int_{-\infty}^{t} \phi(t-t') \frac{\partial E_{ij}(t')}{\partial t'} dt' \tag{2.9}$$

$$2\, E_{ij}(t) = \int_{-\infty}^{t} \psi(t-t') \frac{\partial S_{ij}(t')}{\partial t'} dt' \tag{2.10}$$

For a future reference, integrate Equation (2.7) by parts and neglect all history from $-\infty$ to 0. Assuming the material was at rest prior $t = 0$.

$$\varepsilon(t) = \sigma(t)\, \psi^{v}(t')|_{t'=t} - \int_{0}^{t} \frac{\partial \psi^{v}(t-t')}{\partial t'} \sigma(t') dt' \tag{2.11}$$

This section gives a brief introduction to the mathematical model used for linear viscoelasticity.

More details with an extension to non-homogeneous and anisotropy materials can be found in [67]. The Functions ψ^v, ψ, ϕ^v and ϕ are know as creep and relaxation memory functions for the volumetric and deviatoric components, respectively.

2.1 Linear Viscoelastic Response Functions

Response functions are determined through experimental testing or through interconversion from other known response functions. For asphalt concrete for example, creep compliance $D(t)$ as a function of time can be determined from a simple mechanical test. On the other hand, relaxation modulus $E(t)$ is very difficult to be obtained by laboratory testing because it requires a high capacity and robust testing machine. Therefore, it is often the case where $E(t)$ is obtained through interconversion from $D(t)$ or other response functions.

Response functions are represented in analytical expressions. This mathematical functions may be simplistic or very complicated depending on the smoothness and stability of the experimental data that needs to be fitted. Some of the commonly used analytical expressions used to represent both creep compliance $D(t)$ and relaxation modulus $E(t)$ are the following (from reference [89]):

- Pure Power Law

$$J(t) = J_1\, t^n \tag{2.12}$$

  where J_1 is the value of creep compliance at $t = 1$ and n is obtained by identifying the representative slope of the experimental data over the transient region plotted on a log-log scale.

- Generalized Power Law

$$J(t) = J_0 \,+\, J_1\, t^n \tag{2.13}$$

  where J_0 is the glassy compliance ($J_0 = lim_{t\to 0} J(t)$)

- Modified Power Law

$$J(t) = J_0 + \frac{J_e - J_0}{\left(1 + \frac{\tau}{t}\right)^n} \tag{2.14}$$

where J_e is the long-time equilibrium compliance ($J_e = lim_{t\to\infty} J(t)$), τ and n are determined to fit the data.

- Prony Series

$$J(t) = J_0 + \sum_m^M J_m(1 - e^{-\frac{t}{\tau_m}}) \tag{2.15}$$

where J_0 is the glassy compliance, J_m is the regression coefficient and τ_m is the retardation time. This mechanical model is referred as the generalized Voigt model. Similarly for relaxation modulus

$$E(t) = E_\infty + \sum_m^M E_m\, e^{-\frac{t}{\rho_m}} \tag{2.16}$$

where E_∞ is the long-time equilibrium modulus, E_m is the regression coefficient and ρ_m is the relaxation time. This mechanical model is related to the generalized Maxwell model.

The most commonly used mathematical representation is the Prony Series, because of its ability of describing a wide range of viscoelastic response and its simplicity. This theory has a basis in the mechanical models dealing with linear springs and dashpots, which is explained in more detail in this section.

All the previous response functions are limited to uniaxial models. In order to study a three dimensional isotropic body, consider separating the deformations into deviatoric and volumetric components. In an isotropic medium it is sufficient to focus in any one pair of points inside the body. These points are separated by the flexible properties of the material. Thus, the stress analysis and characterization of the material may be done with an equivalent mechanical model whose individual properties are identical to those in the original body. For example, a massless spring can be considered as the equivalent mechanical model for elasticity while a massless viscous dashpot can be considered the mechanical analog for viscous dissipation. Then, any viscoelastic behavior can be represented by combinations of springs and dashpots. This combination is know

as a mechanical model, and its parameters correspond to the material properties of the equivalent medium.

Two simple viscoelastic models can be constructed by a combination of a single pair of spring and dashpot in parallel or in series. The first one is know as Kelvin body while the second is named Maxwell body (see Figure 2.3). K is the spring constant and η^v is the dashpot parameter; both correspond to the volumetric changes. Even though, the figure shows the same letters for the element parameters, these are not necessary equal. The following discussion will be limited to the volumetric deformations, but the deviatoric ones can be deduced by a change of symbols; E_{ij} for ε, S_{ij} for σ, $2G$ for K, and 2η for η^v.

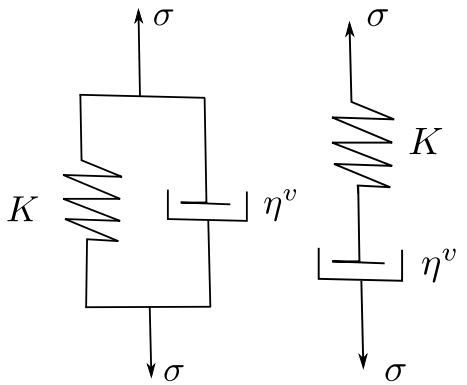

Figure 2.3: *Simple mechanical models.*

To build the stress-strain relations in the Kelvin and Maxwell bodies, it can be observed that in the first one, elements will have equal deformation but not equal load, while the reverse holds in the second one.

In the Kelvin model the total volumetric stress σ is the summation of the first element (elastic) stress σ^e and the second element (viscous) stress σ^v. The stress-strain relation for each of the elements are as follows: For spring element

$$\sigma^e(x,t) \;=\; K(x,t)\,\varepsilon(x,t) \tag{2.17}$$

For dashpot element

$$\sigma^v(x,t) \;=\; \eta^v(x,t)\,\frac{\partial \varepsilon(x,t)}{\partial t} \tag{2.18}$$

Note that Equation (2.18) has been written with a partial derivative, rather than a total one, because of the assumption that in any viscoelastic material the velocities dx_i/dt due to strains are very small and the terms $(\partial\varepsilon/\partial x_i)\cdot(dx_i/dt)$ are of second order compared to $(\partial\varepsilon/\partial t)$.

Adding Equations (2.17) and (2.18), and with initial conditions $\varepsilon(x,0)=0$,

$$\sigma(x,t) \;=\; K(x,t)\,\varepsilon(x,t) \;+\; \eta^v(x,t)\,\frac{\partial \varepsilon(x,t)}{\partial t} \tag{2.19}$$

Introduce a retardation time τ^v defined as $\tau^v = \eta^v/K$ and rewriting Equation (2.19) gives:

$$\frac{\partial \varepsilon(x,t)}{\partial t} \;+\; \frac{\varepsilon(x,t)}{\tau^v(x,t)} \;=\; \frac{\sigma(x,t)}{\eta^v(x,t)} \tag{2.20}$$

by integrating the previous and using the initial condition stated above,

$$\varepsilon(x,t) \;=\; \int_0^t e^{-\frac{t-t'}{\tau^v}}\,\frac{\sigma(x,t')}{\eta^v(x,t')}\,dt' \tag{2.21}$$

with t' as history time, $t' \le t$ and t as the present time. A similar analysis can be performed for the Maxwell body and can be found in [67].

Now, consider a combination of $N+2$ Kelvin models in series with spring constants K_n and coefficients of viscosity η_n. Assume that the first and last Kelvin bodies have the element parameters such that $\eta_0 = K_{n+1} = 0$. This is known as the generalized Kelvin Model (GKM). The load in each Kelvin model is σ and their respective deformation are ε_n with n=0,1,2,...,$N+1$ (see Figure 2.4). The total deformation of this model corresponding to the volumetric strain components at any point in the viscoelastic medium is:

$$\varepsilon(x,t) \;=\; \sum_{n=0}^{N+1} \varepsilon_n(x,t) \tag{2.22}$$

Substituting Equations (2.17), (2.18) and (2.21) into previous yields

$$\varepsilon(x,t) \;=\; \frac{\sigma(x,t)}{K_0(x,t)} \;+\; \sum_{n=1}^{N} \int_0^t e^{-\frac{t-t'}{\tau_n^v(x,t)}} \, \frac{\sigma(x,t')}{\eta_n^v(x,t')} \, dt' \;+\; \int_0^t \frac{\sigma(x,t')}{\eta_{N+1}(x,t')} \, dt' \tag{2.23}$$

with $\tau_n^v = \eta_n^v / K_n$ and n=1,2,3,...,N. The first and last terms in the equation correspond to the instantaneous response and the long term behavior, respectively. The middle term is all the time dependent response in between. This equation represents a form of the volumetric stress-strain relations of a general linear viscoelastic solid. If the parameters representing material properties area not time dependent Equation (2.23) reduces to:

$$\varepsilon(x,t) \;=\; \frac{\sigma(x,t)}{K_0} \;+\; \sum_{n=1}^{N} \frac{1}{\eta_n^v(x)} \int_0^t e^{-\frac{t-t'}{\tau_n^v(x)}} \, \sigma(x,t') \, dt' \;+\; \frac{1}{\eta_{N+1}(x)} \int_0^t \sigma(x,t') \, dt' \tag{2.24}$$

Notice that these integrals are path dependent meaning there is not a unique relation between stress-strain and their behavior depend on history. General viscoelastic behavior that has been described

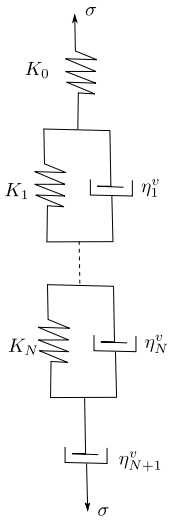

Figure 2.4: *Generalized Kelvin model.*

in terms of Kelvin bodies in series can be also formulated, in a similar way, in terms of Maxwell bodies placed in parallel and is know as generalized Maxwell model (GMM). The derivation can be found in [67].

By comparing Equation (2.11) and Equation (2.24) we get:

$$\psi^v(t')|_{t'=t} \;=\; \frac{1}{K_0(x)} \tag{2.25}$$

$$-\frac{\partial \psi^v(t')}{\partial t'} = \sum_{n=1}^{N} \frac{e^{-\frac{t-t'}{\tau_n^v(x)}}}{\eta_n^v(x)} \;+\; \frac{1}{\eta_{N+1}(x)} \tag{2.26}$$

Integrating equation (2.26) gives the volumetric creep function

$$\psi^v(t')|_{t'=0} \;=\; \psi^v(t) = \frac{1}{K_0(x)} \;+\; \sum_{n=1}^{N} \int_0^t \frac{e^{-\frac{t-t'}{\tau_n^v(x)}}}{\eta_n^v(x)}\, dt' \;+\; \int_0^t \frac{1}{\eta_{N+1}(x)}\, dt' \tag{2.27}$$

Equation (2.27) can further be integrated to yield

$$\psi^v(t) = \frac{1}{K_0(x)} \;+\; \sum_{n=1}^{N} J_n^v(x)\,(1 - e^{-\frac{t}{\tau_n^v(x)}}) \;+\; \frac{1}{\eta_{N+1}(x)} \tag{2.28}$$

Equation (2.28) is the volumetric response function which is similar to the presented Prony series, with J_n^v defined as the volumetric compliance. Later in this document $\psi^v(t)$ is written as $K(t)$, the reason is to make comparisons with linear elasticity easy to observe.

As mentioned before, response functions can be obtained through interconversion from other known response function. Creep compliance and relaxation modulus are two aspects of the same viscoelastic behavior and are related. For the volumetric component for example, if the material is purely elastic, then J^v and K would be reciprocal to each other.

$$K_{elastic}\, J^v_{elastic} \;=\; 1.0 \tag{2.29}$$

In viscoelasticity this is only true in the Laplace domain.

Again, assuming that the body was at rest prior $t = 0$ and therefore no initial strains are present. Apply the Laplace transform to Equation (2.8), using the convolution and derivative theorems for

Laplace transforms we get:

$$\mathfrak{L}\left\{\sigma(t)\right\} = \mathfrak{L}\left\{\int_0^t K(t-t')\frac{\partial \varepsilon(t')}{\partial t'}dt'\right\} = \mathfrak{L}\left\{K(t)\right\}\,\mathfrak{L}\left\{\frac{\partial \varepsilon(t)}{\partial t}\right\} \tag{2.30}$$

$$\bar{\bar{\sigma}}(p) = \mathfrak{L}\left\{K(t)\right\}\,p\,\mathfrak{L}\left\{\varepsilon(t)\right\} = \bar{\bar{K}}(p)\,p\,\bar{\bar{\varepsilon}}(p) \tag{2.31}$$

Notice that the volumetric relaxation modulus in Laplace domain multiplied by the transform variable p acts as a fictitious volumetric modulus of elasticity and it has a relation similar to the case of linear elastic material.

$$p\,\bar{\bar{K}}(p) \;=\; \frac{\bar{\bar{\sigma}}(p)}{\bar{\bar{\varepsilon}}(p)} \tag{2.32}$$

Similarly for Equation (2.7)

$$\bar{\bar{\varepsilon}}(p) = \bar{\bar{J}}^{v}(p)\,p\,\bar{\bar{\sigma}}(p) \tag{2.33}$$

$$p\,\bar{\bar{J}}^{v}(p) = \frac{\bar{\bar{\varepsilon}}(p)}{\bar{\bar{\sigma}}(p)} \tag{2.34}$$

From previous Equations (2.32) and (2.34) we obtain

$$\bar{\bar{K}}(p)\,\bar{\bar{J}}^{v}(p) = \frac{1}{p^2} \tag{2.35}$$

Observed that $p\,\bar{\bar{J}}^{v}(p)$ and $p\,\bar{\bar{K}}(p)$ are reciprocal of each other and one can be use to find the other. Applying the inverse Laplace transform gives their relation in the time domain, which is much more complex:

$$\int_0^t K(t-t')\,J^{v}(t')\,dt' \;=\; \int_0^t J^{v}(t-t')\,K(t')\,dt' \;=\; t \tag{2.36}$$

Computing the inverse of Laplace transform is not always as easy as in this example. Therefore there are also some other methods to approximate this interconversion such as Power-law based, Christensen, and Denby among others [89]. This section is limited to volumetric strain-stress relations. The same mechanical models can be used for the deviatoric components. One only needs to replace K_n by $2G_n$ (deviatoric moduli) and η_n^{v} by $2\eta_n$ (deviatoric viscosity) to obtain the

GKM for the change in shape. More details on the deviatoric formulation can be found in [67].

2.2 Generalization of Constitutive relation in three dimensions

Another way the viscoelastic behavior can be generalized to three dimensions is by using the basis of the similarity between linear viscoelasticity and elasticity as follows. The generalized Hooke's law of linear elasticity is given by

$$\sigma_{ij} = C_{ijkl}\varepsilon_{kl} \tag{2.37}$$

with C_{ijkl} as the elastic modulus tensor. There are 81 components in this tensor, but taking into account the symmetry of both strain and stress tensors only 36 of them are independent. Also, if the elastic solid is describable by a strain energy density function, the number of independent elastic constants reduces to 21. An anisotropic material with the most general type of anisotropy can be described by 21 independent elastic constants. On the other hand, if the material is isotropic, with properties that are independent of direction, it can be described by two independent elastic constants. For isotropic materials, the constitutive equations are

$$\sigma_{ij} = \lambda\varepsilon_{kk}\delta_{ij} + 2\mu\varepsilon_{ij} \tag{2.38}$$

where λ and μ are the two independent Lame elastic constants and δ_{ij} is the Kronecker delta.

Since it only takes two material constants to represent the material behavior in this case, for convenience, the shear modulus (G) and the bulk modulus (K) may be used to separate change in shape and volume, respectively. Both of these elastic constants are different and unrelated and can be computed as follows:

$$G = \mu \tag{2.39}$$

$$K = \lambda + \frac{2\mu}{3} \tag{2.40}$$

For Linear viscoelasticity, the following is the most general case of the integral representation,

assuming that the body was at rest prior to $t = 0$.

$$\sigma_{ij}(t) = \int_0^t C_{ijkl}(t-t') \, \frac{\partial \varepsilon_{kl}(t')}{\partial t'} \, dt' \tag{2.41}$$

As in the linear case this equation is sufficiently general to accommodate any degree of anisotropy. Each independent component of the modulus viscoelastic tensor C can have a different time dependence. Similarly, for isotropic linear viscoelastic material constitutive equations are

$$\sigma_{ij}(t) = \delta_{ij} \int_0^t \lambda(t-t') \, \frac{\partial \varepsilon_{kk}(t')}{\partial t'} \, dt' \; + \; \int_0^t 2\mu(t-t') \frac{\partial \varepsilon_{ij}(t')}{\partial t'} \, dt' \tag{2.42}$$

where $\lambda(t)$ and $\mu(t)$ are two independent viscoelastic functions that can have different time dependence. Likewise to linear elasticity, we can use a shear relaxation function $G(t)$ and a bulk relaxation $K(t)$, to represent the time dependent change in shape and volume, respectively.

Their relation in the Laplace domain are:

$$\bar{\bar{G}}(p) = \bar{\bar{\mu}}(p) \tag{2.43}$$

$$\bar{\bar{K}}(p) = \bar{\bar{\lambda}}(p) + \frac{2\bar{\bar{\mu}}(p)}{3} \tag{2.44}$$

Equation (2.42) transformed to the Laplace domain has the form:

$$\bar{\bar{\sigma}}_{ij}(p) = \bar{\bar{\lambda}}(p) \; p \, \bar{\bar{\varepsilon}}_{kk}(p) \, \delta_{ij} \; + \; 2\bar{\bar{\mu}}(p) \; p \, \bar{\bar{\varepsilon}}_{ij}(p) \tag{2.45}$$

Using shear and bulk relaxation functions:

$$\bar{\bar{\sigma}}_{ij}(p) = 2 \, \bar{\bar{G}}(p) \, [p \, \bar{\bar{\varepsilon}}_{ij}(p) - \frac{1}{3} \, p \, \bar{\bar{\varepsilon}}_{kk}(p) \, \delta_{ij}] \; + \; \bar{\bar{K}}(p) \; p \, \bar{\bar{\varepsilon}}_{kk}(p) \, \delta_{ij} \tag{2.46}$$

Now, separating volumetric and deviatoric components and using relations similar to Equation

(2.2),

$$\bar{\bar{S}}_{ij}(p) = 2\bar{\bar{G}}(p)\; p\; \bar{\bar{E}}_{ij}(p) \tag{2.47}$$

$$\bar{\bar{\sigma}}(p) = \bar{\bar{K}}(p)\; p\; \bar{\bar{\varepsilon}}(p) \tag{2.48}$$

where $\bar{\bar{\sigma}}(p) = \frac{1}{3}\bar{\bar{\sigma}}_{ii}(p)$ and $\bar{\bar{\varepsilon}}(p) = \frac{1}{3}\bar{\bar{\varepsilon}}_{ii}(p)$. Finally, taking the inverse of the Laplace transform and using the convolution and derivative theorems, the time domain the stress-strain relationships for deviatoric and bulk components are:

$$S_{ij}(t) = 2\int_0^t G(t-t')\,\frac{\partial E_{ij}(t')}{\partial t'}\,dt' \tag{2.49}$$

$$\sigma(t) = \int_0^t K(t-t')\,\frac{\partial \varepsilon(t')}{\partial t'}\,dt' \tag{2.50}$$

These are similar Equations to (2.5) and (2.8) presented earlier. Where S_{ij}, E_{ij} and σ, ε are the deviatoric and bulk components of stress tensor, respectively. $G(t)$ corresponds to the shear relaxation function, and $K(t)$ is the bulk stress relaxation.

2.3 Boundary Value Problem for linear viscoelasticity using the correspondence principle

This section presents a three dimensional problem assuming linear viscoelastic isotropic material behavior using the correspondence principle.

Consider a three dimensional domain Ω with boundary $\partial\Omega$ in a three dimensional space as illustrated in Figure 2.5. The boundary is subdivided into Γ^u and Γ^σ. Displacements and tractions are prescribed at Γ^u and Γ^σ, respectively.

The equilibrium equations are given by

$$\frac{\partial \sigma_{ij}(\boldsymbol{x},t)}{\partial x_i} + F_j(\boldsymbol{x},t) = 0 \tag{2.51}$$

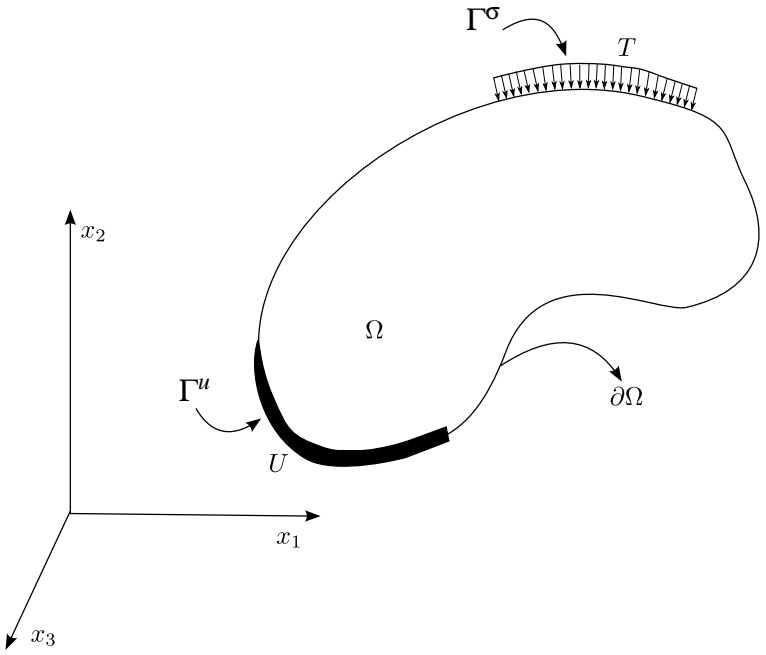

Figure 2.5: *Three dimensional boundary value problem.*

where $\boldsymbol{x}$ refers to the location of any part of the body at time t. The linear viscoelastic stress-strain relation, assuming the body is at rest prior $t = 0$, from Section 2.2 separated in deviatoric and bulk components are

$$S_{ij}(\boldsymbol{x},t) = 2\int_0^t G(t-t')\,\frac{\partial E_{ij}(\boldsymbol{x},t')}{\partial t'}\,dt' \tag{2.52}$$

$$\sigma(\boldsymbol{x},t) = \int_0^t K(t-t')\,\frac{\partial \varepsilon(\boldsymbol{x},t')}{\partial t'}\,dt' \tag{2.53}$$

There are no restrictions on the material functions and they can be different to each other. The strain-displacement relation for small deformations is given by

$$\varepsilon_{ij}(\boldsymbol{x},t) = \frac{1}{2}\left[\frac{\partial u_i(\boldsymbol{x},t)}{\partial x_j} + \frac{\partial u_j(\boldsymbol{x},t)}{\partial x_i}\right] \tag{2.54}$$

The boundary conditions are given by

$$\sigma_{ij}(\boldsymbol{x},t)n_i(\boldsymbol{x}) = T_j(\boldsymbol{x},t) \quad \text{on } \Gamma^{\sigma} \tag{2.55}$$

$$u_j(\boldsymbol{x},t) = U_j(\boldsymbol{x},t) \quad \text{on } \Gamma^{u} \tag{2.56}$$

where $\boldsymbol{n}$ is an outward unit normal vector on $\partial\Omega$ and T_j and U_j are the prescribed tractions and displacements, respectively.

Now lets write the same problem but in Laplace domain using the transform variable p:

Equilibrium equations

$$\frac{\partial \bar{\bar{\sigma}}_{ij}(\boldsymbol{x},p)}{\partial x_i} + \bar{\bar{F}}_j(\boldsymbol{x},p) = 0 \tag{2.57}$$

Constitutive relations; the conversion of the Boltzmann integral into Laplace domain is done similarly to Equation (2.30)

$$\bar{\bar{S}}_{ij}(\boldsymbol{x},p) = 2\bar{\bar{G}}(p)\; p\, \bar{\bar{E}}_{ij}(\boldsymbol{x},p) \tag{2.58}$$

$$\bar{\bar{\sigma}}(\boldsymbol{x},p) = \bar{\bar{K}}(p)\; p\, \bar{\bar{\varepsilon}}(\boldsymbol{x},p) \tag{2.59}$$

Boundary conditions

$$\bar{\bar{\sigma}}_{ij}(\boldsymbol{x},p) n_i(\boldsymbol{x}) = \bar{\bar{T}}_j(\boldsymbol{x},p) \quad \text{on } \Gamma^{\sigma} \tag{2.60}$$

$$\bar{\bar{u}}_j(\boldsymbol{x},p) = \bar{\bar{U}}_j(\boldsymbol{x},p) \quad \text{on } \Gamma^{u} \tag{2.61}$$

This problem could be described as a fictitious elastic problem with elastic modulus, $p\bar{\bar{G}}(p)$ and $p\bar{\bar{K}}(p)$, body force $\bar{\bar{F}}(p)$, prescribed tractions $\bar{\bar{T}}(p)$ and displacements $\bar{\bar{U}}(p)$. Notice that this problem in the Laplace domain is not time dependent anymore. All quantities are functions of the transform parameter p, and it can be solved as a linear elastic problem. If the solution to this problem is obtained, $\bar{\bar{\sigma}}_{ij}(\boldsymbol{x},p)$ and $\bar{\bar{u}}_j(\boldsymbol{x},p)$, then an inverse Laplace transform gives $\sigma_{ij}(\boldsymbol{x},t)$ and $u_j(\boldsymbol{x},t)$, which is the solution in the time domain for the linear viscoelastic problem.

The previous is know as the correspondence principle, and the main idea is to solve a linear elastic problem in which its material constants are functions written in Laplace domain multiplied by the transform parameter. Other time dependent functions are also transformed to Laplace domain. After the elastic problem is solved, the Laplace inverse of its solution gives the solution in

the time domain for the corresponding linear viscoelastic problem.

The main limitation of this approach is that the boundaries Γ^{σ} and Γ^{u} must remain constant with time, although the loads or displacements applied may be time dependent.

2.3.1 Example 1

A one dimensional bar of length L is constrained at $x = 0$, has a time dependent body force $q(t)$, and time dependent traction $P(t)$ acting at $x = L$. It has a constant area throughout its length A and the material is linear viscoelastic with $E(t)$ and $J(t)$ as its relaxation modulus and creep compliance, respectively. It is assumed that the bar is completely at rest prior to $t = 0$ and therefore no initial strains are present. Figure 2.6 shows the described problem.

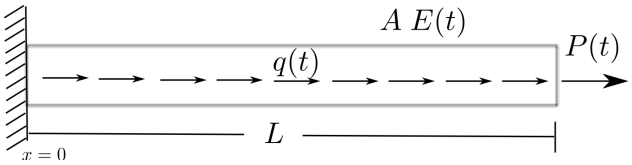

Figure 2.6: *One dimmensional bar problem. Linear viscoelastic material properties.*

First, look at the solution for the linear elastic material; the strong form of this problem is:

$$AE\frac{d^2u(x)}{dx^2} + q(x) = 0 \tag{2.62}$$

with BCs:

$$u(0) = 0 \tag{2.63}$$

$$AE\frac{du(L)}{dx} = P \tag{2.64}$$

An analytical solution can be found to this problem by integrating Equation (2.62) twice and is the following. Taking $q(x) = q$ constant in space.

$$u(x) = -\frac{q}{2AE}x^2 + \frac{P + qL}{AE}x \tag{2.65}$$

Now, the time dependent solution $u(x,t)$ for the linear elastic material is

$$u(x,t) \;=\; u^e(x,t) \;=\; -\frac{q(t)}{2\,A\,E}\,x^2 \;+\; \frac{P(t)+q(t)\,L}{A\,E}\,x \tag{2.66}$$

The Laplace transform of the previous solution is

$$\mathfrak{L}\left\{u^e(x,t)\right\} = \bar{\bar{u}}^e(x,p) \;=\; -\frac{\bar{\bar{q}}(p)}{2\,A\,E}\,x^2 \;+\; \frac{\bar{\bar{P}}(p)+\bar{\bar{q}}(t)\,L}{A\,E}\,x \tag{2.67}$$

Using the correspondence principle, **replace** the material constant by the linear viscoelastic material function transformed in Laplace domain and multiplied by the transform parameter p. Use the other time dependent quantities **transformed** to its Laplace equivalent.

$$\bar{\bar{u}}^v(x,p) \;=\; -\frac{\bar{\bar{q}}(p)}{2\,A\,p\bar{\bar{E}}(p)}\,x^2 \;+\; \frac{\bar{\bar{P}}(p)+L\,\bar{\bar{q}}(p)}{A\,p\bar{\bar{E}}(p)}\,x \tag{2.68}$$

using a similar relation as Equation (2.35) for creep and relaxation functions it yields:

$$\bar{\bar{u}}^v(x,p) \;=\; -\frac{\bar{\bar{q}}(p)p\bar{\bar{J}}(p)}{2A}\,x^2 \;+\; \frac{\bar{\bar{P}}(p)p\bar{\bar{J}}(p)+L\,\bar{\bar{q}}(p)p\bar{\bar{J}}(p)}{A}\,x \tag{2.69}$$

finally, apply the inverse of Laplace transform to previous equation using the convolution and derivative theorems similar to Equations (2.30) and (2.31).

$$u^v(x,t) \;=\; -\frac{x^2}{2A}\int_0^t J(t-\tau)\,\frac{\partial q(\tau)}{\partial\tau}\,d\tau \;+\; \frac{x}{A}\left[\int_0^t J(t-\tau)\,\frac{\partial P(\tau)}{\partial\tau}\,d\tau \;+\; L\int_0^t J(t-\tau)\,\frac{\partial q(\tau)}{\partial\tau}\,d\tau\right] \tag{2.70}$$

This is the solution for the more general case where both, body force and external traction are dependent on time. If these two quantities were constant in time the solutions would reduce to:

$$u^v(x,t) \;=\; -\frac{q}{2A}\,J(t)\,x^2 \;+\; \frac{P+Lq}{A}\,J(t)\,x \tag{2.71}$$

It is not always easy to compute the inverse of Laplace transform analytically, therefore the use

of a numerical method it is in general necessary. For this simple problem a comparison between analytical and numerical is presented in Figures 2.7 and 2.8. A problem with a bar of length $L = 10$ and area $A = 1$ is solved. Only the solution at $x = 10$ is plotted. A numerical inversion of the Laplace transform can be performed with various methods [66]. One in particular used in this problem is the Fourier series method. More details on Laplace numerical inversion methods can be found in Section 3.4.

The relaxation modulus for this problem $E(t)$ is taken as,

$$E(t) \;=\; 1{,}000 \;+\; 3{,}000\, e^{-\frac{t}{2}} \tag{2.72}$$

For the results shown in Figure 2.7, the body force $q(t) = 0.1$ and traction $P(t) = 10$ are both constant in time. On the other hand, for Figure 2.8 the body force is eliminated while the traction $P(t) = 0.1t$ is time dependent.

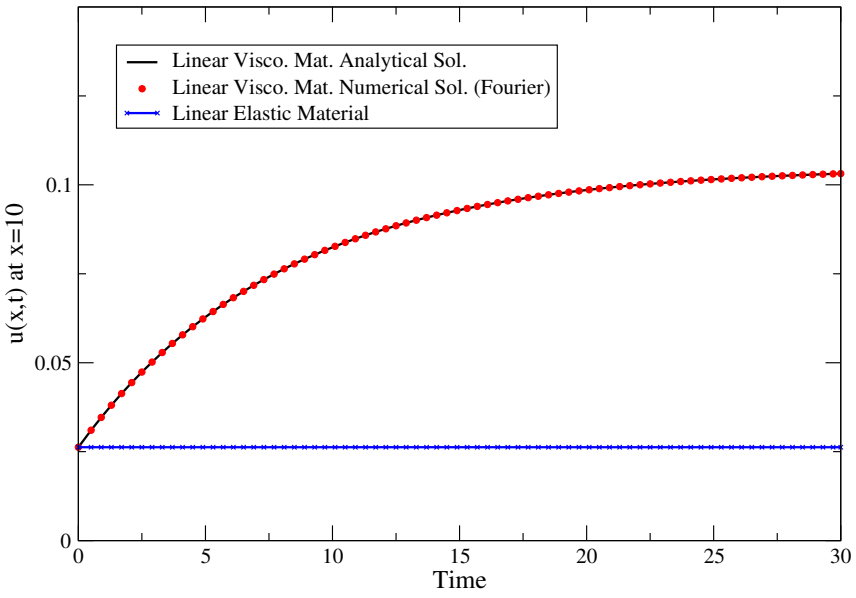

Figure 2.7: *1D Bar problem solution for constant body force and traction.*

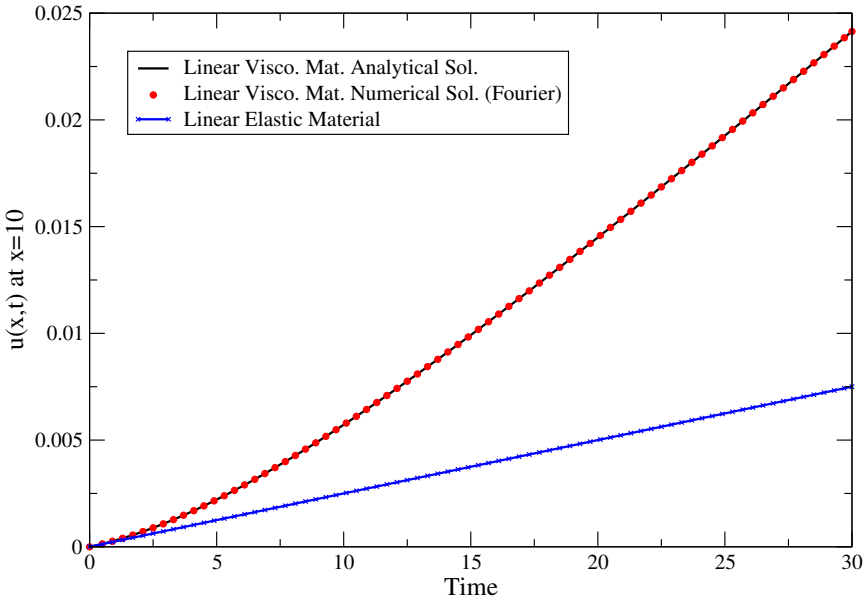

Figure 2.8: *1D Bar problem solution for time dependent traction.*

2.3.2 Example 2

Similar to previous example, consider a one dimensional bar of length L constrained at $x = 0$ and with a time dependent body force $q(t)$. Instead of a traction force a displacement $u(L,t) = u_L(t)$ BCs is applied at $x = L$. It has a constant area throughout its length A and the material is linear viscoelastic with $E(t)$ and $J(t)$ as its relaxation modulus and creep compliance, respectively. It is assumed that the bar is completely at rest prior to $t = 0$ and therefore no initial strains are present. Figure 2.9 shows the described problem.

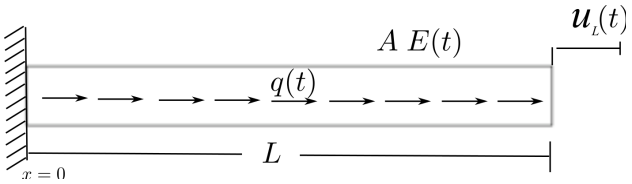

Figure 2.9: *One dimmensional bar problem. Linear viscoelastic material properties.*

The strong form of reference elastic problem is:

$$AE\frac{d^2u(x)}{dx^2} + q(x) = 0 \tag{2.73}$$

with BCs:

$$u(0) = 0 \tag{2.74}$$

$$u(L) = u_L \tag{2.75}$$

An analytical solution can be found to this problem by integrating Equation (2.73) twice and is the following. Taking $q(x) = q$ constant in space.

$$u(x) = -\frac{q\,x}{2\,A\,E}(x-L) + \frac{u_L}{L}x \tag{2.76}$$

Because of the nature of the problem, it is important to look at stresses solution.

$$\sigma_x(x) \;=\; -\frac{q}{A}\,(x-\frac{L}{2}) \;+\; \frac{u_L E}{L} \tag{2.77}$$

Now, the time dependent solution $u^e(x,t)$ and $\sigma^e(x,t)$ for the linear elastic material are:

$$u^e(x,t) \;=\; -\frac{q(t)\,x}{2A\,E}\,(x-L) \;+\; \frac{u_L(t)}{L}\,x \tag{2.78}$$

$$\sigma^e_x(x,t) \;=\; -\frac{q(t)}{A}\,(x-\frac{L}{2}) \;+\; \frac{u_L(t)\,E}{L} \tag{2.79}$$

The Laplace transform of the previous solutions are

$$\mathfrak{L}\left\{ u^e(x,t) \right\} = \bar{\bar{u}}^e(x,p) \;=\; -\frac{\bar{\bar{q}}(p)\,x}{2A\,E}\,(x-L) \;+\; \frac{\bar{\bar{u}}_L(p)}{L}\,x \tag{2.80}$$

$$\mathfrak{L}\left\{ \sigma^e_x(x,t) \right\} = \bar{\bar{\sigma}}^e(x,p) \;=\; -\frac{\bar{\bar{q}}(p)}{A}\,(x-\frac{L}{2}) \;+\; \frac{\bar{\bar{u}}_L(p)\,E}{L} \tag{2.81}$$

Then, using the correspondence principle, **replace** the material constant by the linear viscoelastic material function transformed in Laplace domain and multiplied by the transform parameter p. Use the other time dependent quantities **transformed** to its Laplace equivalent.

$$\bar{\bar{u}}^v(x,p) \;=\; -\frac{\bar{\bar{q}}(p)\,x}{2A\,p\bar{\bar{E}}(p)}\,(x-L) \;+\; \frac{\bar{\bar{u}}_L(p)}{L}\,x \tag{2.82}$$

$$\bar{\bar{\sigma}}^v_x(x,p) \;=\; -\frac{\bar{\bar{q}}(p)}{A}\,(x-\frac{L}{2}) \;+\; \frac{\bar{\bar{u}}_L(p)\,p\bar{\bar{E}}(p)}{L} \tag{2.83}$$

using a similar relation as Equation (2.35) for creep and relaxation functions it yields:

$$\bar{\bar{u}}^v(x,p) \;=\; -\frac{\bar{\bar{q}}(p)p\bar{\bar{J}}(p)\,x}{2A}\,(x-L) \;+\; \frac{\bar{\bar{u}}_L(p)}{L}\,x \tag{2.84}$$

finally, apply the inverse of Laplace transform to previous equation using the convolution and

derivative theorems similar to Equations (2.30) and (2.31).

$$u^v(x,t) \;=\; -\frac{x(x-L)}{2A}\int_0^t J(t-\tau)\,\frac{\partial q(\tau)}{\partial \tau}\,d\tau \;+\; \frac{u_L(t)}{L}\,x \tag{2.85}$$

$$\sigma_x^v(x,t) \;=\; -\frac{q(t)\,(x-\frac{L}{2})}{A} \;+\; \frac{1}{L}\int_0^t E(t-\tau)\,\frac{\partial u_L(\tau)}{\partial \tau}\,d\tau \tag{2.86}$$

This is the solution for the more general case where both, body force and imposed displacement are time dependent. If these two quantities were constant in time the solutions would reduce to:

$$u^v(x,t) \;=\; -\frac{q\,x}{2A}\,J(t)\,(x-L) \;+\; \frac{u_L}{L}\,x \tag{2.87}$$

$$\sigma_x^v(x,t) \;=\; -\frac{q}{A}(x-\frac{L}{2}) \;+\; \frac{u_L}{L}\,E(t) \tag{2.88}$$

A numerical inversion is done using the Fourier series method using values of $b\,t = 4.5$ and $n = 101$. The relaxation modulus for this problem $E(t)$ is taken as

$$E(t) \;=\; 1{,}000 \;+\; 3{,}000\,e^{-\frac{t}{2}} \tag{2.89}$$

For the results shown in Figure 2.10, the body force $q(t) = 0.1$ and the imposed displacement $u_L(t) = 0.025$ are both constant in time. On the other hand, for Figure 2.11 the body force is eliminated while the imposed displacement $u_L(t) = 0.0025t$ is time dependent.

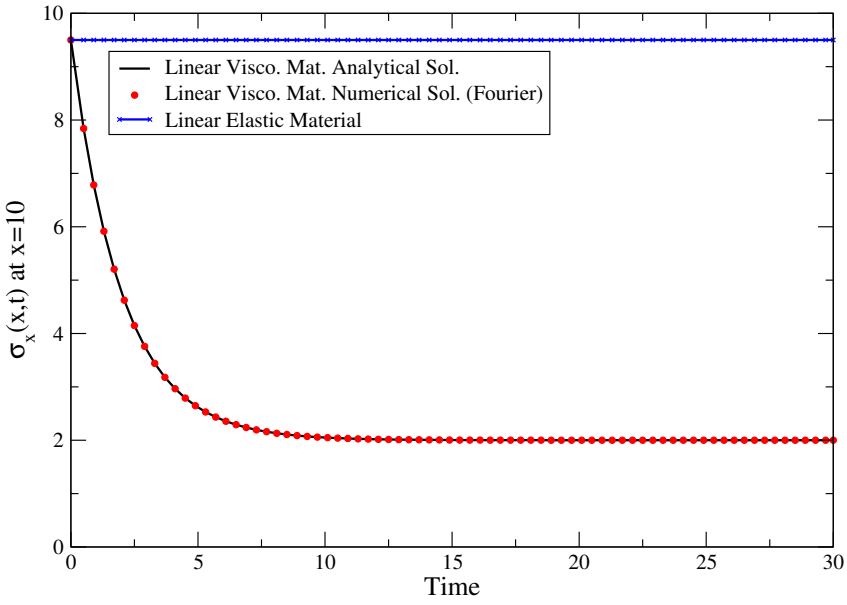

Figure 2.10: *1D Bar problem solution for constant body force and imposed displacement.*

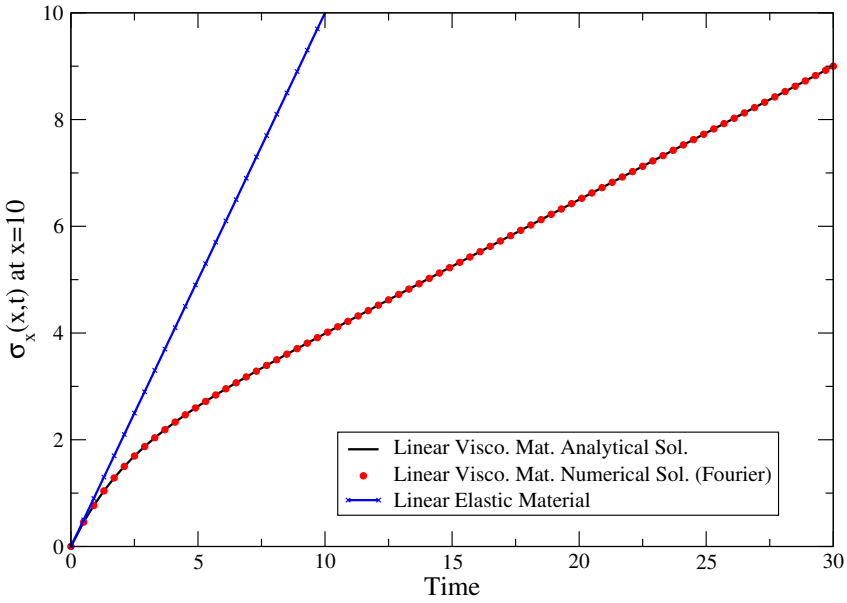

Figure 2.11: *1D Bar problem solution for time dependent imposed displacement.*

Transform Dirichlet to Neumann BCs

In this section, the previous problem is repeated with the objective to obtain the same solutions but instead of imposing a displacement at $x = 10$ a time dependent traction is applied. The difficulty is to find a compatible traction that would not alter in any way previous problem solutions. To find the traction force to be applied for the elastic problem lets equal Equations (2.65) and (2.76).

$$-\frac{q}{2AE}x^2 + \frac{P^e + qL}{AE}x = -\frac{qx}{2AE}(x-L) + \frac{u_L}{L}x \tag{2.90}$$

Solving for P^e we get:

$$P^e = -\frac{qL}{2} + \frac{u_L AE}{L} \tag{2.91}$$

Using the time dependent quantities and applying the correspondence principle the viscoelastic load in Laplace domain $\bar{\bar{P}}^v$ is found.

$$\bar{\bar{P}}^v(p) = -\frac{\bar{\bar{q}}(p)L}{2} + \frac{\bar{\bar{u_L}}(p)Ap\bar{\bar{E}}(p)}{L} \tag{2.92}$$

Finally, applying the inverse of Laplace transform.

$$P^v(t) = -\frac{q(t)L}{2} + \frac{A}{L}\int_0^t E(t-\tau)\frac{\partial u_L(\tau)}{\partial \tau}\,d\tau \tag{2.93}$$

This is the solution for the more general case where both, body force and imposed displacement are time dependent. If these two quantities were constant in time the solutions would reduce to:

$$P^v(t) = -\frac{q(t)L}{2} + \frac{u_L A}{L}E(t) \tag{2.94}$$

This viscoelastic load can be applied at the end of the bar instead of the imposed displacement. In order to verify if this is correct, the previous problem is repeated and the viscoelastic load P^v is applied. Figure 2.12 shows the results for the case where the body force $q(t) = 0.1$ and the imposed displacement $u_L(t) = 0.025$ are both constant in time. Note that this figure shows the

displacements at $x = 5$; at $x = 10$ its unnecessary to check because is constant in time and equal to 0.025. Figure 2.13 shows the comparison of stresses at $x = 10$.

The same verification is done for time dependent imposed displacement $u_L(t) = 0.0025t$ and the solutions can be seen in Figures 2.14 and 2.15.

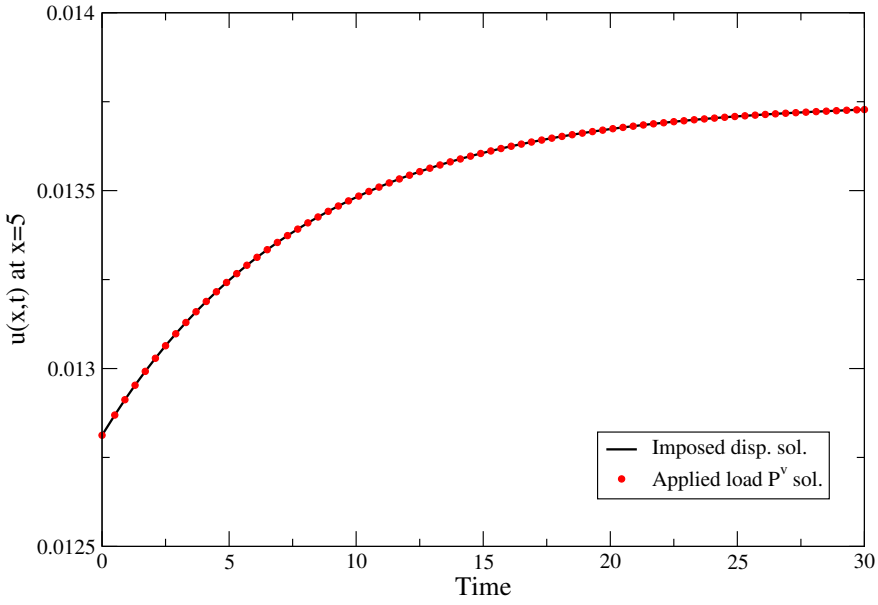

Figure 2.12: *1D Bar problem solution for constant body force and imposed displacement compared to transformed BCs P^v.*

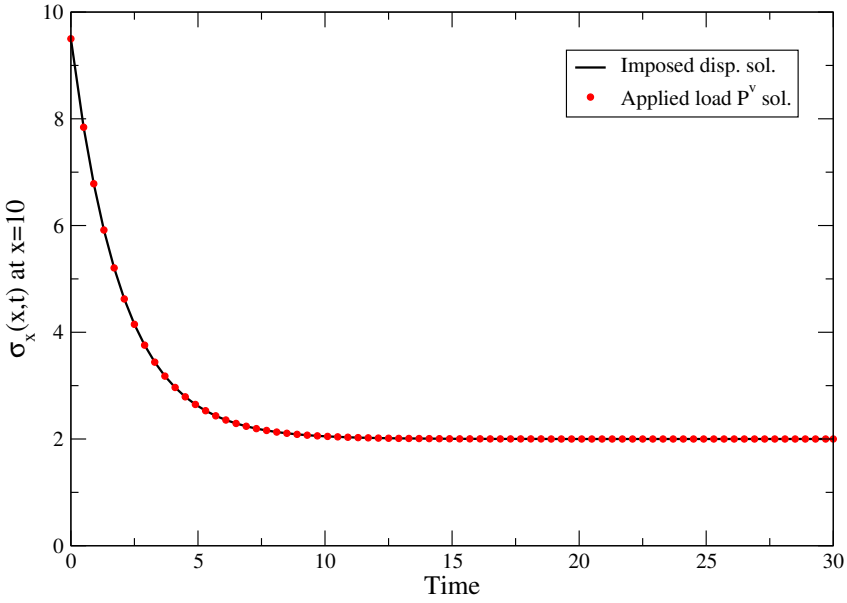

Figure 2.13: *1D Bar problem solution for constant body force and imposed displacement compared to transformed BCs P^v.*

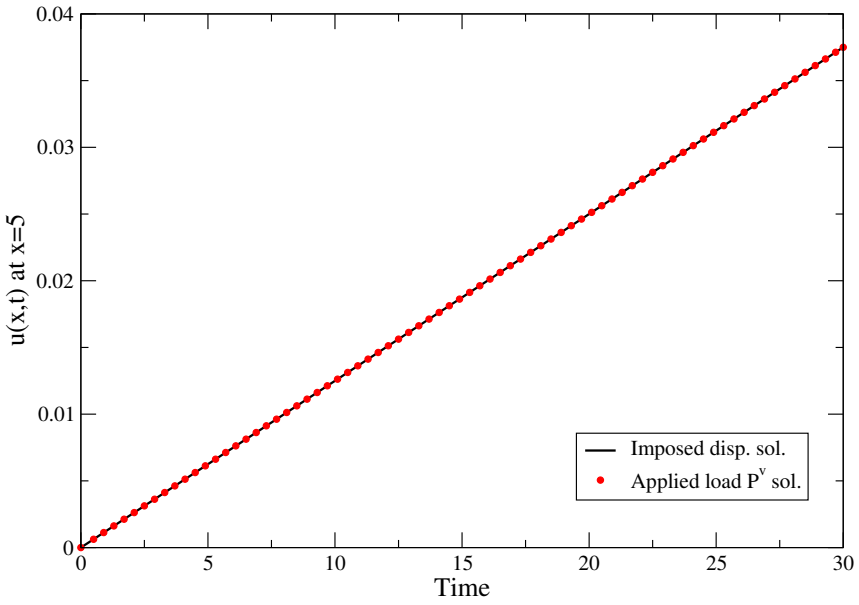

Figure 2.14: *1D Bar problem solution for time dependent imposed displacement compared to transformed BCs P^v.*

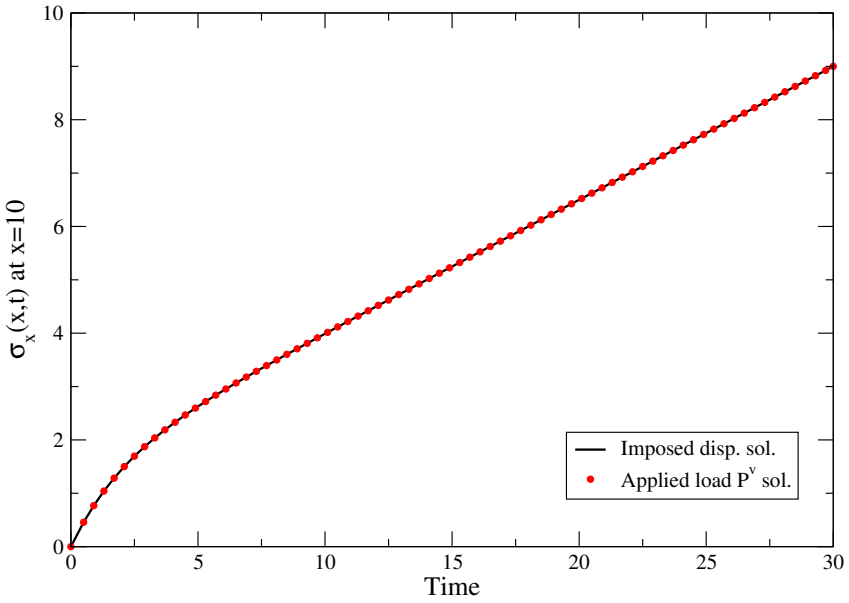

Figure 2.15: *1D Bar problem solution for time dependent imposed displacement compared to transformed BCs P^v.*

2.4 Three Dimensional Implementation in ISET

In this section a numerical implementation for linear viscoelasticity is described. The constitutive models presented in previous sections serve as a base for this implementation. The implementation is performed in ISET (GFEM code) which is a numerical research code use by our research group. There is an extensive literature on the implementation of linear viscoelastic constitutive equations in the FEM. A good literature review by Zocher et al. can be found in [186]. Because of its simplicity and good performance, the chosen algorithm to implement is the one used by Abaqus [2], which is similar to Hinterhoelzl and Schapery [68]. The notation used in this formulation is similar to the notation presented in the Abaqus manual. It is assumed that the shear and the volumetric behaviors are independent in multi-axial stress state. Also, that the viscoelastic material is defined by a Prony series expansion as explained in Section 2.1.

The boundary value problem to be numerically solved here is the same as the one given in Section 2.3. The equilibrium equations, the stress strain relations and the strain displacement relations are given by Equations(2.51)- (2.54). The boundary conditions are given by Equations (2.55) and (2.56).

To find the weak formulation of the problem described above, let the set of kinematically admissible displacement fields be

$$\tilde{H}^1(\Omega) = \left\{ u_j(\boldsymbol{x},t) \mid u_j(\boldsymbol{x},t) \in H^1(\Omega),\ u_j(\boldsymbol{x},t) = U_j(\boldsymbol{x},t) \quad \text{on } \Gamma^u \right\}$$

where H^1 is a Hilbert space.

Let the space of virtual kinematically admissible displacement fields be

$$\overset{o}{H}{}^1(\Omega) = \left\{ v_j(\boldsymbol{x},t) \mid v_j(\boldsymbol{x},t) \in H^1(\Omega),\ v_j(\boldsymbol{x},t) = 0 \quad \text{on } \Gamma^u \right\}$$

The weak form of the equilibrium equations can be stated as follows.

Find $\boldsymbol{u}(\boldsymbol{x},t) \in \tilde{H}^1(\Omega)$ such that

$$B\Big(\boldsymbol{u}(\boldsymbol{x},t),\boldsymbol{v}(\boldsymbol{x},t)\Big) = L\Big(\boldsymbol{v}(\boldsymbol{x},t)\Big) \;\forall\; \boldsymbol{v}(\boldsymbol{x},t) \in \overset{o}{H}{}^1 \tag{2.95}$$

where $B(\cdot,\cdot)$ and $L(\cdot)$ are the bilinear and linear forms, respectively, and are given by

$$\begin{aligned} B\Big(\boldsymbol{u}(\boldsymbol{x},t),\boldsymbol{v}(\boldsymbol{x},t)\Big) &= \int_\Omega \varepsilon_{ij}\Big(\boldsymbol{v}(\boldsymbol{x},t)\Big)\,\sigma_{ij}\Big(\boldsymbol{u}(\boldsymbol{x},t)\Big)\,d\Omega \\ L\Big(\boldsymbol{v}(\boldsymbol{x},t)\Big) &= \int_\Omega \boldsymbol{v}(\boldsymbol{x},t)\,F_j(\boldsymbol{x},t)\,d\Omega + \int_{\Gamma^\sigma} v_j(\boldsymbol{x},t)\,T_j(\boldsymbol{x},t)\,d\Gamma \end{aligned} \tag{2.96}$$

In tensor notation

$$\int_\Omega \boldsymbol{\sigma}\Big(\boldsymbol{u}(\boldsymbol{x},t)\Big) : \boldsymbol{\varepsilon}\Big(\boldsymbol{v}(\boldsymbol{x},t)\Big)\,d\Omega = \int_\Omega \boldsymbol{v}(\boldsymbol{x},t)\cdot\boldsymbol{F}(\boldsymbol{x},t)\,d\Omega + \int_{\Gamma^\sigma} \boldsymbol{v}(\boldsymbol{x},t)\cdot\boldsymbol{T}(\boldsymbol{x},t)\,d\Gamma \tag{2.97}$$

Consider a finite element approximation of $\boldsymbol{u}(\boldsymbol{x},t)$ given by

$$\boldsymbol{u}(\boldsymbol{x},t) \approx \boldsymbol{u}^h(\boldsymbol{x},t) = \sum_{\alpha=1}^{N} \varphi_\alpha(\boldsymbol{x})\boldsymbol{u}_\alpha^h(\boldsymbol{x},t) \tag{2.98}$$

where $\varphi_\alpha(\boldsymbol{x})$ are the FEM shape functions and $\alpha = 1,...,N$, in a FEM mesh with N number of nodes. With no restrictions these shape functions can be replaced by the GFEM shape functions which will be introduce in Section 4.2.1.

Using, $\boldsymbol{\varepsilon}\Big(\boldsymbol{v}(\boldsymbol{x},t)\Big) \approx \sum_{\alpha=1}^{N} \boldsymbol{B}_\alpha(\boldsymbol{x})\boldsymbol{u}_\alpha^h(\boldsymbol{x},t)$, with $\boldsymbol{B}_\alpha(\boldsymbol{x}) = \nabla\varphi_\alpha(\boldsymbol{x})$. in Equation (2.97) gives,

$$\int_\Omega \Big(\boldsymbol{B}_\alpha(\boldsymbol{x})\boldsymbol{u}_\alpha^h(\boldsymbol{x},t)\Big)^T \boldsymbol{\sigma}\Big(\boldsymbol{u}^h(\boldsymbol{x},t)\Big)\,d\Omega = \int_\Omega \Big(\varphi_\alpha(\boldsymbol{x})\boldsymbol{u}_\alpha^h(\boldsymbol{x},t)\Big)\boldsymbol{F}(\boldsymbol{x},t)\,d\Omega + \int_{\Gamma^\sigma} \Big(\varphi_\alpha(\boldsymbol{x})\boldsymbol{u}_\alpha^h(\boldsymbol{x},t)\Big)\boldsymbol{T}(\boldsymbol{x},t)\,d\Gamma$$

For simplicity consider no body force. Let $\boldsymbol{F}^{ext} = \int_{\Gamma^\sigma} \varphi_\alpha(\boldsymbol{x})\boldsymbol{T}(\boldsymbol{x},t)\,d\Gamma$ a vector of external forces and Let $\boldsymbol{F}^{int} = \int_\Omega \boldsymbol{B}_\alpha(\boldsymbol{x})^T\,\boldsymbol{\sigma}\Big(\boldsymbol{u}^h(\boldsymbol{x},t)\Big)\,d\Omega$ a vector of internal forces.

This problem has a nonlinearity in the material, therefore an incremental method like Newton-

Raphson is used to solve it. Let $\boldsymbol{R}$ be the residual defined as

$$\boldsymbol{F}^{int} - \boldsymbol{F}^{ext} = \boldsymbol{R} \tag{2.99}$$

Assume that we know the solution at time t^k. We apply a load increment and need to compute the solution for $t^{k+1} = t^k + \Delta t$. Applying Newton-Raphson for i^{th} iteration

$$\boldsymbol{u}^h_{i+1}(\boldsymbol{x}, t^{k+1}) = \boldsymbol{u}^h_i(\boldsymbol{x}, t^{k+1}) - \left[\frac{\partial \boldsymbol{R}\left(\boldsymbol{u}^h_i(\boldsymbol{x}, t^{k+1})\right)}{\partial \boldsymbol{u}}\right]^{-1} \boldsymbol{R}\left(\boldsymbol{u}^h_i(\boldsymbol{x}, t^{k+1})\right) \tag{2.100}$$

Note that, $\Delta \boldsymbol{u}^h_{i+1} = \boldsymbol{u}^h_{i+1}(\boldsymbol{x}, t^{k+1}) - \boldsymbol{u}^h_i(\boldsymbol{x}, t^{k+1})$ and $\left[\frac{\partial \boldsymbol{R}\left(\boldsymbol{u}^h_i(\boldsymbol{x}, t^{k+1})\right)}{\partial \boldsymbol{u}}\right]^{-1}$ is know as a tangent stiffness matrix $\boldsymbol{K}^{tan}\left(\boldsymbol{u}^h_i(\boldsymbol{x}, t^{k+1})\right)$.

The problem to solve becomes

$$\boldsymbol{K}^{tan}\left(\boldsymbol{u}^h_i(\boldsymbol{x}, t^{k+1})\right) \Delta \boldsymbol{u}^h_{i+1} = -\boldsymbol{R}\left(\boldsymbol{u}^h_i(\boldsymbol{x}, t^{k+1})\right) \tag{2.101}$$

The tangent stiffness matrix can be difficult to evaluated for complex constitutive laws. In this problem, let us use linearization to compute the contribution from element (e) associated with nodes a and b as follows

$$\boldsymbol{K}^{tan(e)}_{ab} = \int_{\Omega^{(e)}} \boldsymbol{B}^T_a(\boldsymbol{x})\, G^{tan}(\Delta t)\, \boldsymbol{B}_b(\boldsymbol{x})\, d\Omega^{(e)} \tag{2.102}$$

where $G^{tan}(\Delta t)$ is called tangent modulus and its computation will be discussed later in this section. The Residual is computed with Equation (2.99). There, most of the quantities can be computed directly. Stresses, used for F^{int}, on the other hand is not as straightforward. For simplicity and following the idea from previous sections, separate the behavior into deviatoric and volumetric parts.

From now on we will concentrate in the computation of the deviatoric stress tensor. The equa-

tions for the volumetric terms can be derived in an analogous way. Using Equation (2.52) in terms of Prony series we get

$$\boldsymbol{S}(\boldsymbol{x},t) = 2\int_0^t \left(G_\infty + \sum_{m=1}^{M} G_m\, e^{\frac{t'-t}{\rho_m}}\right) \frac{\partial \boldsymbol{E}(\boldsymbol{x},t')}{\partial t'}\, dt'$$

where G_∞ is the long-time shear modulus, G_m is the regression coefficient , ρ_m is the relaxation time and M is number of terms in the Prony series.

The instantaneous shear modulus is given by $G_0 = G_\infty + \sum_{m=1}^{M} G_m$ and call $\alpha_m = \frac{G_m}{G_0}$ a relative modulus of term m. Previous equation becomes

$$\boldsymbol{S}(\boldsymbol{x},t) = 2\,G_0\,\boldsymbol{E}(\boldsymbol{x},t) \;-\; 2\sum_{m=1}^{M} \alpha_m \int_0^t \left(1 - e^{\frac{t'-t}{\rho_m}}\right) \frac{\partial \boldsymbol{E}(\boldsymbol{x},t')}{\partial t'}\, dt' \tag{2.103}$$

The integral part of Equation (2.103) is the viscous strain in each term of the series. Name it E_m.

$$\boldsymbol{S}(\boldsymbol{x},t) = 2\,G_0\,\boldsymbol{E}(\boldsymbol{x},t) \;-\; 2\sum_{m=1}^{M} \alpha_m\, \boldsymbol{E}_m(\boldsymbol{x},t) \tag{2.104}$$

and separating E_m in two parts we get

$$\boldsymbol{E}_m(\boldsymbol{x},t^{k+1}) = \int_0^{t^k} \left(1 - e^{\frac{t'-t^{k+1}}{\rho_m}}\right) \frac{\partial \boldsymbol{E}(\boldsymbol{x},t')}{\partial t'}\, dt' \;+\; \int_{t^k}^{t^{k+1}} \left(1 - e^{\frac{t'-t^{k+1}}{\rho_m}}\right) \frac{\partial \boldsymbol{E}(\boldsymbol{x},t')}{\partial t'}\, dt'$$

Observe that $1 - e^{\frac{t'-t^{k+1}}{\rho_m}} = 1 - e^{\frac{-\Delta t}{\rho_m}} + e^{\frac{-\Delta t}{\rho_m}}\,(1 - e^{\frac{t'-t^k}{\rho_m}})$ and also for a finite element analysis this equation must be integrated over a finite increment of time. Therefore, assume that during the small increment Δt, from t^k until t^{k+1}, $\boldsymbol{E}$ varies linearly with t.

$$\begin{aligned}\boldsymbol{E}_m(\boldsymbol{x},t^{k+1}) = \left(1 - e^{\frac{-\Delta t}{\rho_m}}\right) \int_0^{t^k} \frac{\partial \boldsymbol{E}(\boldsymbol{x},t')}{\partial t'}\, dt' \;+\; e^{\frac{-\Delta t}{\rho_m}} \int_0^{t^k} \left(1 - e^{\frac{t'-t^k}{\rho_m}}\right) \frac{\partial \boldsymbol{E}(\boldsymbol{x},t')}{\partial t'}\, dt' \\ + \frac{\Delta \boldsymbol{E}(\boldsymbol{x},t^{k+1})}{\Delta t} \int_{t^k}^{t^{k+1}} \left(1 - e^{\frac{t'-t^{k+1}}{\rho_m}}\right) dt'\end{aligned}$$

The first and last integrals in this expression can be evaluated directly and the second expression

corresponds to the viscous strain $\boldsymbol{E}_m$ for time t^k. Rewriting previous equation we obtain

$$\boldsymbol{E}_m(\boldsymbol{x},t^k)+\Delta\boldsymbol{E}_m(\boldsymbol{x},t^{k+1}) = \left(1-e^{\frac{-\Delta t}{\rho_m}}\right)\boldsymbol{E}(\boldsymbol{x},t^k) \;+\; e^{\frac{-\Delta t}{\rho_m}}\,\boldsymbol{E}_m(\boldsymbol{x},t^k) + \left(\Delta t-\rho_m\,(1-e^{\frac{-\Delta t}{\rho_m}})\right)\frac{\Delta\boldsymbol{E}(\boldsymbol{x},t^{k+1})}{\Delta t}$$

Then the increment in the viscous strain for the m^{th} term at time step t^{k+1} and iteration i

$$\Delta\boldsymbol{E}_{i(m)}(\boldsymbol{x},t^{k+1}) = \left(1-e^{\frac{-\Delta t}{\rho_m}}\right)\left(\boldsymbol{E}(\boldsymbol{x},t^k)-\boldsymbol{E}_m(\boldsymbol{x},t^k)\right) \;+\; \left(\Delta t-\rho_m\,(1-e^{\frac{-\Delta t}{\rho_m}})\right)\frac{\Delta\boldsymbol{E}_i(\boldsymbol{x},t^{k+1})}{\Delta t} \tag{2.105}$$

The first term corresponds to the history since $\boldsymbol{E}(\boldsymbol{x},t^k)$ and $\boldsymbol{E}_m(\boldsymbol{x},t^k)$ are the converged, total strain and viscous strain, at the previous time step. The second term, on the other hand, is the increment at current time step t^{k+1} for current iteration i and previous iteration, with $\Delta\boldsymbol{E}_i(\boldsymbol{x},t^{k+1})$ given by

$$\Delta\boldsymbol{E}_i(\boldsymbol{x},t^{k+1}) = \boldsymbol{E}_i(\boldsymbol{x},t^{k+1}) \;-\; \boldsymbol{E}_{i-1}(\boldsymbol{x},t^{k+1}) \tag{2.106}$$

Note that this recursive Equation (2.105) requires knowledge of solution variables from a previously converged time step and and previous iteration.

The stress for time t^{k+1} and iteration i can then be computed using a deviatoric stress increment

$$\boldsymbol{S}_i(\boldsymbol{x},t^{k+1}) \;=\; \boldsymbol{S}(\boldsymbol{x},t^k) \;+\; \Delta\boldsymbol{S}_i(\boldsymbol{x},t^{k+1}) \tag{2.107}$$

where $\boldsymbol{S}(\boldsymbol{x},t^k)$ is the converged deviatoric stress from previous time step and $\Delta\boldsymbol{S}_i(\boldsymbol{x},t^{k+1})$ is computed similar to Equation (2.104) and has the form

$$\Delta\boldsymbol{S}_i(\boldsymbol{x},t^{k+1}) = 2\,G_0\,\Delta\boldsymbol{E}_i(\boldsymbol{x},t^{k+1}) \;-\; 2\,\sum_{m=1}^{M}\alpha_m\,\Delta\boldsymbol{E}_{i(m)}(\boldsymbol{x},t^{k+1}) \tag{2.108}$$

By differentiating the previous equation with respect to the deviatoric strain increment $\Delta\boldsymbol{E}$, a tan-

gent modulus for a nonlinear formulation and Equation (2.102) is obtained

$$G^{tan}(\Delta t) = G_0 \left[1 - \sum_{m=1}^{M} \alpha_m \left(\Delta t - \rho_m \left(1 - e^{\frac{-\Delta t}{\rho_m}}\right)\right)\right] \tag{2.109}$$

Note that the tangent modulus is only dependent on the time increment, therefore if the increment is fixed, Equations (2.109) gives a constant and (2.102) is a time independent matrix. That means that the tangent matrix only needs to be computed once for all the simulation if the time increment does not change. This is very convenient in large FEM examples because most of the computational time is spend at the assembly and factorization of the tangent stiffness.

At this point we have derived all the necessary equations to solve this nonlinear problem. The volumetric quantities are similar: Substitute $2G_0$, $2G_m$, S_{ij}, E_{ij}, E_m with K_0, K_m, σ, ε, ε_m, respectively.

Temperature effects can be introduce by using a reduced time ξ in previous derivation instead of the real time t, without altering any of the equations. This is possible because of the time temperature superposition principle (TTSP) [55].

$$\xi = \int_0^t \frac{dt'}{a_T(T(t'))} \tag{2.110}$$

where a_T is shift factor depending on temperature $T(t')$. This shift factor is usually obtained from experiments. A commonly used shift function is the William-Landell-Ferry (WLF) for temperature regime other than glassy and rubbery.

$$-\log(a_T) = \frac{C_1(T - T_0)}{C_2 + (T - T_0)} \tag{2.111}$$

where T is the temperature of interest and T_0 is the reference temperature. Coefficients C_1 and C_2 are obtained from experimental data.

Finally, the numerical algorithm to solve this problem with fixed time increment follows these steps:

- 1) Choose a time increment and compute the tangent stiffness matrix with Equation (2.102).
- 2) Time loop, next time step (t^k)
- 3) Compute $\boldsymbol{F}^{ext}$, and residual $\boldsymbol{R}$ with Equation (2.99). Note that if this is iteration $i = 0$ the residual is equal to the external force.
- 4) Iteration loop, next iteration i
- 5) Update the solution computing the increment $\Delta \boldsymbol{u}^{\boldsymbol{h}}$ with Equation (2.101). Also compute strains with $\boldsymbol{B}\boldsymbol{u}^h$, strain increment with (2.106), viscous strain increment for m^{th} term with (2.105) and stress increment with (2.108).
- 6) Update stresses with (2.107) and compute residual with (2.99)
- 7) If residual is greater than tolerance go to 4 otherwise continue to 8.
- 8) Save converged quantities such as strain and stress. If time is not the end time go to 2 otherwise end.

Note that since the material is linear, use of the consistently derived tangent modulus terms leads to convergence in one iteration.

2.4.1 Example

In order to verify the implementation described in Section 2.4, a simple example is created and solved using the commercial software Abaqus and our research code ISET. A cantilever beam is fixed at one end while the other is subject to a load $F(t) = \lambda(t)\,F$. Four different types of loads are studied.

Constant

$$\lambda(t) = 1.0$$

Ramp

$$\lambda(t) = \frac{t}{t_{peak}}$$

Sinusoidal

$$\lambda(t) = \frac{1 - \cos\left(\frac{2\pi t}{t_{peak}}\right)}{2}$$

Impulse

$$\begin{aligned} \lambda(t) &= \frac{1 - \cos\left(\frac{2\pi t}{t_{peak}}\right)}{2} \quad for\ t < 2t_{peak} \\ \lambda(t) &= 0 \quad otherwise \end{aligned}$$

For all these load types, $F = 6.6\,N$ and t_{peak} refers to the time when the maximum load is applied. Figure 2.16 illustrates the problem dimensions (h= $1cm$), finite element mesh and a red circle shows the location where the displacements are extracted for comparison. The temperature considered for this part of the simulation is 0^o Celsius (C).

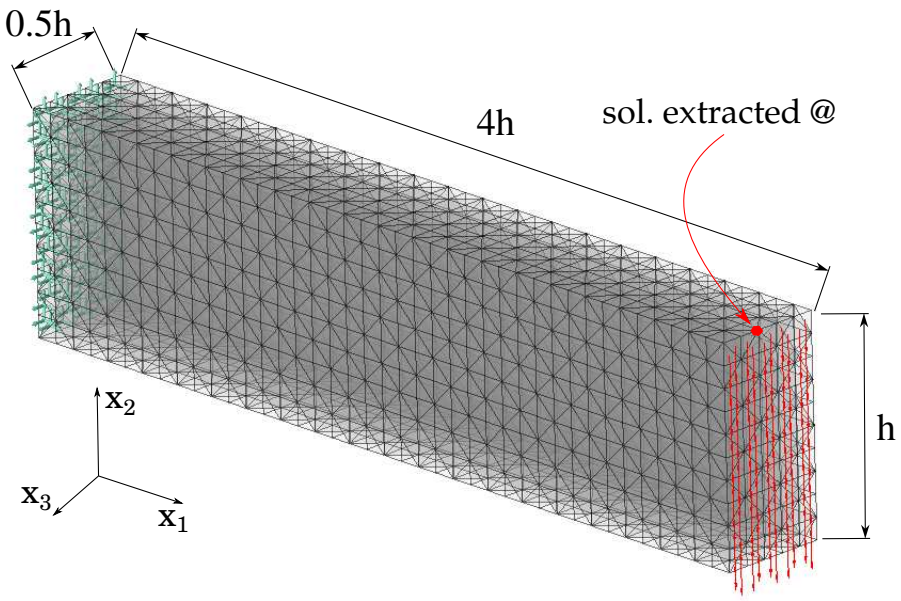

Figure 2.16: *Three dimensional cantilever beam example.*

The mathematical representation of the viscoelastic material response is described by the Prony

Table 2.1: *Mathematical representation of the viscoelastic material (Prony series).*

m	G_m (MPa)	K_m (MPa)	ρ_m (s)
1	89,604	194,142	1.01e-10
2	45,524	98,635	3.26e-05
3	39,161	76,183	0.00115
4	26,313	57,011	0.0429
5	23,658	51,260	1.65
6	7,940	17,204	493
$G_0 = 232,859$ and $K_0 = 504,527$			

series shown in Table 2.1. The same finite element mesh is used in both softwares (Abaqus and ISET). It consist of 10,000 linear tetrahedrons of four nodes and 8,118 degrees of freedom (dofs). The simulation time is 20 seconds with a time increment $\Delta t = 0.02$.

The results for the four different load types are presented in Figure 2.17.

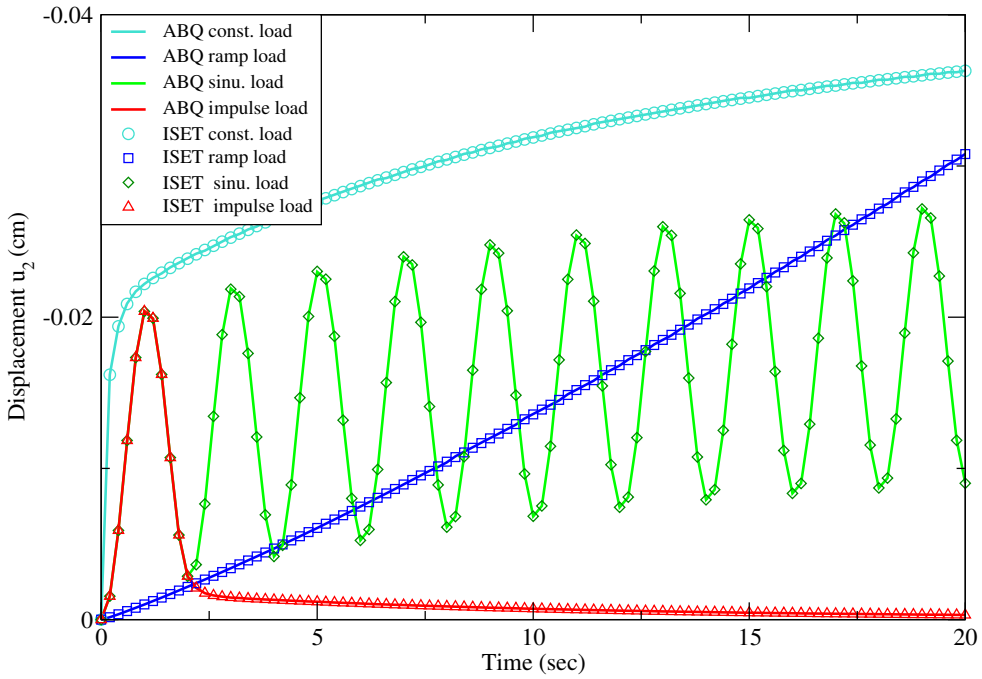

Figure 2.17: *Displacement results u_2 for 4 different type of loads in $0^o\,C$.*

In a second verification test, using only the constant load type, different temperatures are simulated. Figure 2.18 shows the results for $-10^o\,C$, $0^o\,C$, $10^o\,C$, and $20^o\,C$. Again, ISET results are in good accordance with Abaqus results.

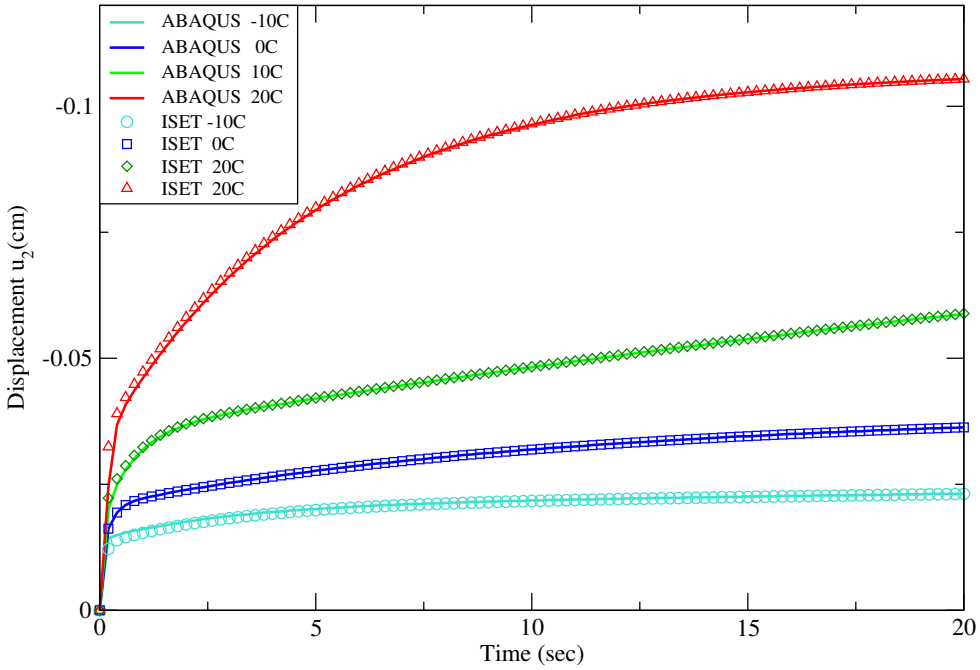

Figure 2.18: *Displacement results u_2 for different temperatures.*

Finally, in order to check convergence of results and see a comparison between FEM and GFEM, a linear, quadratic and cubic approximation at $0^o\,C$ is performed. To perform a quadratic approximation in Abaqus, just like any other FEM software, the original FE mesh needs to be modified. All the four-node tetrahedrons are converted to ten-node tetrahedrons. On the other hand, in ISET or any other GFEM code, the quadratic approximation can be achieved with polynomial enrichments. This is very convenient, because no modifications are needed in the FE model. An overview of GFEM and types of enrichments are given in Chapter 4.

The cubic approximation is also quickly performed in ISET by increasing the degree of the polynomial enrichment. The results of the cubic approximation give exactly the same results as the quadratic, therefore there is no need to go through the process of creating another FE mesh with cubic elements to run the example in Abaqus. Figure 2.19 shows the results of this study. The deformed configuration and VonMisses stress distribution for Abaqus and ISET, quadratic approximation, are shown in Figures 2.20(a) and 2.20(b), respectively. Note that Abaqus and ISET results are the same.

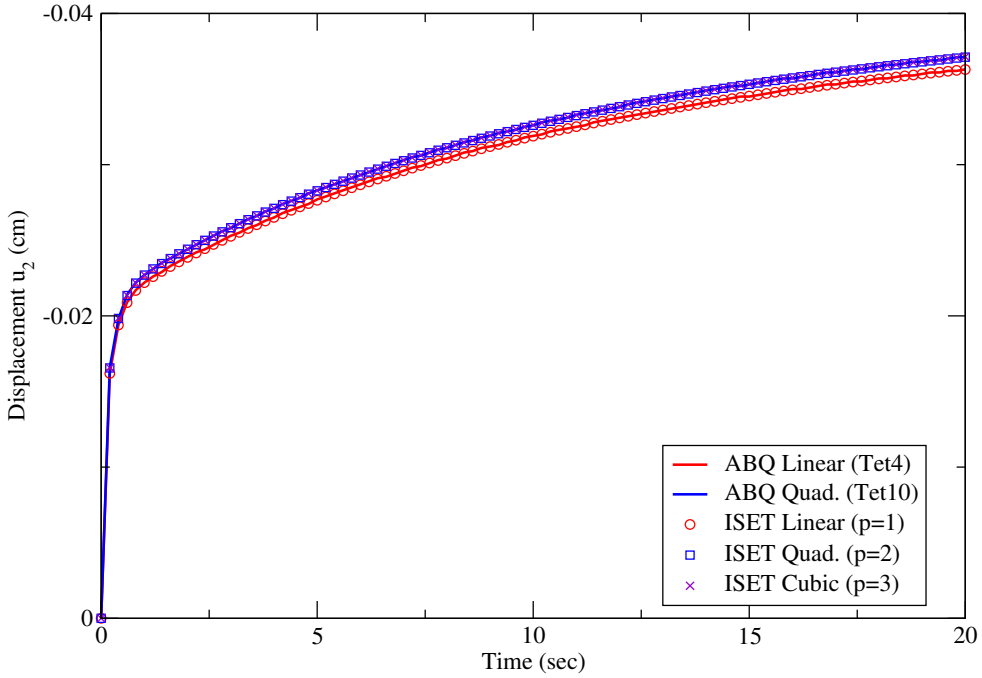

Figure 2.19: *Displacement results u_2 for linear, quadratic and cubic approximations at $0^o\,C$.*

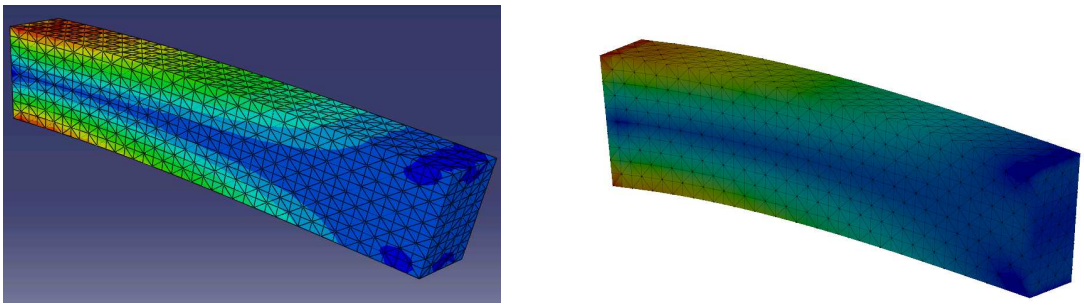

(a) Abaqus (b) ISET (GFEM code)

Figure 2.20: *Deformed configuration and VonMisses stress distribution, for quadratic approximation.*

This example has allowed us to verify the implementation performed in ISET (GFEM code).

Chapter 3

Static Cracks in Linear Viscoelasticity

Cracks in structures such as pavements, tend to have an arbitrary three-dimensional shape and are generally non-planar. In order to understand its fracture behavior it is necessary to compute a representative fracture mechanics parameters. The most common crack front parameters used as a global measure of fracture process are stress intensity factors (SIFs, $\mathcal{K}$) and energy release rate ($\mathcal{G}$). SIFs characterize the stresses, strains and displacements near the crack tip while $\mathcal{G}$ quantifies the net change in potential energy due to an increment in crack size.

In the case of linear elasticity, SIFs are sufficient to accurately describe the fracture behavior, and are square proportional to energy release rate. However, SIFs are not a suitable crack front parameter for linear viscoelasticity, because they are related only to the magnitude of the load and geometry of the structure. In contrast, energy release rate contains material information making it a more appropriate parameter to use.

Other energy based parameters that have been successfully used by researchers to characterize fracture behavior in linear viscoelasticity are:

- Strain energy release rate, proposed by Bayomy et al. [14] as an indicator of fracture toughness in asphalt mixtures.
- A J-like integral as fracture characterizing parameter presented by Schapery [149].
- A time-dependent energy release rate using J-integral computed by Syngellakis et al. [167].

Additionally, Kuai et al. [93] developed a model of fatigue crack propagation of asphalt concrete also based on the J-integral. Wagner et al. [175, 176] developed a disk-shaped compact tension (DC(T)) test as a practical method for obtaining the fracture energy in asphalt concrete.

This Chapter focuses in the computation of a time-dependent energy release rate, which serves to characterize the behavior of the crack front. A derivation to obtain ERR using the correspondence principle is presented in Section 3.1. Additionally, methods to compute the inverse Laplace transform numerically are studied in Section 3.4. This allows the use of complex material functions to characterize the viscoelastic behavior. Finally, examples are presented in Section 3.5 to show the robustness of the method.

3.1 Time Dependent Energy Release Rate (ERR) for Linear Viscoelasticity

In this section the solution of a static fracture problem for a linear viscoelastic body using the correspondence principle [67] is presented. Consider a linear viscoelastic homogeneous and isotropic material in a three dimensional domain Ω with boundary $\partial\Omega$ in a three dimensional space as illustrated in Figure 3.1. The boundary is subdivided into Γ^u, Γ^σ and Γ^c. Displacements are prescribed at Γ^u, while tractions are applied at Γ^σ and Γ^c.

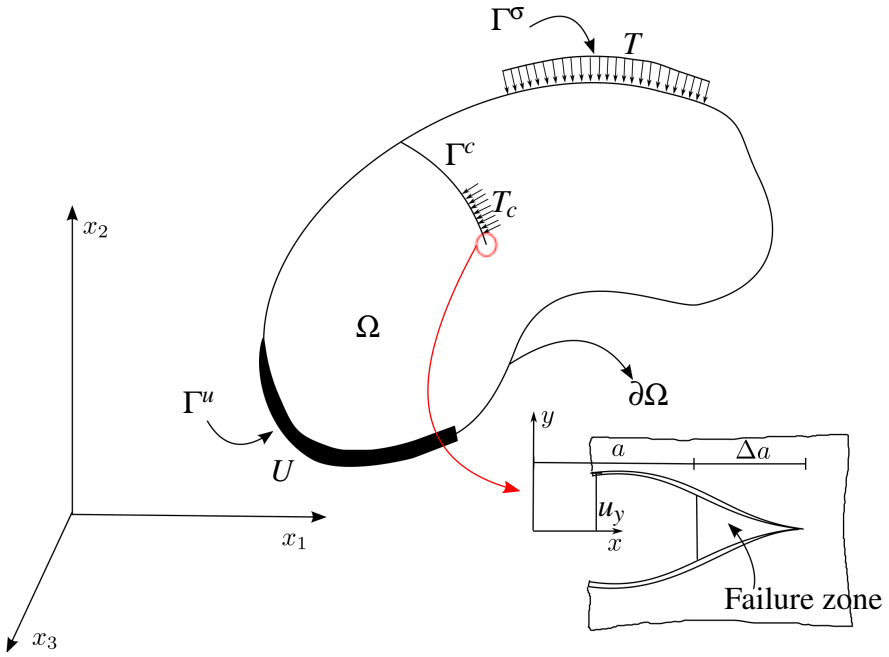

Figure 3.1: *Three dimensional boundary value problem with a crack.*

Following the same ideas from Schapery's papers [145, 146, 148], assume two important regions in a small neighborhood surrounding the crack tip. 1) a linear viscoelastic, homogeneous and isotropic continuum and 2) A zone where material damage develops and failure occurs (failure zone). Many authors have studied this problem [82, 90, 113, 181]; but Schapery's ideas allows an approximate treatment without the need of a precise modeling of the nonlinear behavior at the crack front.

The equilibrium equations, the stress-strain relations and the strain-displacement relations are given by Equations (2.51), (2.52), (2.53) and (2.54). The boundary conditions are

$$\sigma_{ij}(\boldsymbol{x},t)n_i(\boldsymbol{x}) = T_j(\boldsymbol{x},t) \quad \text{on } \Gamma^{\sigma} \tag{3.1}$$

$$\sigma_{ij}(\boldsymbol{x},t)n_i(\boldsymbol{x}) = T_{cj}(\boldsymbol{x},t) \quad \text{on } \Gamma^{c} \tag{3.2}$$

$$u_j(\boldsymbol{x},t) = U_j(\boldsymbol{x},t) \quad \text{on } \Gamma^{u} \tag{3.3}$$

Assume a layer of damaged material which extends along $x < a$ and around the failure zone, small enough that its effect on the prediction of displacement $u^v(t)$ in the neighborhood of the tip is negligible. Call $x = a$ the crack front and failure zone the region $a < x < (a + \Delta a)$. Within the failure zone there is a reaction from the surrounding continuum and it can be represented by a tensile stress distribution σ_f named failure stress. The rest of the body acts as a linear viscoelastic material.

In order to use the correspondence principle for stationary cracks, it is important to mention two restrictive conditions [145]: a) The crack cannot decrease in size $\frac{da}{dt} \geq 0$, and b) The *elastic* stress normal to the surface of crack prolongation must be independent of material functions such as G, and K.

Restriction b) is met as long as all boundary conditions are of Neumann type. In other cases

where the dependence on the Poisson's ratio exists (Dirichlet BCs), if the material of interest has a constant Poisson's ratio, the dependence of the elastic solution on Poisson's ratio does not invalidate the correspondence principle. Assuming a constant Poisson's ratio is an approximation commonly used, and it is said to be true in many situations involving polymeric materials [144]. This assumption means that the two relaxation functions (shear and bulk), are proportional to each other, and hence have the same dependence on time.

As result, if the correspondence principle is applicable with the mentioned restrictions, the stresses near the tip of the crack in a viscoelastic body are the same as those given for an elastic media. Therefore, the stress intensity factor for Mode I, for example, would also be the same and has the form [170],

$$\mathcal{K}_I = \sigma \sqrt{\pi a}\, f \tag{3.4}$$

where $\mathcal{K}_I$ is the stress intensity factor for Mode I fracture, σ is the nominal far field stress, a is the size of the crack and f is a non-dimensional function depending on the size and geometry of the structural component. It is also known as form factor.

The viscoelastic displacements $u^v(t)$ can be computed using a reference elastic solution. Namely, use the solutions of a reference elastic problem in the Laplace domain and invert them back to the time domain. This is known as the correspondence principle and more details can be found in [67]. With this procedure, the released energy available for the fracture process known as Energy Release Rate (ERR) can be computed.

Consider a problem as shown in Figure 3.2, with linear viscoelastic material properties. All boundary conditions are tractions and Poisson's ratio is constant. A crack extension of length Δa is thought to be generated by the quasi-static reduction of stresses acting along the cut Δa. Before crack extension the normal stress ($\sigma_y(x,t)$) for the linear viscoelastic body is the same as the corresponding stress in the reference elastic problem and is given by [170] (neglect H.O.T. for now).

$$\sigma_y^v(x,t) = \sigma_y^e(x,t) = \frac{\mathcal{K}_I(a,t)}{\sqrt{2\pi x}} \tag{3.5}$$

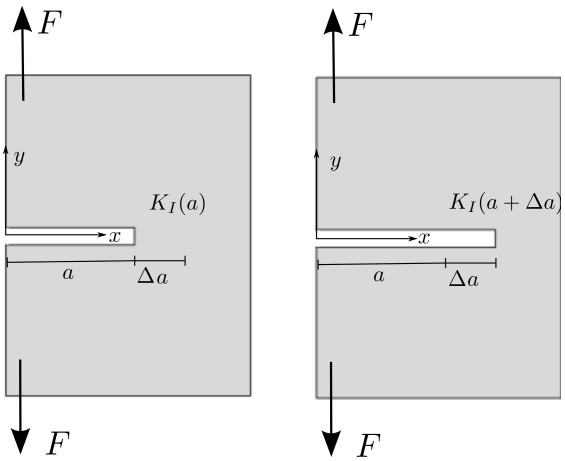

Figure 3.2: *Energy Release Rate for Mode I problem.*

To prove this, use the correspondence principle. First, look at the linear elastic solution.

$$\sigma_y^e(x,t) = \frac{\mathcal{K}_I(a,t)}{\sqrt{2\pi x}} \tag{3.6}$$

Take the Laplace transform

$$\mathfrak{L}\left\{\sigma_y^e(x,t)\right\} = \bar{\bar{\sigma}}_y^e(x,p) = \frac{\bar{\bar{\mathcal{K}}}_I(a,p)}{\sqrt{2\pi x}} \tag{3.7}$$

The viscoelastic solution in the Laplace domain is the same because stresses are not influenced by the material properties under the previous assumptions.

$$\bar{\bar{\sigma}}_y^v(x,p) = \frac{\bar{\bar{\mathcal{K}}}_I(a,p)}{\sqrt{2\pi x}} \tag{3.8}$$

Finally, take the inverse Laplace transform of the previous

$$\mathfrak{L}^{-1}\left\{\bar{\bar{\sigma}}_y^v(x,p)\right\} = \sigma_y^v(x,t) = \frac{\mathcal{K}_I(a,t)}{\sqrt{2\pi x}} \tag{3.9}$$

Equations (3.9) and (3.6) are equivalent. Now, find the viscoelastic displacements ($u_y^v(x,t)$) of the upper and lower crack faces along Δa after crack extension using the correspondence principle.

The displacements for the reference elastic problem are given by [170],

$$u_y^e(x,t) = \frac{\kappa^e + 1}{2\,G^e}\,\mathcal{K}_I(a+\Delta a,t)\,\sqrt{\frac{a+\Delta a-x}{2\,\pi}} \tag{3.10}$$

where G^e is the shear modulus and κ^e is the Kolosov's constant of the reference elastic problem. Assuming plane strain and leaving Equation (3.10) in terms of G^e and K^e (bulk modulus), we get,

$$u_y^e(x,t) = \left(\frac{3}{G^e + 3\,K^e} + \frac{1}{G^e}\right)\,\mathcal{K}_I(a+\Delta a,t)\,\sqrt{\frac{a+\Delta a-x}{2\,\pi}} \tag{3.11}$$

Taking the Laplace transform

$$\mathfrak{L}\left\{u_y^e(x,t)\right\} = \bar{\bar{u}}_y^e(x,p) = \left(\frac{3}{G^e + 3\,K^e} + \frac{1}{G^e}\right)\,\bar{\bar{\mathcal{K}}}_I(a+\Delta a,p)\,\sqrt{\frac{a+\Delta a-x}{2\,\pi}} \tag{3.12}$$

Applying the correspondence principle, replace the material constants by the linear viscoelastic material functions transformed to the Laplace domain and multiplied by the transform parameter p.

$$\bar{\bar{u}}_y^v(x,p) = \left(\frac{3}{p\,\bar{\bar{G}}(p) + 3\,p\,\bar{\bar{K}}(p)} + \frac{1}{p\,\bar{\bar{G}}(p)}\right)\,\bar{\bar{\mathcal{K}}}_I(a+\Delta a,p)\,\sqrt{\frac{a+\Delta a-x}{2\,\pi}} \tag{3.13}$$

Making use of the reciprocal property of material functions in the Laplace domain, use the compliance functions instead of the relaxation functions. $p\,\bar{\bar{J}}^{G+3K}(p) = \frac{1}{p\,\bar{\bar{G}}(p)+3\,p\,\bar{\bar{K}}(p)}$ and $p\,\bar{\bar{J}}^{G}(p) = \frac{1}{p\,\bar{\bar{G}}(p)}$.

$$\bar{\bar{u}}_y^v(x,p) = \left(p\,\bar{\bar{J}}^{G+3K}(p) + p\,\bar{\bar{J}}^{G}(p)\right)\,\bar{\bar{\mathcal{K}}}_I(a+\Delta a,p)\,\sqrt{\frac{a+\Delta a-x}{2\,\pi}} \tag{3.14}$$

Take the inverse of the Laplace transform to obtain the time dependent viscoelastic displacements

$$u_y^v(x,t) = \mathfrak{L}^{-1}\left\{\bar{\bar{u}}_y^v(x,p)\right\} =$$

$$\sqrt{\frac{a+\Delta a-x}{2\,\pi}}\left[3\int_0^t J^{G+3K}(t-t')\frac{\partial\,\mathcal{K}_I(a+\Delta a,t')}{\partial t'}dt' + \int_0^t J^{G}(t-t')\frac{\partial\,\mathcal{K}_I(a+\Delta a,t')}{\partial t'}\,dt'\right] \tag{3.15}$$

Finally, using the concept of work of fracture which is the change of work due to the creation of the new crack surfaces

$$\Delta W_f = \Delta\Pi = -\frac{1}{2}\int_0^{\Delta a} \sigma_y^v(x,t)\,\left[u_y^{v+}(x,t) - u_y^{v-}(x,t)\right] dx \tag{3.16}$$

Substitute Equations (3.9) and (3.15) into (3.16) to obtain,

$$\Delta\Pi = -\int_a^{a+\Delta a} \sqrt{\frac{a+\Delta a - x}{4\,\pi^2\,x}} \left[3\int_0^t J^{G+3K}(t-t')\frac{\partial}{\partial t'}\Big(\mathcal{K}_I(a,t')\;\mathcal{K}_I(a+\Delta a,t')\Big)\,dt' \right.$$

$$\left. + \int_0^t J^{G}(t-t')\frac{\partial}{\partial t'}\Big(\mathcal{K}_I(a,t')\;\mathcal{K}_I(a+\Delta a,t')\Big)\,dt' \right] dx \tag{3.17}$$

Working out the spatial integral,

$$\Delta\Pi = -\frac{\Delta a}{4}\left[3\int_0^t J^{G+3K}(t-t')\frac{\partial}{\partial t'}\Big(\mathcal{K}_I(a,t')\;\mathcal{K}_I(a+\Delta a,t')\Big)\,dt' \right.$$

$$\left. + \int_0^t J^{G}(t-t')\frac{\partial}{\partial t'}\Big(\mathcal{K}_I(a,t')\;\mathcal{K}_I(a+\Delta a,t')\Big)\,dt' \right] \tag{3.18}$$

The energy release rate is equal to $\mathcal{G} = -\frac{\Delta\Pi}{\Delta a}$ and if $\Delta a \to 0$,

$$\mathcal{G}_I^v(t) = \frac{1}{4}\left[3\int_0^t J^{G+3K}(t-t')\frac{\partial \mathcal{K}_I^2(a,t')}{\partial t'}\,dt' + \int_0^t J^{G}(t-t')\frac{\partial \mathcal{K}_I^2(a,t')}{\partial t'}\,dt' \right] \tag{3.19}$$

Equation (3.19) is the time-dependent energy release rate for a linear viscoelastic, homogeneous, isotropic material. The stress intensity factor $\mathcal{K}_I$ can be time dependent and it has a linear relation with the far field stress. Therefore, introduce a time dependent function $\lambda(t)$ that scales $\mathcal{K}_I$. Such that $g(a,t) = \lambda(t)\;\mathcal{K}_I(a)$. Note that $\lambda(t)$ is a normalized function of the applied load. Equation (3.19) becomes,

$$\mathcal{G}_I^v(t) = \frac{1}{4}\left[3\int_0^t J^{G+3K}(t-t')\frac{\partial g_I^2(a,t')}{\partial t'}\,dt' + \int_0^t J^{G}(t-t')\frac{\partial g_I^2(a,t')}{\partial t'}\,dt' \right] \tag{3.20}$$

and finally

$$\mathcal{G}_I^v(t) = \frac{\mathcal{K}_I^2(a)}{4}\left[3\int_0^t J^{G+3K}(t-t')\frac{\partial\lambda^2(t')}{\partial t'}\,dt' + \int_0^t J^{G}(t-t')\frac{\partial\lambda^2(t')}{\partial t'}\,dt'\right] \tag{3.21}$$

The result is a combination of hereditary integrals which account for the load history. It was assumed that loading starts just after zero $t = 0^+$, so no initial conditions are necessary. These convolution integrals can be computed using the Laplace transform or by performing a numerical integration. In this document, both approaches are studied (3.4,7).

The Laplace transform of Equation (3.21) is,

$$\mathfrak{L}\left\{\mathcal{G}_I^v(t)\right\} = \bar{\bar{\mathcal{G}}}_I^v(p) = \frac{\mathcal{K}_I^2(a)}{4}\left[\bar{\bar{J}}^{G+3K}(p)\,p\,\mathfrak{L}\left\{\lambda^2(t)\right\} + \bar{\bar{J}}^{G}(p)\,p\,\mathfrak{L}\left\{\lambda^2(t)\right\}\right]$$

$$\bar{\bar{\mathcal{G}}}_I^v(p) = \left[\frac{3}{p\,\bar{\bar{G}}(p) + 3\,p\,\bar{\bar{K}}(p)} + \frac{1}{p\,\bar{\bar{G}}(p)}\right]\frac{\mathcal{K}_I^2(a)\,\bar{\bar{\lambda}}_2(p)}{4} \tag{3.22}$$

Other fracture modes can be derived analogously and have the following form in Laplace domain.

$$\bar{\bar{\mathcal{G}}}_{II}^v(p) = \left[\frac{3}{p\,\bar{\bar{G}}(p) + 3\,p\,\bar{\bar{K}}(p)} + \frac{1}{p\,\bar{\bar{G}}(p)}\right]\frac{\mathcal{K}_{II}^2(a)\,\bar{\bar{\lambda}}_2(p)}{4} \tag{3.23}$$

and

$$\bar{\bar{\mathcal{G}}}_{III}^v(p) = \left[\frac{1}{2\,p\,\bar{\bar{G}}(p)}\right]\mathcal{K}_{III}^2(a)\,\bar{\bar{\lambda}}_2(p) \tag{3.24}$$

No matter how complicated the relaxation functions (many terms in a Prony series representation), the previous equations can be inverted back to the time domain numerically. Details on the subject are discuss in Section 3.4. Components of ERR in the time domain for all three fracture

modes are as follows:

$$\begin{aligned}
\mathcal{G}_I^v(t) &= \frac{\mathcal{K}_I^2(a)}{4}\left[3\int_0^t J^{G+3K}(t-t')\frac{\partial\lambda^2(t')}{\partial t'}\,dt' + \int_0^t J^{G}(t-t')\frac{\partial\lambda^2(t')}{\partial t'}\,dt'\right] \\
\mathcal{G}_{II}^v(t) &= \frac{\mathcal{K}_{II}^2(a)}{4}\left[3\int_0^t J^{G+3K}(t-t')\frac{\partial\lambda^2(t')}{\partial t'}\,dt' + \int_0^t J^{G}(t-t')\frac{\partial\lambda^2(t')}{\partial t'}\,dt'\right] \\
\mathcal{G}_{III}^v(t) &= \frac{\mathcal{K}_{III}^2(a)}{2}\left[\int_0^t J^{G}(t-t')\frac{\partial\lambda^2(t')}{\partial t'}\,dt'\right]
\end{aligned} \tag{3.25}$$

Note that, $\bar{\bar{\lambda}}_2(p)$ is a Laplace transform of a squared time dependent function $\lambda(t)$, which scales values of $\mathcal{K}_I$. This is possible because in the linear elastic regime there is a linear relation between the load and stress intensity factors.

In conclusion, the inverse Laplace transform of $\bar{\bar{\mathcal{G}}}_I^v(p)$, $\bar{\bar{\mathcal{G}}}_{II}^v(p)$ and $\bar{\bar{\mathcal{G}}}_{III}^v(p)$ gives $\mathcal{G}_I^v(t)$,$\mathcal{G}_{II}^v(t)$ and $\mathcal{G}_{III}^v(t)$ in the time domain, respectively, for the linear viscoelastic material. It is also important to note that stress intensity factors $\mathcal{K}_I$, $\mathcal{K}_{II}$, and $\mathcal{K}_{III}$ are computed using the reference elastic problem.

3.2 Alternative Derivation

An alternative to the previous derivation, is to apply the correspondence principle directly to the energy release rate function of the reference elastic problem. The energy release rate for a linear elastic plane strain problem with a time dependent load is computed by,

$$\mathcal{G}_I^e(t) = \frac{1-\nu^2}{E}\,\mathcal{K}_I^2(a)\,\lambda(t)^2$$

Writing the above in terms of shear and bulk modulus,

$$\mathcal{G}_I^e(t) = \left[\frac{3}{G^e + 3\,K^e} + \frac{1}{G^e}\right]\frac{\mathcal{K}_I^2(a)\,\lambda(t)^2}{4} \tag{3.26}$$

Transforming Equation (3.26) to the Laplace domain,

$$\bar{\bar{\mathcal{G}}}_I^e(p) = \left[\frac{3}{G^e + 3\,K^e} + \frac{1}{G^e}\right] \frac{\mathcal{K}_I^2(a)\,\bar{\bar{\lambda}}_2(p)}{4} \tag{3.27}$$

with $\mathfrak{L}\left\{\lambda^2(t)\right\} = \bar{\bar{\lambda}}_2(p)$. Finally, use the correspondence principle in Equation (3.27).

$$\bar{\bar{\mathcal{G}}}_I^v(p) = \left[\frac{3}{p\,\bar{\bar{G}}(p) + 3\,p\,\bar{\bar{K}}(p)} + \frac{1}{p\,\bar{\bar{G}}(p)}\right] \frac{\mathcal{K}_I^2(a)\,\bar{\bar{\lambda}}_2(p)}{4} \tag{3.28}$$

Which is identical to Equation (3.22).

3.3 Dirichlet Boundary Conditions

Until this moment we have assumed that the boundary conditions applied to the body are of Neumann type or homogeneous Dirichlet. For the case of non-homogeneous Dirichlet boundary conditions, an alternative is to find an equivalent problem where tractions are applied instead of displacements, as done in Example 2.3.2. The difficulty lies in finding the equivalent tractions.

For the purpose of this study, an analytical expression in the Laplace domain for Dirichlet boundary conditions is computed using the $\mathcal{G} - \mathcal{K}$ relationships for viscoelastic cracked bodies presented by Zhang [185]. He showed that the ERR of a cracked body with viscoelastic material properties is equal to the rate of closure energy. Crack-closure energy can be computed using Irwins integral [74]. It is assumed that the energy released due to extending the crack front by Δa is identical to the energy required to close the crack by a same amount. Therefore, he derived the following expression from the computation of the rates of crack-closure energy; plane strain is assumed here.

$$\mathcal{G}_i^v(t) = \left[\frac{1 - v_0^2}{E_0}\right] \mathcal{K}_i^2(a) f_{iu}(t) f_{i\sigma}(t)$$

Transforming above equation in terms of deviatoric and volumetric modulus we obtain,

$$\mathcal{G}_i^v(t) = \left[\frac{3}{G_0+3K_0} + \frac{1}{G_0}\right] \mathcal{K}_i^2(a) f_{iu}(t) f_{i\sigma}(t) \tag{3.29}$$

where G_0 and K_0 correspond to the instantaneous modulus of the viscoelastic body. $f_{iu}(t)$ and $f_{i\sigma}(t)$ are known as time factors. For the case of Dirichlet type boundary conditions, they are given by,

$$\begin{aligned} f_{iu}(t) &= \lambda(t)^2 \\ f_{i\sigma}(t) &= \mathfrak{L}^{-1}\left\{\frac{p\,\bar{\bar{G}}(p)\left(p\,\bar{\bar{G}}(p)+3\,p\,\bar{\bar{K}}(p)\right)}{4p\,\bar{\bar{G}}(p)+3\,p\,\bar{\bar{K}}(p)} * \left(\frac{3}{G_0+3K_0}+\frac{1}{G_0}\right)\right\} \end{aligned} \tag{3.30}$$

with $i = I, II$ and for mode III,

$$\begin{aligned} f_{IIIu}(t) &= \lambda(t)^2 \\ f_{III\sigma}(t) &= \mathfrak{L}^{-1}\left\{\frac{p\,\bar{\bar{G}}(p)}{G_0}\right\} \end{aligned} \tag{3.31}$$

Replace Equations (3.30) and (3.31) into Equation (3.29) in Laplace domain we get,

$$\begin{aligned} \bar{\bar{\mathcal{G}}}_I^v(p) &= \left[\frac{p\,\bar{\bar{G}}(p)\left(p\,\bar{\bar{G}}(p)+3\,p\,\bar{\bar{K}}(p)\right)}{4p\,\bar{\bar{G}}(p)+3\,p\,\bar{\bar{K}}(p)} * \left(\frac{3}{G_0+3K_0}+\frac{1}{G_0}\right)^2\right] \frac{\mathcal{K}_I^2(a)\,\bar{\bar{\lambda}}_2(p)}{4} \\ \bar{\bar{\mathcal{G}}}_{II}^v(p) &= \left[\frac{p\,\bar{\bar{G}}(p)\left(p\,\bar{\bar{G}}(p)+3\,p\,\bar{\bar{K}}(p)\right)}{4p\,\bar{\bar{G}}(p)+3\,p\,\bar{\bar{K}}(p)} * \left(\frac{3}{G_0+3K_0}+\frac{1}{G_0}\right)^2\right] \frac{\mathcal{K}_{II}^2(a)\,\bar{\bar{\lambda}}_2(p)}{4} \\ \bar{\bar{\mathcal{G}}}_{III}^v(p) &= \left[\frac{p\,\bar{\bar{G}}(p)}{2\,G_0^2}\right] \mathcal{K}_{III}^2(a)\,\bar{\bar{\lambda}}_2(p) \end{aligned} \tag{3.32}$$

Equations (3.32) correspond to the time-dependent ERR in the case of non-homogeneous displacement boundary conditions for modes I, II and III written in the Laplace domain. Thus, the Laplace inversion of those equations give its corresponding ERR in the time domain ($\mathcal{G}_I^v(t)$, $\mathcal{G}_{II}^v(t)$

and $\mathcal{G}^{v}_{III}(t)$). The analytical inversion of these equations is very complicated, even more if the material functions have many terms. Therefore, in Section 3.4 methods to compute Laplace inversion numerically are investigated. Additionally, an example with Dirichlet boundary conditions is presented in Section 4.3.1.

Note that, using Equation (3.29) with the time factors corresponding to Neumann type boundary conditions gives Equations equivalent to (3.22) - (3.24).

3.4 Numerical Laplace Inversion

The Laplace transform is widely used because it is a powerful method that has the property of converting complicated relationships and operations of functions in the time domain to corresponding simpler operations in the Laplace domain. In Section 3.1 expressions for a time dependent Energy Release Rate (ERR) were presented. By simple observation it can be concluded that the ERR Equations in the Laplace domain (3.22)-(3.24) and (3.32) are much simpler than their corresponding integral expressions in the time domain. Therefore, it is attractive to attempt to solve these equations in the Laplace domain and invert the solution back to the time domain.

In the case of fracture mechanics in viscoelasticity, if the material functions and applied BCs are simple functions of time, the computation of ERR in Laplace domain and its inversion can be done analytically. This is shown in Examples 3.5.1, 3.5.2 and 4.3.1. Unfortunately, this is not always the case and many viscoelastic materials need to be described with ten or more Prony series terms. This makes the analytical Laplace inversion of the solution almost impossible to achieve. In this section three different numerical Laplace inversion methods are tested, in order to transform the time-dependent ERR solution.

3.4.1 Schapery's method

This method consists on a simple analytical inversion technique [143]. It is applicable when the function in the Laplace domain is in the form $s\,F(s) = A\,s^m$ and $m < 1$. The advantage of this method is the simplicity of the implementation, and it can give approximate solutions on the order of 5% accuracy [77].

$$f(t) \approx \Big[s\,F(s) \Big]_{s=1/b^t} \tag{3.33}$$

where $b = 1.781$.

Table 3.1: *Zakian's method,A_i and α_i for $n = 5$ [65].*

i	α	A
1	12.83767675 + j1.666063445	-36902.08210 + j196990.4257
2	12.22613209 + j5.012718792	+61277.02524 - j95408.62551
3	10.93430308 + j8.409673116	-28916.56288 + j18169.18531
4	8.776434715 + j11.92185389	+4655.361138 - j1.901528642
5	5.225453361 + j15.72952905	-118.7414011 - j141.3036911

3.4.2 Zakian's method

This method approximates the time domain function by an infinite series of weighted evaluations of the domain function using the following [65]:

$$f(t) = \frac{2}{t} \sum_{i=1}^{n} \mathrm{Re}\Big\{ A_i F\big(\frac{\alpha_i}{t}\big) \Big\} \tag{3.34}$$

with A_i and α_i as defined constants for $n = 5$ (see Table 3.1).

This method is a good alternative, but additional A_i and α_i constant terms may be necessary depending on the complexity of the function to be inverted. The constants shown in Table 3.1 are widely found in the literature, but it may not be as easy to find many more terms.

3.4.3 Fourier series method

Dubner et al. [48] presented an inverse Laplace transform using a Fourier cosine series. The implementation of this method is not as simple as previous methods, but it proves to be more robust for complex functions.

$$f(t) = \frac{e^{bt}}{t} \left[\frac{1}{2} F(b) + \mathrm{Re} \sum_{k=1}^{n} F\big(b + j\frac{k\pi}{t}\big)(-1)^k \right] \tag{3.35}$$

where F is the function to be transformed, $j = \sqrt{-1}$ and the parameters b and n must be optimized for increased accuracy. In this dissertation $bt = 4.5$ and $n = 101$. In contrast to Zakian's method, to increase accuracy, additional terms may be added automatically by only increasing the value of n.

In the examples presented in this study the value of n used is 101. Syngellakis et al. [166] reported that increasing number of the transform parameters imposes a heavy computational penalty (time and cost) on the final output, but authors experienced, even with $n = 300$ in a standard laptop the inversion of a complex ERR functions takes less than a couple of seconds.

In the following section examples with simple material functions and different load types are solved. Using the mentioned numerical inversion techniques, Laplace inversion approximations of the solution are computed and compared to analytical solutions. This allows to test their performance.

3.5 Examples

3.5.1 Center-cracked Plate Example

The following example consists of a two dimensional rectangular plate with a crack located at its center. The crack has a length of $2a$ in the direction perpendicular to the applied load. It is assumed to be a plane strain problem. The dimensions of the plate are: height $H = 30$ and width $w = 20$. The value of $a = 3$ and the pressure $\sigma_0 = 100$. The plate is loaded with three different types of loads; $\lambda(t) = 1$ (constant), $\lambda(t) = \frac{t}{t_{peak}}$(ramp) and $\lambda(t) = |\sin(\frac{t\pi}{t_{peak}})|$ (sinusoidal). Figure 3.3 shows the details of the problem. The material is assumed to be linear viscoelastic and the material moduli is characterized by a bulk and shear relaxation functions. Note that, the shear and bulk relaxation functions have the same time dependence. Later, we look at the case when they do not.

$$
\begin{aligned}
K(t) &= 2500 + 7500\, e^{-\frac{t}{2}} \\
G(t) &= 1125 + 3375\, e^{-\frac{t}{2}}
\end{aligned}
$$

First compute the stress intensity factor of the elastic reference problem using the instantaneous

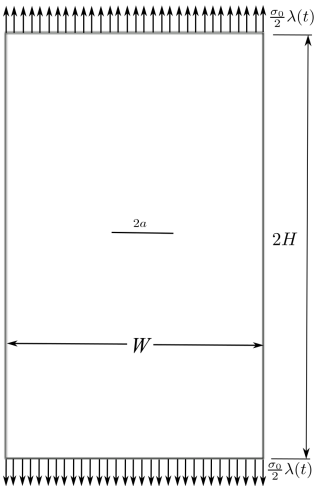

Figure 3.3: *Center-cracked Plate Problem.*

material properties at $t = 0$. The load used is the maximum load for each of the three cases at $t = t_{peak}$. Since this problem is simple, an analytical solution for stress intensity factor $\mathcal{K}_I$ can be found using the following expression [170]:

$$\mathcal{K}_I = \sigma_{max}\sqrt{\pi a \sec\left(\frac{\pi a}{W}\right)} = 325.2334 \tag{3.36}$$

where σ_{max} is the far field stress when the applied load has its maximum value. That is when $\lambda(t) = 1.0$.

The viscoelastic time-dependent ERR $\mathcal{G}_I(t)$ is obtained by using Equation (3.22) and computing its inverse Laplace transform. To compute the solution in Laplace domain (Eq. (3.22)) use the SIF of the reference elastic problem, and compute the Laplace transform of the material and the load $\lambda(t)^2$ functions as follows.

The material functions in Laplace domain are:

$$\begin{aligned}\bar{\bar{K}}(p) &= \frac{2500}{p} + \frac{7500}{p+\frac{1}{2}} \\ \bar{\bar{G}}(p) &= \frac{1125}{p} + \frac{3375}{p+\frac{1}{2}}\end{aligned}$$

The Laplace transform functions $\bar{\bar{\lambda}}_2(p)$ for each load type is:

For a constant load $\lambda(t) = 1$, the Laplace transform is,

$$\bar{\bar{\lambda}}_2(p) = \mathfrak{L}\left\{\lambda(t)^2 = 1.0\right\} = \frac{1}{p} \tag{3.37}$$

For a ramp load $\lambda(t) = \frac{t}{t_{peak}}$, the Laplace transform is,

$$\bar{\bar{\lambda}}_2(p) = \mathfrak{L}\left\{\lambda(t)^2 = \frac{t^2}{t_{peak}^2}\right\} = \frac{2}{t_{peak}^2\, p^3} \tag{3.38}$$

For a sinusoidal load $\lambda(t) = |\sin(\frac{t\,\pi}{t_{peak}})|$, the Laplace transform is,

$$\bar{\bar{\lambda}}_2(p) = \mathfrak{L}\left\{\lambda(t)^2 = \sin^2\left(\frac{t\,\pi}{t_{peak}}\right)\right\} = \frac{1}{2\,p} - \frac{p}{2\,(p^2 + \frac{\pi^2}{t_{peak}^2})} \tag{3.39}$$

The solutions (ERR) in the Laplace domain and time domain computed analytically for each load case are:

Constant Load

$$\begin{aligned} \bar{\bar{G}}_I^v(p) &= \frac{32.7039\,(2\,p+1)}{p\,(8\,p+1)} \\ G_I^v(t) &= 32.7039 - 24.5279\,e^{-0.125\,t} \end{aligned} \tag{3.40}$$

Ramp Load with $t_{peak} = 50$

$$\begin{aligned} \bar{\bar{G}}_I^v(p) &= \frac{0.0262\,(2\,p+1)}{p^3(8\,p+1)} \\ G_I^v(t) &= 0.0131\,t^2 - 0.1570\,t + 1.2559 - 1.2559\,e^{-0.125\,t} \end{aligned} \tag{3.41}$$

Sinusoidal Load with $t_{peak} = 2.5$

$$\begin{aligned} \bar{\bar{G}}_I^v(p) &= \frac{65.4078\,\pi^2\,(2\,p+1)}{p\,(25\,p^2+4\,\pi^2)(8\,p+1)} \\ G_I^v(t) &= 16.3520 - 1.2080\,\sin\left(\frac{\pi}{2.5}\,t\right) - 4.2082\,\cos\left(\frac{\pi}{2.5}\,t\right) - 12.1438\,e^{-0.125\,t} \end{aligned} \tag{3.42}$$

Even though the material model in this problem is simple, the analytical solution in the time domain can be a complicated function to obtain (see Eq. (3.42)). The three numerical inversion techniques shown at the beginning of this Section are used to invert the Laplace domain solutions given by Equations (3.40)-(3.42). Figures 3.4, 3.5 and 3.6 show the analytical and numerical inverse Laplace transforms solutions for constant, ramp and sinusoidal load, respectively, for this example.

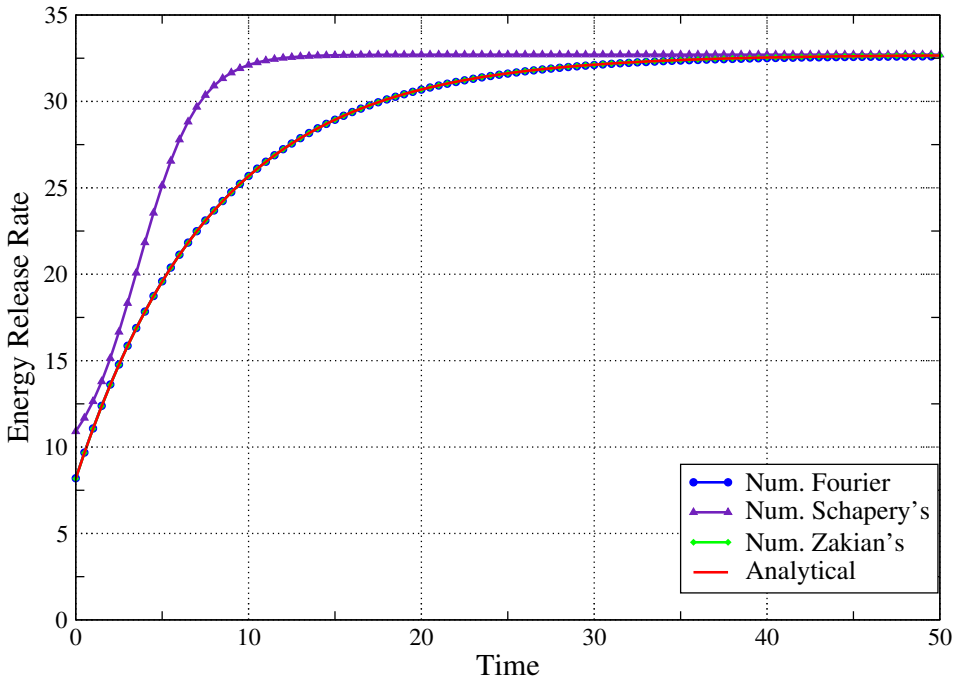

Figure 3.4: *Time dependent Energy Release Rate for simple material functions with same time dependence and constant applied tractions.*

The Fourier numerical Laplace inversion is the only method that gives good approximations for all load cases. Zakian's method works fine for the constant and ramp loads, but in the sinusoidal

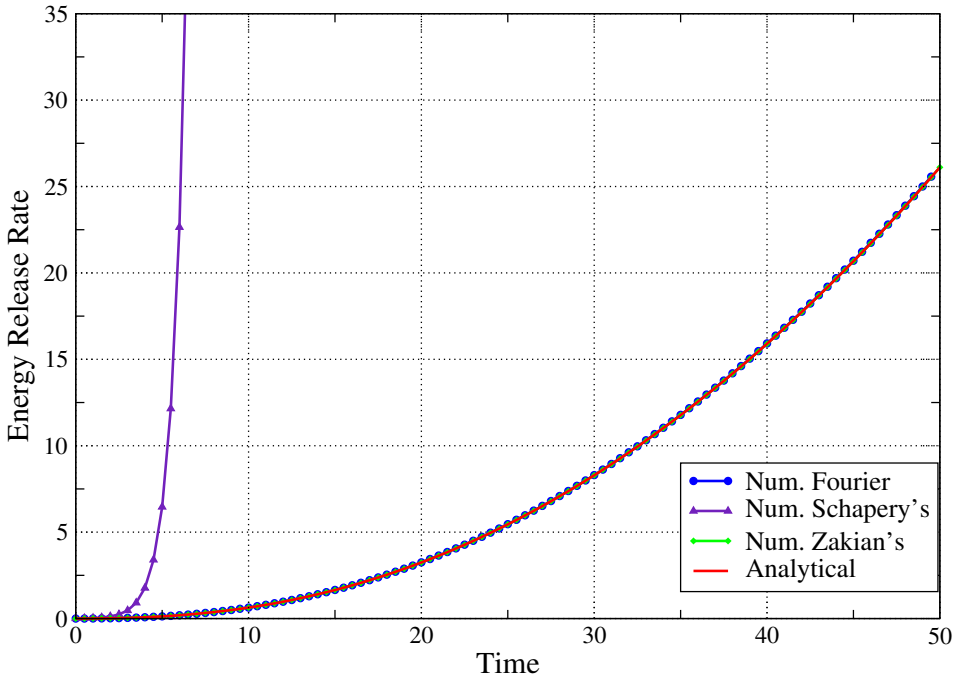

Figure 3.5: *Time dependent Energy Release Rate for simple material functions with same time dependence and ramp type applied tractions.*

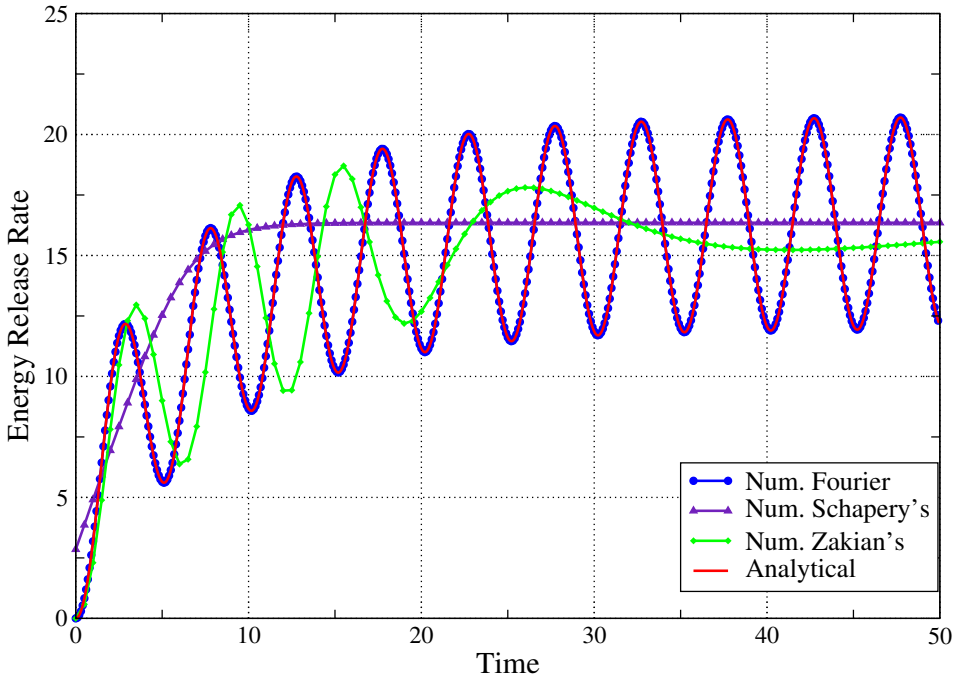

Figure 3.6: *Time dependent Energy Release Rate for simple material functions with same time dependence and sinusoidal type applied tractions.*

load case, there seems to be a need for more weighted evaluation points. Schapery's method does not give a good approximation for this type of Laplace function (ERR).

Now, consider the same problem but with the material functions having different time dependences. The volumetric relaxation function is constant while the shear function is time dependent.

$$\begin{aligned} K(t) &= 10,000 \\ G(t) &= 1,125 + 3,375\, e^{-\frac{t}{2}} \end{aligned}$$

The Laplace transform of these functions are

$$\begin{aligned} \bar{\bar{K}}(p) &= \frac{10,000}{p} \\ \bar{\bar{G}}(p) &= \frac{1,125}{p} + \frac{3,375}{p+\frac{1}{2}} \end{aligned} \tag{3.43}$$

The Laplace transform functions $\bar{\bar{\lambda}}_2(p)$ for each load type and the stress intensity factor of the reference problem are the same as in the previous case. Again, using Equation (3.22) and computing the Laplace inverse we get:

Constant Load

$$\begin{aligned} \bar{\bar{G}}_I^v(p) &= \frac{94.0238\,(2\,p+1)(64\,p+23)}{p\,(8\,p+1)(184\,p+83)} \\ G_I^v(t) &= 26.0548 - 17.6295\, e^{-0.125t} - 0.2493\, e^{-0.4511t} \end{aligned}$$

Ramp Load with $t_{peak} = 50$

$$\begin{aligned} \bar{\bar{G}}_I^v(p) &= \frac{0.0752\,(2\,p+1)(64\,p+23)}{p^3(8\,p+1)(184\,p+83)} \\ G_I^v(t) &= 0.0104\,t^2 - 0.1133\,t + 0.9036 - 0.9026\, e^{-0.125t} - 9.8032 * 10^{-4}\, e^{-0.4511t} \end{aligned}$$

Sinusoidal Load with $t_{peak} = 2.5$

$$\bar{\bar{G}}_I^v(p) = \frac{167.1696\,(2\,p+1)(64\,p+23)}{(2.2518\,p^3+3.5559\,p)(8\,p+1)(184\,p+83)}$$

$$G_I^v(t) = 13.0274 - 0.9079\,\sin\left(\frac{\pi}{2.5}t\right) - 4.1886\,\cos\left(\frac{\pi}{2.5}t\right) - 8.7284\,e^{-0.125t} - 0.1104\,e^{-0.4511t}$$

Figures 3.7, 3.8 and 3.9 show the analytical and numerical inverse Laplace transforms solutions for constant, ramp and sinusoidal load, respectively, for this example.

For the case of a constant load Lee et al. [97] solved the same problem using a boundary element method for linear viscoelasticity. He solved two problems with same characteristics but with a small difference in crack length. Then, he computed the difference in potential energy between them to obtain the ERR. The solution published by him is compared in Figure 3.7.

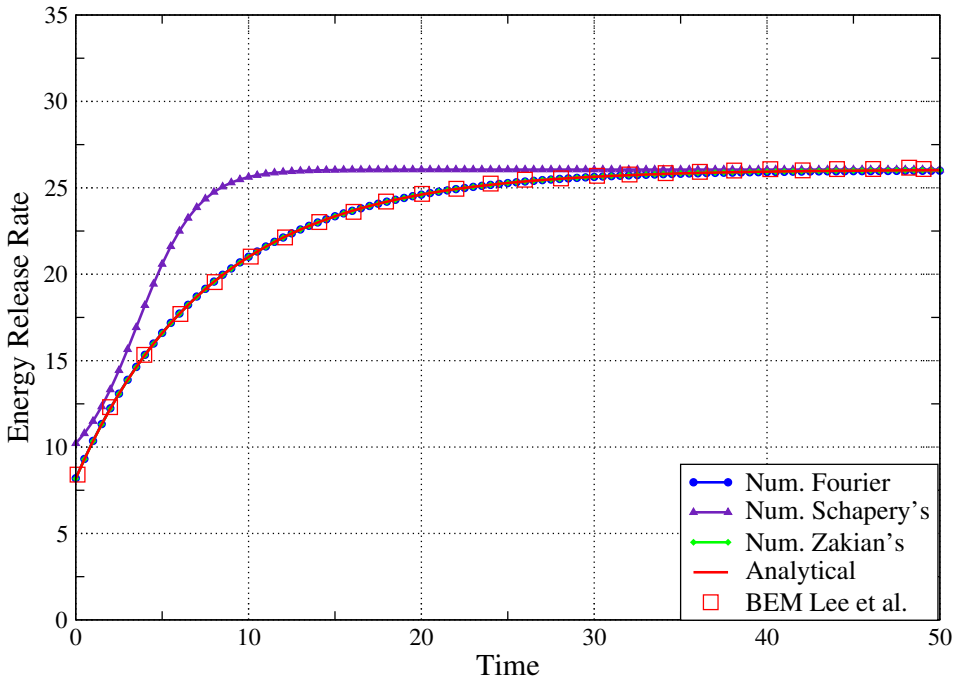

Figure 3.7: *Time dependent Energy Release Rate for simple material functions with different time dependence and constant applied tractions.*

Again, the Fourier numerical Laplace inversion has outperformed the other methods. Herein, the numerical Laplace inversion used in the rest of this study is the Fourier method.

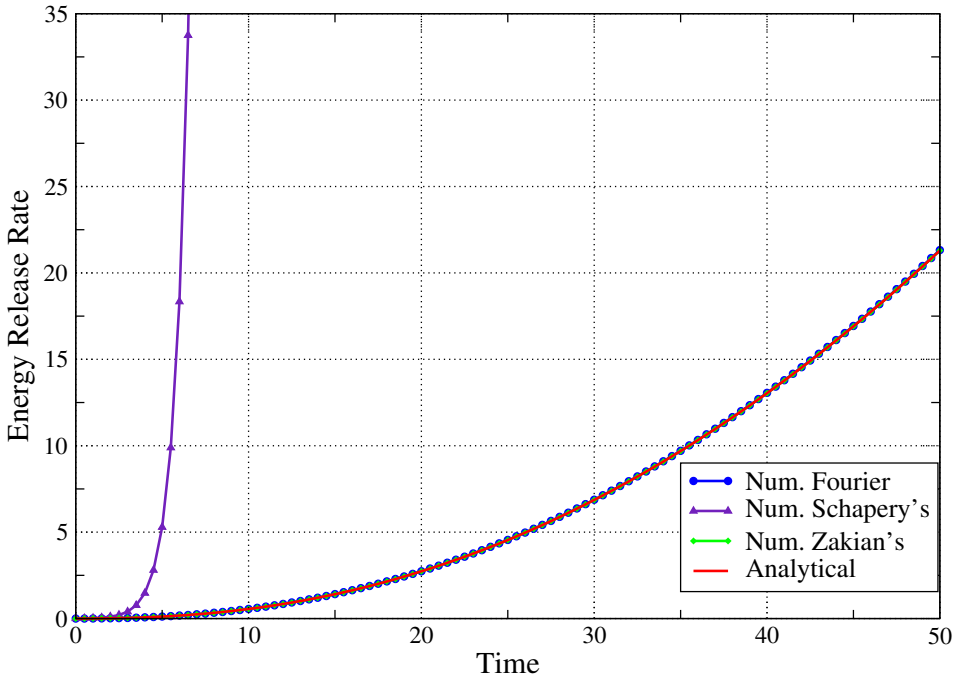

Figure 3.8: *Time dependent Energy Release Rate for simple material functions with different time dependence and ramp type applied tractions.*

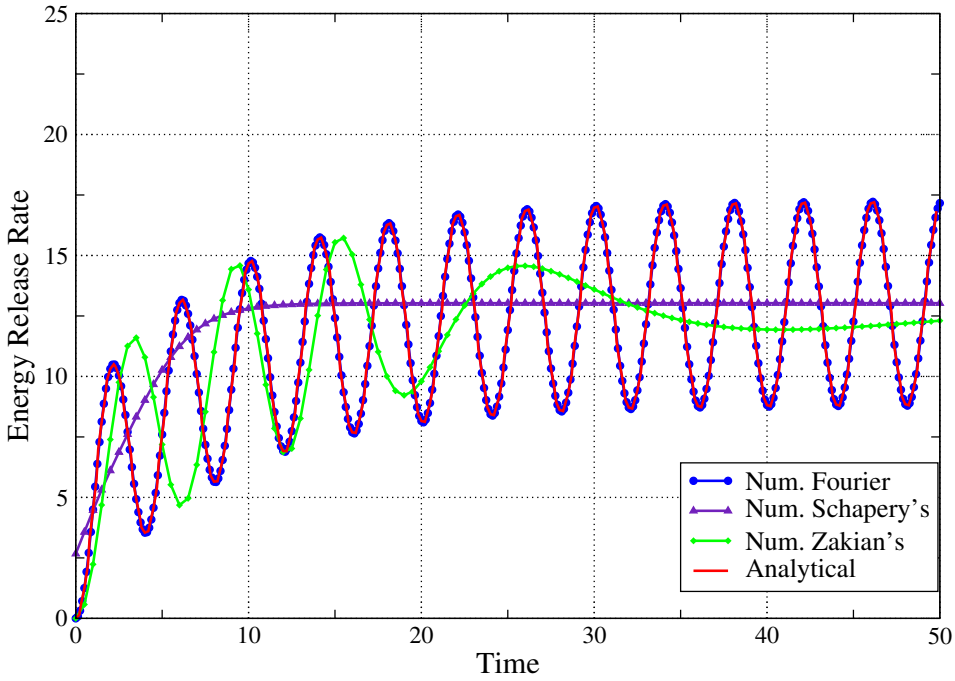

Figure 3.9: *Time dependent Energy Release Rate for simple material functions with different time dependence and sinusoidal type applied tractions.*

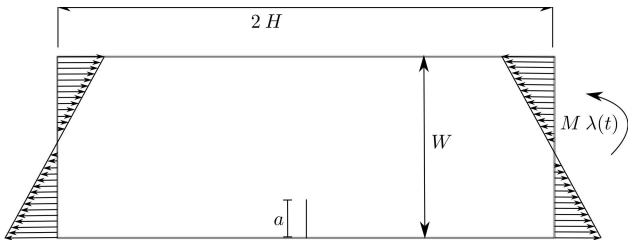

Figure 3.10: *Edge Crack Under Bending Problem.*

3.5.2 Edge-crack Plate Under Bending

A two dimensional rectangular plate of width $W = 10$ and length $H = 30$ is subjected to a pure bending moment $M = 10000$. An edge crack of length $a = 3$ is located at the bottom of the plate as seen in Figure 3.10. The plate is loaded with three load types; $\lambda(t) = 1$ (constant), $\lambda(t) = \frac{t}{t_{peak}}$(ramp) and $\lambda(t) = |\sin(\frac{t\,\pi}{t_{peak}})|$ (sinusoidal).

Assume plane strain and material to be linear viscoelastic. The material moduli is characterized by the following bulk and shear relaxation functions.

$$\begin{aligned} K(t) &= 10000 \\ G(t) &= 1125 + 3375\, e^{-\frac{t}{2}} \end{aligned} \tag{3.44}$$

The stress intensity factor $\mathcal{K}_I$ for the reference elastic problem can be computed using Equation (3.45) found in [170]. The load used is the maximum load for each of the three loading cases at $t = t_{peak}$, and the material moduli is the instantaneous ($t = 0$).

$$\mathcal{K}_I = \frac{6M}{W^2}\sqrt{\pi a}\,F\left(\frac{a}{W}\right) = 2066.71 \tag{3.45}$$

with

$$F\left(\frac{a}{W}\right) = 1.122 - 1.40\left(\frac{a}{W}\right) + 7.33\left(\frac{a}{W}\right)^2 - 13.08\left(\frac{a}{W}\right)^3 + 14.0\left(\frac{a}{W}\right)^4 \tag{3.46}$$

The Laplace transform function $\bar{\bar{\lambda}}_2(p)$ for each load type are given by Equations (3.37)-(3.39) and the Laplace transform of the material functions is Equation (3.43).

The viscoelastic time-dependent ERR $\mathcal{G}_I(t)$ is obtained by using Equation (3.22) and computing its inverse Laplace transform. An analytical and a Fourier numerical inversion of the Laplace transform are obtained and compared. Also, for the case of a constant load, Lee et al. [97] solved the same problem using a boundary element method for linear viscoelasticity. He solved two problems with same characteristics but with a small difference in crack length. In order to find the ERR, he computed the difference in potential energy between them. Figure 3.11 shows the solutions computed here and Lee's solution.

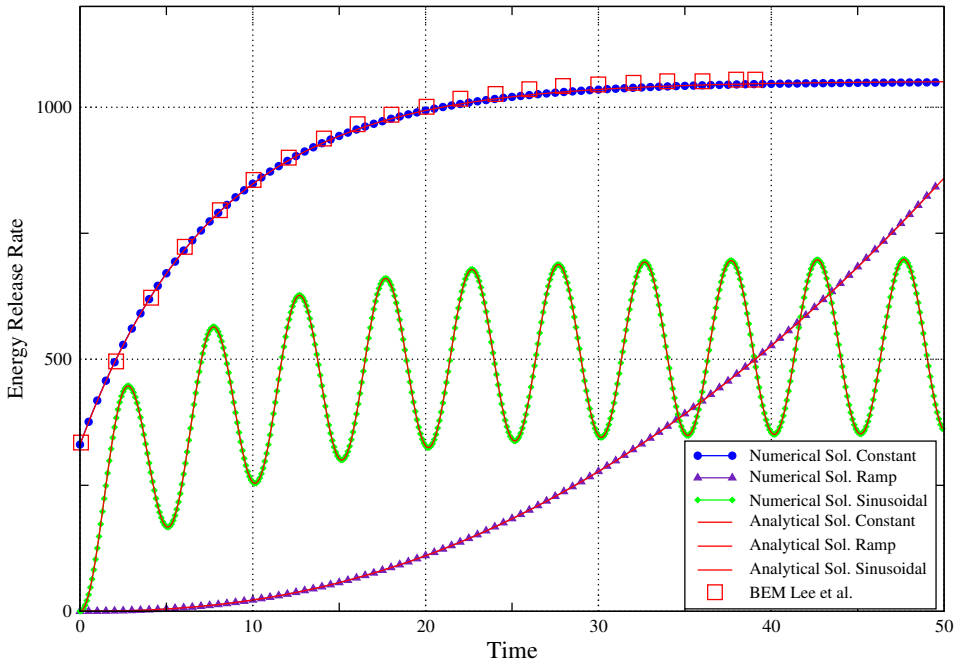

Figure 3.11: *Time dependent Energy Release Rate for material functions with different time dependence.*

In this last example and the second part of Example 3.5.1, we look at the case when the material functions don't have the same time dependency. This means that Poisson's ratio is not constant in time. Even though, this violates one of the first assumptions made at the beginning of this Chapter, results show good agreement with Lee's solutions. The use of two material functions in our derivation relaxes the constrain of a constant Poisson's ratio. This type of problem can not

be solved using Schapery's work of fracture method [149], because he used only one material function (creep compliance) to characterize the material behavior.

The two examples presented in this Chapter are simple enough to understand the methodology to obtain an important crack front parameter in linear viscoelasticity (ERR) using the convenient relation to an elastic reference problem. Stress intensity factors for the elastic problems were found in literature. However, this is not always possible. Therefore, a numerical method for the analysis and computation of stress intensity factors is presented in the next Chapter.

Chapter 4

Numerical Analysis of Static Cracks in Linear Viscoelasticity with the GFEM

In the previous Chapter a detailed formulation of a crack front parameter (ERR) for linear viscoelasticity was presented. This ERR is useful to characterize the fracture behavior in viscoelastic materials. ERR can be computed using Equations (3.22), (3.23) and (3.24) or Equation (3.25). Inherent in either procedure is a need to analyze and solve a reference elastic problem in order to compute stress intensity factors. In examples 3.5, the reference elastic problem had an analytical solution for SIFs and therefore a numerical approach was not necessary. Here, on the other had, we aim to study much more complex problems. Therefore, the objective of this Chapter is to solve three dimensional fracture problems in linear viscoelasticity with a numerical method called Generalized Finite Element Method (GFEM).

Many theoretical and experimental research has been done to understand the behavior of fracture in viscoelastic media [18, 19, 145–147, 149], but limited literature exist for numerical application in this area. In finite elements for example, fracture behavior of polymer matrix composites has been studied by Mackerle [103]. Using the boundary element method (BEM) Syngellakis et al. [167] solved polymer fracture problems. He use a Laplace transform domain and a time domain to solved 2-D viscoelastic problems. In the Laplace transform domain, he solved a series of reference elastic problems where the material constants were replaced by material functions of p (transform parameter) in the transform domain. Then he computed the time-dependent response using Schaperys numerical inversion method [143]. He concluded that although the transform domain gives accurate solutions, it dependents on the transform inversion method and the choice of range and distribution of the transform parameters. Increasing the number of the transform parameters domain solutions imposes a heavy computational penalty on the final output [166]. In the

time domain, he obtained fundamental solutions using relations specific to a viscoelastic material model. In other words, the solution of a specific viscoelastic model is found by applying the correspondence principle and the inverse Laplace transform. This is done analytically as long as the material functions are simple enough and in some cases it may be impossible to find a convenient form of the appropriate fundamental solution.

Yu et al. [183] used the Extended Finite Element Method (*XFEM*) to model 2-D cracked viscoelastic media. He computed time-dependent energy release rate (ERR) components for modes I and II. He implemented an incremental method of viscoelasticity in *XFEM*. This nonlinear analysis of viscoelasticity is very common in numerical methods and a good literature review by Zocher et al. can be found in [186]. The key differences of his implementation is the use of enrichment functions for cracks and the extraction of ERR at each time step. The author of this dissertation has also implemented an incremental method for viscoelasticity in a Generalized Finite Element Method (GFEM) code. Details about this implementation can be found in Section 2.4. This nonlinear solver for viscoelasticity is used for verification (Example 4.3.2) of the correspondence principle method presented in the previous Chapter.

This Chapter focuses in the numerical simulation of 3-D viscoelastic fracture problems using GFEM. In contrast with other methods, here the numerical problem is only solved once and is enough to compute the viscous solution in time. This reduces the simulation time significantly compared to an incremental formulation of viscoelastic fractured media.

The reminder of this Chapter is as follows: Section 4.1 poses the viscoelastic static fracture problem to be solved using the generalized finite element method (GFEM). Section 4.2 describes the basic concepts of GFEM and the construction of enrichment functions used in the elastic reference problem. This method however, is not limited to linear elastic materials. As a matter of fact, an implementation of viscoelasticity in GFEM is used in Example 4.3.2. Numerical examples are presented in Section 4.3 and a reflective crack problem is solved in Section 4.4.

4.1 Problem Description

Consider the same three dimensional domain Ω with boundary $\partial\Omega$ in a three dimensional space as in Section 3.1. The boundary is subdivided into Γ^u, Γ^σ and Γ^c; displacements and tractions are prescribed accordingly.

The material is linear viscoelastic, homogeneous and isotropic. The equilibrium equations, the stress-strain relations and the strain-displacement relations are given by Equations (2.51)-(2.54). The boundary conditions are given by Equations (3.1)-(3.3).

From this problem we create a reference elastic problem with a three dimensional domain Ω^e with boundary $\partial\Omega^e$ in a three dimensional space as illustrated in Figure 4.1. Assume a linear elastic, homogeneous and isotropic material for this reference problem. The boundary is subdivided in a similar manner as the viscoelastic problem.

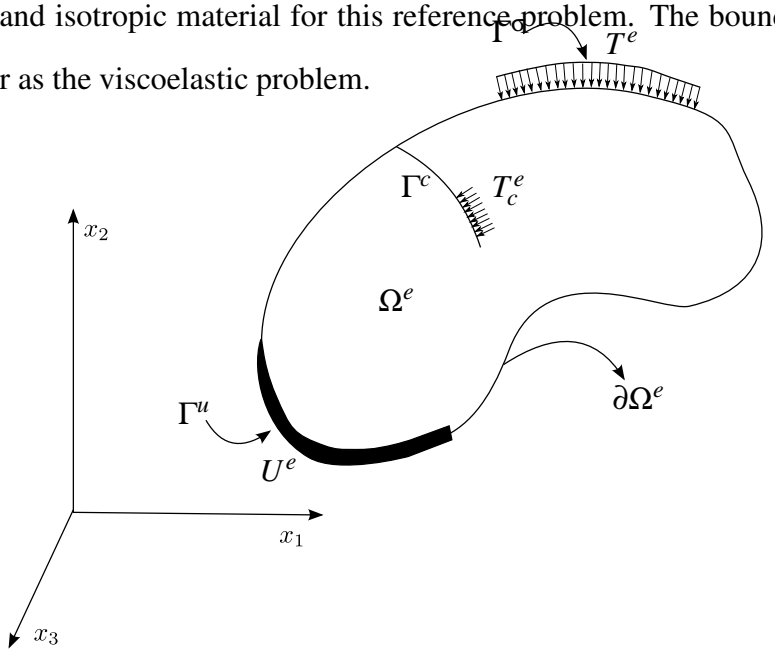

Figure 4.1: *Reference elastic three dimensional boundary value problem with a crack.*

Equilibrium equations for the reference elastic problem are

$$\frac{\partial \sigma_{ij}^e(\boldsymbol{x})}{\partial x_i} + F_j^e(\boldsymbol{x}) = 0 \tag{4.1}$$

where σ_{ij}^e is the Cauchy stress tensor and F_j^e are body forces.

The constitutive relations are given by

$$\sigma^e_{ij}(\boldsymbol{x}) = 2\,G_0\,[\varepsilon^e_{ij}(\boldsymbol{x}) - \frac{1}{3}\,\varepsilon^e_{kk}(\boldsymbol{x})\,\delta_{ij}] \;+\; K_0\,\varepsilon^e_{kk}(\boldsymbol{x})\,\delta_{ij} \tag{4.2}$$

where G_0 and K_0 are the instantaneous shear and bulk modulus of the linear viscoelastic problem, respectively, and δ_{ij} is the Kronecker delta.

The strain-displacement relations for small deformations are given by is

$$\varepsilon^e_{ij}(\boldsymbol{x}) = \frac{1}{2}\left[\frac{\partial u^e_i(\boldsymbol{x})}{\partial x_j} + \frac{\partial u^e_j(\boldsymbol{x})}{\partial x_i}\right] \tag{4.3}$$

Boundary conditions

$$\sigma^e_{ij}(\boldsymbol{x})n_i(\boldsymbol{x}) = T^e_j(\boldsymbol{x}) = T_j(\boldsymbol{x},t_{peak}) \quad \text{on } \Gamma^\sigma \tag{4.4}$$

$$u^e_j(\boldsymbol{x}) = U^e_j(\boldsymbol{x}) \quad \text{on } \Gamma^u \tag{4.5}$$

$$\sigma^e_{ij}(\boldsymbol{x})n_i(\boldsymbol{x}) = T^e_{cj}(\boldsymbol{x}) = T_{cj}(\boldsymbol{x},t_{peak}) \quad \text{on } \Gamma^c \tag{4.6}$$

with $T(\boldsymbol{x},t)$ as the tractions imposed on the viscoelastic problem and t_{peak} as the time when the maximum load is acting on the boundary.

Note that this reference elastic problem is not time dependent. Later, to introduce time in the linear viscoelastic computations, the function $\lambda(t)$ is used. This function is related to the time dependent loads (tractions applied at the boundary and body forces) and it scales the stress intensity factors computed in the reference problem. This is possible because the linear relation that exists between the applied loads and the stress intensity factor in linear elasticity. This function was presented earlier in Section 3.1.

To find the weak formulation of the reference elastic problem described above, let the set of

kinematically admissible displacement fields be

$$\tilde{H}^1(\Omega^e) = \left\{ \boldsymbol{u}^e, u_j^e(\boldsymbol{x}) \mid u_j^e(\boldsymbol{x}) \in H^1(\Omega^e),\ u_j^e(\boldsymbol{x}) = U_j^e(\boldsymbol{x}) \quad \text{on } \Gamma^u \right\} \quad j = 1,2,3$$

where H^1 is the first order Hilbert space.

Let the space of virtual kinematically admissible displacement fields be

$$\overset{o}{H}{}^1(\Omega^e) = \left\{ \boldsymbol{v}^e, v_j^e(\boldsymbol{x}) \mid v_j^e(\boldsymbol{x}) \in H^1(\Omega^e),\ v_j^e(\boldsymbol{x}) = 0 \quad \text{on } \Gamma^u \right\} \quad j = 1,2,3$$

The weak form of the equilibrium equations can be stated as follows.

$$\begin{aligned} &\textit{Find } \boldsymbol{u}^e \in \tilde{H}^1(\Omega^e) \textit{ such that} \\ &B\left(\boldsymbol{u}^e, \boldsymbol{v}^e\right) = L\left(\boldsymbol{v}^e\right) \ \forall\ \boldsymbol{v}^e \in \overset{o}{H}{}^1 \end{aligned} \tag{4.7}$$

where $B(\cdot,\cdot)$ and $L(\cdot)$ are the bilinear and linear forms, respectively, and are given by

$$\begin{aligned} B\left(\boldsymbol{u}^e, \boldsymbol{v}^e\right) &= \int_{\Omega^e} \varepsilon_{ij}^e\left(\boldsymbol{v}^e\right) \sigma_{ij}^e\left(\boldsymbol{u}^e\right) d\Omega^e \\ L\left(\boldsymbol{v}^e\right) &= \int_{\Omega^e} v_j^e(\boldsymbol{x})\, F_j^e(\boldsymbol{x})\, d\Omega^e + \int_{\Gamma^t} v_j^e(\boldsymbol{x})\, T_j^e(\boldsymbol{x})\, d\Gamma + \int_{\Gamma^c} v_j^e(\boldsymbol{x})\, T_{cj}^e(\boldsymbol{x})\, d\Gamma \end{aligned} \tag{4.8}$$

4.2 Overview of GFEM

The Generalized FEM can be regarded as a finite element method with shape functions built using the concept of a partition of unity. This method has its origins in the works of Babuška et al. [10, 12, 106] (under the names "special finite element methods", "generalized finite element method" and "finite element partition of unity method") and Duarte and Oden [39, 45–47, 119] (under the names "*hp* clouds" and "cloud-based *hp* finite element method"). Several meshfree methods proposed in recent years can also be viewed as special cases of the partition of unity method. Details on the mathematical formulation of the GFEM can be found in, e.g., [10, 41, 106, 119, 161].

In this Section, we summarize the main concepts of the method.

The linear finite element shape functions $\varphi_\alpha,\ \alpha = 1,\ldots,N$, in a finite element mesh with N nodes constitute a partition of unity, i.e.,

$$\sum_{\alpha=1}^{N} \varphi_\alpha(\boldsymbol{x}) = 1$$

for all $\boldsymbol{x}$ in a domain Ω^e covered by the finite element mesh. This is a key property used in partition of unity methods and, in particular, in the GFEM.

A GFEM shape function $\phi_{\alpha i}$ is built from the product of a FE shape function φ_α and an enrichment function $L_{\alpha i}$

$$\phi_{\alpha i}(\boldsymbol{x}) = \varphi_\alpha(\boldsymbol{x}) L_{\alpha i}(\boldsymbol{x}) \qquad \text{(no summation on } \alpha\text{)}, \tag{4.9}$$

where α is a node in the finite element mesh. Figure 4.2 illustrates the construction of GFEM shape functions.

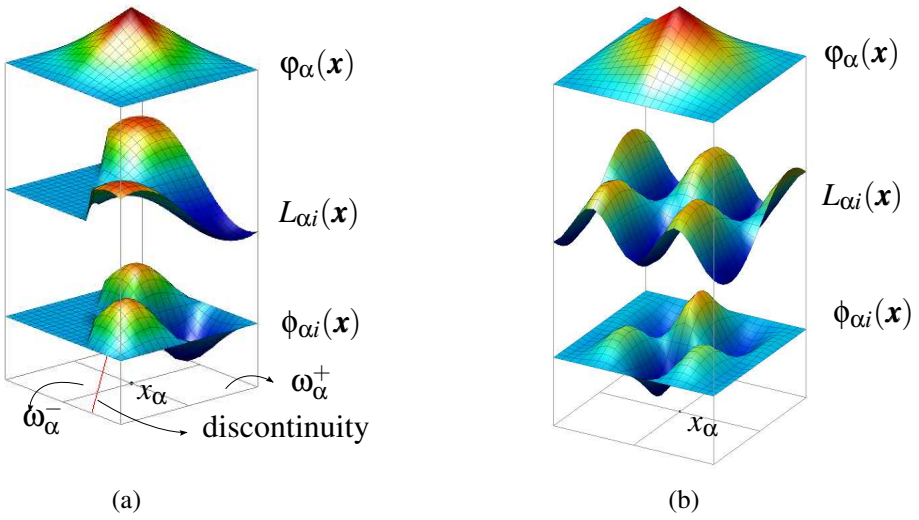

Figure 4.2: *Construction of a generalized FEM shape function using (a) a discontinuous piece-wise polynomial enrichment and (b) a custom-built enrichment. Here, φ_α is the function at the top, the enrichment function, $L_{\alpha i}$, is shown in the middle, and the generalized FE shape function, $\phi_{\alpha i}$, is the resulting bottom function.*

Features such as discontinuities or material interfaces are represented by a judicious choice of enrichment functions $L_{\alpha i}(\boldsymbol{x})$, instead of using a finite element mesh with element faces meticu-

lously placed along the discontinuities or interfaces. Several enrichment functions can be hierarchically added to any node α in a finite element mesh. Thus, if D_L is the number of enrichment functions at node α, the GFEM approximation, $\boldsymbol{u}^{e(hp)}$, of a function $\boldsymbol{u}^e$ can be written as

$$\begin{aligned}\boldsymbol{u}^{e(hp)}(\boldsymbol{x}) &= \sum_{\alpha=1}^{N}\sum_{i=1}^{D_L} \underline{\boldsymbol{u}}^e_{\alpha i}\phi_{\alpha i}(\boldsymbol{x}) = \sum_{\alpha=1}^{N}\sum_{i=1}^{D_L} \underline{\boldsymbol{u}}^e_{\alpha i}\varphi_\alpha(\boldsymbol{x})L_{\alpha i}(\boldsymbol{x}) \\ &= \sum_{\alpha=1}^{N}\varphi_\alpha(\boldsymbol{x})\sum_{i=1}^{D_L} \underline{\boldsymbol{u}}^e_{\alpha i}L_{\alpha i}(\boldsymbol{x}) = \sum_{\alpha=1}^{N}\varphi_\alpha(\boldsymbol{x})\boldsymbol{u}^{e(hp)}_\alpha(\boldsymbol{x}),\end{aligned}$$

where $\underline{\boldsymbol{u}}^e_{\alpha i},\ \alpha = 1,\ldots,N,\ i = 1,\ldots,D_L$, are nodal degrees of freedom and $\boldsymbol{u}^{e(hp)}_\alpha(\boldsymbol{x})$ is a local approximation of $\boldsymbol{u}^e$ defined on $\omega_\alpha = \{\boldsymbol{x} \in \Omega^e : \varphi_\alpha(\boldsymbol{x}) \neq 0\}$, the support of the partition of unity function φ_α. In the case of a finite element partition of unity, the support ω_α (often called a cloud or a patch) is given by the union of the finite elements sharing a vertex node $\boldsymbol{x}_\alpha$ [41]. These local approximations, $\boldsymbol{u}^{e(hp)}_\alpha(\boldsymbol{x})$, belong to local spaces $\chi_\alpha(\omega_\alpha) = \text{span}\{L_{i\alpha}\}_{i=1}^{D_L}$ defined on the cloud $\omega_\alpha,\ \alpha = 1,\ldots,N$. The selection of the enrichment or basis functions for a particular local space $\chi_\alpha(\omega_\alpha)$ depends on the local behavior of the function $\boldsymbol{u}^e$ over the cloud ω_α. In the case of a fracture mechanics problem for example, the discontinuities in the displacement field can be approximated independently of the underlying finite element mesh. For instance, the elasticity solution $\boldsymbol{u}^e$ may be written as

$$\boldsymbol{u}^e = \hat{\boldsymbol{u}}^e + \tilde{\tilde{\boldsymbol{u}}}^e + \breve{\boldsymbol{u}}^e \tag{4.10}$$

where $\hat{\boldsymbol{u}}^e$ is a continuous function, $\tilde{\tilde{\boldsymbol{u}}}^e$ is a discontinuous function but non-singular and $\breve{\boldsymbol{u}}^e$ is a discontinuous and singular function.

Any *a priori* knowledge about the solution $\boldsymbol{u}^e$ is used to select basis functions for a local space $\chi_\alpha(\omega_\alpha)$. For the discontinuous part of the domain, for example, discontinuous functions like the one shown in Figure 4.2(a) can be used as enrichment functions [44, 108, 156, 163, 179]. At nodes near a crack front, expansions of the elasticity solution in the neighborhood of a crack (Westergaard functions) can be taken as enrichment functions as described in [41, 42, 108, 117, 118, 163]. Both are discussed in Section 4.2.1. Other custom-built enrichment functions shown in Figure 4.2(b)

that are solutions of local boundary value problems can also be used [40, 43, 162]. These so-called global-local enrichment functions are briefly described in Section 5.1. The main strength of the generalized FEM, is the freedom to choose any enrichment function, polynomial or not. More details about different enrichment functions can be found in the next sections.

4.2.1 Enrichment Functions for 3-D Cracks

In this section, enrichment functions for 3-D cracks are briefly described; further details can be found in [128]. Cosider a three-dimensional (3-D) domain with a crack surface representation inside. The explicit crack surface describes the location of the discontinuities and singularities in the body. Figure 4.3 shows the details. Light blue lines are intersections of the crack surface with the 3-D domain boundary, while red lines represent the crack front.

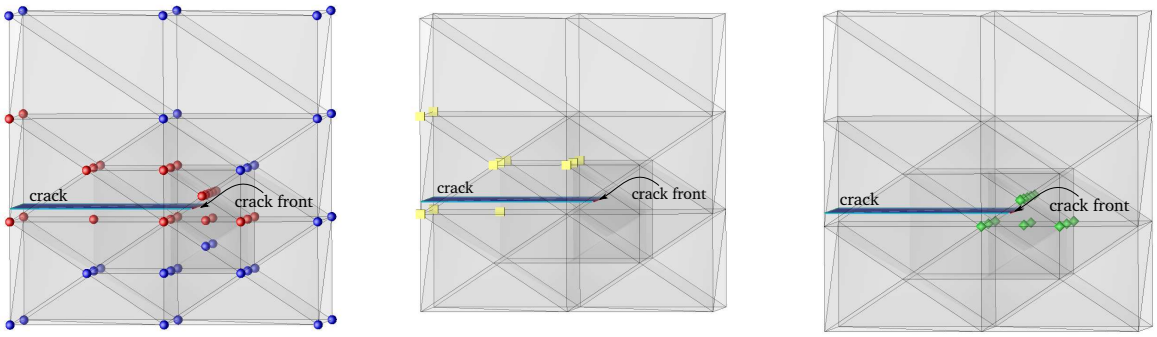

(a) Blue glyphs show enrichments for clouds ω_α that do not intersect the crack surface.

(b) Yellow glyphs show high-order step function enrichments for clouds ω_α

(c) Green glyphs show crack front enrichments for clouds ω_α

Figure 4.3: *Enrichment Functions for 3-D Cracks.*

In this fracture problem, three types of enrichment functions are considered.

(i) Enrichment for clouds ω_α that do not intersect the crack surface.

In this case, the elasticity solution $\boldsymbol{u}^e$ is continuous over ω_α. A local approximation, $\hat{\boldsymbol{u}}^e(\boldsymbol{x})$ of $\boldsymbol{u}^e$ over ω_α can be written as

$$\hat{\boldsymbol{u}}_\alpha^{e(hp)}(\boldsymbol{x}) = \sum_{i=1}^{\hat{D}_L} \underline{\hat{\boldsymbol{u}}}_{\alpha i}^e \hat{L}_{\alpha i}(\boldsymbol{x}) \tag{4.11}$$

where $\hat{D}_L$ is the dimension of a set of polynomial enrichment functions. Our implementation follows [41, 119], and the enrichments functions $\{\hat{L}_{\alpha i}\}_{i=1}^{\hat{D}_L}$ for a cloud associated with node $\boldsymbol{x}_\alpha = (x_\alpha, y_\alpha, z_\alpha)$ are given by

$$\left\{\hat{L}_{\alpha i}\right\}_{i=1}^{\hat{D}_L} = \left\{1, \frac{(x-x_\alpha)}{h_\alpha}, \frac{(y-y_\alpha)}{h_\alpha}, \frac{(z-z_\alpha)}{h_\alpha}, \frac{(x-x_\alpha)^2}{h_\alpha^2}, \frac{(y-y_\alpha)^2}{h_\alpha^2}, \dots\right\} \tag{4.12}$$

with h_α being a scaling factor [41, 119]. Figure 4.3(a) shows blue glyphs at the location of these continuous enrichments. The red glyphs correspond to a combination of this continuous enrichments and other enrichments discussed next.

Notice that enrichment functions can be added hierarchically to any node α in the domain. This results in high-order approximations of the displacement field at the corresponding cloud. This can be compared to the use of high-order elements in standard FEM, but the benefit of GFEM is that the user does not have to change its original FE mesh to achieve it.

(ii) Enrichment for clouds completely cut by the crack surface.

In this case, the crack surface divides ω_α into two sub-domains, ω_α^+ and ω_α^- such that $\omega_\alpha = \omega_\alpha^+ \cup \omega_\alpha^-$. With α belonging to a subset of indices in which corresponding clouds ω_α intersect the crack surface but not the crack front. The displacement field $\boldsymbol{u}^e$ for this case can be decomposed into:

$$\boldsymbol{u}^e = \hat{\boldsymbol{u}}^e + \tilde{\tilde{\boldsymbol{u}}}^e = \hat{\boldsymbol{u}}^e + \mathcal{H}\tilde{\boldsymbol{u}}^e \tag{4.13}$$

where $\hat{\boldsymbol{u}}^e$ and $\tilde{\boldsymbol{u}}^e$ are continuous functions and $\mathcal{H}(\boldsymbol{x})$ denotes a discontinuous function defined by

$$\mathcal{H}(\boldsymbol{x}) = \begin{cases} 1 & \text{if } \boldsymbol{x} \in \omega_\alpha^+ \\ 0 & \text{otherwise} \end{cases} \tag{4.14}$$

A local approximation, $\boldsymbol{u}_\alpha^{e(hp)}(\boldsymbol{x})$, of $\boldsymbol{u}^e$ over the selected ω_α can be written as

$$\boldsymbol{u}_\alpha^{e(hp)}(\boldsymbol{x}) = \hat{\boldsymbol{u}}_\alpha^{e(hp)}(\boldsymbol{x}) + \mathcal{H}\tilde{\boldsymbol{u}}_\alpha^{e(hp)}(\boldsymbol{x}) = \sum_{i=1}^{\hat{D}_L} \underline{\hat{\boldsymbol{u}}}_{\alpha i}^e \hat{L}_{\alpha i}(\boldsymbol{x}) + \sum_{i=1}^{\tilde{D}_L} \underline{\tilde{\boldsymbol{u}}}_{\alpha i}^e \mathcal{H}\hat{L}_{\alpha i}(\boldsymbol{x}) \tag{4.15}$$

where $\hat{\boldsymbol{u}}_{\alpha}^{e(hp)}(\boldsymbol{x})$ and $\tilde{\boldsymbol{u}}_{\alpha}^{e(hp)}(\boldsymbol{x})$ are local approximations of $\hat{\boldsymbol{u}}^{e}$ and $\tilde{\boldsymbol{u}}^{e}$, respectively, and $\hat{L}_{\alpha i}$ is a polynomial enrichment function previously defined. The enrichment functions are taken as

$$\mathcal{H}\hat{L}_{\alpha i}(\boldsymbol{x}) = \left\{\tilde{L}_{\alpha i}\right\}_{i=1}^{\tilde{D}_L} = \left\{\mathcal{H}, \mathcal{H}\frac{(x-x_{\alpha})}{h_{\alpha}}, \mathcal{H}\frac{(y-y_{\alpha})}{h_{\alpha}}, \mathcal{H}\frac{(z-z_{\alpha})}{h_{\alpha}}, \mathcal{H}\frac{(x-x_{\alpha})^2}{h_{\alpha}^2}, \ldots\right\} \tag{4.16}$$

These functions are known as high-order step functions and can approximate discontinuities in the solution $\boldsymbol{u}^{e}$ *inside* a finite element that belongs to the subset of clouds ω_{α} that intersect with the crack surface. Figure 4.3(b) shows yellow glyphs at the location where the GFEM shape functions are given by

$$\varphi_{\alpha} \times \left\{1, \frac{(x-x_{\alpha})}{h_{\alpha}}, \frac{(y-y_{\alpha})}{h_{\alpha}}, \frac{(z-z_{\alpha})}{h_{\alpha}}, \mathcal{H}, \mathcal{H}\frac{(x-x_{\alpha})}{h_{\alpha}}, \mathcal{H}\frac{(y-y_{\alpha})}{h_{\alpha}}, \mathcal{H}\frac{(z-z_{\alpha})}{h_{\alpha}}, \ldots\right\} \tag{4.17}$$

(iii) Enrichment for clouds that intersect the crack front.

Terms from the asymptotic expansion of the elasticity solution near a crack front are used as enrichment functions in clouds that intersect the crack front. Three dimensional asymptotic expansions are quite complex, especially at the regions where the crack surface intersects the domain boundary. Therefore, it is more practical to use two dimensional expansions of the elastic solution as enrichment functions in a finite size domain. As a result, in order to obtain good accuracy it is necessary to have a sufficiently fine mesh around the crack front.

The enrichment functions explained here are for all those nodes with indices α that belong to a subset in which their corresponding cloud ω_{α} intersect with the crack front. A local approximation $\breve{\boldsymbol{u}}_{\alpha}^{e(hp)}(\boldsymbol{x})$, of $\boldsymbol{u}^{e}$ over the cloud ω_{α} can be written as [41, 128]

$$\breve{\boldsymbol{u}}_{\alpha}^{e(hp)} = \sum_{i=1}^{2} \begin{bmatrix} \underline{\breve{u}}_{\alpha i}^{e(\xi)}\, \breve{L}_{\alpha i}^{\xi}(r,\theta) \\ \underline{\breve{u}}_{\alpha i}^{e(\eta)}\, \breve{L}_{\alpha i}^{\eta}(r,\theta) \\ \underline{\breve{u}}_{\alpha i}^{e(\zeta)}\, \breve{L}_{\alpha i}^{\zeta}(r,\theta) \end{bmatrix} \tag{4.18}$$

where ξ, η and ζ are directions in a Cartesian coordinate system at the crack front, r and θ are

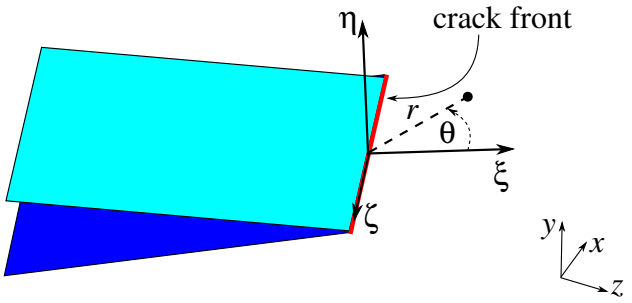

Figure 4.4: *Crack front coordinate system.*

polar coordinates, as illustrated in Figure 4.4, $\breve{u}^{e(\xi)}_{\alpha i}$, $\breve{u}^{e(\eta)}_{\alpha i}$ and $\breve{u}^{e(\zeta)}_{\alpha i}$ are degrees of freedom in the crack front coordinate system.

The enrichment functions are given by [41, 42, 117, 118],

$$
\begin{aligned}
\breve{L}^{\xi}_{\alpha 1}(r,\theta) &= \sqrt{r}\left[(\kappa^e - \frac{1}{2})\cos\frac{\theta}{2} - \frac{1}{2}\cos\frac{3\theta}{2}\right] \\
\breve{L}^{\eta}_{\alpha 1}(r,\theta) &= \sqrt{r}\left[(\kappa^e + \frac{1}{2})\sin\frac{\theta}{2} - \frac{1}{2}\sin\frac{3\theta}{2}\right] \\
\breve{L}^{\zeta}_{\alpha 1}(r,\theta) &= \sqrt{r}\sin\frac{\theta}{2} \\
\breve{L}^{\xi}_{\alpha 2}(r,\theta) &= \sqrt{r}\left[(\kappa^e + \frac{3}{2})\sin\frac{\theta}{2} + \frac{1}{2}\sin\frac{3\theta}{2}\right] \\
\breve{L}^{\eta}_{\alpha 2}(r,\theta) &= \sqrt{r}\left[(\kappa^e - \frac{3}{2})\cos\frac{\theta}{2} + \frac{1}{2}\cos\frac{3\theta}{2}\right] \\
\breve{L}^{\zeta}_{\alpha 2}(r,\theta) &= \sqrt{r}\sin\frac{3\theta}{2}
\end{aligned}
\tag{4.19}
$$

where the material constant $\kappa^e = 3 - 4\nu^e$ (assuming plane strain) is known as Kolosov's constan and ν^e is Poisson's ratio.

Notice that the basis functions come from the components of the asymptotic expansion of the elasticity solution of a straight crack front, far from the vertices and with a traction-free flat crack surface [168]. These are the first terms of Modes *I*, *II* and the first and second terms of the Mode *III*, which can approximate the singularity of the exact solution along the crack front and the discontinuity of the displacement field. For the x, y and z components of the displacement vector

the enrichment functions are given by the following expressions, respectively:

$$\varphi_\alpha \times \left\{ 1, \breve{L}^x_{\alpha 1}, \breve{L}^x_{\alpha 2}, \frac{(x-x_\alpha)}{h_\alpha}, \frac{(y-y_\alpha)}{h_\alpha}, \frac{(z-z_\alpha)}{h_\alpha}, \dots \right\},$$

$$\varphi_\alpha \times \left\{ 1, \breve{L}^y_{\alpha 1}, \breve{L}^y_{\alpha 2}, \frac{(x-x_\alpha)}{h_\alpha}, \frac{(y-y_\alpha)}{h_\alpha}, \frac{(z-z_\alpha)}{h_\alpha}, \dots \right\},$$

$$\varphi_\alpha \times \left\{ 1, \breve{L}^z_{\alpha 1}, \breve{L}^z_{\alpha 2}, \frac{(x-x_\alpha)}{h_\alpha}, \frac{(y-y_\alpha)}{h_\alpha}, \frac{(z-z_\alpha)}{h_\alpha}, \dots \right\}$$

Figure 4.3(c) shows green glyphs at the location where these GFEM shape functions are used. It is important to note that the basis functions (4.19) are defined in a coordinate system located along the crack front. Therefore, they must be transformed to the global Cartesian coordinate system (x, y, z) prior to their use in the definition of the just mentioned, GFEM shape functions. Details about this transformation can be found in [41, 42].

The numerical examples presented in this study show that the GFEM shape functions presented here, combined with sufficiently fine meshes at the crack front, are able to deliver accurate solution of stress intensity factors. The extraction of SIFs is done using the Contour Integral method (CIM) or the Cut-off Function Method (CFM), both explained in detail in Appendix A.

4.3 GFEM examples

In this section three example problems are solved using the correspondence principle method explained in Section 3.1. Furthermore, GFEM is used to solve the reference elastic models and compute stress intensity factors.

In the first problem Dirichlet type boundary condition are considered and the solution is compared to an analytical ERR expression. The second problem serves to verify the application of the correspondence principle (C.P.) by comparing results (crack mouth opening displacement CMOD) with the nonlinear implementation of viscoelasticity derived in Section 2.4. The last problem is a 3-D fracture problem solved using GFEM. There the solution is analyzed along the whole crack

front, and thus the ERR is not a curve dependent in time anymore but a surface.

4.3.1 Edge-crack Plate Under Displacements

Consider a viscoelastic plate with dimensions $b = 7$ m, $L = 16$ m and $t = 1$ m with a through the thickness edge crack of size $a = 3.5$ m. The plate is subjected to displacement boundary condition $\delta\lambda(t)$ in the form of three different types of functions; $\lambda(t) = 1$ (constant), $\lambda(t) = \frac{t}{t_{peak}}$ (ramp) and $\lambda(t) = |\sin(\frac{t\,\pi}{t_{peak}})|$ (sinusoidal). The maximum value of δ is 0.00156. The material is assumed

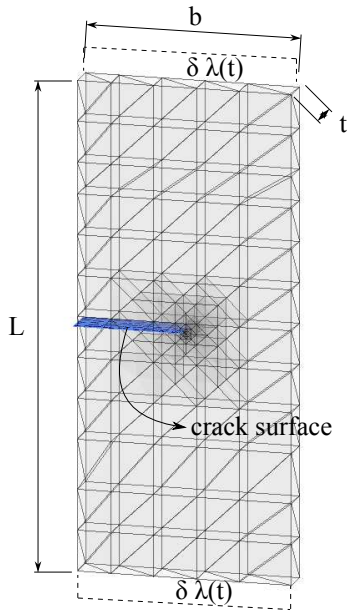

Figure 4.5: *Edge-crack Plate Under Displacements problem description.*

to be linear viscoelastic and the material moduli is characterized by a bulk and shear relaxation functions with same time dependence.

$$\begin{aligned} K(t) &= 300.00 + 169.02\, e^{-\frac{t}{269.484}}\ Pa \\ G(t) &= 230.00 + 112.68\, e^{-\frac{t}{269.484}}\ Pa \end{aligned} \tag{4.20}$$

The stress intensity factor $\mathcal{K}_I$ for the reference elastic problem is found using GFEM. There, the material modulus consider is the instantaneous and the displacement imposed is $\delta = 0.00156$. The

mesh and the crack surface can be seen in figure 4.5. GFEM shape functions of degree $p = 3$ are used. Furthermore, Heaviside and branch functions are used as enrichments to represent the discontinuity and singularity created by the presence of the crack. Details about GFEM enrichments for 3-D fracture problems can be found in [128, 129].

The stress intensity factor found is:

$$\mathcal{K}_I = 0.3801\ Nm^{(-3/2)} \tag{4.21}$$

Same as in previous examples, the Laplace transform functions $\bar{\bar{\lambda}}_2(p)$ for each load type are given by Equations (3.37)-(3.39) and the Laplace transform of the material functions is Equation (3.43).

The viscoelastic time-dependent ERR $\mathcal{G}_I(t)$ is obtained by using Equation (3.32) and computing its inverse Laplace transform. An analytical solution for plane strain, constant Poisson's ratio v and constant imposed displacement can be computed using the following equation given by Zhang [185].

$$\mathcal{G}_I(t) = \frac{1-v^2}{E}\,\mathcal{K}_I^2\, f_{Iu}(t) f_{I\sigma}(t) \tag{4.22}$$

with $f_{I\sigma}(t)$ and $f_{Iu}(t)$ as the time factors. The mathematical representation for these time factors is presented in [185]. For these particular material functions, they are as follows,

$$f_{Iu}(t) = H(t) \quad \text{Heaviside function} \tag{4.23}$$

and

$$f_{I\sigma}(t) = \frac{1}{1+\frac{E_1}{E_2}}\left(1 + \frac{E_1}{E_2} e^{-p_1 t}\right) \tag{4.24}$$

E_1 and E_2 correspond to the spring components of a standard linear body and p_1 is the relaxation time. The material functions of this problem can be converted to represent a standard linear body with $E_1 = 600$ Pa, $E_2 = 465$ Pa and $\eta_2 = 287x10^3$ Pa. s. The Poisson's ratio used in the conversion is $v = 0.0$.

Then, the analytical solution of this problem for a constant imposed displacement is

$$\mathcal{G}_I(t) = 9.7392x10^{-4} + 1.2567x10^{-4}e^{-\frac{t}{269.484}} \tag{4.25}$$

Also, YU et al. [183] solved the same problem for the case of a constant imposed displacement. He used a nonlinear viscoelastic implementation in *XFEM* and extracted energy release rate at every time step. The draw-back of using his method is that a *XFEM* problem needs to be solved for every time step. With the correspondence principle presented here only one reference elastic problem is solved using GFEM to obtain SIFs, then the solution is computed using Equations (3.32) and numerically inverting it to the time domain.

Figure 4.6 shows the solution computed here, YU's solution and Zhang's analytical solution for constant imposed displacement. Figure 4.7 shows the solution of all the load cases considered in this problem.

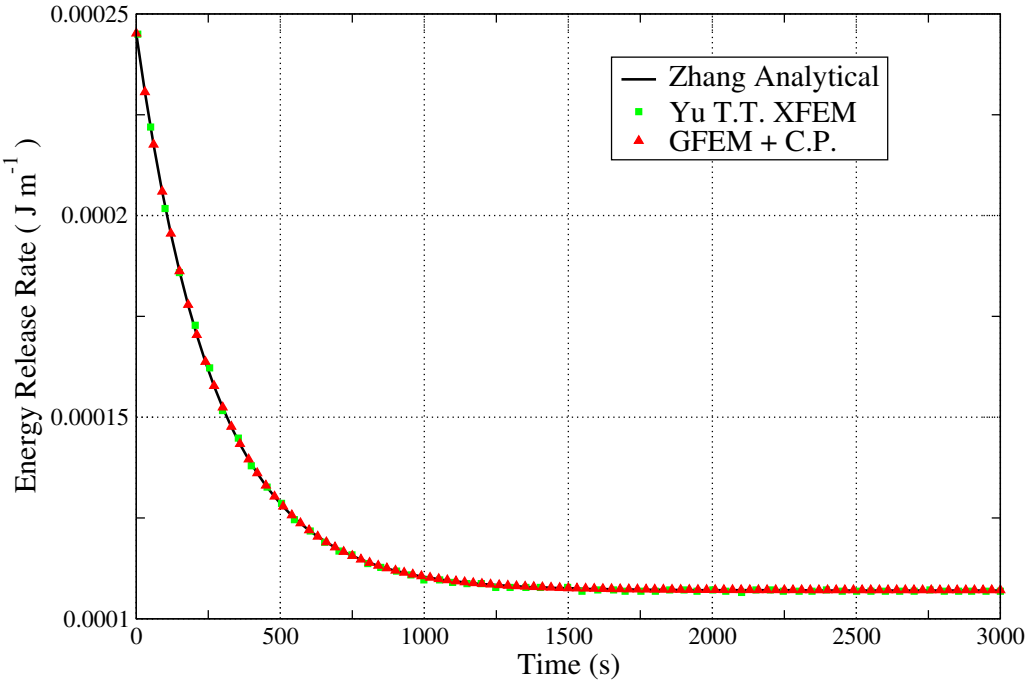

Figure 4.6: *Time dependent Energy Release Rate for material functions with same time dependence and constant imposed displacement.*

Now, consider the same problem but with the material functions having different time depen-

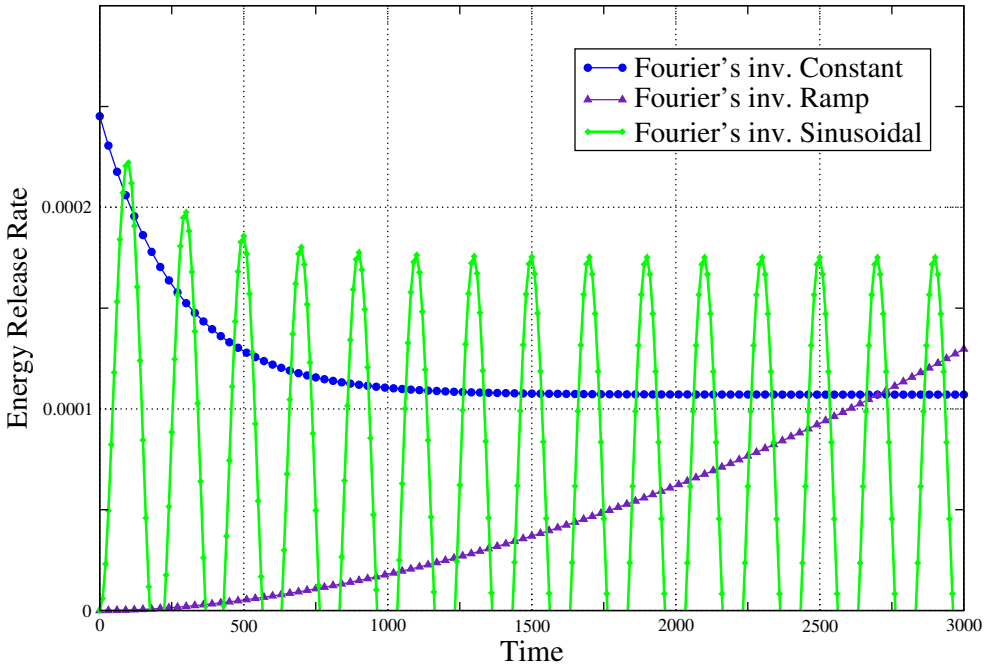

Figure 4.7: *Time dependent Energy Release Rate for material functions with same time dependence for constant, ramp and sinusoidal imposed displacements, using GFEM + C.P.*

dence. The volumetric relaxation function is constant while the shear function is time dependent.

$$\begin{aligned} K(t) &= 300.00\ Pa \\ G(t) &= 230.00 + 112.68\, e^{-\frac{t}{269.484}}\ Pa \end{aligned} \tag{4.26}$$

Similarly to previous, an analytical solution for plane strain and constant imposed displacement can be computed using Equation (4.22) and taking the corresponding time factors given in [185].

The computed analytical solution of this case is

$$\mathcal{G}_I(t) = 1.399x10^{-4} + 8.631x10^{-5}e^{-\frac{t}{269.484}} + 1.886x10^{-5}e^{-\frac{t}{490.605}} \tag{4.27}$$

Figure 4.8 shows the solution computed here and Zhang's analytical solution for constant imposed displacement and material functions with different time dependence.

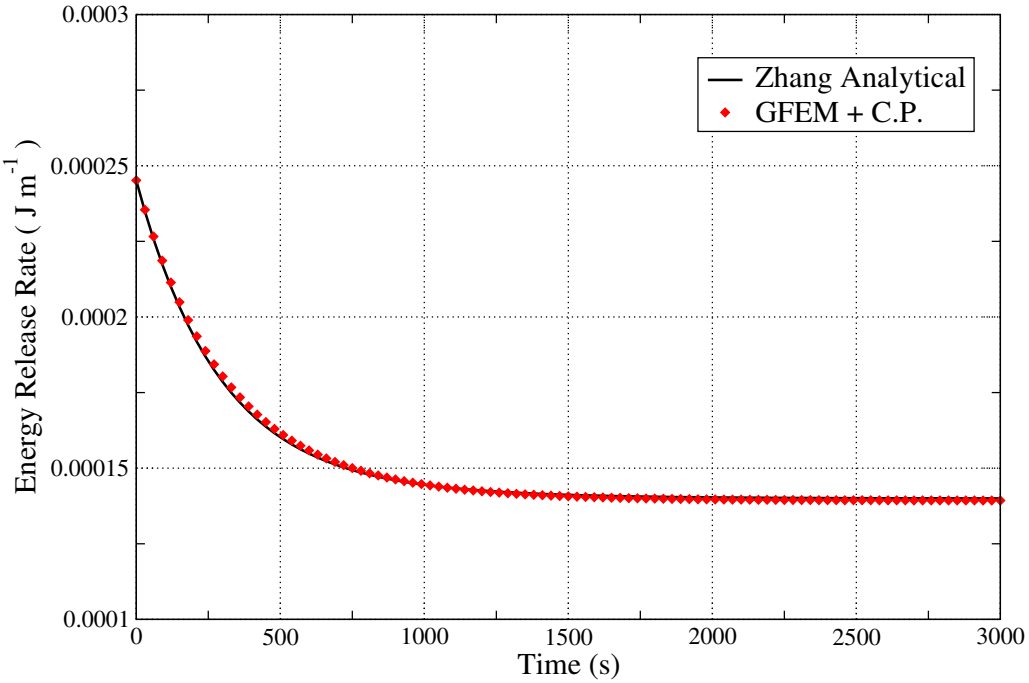

Figure 4.8: *Time dependent Energy Release Rate for material functions with different time dependence and constant imposed displacement.*

4.3.2 Center cracked plate

This problem consists of a rectangular plate with an inserted crack through the entire thickness, as illustrated in Figure 4.9(a). The model is subject to a uniform load $\sigma\lambda(t)$ at top and bottom faces of the domain. Three different time functions for the load are examined; $\lambda(t) = 1$ (constant), $\lambda(t) = \frac{t}{t_{peak}}$(ramp) and a sinusoidal load.

The dimensions of the plate are: $H = 30$ cm and $w = 10$ cm. The material properties are linear viscoelastic, isotropic and are represented by the Prony series shown in Table 4.1.

A crack is inserted in the center of the plate with a dimension of $a = 3.0$ cm. Three different methodologies are used to solve this problem. The first one corresponds to the nonlinear formulation described in Section 2.4. The second is to use the correspondence principle with a 2-D analytical solution of a reference elastic problem. Finally, the third method consists on using again the correspondence principle but this time with a GFEM reference elastic problem.

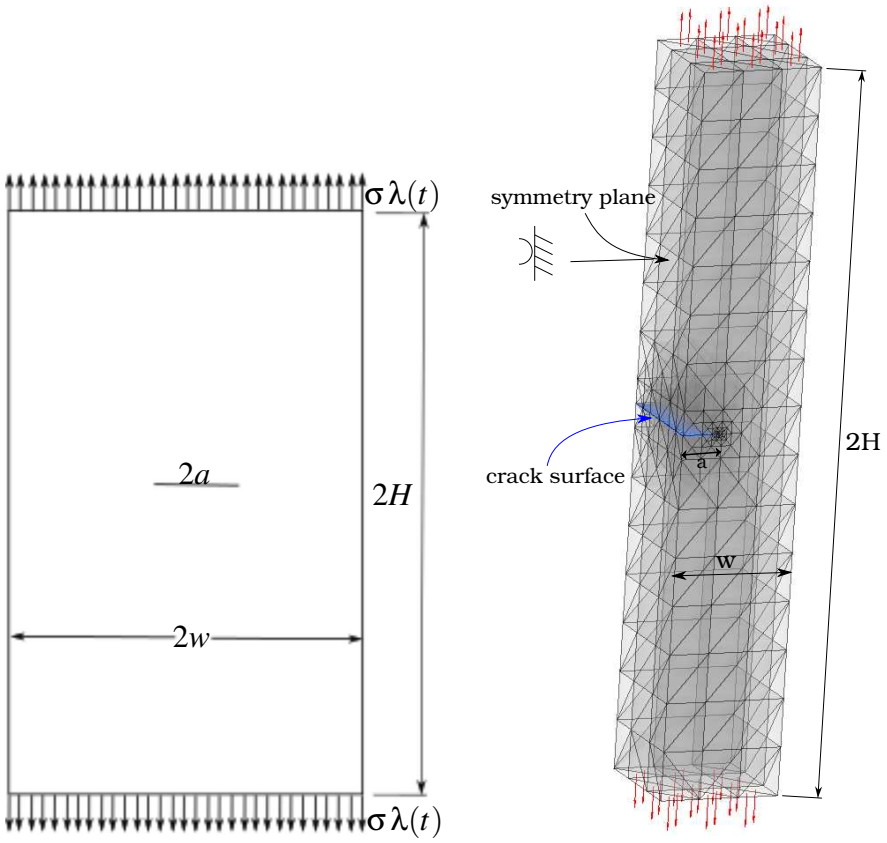

(a) Problem description. (b) GFEM mesh details.

Figure 4.9: *Center crack plate problem details.*

Non-linear solver

Here, the simulation consists of solving the problem for each time increment using the nonlinear formulation presented in Section 2.4. At each time step the crack mouth opening displacement (CMOD) is measured. To reduce the simulation time, and because of the symmetry of the problem, only the right half of the problem is modeled. Figure 4.9(b) shows the GFEM mesh including the position of the crack surface.

The discontinuity and singularity of the crack is modeled via enrichments as described in Section 4.2.1. Also, the resulting polynomial order used to approximate the continuous part of the problem is $p - order = 3$.

The total simulation time is 240 seconds and it is divided in 100 steps with a fixed increment of 2.4 seconds. Solutions for all load types are shown in Figure 4.10.

Table 4.1: *Mathematical representation of the viscoelastic material (Prony series).*

m	G_m (MPa)	K_m (MPa)	ρ_m (s)
1	74.633	161.705	2e-2
2	108.87	235.88	2e-1
3	213.12	461.77	2
4	231.59	501.78	2e1
5	149.26	323.40	2e2
6	60.013	130.03	2e3
7	15.773	34.174	2e4
8	5.3088	11.502	2e5
9	1.4155	3.0669	2e6
10	0.3041	0.6589	2e7
11	0.3696	0.8008	2e8
$G_0 = 861.54$ and $K_0 = 1866.67$			

Correspondence Principle with 2-D Analytical Solution

In this section, the problem is solved using the correspondence principle with an analytical solution of the reference elastic problem. The 2-D linear elastic solution (CMOD) for this problem is given by [170].

$$\delta^e_{CMOD} = \sigma\,\lambda(t)\,a\left[\frac{3}{G^e + 3\,K^e} + \frac{1}{G^e}\right] V_I\left(\frac{a}{w}\right) \tag{4.28}$$

with

$$V_I\left(\frac{a}{w}\right) = -0.071 - 0.535\left(\frac{a}{w}\right) + 0.169\left(\frac{a}{w}\right)^2 - 0.090\left(\frac{a}{w}\right)^3 + 0.020\left(\frac{a}{w}\right)^4 - 1.071\frac{w}{a}\,ln\left(1 - \frac{a}{w}\right)$$

Writing Equation (4.28) in the Laplace domain,

$$\bar{\bar{\delta}}^e_{CMOD} = \sigma\,\bar{\bar{\lambda}}(p)\,a\left[\frac{3}{G^e + 3\,K^e} + \frac{1}{G^e}\right] V_I\left(\frac{a}{w}\right) \tag{4.29}$$

Using the correspondence principle, the viscoelastic CMOD in Laplace domain is

$$\bar{\bar{\delta}}^{v}_{CMOD} = \sigma\,\bar{\bar{\lambda}}(p)\,a\left[\frac{3}{p\,\bar{\bar{G}}(p)+3\,p\,\bar{\bar{K}}(p)}+\frac{1}{p\,\bar{\bar{G}}(p)}\right]V_I\left(\frac{a}{w}\right) \tag{4.30}$$

Correspondence Principle with GFEM

This method consists of using the correspondence principle with a GFEM reference elastic problem. The GFEM reference elastic problem has the same mesh and boundary conditions as the nonlinear problem, see Figure 4.9(b). The only difference is that the material properties are considered linear elastic and therefore the instantaneous shear and bulk modulus are used as the elastic material constants.

After solving the numerical reference elastic numerical problem with GFEM, the CMOD is computed,

$$\delta^{e}_{CMOD} = 0.51538\,cm$$

In linear elasticity, the CMOD is inversely proportional to the material stiffness (Cf. Equation (4.28)). Therefore other CMODs for different material constants and load in the linear elastic regime can be computed using,

$$\delta^{e}_{CMOD}(t) = \frac{\delta^{e}_{CMOD}(0)\,E^{e}_{0}}{E^{e}_{t}}\,\lambda(t)$$

with $\delta^{e}_{CMOD}(0)$ as the initially computed CMOD, E^{e}_{0} the elastic material constant used to compute the initial CMOD, E^{e}_{t} as an elastic material constant and $\lambda(t)$ the value for the load function for time t.

Changing the material constants to the deviatoric and volumetric parts we have,

$$\delta^{e}_{CMOD}(t) = \frac{\delta^{e}_{CMOD}(0)\,G^{e}_{0}\,K^{e}_{0}\left(3\,K^{e}_{t}+G^{e}_{t}\right)}{G^{e}_{t}\,K^{e}_{t}\left(3\,K^{e}_{0}+G^{e}_{0}\right)}\,\lambda(t) \tag{4.31}$$

Transforming Equation (4.31) to the Laplace domain we get,

$$\delta^e_{CMOD}(p) = \frac{\delta^e_{CMOD}(0)\, G^e_0\, K^e_0 \left(3\, K^e_t + G^e_t\right)}{G^e_t\, K^e_t \left(3\, K^e_0 + G^e_0\right)} \bar{\bar{\lambda}}(p)$$

Finally applying the correspondence principle and knowing that $G^e_0 = G_0$ and $K^e_0 = K_0$ correspond to the viscoelastic instantaneous shear and bulk modulus:

$$\bar{\bar{\delta}}^v_{CMOD}(p) = \frac{\delta^e_{CMOD}\, G_0\, K_0 \left(3\, p\bar{\bar{K}}(p) + p\bar{\bar{G}}(p)\right)}{p\bar{\bar{G}}(p)\, p\bar{\bar{K}}(p) \left(3\, K_0 + G_0\right)} \bar{\bar{\lambda}}(p) \tag{4.32}$$

δ^e_{CMOD} is the CMOD computed with the GFEM reference elastic problem using the instantaneous shear and bulk modulus as elastic material constants.

Equations (4.30) and (4.32) are transformed back to the time domain giving the time-dependent CMOD for the linear viscoelastic material. This transformation can be performed numerically using Equation (3.35).

The Laplace transform of the load functions $\lambda(t)$ are as follows.

For a constant load $\lambda(t) = 1$,

$$\bar{\bar{\lambda}}(p) = \mathfrak{L}\left\{\lambda(t) = 1.0\right\} = \frac{1}{p} \tag{4.33}$$

For a ramp load $\lambda(t) = \frac{t}{t_{peak}}$,

$$\bar{\bar{\lambda}}(p) = \mathfrak{L}\left\{\lambda(t) = \frac{t}{t_{peak}}\right\} = \frac{1}{t_{peak}\, p^2} \tag{4.34}$$

For a sinusoidal load $\lambda(t) = \frac{1}{2} - \frac{\cos(\frac{\pi t}{t_{peak}})}{2}$,

$$\bar{\bar{\lambda}}(p) = \mathfrak{L}\left\{\lambda(t) = \frac{1}{2} - \frac{\cos(\frac{\pi t}{t_{peak}})}{2}\right\} = \frac{1}{2\, p} - \frac{p}{2\,(p^2 + \frac{\pi^2}{t^2_{peak}})} \tag{4.35}$$

The Prony series function in Laplace domain is given by,

$$\bar{\bar{G}}(p) = G_\infty + \sum_m^M \frac{G_m}{\frac{1}{\rho_m} + p} \tag{4.36}$$

$$\bar{\bar{K}}(p) = K_\infty + \sum_m^M \frac{K_m}{\frac{1}{\rho_m} + p} \tag{4.37}$$

where G_∞ and K_∞ are the long-time equilibrium shear and bulk modulus, respectively.

With all these equations, we can quickly compute the time-dependent CMOD for the linear viscoelastic material. Figure 4.10 shows the results for all load types using the correspondence principle with the analytical solution compared to the nonlinear analysis.

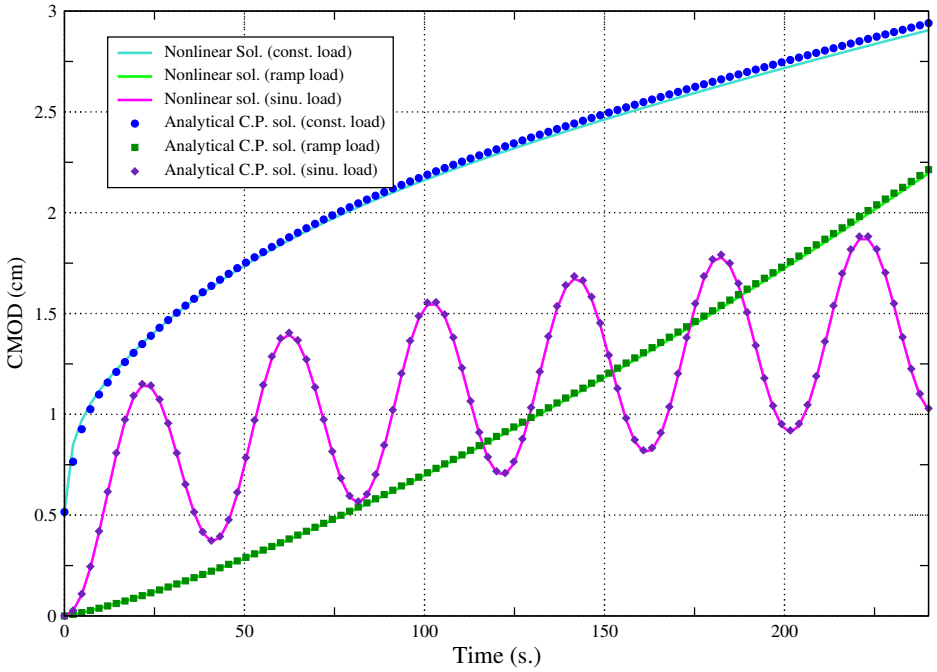

Figure 4.10: *The time-dependent CMOD. Non-linear analysis vs. correspondence principle with analytical solution.*

Figure 4.11 shows the results for all load types using the correspondence principle with GFEM compared to the nonlinear analysis. Notice the good agreement in the results.

Just to verify that results are not frequency dependent, we solve again the problem with the sinusoidal load with the three methodologies using $t_{peak} = 2$s. and $t_{peak} = 0.2$ s. Figures 4.12 and

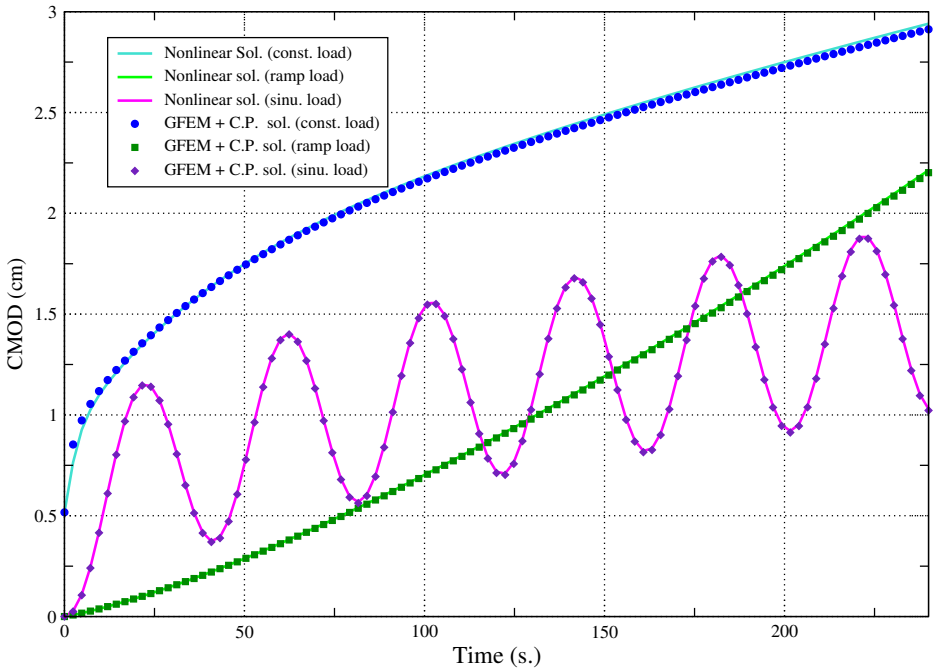

Figure 4.11: *The time-dependent CMOD. Non-linear analysis vs. correspondence principle with GFEM.*

4.13 show the results.

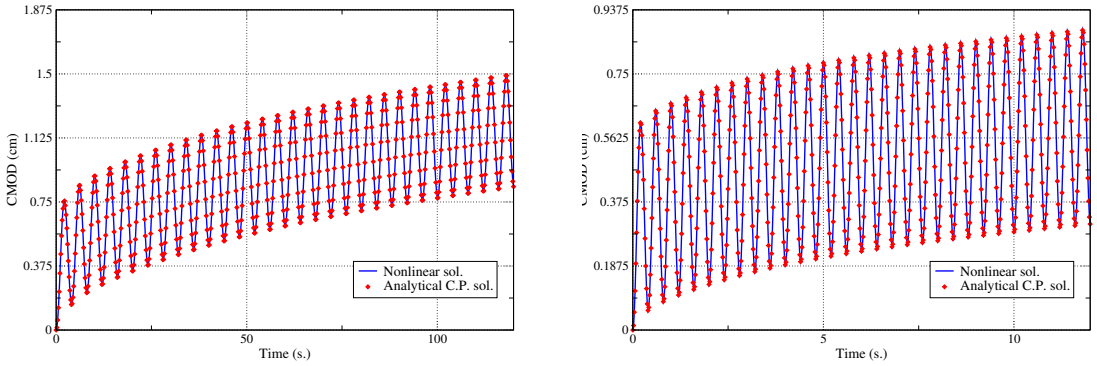

(a) CMOD for sinusoidal load with $t_{peak} = 2$s. (b) CMOD for sinusoidal load with $t_{peak} = 0.2$s.

Figure 4.12: *Time dependent CMOD. Non-linear analysis vs correspondence principle with analytical solution.*

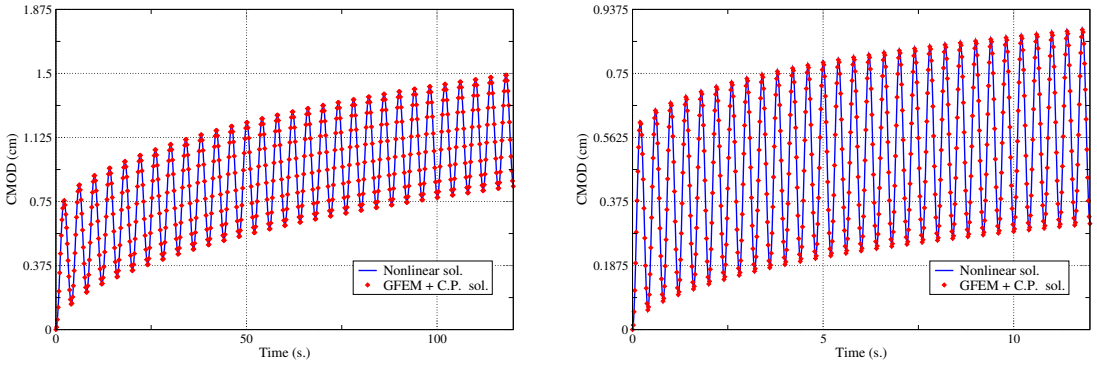

(a) CMOD for sinusoidal load with $t_{peak} = 2$ s.

(b) CMOD for sinusoidal load with $t_{peak} = 0.2$ s.

Figure 4.13: *Time dependent CMOD. Non-linear analysis vs correspondence principle with GFEM.*

4.3.3 Inclined Elliptical Crack

For this problem, an elliptical crack surface is inserted into a viscoelastic cube. The crack surface has an inclination of 30° with respect to the horizontal axis. The ratio between the minor and major axes of the crack surface is $\frac{a}{c} = \frac{9}{15}$. The cube dimension is taken as $\frac{c}{b} = \frac{3}{40}$. Details are shown in Figure 4.14.

The linear viscoelastic material properties are described by a Prony series shown in Table 4.2. The simulation time is 20 seconds and the temperature is 20° C.

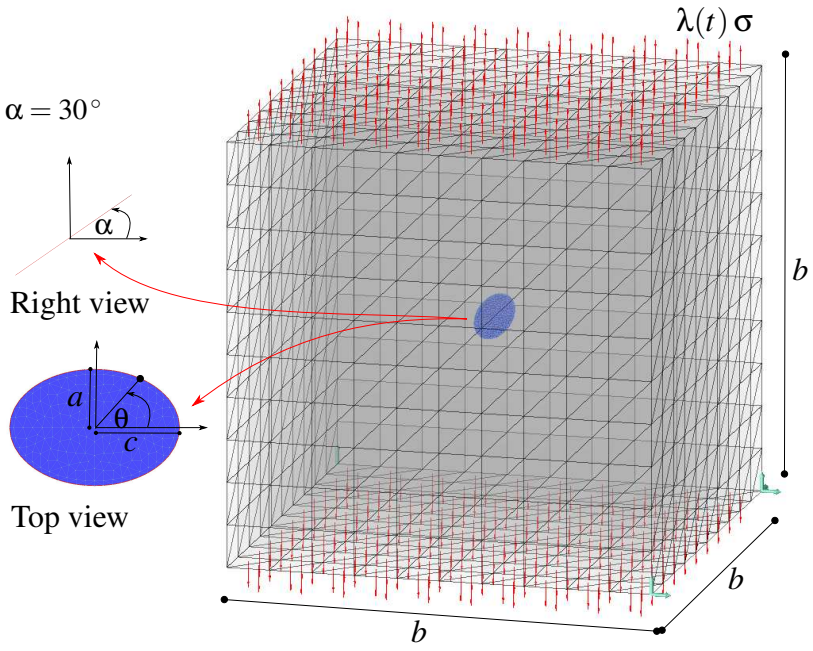

Figure 4.14: *Geometrical details of elliptical crack problem.*

The cube is loaded by $\lambda(t)\,\sigma$ at top and bottom. Three different time functions for the load are examined; $\lambda(t) = 1$ (constant), $\lambda(t) = \frac{t}{t_{peak}}$(ramp) and $\lambda(t) = |\sin(\frac{t\,\pi}{t_{peak}})|$ (sinusoidal).

In order to compute the time-dependent energy release rate (ERR) for this problem a reference elastic problem is created. The instantaneous shear and bulk modulus are used as material properties. The imposed tractions on top and bottom of the cube are σ.

The extracted stress intensity factors for Modes I, II, and III using the GFEM on the elastic reference problem are compared with the analytical solution for an infinite domain and are presented

Table 4.2: *Mathematical representation of the viscoelastic material (Prony series).*

m	G_m	K_m	ρ_m
1	0.1539	0.2565	1.01e-10
2	0.0782	0.1303	3.26e-05
3	0.0604	0.1007	0.00115
4	0.0452	0.0753	0.0429
5	0.0406	0.0677	1.65
6	0.0136	0.0227	493
$G_0 = 0.40$ and $K_0 = 0.67$			

in Figure 4.15. SIFs are normalized using

$$\bar{\mathcal{K}}_I = \frac{\mathcal{K}_I}{\sigma\sqrt{\pi b}} \tag{4.38}$$

Excellent agreement is observed for all SIFs.

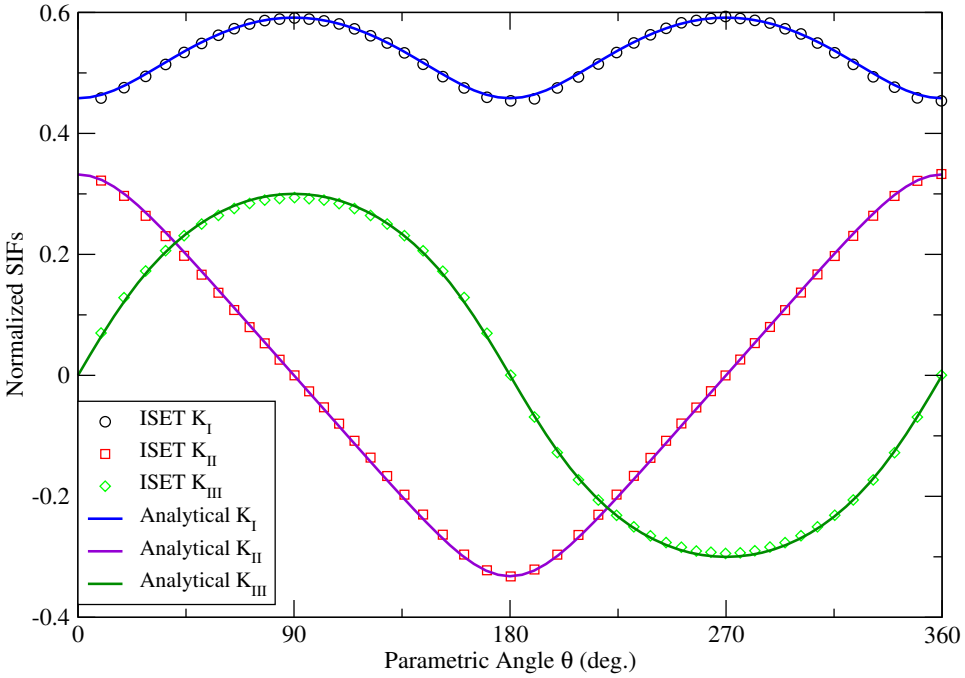

Figure 4.15: *The SIFs for Modes I, II, and III using the GFEM methodology on the elastic reference problem.*

To compute the three components of the viscoelastic ERR, Equations (3.22), (3.23), and (3.24) are used. Note that these equations are in the Laplace domain, therefore the material functions

in this domain are needed. The Prony series function in Laplace domain are given by Equations (4.36) and (4.37).

The Laplace transform functions $\bar{\bar{\lambda}}_2(p)$ for each load type are

for a constant load $\lambda(t) = 1$,

$$\bar{\bar{\lambda}}_2(p) = \frac{1}{p} \tag{4.39}$$

for a ramp load $\lambda(t) = \frac{t}{t_{peak}}$,

$$\bar{\bar{\lambda}}_2(p) = \frac{2}{t_{peak}^2 p^3} \tag{4.40}$$

for a sinusoidal load $\lambda(t) = |\sin(\frac{t\pi}{t_{peak}})|$,

$$\bar{\bar{\lambda}}_2(p) = \frac{1}{2p} - \frac{p}{2(p^2 + \frac{\pi^2}{t_{peak}^2})} \tag{4.41}$$

After computing $\bar{\bar{G}}_I(p)$, $\bar{\bar{G}}_{II}(p)$ and $\bar{\bar{G}}_{III}(p)$, the corresponding ERR in the time domain are obtained by a Fourier's numerical inversion using Equation (3.35). Figures 4.16(a), 4.16(c) and 4.16(e) show the components of the time-dependent energy release rate at the crack front location $\theta = 90$ degrees, while Figures 4.16(b), 4.16(d) and 4.16(f) correspond to the crack front location $\theta = 180^\circ$.

In order to visualize how the ERR along the front evolves in time, it is necessary to create a three dimensional surface. Figure 4.17 shows the components of ERR for the constant load type. Figure 4.18 shows the components of ERR for the ramp load type. Figure 4.19 shows the components of ERR for the sinusoidal load type.

The deformed configuration and von Mises stress of a planar cut of the cube is shown in Figure 4.20.

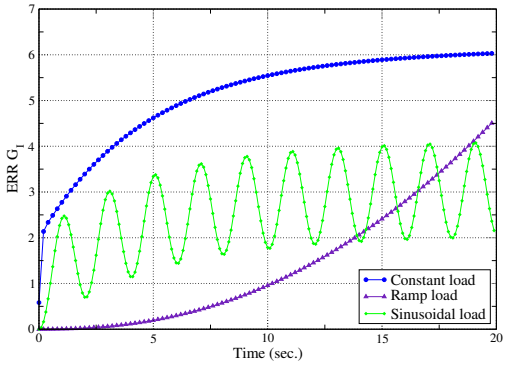

(a) ERR $\mathcal{G}_I$ for vertex located at $\theta = 90$ deg.

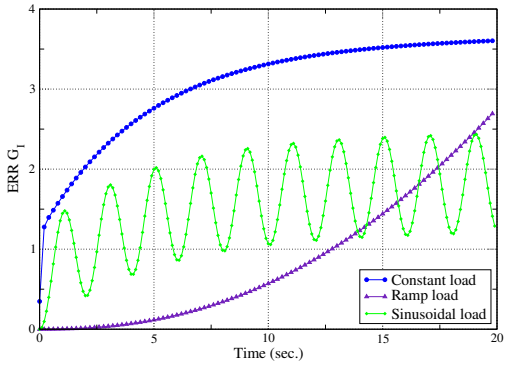

(b) ERR $\mathcal{G}_I$ for vertex located at $\theta = 180$ deg.

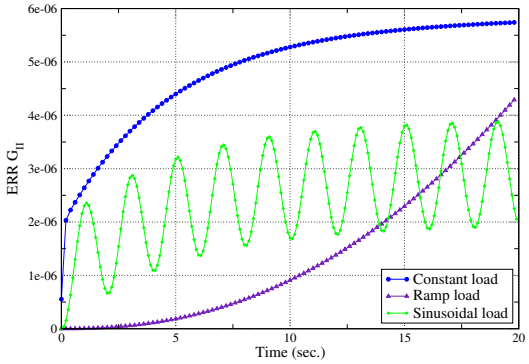

(c) ERR $\mathcal{G}_{II}$ for vertex located at $\theta = 90$ deg.

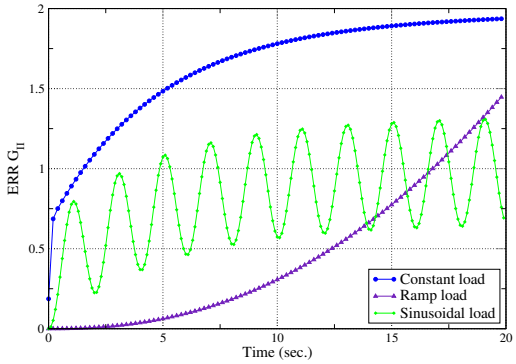

(d) ERR $\mathcal{G}_{II}$ for vertex located at $\theta = 180$ deg.

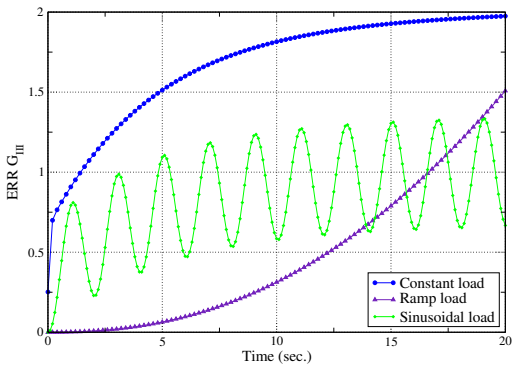

(e) ERR $\mathcal{G}_{III}$ for vertex located at $\theta = 90$ deg.

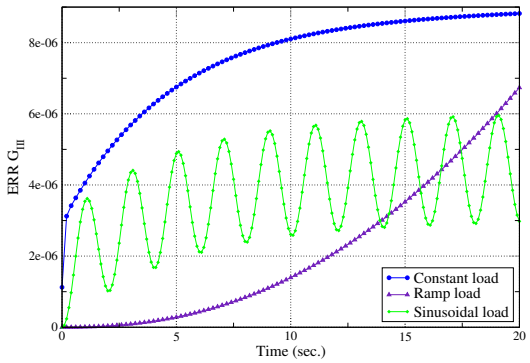

(f) ERR $\mathcal{G}_{III}$ for vertex located at $\theta = 180$ deg.

Figure 4.16: *Time dependent energy release rate for all load types.*

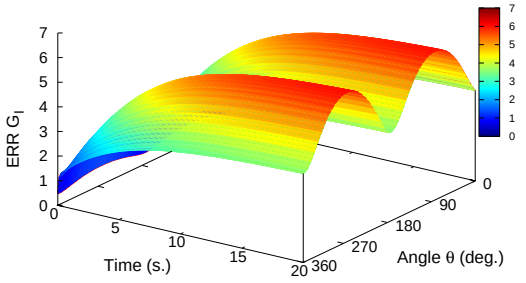

(a) ERR $\mathcal{G}_I$, constant load type.

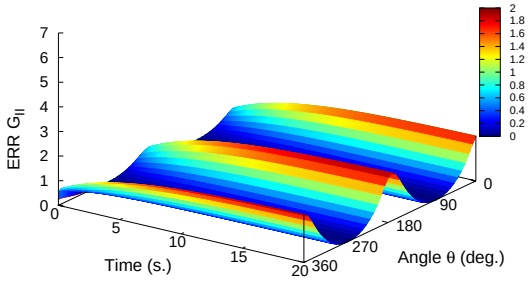

(b) ERR $\mathcal{G}_{II}$, constant load type.

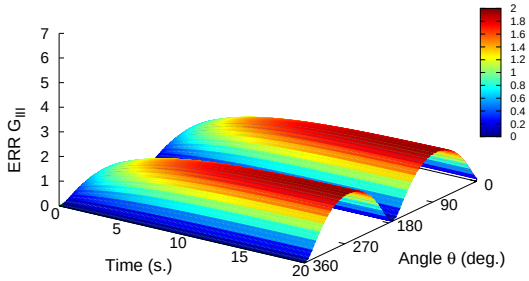

(c) ERR $\mathcal{G}_{III}$, constant load type.

Figure 4.17: *Time dependent energy release rate along crack front for constant load.*

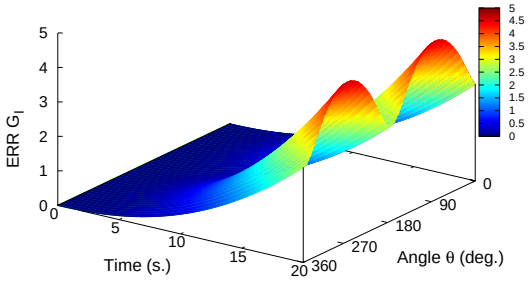

(a) ERR $\mathcal{G}_I$, ramp load type.

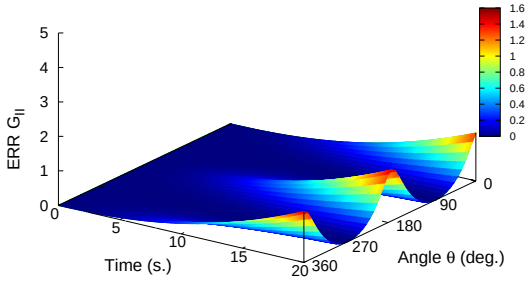

(b) ERR $\mathcal{G}_{II}$, ramp load type.

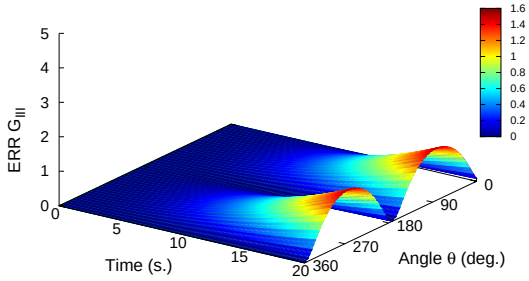

(c) ERR $\mathcal{G}_{III}$, ramp load type.

Figure 4.18: *Time dependent energy release rate along crack front for ramp load.*

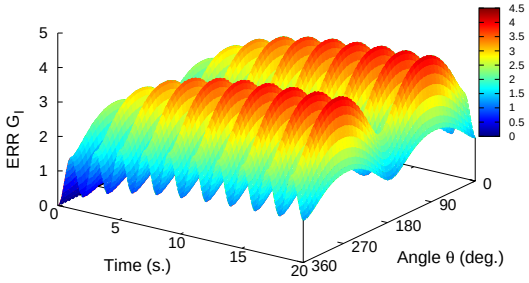

(a) ERR $\mathcal{G}_I$, sinusoidal load type.

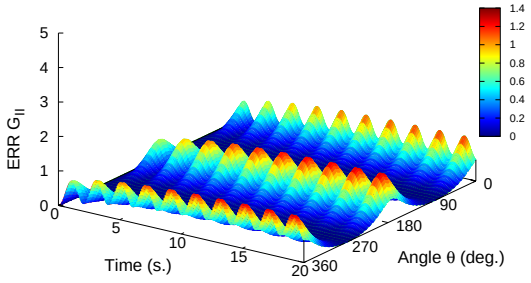

(b) ERR $\mathcal{G}_{II}$, sinusoidal load type.

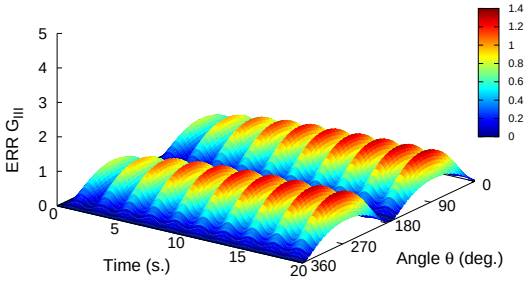

(c) ERR $\mathcal{G}_{III}$, sinusoidal load type.

Figure 4.19: *Time dependent energy release rate along crack front for sinusoidal load.*

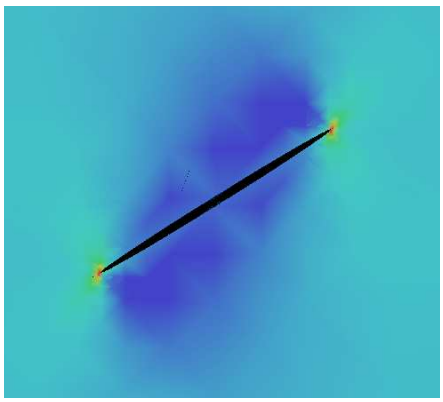

Figure 4.20: *Deformed configuration and von Mises stress on a cutting plane.*

4.4 Reflective Crack (RC) Simulation with GFEM

In this section, we simulate the problem of a static reflective crack in an airfield pavement making use of the correspondence principle together with the GFEM previously described. Modes *I*, *II* and *III* energy release rate (ERR) are computed along the crack front in order to investigate the three-dimensional, mixed mode crack-driving mechanisms in a typical airfield pavement.

A pavement section of an airport that serves the Boeing 777 aircraft is selected to be modeled. The model geometry and pavement cross sections for the underlying Portland Cement Concrete (PCC) are arbitrarily selected as the standard section of runway 4L-22R at O'Hare Airport.

The pavement model encompasses half of two adjacent slabs and one PCC joint, as illustrated by the shaded region in Figure 4.21(a). The simulated airfield pavement is composed of a 20 cm asphalt overlay; 23 cm concrete slabs, each with plan dimensions of 6 m $\times$ 5.7 m (PCC), and; a 28 cm cement treated base (CTB). A saw cut of 13 mm width is modeled in the PCC layer.

The dimensions of the reflective crack surface are 2.54 cm in height and 5 cm in depth. The curved portion of the crack has a radius of 2.54 cm and starts at the midpoint of its depth. Figure 4.21(b) shows the geometry of the crack surface.

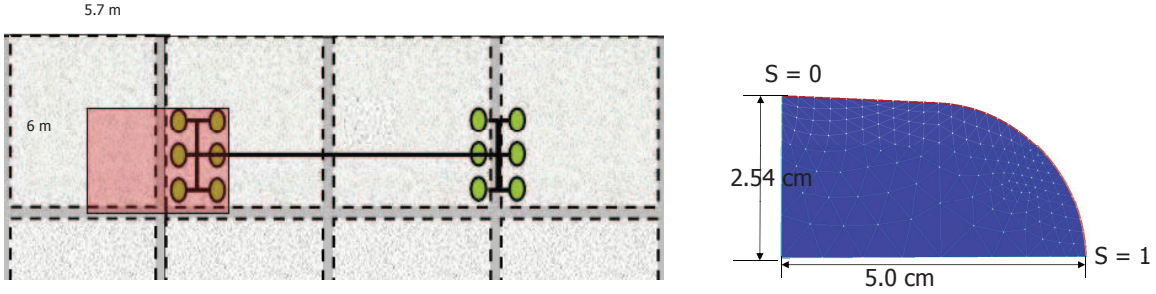

(a) Airfield pavement analyzed. The shaded rectangle represents the portion of pavement modeled in this study.

(b) Crack surface geometry details

Figure 4.21: *Reflective cracking problem analyzed.*

Table 4.3: *Mathematical representation of the viscoelastic material (Prony series).*

m	G_m (MPa)	K_m (MPa)	ρ_m (s)
1	44.244	132.73	2e-2
2	64.541	193.62	2e-1
3	126.34	379.04	2
4	137.29	411.88	2e1
5	88.488	265.46	2e2
6	35.577	106.73	2e3
7	9.3506	28.051	2e4
8	3.1472	9.4415	2e5
9	0.8391	2.5174	2e6
10	0.1803	0.5409	2e7
11	0.2191	0.6573	2e8

$G_0 = 510.74$ and $K_0 = 1532.22$

4.4.1 Pavement Layer Profile and Material

The asphalt overlay is assumed to be composed of a linear viscoelastic material represented by the Prony series given in Table 4.3. All other layers are assumed to have elastic material properties.

The concrete slabs are assumed to have a Young's modulus of 27,579 MPa, while the CTB modulus was taken as 6,895 MPa. The Poisson's ratio for the concrete slabs and the CTB layer are assumed to be 0.15 and 0.20, respectively. Figure 4.22(a) shows details of the pavement considered. Furthermore, the interface between asphalt overlay and Portland cement concrete layer is assumed to be fully bonded.

The Boeing 777-200 aircraft has two main landing gears with a main gear width of 11 m. Due to the very large width of the gear, we assume here that the distance between gears is large enough such that interactions may be neglected for the purposes of studying the mixed mode behavior and 3-D responses. One side of the dual-tridem main gear carries about 47.5% of the gross taxiway weight (288 Ton) of the Boeing 777-200 aircraft, and is composed of six wheels with an individual contact tire pressure of 1,482 MPa [3]. Details are shown in Figure 4.22(b).

Two gear loading positions of the aircraft are considered in this section, as shown in Figure 4.23. Load Position A (Cf. Figure 4.23a) loads the pavement symmetrically with respect to the

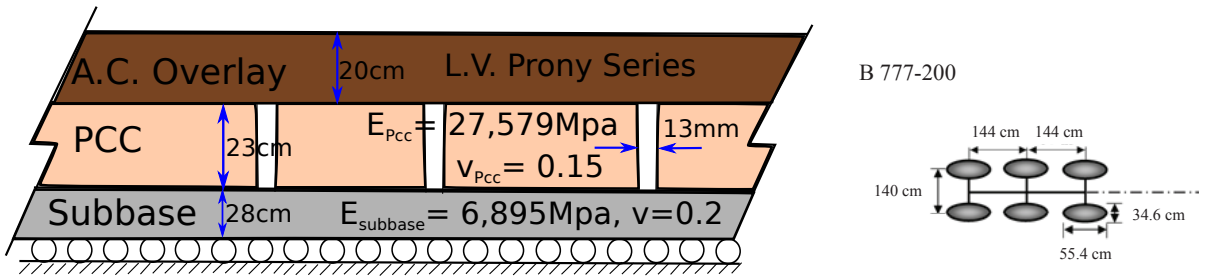

(a) Material properties and details of a standard section of runway 4L-22R at O'Hare Airport.

(b) Boeing 777-200 aircraft wheel loading detail

Figure 4.22: *Cross section of pavement analyzed and load.*

PCC joint, while Position B leads to strong shear deformations at the PCC joint. These loading configurations are expected to show different fracture deformation modes and provide information about possible crack growth mechanisms.

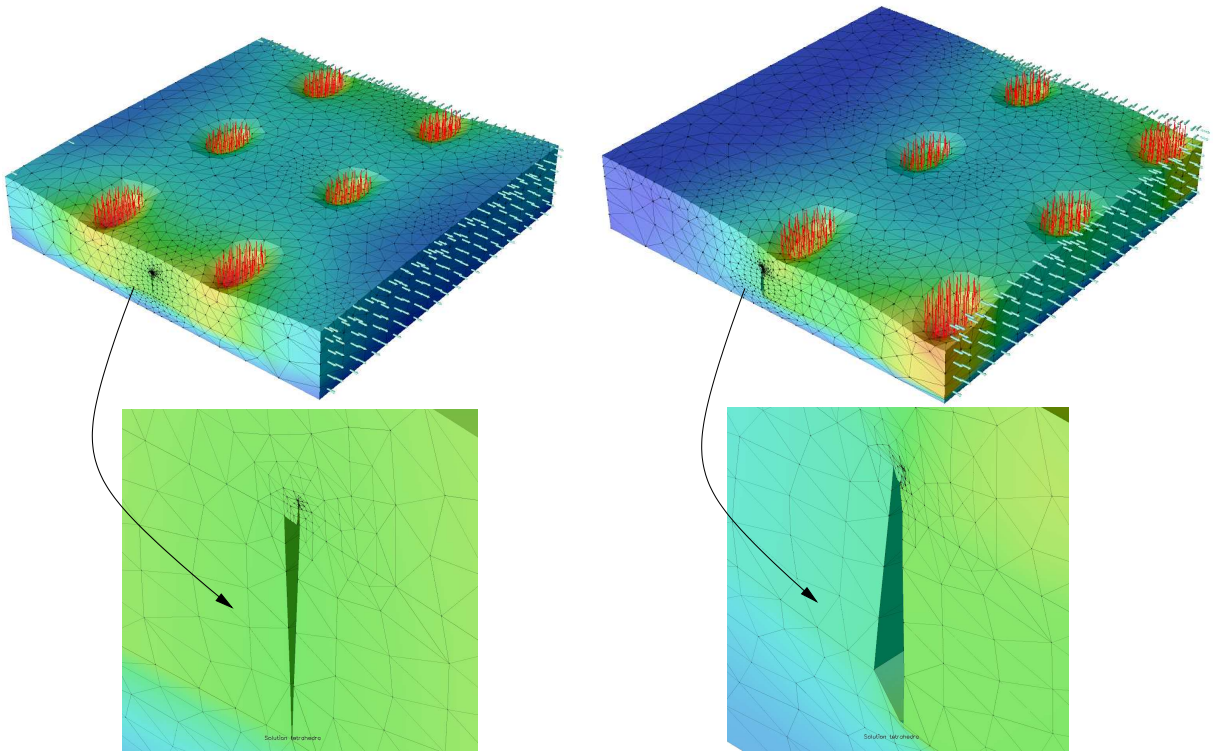

(a) Load position A and corresponding deformed configuration at the PCC joint.

(b) Load position B and corresponding deformed configuration at the PCC joint.

Figure 4.23: *Gear load positions considered in this study. Position A loads the pavement symmetrically with respect to the PCC joint, while Position B leads to strong shear deformations at the PCC joint.*

4.4.2 Finite Element Geometry and Boundary Conditions

A relatively coarse 3-D mesh *without any crack discretization* is created using the software program Patran [124]. Smaller elements are created around the PCC joint and locations where wheel loads are applied, as shown in Figures 4.24(a) and 4.24(b), respectively.

Two-dimensional triangular elements are used to represent the geometry of the crack surface as illustrated in Figure 4.21(b). As it will be explained in Chapter 6, these elements are used to define discontinuous enrichment functions. Details on these functions are described in Section 4.2.1. The 2-D elements do not have any degrees of freedom. Furthermore, the crack triangulation is completely independent of the 3-D mesh.

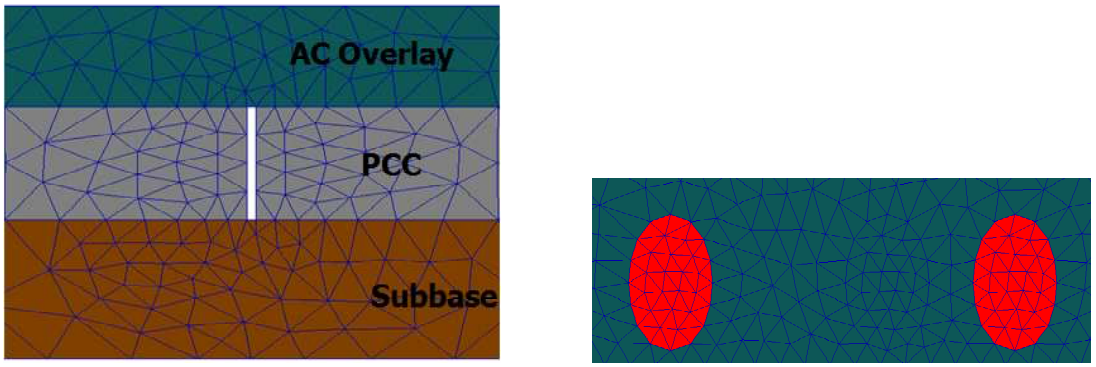

(a) Tetrahedral mesh around PCC joint

(b) Discretization around locations where wheel loads are applied

Figure 4.24: *Details of discretization used in the GFEM model.*

In order to compute all components of ERR along the crack front, first we create a reference elastic problem using the instantaneous material properties for the asphalt overlay. We then, solve this reference problem using our GFEM research code (ISET) and extract the stress intensity factors (SIFs) for all modes. In ISET, the mesh is automatically refined around the crack front in order to obtain a sufficiently fine mesh. The ratio of characteristic element size to crack radius, L_e/a, along the crack front is $0.004 \leq L_e/a \leq 0.1$. Even though this ratio may seem large compared to what is normally used in finite element models for 3-D cracks, the GFEM methodology is able to deliver accurate solutions due to the analytical enrichments used at nodes near the crack front.

Third and fourth degree polynomial shape functions are also used to approximate the continuous part of the solution. Figure 4.25 shows the resulting tetrahedral mesh used in the model along with a detailed zoom-in at the location where the crack is placed. Extraction of stress intensity factors is performed using the Cut-off Function Method (CFM, ref. A) for all the fracture modes.

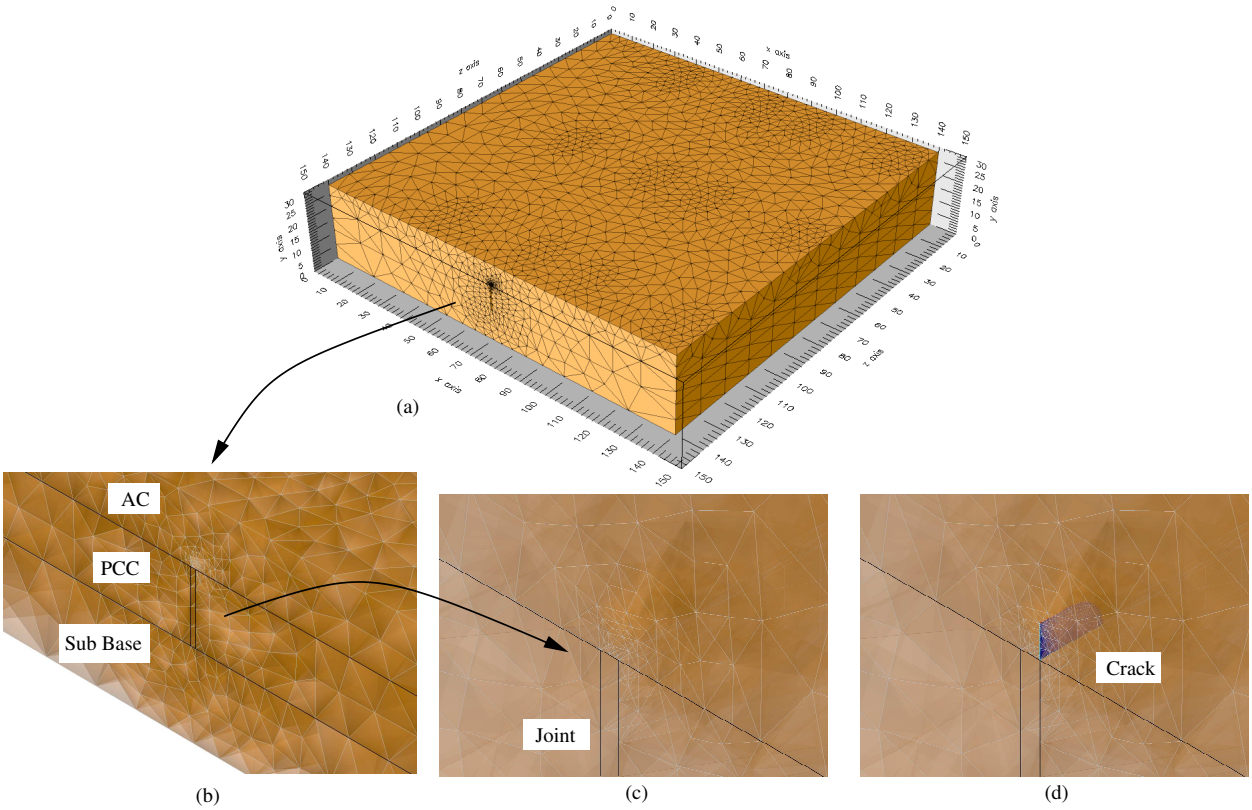

Figure 4.25: *Modeling of a 3-D reflective crack with the Generalized FEM. The crack is modeled using discontinuous and singular GFEM shape functions, instead of a finite element mesh with element faces oriented with the crack. (a) 3-D mesh without crack. (b) and (c) Details of mesh in vicinity of joint. (d) Reflective crack inserted into existing uncracked FE mesh.*

After completing the simulation of the reference elastic problem, components of ERR of the viscoelastic problem are computed using Equations (3.22)- (3.24) transformed back numerically to the time domain using Equation (3.35).

The linear viscoelastic material properties represented with Prony series in the Laplace domain have the form of Equations (4.36) and (4.37). The load is considered to be a time function $\lambda(t)\,\sigma$,

with σ as the pressure applied by the landing gears of the aircraft and $\lambda(t)$ as a sinusoidal load $|\sin(\frac{t\,\pi}{t_{peak}})|$. The Laplace transform of the squared function $\lambda(t)$ is

$$\bar{\bar{\lambda}}_2(p) = \frac{1}{2\,p} - \frac{p}{2\,(p^2 + \frac{\pi^2}{t_{peak}^2})} \tag{4.42}$$

The simulation time considered here is 240s with $t_{peak} = 10$s.

4.4.3 Analysis of Results

Figure 4.26 shows the SIFs of the reference elastic problem while Figures 4.27(a)-4.27(c) show the ERR along the crack front for load position A.

It can be observed that this is clearly a Mode *I* dominated case. Also, $\mathcal{K}_I$ and $\mathcal{G}_I$ varies significantly along the crack front, reaching a maximum value at $s = 1$, where s is a non-dimensional coordinate along the crack front. This demonstrates that, under this loading position, the reflective crack will grow faster at $s = 1$ than at $s = 0$ and thus it will exhibit significant channeling behavior. Even though $\mathcal{G}_{II}$ and $\mathcal{G}_{III}$, shown in Figures 4.27(b) and 4.27(c), are very small, they are not zero. This is caused by the fact that the crack is inserted above the right hand side of the PCC joint, as illustrated in Figure 4.23(a), and therefore shifted from the plane of symmetry.

Figures 4.28 and 4.27 show the same results as above but for load position B. The distribution of $\mathcal{K}$ and $\mathcal{G}$ along the crack front is significantly different from that of load position A. An interplay between Modes *II* and *III* can be observed. At $s = 0$ Mode *II* dominates; at $s = 1$ Mode *III* becomes dominant while Mode *II* almost drops to zero. Thus, at $s = 0$ the crack will grow by shear action while at $s = 1$ it must tear in order to grow. This decrease in values for $\mathcal{K}_{II}$ and increase for $\mathcal{K}_{III}$, is because the crack front changes direction. It starts as a horizontal line in the YZ plane but it curves and becomes almost a vertical line in the same plane. If the crack front were to stay in the horizontal direction $\mathcal{K}_I$ would remain the dominant case in this example. This type of behavior can only be seen in a three-dimensional simulation.

It is clear that reflective cracks in airfield pavements are subjected to mixed mode behavior with

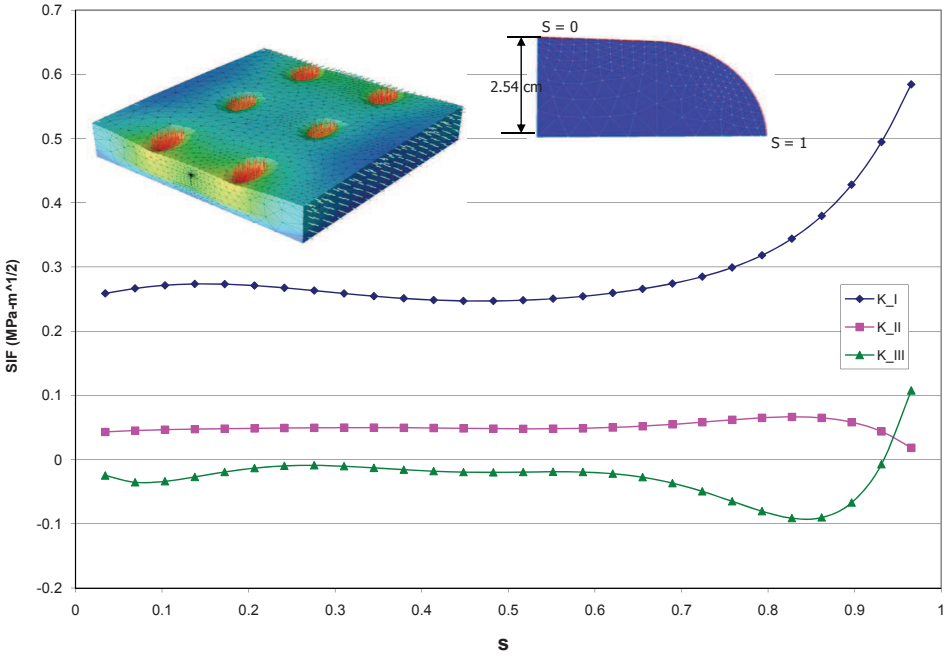

Figure 4.26: *Stress Intensity Factors (SIFs) along crack front for load position A.*

all three modes present and thus realistic simulations must be performed in three dimensions. Such 3-D analyses can be used to determine if the crack will propagate towards the pavement surface or across the pavement, in a channeling orientation. This information may aid in the design of preventive measures against reflective crack growth and in the determination of critical parameters controlling their propagation.

The mixed mode behavior demonstrated here leads to non-planar crack growth, which makes the simulation of this class of problems quite challenging specially for standard finite element methods. The simulation of three-dimensional crack growth in airfield pavements is presented in Chapter 7.

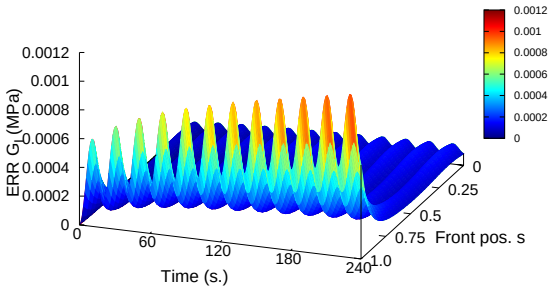

(a) Energy Release Rate (ERR) $\mathcal{G}_I$.

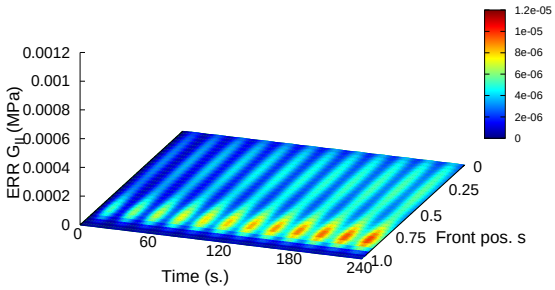

(b) Energy Release Rate (ERR) $\mathcal{G}_{II}$.

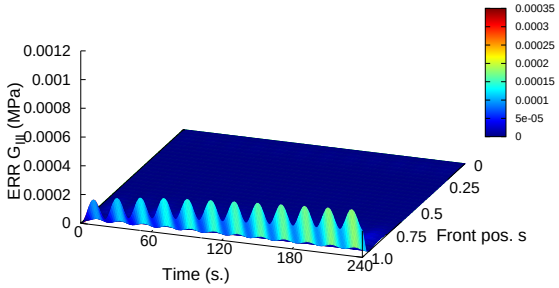

(c) Energy Release Rate (ERR) $\mathcal{G}_{III}$.

Figure 4.27: *Energy Release Rate (ERR) along crack front for load position A.*

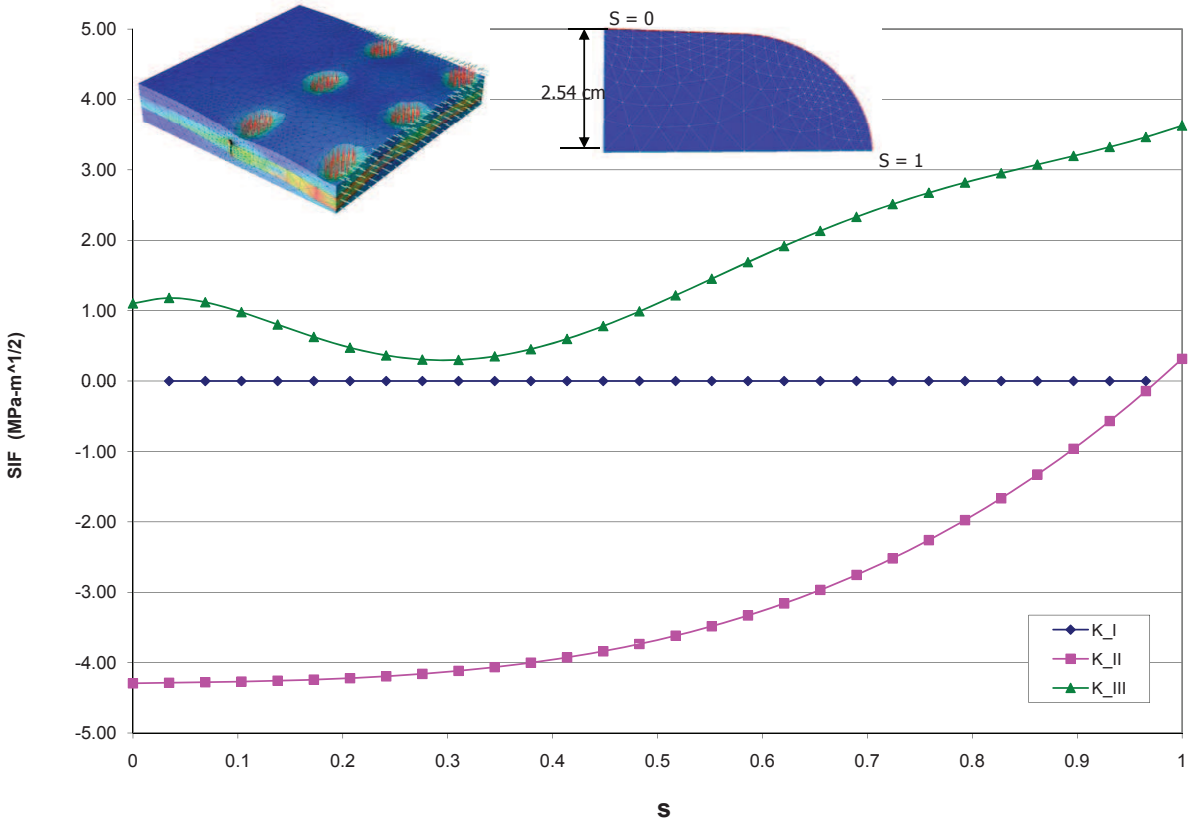

Figure 4.28: *Stress Intensity Factors (SIFs) along crack front for load position B.*

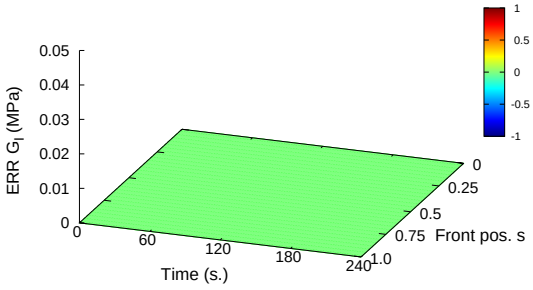

(a) Energy Release Rate (ERR) $\mathcal{G}_I$.

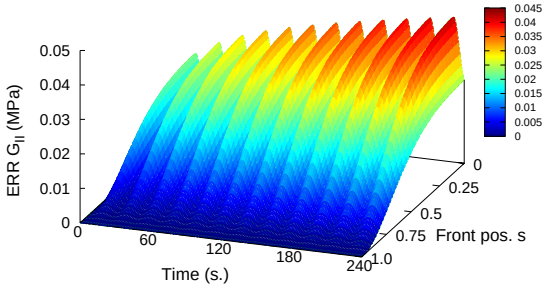

(b) Energy Release Rate (ERR) $\mathcal{G}_{II}$.

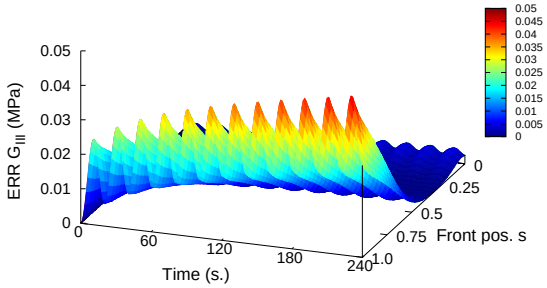

(c) Energy Release Rate (ERR) $\mathcal{G}_{III}$.

Figure 4.29: *Energy Release Rate (ERR) along crack front for load position B.*

Chapter 5

Two-Scale Simulation of Cracks in Linear Viscoelastic Materials

Even though in the GFEM previously described, the three-dimensional finite element mesh does not need to match the analyzed surface crack, available enrichment functions for cracks do not provide, in general, sufficient accuracy and local refinement of the mesh must also be applied [128, 129]. Modeling airfield pavements to study reflective cracking for example, is difficult and computationally expensive since the area of interest is orders of magnitude smaller than the domain of the problem. A representative model of an airfield pavement can easily have around ten meters in length, while the size of the reflective crack for a simulation would be around three centimeters. In order to obtain accurate results in an analysis of fracture using the GFEM, experience has shown that mesh refinement is needed along the crack front. Although the refinement is not as strong as in the case of the standard FEM, the elements should be around 3% of the crack size [50, 128, 129]. Therefore, in the case of an airfield model, the element size along the crack front should be approximately 0.09 cm. This is about 10,000 times smaller than the typical pavement model size. In this type of problem, even using GFEM, the resulting system of equations [13] becomes ill-conditioned due to the extremely large ratio between min. and max. element sizes in the FEM mesh. One workaround for this issue is to perform the computations using high-precision 128-bit floating-point arithmetic [155]. However, few compilers or software libraries can handle high-precision arithmetic, and those that can are extremely slow-often 50 to 100 times slower than conventional 64-bit floating-point arithmetic [155].

Structural problems involving multiple spatial scales of interest, like reflective cracking problems, are commonly solved using a global-local or sub-modeling procedure [36, 54, 115]. This approach is known to be sensitive to the quality of boundary conditions used in the local domains.

Accurate local solutions require the use of sufficiently large local domains. However, the optimal size of the local domain is, in general, problem dependent.

In this section, the problem of reflective cracking in airfield pavements using the GFEM with global-local enrichment functions (hereafter denoted *GFEM*$^{g\text{-}l}$) [40, 84], is analyzed. In this method local solutions computed using a standard global-local finite element analysis are used as enrichment functions for the GFEM; therefore global (structural-scale) meshes can be coarse even in the presence of small cracks. A detailed study of the performance of the *GFEM*$^{g\text{-}l}$ for this class of problems is presented using representative three-dimensional simulations including reflective cracks in airfield pavements. The effects of local domain size on the accuracy of the *GFEM*$^{g\text{-}l}$ and standard global-local finite element analysis (GL-FEM) are investigated. The influence of the global enrichment zone size used in the *GFEM*$^{g\text{-}l}$ is also analyzed. A brief review of the *GFEM*$^{g\text{-}l}$ is presented next.

5.1 *GFEM*$^{g\text{-}l}$ overview

Global-local enrichment functions can be defined for many classes of problems, like interacting 3-D cracks [83], propagating 3-D fractures [131] or problems exhibiting sharp thermal gradients [120, 121]. These functions can also be developed for problems involving localized nonlinear material responses [85]. They are able to represent fine-scale responses on *coarse*, macroscale, finite element meshes and to fully account for interactions among scales. Detailed mathematical analysis of this class of GFEM is presented in [40, 64]. In this section, we consider the case of 3-D simulations of propagating mechanically-short cracks. These cracks are much smaller than any dimension of a structural component but larger than the details of the material micro-structure [171]. This formulation also works for the case of static cracks when only one crack growth step is considered. Furthermore, a review of the global-local approach to build enrichment functions for the GFEM is presented. Additional details can be found in [40, 43].

5.1.1 Initial Global Problem

Consider a three-dimensional domain composed of linear viscoelastic, isotropic and homogeneous material. As done in Chapters 3 and 4, in order to compute stress intensity factors (SIFs), consider a reference elastic domain $\bar{\Omega}^e_G$ with boundary $\partial\Omega^e_G$ decomposed as $\partial\Omega^e_G = \Gamma^u_G \cup \Gamma^\sigma_G$ with $\Gamma^u_G \cap \Gamma^\sigma_G = \emptyset$. The domain is cracked, but that is not considered at this stage of the methodology.

The equilibrium equations, constitutive and kinematic relations for the reference elastic problem are given by

$$\begin{aligned} \frac{\partial \sigma^e_{ij}(\boldsymbol{x})}{\partial x_i} + F^e_j(\boldsymbol{x}) &= 0 \quad \text{in} \quad \Omega^e_G, \\ \sigma^e_{ij}(\boldsymbol{x}) &= 2\,G_0\,[\varepsilon^e_{ij}(\boldsymbol{x}) - \frac{1}{3}\,\varepsilon^e_{kk}(\boldsymbol{x})\,\delta_{ij}] + K_0\,\varepsilon^e_{kk}(\boldsymbol{x})\,\delta_{ij}, \\ \varepsilon^e_{ij}(\boldsymbol{x}) &= \frac{1}{2}\left[\frac{\partial u^e_i(\boldsymbol{x})}{\partial x_j} + \frac{\partial u^e_j(\boldsymbol{x})}{\partial x_i}\right] \end{aligned} \tag{5.1}$$

where σ^e_{ij} is the Cauchy stress tensor, F^e_j are body forces, ε^e_{ij} is the linear strain tensor and G_0, K_0 are the instantaneous shear and bulk modulus of the viscoelastic problem, respectively.

The boundary conditions prescribed at $\partial\Omega_G$ are as follows

$$\begin{aligned} \sigma^e_{ij}(\boldsymbol{x}) n_i(\boldsymbol{x}) &= T^e_j(\boldsymbol{x}) = T_j(\boldsymbol{x}, t_{peak}) \quad \text{on} \quad \Gamma^\sigma, \\ u^e_j(\boldsymbol{x}) &= U^e_j(\boldsymbol{x}) \quad \text{on} \quad \Gamma^u \end{aligned} \tag{5.2}$$

where n_i is an outward unit normal vector on Γ^σ_G, T^e_j are prescribed tractions, U^e_j are prescribed displacements, $T(\boldsymbol{x},t)$ are the tractions imposed at the viscoelastic problem and t_{peak} is the time when the maximum load is acting on the boundary.

Here, we analyze three dimensional cracks in the reference problem with elastic, isotropic and homogeneous material behavior. The solution methodology based on the $GFEM^{\text{g-l}}$ is, however, applicable to other material models, such as visco-plastic behavior or viscoelastic material with no use of correspondence principle.

Let $\boldsymbol{u}_G^{e(k)}$ denote a generalized FEM approximation of the solution $\boldsymbol{u}^{e(k)}$ of Problem (5.1), (5.2). For simplicity, we assume no body force. The approximation $\boldsymbol{u}_G^{e(k)}$ is the solution at damage evolution (or propagation) step k, of the following global problem:

Find $\boldsymbol{u}_G^{e(k)} \in \boldsymbol{X}_G^{hp,k}(\Omega_G^e) \subset H^1(\Omega_G^e)$ such that $\forall\, \boldsymbol{v}_G^{e(k)} \in \boldsymbol{X}_G^{hp,k}(\Omega_G^e)$

$$\int_{\Omega_G^e} \boldsymbol{\sigma}^e(\boldsymbol{u}_G^{e(k)}) : \boldsymbol{\varepsilon}^e(\boldsymbol{v}_G^{e(k)}) \mathrm{d}\boldsymbol{x} + \eta \int_{\Gamma_G^u} \boldsymbol{u}_G^{e(k)} \cdot \boldsymbol{v}_G^{e(k)} \mathrm{d}\boldsymbol{s} = \int_{\Gamma_G^\sigma} \boldsymbol{T}^e \cdot \boldsymbol{v}_G^{e(k)} \mathrm{d}\boldsymbol{s} + \eta \int_{\partial\Omega_G^u} \boldsymbol{U}^e \cdot \boldsymbol{v}_G^{e(k)} \mathrm{d}\boldsymbol{s}, \quad (5.3)$$

where $\boldsymbol{X}_G^{hp,k}(\Omega_G^e)$ is a discretization of the Hilbert space at propagation step k, $H^1(\Omega_G^e)$ generated by the GFEM shape functions defined in (4.9), and η is a penalty parameter. Problem (5.3) leads to a system of linear equations for the unknown degrees of freedom of $\boldsymbol{u}_G^{e(k)}$.

Hereafter, this problem is denoted as the *global problem*. At the initial propagation step $k = 0$ cracks are not considered when solving the initial global problem. Thus, only polynomial enrichment functions like those defined in Equation (4.12) are used in the computation of GFEM shape functions. The standard finite element can also be used. For subsequent steps the enrichment functions in $\boldsymbol{X}_G^{hp,k}(\Omega_G^e)$ are defined in local spaces and *have to be computed on-the-fly*. We describe a fine-scale problem in the next subsection to achieve this goal. The mesh used to solve this problem is typically a coarse quasi-uniform mesh like the one shown in Figure 5.1.

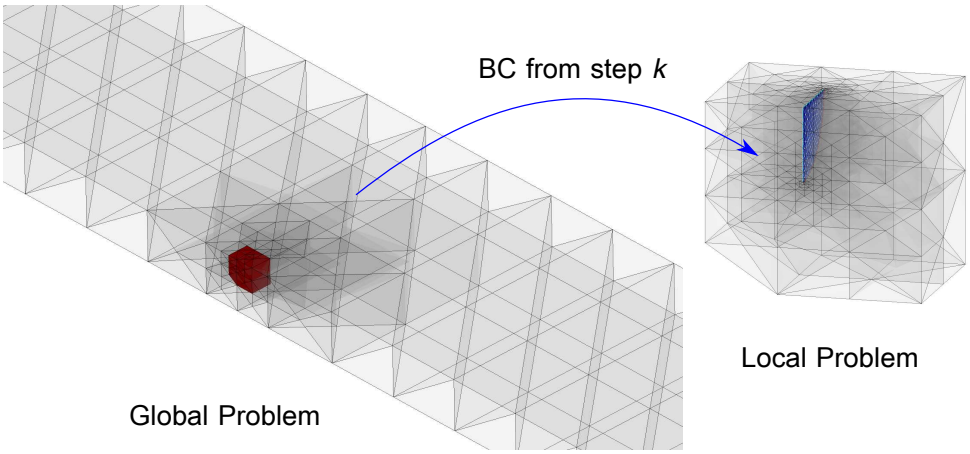

Figure 5.1: *Illustration of the* GFEM$^{g\text{-}l}$ *for static crack analysis or propagation. The figure shows the neighborhood* Ω_L^e *of a small propagating or static crack in the global domain. The solution of the global problem at simulation step k provides boundary conditions for the extracted local domain.*

5.1.2 Local Problem

Let Ω_{L}^e denote a subdomain of Ω_G^e as shown in Figure 5.1. This local domain contains a fine-scale feature like the crack surface shown in the same figure or other local features of interest. The following local problem is solved on Ω_{L}^e after the global solution $\boldsymbol{u}_G^{e(k)}$ is computed as described above:

Find $\boldsymbol{u}_{\mathrm{L}}^{e(k)} \in \boldsymbol{X}_{\mathrm{L}}^{hp,k}(\Omega_{\mathrm{L}}^e) \subset H^1(\Omega_{\mathrm{L}}^e)$ such that $\forall\ \boldsymbol{v}_{\mathrm{L}}^{e(k)} \in \boldsymbol{X}_{\mathrm{L}}^{hp,k}(\Omega_{\mathrm{L}}^e)$

$$
\begin{aligned}
&\int_{\Omega_{\mathrm{L}}^e} \boldsymbol{\sigma}^e(\boldsymbol{u}_{\mathrm{L}}^{e(k)}) : \boldsymbol{\varepsilon}^e(\boldsymbol{v}_{\mathrm{L}}^{e(k)}) \mathrm{d}\boldsymbol{x} + \eta \int_{\partial\Omega_{\mathrm{L}}^e \cap \Gamma_G^u} \boldsymbol{u}_{\mathrm{L}}^{e(k)} \cdot \boldsymbol{v}_{\mathrm{L}}^{e(k)} \mathrm{d}\boldsymbol{s} + \\
&\kappa \int_{\partial\Omega_{\mathrm{L}}^e \setminus (\partial\Omega_{\mathrm{L}}^e \cap \partial\Omega_G^e)} \boldsymbol{u}_{\mathrm{L}}^{e(k)} \cdot \boldsymbol{v}_{\mathrm{L}}^{e(k)} \mathrm{d}\boldsymbol{s} = \int_{\partial\Omega_{\mathrm{L}}^e \cap \Gamma_G^\sigma} \boldsymbol{T}^{e(k)} \cdot \boldsymbol{v}_{\mathrm{L}}^{e(k)} \mathrm{d}\boldsymbol{s} + \\
&\eta \int_{\partial\Omega_{\mathrm{L}}^e \cap \Gamma_G^u} \boldsymbol{U}^{e(k)} \cdot \boldsymbol{v}_{\mathrm{L}}^{e(k)} \mathrm{d}\boldsymbol{s} + \int_{\partial\Omega_{\mathrm{L}}^e \setminus (\partial\Omega_{\mathrm{L}}^e \cap \partial\Omega_G^e)} (\boldsymbol{t}(\boldsymbol{u}_G^{e(k)}) + \kappa \boldsymbol{u}_G^{e(k)}) \cdot \boldsymbol{v}_{\mathrm{L}}^{e(k)} \mathrm{d}\boldsymbol{s}, \qquad (5.4)
\end{aligned}
$$

where $\boldsymbol{X}_{\mathrm{L}}^{hp,k}(\Omega_{\mathrm{L}}^e)$ is a discretization of $H^1(\Omega_{\mathrm{L}}^e)$ using GFEM shape functions. This local domain contains a crack, and therefore the GFEM space $\boldsymbol{X}_{\mathrm{L}}^{hp,k}(\Omega_{\mathrm{L}})$ has shape functions built with discontinuous and singular enrichment functions-refer to Section 4.2.1. A key aspect of Problem (5.4) is the use of the coarse-scale solution at simulation step k, $\boldsymbol{u}_G^{e(k)}$, to compute the boundary condition on $\partial\Omega_L^e \setminus (\partial\Omega_L^e \cap \partial\Omega_G^e)$. The numerical nature of the coarse-scale solution used for the fine-scale boundary conditions leads to the use of the terminology "inexact boundary conditions". Exact boundary conditions are prescribed on portions of $\partial\Omega_L^e$ that intersect either Γ_G^u or Γ_G^σ. This allows the solution of problem (5.4) using finite element meshes that do not fit the crack surface. The traction vector, $\boldsymbol{t}(\boldsymbol{u}_G^k)$ is computed from the initial global problem using Cauchy's relation, i.e.,

$$
\boldsymbol{t}(\boldsymbol{u}_G^k) = \hat{\boldsymbol{n}} \cdot \boldsymbol{\sigma}^e(\boldsymbol{u}_G^{e(k)}) = \hat{\boldsymbol{n}} \cdot (\boldsymbol{C} : \boldsymbol{\varepsilon}^e(\boldsymbol{u}_G^{e(k)}), \qquad (5.5)
$$

where $\hat{\boldsymbol{n}}$ is the outward unit normal vector to $\partial\Omega_{\mathrm{L}}^e$ and κ is the stiffness of a distributed spring used on $\partial\Omega_{\mathrm{L}}^e \setminus \partial\Omega_{\mathrm{L}}^e \cap \partial\Omega_G^e$.

The spring stiffness, κ, can be selected using [84, 85]

$$\kappa = \frac{E_0}{\sqrt[nd]{V_0 J}}, \tag{5.6}$$

where E_0 is the instantaneous relaxation modulus of the linear viscoelastic problem, *nd* is the number of spatial dimensions of the problem, V_0 is the volume of the master element used, and J is the Jacobian of the global element across the local boundary where the spring boundary condition is imposed.

5.1.3 Enriched Global Problem

The approach described in the previous two sections for step $k = 0$ corresponds to a standard global-local finite element analysis, except that the GFEM is used at the local problem. Therefore, the accuracy of the local solution $\boldsymbol{u}_{\mathrm{L}}^{e(k=0)}$, for example, depends not only on the discretization used in the local domain Ω_{L}^{e} but also on the quality of the boundary conditions used on $\partial\Omega_{\mathrm{L}}^{e} \backslash (\partial\Omega_{\mathrm{L}}^{e} \cap \partial\Omega_{G}^{e})$. In the *GFEM*$^{\text{g-l}}$ [40, 43] quantities of interest are *not* computed from the local solution $\boldsymbol{u}_{\mathrm{L}}^{e(k)}$. Instead, $\boldsymbol{u}_{\mathrm{L}}^{e(k)}$ is used as an enrichment function in the global reference mesh. Figure 5.2 illustrates this process. The corresponding GFEM shape functions are given by

$$\boldsymbol{\phi}_{\alpha}^{k+1} = \varphi_{\alpha} \boldsymbol{u}_{\mathrm{L}}^{e(k)}, \tag{5.7}$$

where φ_{α} denotes a finite element shape function defined in the coarse *global* mesh used to solve the global problem presented in Section 5.1.1. This GFEM shape function (5.7) is used at nodes $\boldsymbol{x}_{\alpha}$ of the global mesh whose support, ω_{α}, is contained in the local reference domain Ω_{L}^{e}. Each component of the displacement vector is enriched with the corresponding components of the local solution $\boldsymbol{u}_{\mathrm{L}}^{e(k)}$. Thus, a global-local enrichment adds three degrees of freedom to a node when solving a three-dimensional reference elastic problem. The global problem defined in Section 5.1.1 is then solved again using the same mesh enriched with GFEM shape functions (5.7). The solution

of this so-called *enriched global problem* is denoted $\boldsymbol{u}_G^{e(k+1)}$. It can be computed very efficiently using the available factorization of the global stiffness matrix of the initial global problem [40].

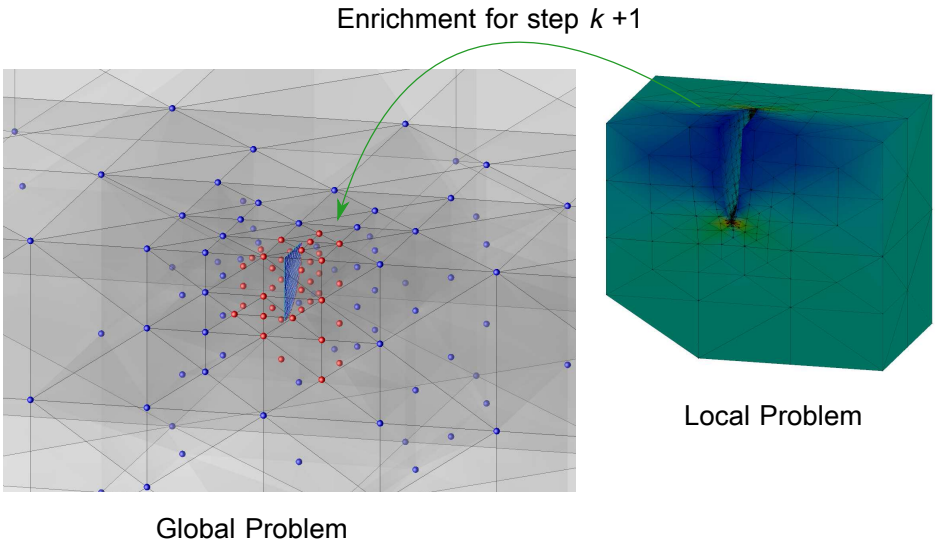

Figure 5.2: *Hierarchical enrichment of the coarse global reference mesh with local solutions computed on locally refined mesh. Only three degrees of freedom are added to these global nodes (shown with red spheres in the global mesh). These enrichments are used to approximate the global solution in the neighborhood of the crack at simulation step* $k+1$.

For a static crack problems the simulation will end at simulation step $k = 1$, after computing the solution of the enriched global problem, extracting stress intensity factors and computing the time-dependent energy release rate of the viscoelastic problem. On the other hand, in crack propagation problems at simulation step $k+1$ (with $k > 1$), the crack surface representation is updated with its new crack front position, and the simulation continues until the final step has been reached. More details about crack propagation are be discussed in Chapter 7.

5.2 Linear Viscoelastic Problems with *GFEM*$^{\text{g-l}}$ and Verification

This section presents applications of the *GFEM*$^{\text{g-l}}$ described in Section 5.1. Two verification problems are solved. The first one consists of a quarter-penny-shaped edge crack on a bar, while the

second one is an elliptical, inclined crack surface in a viscoelastic cube. The second problem has already been solved in Section 4.3.3 using GFEM and its solution is compared here.

5.2.1 Quarter-Penny-Shaped Crack

This problem deals with a static, quarter-penny-shaped crack in a linear viscoelastic bar, as illustrated in Figure 5.3. Even though the solution of this problem is for a linear viscoelastic medium, the reference elastic problem is used in the verification of the $GFEM^{g\text{-}l}$ method, with the solutions by Raju and Newman [136] and Ali [4] for corner cracks.

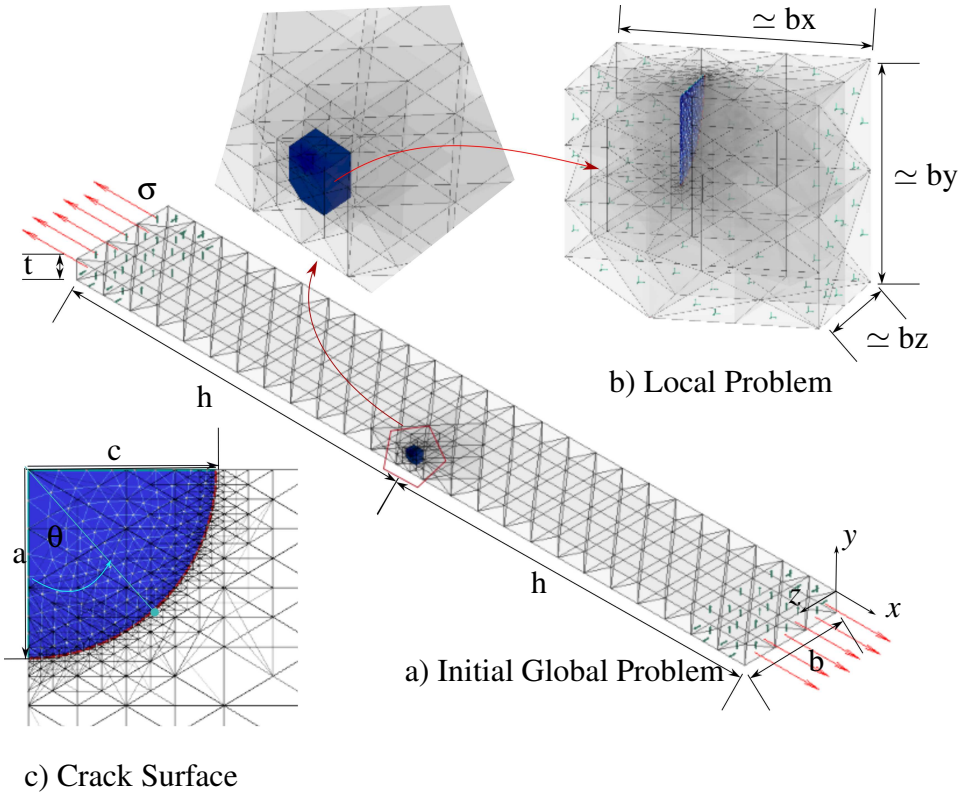

Figure 5.3: *Corner-cracked plate problem subjected to tensile axial load.*

The quarter penny-shaped crack is located at the corner of viscoelastic plate subjected to a uniform tensile load $\sigma\lambda(t)$ at its ends (cf. Figure 5.3). Displacement constraints are also imposed near the ends of the plate in order to minimize rotations under the applied loads. In this problem we consider a quarter circular crack so, in Figure 5.3(c), $a = c$. The material properties of this problem

Table 5.1: *Mathematical representation of the viscoelastic material (Prony series).*

m	G_m (MPa)	K_m (MPa)	ρ_m (s)
1	74.633	161.70	2e-2
2	108.87	235.88	2e-1
3	213.12	461.77	2
4	231.59	501.78	2e1
5	149.26	323.40	2e2
6	60.013	130.03	2e3
7	15.773	34.174	2e4
8	5.3088	11.502	2e5
9	1.4155	3.0669	2e6
10	0.3041	0.6589	2e7
11	0.3696	0.8008	2e8

$G_0 = 861.54$ and $K_0 = 1866.67$

are represented by a Prony Series shown in Table 5.1. The simulation time is 200s. Constant, ramp and sinusoidal loads with $t_{peak} = 10$s, are examined.

To solve this problem, a reference elastic problem with the instantaneous relaxation modulus as material properties is created and solved using *GFEM*$^{\text{g-l}}$. The load for this reference elastic problem is given by σ. The first step in the *GFEM*$^{\text{g-l}}$ involves the solution of the global problem on a mesh enriched with polynomial functions only. Thus, no cracks are considered at this stage. In this example polynomials of degree $p = 3$ are used. This problem is hereafter denoted as the *initial global problem* and is illustrated in Figure 5.3a. The global mesh is quasi-uniform while in the local problem the mesh is strongly refined at the crack front. The ratio between the element size at the crack front, L_e^L, and the crack size, a, is taken as $L_e^L/a \simeq 0.03$. The ratio between the size of the smallest element in the mesh of the global problem, L_e^G, and the crack size, a, is $L_e^G/a = 0.5$. Note that in the *GFEM*$^{\text{g-l}}$, cracks are not explicitly discretized in the global problem. Instead, they are represented through global-local enrichments, i.e., the solution of local problems. Thus, the global mesh does not change during a simulation. The following dimensions are adopted for the plate: $2h/c = 180.5$, $a/t = 0.2$ and $a/b = 0.04$.

Figure 5.3b shows the local problem where the crack is discretized using analytically defined enrichment functions as described in Section 4.2.1. Also polynomial enrichments of degree $p =$

3 are used to approximate the continuous part of the solution. The size of the local reference domain is significantly smaller than the global one. The local domain is defined by global elements contained in a bounding box with dimensions $bx/a = 2,\ by/a = 2,\ bz/a = 2$ in the $x-$, $y-$ and $z-$ directions, respectively. The size of the local domain is about 2% of the original reference problem size.

The solution of the global problem enriched with global-local functions is shown in Figure 5.4. This problem is hereafter denoted as the *enriched global problem*. Note that, the global mesh is quite coarse and yet it can capture the singularity at the crack front.

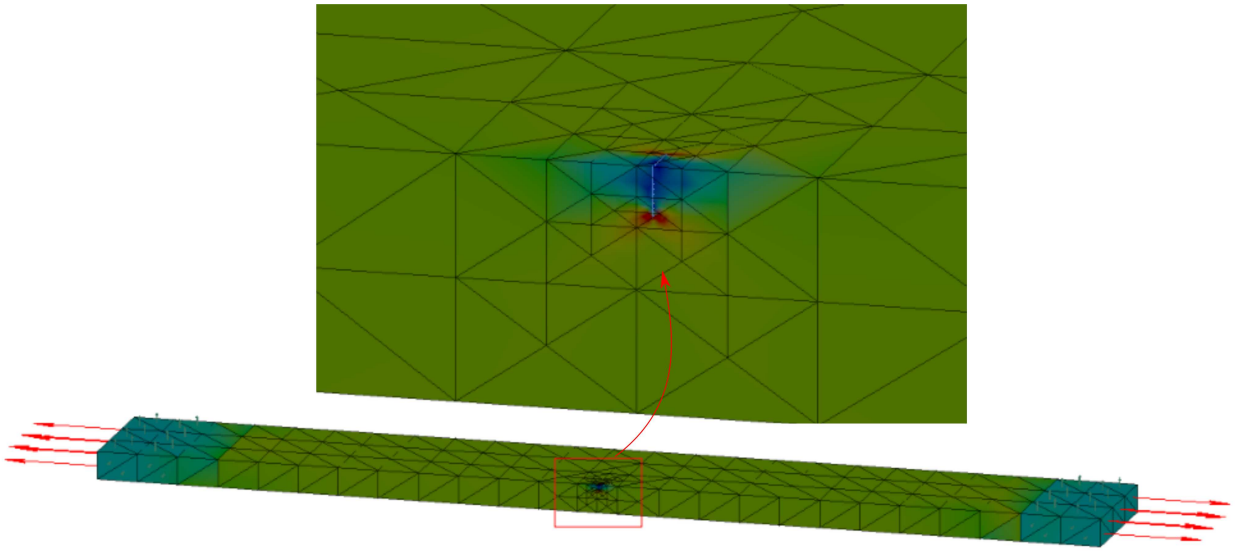

Figure 5.4: *Enriched global problem solution.*

Figure 5.5 shows the normalized Mode I stress intensity factor $\mathcal{K}_I/\mathcal{K}_r$ extracted from the solution of the enriched global and local problems. They are denoted as $GFEM^{\text{g-l}}$ and GL-FEM in the figure, respectively.

The solutions by Raju and Newman [136] and Ali [4] are also shown for comparison. The horizontal axis in the figure denotes the angular position at the crack front as illustrated in Figure 5.3(c). The normalizing factor, $\mathcal{K}_r$, is taken as

$$\mathcal{K}_r = \sigma\sqrt{\frac{\pi a}{Q}} \tag{5.8}$$

with Q

$$Q = 1 + 1.464\left(\frac{a}{c}\right)^{1.65}. \tag{5.9}$$

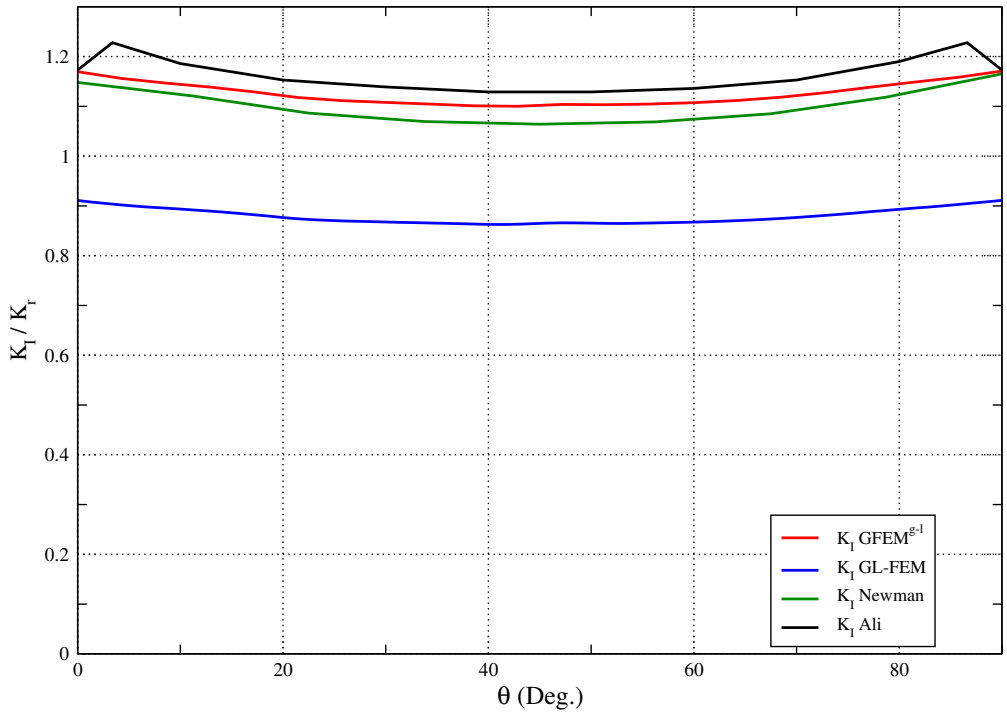

Figure 5.5: *Normalized Mode I stress intensity factors for corner crack, $a/t = 0.2$.*

With the solutions (SIFs) of the reference elastic problem in hand, we proceed to compute the viscoelastic ERR using Equation (3.22). Other modes are neglected in this simulation because clearly it is a Mode I dominated problem. As done before, the Laplace transform functions $\bar{\bar{\lambda}}_2(p)$ for each load type are given by Equations (4.39) - (4.41). The material properties in Laplace domain are computed using Equations (4.36) and (4.37).

After computing $\bar{\bar{G}}_I(p)$, the ERR in the time domain is obtained by a Fourier's numerical inversion using Equation (3.35). Figure 5.6 shows the energy release rate $\mathcal{G}_I$ along the front for each of the load types in this problem.

The stress intensity factors (SIFs) extracted from the $GFEM^{\text{g-l}}$ solution are significantly more accurate than those extracted from the local solution and agrees very well with the literature solu-

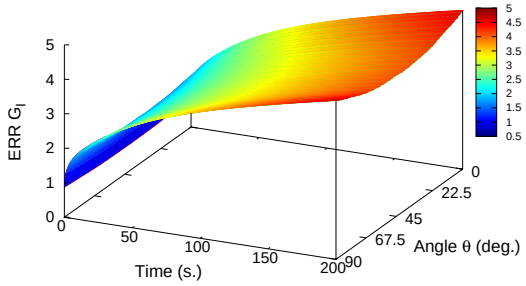

(a) Constant load.

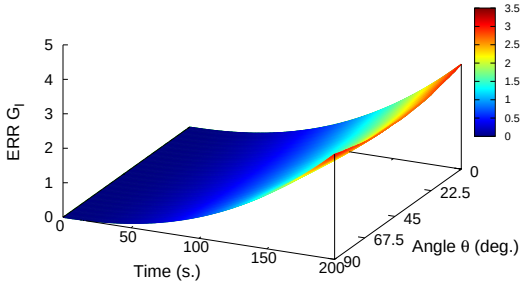

(b) Ramp load.

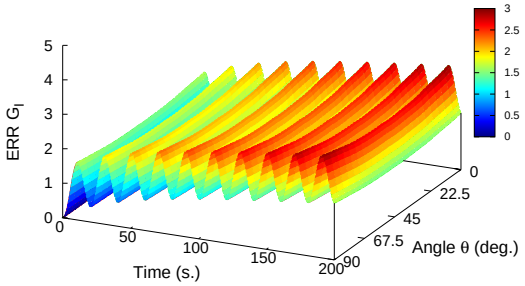

(c) Sinusoidal load.

Figure 5.6: *Energy Release Rate (ERR) $\mathcal{G}_I$ along the crack front (enriched global problem).*

tions. The local solution is equivalent to one provided by a global-local FEM analysis, which is commonly used in the industry to handle problems involving multiple spatial scales of interest.

Table 5.2 shows the size of the various discretizations used in the solution of the reference elastic problem. The enriched global problem captures $\mathcal{K}_I$ very well while adding only 120 global-local enrichment degrees of freedom to the initial global problem. The computational cost of the local problem must also be considered in the total cost of the $GFEM^{g\text{-}l}$. However, in most practical problems the global problem is much larger than the local one. Furthermore, the solution of the enriched global problem can be efficiently computed using the solution of the initial global problem [84, 131].

Table 5.2: *Size of the various discretizations in terms of number of degrees of freedom (DOFs).*

Problem	Number of DOFs
Initial Global	10,170
Local	53,436
Enriched Global	10,290

5.2.2 Inclined, Elliptical Crack with *GFEM*$^{\text{g-l}}$

This problem is the same as the one described in Section 4.3.3. The only difference is that here we use the *GFEM*$^{\text{g-l}}$ methodology to solve it. The linear viscoelastic material properties are described by the Prony series shown in Table 4.2. The simulation time is 20 seconds and the temperature is 20° C. The cube is again loaded by $\lambda(t)\,\sigma$ at top and bottom. Three different time functions for the load are investigated: constant, ramp and sinusoidal.

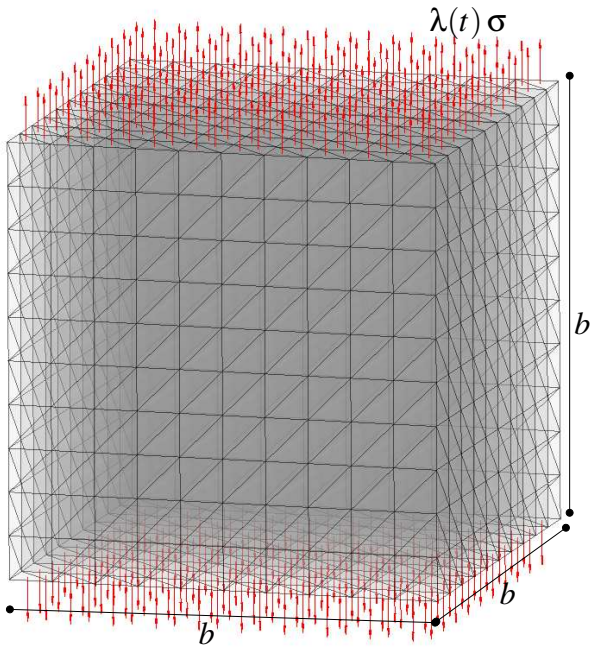

Figure 5.7: *Details of global reference problem.*

In order to compute the time-dependent energy release rate (ERR) for this problem a reference elastic problem is created. The instantaneous shear and bulk modulus are used as material properties. The imposed stress on top and bottom of the cube is in the reference elastic problem is σ. The initial global reference elastic problem is solved using the cube mesh shown in Figure 5.7.

Notice that at this stage the crack is not discretized. Spring boundary conditions computed from this initial global solution are next applied to a local reference problem defined around the crack surface. The local mesh is refined, and nodes are enriched in order to obtain the local solution. Figure 5.8 shows the reference local problem and the refinement of the mesh. The global refer-

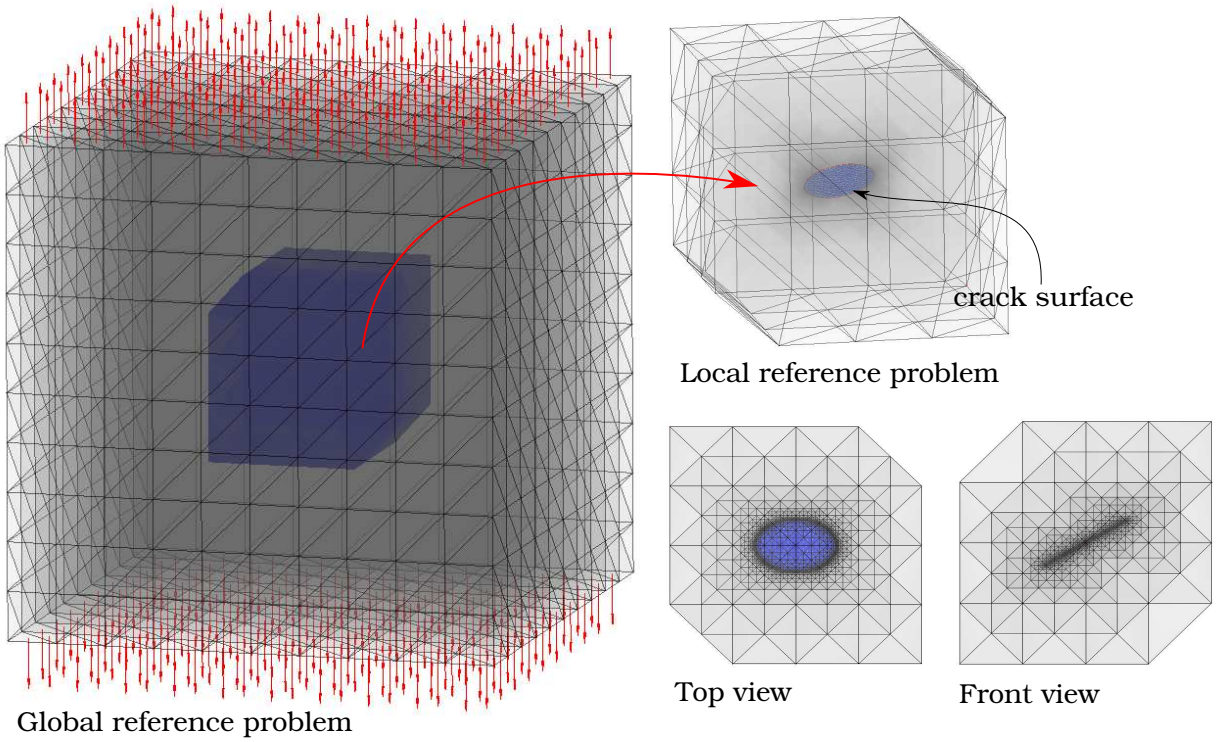

Figure 5.8: *Details of local reference problem.*

ence problem is then enriched with the local solution and solved as described in previous sections. The extracted stress intensity factors for Modes *I*, *II*, and *III* using the $GFEM^{g\text{-}l}$ methodology are shown in Figure 5.9. These results are compared with the analytical solution for an infinite domain and the solution computed with the GFEM. SIFs are normalized using Equation (4.38). Excellent agreement among all three solutions can be observed for all SIFs.

To compute every component of the viscoelastic ERR Equations (3.22)- (3.24) are used. Note that these equations are in Laplce domain; therefore, the material functions in this domain are needed. The Prony series function in Laplace domain is given by Equations (4.36) and (4.37). Also, the Laplace transform functions for each load type are given by Equations (4.39)-(4.41).

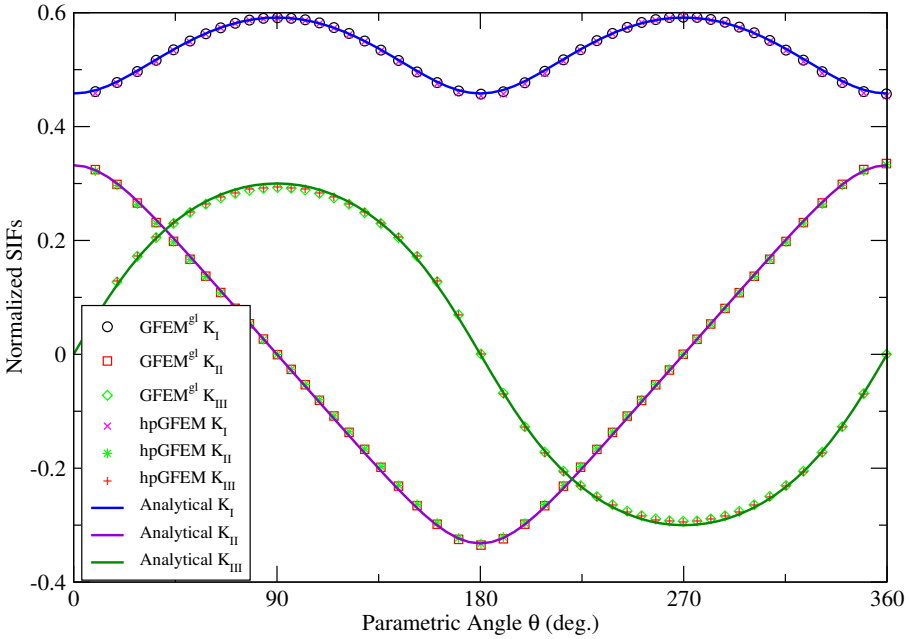

Figure 5.9: *The SIFs for Modes I, II, and III of* GFEM$^{g\text{-}l}$*, GFEM and analytical solution for an infinite domain.*

Finally, the ERR in the time domain are obtained by a Fourier's numerical inversion using Equation (3.35). Figure 5.10 shows the components of ERR for the constant load type. Figure 5.11 shows the components of ERR for the ramp load type. Figure 5.12 shows the components of ERR for the sinusoidal load type.

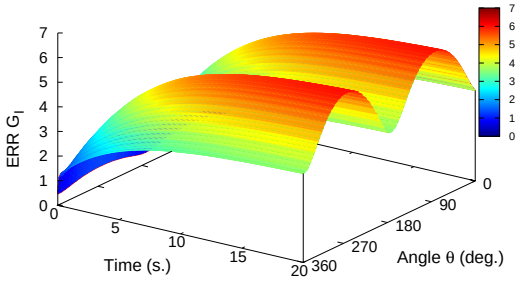

(a) ERR $\mathcal{G}_I$, constant load type.

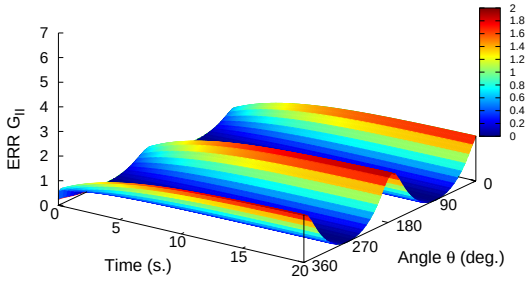

(b) ERR $\mathcal{G}_{II}$, constant load type.

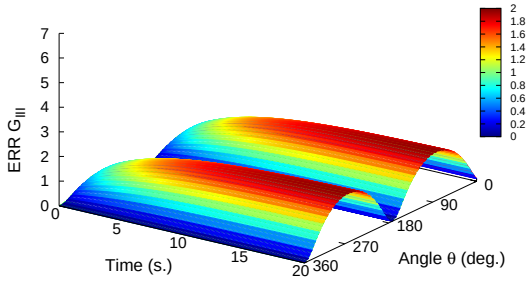

(c) ERR $\mathcal{G}_{III}$, constant load type.

Figure 5.10: *Time dependent energy release rate along crack front for constant load.*

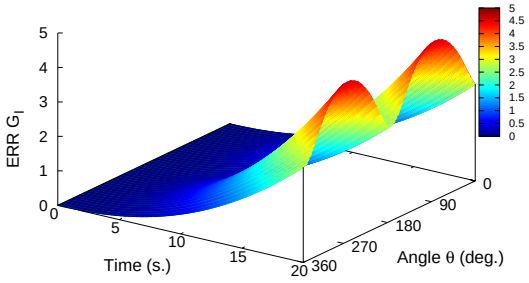

(a) ERR $\mathcal{G}_I$, ramp load type.

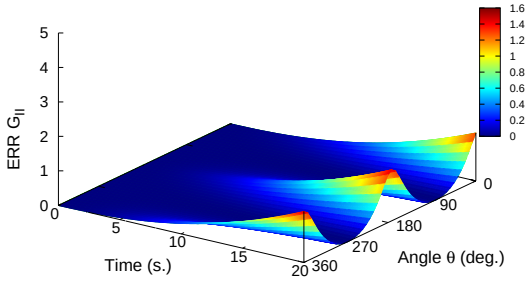

(b) ERR $\mathcal{G}_{II}$, ramp load type.

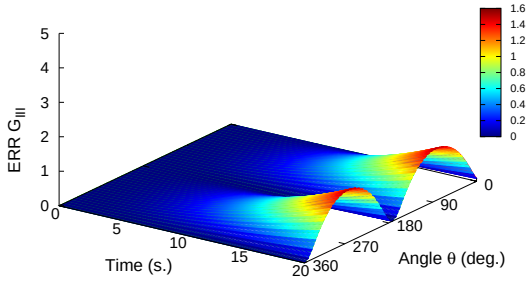

(c) ERR $\mathcal{G}_{III}$, ramp load type.

Figure 5.11: *Time dependent energy release rate along crack front for ramp load.*

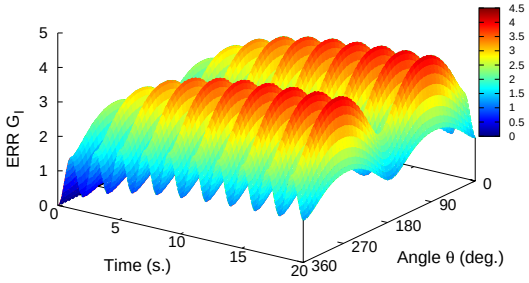

(a) ERR $\mathcal{G}_I$, sinusoidal load type.

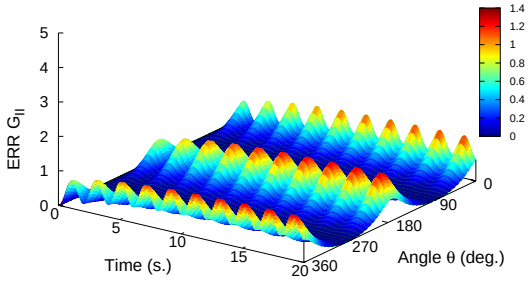

(b) ERR $\mathcal{G}_{II}$, sinusoidal load type.

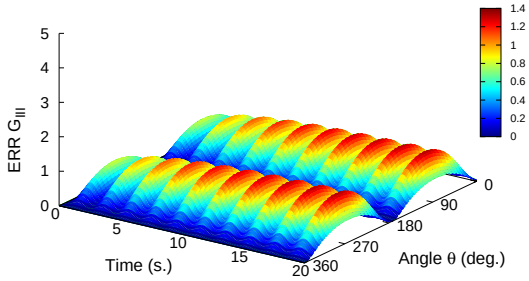

(c) ERR $\mathcal{G}_{III}$, sinusoidal load type.

Figure 5.12: *Time dependent energy release rate along crack front for sinusoidal load.*

5.3 Reflective Crack Simulation with the *GFEM*$^{\text{g-l}}$

In this section, we analyze a typical pavement section of an airport that serves the Boeing 777 aircraft, using the *GFEM*$^{\text{g-l}}$.

5.3.1 Pavement Layer Profile and Material

The selected model geometry and pavement cross sections for the underlying PCC are from a section of runway 4L-22R at O'Hare Airport, located in Illinois, USA. Details of the cross section are shown in Figure 5.13(b). The interface between the asphalt overlay and Portland cement concrete layer is assumed to be fully bonded.

To enhance model efficiency, the subgrade is idealized as a dense liquid (Winkler) foundation. Therefore, a series of springs is used to model the subgrade in the 3-D pavement model. The simulated airfield pavement is composed of a 20 cm asphalt overlay; 23 cm concrete slabs, each with plan dimensions of 6 m $\times$ 5.7 m (PCC), and a 28 cm cement treated base (CTB). A saw-cut joint having a width of 13 mm is assumed to exist and is modeled accordingly.

Figures 5.13(a) and 5.13(b) show details of the pavement portion considered and details concerning the material properties adopted. The asphalt overlay is assumed to be composed of a linear viscoelastic material represented by a Prony series given in Table 5.3. All other layers are assumed to have elastic material properties.

The concrete slabs are assumed to have a Young's modulus of 27,580 MPa, while the CTB modulus is taken as 6,900 MPa. A Winkler-type subgrade, modeled with springs, is assumed to have a stiffness of $k = 55\frac{N}{cm^3}$. The Poisson's ratios for the concrete slabs and the CTB layer are assumed to be 0.15 and 0.20, respectively.

5.3.2 Finite Element Geometry and Boundary Conditions

In order to compute all components of energy release rate (ERR) along the crack front, a reference elastic problem using the instantaneous material properties for the asphalt overlay is created. This

Table 5.3: *Mathematical representation of the viscoelastic material (Prony series).*

m	G_m (MPa)	K_m (MPa)	ρ_m (s)
1	44.244	132.73	2e-2
2	64.542	193.62	2e-1
3	126.35	379.04	2
4	137.29	411.88	2e1
5	88.488	265.46	2e2
6	35.577	106.73	2e3
7	9.3506	28.051	2e4
8	3.1472	9.4415	2e5
9	0.8391	2.5174	2e6
10	0.1803	0.5409	2e7
11	0.2191	0.6573	2e8

$G_0 = 510.74$ and $K_0 = 1532.22$

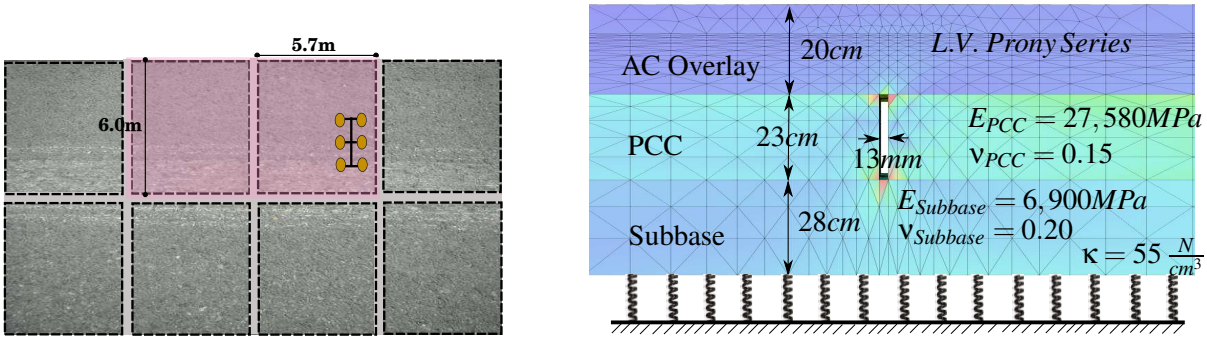

(a) The shaded square represents the portion of pavement modeled in this study. The Boeing 777 gear configuration is also illustrated.

(b) Material properties and details of a standard section of runway 4L-22R at O'Hare Airport.

Figure 5.13: *Airfield pavement analyzed.*

reference problem is solved using the *GFEM*$^{g\text{-}l}$ methodology described in Section 5.1 and the stress intensity factors (SIFs) for all modes are extracted.

A 3-D global model of the reference elastic problem loaded with one main gear of a Boeing 777, aircraft is simulated using the *GFEM*$^{g\text{-}l}$ enrichment functions. Figure 5.14(a) shows the global and local models as well as the crack surface. The global discretization is composed of a relatively coarse 3-D mesh *without any crack discretization* created using the software program Patran [124]. A single gear of a Boeing 777-200 aircraft is modeled, and it is assumed that the distance between gears is large enough such that interactions between them may be neglected for the purposes of

studying the mixed mode behavior and 3-D responses above a given PCC joint.

The local reference model is created automatically by extracting elements from the global coarse mesh that are confined in a specified bounding box. For this problem, 4 percent of the global problem length is used $25 \times 10 \times 25$cm (Figure 5.14(b)). Here, a half-penny-shaped reflective crack with a radius of 1.3 cm, as shown in Figure 5.14(c), is inserted into the AC overlay, above the PCC joint.

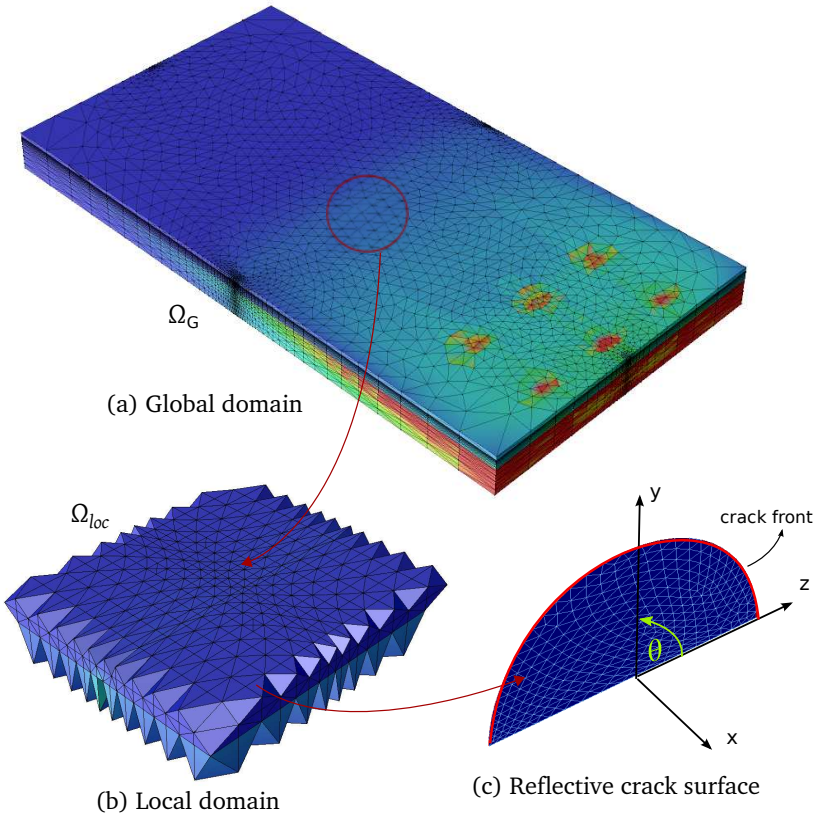

(a) Global domain

(b) Local domain

(c) Reflective crack surface

Figure 5.14: *Discretization of the airfield pavement with a single landing gear and a reflective crack.*

The resulting polynomial order of the initial global problem is $p-order = 2$. The solution of this analysis are used to impose boundary conditions on the local model, where spring boundary conditions are used, as explained in Section 5.1.2.

The reflective crack is inserted in the local model at the bottom of the asphalt overlay. Figure 5.15 shows the crack opening in the local reference model. The elements intersecting the crack

front are bisected automatically until an acceptable level of mesh refinement is achieved. Furthermore, enrichments are assigned to local nodes in order to model the discontinuity across the crack surface and singularity along the crack front. Also, the resulting polynomial order to approximate the continuous part of the solution is $p-order=3$. For details about crack enrichment functions refer to Section 4.2.1. The ratio of characteristic element size to crack radius, L_e/a, along the crack front is $0.008 \leq L_e/a \leq 0.07$.

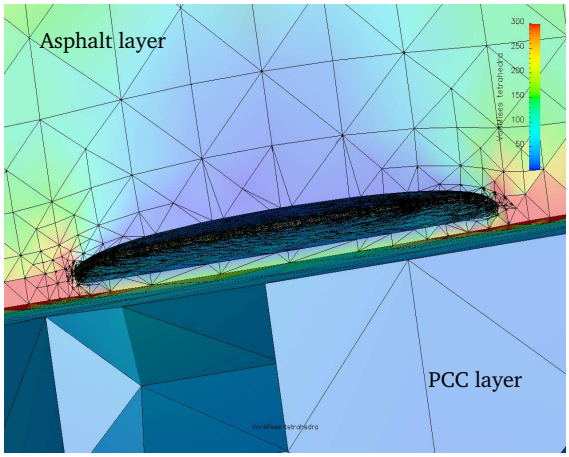

Figure 5.15: *Local model, bottom view in the interior of the PCC joint. Reflective crack opening.*

Global-local enrichment functions, discussed in Section 5.1.3, are obtained from the solution of the local problem and are used to enrich the coarse global problem. Cubic polynomial shape functions are used in a boxed region with dimensions $25 \times 10 \times 25$ cm close to the crack surface. Elsewhere in the domain, quadratic shape functions are used.

After completing the simulation of the reference elastic problem, components of ERR for the viscoelastic problem are computed using Equations (3.22)- (3.24). These Laplace functions are transformed back to the time domain numerically using Equation (3.35).

The linear viscoelastic material properties represented with Prony series in Laplace domain have the form of Equations (4.36) and (4.37). The load is considered to be a time function $\lambda(t)\,\sigma$, with σ the pressure applied by the landing gears of the aircraft and $\lambda(t)$ a sinusoidal load

$|\sin(\frac{t\,\pi}{t_{peak}})|$. The Laplace transform of the squared function $\lambda(t)^2$ is

$$\bar{\bar{\lambda}}_2(p) = \frac{1}{2\,p} - \frac{p}{2\,(p^2 + \frac{\pi^2}{t_{peak}^2})} \tag{5.10}$$

The simulation time considered here is 240s, with a $t_{peak} = 10$s.

5.3.3 Analysis of Results

The stress intensity factors (SIFs) extracted from the reference elastic *GFEM*$^{\text{g-l}}$ solution of the three-dimensional reflective crack problem are compared with the solution provided by solving the same problem using the GFEM approach applied directly to the global problem as described in Section 4.2. Also, SIFs from a global-local generalized FEM are presented. This global-local generalized FEM method suffers from the same limitations as the global-local FEM (GL-FEM) [83]. Therefore, it is reasonable to assume that the conclusions drawn here are also valid for the global-local FEM. The main difference between these two is that the local solution is computed with the GFEM.

In order to quantify the error of the stress intensity factor (SIF) extracted along the crack front, the normalized discrete L^2-norm of the relative difference between the computed SIF and the verification solution,

$$e^r(\mathcal{K}_i) := \frac{\|e_i\|_{L^2}}{\|\hat{\mathcal{K}}_i\|_{L^2}} = \frac{\sqrt{\sum_{j=1}^{N_{ext}} \left(\mathcal{K}_i^j - \hat{\mathcal{K}}_i^j\right)^2}}{\sqrt{\sum_{j=1}^{N_{ext}} \left(\hat{\mathcal{K}}_i^j\right)^2}} \tag{5.11}$$

is used. In the equation above, N_{ext} is the number of extraction points along the crack front, $\hat{\mathcal{K}}_i^j$ and $\mathcal{K}_i^j$ are the verification and computed stress intensity factor values for Mode i at the crack front point j, respectively.

Figure 5.16(a) shows $\mathcal{K}_I$, $\mathcal{K}_{II}$ and $\mathcal{K}_{III}$ computed with the three methods investigated herein, namely, the GL-FEM, the *GFEM*$^{\text{g-l}}$ and the GFEM. The x-axis represents the position along the

crack front given by the angle θ (cf. Figure 5.14(c)). Since the values of the SIFs for $\mathcal{K}_I$ are about ten times greater than those for $\mathcal{K}_{II}$ and $\mathcal{K}_{III}$, the comparison of accuracy is only performed for $\mathcal{K}_I$. Figure 5.17(a) shows $\mathcal{K}_I$ computed with the three methods.

The global-local FEM (GL-FEM) solutions consists of SIFs computed from the solution of the local problem and subjected to spring boundary conditions provided by the initial global problem, refer to Section 5.1.2. The relative error obtained with this method for $\mathcal{K}_I$, is $e^r(\mathcal{K}_I) = 0.055$. The $GFEM^{\text{g-l}}$ corresponds to the solution computed with the GL-FEM used as enrichment function for the coarse global mesh. The relative error of the $GFEM^{\text{g-l}}$ for $\mathcal{K}_I$, is $e^r(\mathcal{K}_I) = 0.011$. Observe that this value is 5 times smaller than the one obtained by the GL-FEM.

To show one of the major limitations of the global-local FEM (GL-FEM) the quality of the boundary conditions for the local problem is reduced by solving the initial global problem using linear polynomial shape functions, instead of quadratic, without changing the order of polynomials in the local and enriched global problems. Figure 5.16(b) shows $\mathcal{K}_I$, $\mathcal{K}_{II}$ and $\mathcal{K}_{III}$ computed with the three methods–the GL-FEM, the $GFEM^{\text{g-l}}$ and the GFEM. Notice that SIFs for Modes *I*, *II* and *III* for the global-local FEM (GL-FEM) have shifted downwards, meaning that decreasing the quality of the boundary conditions has led to a decrease in the accuracy of the solution. On the other hand the $GFEM^{\text{g-l}}$ is still delivering a very accurate solution. The relative errors of the GL-FEM and $GFEM^{\text{g-l}}$ for $\mathcal{K}_I$, are $e^r(\mathcal{K}_I) = 0.296$ and $e^r(\mathcal{K}_I) = 0.011$, respectively. Figure 5.17(b) shows $\mathcal{K}_I$ computed with the three methods.

The size of the initial global problem, local problem and enriched global problem in terms of degrees of freedom (dofs) are shown in Table 5.4. The size of the local problem is the same for both cases because the amount of refinement and enrichment used is equal. Similarly in the enriched global problem, polynomial enrichment and corresponding global-local enrichment used is the same. By, keeping these two equal we can observe the influence of the quality of the initial global problem approximation.

Figure 5.18 shows the viscoelastic time-dependent ERR for Mode *I* along the crack front for this reflective crack. Other modes are not computed because this is clearly a Mode *I* dominated

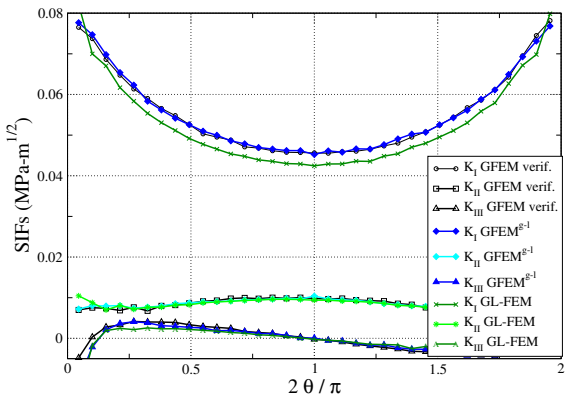

(a) A quadratic approximation is used in the initial global problem.

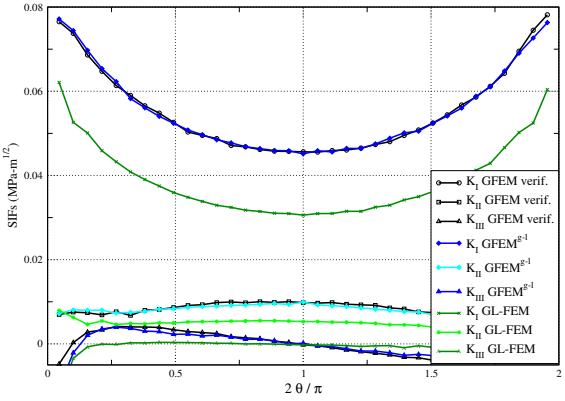

(b) A linear approximation is used in the initial global problem.

Figure 5.16: *Stress Intensity Factors (SIFs) along the crack front for the GL-FEM and the* GFEM^{g-l}. *The GFEM solution is taken as verification.*

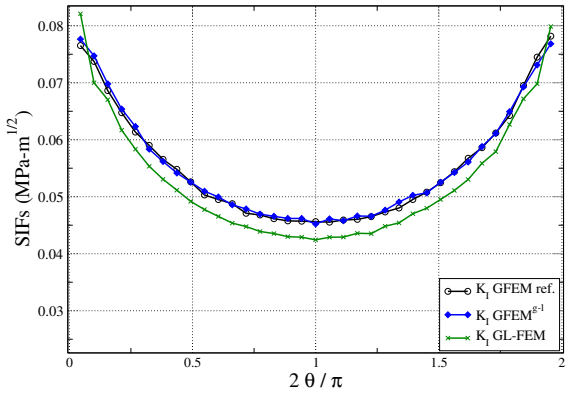

(a) A quadratic approximation is used in the initial global problem.

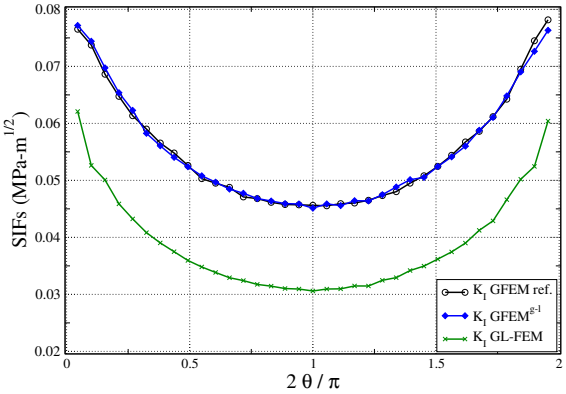

(b) A linear approximation is used in the initial global problem.

Figure 5.17: *$\mathcal{K}_I$ Stress Intensity Factor (SIF) along the crack front for the GL-FEM and the* GFEM^{g-l}. *The GFEM solution is taken as verification.*

problem.

The example presented in this section shows that stress intensity factors extracted from reference elastic problem using the *GFEM*$^{g-l}$ methodology are significantly more accurate than those extracted from a standard global-local analysis. Even though the *GFEM*$^{g-l}$ does not require refinement of the global mesh, the accuracy of the solution is comparable with that of the GFEM. This enables, for example, the use of meshes for airfield pavements with many slabs which are orders of magnitude larger than the reflective crack dimensions. Furthermore, in the *GFEM*$^{g-l}$, the initial

Table 5.4: *Size of problems in terms of degrees of freedom.*

Domain	DOFs
Initial Global (linear)	147,348
Initial Global (quadratic)	589,392
Local	224,736
Enriched Global	700,371

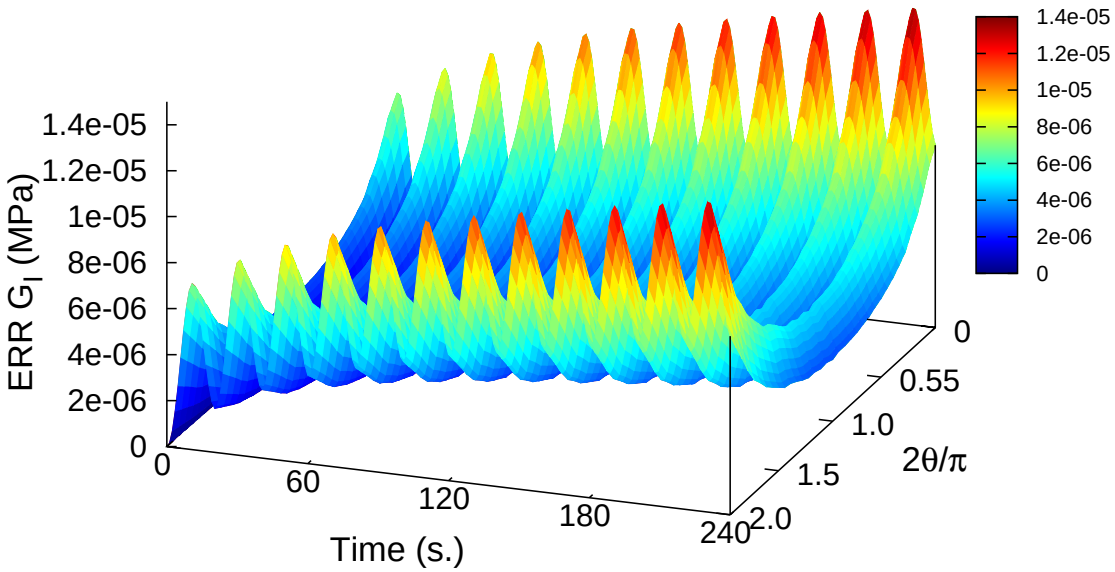

Figure 5.18: *Energy Release Rate (ERR) $\mathcal{G}_I$ along the crack front.*

global problem only needs to be solved once, and the same global coarse mesh can be used for any crack configuration [40]. In other words, many reflective cracks can be studied at different parts of the airfield pavement without having to solve the initial, large domain from scratch several times. This brings substantial computational savings. Similar conclusions are observed in the case of crack propagation simulations [131].

5.4 Analysis of *GFEM*$^{g\text{-}l}$ Parameters

As in the previous section, we analyze a typical section of an airport pavement using the *GFEM*$^{g\text{-}l}$. Here, the effects of local domain size on the accuracy of the *GFEM*$^{g\text{-}l}$ and standard global-local finite element analysis (GL-FEM) are investigated. Furthermore, the influence of the global enrichment zone size used in the *GFEM*$^{g\text{-}l}$ is also analyzed. Again, the global model is denoted as the initial large domain that represents the entire airfield pavement being modeled. The local model is the small domain extracted from the global model. At the local model a three-dimensional reflective crack is discretized and modeled using the GFEM. Mode *I*, *II* and *III* stress intensity factors are computed at local and enriched global reference elastic problems. The viscoelastic time-dependent energy release rate is computed afterwards with the most accurate solution of the reference elastic problem analysis.

5.4.1 Pavement Layer Profile and Material

A pavement section similar to the previous example is used. Figure 5.19 provides the material properties used. In this example the subbase is removed and rollers are placed beneath the concrete slab. This simulated airfield pavement is composed of a 13 cm asphalt overlay, 20 cm concrete slabs each with plan dimensions of 4.5 m $\times$ 9.15 m (PCC). A saw cut joint of 13 mm width is modeled within the PCC layer.

The asphalt overlay is assumed to be composed of a linear viscoelastic material represented by the Prony series given in Table 5.3. All other layers are assumed to have elastic material properties.

The concrete slabs are assumed to have a Young's modulus of 27,580 MPa. The Poisson's ratio for the concrete slabs is assumed to be 0.15.

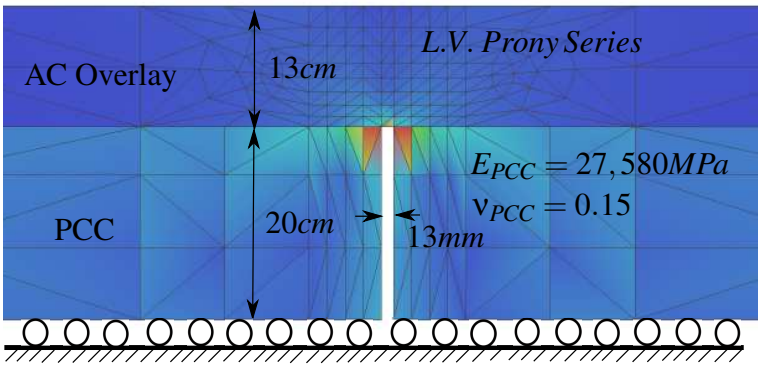

Figure 5.19: *Material properties and details of a standard section.*

5.4.2 Finite Element Geometry and Boundary Conditions

Following the same idea as in the previous problem, a reference elastic problem is created and analyzed using $GFEM^{g\text{-}l}$. Results for both GL-FEM and $GFEM^{g\text{-}l}$ are presented.

The goals of this example are to address the following issues: (i) What size should the local problem be? (ii) What effect do the initial local problem boundary conditions have in the solutions of the local problem and the enriched global problem? (iii) How many nodes should be enriched with the solution of the local problem in the enriched global problem? To answer these questions, different sizes of local domains are analyzed, and also the size of the enrichment zone at the enriched global problem is varied to investigate the effect on the stress intensity factors (SIFs). The analysis is separated in two sections: 1) Effect of local domain size and, 2) Effect of enrichment zone size. In both cases, the same global model is used. This consists of two slabs and one PCC joint as illustrated in Figure 5.20, which uses a relatively coarse 3-D mesh *without any crack discretization*. The smallest elements are created to represent the PCC joint.

Due to temperature variation, the concrete slabs that lie under the asphalt layer expand and contract inducing the opening and closing of the PCC joint. In this problem, displacement boundary conditions are applied at the sides of the PCC slabs to simulate an opening of the joint, which

in turn creates tension at the bottom of the asphalt overlay. The prescribed displacements are indicated by $\Delta = 0.05$ cm in Figure 5.20(a).

A half-penny-shaped reflective crack with a radius of 2.5 cm, as shown in Figure 5.20(c), is inserted into the AC overlay, above the PCC joint in the local model.

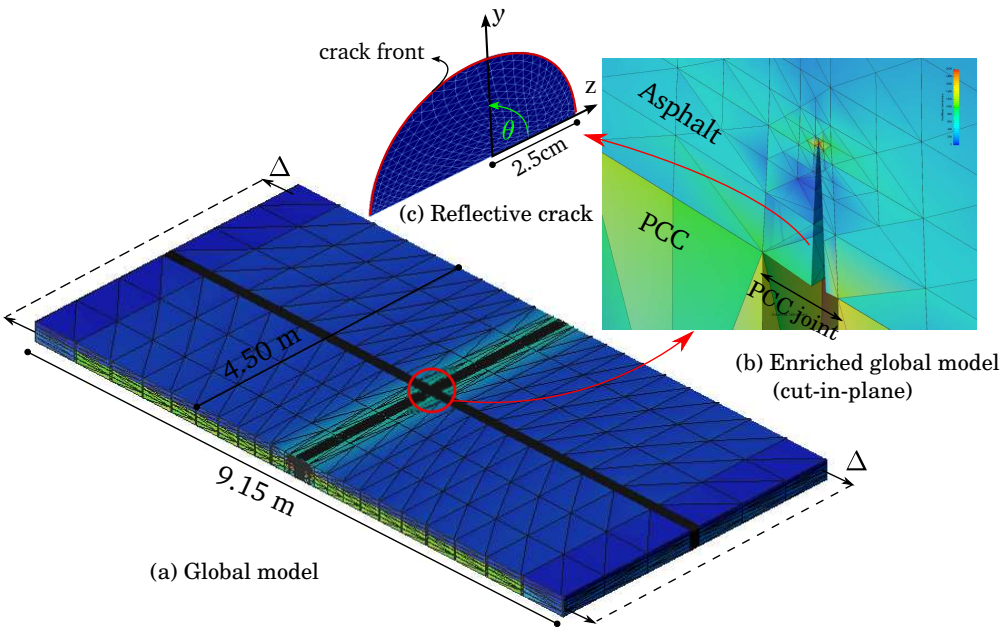

Figure 5.20: *(a) Global model used as initial and enriched global domain. (b) Deformed configuration of enriched global problem (cutting plane). (c) Reflective crack surface.*

5.4.3 Effect of Local Domain Size

The local model is created automatically by extracting elements from the global coarse mesh that are in contact with the crack surface. To increase the size of the local problem, layers of elements may be added as desired. In this section, three sizes of local domains are studied with two different boundary conditions. Recall that the boundary conditions are provided by the solution of the initial global problem. Therefore, the latter will be solved using linear and quadratic approximations. The global-local enrichment zone size in both cases is fixed and is minimized in size by including only nodes of global elements cut by the crack surface. Figure 5.21 shows the three local domains considered, while Figure 5.22 shows the global nodes enriched with global-local functions (indi-

cated by red spheres). The same reflective crack is inserted in all local domains for the purpose of stress intensity factor investigation.

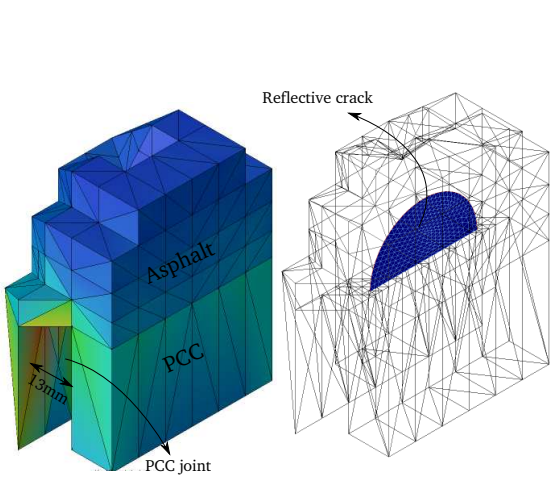

(a) Local domain defined using one global layer of elements around the crack surface

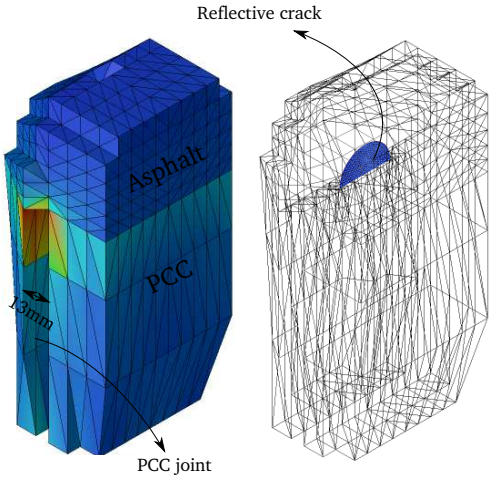

(b) Local domain defined using three global layers of elements around the crack surface

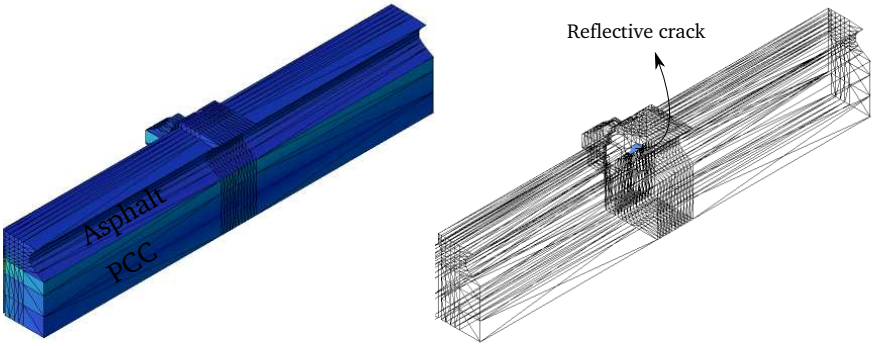

(c) Local domain defined using five global layers of elements around the crack surface

Figure 5.21: *Local domains for the study of size effect on SIFs for GL-FEM and* GFEM$^{g\text{-}l}$.

First, the initial global problem is solved using a linear approximation, i.e., no polynomial enrichments and no crack surface are used. The solution then provides boundary conditions for the local problem. In the local problem, the mesh is automatically refined to have a $L_e/a = 0.027$ for all three cases. Third order polynomial, step function, and singular function enrichments are used to discretize the reflective crack in the local domain. Finally, the enriched global problem is solved using enrichment functions generated from the solution of the local problem. The polynomial order is the same as in the initial global problem, i.e., linear. Stress intensity factors are extracted

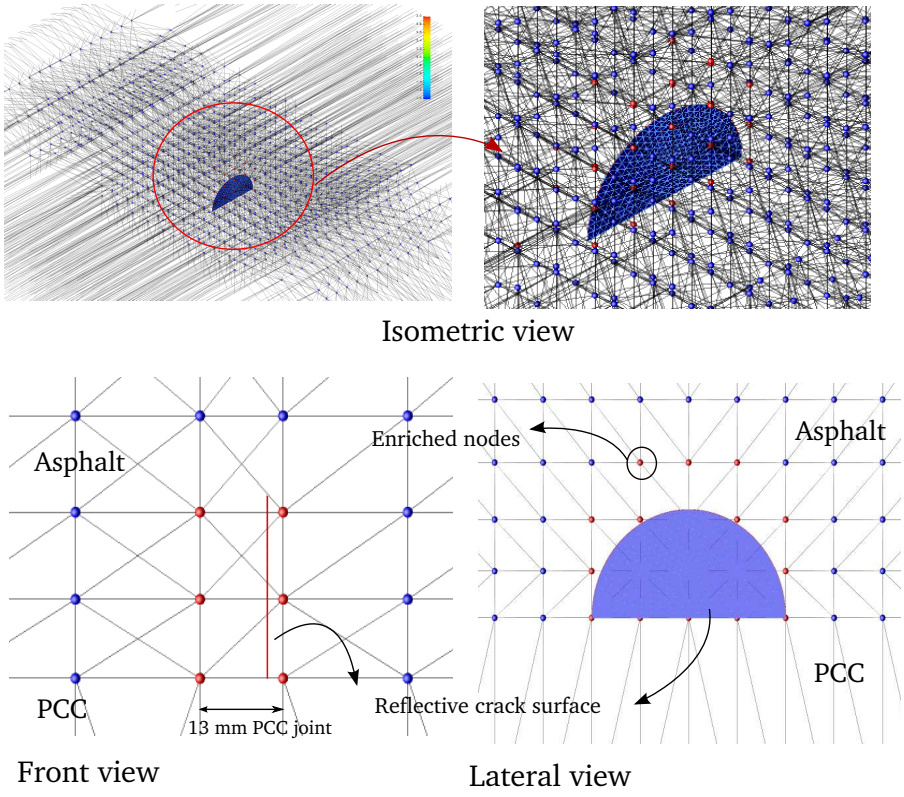

Figure 5.22: *Global nodes enriched with global-local functions (indicated by red spheres). The same set of nodes is used regardless of the size of the local domain.*

from the local and enriched global solutions. Figure 5.23(a) shows $\mathcal{K}_I$ only, as this is a Mode *I* dominated problem. It is observed that the size of the local domain significantly affects the solution of the standard global-local approach (GL-FEM). With a bigger local domain, we obtain a more accurate solution for SIFs. On the other hand, in the *GFEM*$^{\text{g-l}}$ the size of the local domain has almost no influence on the results for the SIFs. This means that even with the smallest local domain, where the solution is not accurate, the *GFEM*$^{\text{g-l}}$ is able to obtain results that are as accurate as those of the largest local domain. Both GL-FEM and *GFEM*$^{\text{g-l}}$ solutions are not yet close to the verification solution, due to the linear approximation used in the initial global problem. The same process is then repeated, but this time using a quadratic approximation in the global domain along with a cubic approximation in a boxed region of size $25 \times 10 \times 25$ cm close to the crack surface region. Again, no crack is inserted at this stage. The local problem and enriched global problem are solved in the same manner as before. The polynomial order in the enriched global problem is the same as in the initial global problem. Figure 5.23(b) shows the results. Again, it can be seen that the effect of the size of the local domain significantly affects the solution of the standard GL-FEM. The GL-FEM solution of the largest local domain and all *GFEM*$^{\text{g-l}}$ solutions are close to the verification solution. Table 5.5 shows the relative error $e^r(\mathcal{K}_I)$ for all cases.

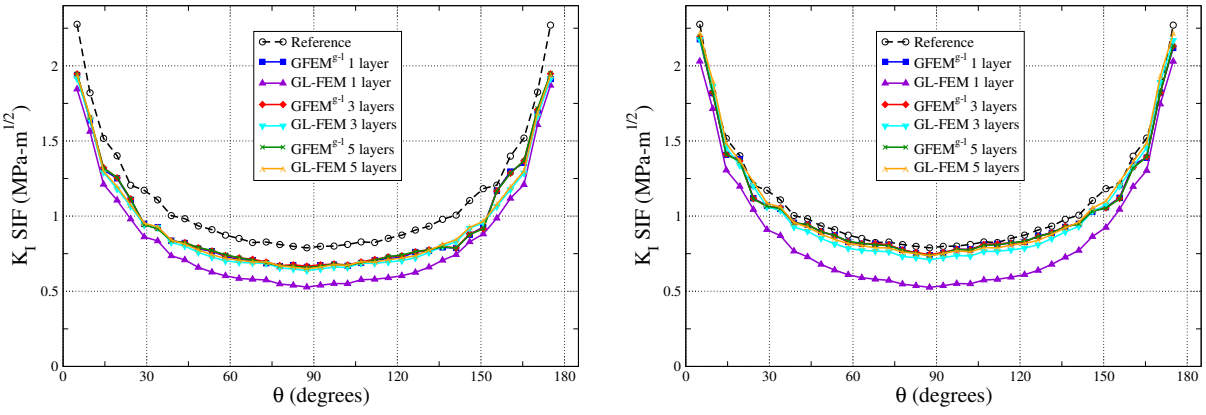

(a) Linear approximation in initial global problem.

(b) Quadratic and cubic approximations in initial global problem.

Figure 5.23: *Stress Intensity Factor* $\mathcal{K}_I$ *for GL-FEM and* GFEM$^{g\text{-}l}$.

Table 5.5: *Relative error $e^r(\mathcal{K}_I)$ of the stress intensity factor (SIF); In column one of the table, p refers to the approximation order used in the initial global problem.*

Local Domain Size	*GFEM*$^{\text{g-l}}$	GL-FEM
$p = 1$		
1 layer	0.123	0.205
3 layers	0.121	0.130
5 layers	0.121	0.121
$p = 2$		
1 layer	0.040	0.194
3 layers	0.040	0.060
5 layers	0.040	0.040

5.4.4 Effect of Enrichment Zone Size

The main goal of this analysis is to investigate the accuracy of the *GFEM*$^{\text{g-l}}$ approach as a function of the number of enriched nodes in the enriched global problem. Accuracy is again assessed in the context of stress intensity factors along the crack front in the asphalt layer. Figure 5.24 shows the local domain that is used for all the cases studied in this section, which is a rectangular prism of size $25 \times 10 \times 25$ cm, centered around the reflective crack site. In other words, the local domain is defined as a rectangular box, rather than layers of elements that contain the crack surface (the selection of one approach over the other is arbitrary). As before, two different boundary conditions for the local problem are considered. The enriched global problem uses the same polynomial shape functions as the initial global problem. Global-local enrichments are added as described below.

Four global-local enrichment zone sizes are studied in this section. They are denoted cases 1, 2, 3 and 4 hereafter. The first case utilizes a very small enrichment zone size, including only nodes of the first layer of elements close to the crack front (cf. Figure 5.25). In the second case, the enrichment zone contains global nodes within an $8 \times 8 \times 8$ cm bounding box (cf. Figure 5.26). In the third case, a $13 \times 8 \times 13$ cm bounding box is used (cf. Figure 5.27). Finally, the fourth case involves the largest possible enrichment zone size, which consists of all the nodes of the global elements that comprise the local domain (cf. Figure 5.28).

Stress intensity factors are computed for two different boundary conditions used at local problems, as done in Section 5.4.3. Figure 5.29(a) shows the stress intensity factors obtained for the

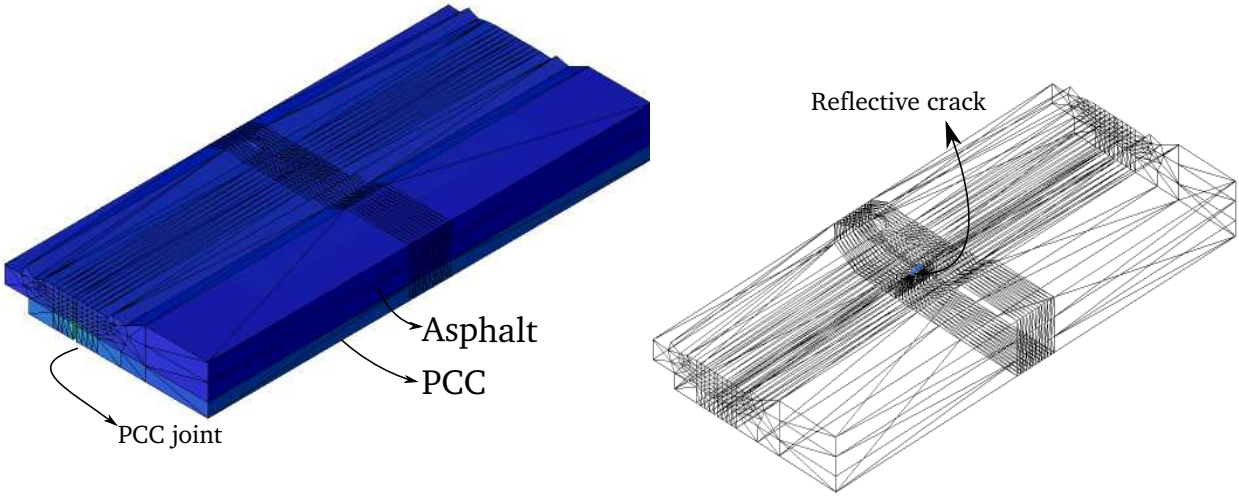

Figure 5.24: *Local domain defined using a* $25 \times 10 \times 25$ *cm bounding box.*

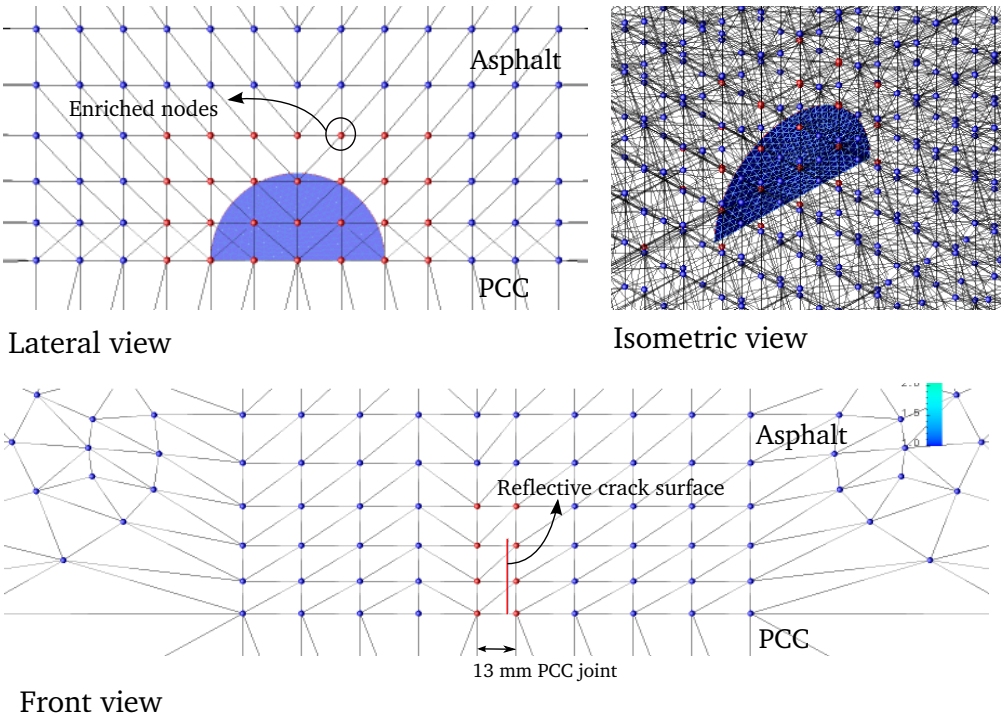

Figure 5.25: *Enrichment zone case 1.*

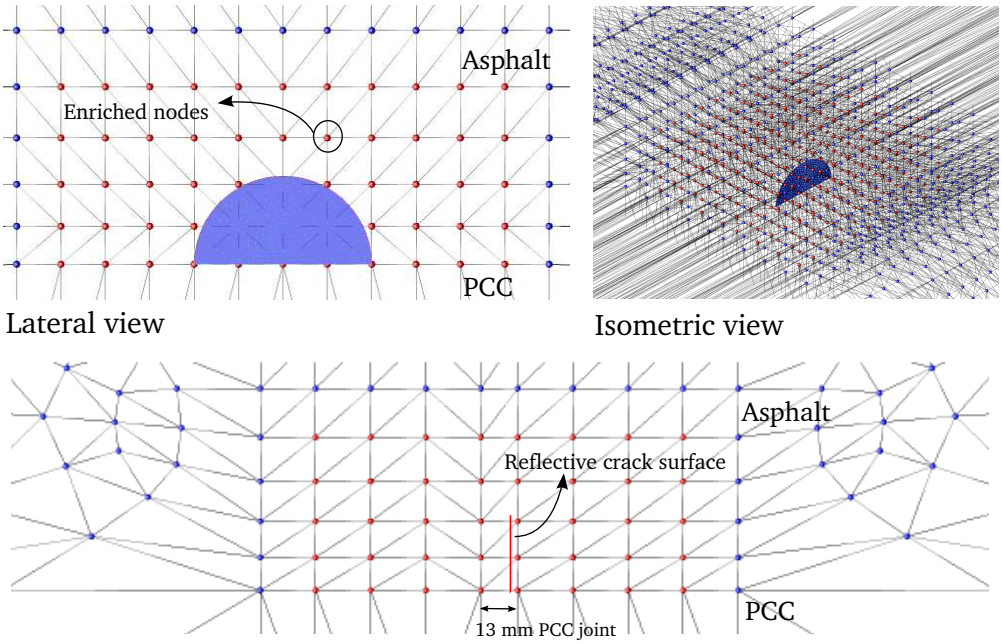

Figure 5.26: *Enrichment zone case 2.*

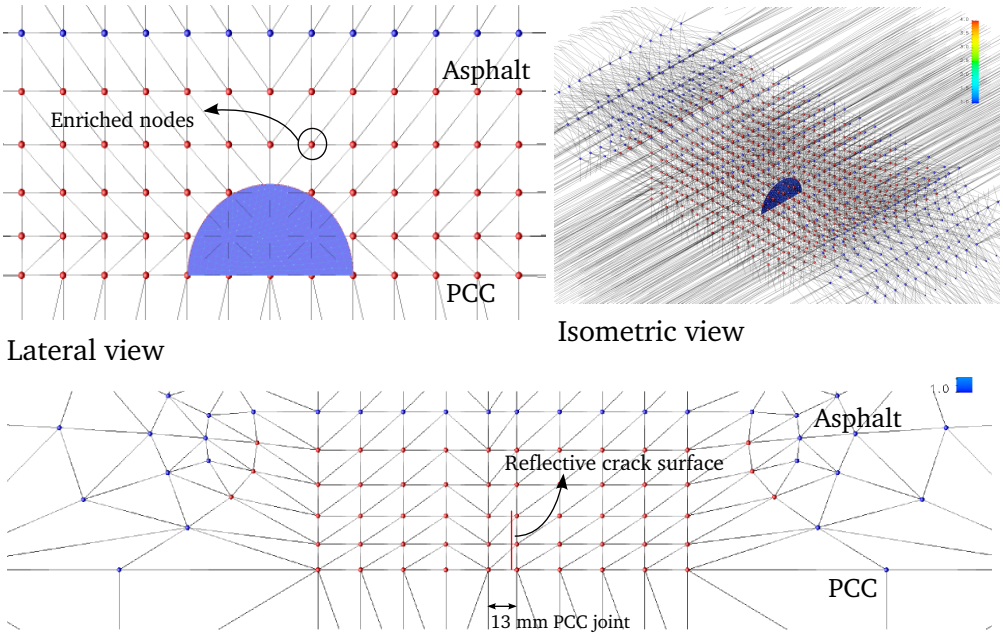

Figure 5.27: *Enrichment zone case 3.*

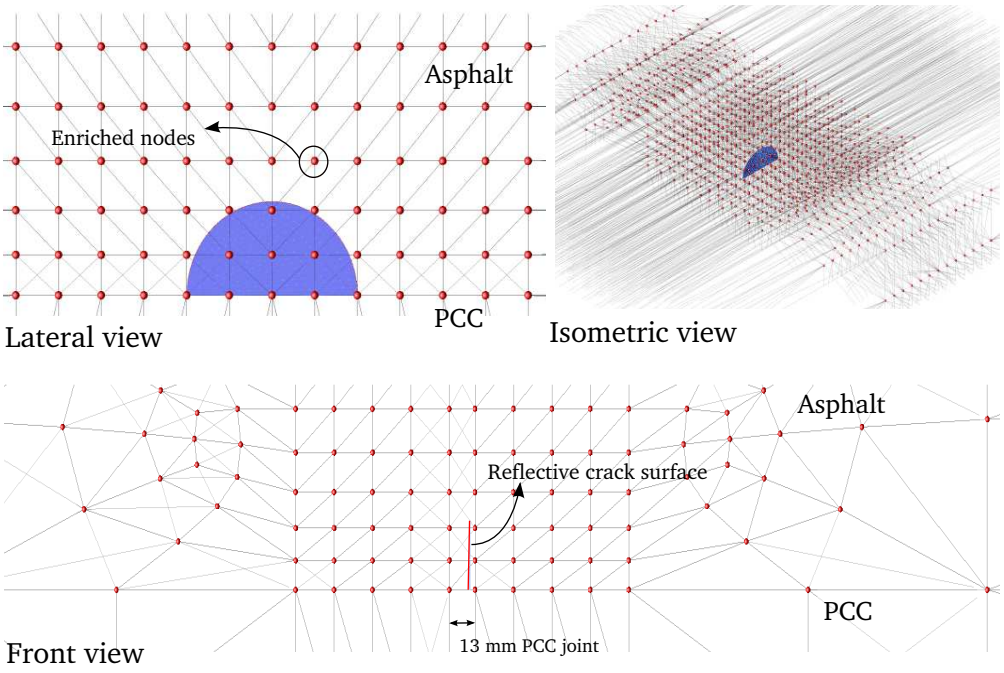

Figure 5.28: *Enrichment zone case 4.*

Table 5.6: *Relative error $e^r(\mathcal{K}_I)$ of the stress intensity factor (SIF); p refers to the approximation order used in the initial and enriched global problems. Case 4 with $p = 2;3$ is take as the verification solution.*

Case	$p = 1$	$p = 2;3$
1	0.105	0.0287
2	0.091	0.0196
3	0.030	0.0089
4	0.030	n/a

case where both the initial and enriched global problem use a linear approximation and Figure 5.29(b) shows those obtained for the quadratic/cubic case. The verification solution used is taken from case 4, with quadratic and cubic polynomial enrichments in the initial and enriched global problems.

This analysis in the elastic problem clearly shows that having more enriched nodes in the global problem improves the accuracy of the SIF prediction. This improvement is more clearly seen in the case of the linear initial global problem. Table 5.6 shows the relative error $e^r(\mathcal{K}_I)$ for all cases studied. Table 5.7 shows the size of the last problem, Case 4, as an example.

The time-dependent ERR is computed using the stress intensity factors of the reference elastic

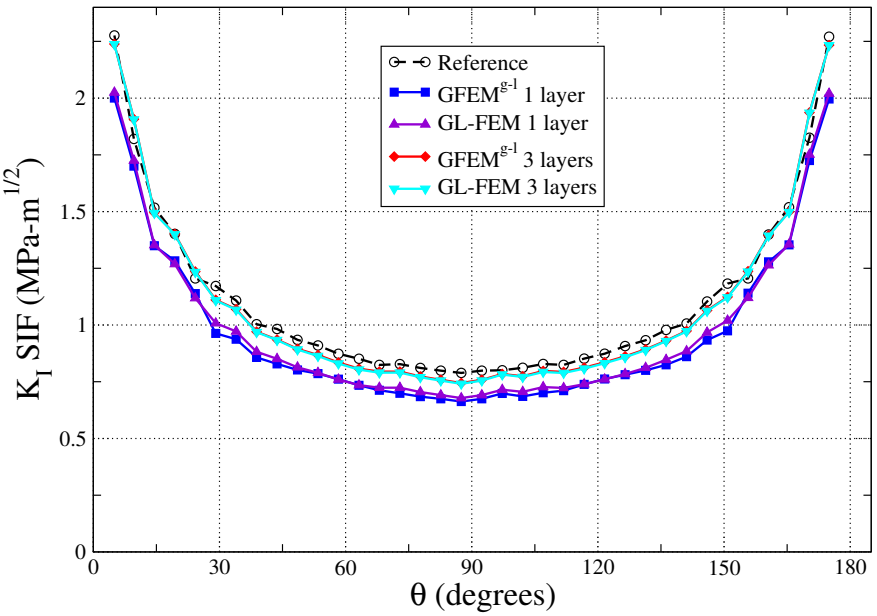

(a) Linear approximation in initial and enriched global problems.

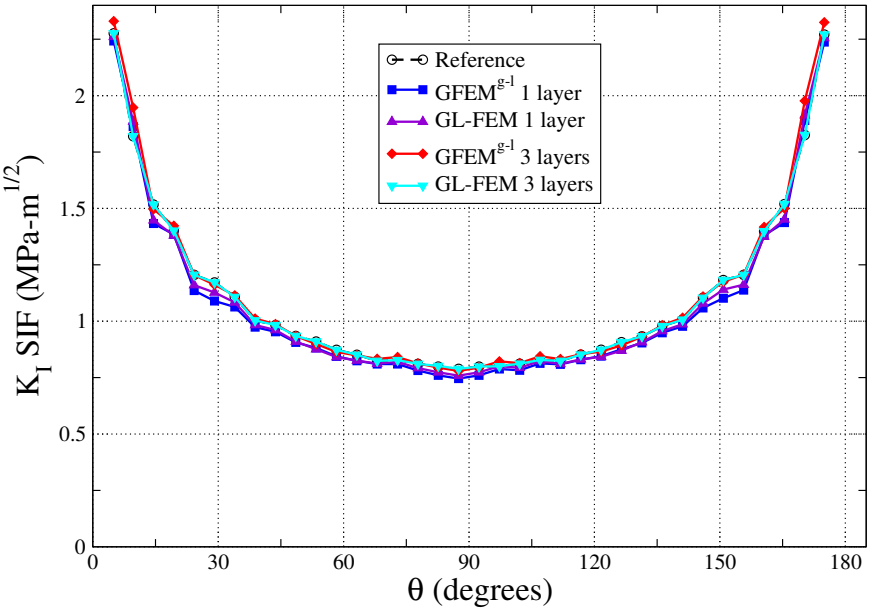

(b) Quadratic and cubic approximations in initial and enriched global problems. Note that the verification solution shown in the figure corresponds to case 4.

Figure 5.29: *Stress Intensity Factor $\mathcal{K}_I$ for* GFEM$^{g\text{-}l}$*, all cases.*

problem case 4. The Mode *I* component of ERR of the viscoelastic problem are computed using Equation (3.32). This Laplace functions is is numerical inverted to the time domain using Fourier's

Table 5.7: *Size of last example Case 4 in terms of degrees of freedom (dofs).*

Problem	Linear	Quadratic and Cubic
Initial Global	22,050	109,260
Local	102,516	102,516
Enriched Global	36,090	112,770

method.

The linear viscoelastic material properties represented with Prony series in Laplace domain have the form of Equations (4.36) and (4.37). The imposed displacement is considered to be a time function $\lambda(t)\,\Delta$. With Δ as the displacement produced by the contraction/expansion of the underlaying PCC and $\lambda(t)$ as a sinusoidal load $|\sin(\frac{t\,\pi}{t_{peak}})|$. The Laplace transform of the squared function $\lambda(t)$ is given by Equation (5.10). The simulation time considered here is of 240s. with a $t_{peak} = 10$s. Figure 5.30 shows the time-dependent ERR for Mode I along the crack front for this reflective crack problem.

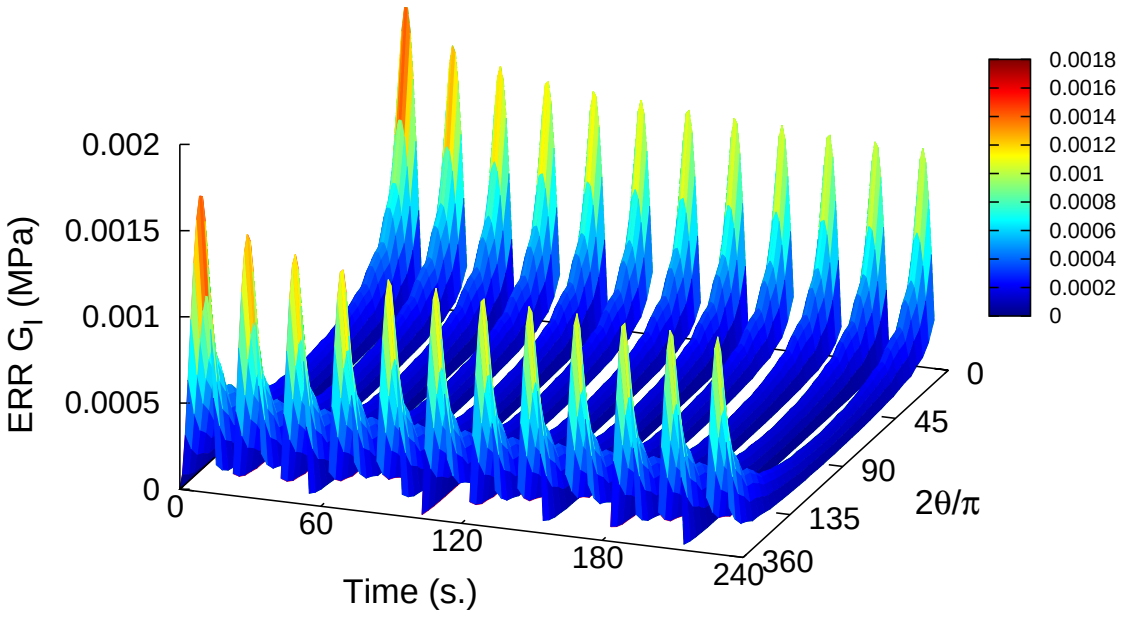

Figure 5.30: *Energy Release Rate (ERR) $\mathcal{G}_I$ along the crack front.*

Chapter 6

Computational Considerations and Improvements to Crack Propagation Algorithm

Crack growth analysis of industrial complexity problems has been broadly done for decades using the standard finite element method (FEM) [53, 114, 152, 178, 184]. In FEM, the discontinuity of the solution is represented by meshes with double nodes and the crack surface is defined by the faces of the elements connected to the double nodes at each side of the crack surface. For three dimensional crack propagation with the FEM, re-meshing of the volume mesh is required at each crack propagation step. Even if the generation of meshes in complex 3-D geometries (re-meshing) is fully automated, it is a demanding task to satisfy discontinuities and element aspect ratio requirements. Poor aspect ratios call into question the accuracy of the approximations. Robustness of the methods may also prove lacking in the case of multiple cracks interacting with each other as well as domain boundaries. The generation of appropriate volume meshes at each propagation step combined with the extremely large problems resulting from the highly refined meshed leads to excessive computational cost [173], as well as poorly conditioned system matrices resulting from the large discrepancy in element sizes used to sufficiently mesh the domain. Figure 6.1 shows an example of a half-penny shaped crack discretized with the FEM.

The partition-of-unity (PoU) based Generalized FEM (GFEM) [10], explained in Section 4.2, also refered to in the literature as the eXtended FEM (*XFEM*) [163] is a promising technique to overcome the shortcomings of the standard FEM in crack growth simulations. In these methods, singularities and discontinuities in the solution are represented using appropriately selected enrichment functions. Geometrical description of crack surfaces, which *do not fit the volume mesh*, provide the necessary information to select the proper location and type of enrichment functions to be used. For crack modeling, fully discontinuous enrichment functions are typically needed for

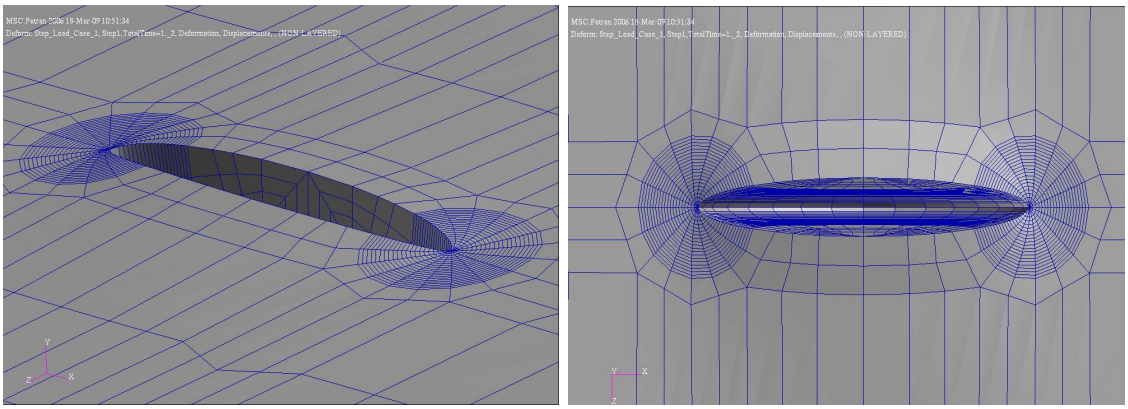

Figure 6.1: *Half penny shaped crack discretized in FEM.*

the crack surface representation and additional singular enrichment functions are required at the crack front.

Since elements in GFEM or *XFEM* have no requirement to fit the crack surface, mesh refinement can be easily applied in localized regions of the discretization. A survey of 3-D crack growth modeling with PoU methods is presented in [135]. In the case of a 3-D fracture mechanics problem, PoU methods rely on a computational geometry technique for the representation of the crack surface. This representation allows the correct assignment of enrichment functions which approximate the discontinuous and singular components of the solution, thus inserting the proper physics into the discretized problem. Two basic types of computational geometry techniques are utilized: (1) implicit methods, which rely upon the volume mesh for the crack surface representation, and (2) explicit methods in which the crack surface is explicitly meshed independently of the volume mesh.

In the case of implicit methods, a three-dimensional volume mesh is used in order to represent a crack surface. Therefore, in these methods the quality of the crack surface descriptions depends upon the refinement of the volume mesh. One example of this type of crack surface representation is the level set method [153]. This method was originally created to model motion of interfaces. These interfaces are represented as the zero level set of a function of one higher dimension. A crack is described by two level sets; a normal level set which is the signed distance to the crack surface, and a tangent level set which is the signed distance to the plane including the crack front and

perpendicular to the crack surface. Belytschko and co-workers coupled the *XFEM* with the level set method for static crack and crack growth simulations [63, 109, 163]. Duan et al. [38] introduced the element local level set method for 3-D dynamic crack growth analysis with the *XFEM*. A detailed review of crack surface representation with level set methods in *XFEM* simulations can be found in [49].

In order to circumvent the often expensive computation to update the level sets in a crack propagation analysis, Chopp et al. [33, 164] proposed use of the fast marching method (FMM) to track the evolution of three-dimensional crack surfaces in *XFEM* simulations. The FMM is an interface capturing technique in which the location of the interface is updated using a finite difference, upwinding scheme. The authors note that one of the strongest features of FMM is the capability of handling multiple, merging interfaces and they apply their technique to simulate crack coalescence. While solved on a 3-D domain, all crack configurations considered involved co-planar, Mode *I* cracks. It is reported by the authors that there are still issues in the corresponding implementation of the *XFEM*, particularly in the proper application of enrichment when interfaces, such as multiple cracks, approach one another. In this case, there may be nodes which are enriched twice due to the proximity to two different crack fronts in conjunction with the use of a quasi-uniform mesh. Errors in the evaluation of the distance functions can be introduced if only one distance function is used, and this issue was handled by using multiple independent distance functions for each crack. It should be noted that the crack surface representation in [33] is implicit and the level set method is used, the FMM is used merely to update the interface location.

Although the level set method combined with *XFEM* has been a good candidate for crack growth simulations, the approach suffers from some limitations, in particular, when applied to problems in which the crack surface geometry is complex. Some of the most important limitations are: (i) The inability to represent a crack surface with sharp turns, which is a common feature of crack surfaces in fatigue crack growth under mixed-mode loading. (ii) Unnecessary degrees of freedom in the simulation, due to the mesh refinement all around the surface region in order to accurately update and represent the crack surface. (iii) Potentially inaccurate representation of the

crack front, in some cases [50], consequence of using two level set functions which are attempting to represent a crack surface. Limitation (ii) is clearly illustrated in Figures 2-3 in Moes et al. [110] and Figure 6.2 from Fries et al. [60]. This property forces a trade-off between problem size

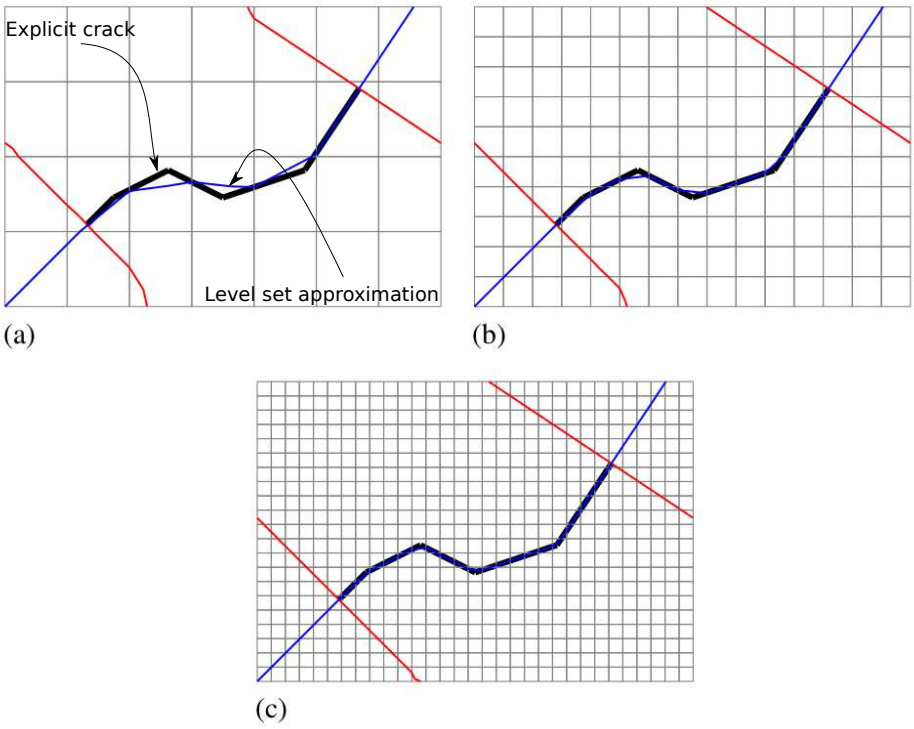

Figure 6.2: *Approximation of the crack path by means of discretized level set functions on different meshes (this figure is from [60]).*

and accuracy of crack surface representation which is absent in explicit methods. While loss of accuracy far from the crack front may not influence the solution in a great manner, it is important to have an accurate description of the crack front itself. Local coordinate systems are placed at the crack front to compute important crack propagation parameters such as crack propagation direction. The computed angle for propagation is directly influenced by the local coordinate system at the crack front, and therefore, an inaccurate description of the front by the level sets functions will give, in turn, an incorrect angle of propagation for the true front.

Mixed mode problems, in particular, tend to exhibit sharp turns in the initial propagation steps. Furthermore, depending on the problem and the geometry of the crack surface, the speed of propagation can vary significantly along the front. This means that part of the crack front advances

across elements ahead of it while other parts stay inside of the same elements containing the front before propagation. Consider the part of the front that has partially cut an element as illustrated, for simplicity in 2-D, in Figure 6.3. The black solid line represents the explicit crack surface or path, the dashed line is the extension of the true front and the blue line is the level set approximation. Clearly there is an inconsistency between the level set description and the true crack path. This will result in an inaccurate computation of the crack propagation direction.

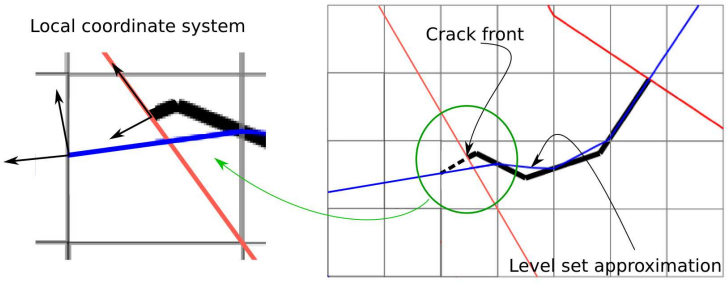

Figure 6.3: *Approximation of the crack front by means of discretized level set functions.*

Other methods that tie the surface representation to the volume mesh are the methods based on a collection of planar cuts or crack planes in tetrahedral elements [76]. These methods are subdivided into four categories depending on the crack path tracking strategy: 1) Fixed.- Uses a standard interface elements (e.g. cohesive elements) and it requires the crack path to be known beforehand. 2) Local.- The crack growth is driven by the normal direction of the maximum principal stress and represented by planar cuts in the tetrahedral elements. Each element has its own independent crack plane. 3) Non-local.- The crack surface in the neighborhood of the crack front is smoothed out in a least-square sense by a post-processing corrector step. The element crack planes on the neighborhood of the crack front are adjusted to provide a smooth crack front for each crack growth step and, consequently, a smooth crack surface representation. 4) Global.- The crack surface is represented by an iso-surface of the solution for the heat conduction-like problem which, in turn, is represented by a collection of planes defined at the element level. It uses an auxiliary problem to trace the crack surface path. Even though, these methods are a good alternative to the level set method they also suffers from some limitations: a predetermined crack path in the case of fixed

tracking scheme; discontinuities in the crack surface representation due to variations of crack plane normals between adjacent elements in the local tracking scheme; and the need to apply an auxiliary problem to trace the crack surface path in case of a global tracking scheme. The bottom line is that the accuracy of the crack surface representation in these methods is still mesh dependent, since the crack surface is represented by the same mesh used for the solution of the problem. A remedy for this problem is to incorporate an auxiliary mesh of same spatial dimension as the mesh used in the analysis process to represent the crack [132]. However, this requires additional bookkeeping and computational cost in order to transfer information between meshes.

Explicit methods use one-dimensional segments embedded in a two dimensional space or two-dimensional polyhedral in a three-dimensional space to represent the crack path and crack surface, respectively. This type of representation provides a continuous crack path/surface completely independent from the 2-D/3-D mesh, adding no extra computational cost to the solution of the problem. Moreover, no mesh refinement is required to improve the accuracy of the crack representation. The crack can have an arbitrary shape and special geometrical features, such as sharp turns, can be easily represented. The accuracy of the crack surface representation depends only on the 2-D elements (facets) used for its discretization. Problems such as hydraulic fracture, propagation with cohesive models and crack closure are some examples where a good crack surface representation is important. This explicit methodology was successfully applied in conjunction with the GFEM in [42, 44, 83, 84, 128–130] as well as the element-free Galerkin method [92]. More recently, the explicit method was extended to represent interfaces in fluid-structure interaction problems using the *XFEM* [105].

Fries et al. [60] combine explicit and implicit crack descriptions within the *XFEM*. The authors use three level set functions which are computed from an explicit crack surface representation and serve as a basis for the enrichments. The explicit representation is employed to determine exactly the crack increment and to update the crack representation without the drawbacks of the purely implicit level sets. The authors state their motivation in the development of a hybrid explicit-implicit crack surface representation as seeking to avoid several shortcomings of the use of level

sets, in particular: 'the update of the level set function is not simple and may introduce additional inaccuracies'. The use of the explicit surface allows for both the de-coupling of the volume and crack surface discretizations as well as the avoidance of solving the advection-type equations required for level set updating. A fully explicit crack surface representation within the *XFEM* is presented by Sukumar et al. [112] with the use of a rasterized crack path corresponding to element boundaries from a sub-grid mesh.

Pereira et al. [128, 130] use the GFEM in conjunction with fully explicit surface meshes composed of flat triangles in order to represent complex 3-D crack surfaces. This method allows automatic local refinement (at regions of interest) in complex 3-D meshes preserving the aspect ratio of volume elements regardless of crack geometry. In this technique, the volume mesh in completely independent of the surface mesh. Therefore, the size of the elements in the volume mesh does not affect the accuracy of the crack surface representation, nor does the size of the facets in the explicit crack surface mesh impact the size of the problem discretized by the volume mesh. Furthermore, the explicit crack surface representation using triangular facets can preserve special features (i.e. kinking and twisting), throughout the crack growth simulation. Figures 6.4 and 6.5 show an example of an explicit crack surface representation in a 3-D GFEM problem. The green and yellow glyphs are crack enrichments as discussed in Section 4.2.1

For crack evolution, Pereira et al. [130] use the face offsetting method (FOM) [78] to track the evolution of complex 3-D crack fronts. Originally this numerical technique (FOM) was developed to track the evolution of general 3-D surfaces, with particular application to burning of solid propellants. The key features of this method are the computation of an increment limit at each step to avoid self-intersection of the front, and the adaptive smoothing of the surface mesh along the tangential direction. In short, at each crack growth step FOM computes a new crack front position avoiding self intersection based on the GFEM solution, additionally it redistributes the vertices to maintain or improve the quality of the surface mesh. The surface mesh update after the front has been propagated is performed with one of two techniques termed: Propagate and Extrude (PAE) and Propagate and Smooth (PAS). More details about FOM and its use in crack propagation can

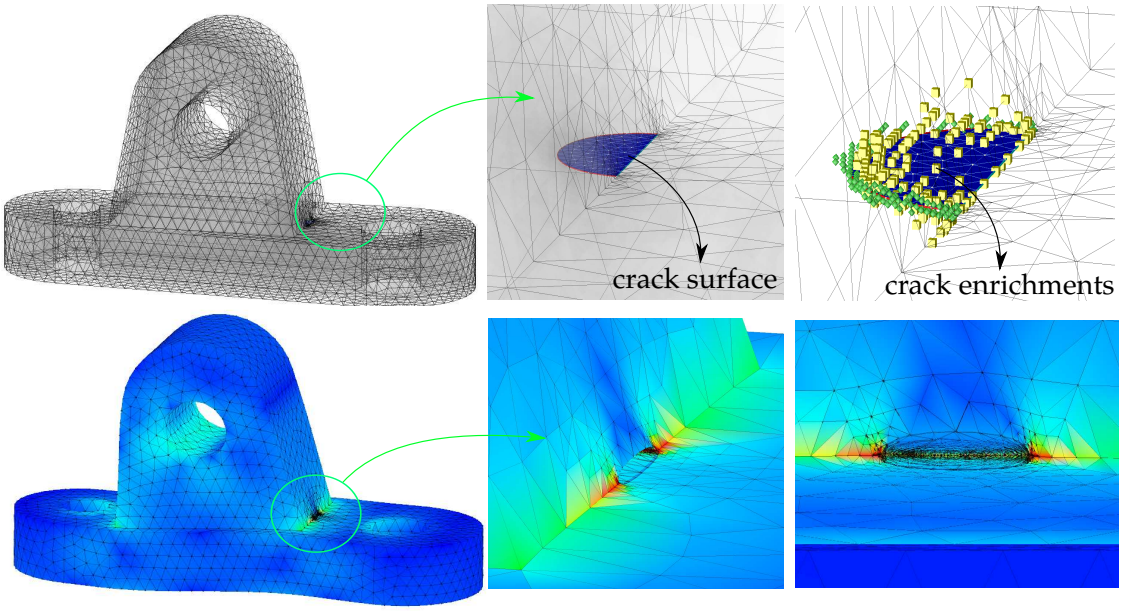

Figure 6.4: *Explicit crack surface representation in GFEM.*

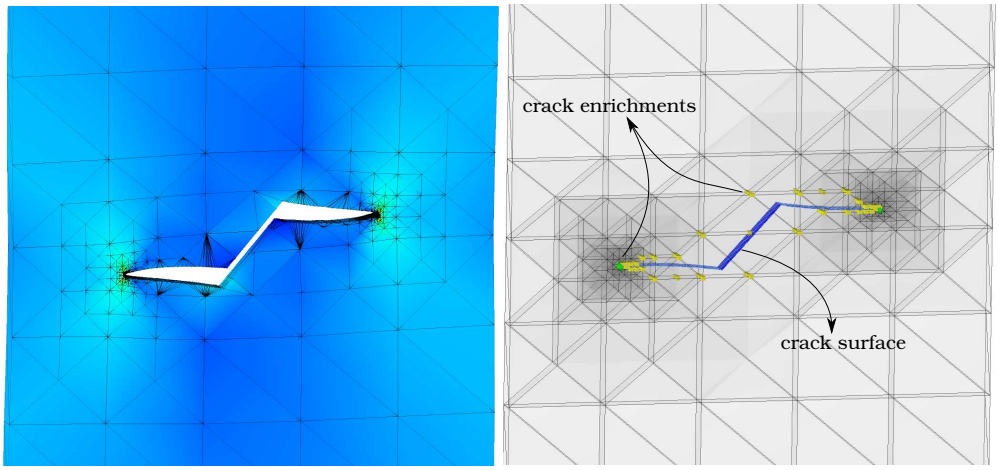

Figure 6.5: *Explicit crack surface representation with a sharp turn (kink) in a GFEM simulation.*

be found in [130]. In the first technique front (PAE) vertices are cloned, then the coordinates of these vertices are set based on the new front position. Additionally, edges and triangular facets are created between the original and cloned front. While not explicitly noted, Fries et al. [60] for example, use a similar form of PAE for crack evolution. The use of this technique is evidenced by the deterioration seen in the crack front representation when an initially (roughly) circular crack front propagates into a highly decagonal front if no additional efforts are made to improve the representation of the crack surface. A second drawback of this technique is the creation of layers of excessive numbers of potentially small and unnecessary triangular facets if propagation increments are small and PAE is used at every increment.

The second technique (PAS) propagates the front by simply moving the vertices at the front, without the creation of any new facets. As in PAE, the coordinates of the crack front vertices are updated to the new crack front position. If this technique is used at every crack propagation step the aspect ratio quality of the facets can become deteriorated. As such, a good combination of both techniques is required. In general, FOM works well when the crack front propagation speed is uniform along the front. However this is not always the case (e.g. reflective cracks in airfield pavements [61, 62]), and in general different crack speeds are expected in different regions of the crack front. More details about FOM and its use in crack propagation can be found in [130]. Figure 6.6 illustrates FOM techniques for crack evolution, this figure is from the Paper [130].

This work takes the work of Pereira et al. [130] as a starting point and improves upon the crack propagation strategies proposed in [130]. Shortcomings of the strategies as proposed in [130] are highlighted and improved algorithms are presented which are geared towards the development of a robust, explicit algorithm for long duration crack propagation analyses. Furthermore, we illustrate the ability of the method to model the accurate evolution, interaction with boundaries and coalescence of multiple crack surfaces.

In the following Section a crack propagation example with significantly different crack front speed is investigated and improvements in the crack evolution algorithm are presented.

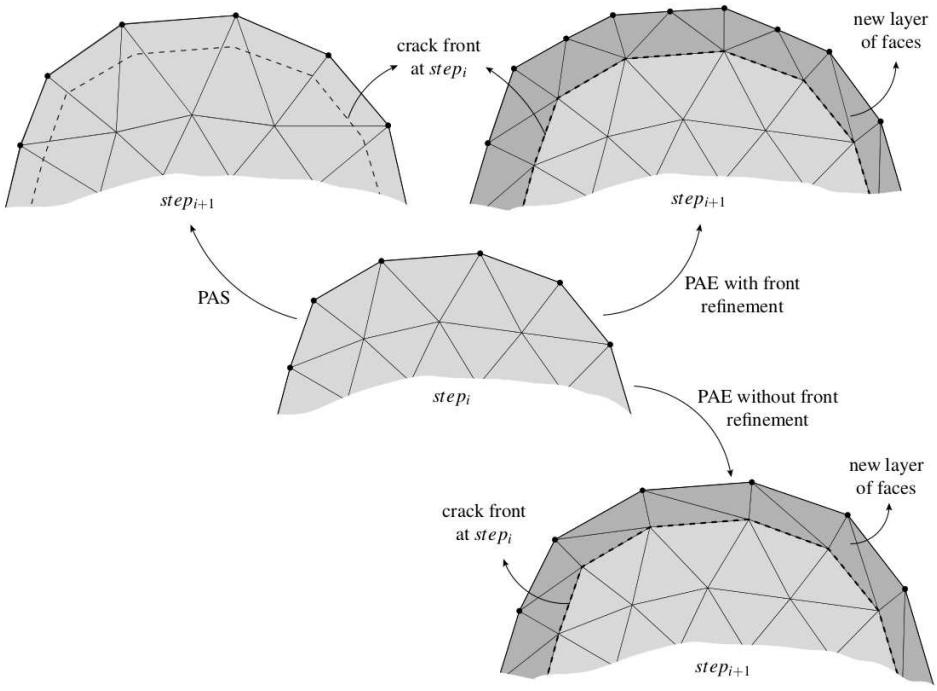

Figure 6.6: *Pereira et al. [130], use the FOM method for crack front evolution in 3-D.*

6.1 Improvements to Crack Propagation Algorithm

The method used to represent a crack surface within the GFEM framework in this paper is the same as that presented by Pereira et al. [128, 129]. It consists of an explicit representation in the form of a polyhedron surface composed of flat triangles with straight edges as illustrated in Figure 6.7. As mentioned before, this explicit representation is independent of the GFEM mesh and does not change the problem size. Furthermore the polyhedron surface provides the necessary geometrical information for the construction of crack front coordinate system, crack front enrichment functions and integration elements cut by the crack surface. The creation of integration elements is a common approach to deal with discontinuities which may be located inside of a finite element. It consists of subdividing each finite element into sub-domains with faces fitting the crack surface. These sub-domains (integration elements) are used for *integration purposes only* and a standard quadrature rule can be used over each of them. More details can be found in [128, 129].

During crack propagation simulations, the crack surface evolution is represented by a sequence

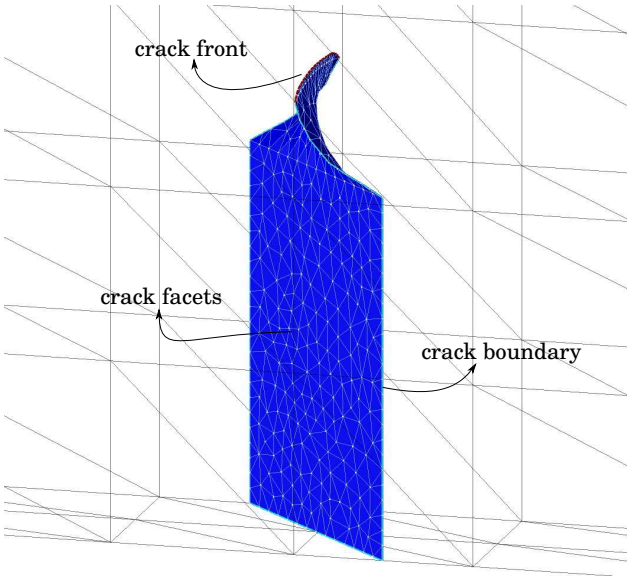

Figure 6.7: *Non-planar, explicit crack surface representation used in GFEM.*

of crack front steps using an explicit crack surface representation at each step. The geometry of the crack evolves based on crack front parameters computed using the physics of the problem at each crack growth step. At the crack front, the deflection angles and the growth amounts are computed using a defined criterion. Refer to Section 7.3 for details.

Consider a crack propagation problem similar to the reflective cracking in airfield pavements. A small quarter-penny-shaped crack is inserted into a rectangular domain. Boundary conditions consist of applied displacements at the bottom faces of the domain. They are such that they simulate the opening and closing of the joint on the underlaying pavement as seen in Figure 6.8. The maximum applied opening of the joint is $0.03\,a_0$ inches along the x-direction. The geometric parameters of the crack surface are $a_0/L = 0.2$, where a_0 is the radius of the initial crack. The maximum crack front increment allowed at each step is $\Delta a_{max} = 0.05\,a_0$. The simulation consists of 50 propagation steps. Linear elastic material properties are assumed with a Young's Modulus, $E = 3318.94$ ksi and a Poisson's ratio, $v = 0.3$. The propagation criteria used here is the one explained in Section 7.3 with Paris law material constants of $C = 1.0$ and $m = 2.5$. Since the purpose of this section is to study the performance of different computational geometry techniques to track the crack evolution of the crack, same type of enrichments and same amount of refinement

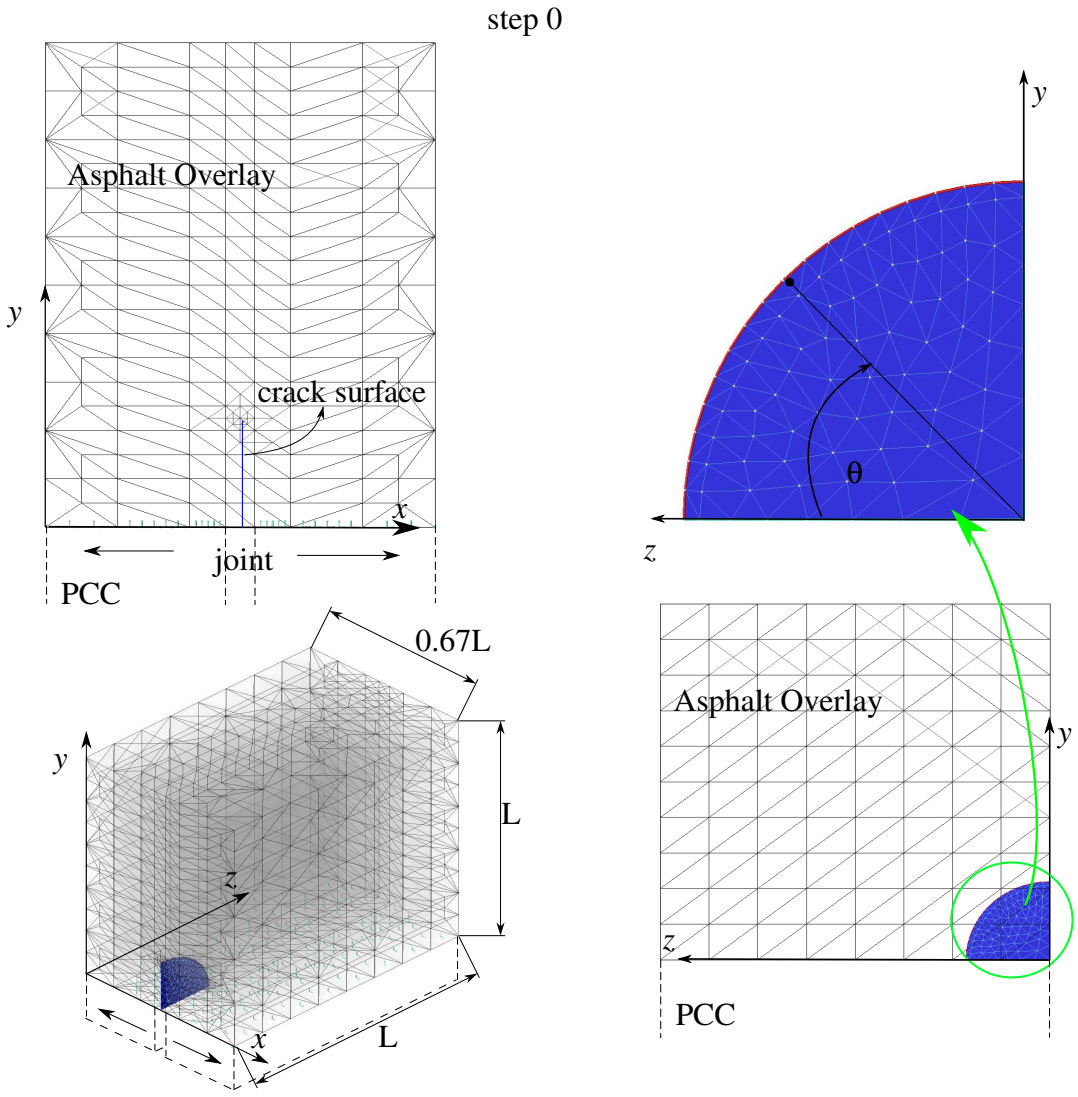

Figure 6.8: *Model description.*

are used in all cases. This allows the evaluation of the computational geometry algorithms with no other influences aside from their own capabilities. In this type of problem the initial stress intensity factors (SIFs) vary along the front, having the highest values when θ approaches 0 degrees, see Figure 6.9. This crack configuration will tend to propagate faster in the z-direction of the rectangular domain than towards its surface (y-direction).

The following subsections show the results of crack propagation when performed using the two aforementioned FOM techniques and illustrate some limitations of their usefulness. In addition, novel techniques are presented to address these geometric difficulties arising in this type of

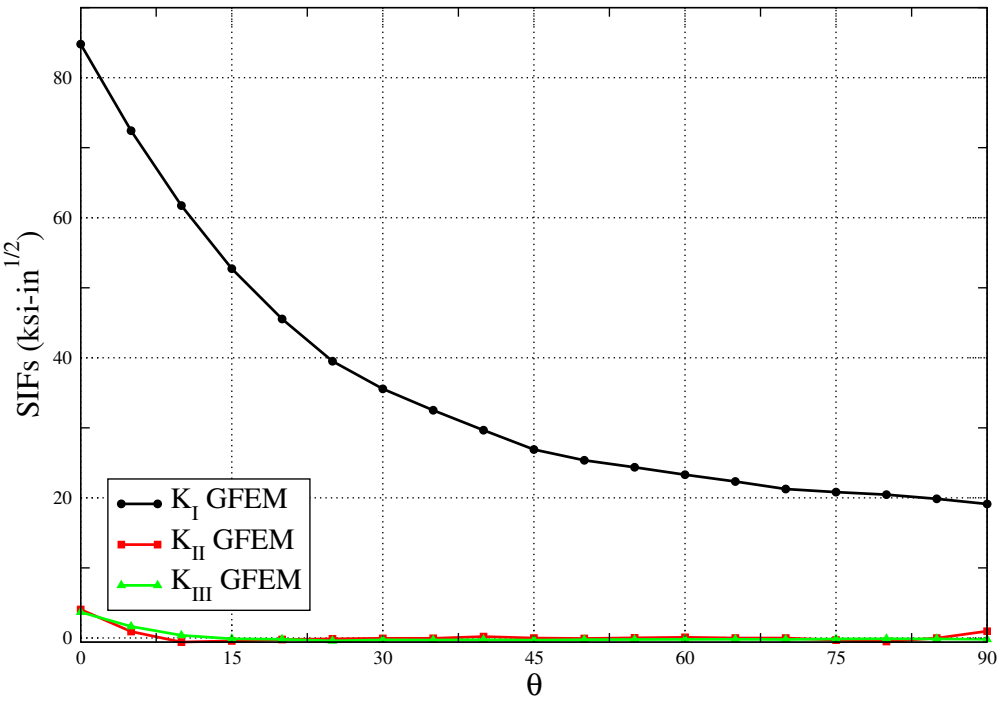

Figure 6.9: *Stress intensity factors along crack front for Crack Step 0.*

problem.

6.1.1 Propagation with FOM

The fist propagation technique investigated is Propagate and Smooth (PAS). Again, this indicates that the front propagates by only moving the crack front vertices, without the creation of any new facets. Figure 6.10 shows the results of this propagation strategy. This technique works fine until the facets close to the front $(\theta = 0^o)$ become significantly larger than facets in other regions of the crack front. For practical considerations, the opposite is desired. Smaller facets close to the front of the crack give a better representation of the crack front. All other facets can have a large size as long as they can represent the crack surface geometry well. As such, this propagation strategy is insufficient in the present case.

We solve the problem again using Propagate and Extrude (PAE). In this technique triangular facets are created between the original geometry and propagated front. Figure 6.11 shows the results of this propagation. With PAE at initial steps the crack front can be better approximated be-

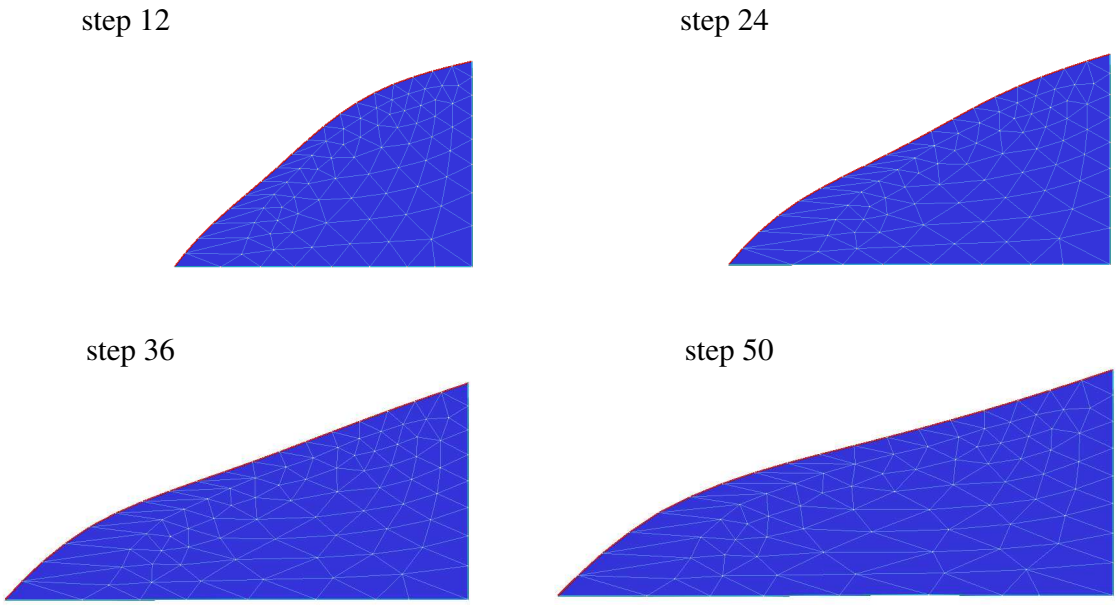

Figure 6.10: *Crack propagation using FOM, Propagate and Smooth (PAS).*

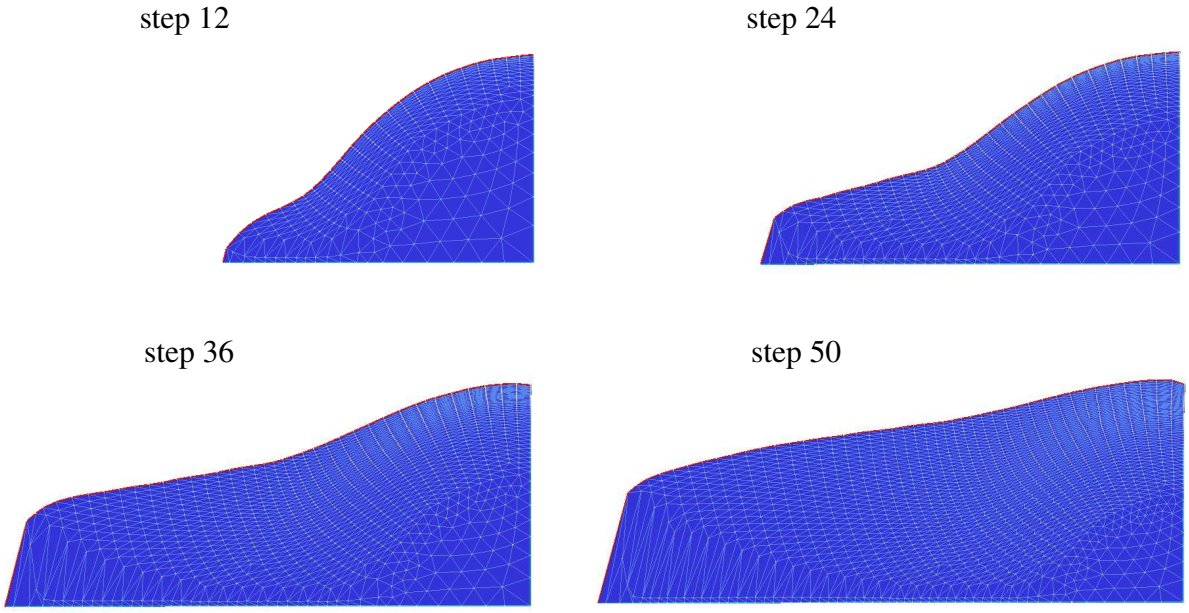

Figure 6.11: *Crack propagation using FOM, Propagate and Extrude (PAE).*

cause the algorithm adds vertices to bisect segments of the front that have become too large. This is not the case for the first and last crack front edges, and therefore the crack front representation further deteriorates after each crack step. Furthermore, the creation of elements at every step leads to many unnecessary facets in the crack surface. Especially at $\theta = 90^o$ where not only is there an excessive number of facets but they are also squeezed together, which can lead to geometric inaccuracies in the creation of integration elements. In the creation of integration elements, each segment of the crack surface facets is checked for possible intersections with the 3-D finite elements. This means that an excessive number of triangular facets increases the computational time. Also, the possibility of round-off errors rises due to intersections found in very close proximity to one another.

Similar results are obtained by combining both FOM techniques (PAE and PAS) within a simulation. Figure 6.12 shows the results when both techniques are used in combination. Here, we propagate most of the time using PAS and every 5 propagation steps we switch to PAE.

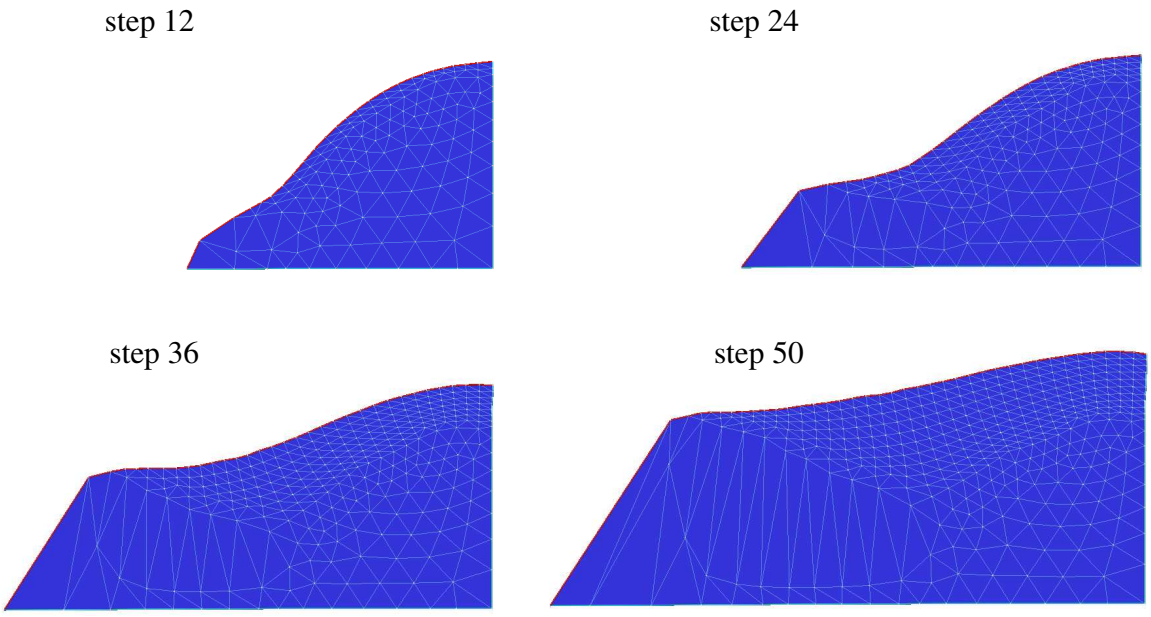

Figure 6.12: *Crack propagation using FOM, mixed PAS and PAE.*

Even though, combining FOM techniques reduces the number of facets on the crack surface, at step 50 the crack front representation has completely deteriorated. Also, we find again that there

are very large facets close to the front at $\theta = 0^o$ and an excessive number of small facets are found at $\theta = 90^o$. Furthermore, switching between PAS and PAE is not an automated process and it requires some undesirable trial and error in order obtain relatively mediocre results.

The main objective of this study is to develop a robust crack propagation algorithm which is suitable for relatively long crack propagation. The problem of reflective cracking for example, often deals with crack surfaces which may have to increase to 10 times or more their original size to reach to the surface. These types of long propagation problems require large numbers of propagation steps, and therefore present ample opportunity for deterioration of the quality of the crack surface representation. With this in mind, this type of problem may not be possible using FOM as presented previously, since the quality of the crack surface representation decreases with the number of crack propagation steps.

The variation of propagation speed along the crack front is what leads to the generation of facets with significantly different sizes when using FOM. While part of the front moves relatively large amounts, the remainder of the front moves very little. FOM only allows us to either stretch the whole front using PAS or create a complete new layer of facets along the front with PAE, neither of which generate acceptably accurate results. In the following section a hybrid approach is presented which seeks to address the issue of using either technique on its own.

6.1.2 Adaptive Crack Front Advancement

In this section we propose a hybrid technique which employs PAE in certain regions of the crack front and PAS in other crack front regions *within a crack propagation step*, as appropriate. In a typical crack propagation step layers of facets will be created at portions of the front with relatively large front increments (PAE) while other portions of the front would simply be moved, with no facet creation (PAS). Figure 6.13 illustrates this adaptive crack front advancement technique.

We again analyze the same propagation example, utilizing the hybrid propagation technique. The majority of the propagation is performed using PAS only, until the facets close to $\theta = 0^o$ are large enough (every 4 steps) such that a new layer of facets is required in this region. Therefore,

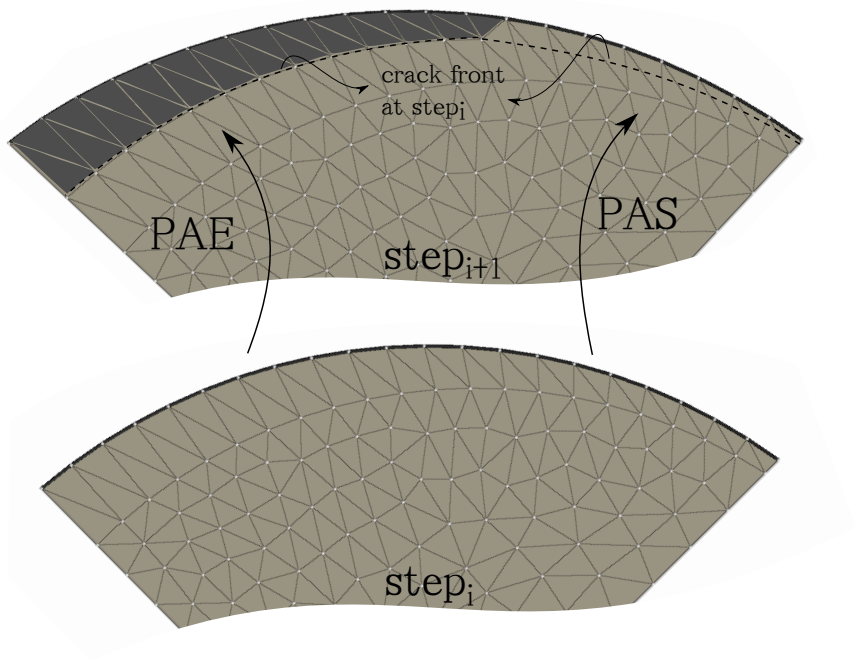

Figure 6.13: *Adaptive crack front advancement technique.*

the adaptive crack front advancement (PAS & PAE) is then used and a new layer of facets is created only in that portion of the front. Figure 6.14 shows the result of the propagation.

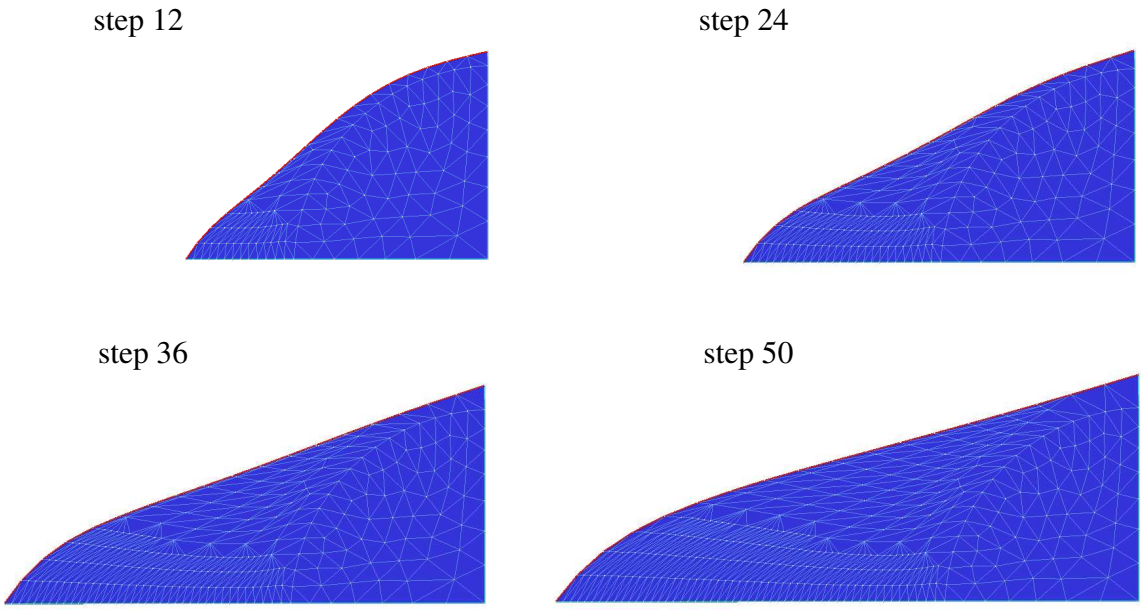

Figure 6.14: *Crack propagation using adaptive front evolution.*

Note that now we have a better control of the facet size along the crack front even though the crack evolution is non-uniform. Also, the crack front geometry is well-represented. Although this method is an improvement, for large crack propagations, it suffers from some of the same limitations as FOM. Namely, after many crack propagation steps the crack surface again contains large numbers of unnecessary, small triangular facets.

6.1.3 Crack Surface Simplification

In order to reduce the number of unnecessary facets on the crack surface representation, a mesh simplification method is presented. The idea is to reduce the number of facets while preserving the surface shape and boundaries. This is not trivial since the crack surface that results from a simplification will always deviate somewhat from the original crack surface. Therefore, it is necessary to measure such a deviation. This measurement along with the removal of edges is done using a function of the Computational Geometry Algorithms Library (CGAL) [1]. The method consists of measuring the cost of each individual edge removal due to the local deviation introduced. A rough measure of this cost is discussed subsequently. As a consequence, it plans the entire process as a sequence of steps of increasing cost. The removed edges are replaced by a vertex and the cost of all edges now incident on the replacement vertex is recalculated, affecting the order of the remaining unprocessed edges.

In the case of a planar crack surface like in this example, the cost of removal mainly involves the size of the edges. Therefore, the smallest edges will be removed first. In the case of a non-planar crack surface, the cost is not only the size of the edge but also the impact on the whole shape of the crack surface when removing that particular edge. The cost and placement strategy is know as Lindstrom-Turk and more details can be found in [1]. Additionally, the algorithm constrains edges recognized as crack fronts to avoid their removal.

The previous propagation example is again simulated using the adaptive crack front advancement along with this crack surface simplification algorithm. Figure 6.15 shows the results of this propagation. The same procedure used in the previous section is repeated, the only modification is

that at every 4 steps the mesh simplification algorithm is called. Notice that most of the smallest

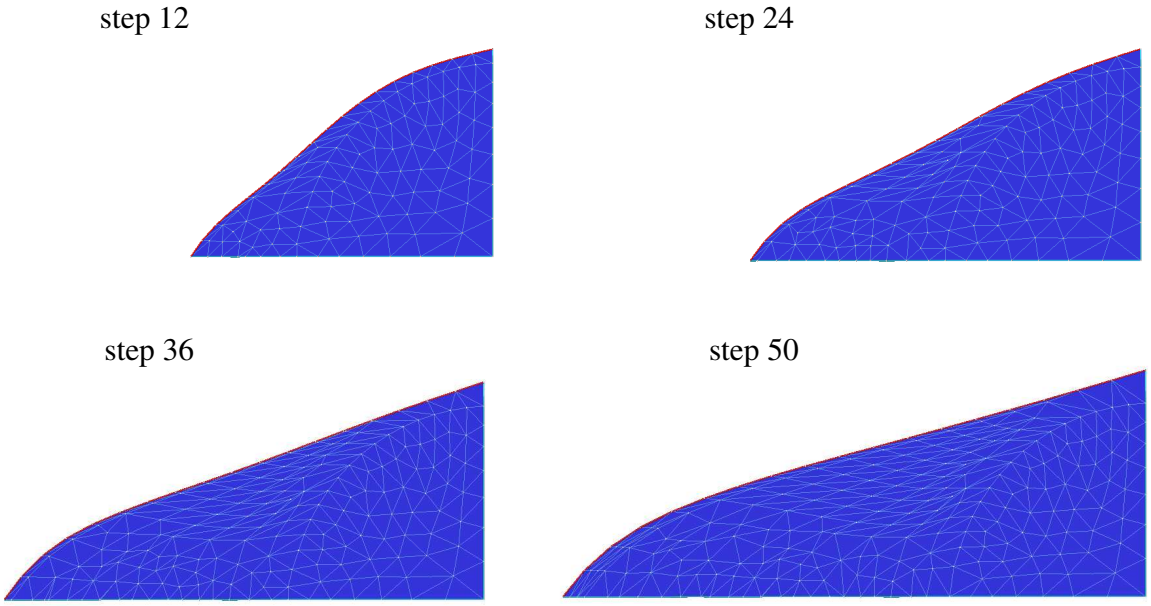

Figure 6.15: *Crack propagation using adaptive front evolution and simplification.*

edges have been removed during the simulation and therefore the number of facets in the interior of the crack surface has reduced significantly. The major drawback is that the user does not have control of the size and quality of the facets used in the crack surface representation after simplification has been performed. This may cause problems in large crack propagations if the simplification algorithm is called excessively. To account for this problem, the next section presents a crack surface re-meshing algorithm.

6.1.4 Crack Surface Re-Meshing

The re-meshing algorithm consists of creating an entire new crack surface representation using flat triangles as facets. The difference with the simplification algorithm is that here all previous facets are removed. The objective is to reproduce the crack surface representation using a small number of facets while preserving its shape and boundaries. The advantage of performing re-meshing of the crack surface is that the user has control of the size and aspect ratio of the facets used. This technique may not be necessary in small crack propagation simulations, but it is essential in the

case of large crack evolution. Previous crack propagation techniques have shown an excessive accumulation of small facets even after the crack surface has only doubled its original size.

The shape and number of facets used to define the crack surface depends on the user input criteria. The criteria consists of the characteristic facet size and the value of the limit angle. The limit angle is a minimum value set by the user for the interior angles of triangular facets. Based on our experience, an increment in the characteristic facet size is desired after each step and a constant 20^o as a limit angle gives a good shape for the triangular elements.

The re-meshing of the crack surface representation is done using a CGAL [1] function for 3-D surface generation. Certain restrictions have to be put in place in order to preserve the crack front and some other important characteristics like sharp turns in the case on non-planar crack surfaces. The CGAL meshing algorithm is based on the notion of the restricted Delaunay triangulation. In short, the algorithm computes a set of sample points on the surface, and extracts an interpolating surface mesh from the three dimensional triangulation of these sample points. As done in a Delaunay refinement process, points are iteratively added until the size and shape criteria, set by the user, are satisfied. More detail about the meshing process can be found in [1].

The previous propagation example is once again simulated using the re-meshing algorithm. This algorithm can be called at every propagation since it takes less than a second to execute. Before performing re-meshing, the adaptive crack front advancement algorithm is used to update the new crack front position. Figure 6.16 shows the results of this simulation.

It is clearly shown that after re-meshing, the crack surface representation has fewer facets in its interior. The crack surface shape and boundaries are preserved with only a single layer of relatively smaller facets used immediately behind to the front in order to maintain a good front representation. Figure 6.17 shows the deformed configuration, von Mises stress of a bottom view of this problem. The previous example (Mode *I*, planar crack) is a good starting point, but very often in 3-D simulation, Modes *I*, *II* and *III* are present. Therefore, most of the crack propagation simulations require non-planar crack surface representations. The following example shows the robustness of the previous techniques in the case of a non-planar crack propagation.

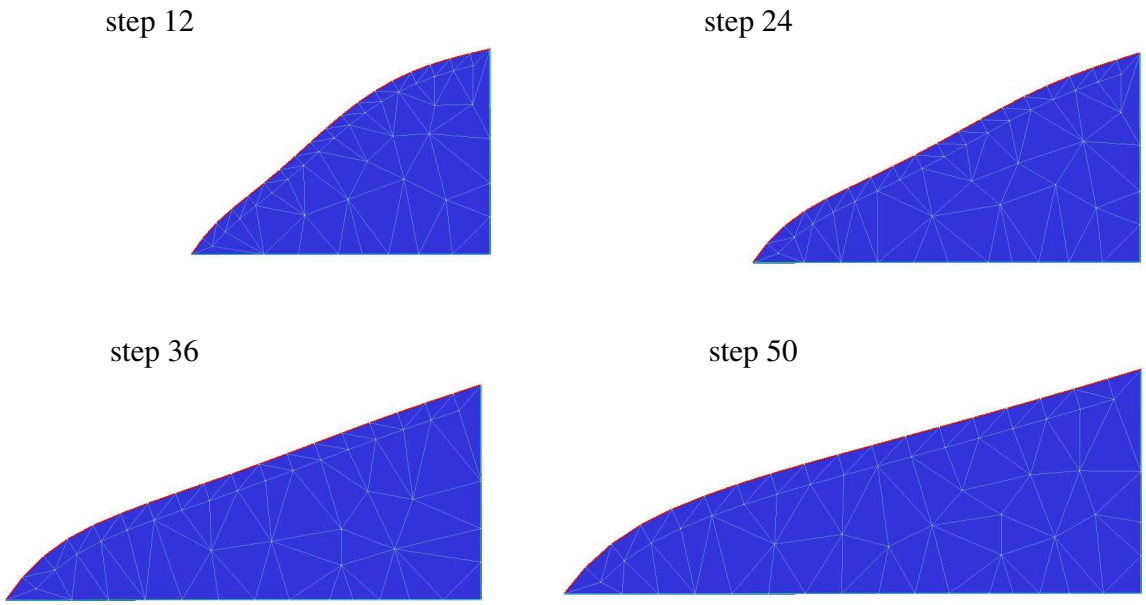

Figure 6.16: *Crack propagation using adaptive front evolution and surface re-mesh.*

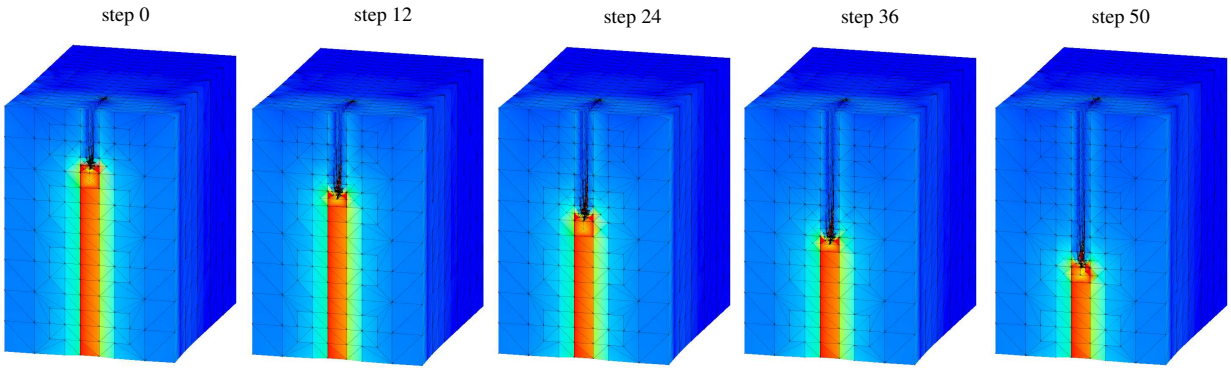

Figure 6.17: *Deformed configuration, von Mises stress of a bottom view of planar crack problem.*

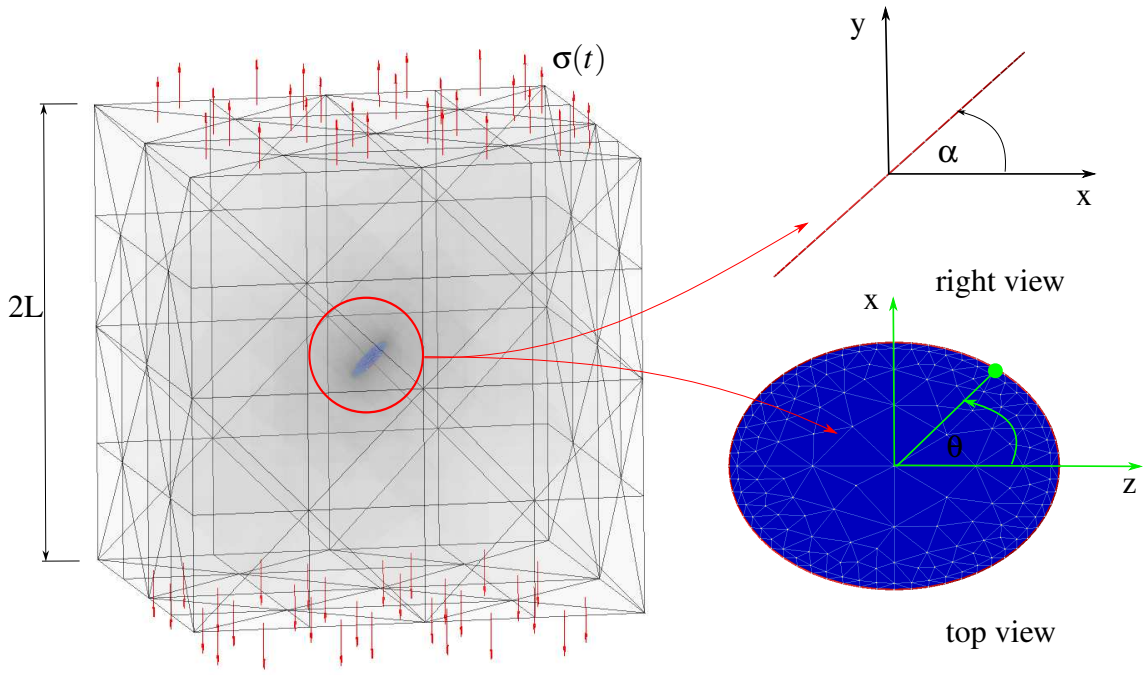

Figure 6.18: *Inclined penny-shaped problem details.*

6.2 Non-planar Crack Propagation

This example consists of an inclined penny-shaped crack inside of a cube with dimension '$2L$'. The cube is subjected to a uniform cyclic tensile load of maximum magnitude $\sigma_{max} = 1$ MPa along the y-direction. The initial coarse mesh and the initial crack surface configuration are illustrated in Figure 6.18. The geometric parameters of the crack surface are $a_0/L = 0.1$ and $\alpha = 45^o$, where a_0 is the radius of the initial crack and α is the inclination with respect to the xz-plane. The maximum crack front increment allowed in each step is taken as $\Delta a_{max} = 0.02\, a_0$. The simulation consists of 23 propagation steps and elastic material properties are assumed. Young's Modulus is taken as $E = 1{,}000$ MPa and Poisson's ratio, $\nu = 0.30$. Details about the criterion for this fatigue crack propagation can be found in [130] and in Section 7.3. Here, the interest is in the computational geometry aspects of the crack surface. Therefore, three different proposed crack evolution techniques are investigated in the analysis of the model problem: (1) FOM, (2) adaptive crack front advancement with simplification and (3) adaptive crack front advancement with re-meshing.

Because of the nature of the problem, all three fracture modes are present, therefore a non-planar propagation is expected. The computed crack front parameters (SIFs) for Propagation Step 0 are plotted in Figure 6.19 illustrating the highly mixed-mode nature of the example. These results are compared to the analytical solution computed for an infinite domain [170], illustrating very good agreement between the numerical and analytical results.

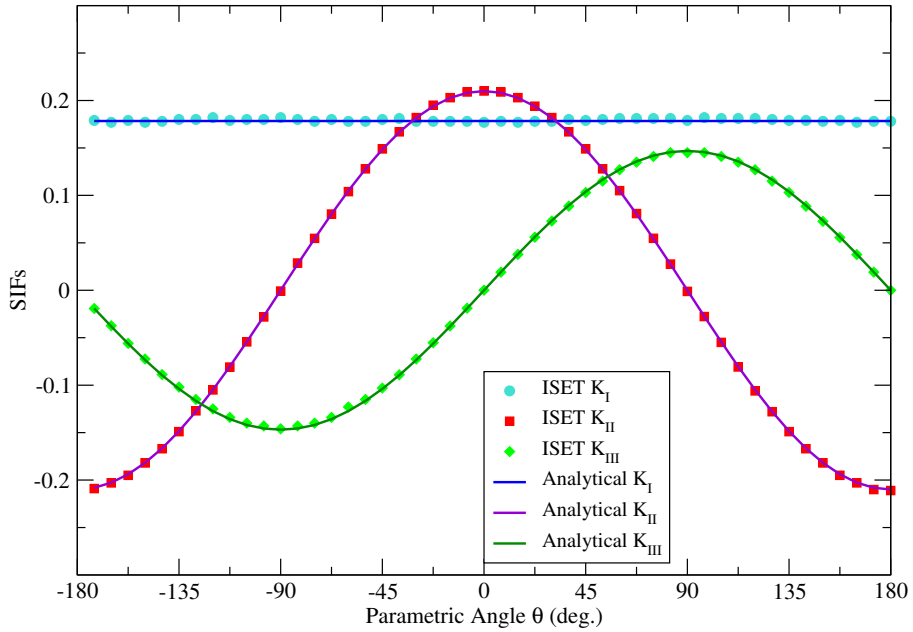

Figure 6.19: *The SIFs for Modes I, II, and III of GFEM Propagation Step 0 and analytical solution for an infinite domain.*

For all crack evolution methods, the same type of enrichments, and the same amount of refinement are used. This allows the evaluation of the computational geometry algorithms with no other influences but its own performance. Figure 6.20 shows the GFEM mesh refinement along the front for different propagation steps. Notice how the smaller facets follow the position of the crack front at each step. Figure 6.21 shows the deformed configurations of the problem in a cutting plane view. The first method used is FOM with PAE only. Figure 6.22 shows the crack surface representations for different propagation steps. Similarly as seen in the planar crack propagation, after many propagation steps, an excessive number of small facets are created.

The second method used is the adaptive crack front advancement of Section 6.1.2 combined

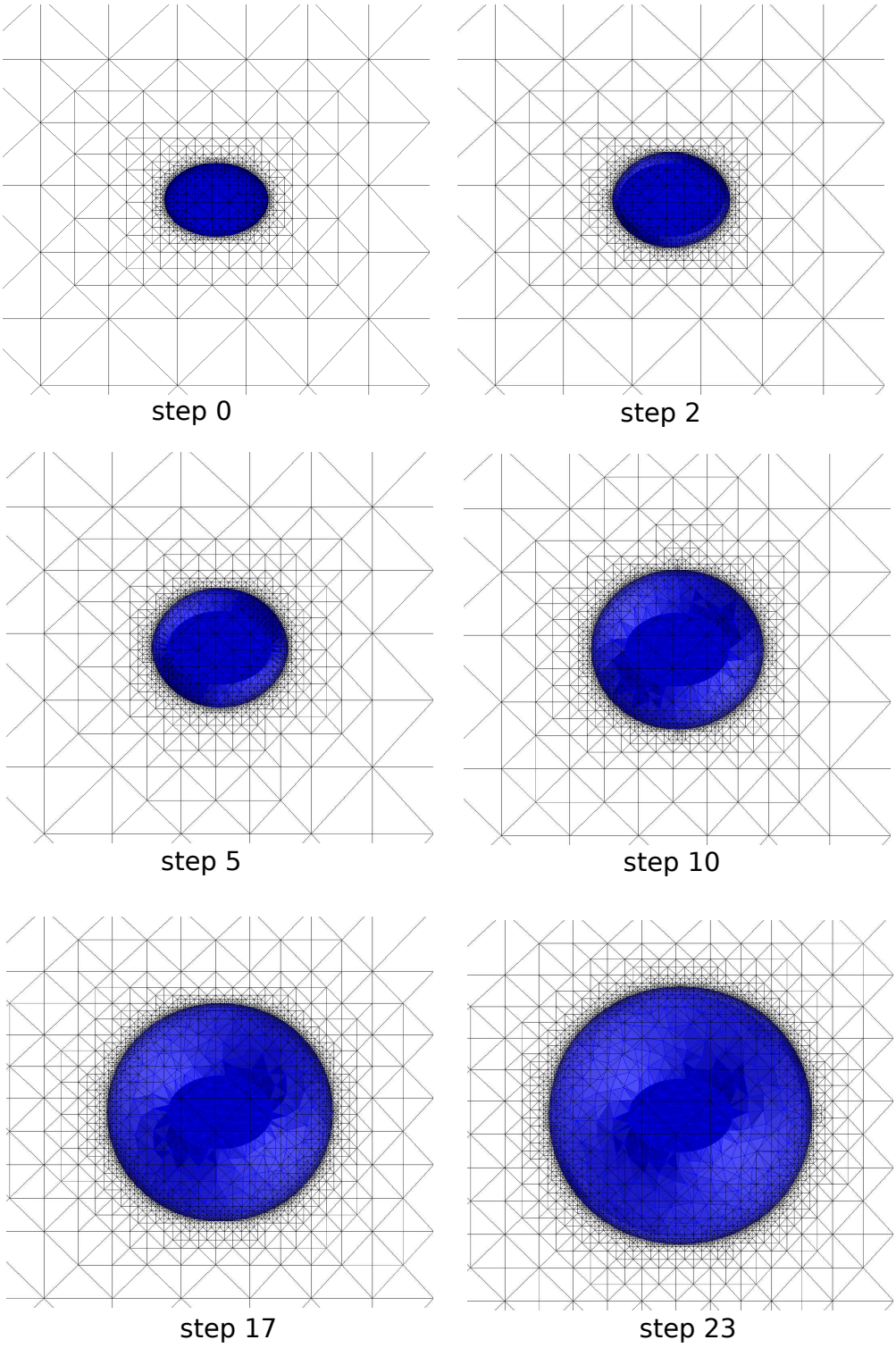

Figure 6.20: *Refinement of GFEM mesh follows the crack front in all cases.*

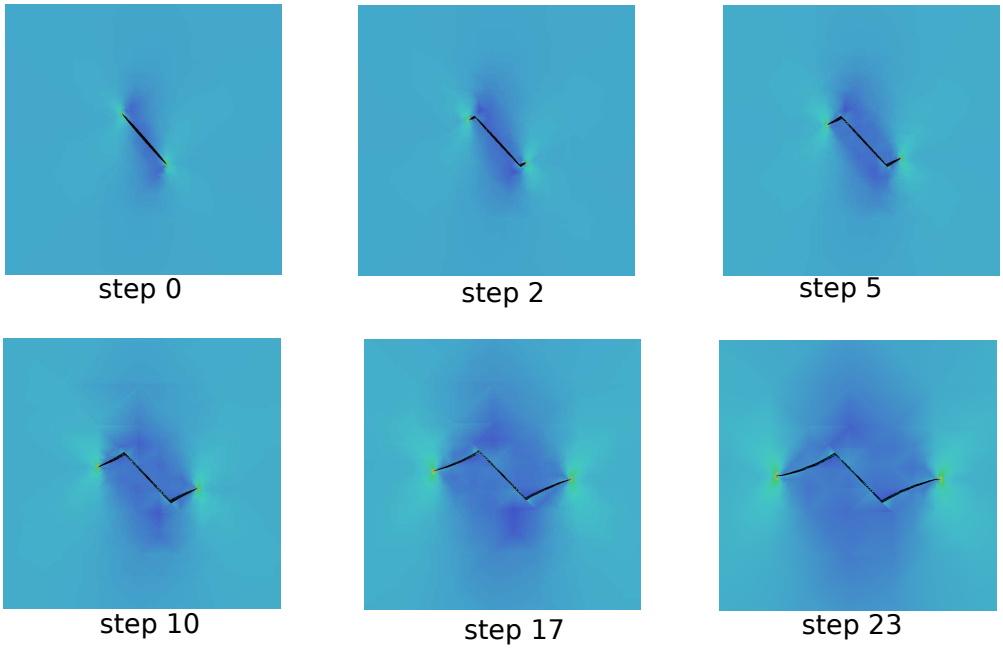

Figure 6.21: *Deformed configuration, von Mises stress on a cutting plane for different crack propagation steps.*

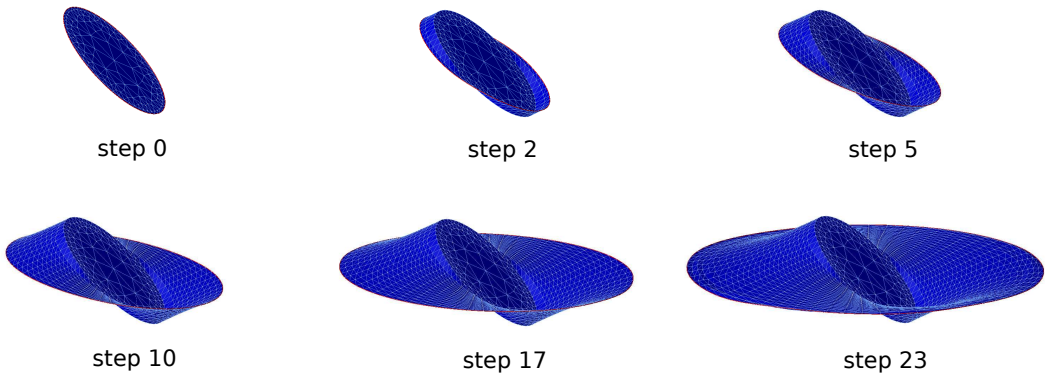

Figure 6.22: *Crack surface representation for different propagation steps using FOM with PAE (Section 6.1.1).*

with mesh simplification (Section 6.1.3). This method is able to provide a good crack surface representation while removing many small facets. The initial sharp turn of the surface is preserved as illustrated in Figure 6.23. The limitation of this method is that we do not have control on the shape and size of the facets used for the crack surface representation.

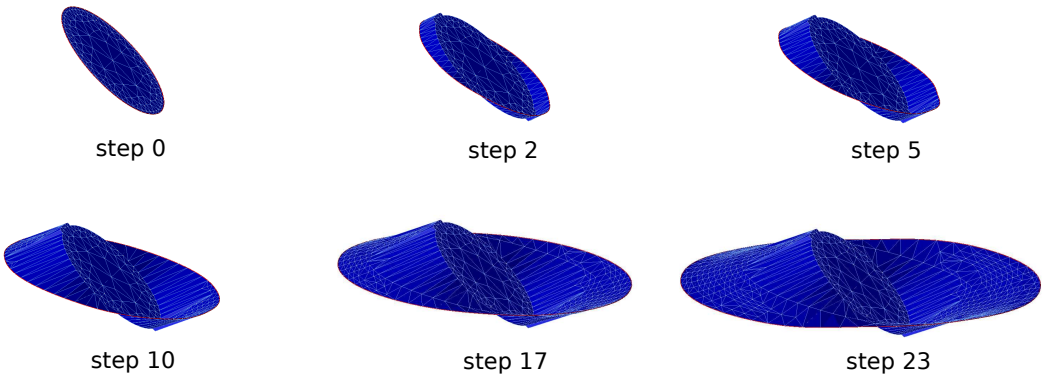

Figure 6.23: *Crack surface representation for different propagation steps using an adaptive crack front advancement (Section 6.1.2) combined with mesh simplification (Section 6.1.3).*

The third method consists of using the adaptive crack front advancement (Section 6.1.2) combined with re-meshing (Section 6.1.4). Figure 6.24 shows the result for this case. The crack front geometry is well-represented and it exhibits the same basic behavior as in the two previous methods. This is not the case for the overall crack surface shape, since it has completely changed. The sharp initial kink in the propagation has dies out after several propagation steps, leading to a deterioration of the overall geometry of the crack surface. In some problems this may be acceptable as long as the crack front is approximated well and the crack faces are in fact traction-free. On the other hand, problems such as hydraulic fracturing, or contact, for example, require a good representation of the entire surface in order to properly account for the applied tractions on the crack faces. As a consequence, the simulation with re-meshing is repeated but this time preserving the initial crack front. Figure 6.25 shows the crack surface representation for same propagation steps. Even though the crack surface mesh is changing constantly, its shape is preserved. Also, with this methodology there is a complete control of the facet size and shape used in the crack surface representation. Furthermore, the crack front geometry is still approximated well with the use of

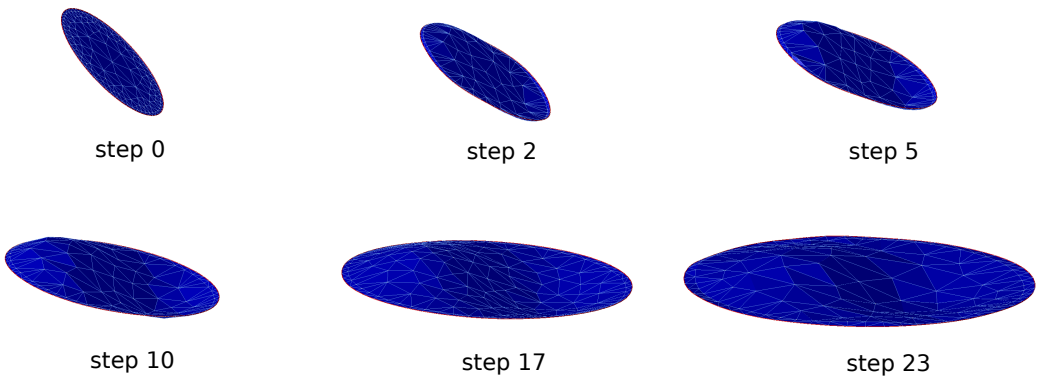

Figure 6.24: *Crack surface representation for different propagation steps using adaptive crack front advancement (Section 6.1.2) and the re-meshing algorithm of Section 6.1.4.*

only a single band of small facets behind it.

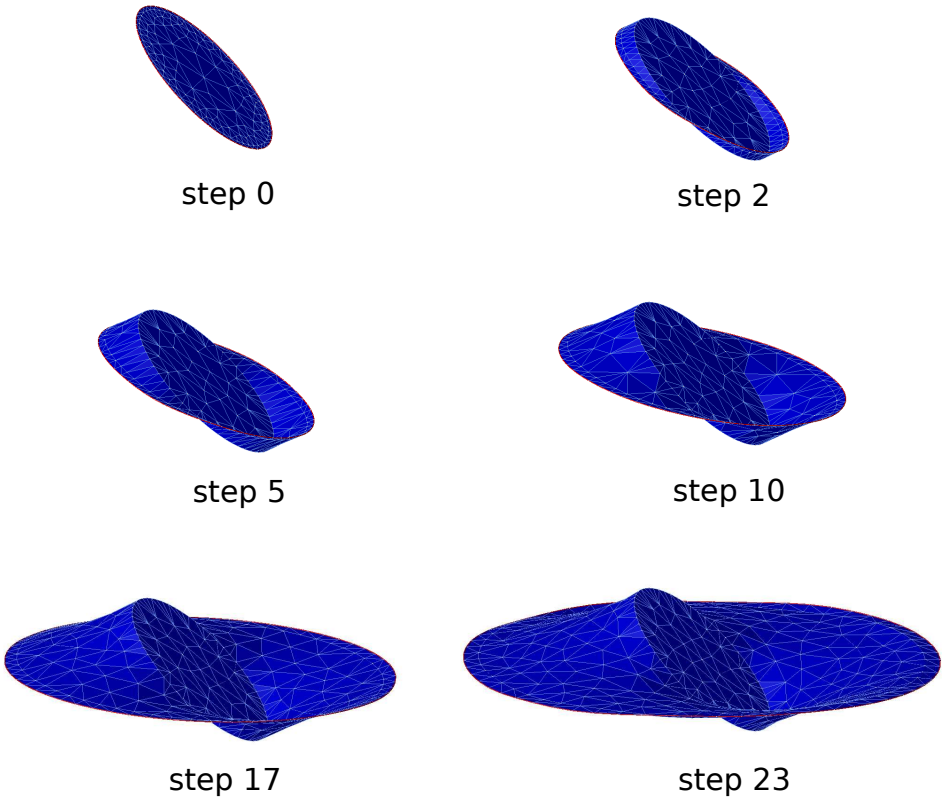

Figure 6.25: *Crack surface representation for different propagation steps using adaptive crack front advancement of Section 6.1.2 combined with re-meshing algorithm (Section 6.1.4) and preservation of the initial crack front.*

6.3 Moving Least Squares Method for Crack Front Evolution (MLSM)

In addition to the previously investigated improvements to the crack surface evolution algorithm, we can further improve the robustness of the algorithm by smoothing out the distribution of crack front vertices between crack propagation steps. As noted previously, at each crack growth step, a new crack front position is computed based on the numerical solution and the crack growth criteria as presented in Section 7.3. The vertices that conform the new crack front may need to be redistributed after each crack growth step to prevent self-intersection. Since the extraction of SIFs and the computation of the new crack front position is done independently at each crack front vertex, it is conceivable that two or more crack front vertices may tend to propagate very close to each other, with the risk of overlapping. This type of surface interpenetration is avoided by design with the use of only FOM, but this is not necessarily the case for the improved techniques presented in Chapter 6. The redistribution of the front vertices is performed using the moving east squares method (MLSM) [96], which guarantees an equidistant positioning of the crack front vertices while preserving the overall shape of the front. The use of MLS smoothing of crack front vertices in conjunction with small crack increments has the ability to avoid self-intersection in the propagation of non-convex crack fronts, thus providing that necessary feature when FOM is not used.

The MLSM for the approximation of the crack front positions can be stated as follows. Let $X(s) : \Gamma_c \rightarrow \Re$ be a continuous function which represent the crack front vertex coordinates of directions 1, 2 or 3 along the crack front Γ_c. The crack front coordinate value $X^L \equiv X(s_L)$, $L = 1,...,N$, is given at each crack front vertex $s_L \in \Gamma_c$, where N is the total number of vertices on the crack front and s is a parametric coordinate system along the crack front (cf. Figure 6.26).

A *global* MLSM approximation, $GX(s)$, of function $X(s)$ is defined by first forming, at each

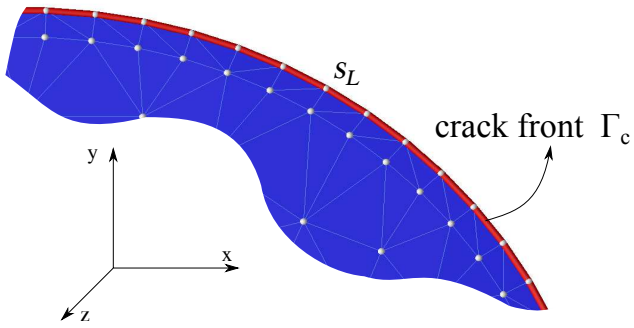

Figure 6.26: *Piece-wise explicit crack front representation.*

point $\bar{s} \in \Gamma_c$, a *local* weighted least square approximation $(L_{\bar{s}}X)(s)$. This function is defined as

$$L_{\bar{s}}X(s) \;=\; \sum_{k=1}^{n} a_k(\bar{s})\, P_k(s) \tag{6.1}$$

where the set $\{P_k\}_{k=1}^{n}$, $n \leq N$ forms a complete 1-D polynomial basis of dimension n and has the following properties:

- $P_1 \equiv 1$
- $P_k \in C^{\infty}(\Gamma_c), k = 1,...,n$
- $\{P_k\}_{k=1}^{n}$ is linearly independent with respect to the inner product (6.3) computed over N vertices $s_L \in \Gamma_c$.

Figure 6.27 illustrates the local approximation $L_{\bar{s}}X(s)$.

The coefficients $a_k(\bar{s}), k = 1,...,n$, are found by solving the following problem:

Find $\boldsymbol{a}^*(s) \in \Re^n$ such that $\forall\, \boldsymbol{a}(s) \in \Re^n$

$$\begin{aligned} J(\boldsymbol{a}^*) \;&:=\; (X - \sum_{k}^{n} a_k^* P_k,\; X - \sum_{k}^{n} a_k^* P_k)_{\bar{s}} \\ &\leq\; (X - \sum_{k}^{n} a_k P_k,\; X - \sum_{k}^{n} a_k P_k)_{\bar{s}} \end{aligned} \tag{6.2}$$

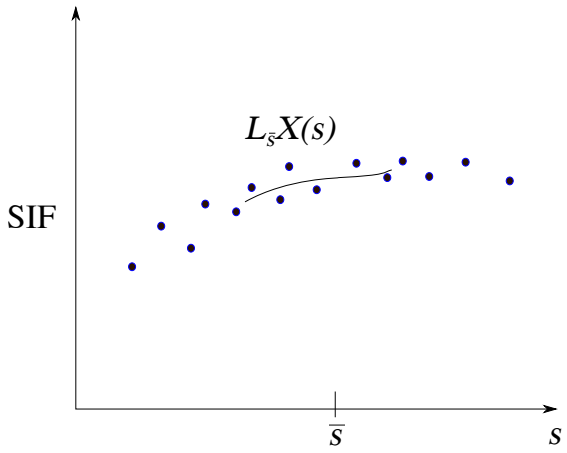

Figure 6.27: *Local weighted least square approximation.*

where $(.,.)_{\bar{s}}$ is a weighted inner product that depends on the point $\bar{s}$ and is defined by [96]

$$(u,\, v)_{\bar{s}} = \sum_{L}^{N} u(s_L)\, W_L(\bar{s})\, v(s_L)\,, \tag{6.3}$$

where $W_L(\bar{s}), L = 1,\ldots,N$, are weight functions such that $W_L(\bar{s}) > 0\ \forall\, \bar{s} \in \Gamma_c$ and $u, v \in C^0(\Gamma_c)$. The above can be written as

$$J(\boldsymbol{a}^*) = \sum_{L=1}^{N} W_L(\bar{s}) \left[X(s_L) - \sum_{k}^{n} a_k^* P_k\right]^2$$

Inequality (6.2) implies that

$$\left(X - \sum_{i=1}^{n} a_i^* P_i,\, P_j\right)_{\bar{s}} = 0 \qquad j = 1,...,n \tag{6.4}$$

Thus

$$\sum_{i=1}^{n} \left(P_i,\, P_j\right)_{\bar{s}} a_i^* = \left(X, P_j\right)_{\bar{s}} \qquad j = 1,...,n \tag{6.5}$$

Using the inner product (6.3) and the values of the coordinates function X at crack front vertices $s_L,\ L = 1,...,N$, the right-hand-side of Eq. (6.5) can be evaluated at each point $\bar{s} \in \Gamma_c$.

Equation (6.5) can be written in a matrix form as follows

$$\boldsymbol{A}(\bar{s})\,\boldsymbol{a}^*(\bar{s}) \;=\; \boldsymbol{B}(\bar{s})\,\boldsymbol{X}$$

where

$$A_{ij}(\bar{s}) \;=\; (P_i,\, P_j)_{\bar{s}}$$

$$\boldsymbol{a}^*(\bar{s}) \;=\; \left\{a_1^*(\bar{s})\;\; a_2^*(\bar{s})\;\; \ldots\;\; a_n^*(\bar{s})\right\}^T$$

$$\boldsymbol{X} \;=\; \left\{X^1\;\; X^2\;\; \ldots\;\; X^N\right\}^T, \qquad X^L \equiv X(s_L)$$

$$\boldsymbol{B}(\bar{s}) \;=\; \begin{bmatrix} W_1(\bar{s})\,P_1(s_1) & W_1(\bar{s})\,P_2(s_1) & \ldots & W_1(\bar{s})\,P_n(s_1) \\ W_2(\bar{s})\,P_1(s_2) & W_2(\bar{s})\,P_2(s_2) & \ldots & W_2(\bar{s})\,P_n(s_2) \\ \vdots & \vdots & \ddots & \vdots \\ W_N(\bar{s})\,P_1(s_N) & W_N(\bar{s})\,P_2(s_N) & \ldots & W_N(\bar{s})\,P_n(s_N) \end{bmatrix}$$

Thus

$$a_k^*(\bar{s}) \;=\; \sum_L^N \sum_j^n A_{kj}^{-1}(\bar{s})\,B_{jL}(\bar{s})\,X^L \qquad k = 1,\ldots,n$$

The local approximation (6.1) can be written as

$$\begin{aligned} L_{\bar{s}}X(s) \;&=\; \sum_{k=1}^n a_k^*(\bar{s})\,P_k(s) \\ &=\; \sum_L^N \sum_j^n \sum_k^n P_k(s)\,A_{kj}^{-1}(\bar{s})\,B_{jL}(\bar{s})\,X^L \end{aligned}$$

Finally, the global MLSM approximation $GX(s)$ is defined by taking $s = \bar{s}$ above, i.e.,

$$GX(\bar{s}) = L_{\bar{s}}X(\bar{s}) \;=\; \sum_{k=1}^n a_k^*(\bar{s})\,P_k(\bar{s}) \quad \forall \bar{s} \in \Gamma_c \tag{6.6}$$

$$\;=\; \sum_L^N \sum_j^n \sum_k^n P_k(\bar{s})\,A_{kj}^{-1}(\bar{s})\,B_{jL}(\bar{s})\,X^L \tag{6.7}$$

There is a great flexibility in selecting the weight functions, $W_L,\ L = 1, ldots, N$, and the basis, $\{P_k\}_{k=1}^{n}$, of the MLSM approximation. Here, the selected weight functions are defined as translations and scaling of a single function as follows:

$$W_L(\bar{s}) := W\left(\frac{2|\bar{s} - s_L|}{\rho_L}\right)$$

where ρ_L defines the support of W_L and controls the number of vertices that contribute to the MLSM approximation at a point $\bar{s}$ on the crack front. Function W is given by [165]

$$W(z_L(\bar{s})) = \begin{cases} \frac{2}{3\rho}\left(1 - \frac{3}{2}z_L^2 + \frac{3}{4}z_L^3\right) & 0 \leq z_L < 1 \\ \frac{1}{6\rho}\left(2 - z_L\right)^3 & 1 \leq z_L < 2 \\ 0 & z_L \geq 2 \end{cases}$$

where

$$z_L(\bar{s}) = \frac{2|\bar{s} - s_L|}{\rho_L}$$

The basis functions are taken as monomials

$$\{P_k\}_{k=1}^{n} = \{1, \bar{s}, ..., \bar{s}^n\}$$

In the numerical examples presented here, $n = 3$ is adopted, which leads to a quadratic basis.

The moving least-square method is a well known method for the approximation of scattered data, which is the case of vertex coordinates at the crack front. The MLSM approximation $GX(\bar{s})$ is not interpolant. Thus, $GX(s_L) \neq X^L$.

Equation (6.7) provides an approximation of the crack front coordinates X along the crack front. It facilitates the redistribution of the vertices to avoid crack front self-intersection and provides a uniform distribution of the vertices along the crack front. This technique is essential for propagation of highly non-convex crack surfaces, such as those which result from the coalescence of multiple cracks (C.f. 6.5).

6.4 Boundary Interaction

In problems like those shown in Figures 6.7 and 6.8 the crack surface has a front which can be divided into two sets of vertices. One set is comprised of all front vertices which are inside the solid domain (termed *on crack front*), while the other is the collection of all front vertices which do not lie inside the solid domain (termed *on domain boundary*). Two consecutive front vertices with status *on crack front* define an edge on the crack front within the domain. Similarly, two consecutive front vertices with status *on domain boundary* corresponds to an edge on the solid domain boundary. If an edge on the crack front has a vertex in each set, this indicates that the vertex with status (*on crack front*) corresponds to the end of the front. Figure 6.28 shows an illustration of the described sets.

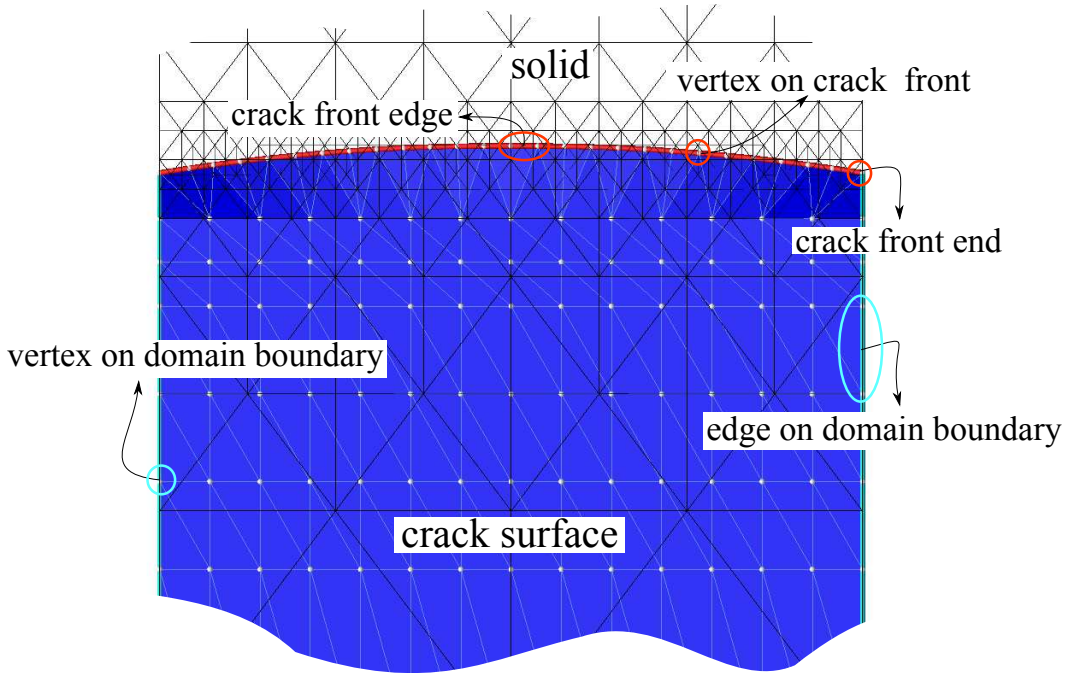

Figure 6.28: *Description of crack surface and its frontier sets.*

At each crack growth step, a new crack front position is computed based on the numerical solution and the crack growth criteria in Section 7.3. The new crack front is represented with a new set of crack front vertices. The position of the new vertices depends on the extraction of SIFs and the growth criteria. In many instances one or more new crack front vertices may be positioned

outside of the domain.

Even though the new position of the crack front may be correct based on the extracted SIFs, etc., some regions of the surface may propagate outside of the domain. In order to continue on with the crack propagation simulation, some special treatment of the crack front near the boundary region is necessary.

After each propagation step, all new crack front edges are queried to determine if any edge has a vertex outside (named A) and a vertex inside (B) of the solid domain. This edge then intersects with an element face on the boundary of the domain. Coordinates of vertex A are then replaced by the coordinates of the edge's intersection with the domain boundary, and all other vertices and facets outside of the domain are eliminated. Essentially any edge completely outside the domain is neglected, and the edge which protrudes out from the domain is in effect trimmed, to now lie on the boundary. Subsequently, all crack front vertices are collected into the appropriate sets for subsequent use. Figure 6.29 illustrates the process. This procedure ensures that all crack front edges are contained within the solid domain (cut elements) or coincident with the domain boundary.

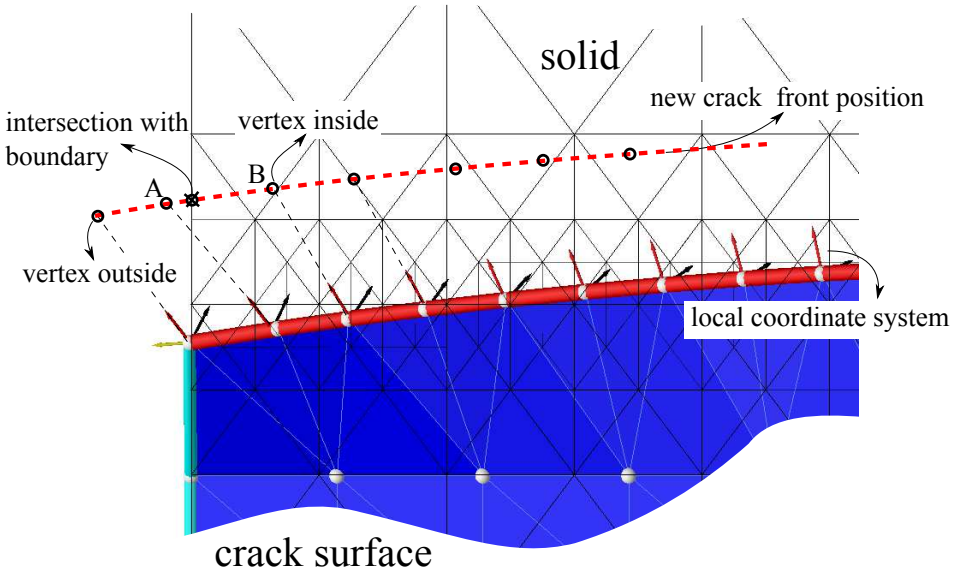

(a) Before propagation

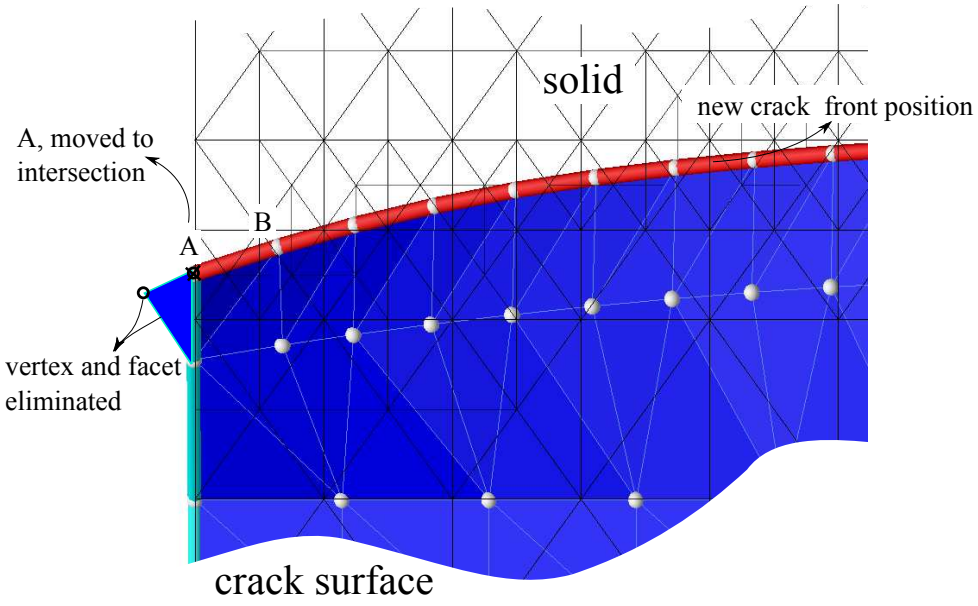

(b) After propagation

Figure 6.29: *Procedure to handle boundary interaction.*

6.5 Coalescence of Multiple Crack Surfaces

Coalescence of adjacent crack surfaces within the GFEM is relatively straightforward, particularly with the use of re-meshing and MLS smoothing of crack front vertices. At each propagation step the minimum distance between two adjacent surfaces is computed and compared to a tolerance distance. If the minimum distance is less than the tolerance distance, the crack surfaces will be joined. At this point crack front vertices are looped over again to determine if any additional pairs of crack front vertices are also within the tolerance distance. Control points are then passed to the crack surface re-mesher corresponding now to the crack front vertices for both surfaces, minus those that are in the coalesced portion of the new crack surface. The use of relatively small crack front increments along with moving least squares for the crack front vertex locations is sufficient to avoid self-intersection of the crack surface in the highly non-convex coalesced regions of the crack front during subsequent propagation steps. After the point of coalescence, one of the cracks is 'turned off' for the remainder of the analysis as it has been coalesced into the one, larger crack surface.

The use of the tolerance distance in the coalescing process essentially makes the assumption that a small portion of the un-cracked ligament remaining between the crack surfaces no longer carries load. This assumption is reasonable because in reality there is a small plastic zone ahead of the crack front, with a limited load-carrying capacity. Figure 6.31 shows the effect of the tolerance distance (effective plastic zone size) on the local shape of the coalesced crack surface.

For the numerical examples considered in this work, the tolerance distance is a user-prescribed value. One potential improvement to the algorithm would be to compute the tolerance distance based on an estimate of the effective plastic zone size computed from extracted stress intensities, $r_p = \frac{\left(\mathcal{K}_{eq}\right)^2}{\pi\sigma_y^2}$, as proposed in [8] or a similar expression using energy release rate.

The manner in which crack vertices are advanced also poses an area for potential improvement. The advancement of a crack front vertex is given by (7.28), ensuring that each crack front vertex is subjected to the same number of loading cycles. In a multi-site damage analysis, it is conceivable

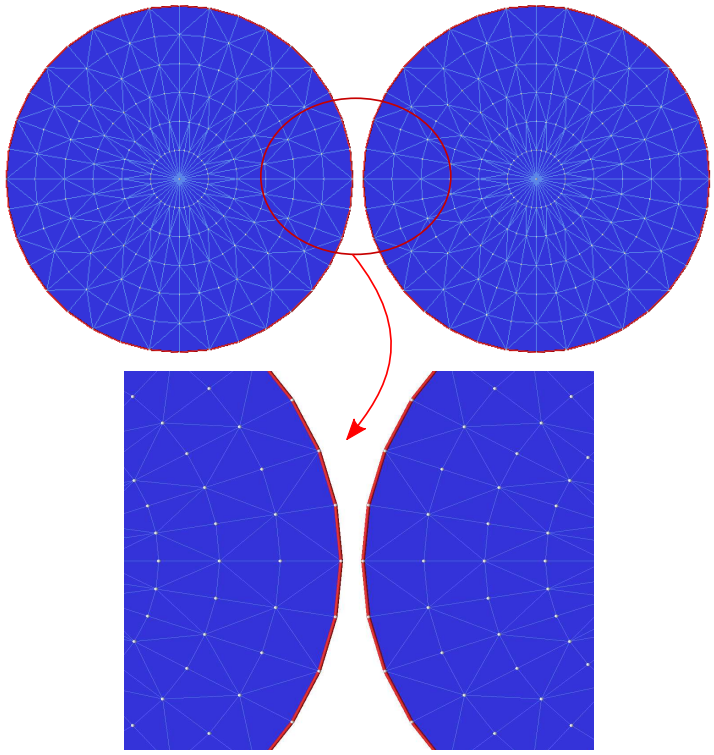

Figure 6.30: *Circular crack surfaces before coalescence.*

that $\Delta\mathcal{G}_{eq}^{max}$ will be different for each crack, indicating different growth rates. As such, $\Delta\mathcal{G}_{eq}^{max}$ must be selected considering all of the crack front vertices for all of the cracks in the analysis, and then each vertex may be scaled according to (7.28). In this manner we ensure that every crack front vertex in the entire analysis is subjected to the same number of loading cycles. In this manner the fatigue life may still be legitimately estimated based on (7.29), where $\Delta\mathcal{G}_{eq}^{max}$ again considers each crack front vertex in the entire analysis. With this in mind, most of the crack surfaces in the present work are symmetric with respect to size, shape, orientation, boundary conditions and domain boundaries, and therefore do not show any significant discrepancies in the $\Delta\mathcal{G}_{eq}^{max}$ computed for each crack surface.

It may be noted that propagation techniques which do not consider stress intensity factors nor energy release rate and have no notion of loading cycles, while perhaps more computationally efficient, will miss this important aspect of the analysis. While the final crack surface configuration may be of interest, in practical engineering scenarios the most critical information is often the

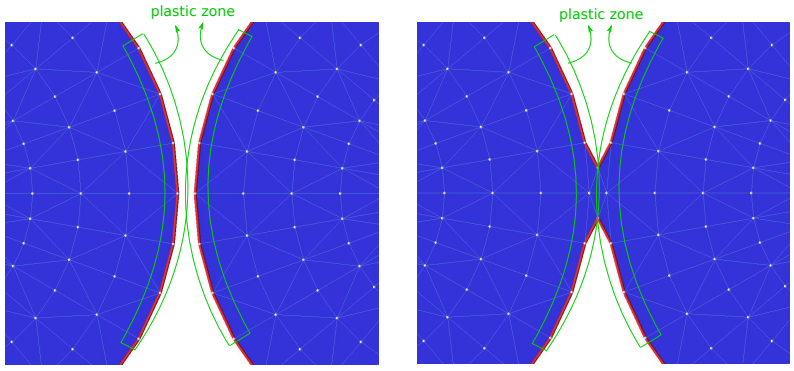

(a) Plastic Zone 1

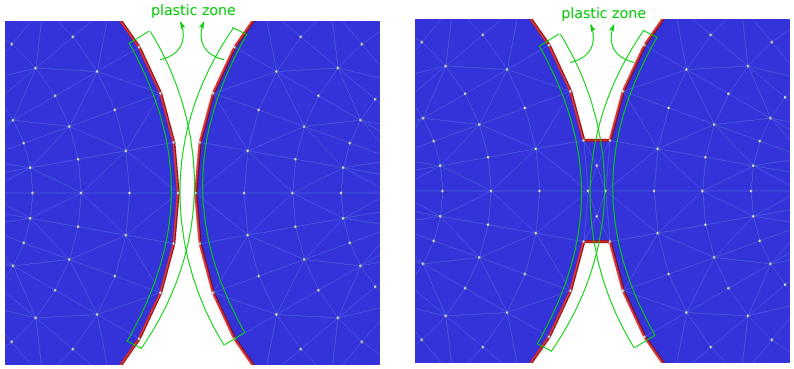

(b) Plastic Zone 2

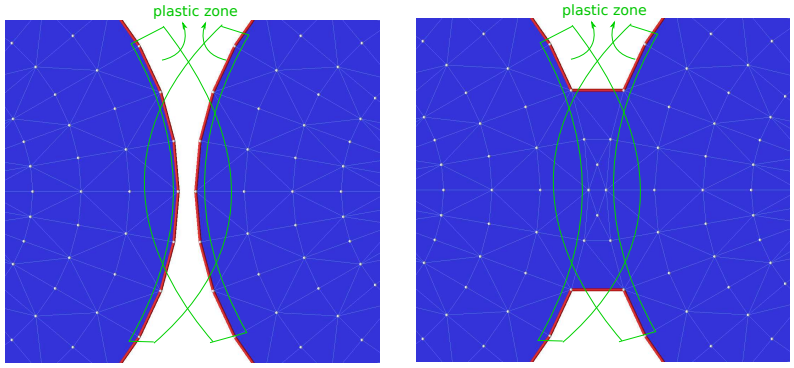

(c) Plastic Zone 3

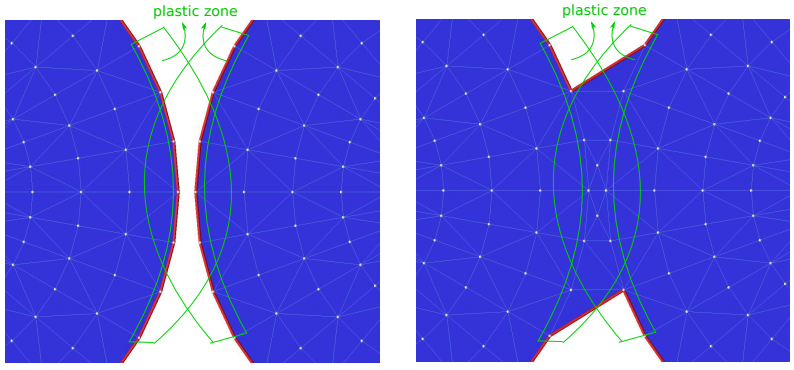

(d) Plastic Zone 4

Figure 6.31: *Crack coalescence with different tolerance distances.*

fatigue life estimate of the component, as this ultimately governs its final design and overall useful lifespan.

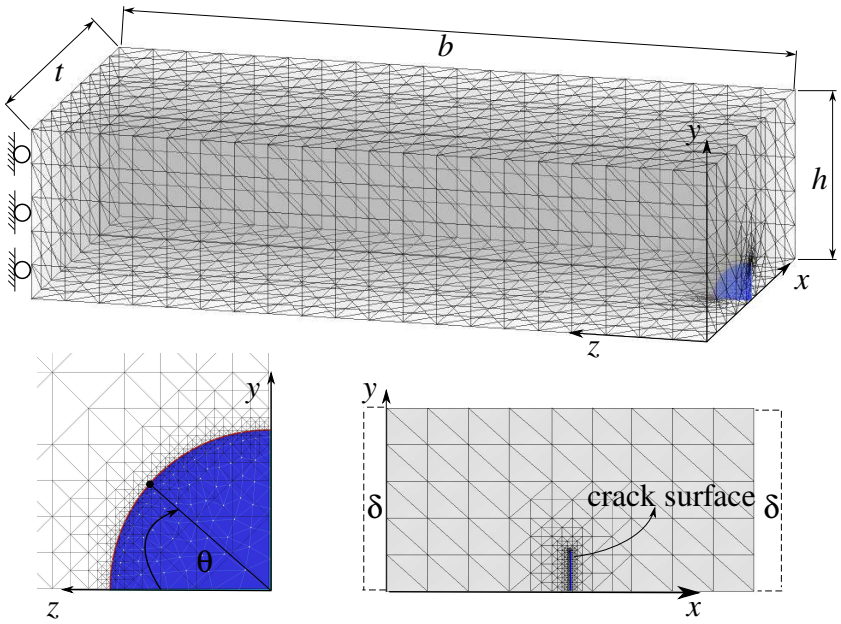

Figure 6.32: *Large Crack Propagation problem description.*

6.6 Numerical Examples

6.6.1 Large Crack Propagation and Boundary Interaction

In this example we consider a fatigue crack growth simulation of an initially quarter-penny-shaped crack in a linear elastic rectangular domain, as illustrated in Figure 6.32. The dimensions of the rectangular domain are $t = 10.0$, $h = 5.0$, $b = 20$ and the crack has an initial radius of $a = 1.0$. All dimensions are in inches. The assumed elastic material properties are Youngs modulus $E = 3,318.94$ ksi and Poissons ratio $\nu = 0.30$. Boundary conditions consist of a cyclically applied displacement of maximum magnitude $\delta = 0.015$ inches at the left and right faces of the rectangular domain. Additionally, the back face of the domain is constrained against motion in the z-direction.

At every crack growth step, stress intensity factors (SIFs) are extracted using the Contour Integral Method (CIM, ref. A) These SIFs are used to compute the direction and magnitude of propagation using the growth criteria presented in Section 7.3. Additionally, techniques such as

ACFA 6.1.2, re-meshing of the crack surface 6.1.4, MLSM 6.3 and boundary interaction 6.4 are used at every crack propagation step.

It is important also to mention that mesh refinement is only performed along the crack front. This localized refinement follows the crack front evolution using the refinement and un-refinement technique presented in [130].

Figures 6.33 and 6.34 show the evolution of the crack surface and the von Mises stress plotted on the deformed configuration, respectively, for several propagation steps. Note that at the end of the simulation the crack surface has grown throughout the entire domain and its final surface is over a hundred times larger than it was initially. It should also be noted that at the end of the simulation the domain is completely fractured into two disjoint sub-domains.

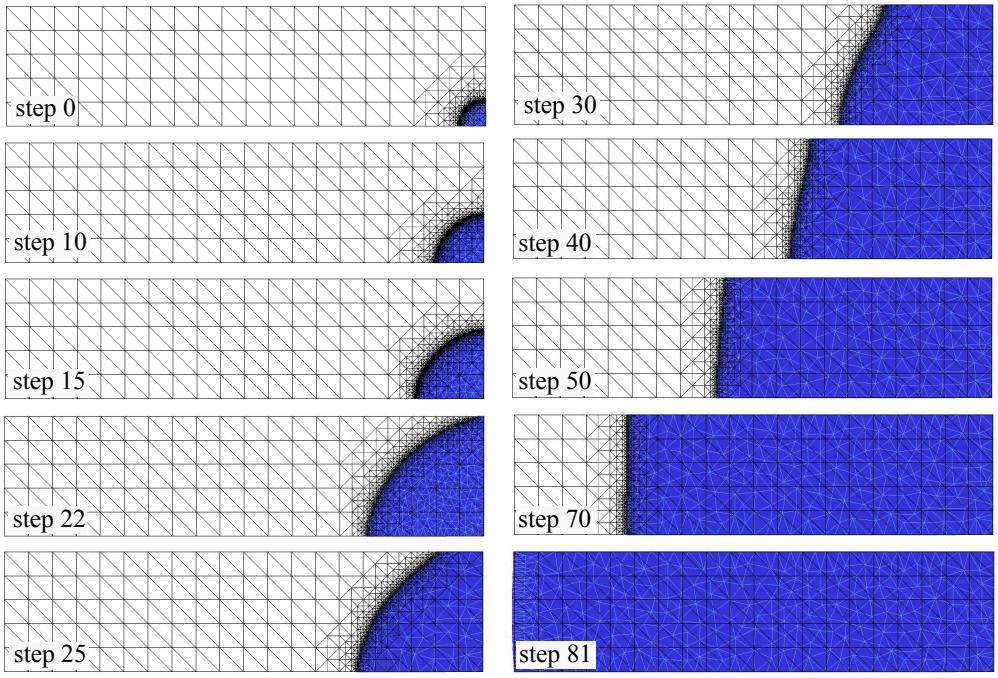

Figure 6.33: *Surface crack evolution.*

Observe that at step 22 the crack front has reached the top boundary of the rectangular domain. At this point a transition from a 2-D propagation to a pseudo-1-D propagation occurs. This type of transition is difficult to simulate using the standard FEM approach since the creation of strongly graded meshes fitting the crack surface while preserving the aspect ratio of the elements is not

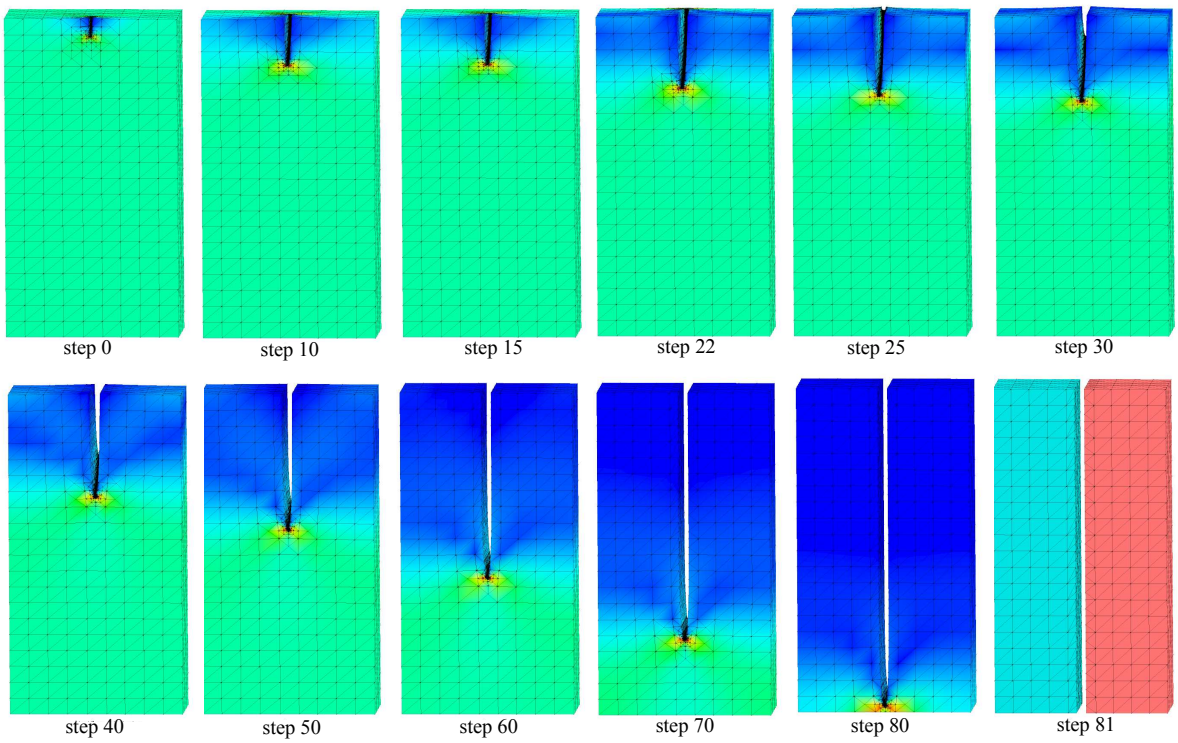

Figure 6.34: *Crack propagation: von Mises stress plotted on deformed configuration.*

always possible in this case unless extremely small elements are used. It is also very difficult to obtain the layer of degenerate quarter-point elements, commonly used for accurate approximations, encompassing the entire the crack front due to the non-normal intersection of the crack front with the domain boundary. In the GFEM this can be handled without much difficulty by simply trimming the portion of the crack surface that may have advanced beyond the physical domain and snapping the crack front to the boundary of the domain, as explained in Section 6.4. Figure 6.35 shows Mode *I* SIFs, $\mathcal{K}_I$, for different crack growth steps. The x-axis corresponds to the normalized position along the crack front. Notice the significant increase in $\mathcal{K}_I$ at the normalized coordinate $x = 1$ observed between steps 21 and 23. This increase occurs just after the transition point, and is the cause for faster front vertex advancement in this region of the crack front which ultimately causes the vertices near $x = 1$ to 'catch up' with the front vertices near $x = 0$ by the end of the simulation.

The second challenge posed in this simulation is the significant change in size of the crack

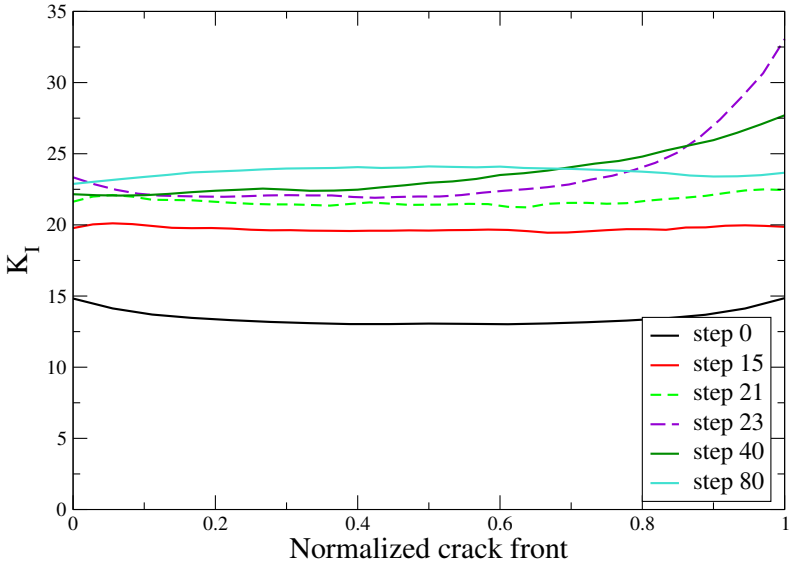

Figure 6.35: *Stress intensity factor $\mathcal{K}_I$ for steps 0, 15, 21, 23, 40, and 80.*

surface. This requires that the geometrical representation of the crack be adapted during the simulation. This process preserves a geometrically accurate representation of the crack front while reducing the number of facets at portions of the surface which are nearly flat or are far from the crack front; which is achieved using the techniques explained in this Chapter.

6.6.2 Coalescence of Two Circular Crack Surfaces

In this section we analyze a problem with two initially parallel, co-planar circular cracks in a domain with dimensions $6x2x6$. The material properties are taken as Young's modulus, $E = 2e5$, and Poisson ratio, $\nu = 0.3$. The domain is subjected to unit, normal tractions (red arrows) applied to the top and bottom surfaces, and point boundary conditions (green arrows) are applied only to prevent rigid body motions, as shown in Figure 6.36.

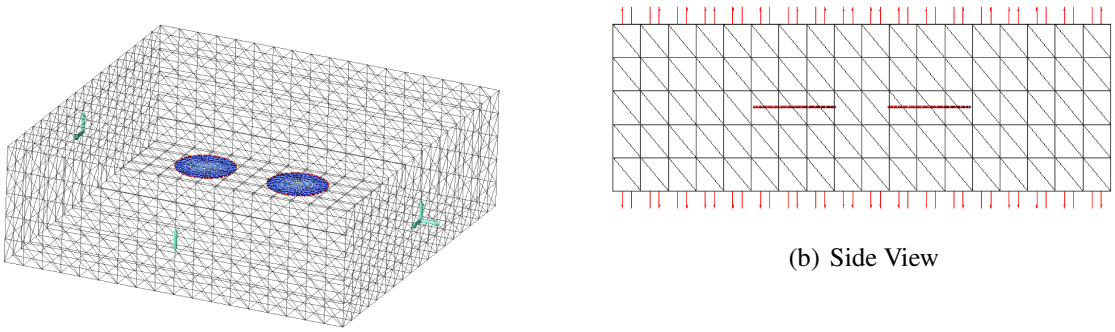

(a) 3-D View

(b) Side View

Figure 6.36: *Initial configuration for two, co-planar circular crack surfaces.*

In this example, the cracks propagate towards one another, and coalesce. After this point the stress intensities are greatest near the point of coalescence, and these vertices propagate greater distances for a given number of load cycles. As such, the coalesced surface tends to grow into a large circular crack surface. Figure 6.37 shows the crack surface(s) at various propagation steps. As can be seen, the shape of the coalesced crack surface evolves from its initial 'peanut' shape, into a nearly circular crack surface as the crack fronts reach the boundary of the domain. Similar results are obtained by Chopp et al. in [33] in which the same numerical example is analyzed. Figure 6.38(a) shows a side view of the final crack configuration illustrating that the coalesced crack surface has remained essentially planar, as would be expected.

Crack coalescence problems in general are a good candidate application area for the crack surface re-meshing algorithm proposed in this work because in the general case they fall into the category of long crack propagation. Upon coalescence, the newly formed crack surface is 'artifi-

cially enlarged' because it now encompasses multiple crack surfaces. In the particular numerical example analyzed here, the initial crack radii are $r_c^{init} = 0.5$, while the final crack surface has a radius of $r_c^{final} \simeq 3.0$, yielding a final crack surface with roughly 36 times the initial surface area, yet the same basic shape. As such, significant savings in the number of elements required to mesh the surface is realized through the use of crack surface re-meshing. The circular shape is still able to be sufficiently maintained through the use of a single band of relatively small facets just behind the crack front, which quickly transition into much larger elements used throughout the rest of the surface, as explained in Section 6.1.4.

One final area of interest is illustrated in Figure 6.38(b). The figure shows a side view of the final crack surface configuration where instead of point constraints to prevent rigid body motion (as used previously), the domain is subjected to unit normal tension on the top surface, and built-in Dirichlet boundary conditions (fully-constrained displacement) are applied to the bottom surface. As can be seen in this instance, while initially (essentially) planar, the coalesced crack surface propagates into a non-planar configuration as the crack front approaches the domain boundary and the effect of the built-in support and non-zero Poisson's ratio impact the crack front trajectory upon advancement. Even though the domain boundary and loading conditions are essentially Mode I, the propagated crack surface shows significant influence of the mixed mode conditions present in the region of the crack front due solely to the selection of a more restrictive Dirichlet boundary condition. This slight change in the model problem illustrates the significant dependence of crack propagation paths on the applied boundary conditions, as discussed in Section 7.3. It also highlights the importance of selecting a physically accurate and appropriately representative model in order to avoid erroneous results and potentially misguided conclusions.

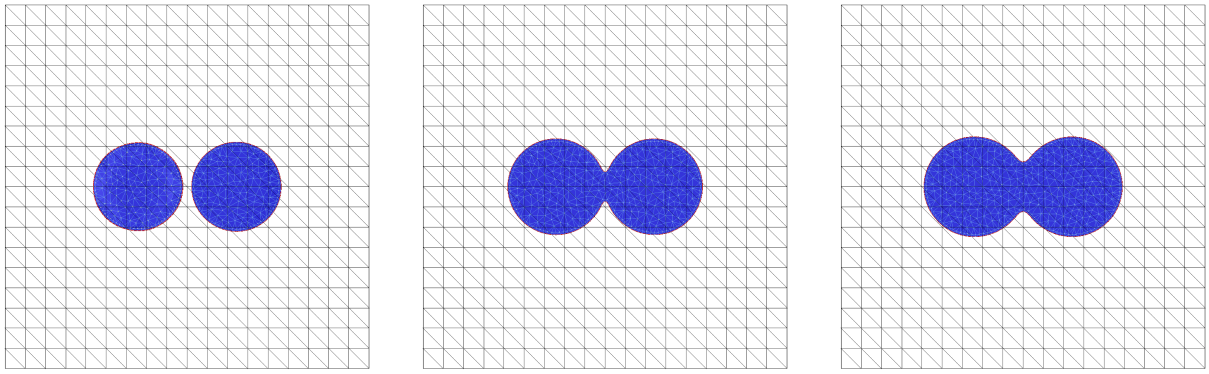

(a) Step 3 (b) Step 5 (c) Step 9

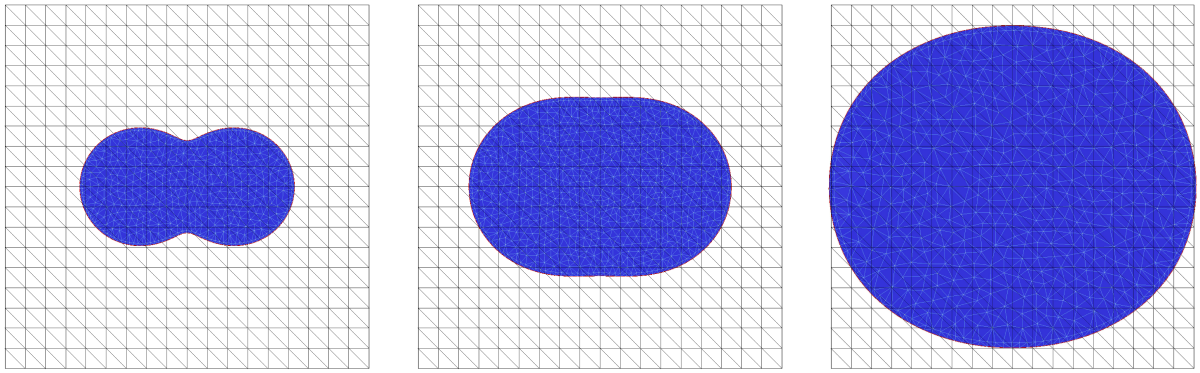

(d) Step 15 (e) Step 25 (f) Step 38

Figure 6.37: *Illustration of crack coalescence for two, cirular crack surfaces.*

(a) Rigid Body Point Constraints (b) Built-in Support

Figure 6.38: *Side view of final coalesced crack surfaces for different Dirichlet boundary conditions.*

6.6.3 Coalescence of Two Quarter-Penny Reflective Cracks

We now consider the same example as in the beginning of this Section 6.1. In this instance there are two quarter-penny-shaped cracks, as illustrated in Figure 6.39. The same domain dimensions, material properties and BCs are used. The new crack is a mirror imagine of the original crack surface, meaning that it has an identical geometry, simply flipped in the opposite direction.

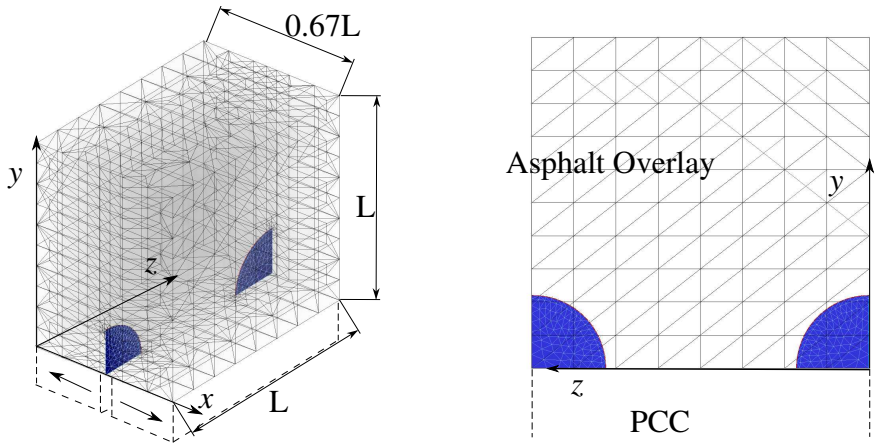

Figure 6.39: *Model description.*

The SIFs are extracted using the Contour Integral Method (CIM, ref. A) and the propagation path is again computed as in Section 7.3. Also, some techniques previously described such as ACFA 6.1.2, re-meshing of the crack surface 6.1.4, MLSM 6.3 and boundary interaction 6.4 are used at every crack propagation step. Due to the loading conditions and proximity to the domain boundary, the improved techniques for surface representation are more relevant in the pre-coalesced portion of the simulation than in the previous example, where the crack surfaces were completely internal and the effective SIFs were essentially uniform along the crack front. In this case, however; we have no existing numerical results against which to compare, and due to the large discrepancy in the crack increments along the front, the coalesced region of the crack surface is not as highly non-convex. Therefore, in this example propagation beyond the coalescence point doesn't pose the same potential for surface interpenetration so the MLSM smoothing or crack front vertices in the coalesced region of the front is not as critical.

Figures 6.41 and 6.40 show the evolution of the crack surface and the von Mises stress plotted

on the deformed configuration, respectively, for several crack propagation steps. We note that in this case the merged crack surface proceeds to propagate throughout the entire domain until it is completely separated into two, disjoint sub-domains.

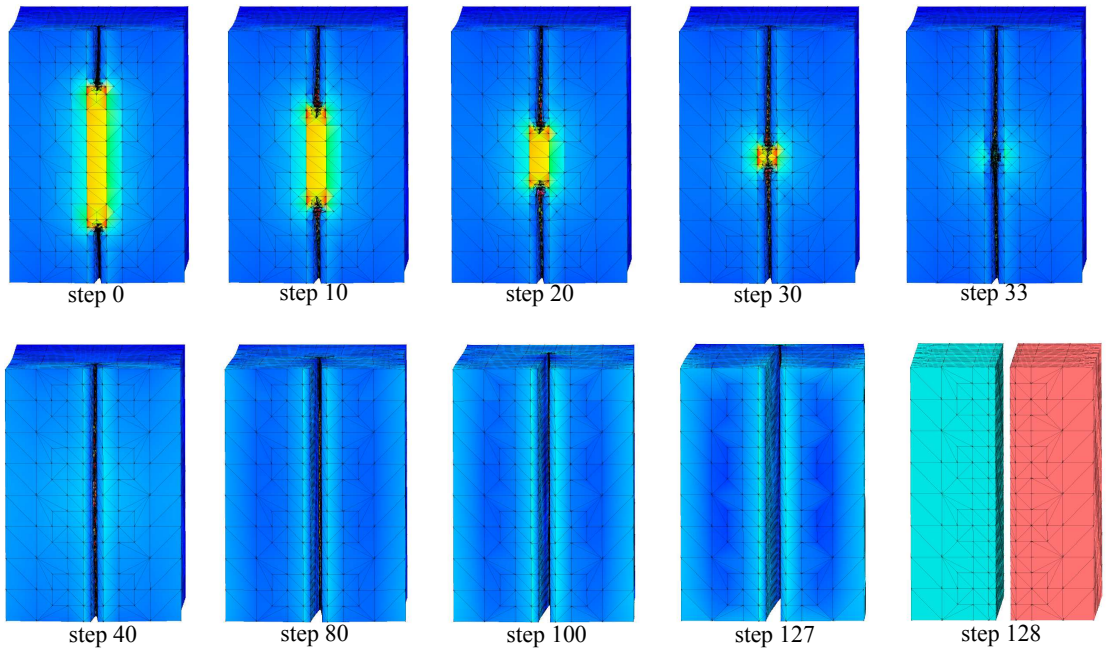

Figure 6.40: *Crack propagation: von Mises stress plotted on deformed configuration.*

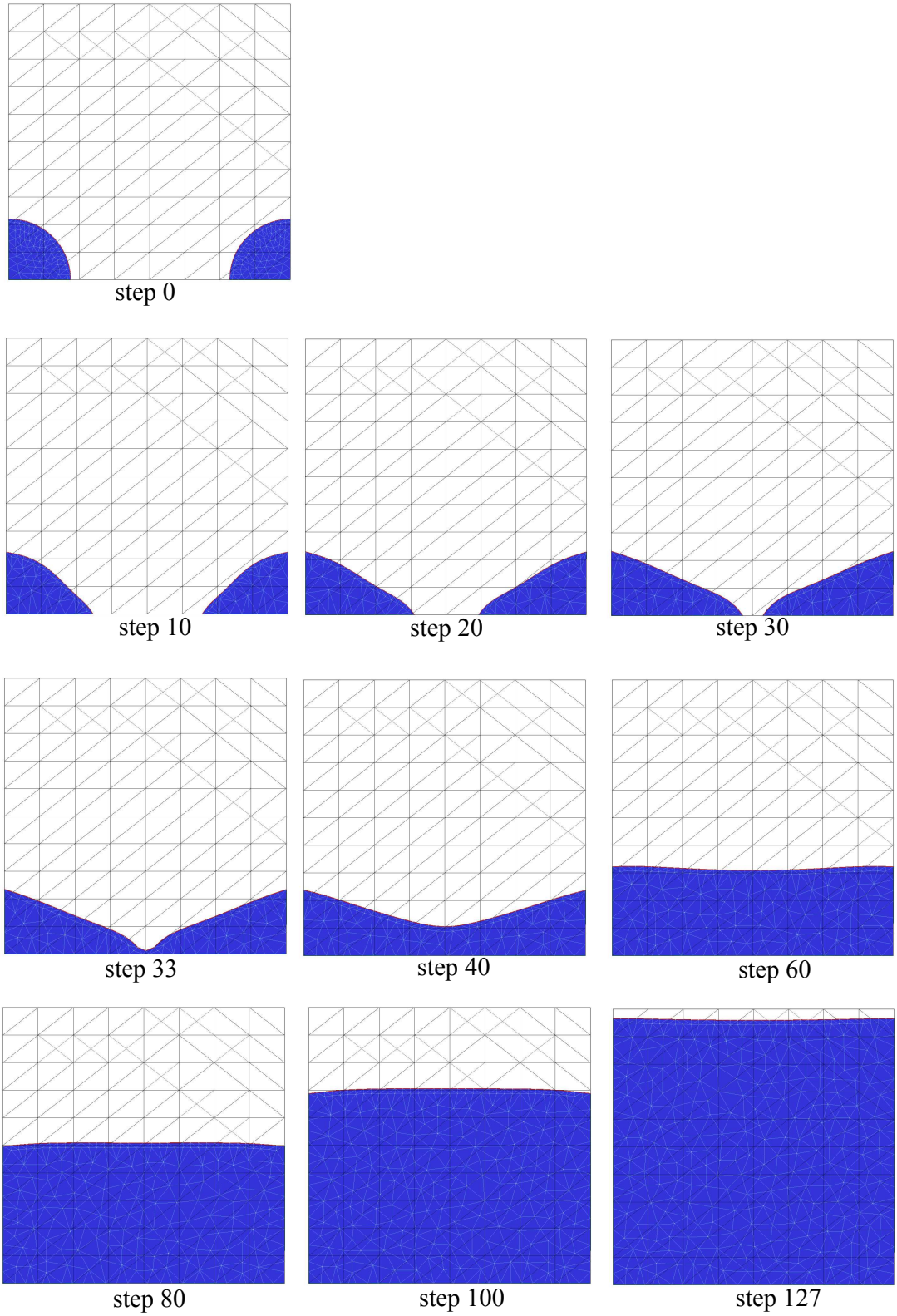

Figure 6.41: *Surface crack evolution. Mesh refinement along the front is not shown for clarity of illustration.*

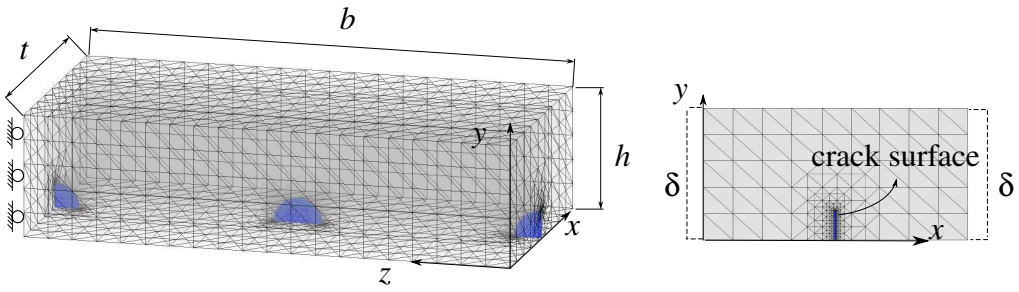

Figure 6.42: *Coalescence of Half-Penny and Two Quarter-Penny Cracks problem description.*

6.6.4 Coalescence of Half-Penny and Two Quarter-Penny Cracks

Consider the same domain as in Example 6.6.1 but with 3 initial crack surfaces. Two quarter-penny shaped cracks at the sides of the specimen and one half-penny shaped crack right at the middle. The dimensions of the rectangular domain are $t = 10.0$, $h = 5.0$, $b = 20$ and the initial radius for all cracks is $a = 1.0$. All dimensions are in inches. The assumed elastic material properties are Youngs modulus $E = 3,318.94$ ksi and Poissons ratio $\nu = 0.30$. Boundary conditions are the same as used in Example 6.6.1 with maximum magnitude of $\delta = 0.015$ inches at the side faces of the rectangular domain. Also, the back face of the domain is constrained against motion in the z-direction. Although this violates the symmetry assumption made in Section 6.5, only in this example, the influence of BCs on crack propagation is checked.

Figure 6.42 shows details about the problem.

SIFs are extracted using CIM (ref. Appendix A) at every crack growth step. These SIFs are used to compute the direction and magnitude of propagation using the growth criteria presented in Section 7.3. Also, techniques presented in this Chapter including crack coalescence 6.5 are used in this simulation. Figures 6.44 and 6.43 show the evolution of the crack surface and the von Mises stress plotted on the deformed configuration, respectively, for several propagation steps.

Observe that propagation of the quarter-penny shaped cracks is similar to the propagation in Example 6.6.1, until they approximate to the crack in the middle. Then, the portion of crack front located at the bottom of the domain ($\theta = 0$) tends to advance faster towards the half-penny shaped crack. After the 3 cracks have coalesced, the right side of the crack hits the boundary of the domain. This does not happen with the left side, because of the boundary condition placed there.

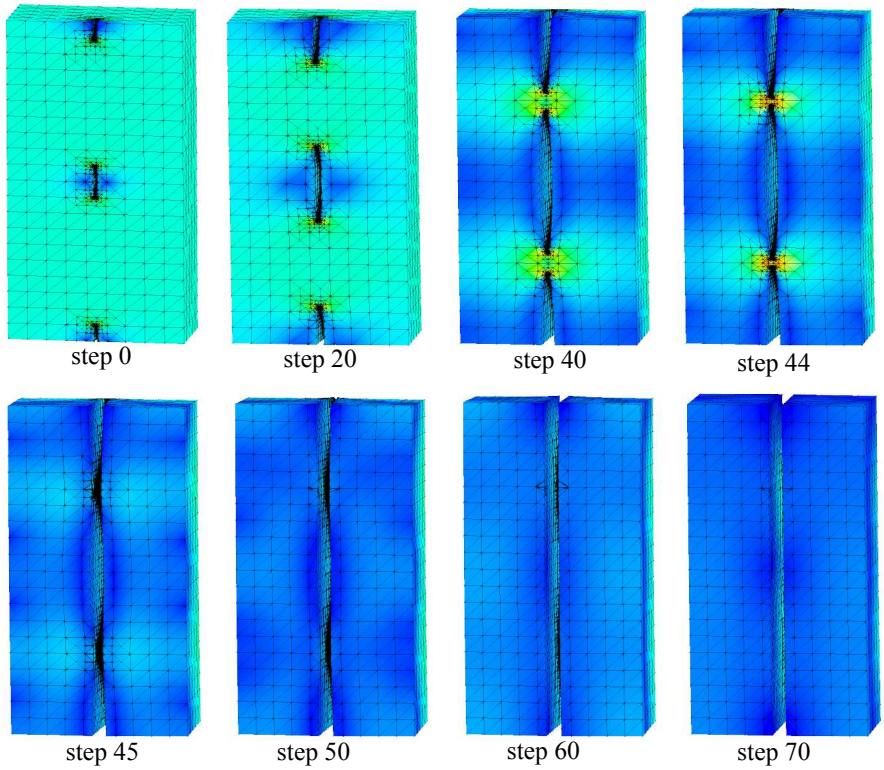

Figure 6.43: *Crack propagation: von Mises stress plotted on deformed configuration.*

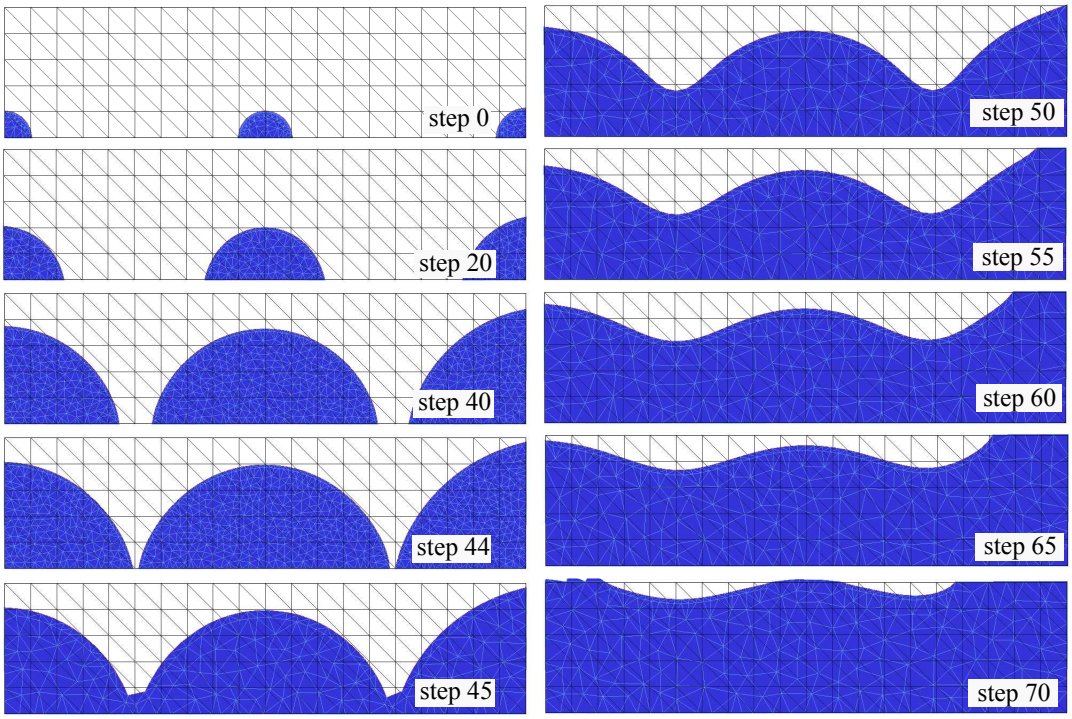

Figure 6.44: *Surface crack evolution.*

This means, that the portion of the crack front that is at the edge of the domain advances faster than it's portions on the interior.

The challenges encountered in this simulation includes, significant change in size of the crack surfaces, crack coalescence and boundary interaction of many parts of the crack front. This is only possible using the techniques proposed in this Chapter.

Chapter 7

Fatigue Crack Growth in Linear Viscoelasticity

In engineering practice, design life of structures and structural components is often governed by fatigue crack considerations. Fatigue assessment is highly relevant in design decisions put forth by the civil, mechanical and aerospace design communities. Fatigue itself is a process in which damage accumulates due to the repetitive application of cyclic loading that may be well below the yield point of the material. The process is inherently dangerous because a single application of the load would not produce any ill effects and a conventional stress analysis will likely lead to the assumption of design safety which may not exist. As such, fatigue assessment is critical in accurate life prediction for engineering structures.

The problem of reflective cracking is an example of a three dimensional fatigue crack growth problem. The cracking in the asphalt overlay is a result of hundreds/thousands of traffic and environmentally induced (fatigue) load cycles, in conjunction with the stress concentrations due to the existing joints or cracks in the underlaying pavement. Not only in the pavements, but also in other structures as well, it is vital that engineers be able to predict the rate of crack growth during load cycling, so any assessment, such as a repair or a replacement of the part in question, can be done before the crack reaches a critical length.

Most of the equations utilized to describe fatigue crack growth behavior are based on observations of the physical phenomenon and extensive material testing. Crack growth laws as well as life estimates are often based upon fracture mechanics quantities such as energy release rate or stress intensity factors [150] which can be computed from numerical solutions. Therefore, accurate simulation data is critical if quantities derived from the numerical solutions are to yield accurate life estimates.

This chapter focuses on the simulation of three-dimensional crack growth in viscoelastic solids under fatigue. From a macro-scale point of view, fatigue can be regarded as a quasi-static phenomenon. Moreover, the crack growth mechanism in fatigue can be characterized by a linear viscoelastic fracture mechanics parameter, i.e., the energy release rate [93]. Therefore, a robust and accurate method to analyze linear viscoelastic fracture mechanics problems, such as the combination of the correspondence principle and the GFEM presented in Chapter 4, is essential for successful crack path and fatigue life predictions.

The rest of this chapter describes the problem to be analyzed and the assumptions of the fatigue crack growth model. Also, the details about the three-dimensional criterion for crack growth advancement and direction are discussed.

7.1 Problem Description

Consider a three-dimensional body subjected to repeated cyclic loading with an existing embedded surface crack as illustrated in Figure 7.1. This is a typical fatigue crack growth problem. Fatigue life prediction is still very much an empirical art more so than a strict science. Fatigue is a complex material process where damage accumulates and it is difficult to accurately describe or model, because often it shows disperse outcomes even in controlled environments [158, 174]. It is influenced by a variety of factors such as load, temperature, material behavior, micro-structure, presence of chemicals, residual stresses, contact, etc. Fatigue is treated as a probabilistic problem and existing theories are based almost entirely on observations of the physical phenomena rather than physical laws and mathematical formulations.

Fatigue is characterized by a large number of cycles (above 10^2) to failure where stress is low compared with the stress capacity (limit) of the material. From a macro-scale point of view, fatigue can be regarded as a quasi-static phenomena. Many phenomenological laws have been used to predict fatigue crack propagation by relating crack growth rate and the amplitude of a characteristic crack front parameter, such as stress intensity factors (SIFs). The most well known

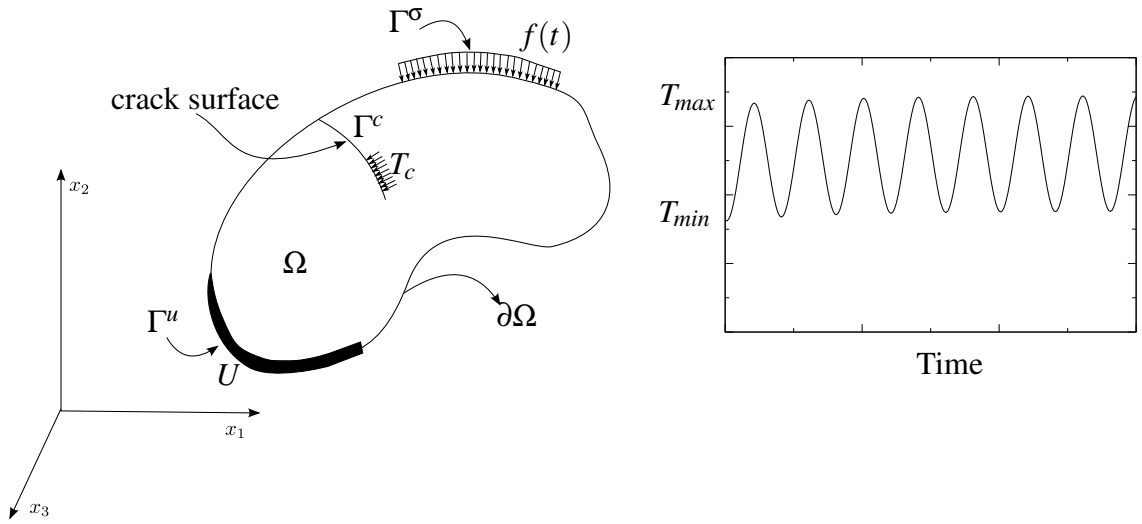

Figure 7.1: *Notation for Fatigue Problem.*

work is that of Paris and Erdogan [123]. This law describes the experimental data under constant amplitude loading and, most importantly, under small-scale yielding. In this type of fatigue, crack growth behavior is commonly idealized in a diagram subdivided into three stages:

- Stage 1: *Crack initiation*; which is governed by the material micro-structure. At this stage there are only micro-cracks which coalesce in formulation of macro-cracks.

- Stage 2: *Stable crack growth*; characterized by a power law based on empirical parameters. In this stage, a macro-crack exists and has stable behavior. In Figure 7.2, this stage starts at the slow crack growth limit and ends in the rapid growth limit.

- Stage 3: *Unstable crack growth*; owing to the fact that at this point the material has reached its critical fracture toughness and the crack exhibits an unstable propagation behavior leading to ultimate failure.

The present study focuses on the simulation of stable crack growth under fatigue and as such, Stage 2 crack growth behavior is assumed. Furthermore, the class of problems analyzed here are subject to constant amplitude cyclic mechanical loading ($T_{max} > 0$ and $T_{min} \geq 0$ Figure 7.1) and quasi-static crack growth.

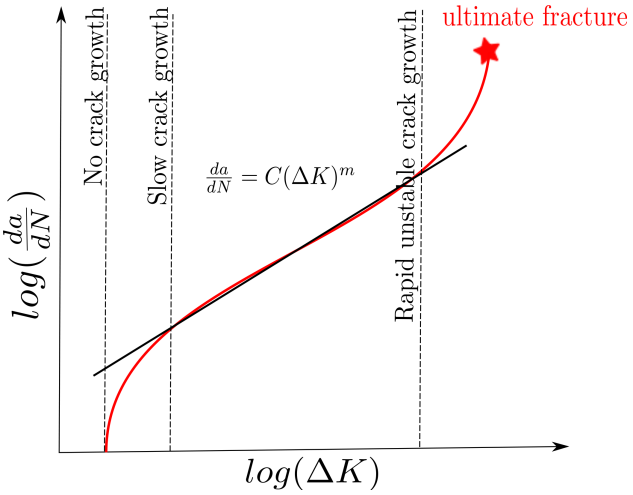

Figure 7.2: *Idealized fatigue crack growth rate diagram.*

7.2 Crack Growth Model for Linear Viscoelasticity

Since fatigue can be regarded as a quasi-static phenomenon, it can be simulated as a sequence of incremental steps. Each step constitutes a fracture mechanics problem with a fixed crack size and it depends on the solution and crack front evolution prediction of the previous steps.

In linear viscoelasticity, each fracture mechanics step can be simulated using the GFEM or *GFEM*$^{\text{g-l}}$ in combination with the nonlinear solver described in Section 2.4. The drawback of this methodology is that the simulation takes a large amount of time since each load cycle has to be simulated with a small time increment. The number of cycles in a fatigue problem for each crack propagation step is above 10^2 which in turn would give more than 10^3 load steps to be simulated, making this a very inefficient way to solve the problem. As an alternative, each fracture step can be solved using the GFEM or *GFEM*$^{\text{g-l}}$ in conjunction with the correspondence principle as described in Chapters 4 and 5, respectively. This is a very efficient simulation because at each step, the numerical simulation only involves a unique reference elastic problem, and the use of correspondence principle allows the computation of the solutions in time.

In order to better understand this process, consider a crack surface of size $a = a_0$ growing in a linear viscoelastic solid under a fatigue process. After several load cycles, the crack surface has increased (slowly) its original size to $a = a_2 > a_0$. This problem can be analyzed as a quasi-static

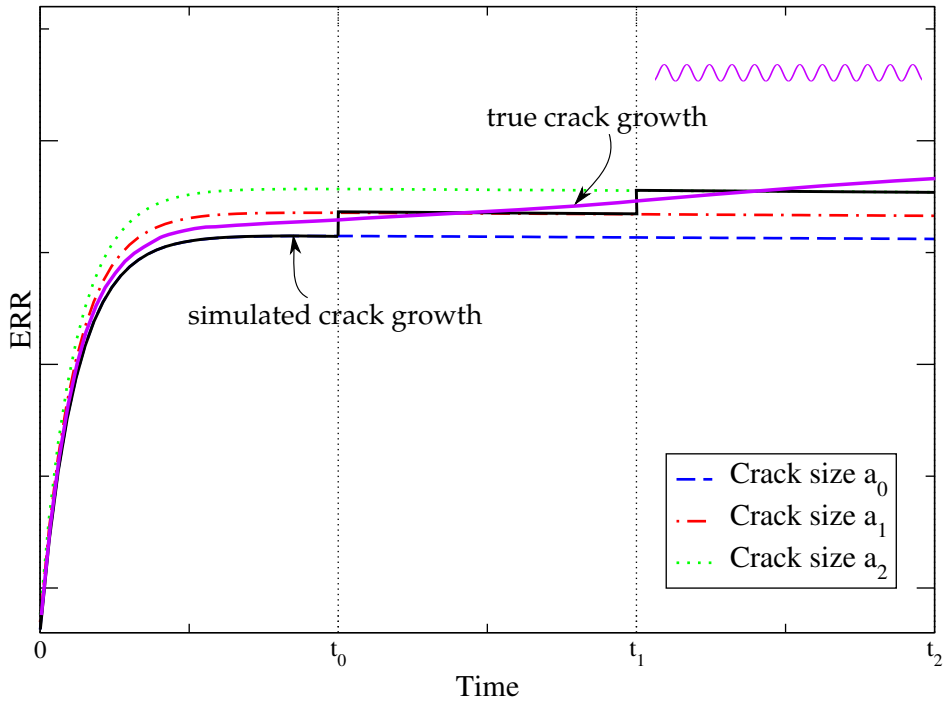

Figure 7.3: *Quasi-static crack growth.*

crack growth by separating the crack evolution into three steps. At Step 0 the crack size is $a = a_0$, Step 1 $a = a_1 > a_0$ and Step 2 $a = a_2 > a_1$. Each step can be analyzed independently as a static problem with its corresponding crack size, and important quantities such as ERR can be computed. Figure 7.3 illustrates the difference of treating this problem as a quasi-static growth and the actual crack growth.

The equations to compute the ERR of this problem are:

$$
\begin{aligned}
G_I^v(t) &= \frac{K_I^2(a_0)}{4}\left[3\int_0^t J^{G+3K}(t-t')\frac{\partial\lambda^2(t')}{\partial t'}\,dt'\right. \\
&+ \left.\int_0^t J^{G}(t-t')\frac{\partial\lambda^2(t')}{\partial t'}\,dt'\right] \quad \text{for} \quad 0 \le t < t_0 \\
G_I^v(t) &= \frac{K_I^2(a_1)}{4}\left[3\int_0^t J^{G+3K}(t-t')\frac{\partial\lambda^2(t')}{\partial t'}\,dt'\right. \\
&+ \left.\int_0^t J^{G}(t-t')\frac{\partial\lambda^2(t')}{\partial t'}\,dt'\right] \quad \text{for} \quad t_0 \le t < t_1 \\
G_I^v(t) &= \frac{K_I^2(a_2)}{4}\left[3\int_0^t J^{G+3K}(t-t')\frac{\partial\lambda^2(t')}{\partial t'}\,dt'\right. \\
&+ \left.\int_0^t J^{G}(t-t')\frac{\partial\lambda^2(t')}{\partial t'}\,dt'\right] \quad \text{for} \quad t_1 \le t \le t_2
\end{aligned} \tag{7.1}
$$

It is not only important to compute the values of energy release rate but also to study the variation of its maximum and minimum values ($\Delta\mathcal{G}$). This information is useful for the computation of the number of cycles corresponding to a crack increment, depending on the criterion selected. Section 7.3 presents in detail the criterion used in this study.

Consider a linear elastic and a linear viscoelastic material during crack propagation. Figure 7.4 shows six propagation steps in a 150 seconds simulation. A three percent increment in crack length every 25 seconds is assumed for each crack propagation step. The energy release rate is computed for both materials.

In both linear elastic and linear viscoelastic materials, an increment in the variation of energy release rate $\Delta\mathcal{G}$ is caused by of an increment in crack size. In linear elasticity $\Delta\mathcal{G}$ is constant within each crack step, therefore only one GFEM simulation is necessary to compute a representative $\Delta\mathcal{G}$ for each crack step. In linear viscoelasticity, on the other hand, $\Delta\mathcal{G}$ is not constant, but it stabilizes after some time. Thus, *the time considered in each crack step must be large enough to compute a representative* $\Delta\mathcal{G}$. This is assuming that $\Delta\mathcal{G}$ of the viscoelastic material in question stabilizes after certain time.

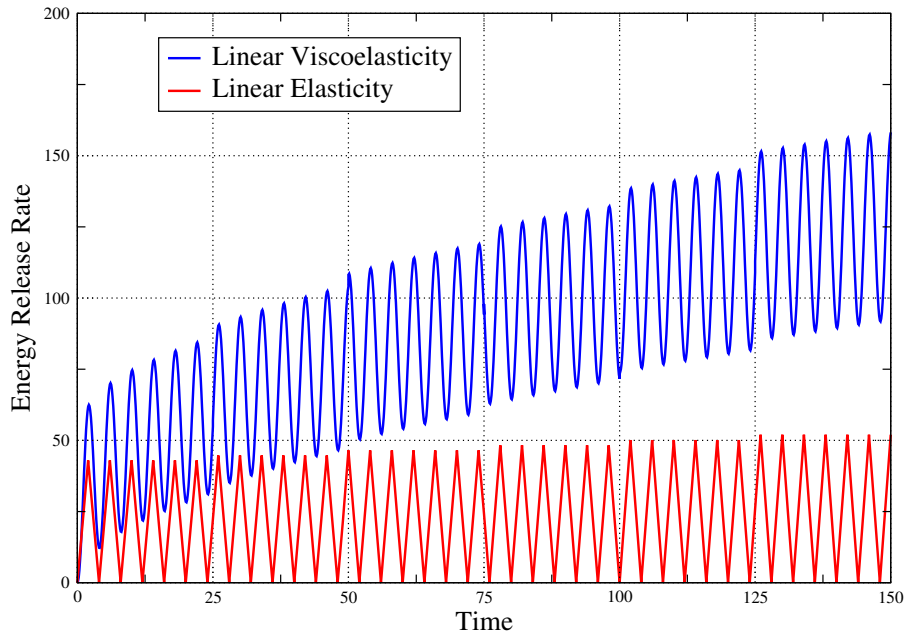

Figure 7.4: *Illustration of crack propagation for linear elastic and viscoelastic materials.*

To analyze this behavior, a static crack in a viscoelastic medium is studied. The material properties are represented by the Prony series shown in Table 7.4. Assume a sinusoidal load $|\sin(\frac{t\,\pi}{t_{peak}})|$ applied to the body with three different values for $t_{peak} = 0.8, 3.2$ and 6.4 seconds. Let us call t_s the time required to reach a stabilized solution ($\Delta\mathcal{G}$). Energy release rate $\mathcal{G}$ and the time t_s are computed for the 3 cases at temperatures of $0^o, 10^o$ and 20^o C. A $\Delta\mathcal{G}$ stabilized is considered when the difference of two consecutive $\Delta\mathcal{G}_i$ and $\Delta\mathcal{G}_{i+1}$ is less than 0.1 percent. Tables 7.1-7.3 and Figures 7.5-7.7 show the results.

It can be seen that the time to find a stabilized value of $\Delta\mathcal{G}$ depends on temperature and frequency. This stabilized time t_s can be used at each crack propagation step to compute a representative $\Delta\mathcal{G}$ when performing a crack growth simulation. This observation agrees with the experimental results found by Kuai et al. [93].

The stabilized time found here only applies for the given material properties, loading condition and temperatures. Therefore a study is necessary, for every particular case, to correctly choose the simulation time for every crack step. This simulation time should be greater than t_s in order to compute a representative $\Delta\mathcal{G}$.

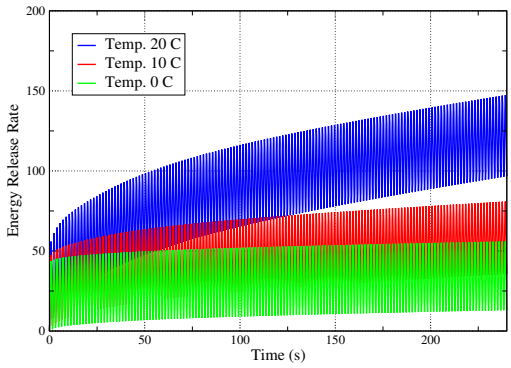

(a) G vs. Time

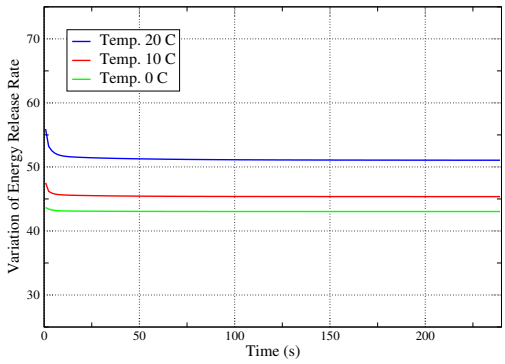

(b) $\Delta\mathcal{G}$ vs. Time

Figure 7.5: *Static crack in linear viscoelastic material.* $t_{peak} = 0.8$ *seconds.*

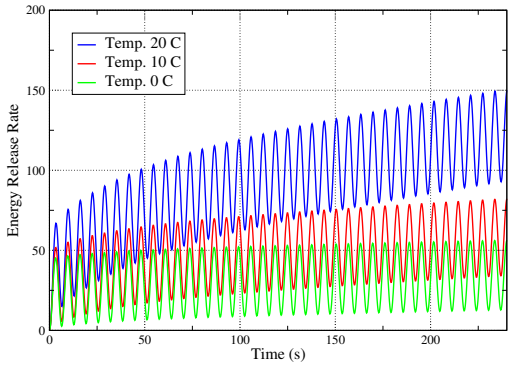

(a) G vs. Time

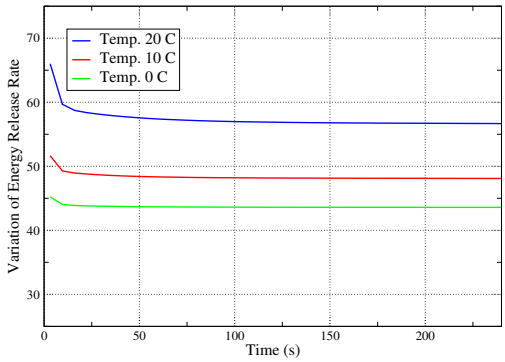

(b) $\Delta\mathcal{G}$ vs. Time

Figure 7.6: *Static crack in linear viscoelastic material.* $t_{peak} = 3.2$ *seconds.*

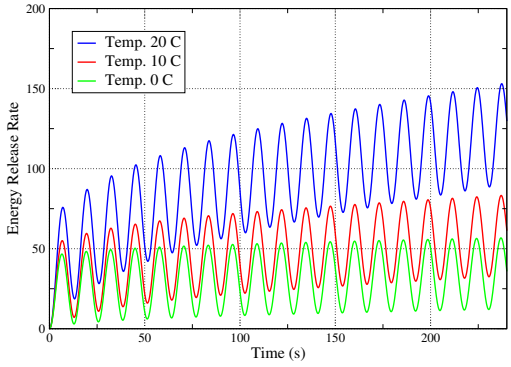

(a) G vs. Time

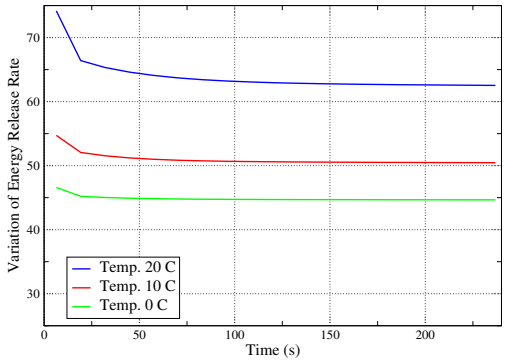

(b) $\Delta\mathcal{G}$ vs. Time

Figure 7.7: *Static crack in linear viscoelastic material.* $t_{peak} = 6.4$ *seconds.*

In conclusion, it is not necessary to simulate hundreds or thousands of cycles. Instead only the number of cycles within t_s time frame. In these examples the number cycles to find a representative

Table 7.1: *Stabilized time for temperature* 0^oC.

t_{peak} (s)	t_s (s)	$Cycles$ (u)
0.8	8.0	5
3.2	32.0	5
6.4	76.8	6

Table 7.2: *Stabilized time for temperature* 10^oC.

t_{peak} (s)	t_s (s)	$Cycles$ (u)
0.8	9.6	6
3.2	57.6	9
6.4	115.2	9

Table 7.3: *Stabilized time for temperature* 20^oC.

t_{peak} (s)	t_s (s)	$Cycles$ (u)
0.8	12.8	9
3.2	89.6	14
6.4	153.6	12

$\Delta\mathcal{G}$ were less than 14.

In the next Section, a propagation problem is solved using the correspondence principle with a FEM reference elastic solution. Additionally, the problem is solved using the viscoelastic nonlinear algorithm explained in Section 2.4 and serves as verification.

7.2.1 Verification Example

In order to verify the use of the correspondence principle for quasi-static crack propagation in linear viscoelastic materials a two-dimensional problem is solved and compared to a nonlinear solver solution.

The problem consists of a rectangular plate with a center crack, as illustrated in Figure 7.8. The model is subjected to a sinusoidal load $\sigma\lambda(t)$ prescribed at top and bottom. The dimensions of the plate are: $H = 10$ cm and $w = 10$ cm. The material properties are linear viscoelastic, homogeneous, isotropic and are represented by the Prony series shown in Table 7.4.

A crack is located at the center of the plate with a initial dimension of $a_0 = 1.0$ cm. The temperature assumed in this problem is 20^oC. Two methodologies are used to solve this problem.

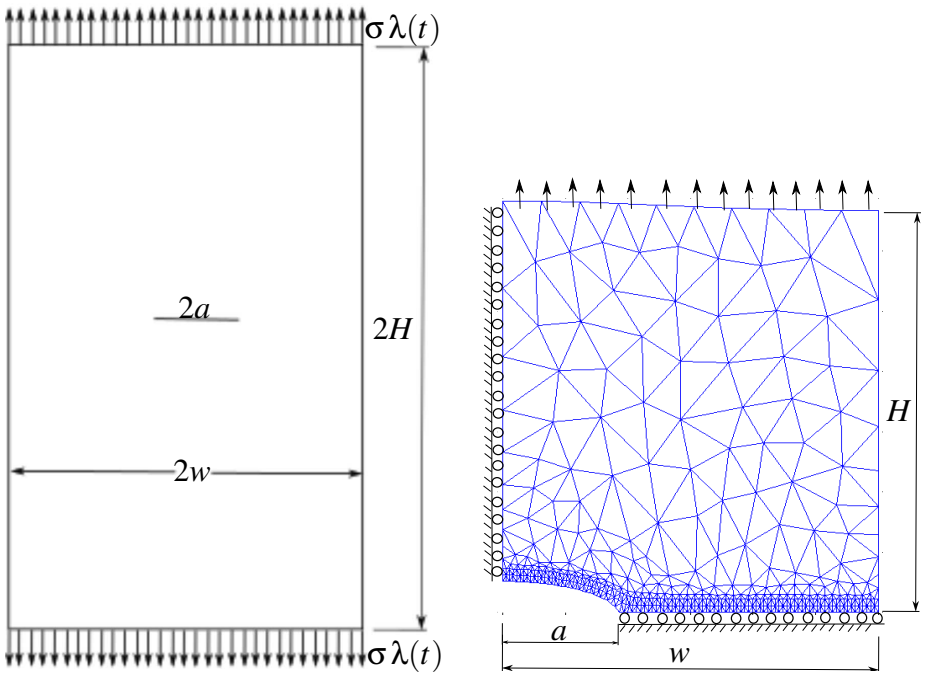

(a) FEM mesh (deformed configuration). (b) Problem description.

Figure 7.8: *Center crack plate problem details.*

The first one corresponds to the nonlinear solver described in Section 2.4. The second uses the correspondence principle with a FEM reference elastic problem for each propagation step.

Crack propagation is analyzed using the idea of quasi-static crack growth. Crack evolution is separated in three steps; step 0 with crack size $a = a_0$, step 1 with $a = a_1 = 1.3\,a_0$ and step 2 with $a = a_2 = 1.6\,a_0$. The total simulation time is 240 seconds and it is divided in 3 time intervals of 80 seconds each ($t_0 = 80$s, $t_1 = 160$s and $t_2 = 240$s). Four different time frequencies are tried for comparison. The first one consists of 50 load cyles per crack step, the second is 20 load cycles, the third is 10 cycles and the fourth one is only 5 cycles. Normally, the time and number of cycles corresponding to an increment in crack length are computed using a defined criterion. Here we assume both for simplicity. The main purpose is to see the difference between the two methodologies with change in crack size.

Table 7.4: *Mathematical representation of the viscoelastic material (Prony series).*

m	G_m (MPa)	K_m (MPa)	ρ_m (s)
1	74.633	161.705	2e-2
2	108.87	235.88	2e-1
3	213.12	461.77	2
4	231.59	501.78	2e1
5	149.26	323.40	2e2
6	60.013	130.03	2e3
7	15.773	34.174	2e4
8	5.3088	11.502	2e5
9	1.4155	3.0669	2e6
10	0.3041	0.6589	2e7
11	0.3696	0.8008	2e8
$G_0 = 861.54$ and $K_0 = 1866.67$			

Non-linear solver

Here, the simulation consists of solving the problem for each time increment using the nonlinear solver explained in Section 2.4. At each time step the crack mouth opening displacement (CMOD) is measured. To save simulation time, because of the double symmetry of the problem, only the right top quarter of the problem is modeled. Figure 7.8(b) shows the FEM mesh including the position of the crack.

The solution process is similar to the static crack simulation, the only difference is that at time t_0, for example, the crack propagates and therefore the crack size changes from a_0 to $a_1 = 1.3\,a_0$. In the FEM mesh this is accomplished by removing some of the displacement boundary conditions at the crack front. This is done during the simulation, so all state variables from previous step are carried out and used at the current crack step.

This simulation can take a significant amount of time to complete. For the case of 50 load cycles per crack step for example, the time increment is 0.08s and the FEM problem has to be solved at least $3,000$ times. The time increment chosen here subdivides each load cycle in 20 increments, which should be enough to accurately simulate the problem.

Correspondence Principle with FEM

This method consists of using the correspondence principle with a FEM reference elastic problem. The FEM reference elastic problem has the same mesh and boundary conditions as the nonlinear problem, see Figure 7.8(b). The only difference is that the material properties are considered linear elastic and therefore the instantaneous shear and bulk modulus are used as the elastic material constants.

The solution process consists of solving three reference elastic problems with their corresponding crack size. Then, using the correspondence principle, the time dependent CMOD is computed as follows:

$$\begin{aligned} \delta^e_{0,CMOD} &= 0.0294\,cm \\ \delta^e_{1,CMOD} &= 0.0307\,cm \\ \delta^e_{2,CMOD} &= 0.0318\,cm \end{aligned}$$

$$\bar{\bar{\delta}}^v_{i,CMOD}(p) = \frac{\delta^e_{i,CMOD}\, G_0\, K_0 \left(3\, p\bar{\bar{K}}(p) + p\bar{\bar{G}}(p)\right)}{p\bar{\bar{G}}(p)\, p\bar{\bar{K}}(p) \left(3\, K_0 + G_0\right)} \bar{\bar{\lambda}}(p) \tag{7.2}$$

where $\delta^e_{i,CMOD}$ is the ith propagation step CMOD computed from the FEM reference elastic problem.

Equation (7.2) is transformed back to the time domain giving the time-dependent CMOD for the linear viscoelastic material. This transformation can be performed numerically using Equation (3.35).

The Laplace transform of the load function $\lambda(t)$ for a sinusoidal load $\lambda(t) = \frac{1}{2}\left(1 - \cos(\frac{\pi t}{t_{peak}})\right)$ is,

$$\bar{\bar{\lambda}}(p) = \mathfrak{L}\left\{\lambda(t) = \frac{1}{2}\left(1 - \cos(\frac{\pi\, t}{t_{peak}})\right)\right\} = \frac{1}{2\,p} - \frac{p}{2\,(p^2 + \frac{\pi^2}{t^2_{peak}})} \tag{7.3}$$

The Prony series functions in Laplace domain are given by,

$$\bar{\bar{G}}(p) = G_\infty + \sum_m^M \frac{G_m}{\frac{1}{\rho_m} + p} \tag{7.4}$$

$$\bar{\bar{K}}(p) = K_\infty + \sum_m^M \frac{K_m}{\frac{1}{\rho_m} + p} \tag{7.5}$$

where G_∞ and K_∞ are the long-time equilibrium shear and bulk modulus, respectively.

The time-dependent CMOD for the linear viscoelastic material using both methods is shown in Figures 7.9-7.12. Also, the deformed configuration for the 3 propagation steps are illustrated in Figure 7.13.

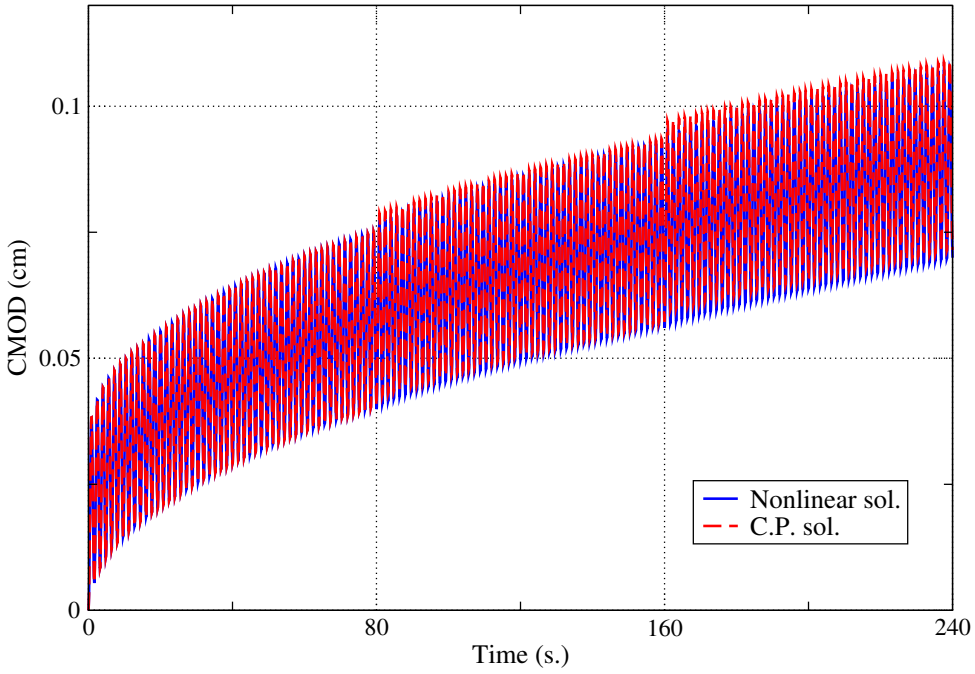

Figure 7.9: *The time-dependent CMOD. Non-linear analysis vs. correspondence principle for 50 load cycles per crack step.*

Results are very similar for both methodologies. The only difference found is at the transition stage from one crack size to another. The reason is that the correspondence principle methodology does not consider the true history of the problem; *it assumes no change in crack size in the past*. This difference is reduced in time, and suggests that the correspondence principle can be used as

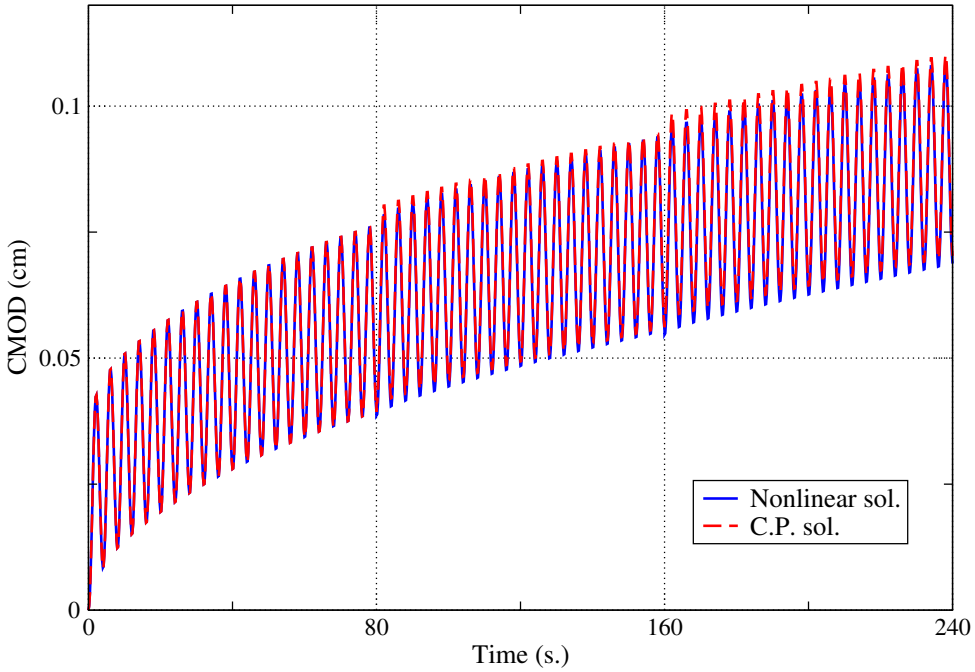

Figure 7.10: *The time-dependent CMOD. Non-linear analysis vs. correspondence principle for 20 load cycles per crack step.*

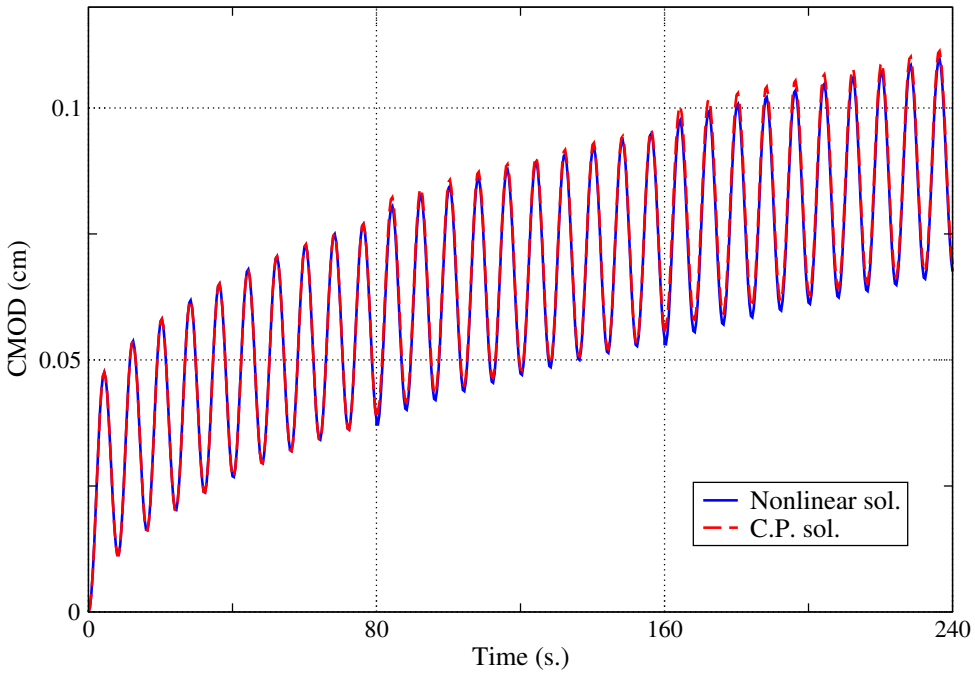

Figure 7.11: *The time-dependent CMOD. Non-linear analysis vs. correspondence principle for 10 load cycles per crack step.*

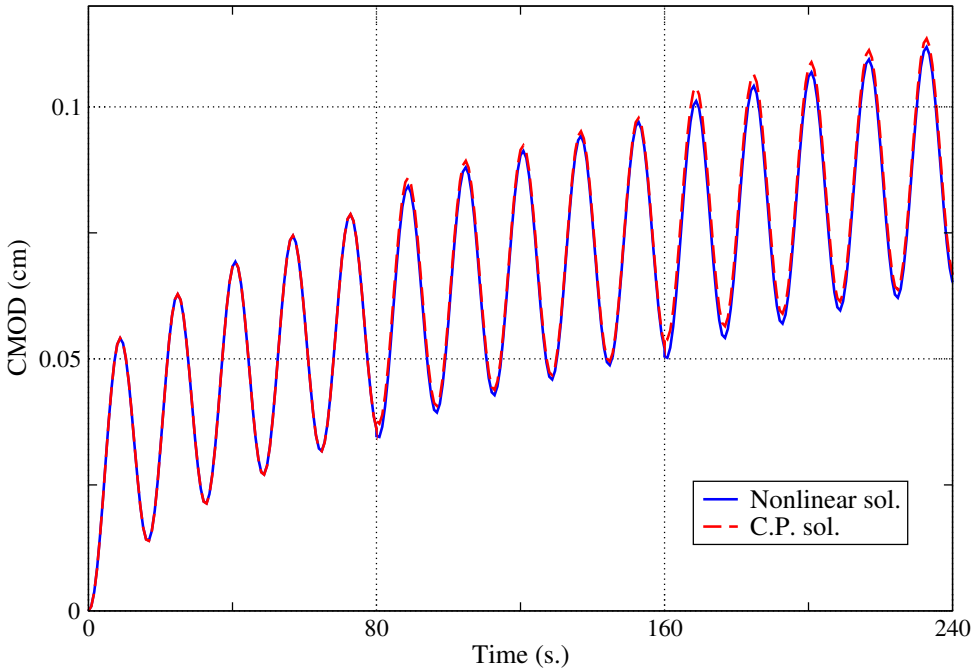

Figure 7.12: *The time-dependent CMOD. Non-linear analysis vs. correspondence principle for 5 load cycles per crack step.*

long as enough time is considered in the simulation.

Not only the values of CMOD are important but also the variation of CMOD (ΔCMOD) because similar crack front parameters may be used in the computation of life prediction (see Section 7.3). For the above example, we consider the case of 50 load cycles per crack propagation step and compute ΔCMOD at each load cycle. ΔCMOD is the difference between the maximum and minimum values. Figure 7.14 shows the ΔCMOD for this case.

Results show that the correspondence principle fails to compute the values for ΔCMOD at the transition from one crack size to another, but the method accurately matches the nonlinear solution after some time. The differences are of very small magnitude, only in the order of 0.12 percent.

In conclusion, the correspondence principle method can be used to compute a representative value for ΔCMOD at each crack propagation step if this computation is done after a stabilization time has passed. This method may not accurately compute the values of CMOD throughout the quasi-static simulation because it does not consider the true history of the problem. Nevertheless,

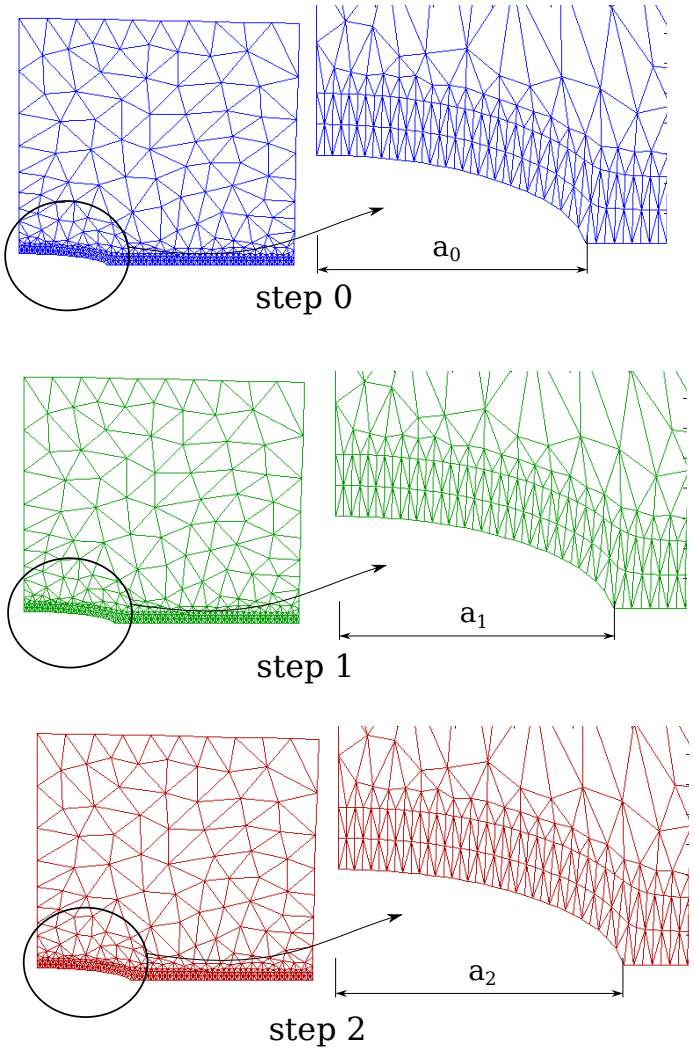

Figure 7.13: *Deformed configuration of the 2-D mesh, at every crack stage.*

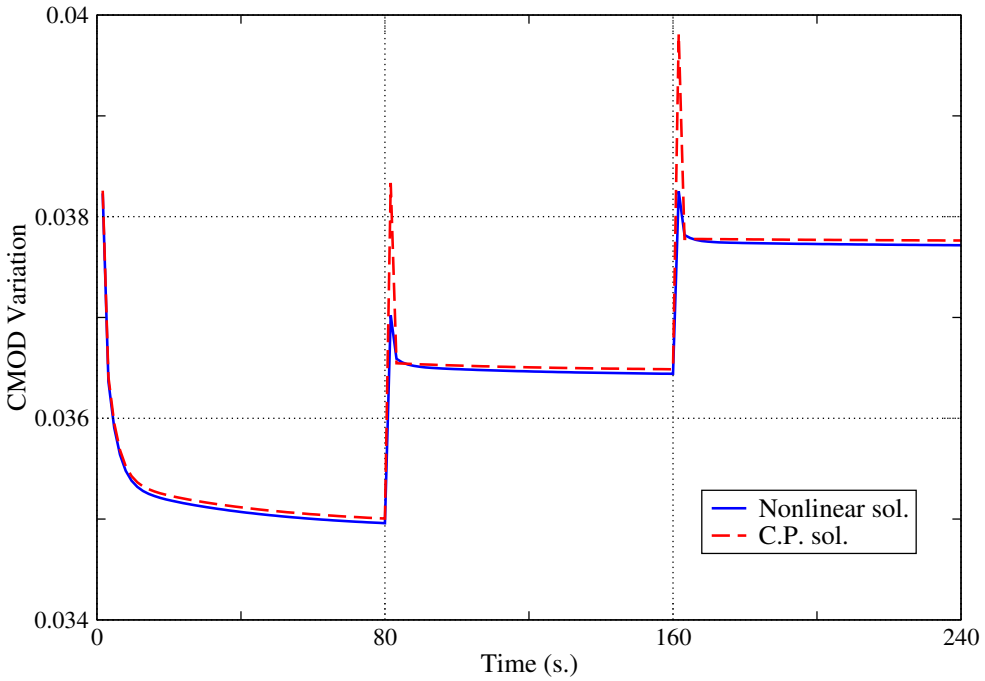

Figure 7.14: *The variation of CMOD (ΔCMOD). Non-linear analysis vs. correspondence principle for 50 load cycles per crack step.*

a characteristic crack front parameter (e.g. ΔCMOD, $\Delta\mathcal{G}$) can be computed at each propagation step. $\Delta\mathcal{G}$, for example, is used for life prediction using a specific criterion (see Section 7.3).

In case the actual value of CMOD is necessary, it can be computed in the time domain considering the total history of the quasi-static propagation using the inverse Laplace transform of Equation (7.2).

$$
\begin{aligned}
\delta^{v}_{CMOD}(t) &= \frac{\delta^{e}_{0,CMOD}\,G_0\,K_0}{3\,K_0+G_0}\left[3\int_0^t J^G(t-t')\frac{\partial\lambda(t')}{\partial t'}\,dt' + \int_0^t J^K(t-t')\frac{\partial\lambda(t')}{\partial t'}\,dt'\right] \quad \text{for} \quad 0 \le t < t_0 \\
\delta^{v}_{CMOD}(t) &= \frac{\delta^{e}_{0,CMOD}\,G_0\,K_0}{3\,K_0+G_0}\left[3\int_0^{t_0} J^G(t-t')\frac{\partial\lambda(t')}{\partial t'}\,dt' + \int_0^{t_0} J^K(t-t')\frac{\partial\lambda(t')}{\partial t'}\,dt'\right] \\
&+ \frac{\delta^{e}_{1,CMOD}\,G_0\,K_0}{3\,K_0+G_0}\left[3\int_{t_0}^t J^G(t-t')\frac{\partial\lambda(t')}{\partial t'}\,dt' + \int_{t_0}^t J^K(t-t')\frac{\partial\lambda(t')}{\partial t'}\,dt'\right] \quad \text{for} \quad t_0 \le t < t_1 \\
\delta^{v}_{CMOD}(t) &= \frac{\delta^{e}_{0,CMOD}\,G_0\,K_0}{3\,K_0+G_0}\left[3\int_0^{t_0} J^G(t-t')\frac{\partial\lambda(t')}{\partial t'}\,dt' + \int_0^{t_0} J^K(t-t')\frac{\partial\lambda(t')}{\partial t'}\,dt'\right] \\
&+ \frac{\delta^{e}_{1,CMOD}\,G_0\,K_0}{3\,K_0+G_0}\left[3\int_{t_0}^{t_1} J^G(t-t')\frac{\partial\lambda(t')}{\partial t'}\,dt' + \int_{t_0}^{t_1} J^K(t-t')\frac{\partial\lambda(t')}{\partial t'}\,dt'\right] \\
&+ \frac{\delta^{e}_{2,CMOD}\,G_0\,K_0}{3\,K_0+G_0}\left[3\int_{t_1}^t J^G(t-t')\frac{\partial\lambda(t')}{\partial t'}\,dt' + \int_{t_1}^t J^K(t-t')\frac{\partial\lambda(t')}{\partial t'}\,dt'\right] \quad \text{for} \quad t_1 \le t \le t_2
\end{aligned}
\tag{7.6}
$$

This Equation is the exact solution for this problem and it can be evaluated using different integration methods.

Integration in Time Domain

Equation (7.6) can be integrated using Gauss quadrature. The number of integration points in this method depends on the complexity of the function to be integrated. In order to use a low number of integration points the integral can be separated in small time increments as follows:

$$
\begin{aligned}
\delta^{v}_{CMOD}(t) &= \frac{\delta^{e}_{i,CMOD}\,G_0\,K_0}{3\,K_0+G_0}\left[3\int_0^{\Delta t} J^G(t-t')\frac{\partial\lambda(t')}{\partial t'}\,dt' + \int_0^{\Delta t} J^K(t-t')\frac{\partial\lambda(t')}{\partial t'}\,dt'\right. \\
&+ 3\int_{\Delta t}^{2\Delta t} J^G(t-t')\frac{\partial\lambda(t')}{\partial t'}\,dt' + \int_{\Delta t}^{2\Delta t} J^K(t-t')\frac{\partial\lambda(t')}{\partial t'}\,dt' + \ldots \\
&+ \left. 3\int_{(n-1)\Delta t}^{n\Delta t} J^G(t-t')\frac{\partial\lambda(t')}{\partial t'}\,dt' + \int_{(n-1)\Delta t}^{n\Delta t} J^K(t-t')\frac{\partial\lambda(t')}{\partial t'}\,dt'\right]
\end{aligned}
\tag{7.7}
$$

with $i = 0$ from $0 < t < t_0$, $i = 1$ from $t_0 < t < t_1$ and $i = 2$ from $t_1 < t < t_2$. Also, n is the number of intervals used to reach time t.

If Δt is very small, as few as 2 integration points can be used to accurately integrate the equation. Figures 7.15-7.18 show the solution of this problem for each load frequency. This solution is compared to the nonlinear analysis results.

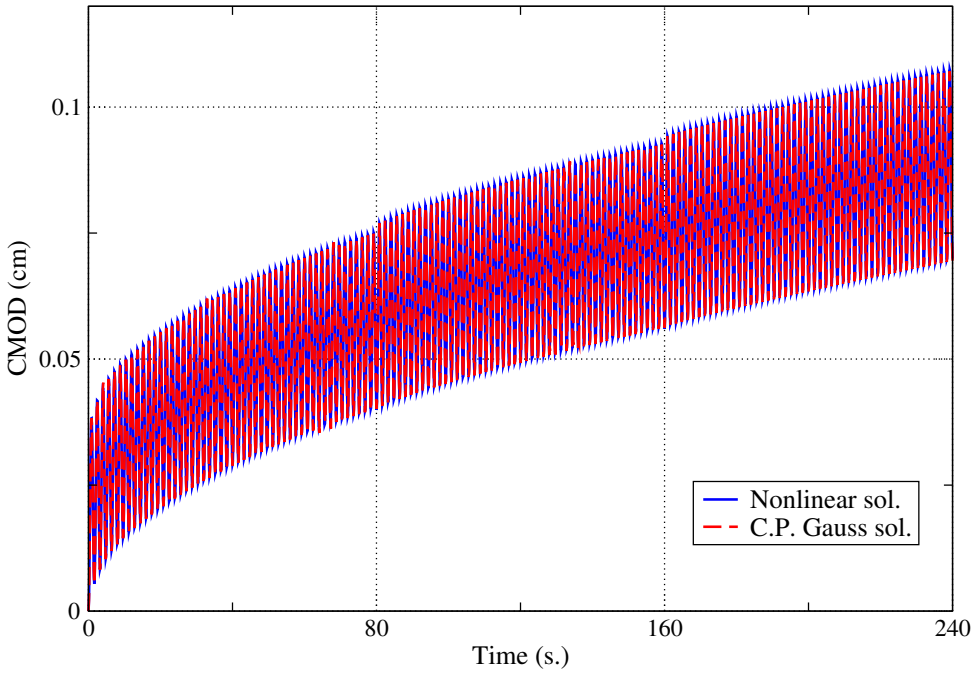

Figure 7.15: *The time-dependent CMOD. Non-linear analysis vs. Gauss integration for 50 load cycles per crack step.*

Notice that the Gauss solutions are on top of the nonlinear solution, even at the point where the crack changes in size. This is because now the complete history (change in crack size) of the problem is considered. The drawback of this method is that for every specific time t all integrals need to be re-evaluated. This is because of the nature of the convolution integral. Thus, the computational time increases as the evaluation time t increases.

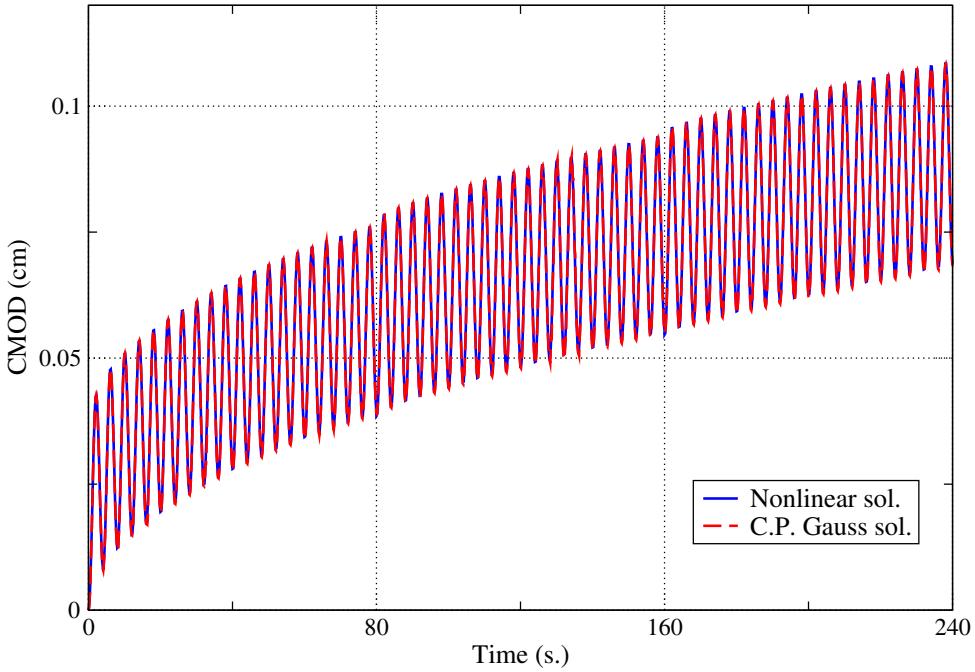

Figure 7.16: *The time-dependent CMOD. Non-linear analysis vs. Gauss integration for 20 load cycles per crack step.*

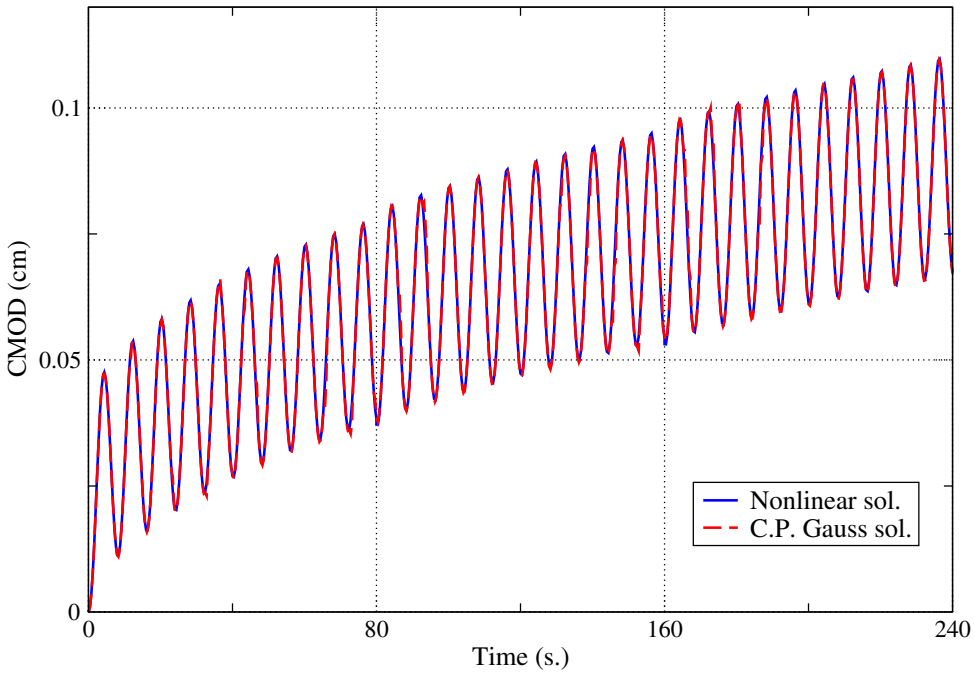

Figure 7.17: *The time-dependent CMOD. Non-linear analysis vs. Gauss integration for 10 load cycles per crack step.*

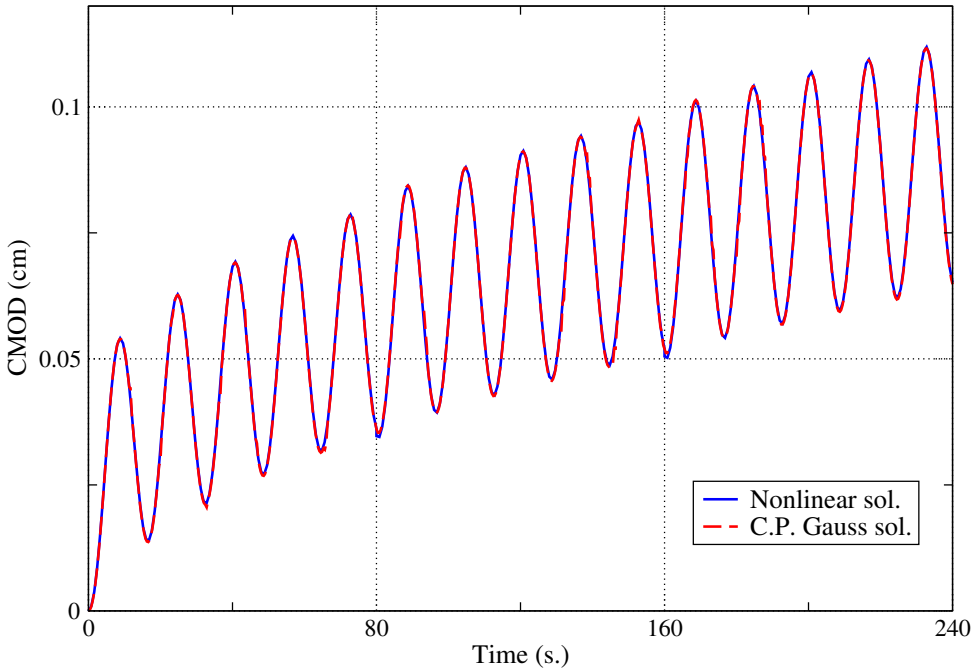

Figure 7.18: *The time-dependent CMOD. Non-linear analysis vs. Gauss integration for 5 load cycles per crack step.*

Incremental Evaluation

A more efficient alternative is to use an incremental formulation similar to the one presented in Section 2.4. Assuming material functions given in terms of Prony series and with $\alpha_m = \frac{J_m}{J_0}$, Equation (7.6) can also be written as:

$$\begin{aligned}\delta^v_{CMOD}(t) &= \frac{\delta^e_{i,CMOD}\, G_0\, K_0}{3\,K_0 + G_0}\left[3\,J^G_0\,\lambda(t) + 3\sum_{m=1}^{M}\alpha^G_m\int_0^t\left(1-e^{\frac{t'-t}{\rho_m}}\right)\frac{\partial\lambda(t')}{\partial t'}\,dt'\right.\\ &+ \left. J^K_0\,\lambda(t) + \sum_{m=1}^{M}\alpha^K_m\int_0^t\left(1-e^{\frac{t'-t}{\rho_m}}\right)\frac{\partial\lambda(t')}{\partial t'}\,dt'\right] \qquad (7.8)\end{aligned}$$

where J^G_0 and J^K_0 are the instantaneous relaxation modulus for the deviatoric and volumetric parts, respectively. J^G_m and J^K_m are the regression coefficients, ρ_m is the relaxation time and M is the number of terms in the Prony series. The integral part of Equation (7.8) is the viscous portion of

each term in the series. Name it A_m.

$$\delta^v_{CMOD}(t) = \frac{\delta^e_{i,CMOD}\, G_0\, K_0}{3\,K_0 + G_0}\left[3\,J_0^G\,\lambda(t) + 3\sum_{m=1}^{M}\alpha_m^G\,A_m^G(t) + J_0^K\,\lambda(t) + \sum_{m=1}^{M}\alpha_m^K\,A_m^K(t)\right] \tag{7.9}$$

and separating A_m in two parts we get

$$A_m(t^{k+1}) = \int_0^{t^k}\left(1 - e^{\frac{t'-t^{k+1}}{\rho_m}}\right)\frac{\partial\lambda(t')}{\partial t'}\,dt' + \int_{t^k}^{t^{k+1}}\left(1 - e^{\frac{t'-t^{k+1}}{\rho_m}}\right)\frac{\partial\lambda(t')}{\partial t'}\,dt'$$

Observe that $1 - e^{\frac{t'-t^{k+1}}{\rho_m}} = 1 - e^{\frac{-\Delta t}{\rho_m}} + e^{\frac{-\Delta t}{\rho_m}}\,(1 - e^{\frac{t'-t^k}{\rho_m}})$, and also this equation can be integrated over a finite increment of time. Therefore, assume that during a small increment Δt, from t^k until t^{k+1}, λ varies linearly with t.

$$\begin{aligned} A_m(t^{k+1}) = \left(1 - e^{\frac{-\Delta t}{\rho_m}}\right)\int_0^{t^k}\frac{\partial\lambda(t')}{\partial t'}\,dt' + e^{\frac{-\Delta t}{\rho_m}}\int_0^{t^k}\left(1 - e^{\frac{t'-t^k}{\rho_m}}\right)\frac{\partial\lambda(t')}{\partial t'}\,dt' \\ + \frac{\Delta\lambda(t^{k+1})}{\Delta t}\int_{t^k}^{t^{k+1}}\left(1 - e^{\frac{t'-t^{k+1}}{\rho_m}}\right)dt' \end{aligned}$$

The first and last integrals in this expression can be evaluated directly. The second expression corresponds to the viscous portion of A_m for time t^k. Rewriting previous equation we obtain

$$\begin{aligned} A_m(t^k) + \Delta A_m(t^{k+1}) = \left(1 - e^{\frac{-\Delta t}{\rho_m}}\right)\lambda(t^k) + e^{\frac{-\Delta t}{\rho_m}}\,A_m(t^k) \\ + \left(\Delta t - \rho_m\,(1 - e^{\frac{-\Delta t}{\rho_m}})\right)\frac{\Delta\lambda(t')(t^{k+1})}{\Delta t} \end{aligned}$$

Then the increment in the viscous portion for the m^{th} term at time step t^{k+1}.

$$\Delta A_m(t^{k+1}) = \left(1 - e^{\frac{-\Delta t}{\rho_m}}\right)\left(\lambda(t^k) - A_m(t^k)\right) + \left(\Delta t - \rho_m\,(1 - e^{\frac{-\Delta t}{\rho_m}})\right)\frac{\Delta\lambda(t^{k+1})}{\Delta t} \tag{7.10}$$

The first term corresponds to the history since $\lambda(t^k)$ and $A_m(t^k)$ are the values computed at the previous time step. The second term, on the other hand, is the increment at current time step t^{k+1}

for current iteration i and previous iteration, with $\Delta\lambda_i(t^{k+1})$ given by

$$\Delta\lambda_i(t^{k+1}) = \lambda_i(t^{k+1}) \; - \; \lambda_{i-1}(t^{k+1}) \tag{7.11}$$

Note that this recursive Equation (7.10) requires knowledge of solution variables from a previous time step.

The CMOD for time t^{k+1} can then be computed using the increment

$$\delta^v_{CMOD}(t^{k+1}) \; = \; \delta^v_{CMOD}(t^k) + \Delta\delta^v_{CMOD}(t^{k+1}) \tag{7.12}$$

where $\delta^v_{CMOD}(t^k)$ is the viscoelastic CMOD from a previous time step and $\Delta\delta^v_{CMOD}(t^{k+1})$ is computed using an Equation similar to (7.9) and has the form:

$$\begin{aligned} \Delta\delta^v_{CMOD}(t^{k+1}) \;\; &= \;\; \frac{\delta^e_{i,CMOD}\, G_0\, K_0}{3\,K_0 + G_0} \left[3\, J^G_0 \; \Delta\lambda(t^{k+1}) \; + \; 3 \sum_{m=1}^{M} \alpha^G_m \; \Delta A^G_m(t^{k+1}) \right. \\ &+ \;\; \left. J^K_0 \; \Delta\lambda(t^{k+1}) \; + \; \sum_{m=1}^{M} \alpha^K_m \; \Delta A^K_m(t^{k+1}) \right] \end{aligned} \tag{7.13}$$

Figures 7.19-7.22 show the solution of this problem by evaluation of Equation (7.6) using this incremental formulation. The solution is compared to the nonlinear analysis results.

The solutions obtained with this method are not as accurate as the Gauss quadrature results, but it is a good alternative if computational time is a concern.

All the previous solutions were computed using a temperature of 20^o C. Other temperatures can be considered using William-Landell-Ferry (WLF) shift function as explained in Section 2.4. Reflective cracking normally appears at cold temperatures. Therefore, let us consider temperatures of $T = 10^o, 0^o$ and -10^o C and repeat the previous example for the case of 20 load cycles per crack step. Figure 7.23 shows the results of CMOD using the Non-linear analysis. Figures 7.24-7.26 show the results of correspondence principle method compared to the nonlinear analysis for all temperature cases.

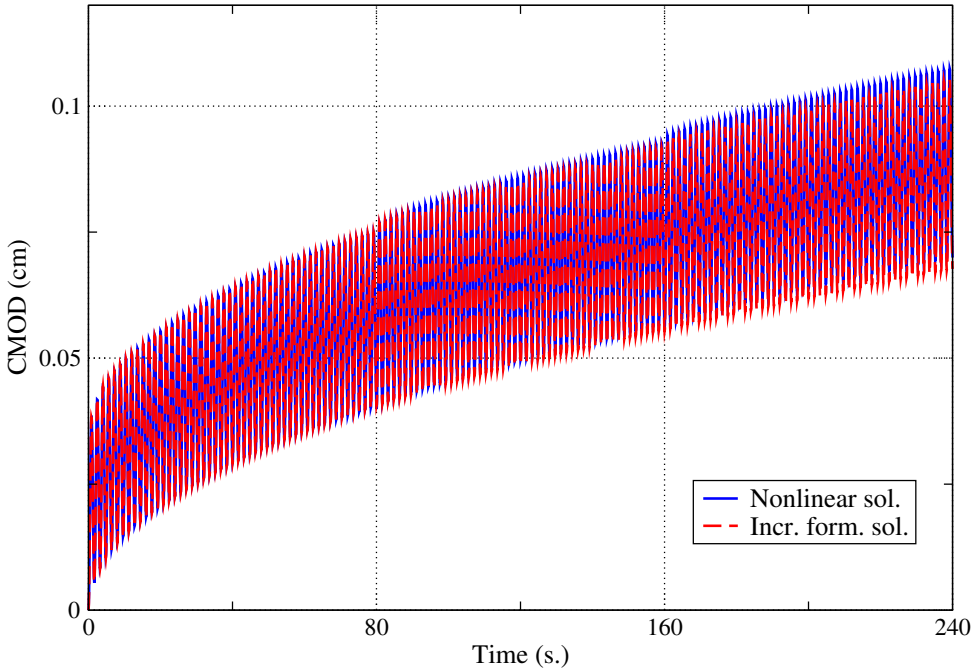

Figure 7.19: *The time-dependent CMOD. Non-linear analysis vs. incremental formulation for 50 load cycles per crack step.*

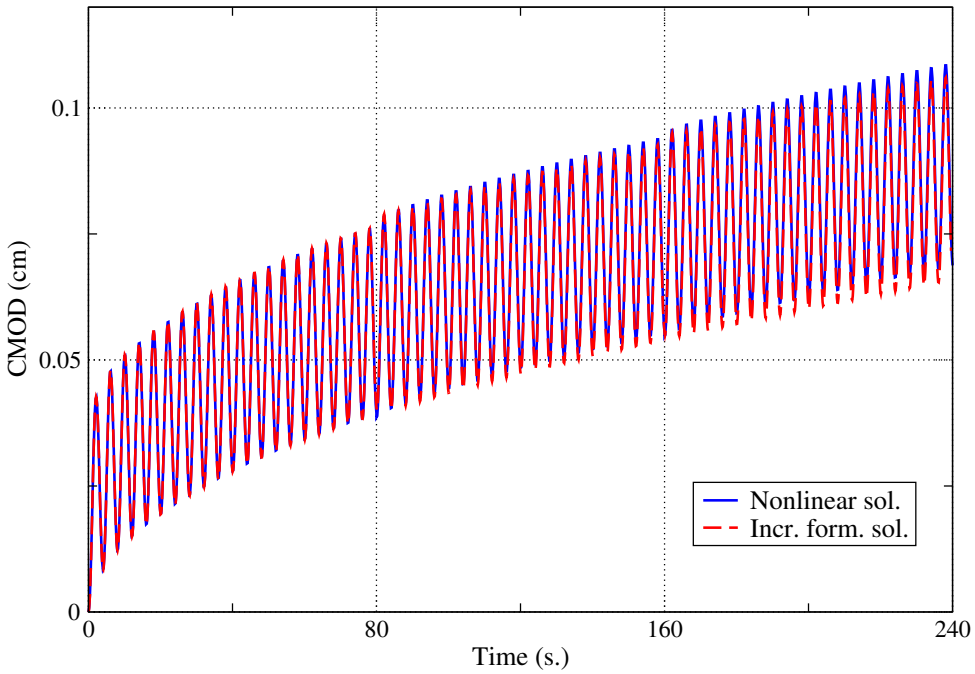

Figure 7.20: *The time-dependent CMOD. Non-linear analysis vs. incremental formulation for 20 load cycles per crack step.*

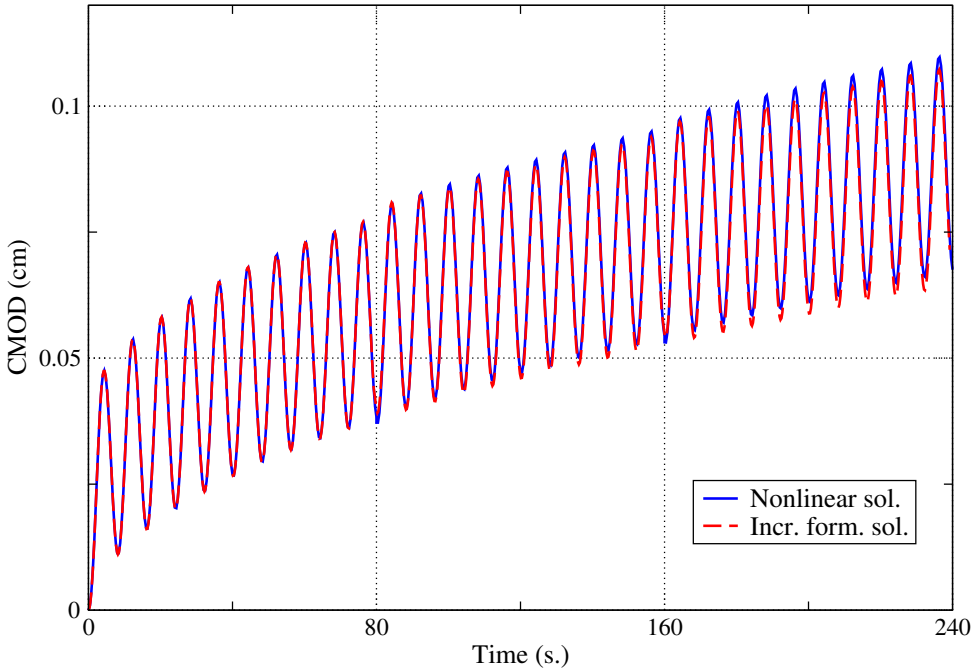

Figure 7.21: *The time-dependent CMOD. Non-linear analysis vs. incremental formulation for 10 load cycles per crack step.*

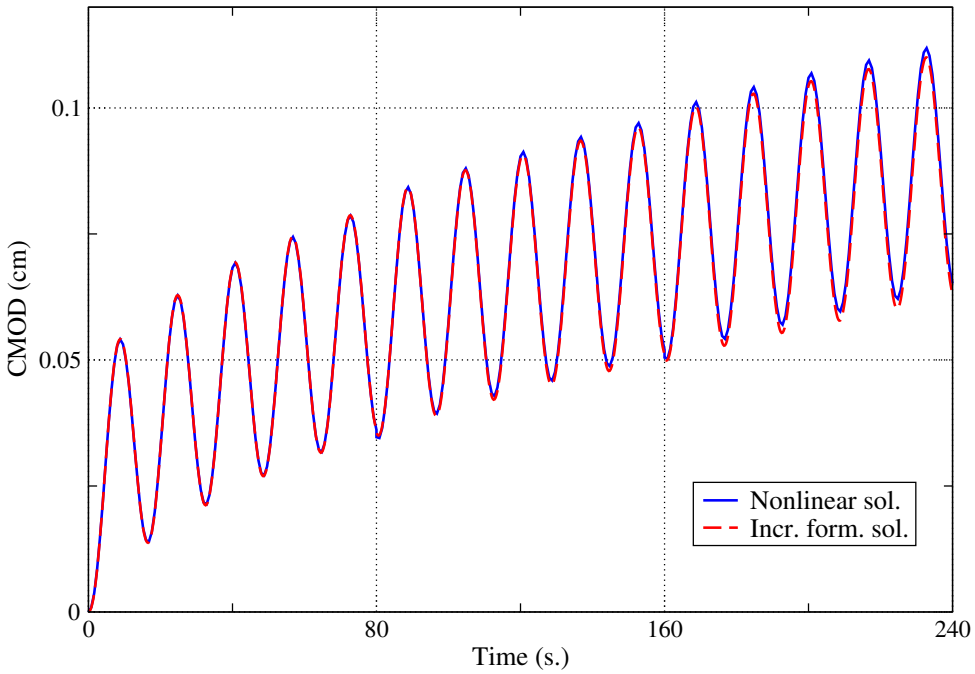

Figure 7.22: *The time-dependent CMOD. Non-linear analysis vs. incremental formulation for 5 load cycles per crack step.*

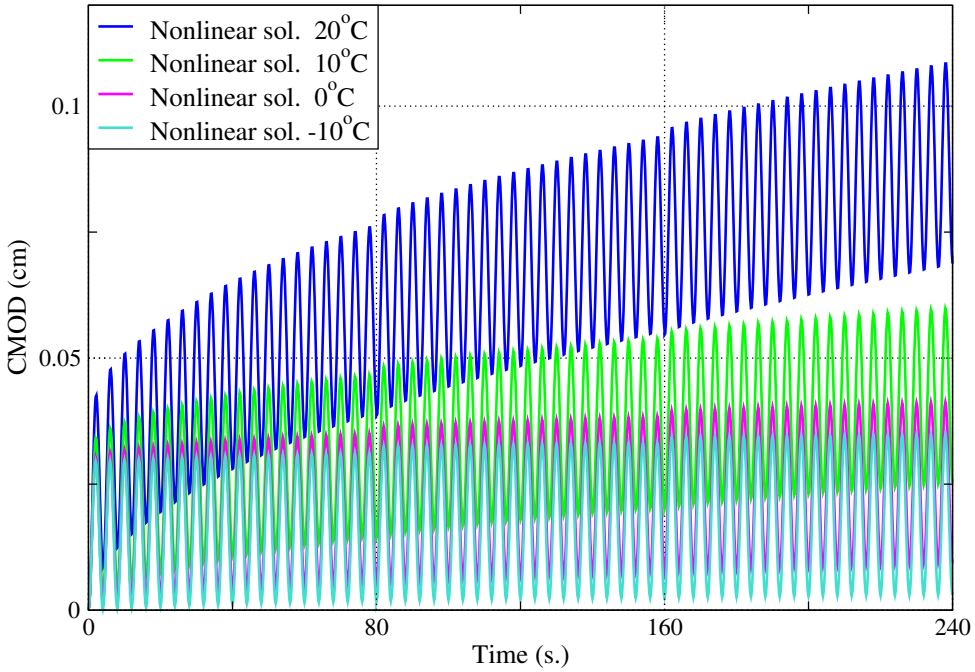

Figure 7.23: *The time-dependent CMOD. Non-linear analysis for 20 load cycles per crack step at different temperatures.*

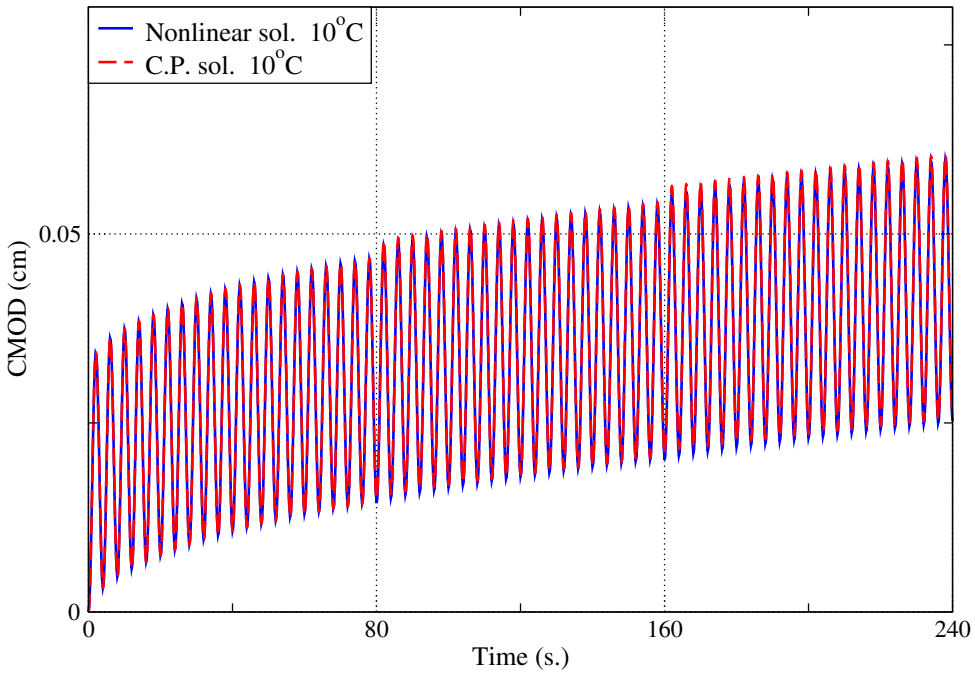

Figure 7.24: *The time-dependent CMOD. Non-linear analysis vs. correspondence principle for 20 load cycles per crack step at* $10^{o}C$.

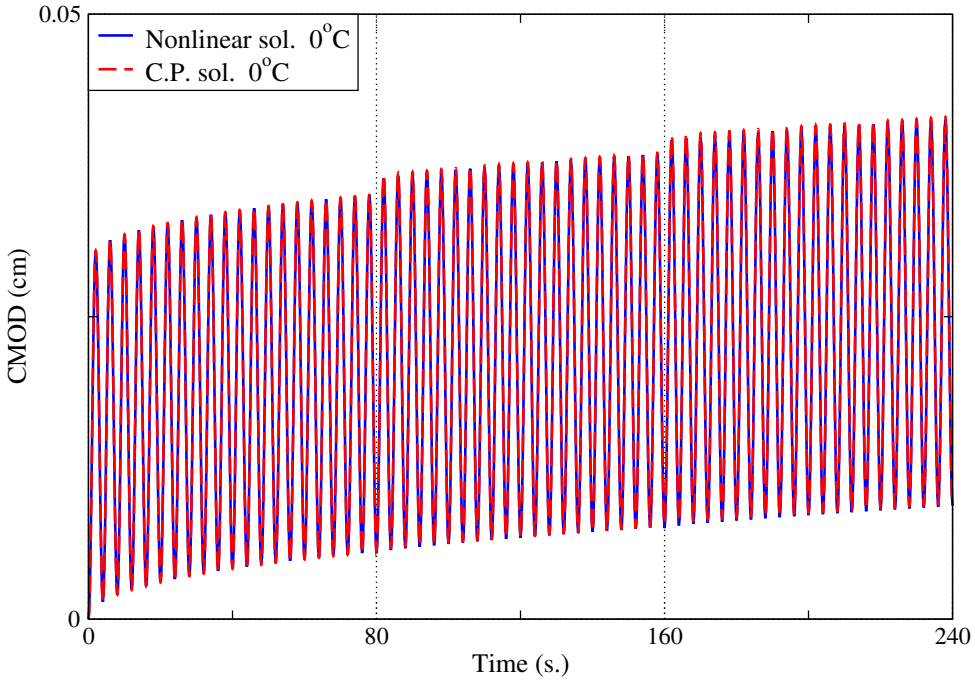

Figure 7.25: *The time-dependent CMOD. Non-linear analysis vs. correspondence principle for 20 load cycles per crack step at* 0^oC.

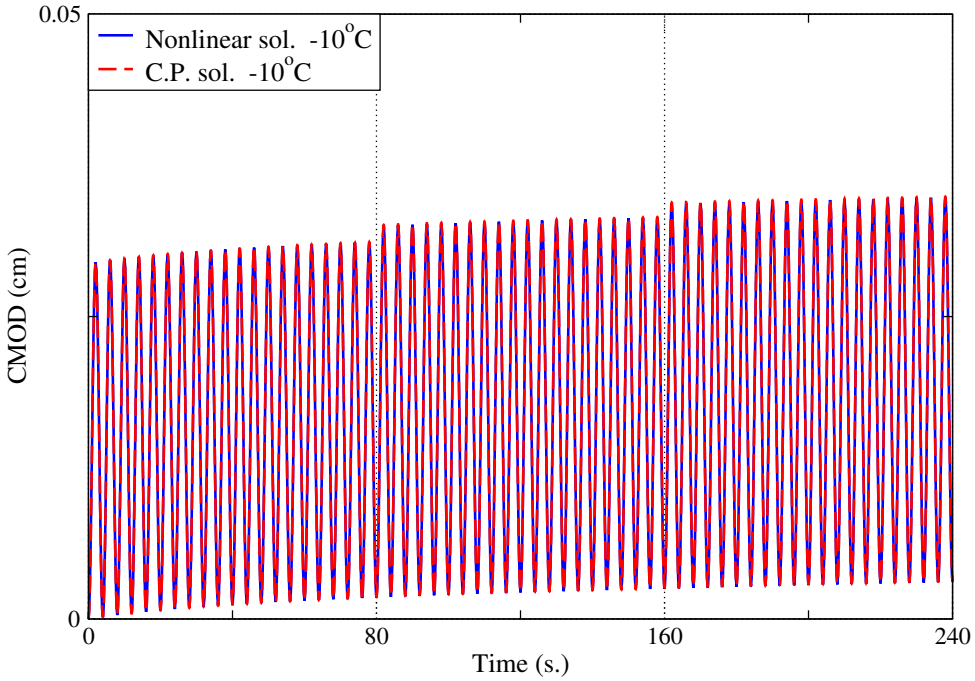

Figure 7.26: *The time-dependent CMOD. Non-linear analysis vs. correspondence principle for 20 load cycles per crack step at* -10^oC.

Figures 7.27-7.29 show the results of the incremental method compared to the Non-linear analysis.

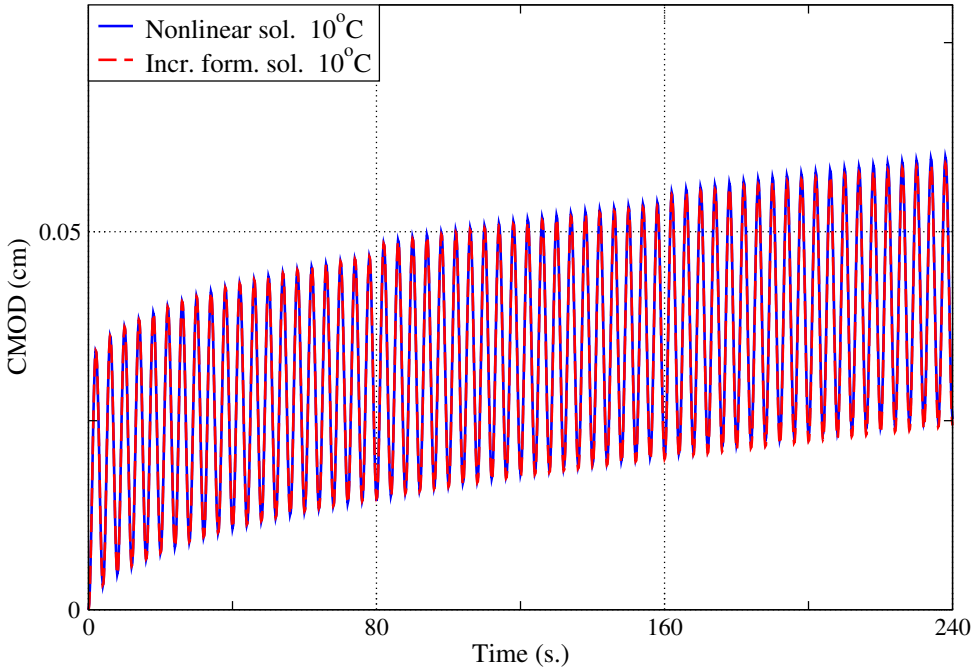

Figure 7.27: *The time-dependent CMOD. Non-linear analysis vs. incremental formulation for 20 load cycles per crack step at* $10^o C$.

Results show that the correspondence principle method for quasi-static crack propagation proposed here can be used at low temperatures. In this example, for temperatures lower than 0^o C results show no difference when compared to the nonlinear solver, even though the method does not consider the true history of the problem. Figure 7.30 shows the difference in percentage between values computed with the nonlinear solver and the correspondence principle method for the case with 20 load cycles per crack step. Figure 7.31 shows a similar comparison but with Gauss integration method. Other alternatives have been studied to evaluate the solution in the time space. They prove to be more accurate but also more expensive in terms of computational time. Therefore, it is important to identify the type of solution needed and the level of accuracy in order to choose the best method.

The interest of this work is to predict fatigue life of a cracked specimen. The criteria used, as it

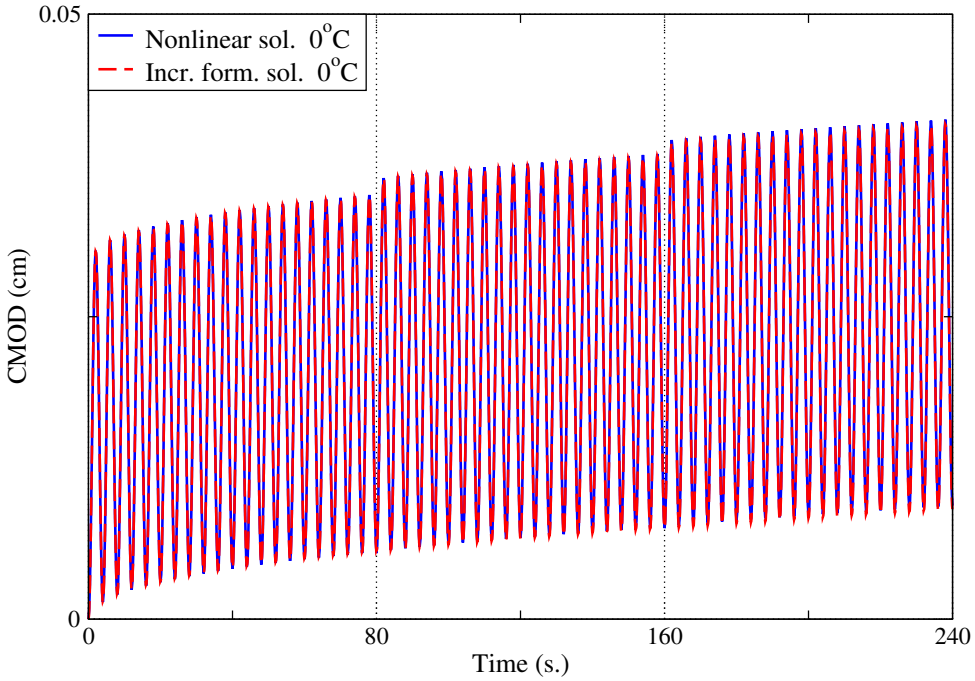

Figure 7.28: *The time-dependent CMOD. Non-linear analysis vs. incremental formulation for 20 load cycles per crack step at* 0^oC.

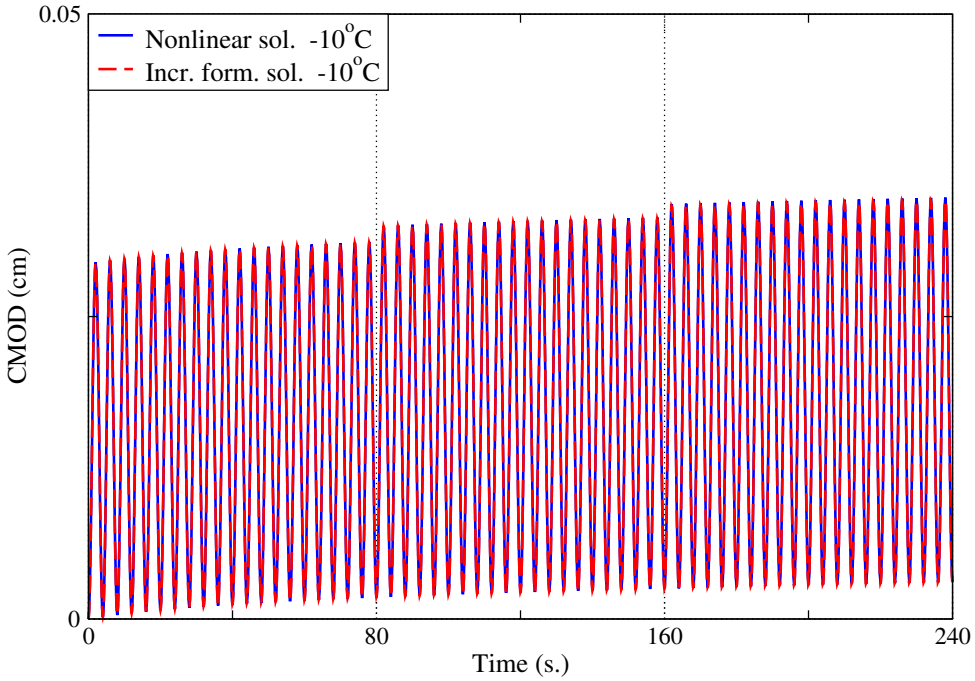

Figure 7.29: *The time-dependent CMOD. Non-linear analysis vs. incremental formulation for 20 load cycles per crack step at* -10^oC.

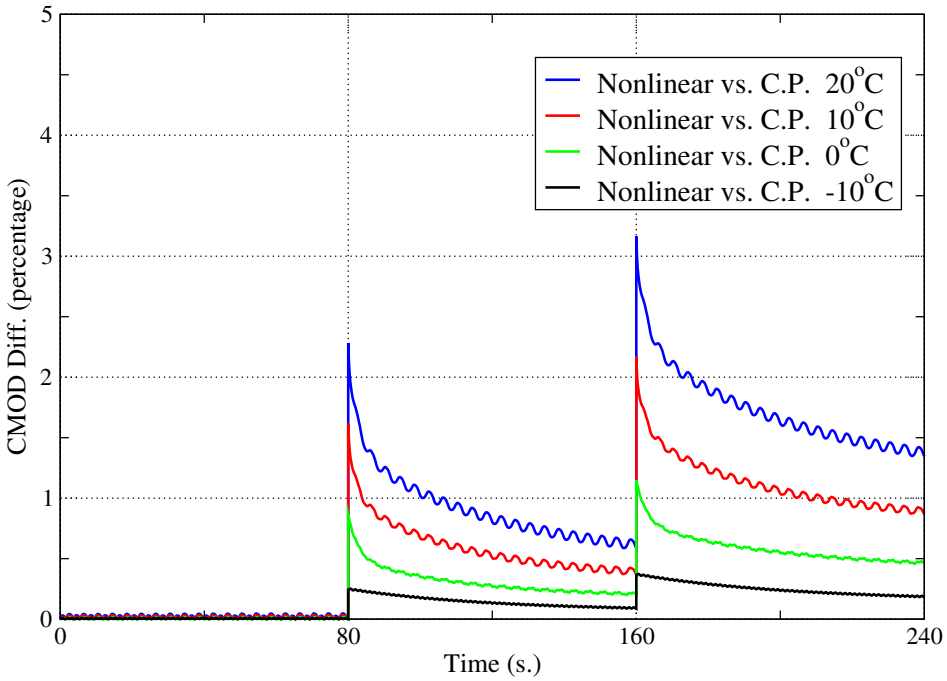

Figure 7.30: *Difference in percentage between values computed with the nonlinear solver and the correspondence principle method for all temperatures.*

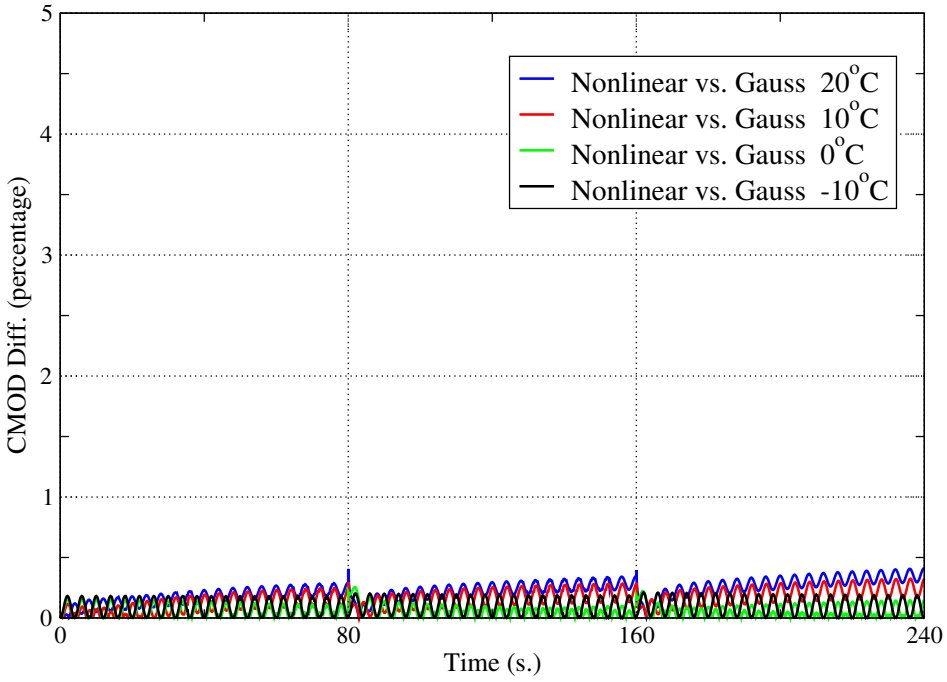

Figure 7.31: *Difference in percentage between values computed with the nonlinear solver and the Gauss integration method for all temperatures.*

will be seen in the next Section, is based on $\Delta\mathcal{G}$. Thus, the correspondence principle with GFEM and Fourier's Laplace numerical inversion is sufficient to simulate quasi-static crack propagation in linear viscoelastic materials. On the condition all assumption made are met (low temperature, small crack increments and sufficient stabilization time).

7.3 Criteria for Fatigue Life Prediction and Crack Growth Direction

A great deal of experimental evidence supports the view that under certain conditions the crack growth rate can be correlated with the cyclic variation in stress intensity factors [158]. There are several empirical fatigue crack growth equations and this work focuses on the fatigue of macro-cracks with cyclic loads of constant amplitude only. Therefore, it is convenient to make use of the Paris-Erdogan equation to predict the crack growth rate [5]

$$\frac{da}{dN} = C\,(\Delta K)^m \tag{7.14}$$

where $\frac{da}{dN}$ is the fatigue crack growth rate per loading cycle, $\Delta K = \mathcal{K}_{max} - \mathcal{K}_{min}$ is the stress intensity factor range during one cycle, and C and m are parameters that depend on the material, environment, frequency, temperature, stress ratio, etc.

Since this work focuses on viscoelasticity and the crack front parameter chosen to characterize the fracture behavior is the energy release rate, some modifications are needed. Kuai et al. [93] developed a model of fatigue crack propagation in asphalt concrete under a repeated Mode I loading condition on the basis of a generalized J-integral approach. He conducted a series of laboratory fatigue crack propagation tests for three types of asphalt concrete under varying loading magnitude, frequency, and temperature conditions. The model was verified by comparing the predicted fatigue lives with experimental data. Other researchers [37, 95] also used a J-integral method instead of the stress intensity factors in crack propagation problems with large scale yielding.

The growth law has the form:

$$\frac{da}{dN} = A\,(\Delta J)^n \tag{7.15}$$

where $\Delta J = J_{max} - J_{min}$ is the change in J for cyclic loading and A and n are material, environment, frequency, temperature, and stress ratio parameters to be determined. In this study this modified law is used with $\Delta\mathcal{G}$ instead of ΔJ. Both represent a change in energy release rate and are equal

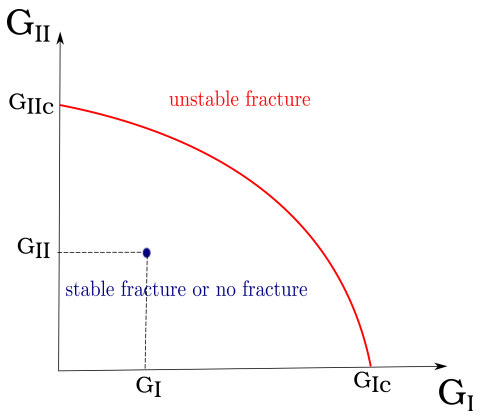

Figure 7.32: *Fracture limit curve.*

in Mode I conditions, but they are computed differently. As mentioned before, for viscoelastic materials, the energy release rate $\mathcal{G}$ is a more suitable quantity to characterize conditions at the crack tip compared to stress intensity factors $\mathcal{K}$.

Equation (7.15) take into account Mode I only, and it is is assume that $\mathcal{J}_{max} < \mathcal{J}_{Ic}$ is well below the fracture toughness so that unstable crack growth does not occur. This crack growth law can not be used in mixed mode behavior, because it would underestimate the risk of fracture. Modes I, II and III contribute to the fracture energy and thus, they all influence the beginning of unstable crack growth. Instead, $\Delta\mathcal{J}$ can be replaced by an equivalent comparative crack energy release rate $\Delta\mathcal{G}_{eq}$ which considers the mixed-mode effects. This is commonly done also with stress intensity factors and there are different criteria in the literature to compute $\Delta\mathcal{K}_{eq}$, which will be explained later in this section.

The beginning of unstable crack growth can be described by a fracture limit curve, see Figure 7.32 for an example with Modes I and II. The fracture toughness $\mathcal{G}_{Ic}$ is the limiting value on the $\mathcal{G}_I$ -axis, and similarly $\mathcal{G}_{IIc}$ for Mode II axis. This limit curve can be extended to a limit surface if Modes I, II, and III are considered. Unfortunately, no much information exists in the determination of $\mathcal{G}_{IIc}$ or $\mathcal{G}_{IIIc}$, experimentally. Braham et al. [18] used a four point shear test of a double notched beam to measure crack tip sliding displacement (CTSD) and crack tip opening displacement (CTOD). Both quantities are necessary because this is a mixed-mode test. He computed fracture energy of tree different asphalt mixtures at very low temperatures (below 0^oC.) by

taking the area under the load displacement (CSTD or CTOD) and dividing it by the fracture face area. It was expected that the mixed-modality ratio (Mode *II*/Mode *I*) be large in this test but it was not the case. The largest ratio obtained was of 2.3. The peak load on this test was found to be 6 times larger than a peak load for a pure Mode *I* test. The reasons Braham et al. suggested are that the shear strength of asphalt concrete greatly exceeds the tensile strength; and that Mode *II* shearing failure involves the simultaneous mobilization of a larger failure area (fracture process zone) than Mode *I*. As a result, the shear failure involves more work and a much higher peak load before significant inelastic behavior occurs as compared to Mode *I*. Finally, he concluded that pure Mode *II* fracture properties are extremely difficult to capture and that his research testing work be viewed as preliminary. Many researchers have reported similar conclusions and that pure Mode *II* testing is difficult to perform in a laboratory setting. As a consequence, researchers only use values for $\mathcal{G}_{Ic}$ as a limit for all three modes. Figure 7.33 shows a fracture limit surface for all three modes and $\mathcal{G}_{Ic}$ as the fracture toughness. This figure was created using Schöllmann's criterion for $\mathcal{G}_{eq}$ (ref. Section 7.3.3), other criteria give very similar fracture limit surfaces.

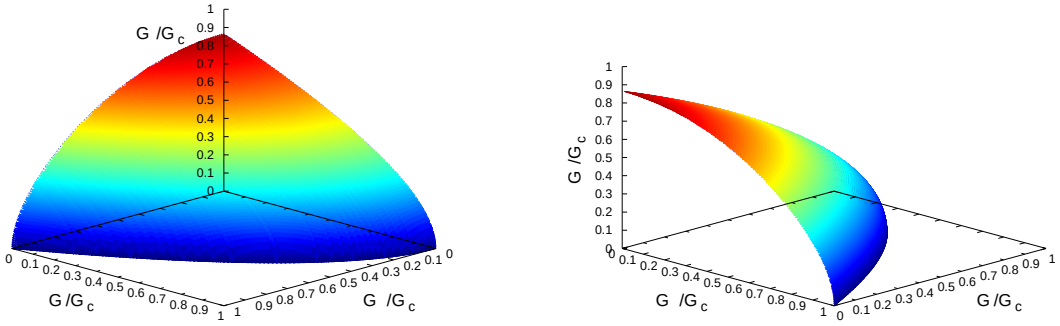

(a) (b)

Figure 7.33: *Fracture limit surface for mixed-mode.*

Crack propagation trajectories depend on many factors including: loading conditions, geometry, material behavior, pre-existing micro flaws, etc. In a purely macro-scale analysis, crack growth direction may be characterized by crack front parameters such as stress intensity factors or the components of energy release rate. A literature review of mixed mode fatigue crack growth can

be found in [134]. In the general case crack growth trajectory may be defined by a kinking angle (θ) and twisting angle (ψ) at the crack tip as illustrated in Figure 7.34. Note that this is merely a schematic plot and the crack surfaces used in subsequent analyses are always continuous. There are different manners in which these angles may be computed, depending on selection of criteria.

In the following subsections an overview of some fracture criteria is presented. These criteria serve as an instrument to determine the beginning of unstable crack growth as well as the crack growth direction.

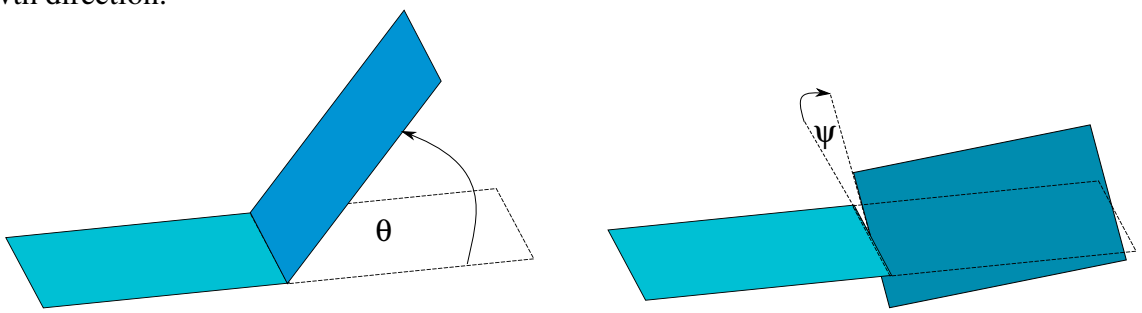

(a) Kinking angle (b) Twisting angle

Figure 7.34: *Crack growth direction angles.*

7.3.1 Nuismer and Hussain Criteria

The criteria of maximum energy release rate by Nuismer [116] and Hussain [72] are based on the assumption of a short kinked crack. At the tip of the kinked crack the stress intensity factors $\hat{K}_I$, $\hat{\mathcal{K}}_{II}$ and $\hat{\mathcal{K}}_{III}$ are given by:

Nuismer

$$\begin{aligned}
\hat{\mathcal{K}}_I &= \frac{1}{2}\cos\frac{\theta}{2}\left[\mathcal{K}_I\,(1+\cos\theta) - 3\,\mathcal{K}_{II}\sin\theta\right] \\
\hat{\mathcal{K}}_{II} &= \frac{1}{2}\cos\frac{\theta}{2}\left[\mathcal{K}_I\,\sin\theta + \mathcal{K}_{II}\,(3\cos\theta - 1)\right] \\
\hat{\mathcal{K}}_{III} &= \mathcal{K}_{III}\cos\frac{\theta}{2}
\end{aligned} \tag{7.16}$$

Hussain

$$\begin{aligned}
\hat{\mathcal{K}}_I &= \left(\frac{\pi-\theta}{\pi+\theta}\right)^{\frac{\theta}{2\pi}} \frac{4}{3+cos^2\theta}\left(\mathcal{K}_I\, cos\,\theta+\frac{3}{2}\mathcal{K}_{II}\, sin\,\theta\right)\\
\hat{\mathcal{K}}_{II} &= \left(\frac{\pi-\theta}{\pi+\theta}\right)^{\frac{\theta}{2\pi}} \frac{4}{3+cos^2\theta}\left(-\frac{1}{2}\mathcal{K}_I\, sin\,\theta+\mathcal{K}_{II}\, cos\,\theta\right)\\
\hat{\mathcal{K}}_{III} &= \left(\frac{\pi-\theta}{\pi+\theta}\right)^{\frac{\theta}{2\pi}} \mathcal{K}_{III}
\end{aligned} \tag{7.17}$$

The relationship between Energy Release Rate and stress intensity factors assuming plane strain condition is:

$$\mathcal{G}_{eq}(\theta) = \frac{1-\nu^2}{E}\left(\hat{\mathcal{K}}_I^2+\hat{\mathcal{K}}_{II}^2\right)+\frac{1+\nu}{E}\hat{\mathcal{K}}_{III}^2 \tag{7.18}$$

According to both, Nuismer and Hussain criteria, the crack propagates into the direction of the maximum energy release rate and unstable crack growth occurs if $\mathcal{G}_{eq}=\mathcal{G}_{Ic}$. The following equation is found by replacing Equation (7.16) into Equation (7.18).

$$\begin{aligned}
\mathcal{G}_{eq}(\theta) = \frac{1}{2}\left(cos\frac{\theta}{2}\right)^2\left[\frac{1-\nu^2}{E}\mathcal{K}_I^2\,(cos\,\theta+1)-4\,\frac{1-\nu^2}{E}\mathcal{K}_I\,\mathcal{K}_{II}\,sin\,\theta\right]+\\
+\frac{1}{2}\left(cos\frac{\theta}{2}\right)^2\left[\frac{1-\nu^2}{E}\mathcal{K}_{II}^2\,(5-3cos\,\theta)+\frac{2\,(1+\nu)}{E}\mathcal{K}_{III}^2\right]
\end{aligned} \tag{7.19}$$

Finding the maximum of the previous equations gives the direction for crack propagation, kinking angle. Equation (7.19) can also be expressed in terms of components of energy release rate.

$$\mathcal{G}_{eq}(\theta) = \frac{1}{2}\left(cos\frac{\theta}{2}\right)^2\left[\mathcal{G}_I\,(cos\,\theta+1)-4\sqrt{\mathcal{G}_I\,\mathcal{G}_{II}}\,sin\,\theta+\mathcal{G}_{II}\,(5-3cos\,\theta)+2\,\mathcal{G}_{III}\right]$$

Every possible combination of Modes *I*, *II*, and *III* loadings result in different deflection angles. These variations of deflection angles can be visualized in a barycentric coordinate system, as pre-

sented in [138, 139, 151]. Figure 7.35 shows the barycentric coordinate system. Consider $\mathcal{G}_I$, $\mathcal{G}_{II}$ and $\mathcal{G}_{III}$ as normalized components of energy release rate. Any combination of these values can be represented by a point in the triangle. The vertices of the triangle are pure Modes I, II and III. Figure 7.36(a) shows the variation of the deflection angle θ with respect to the components

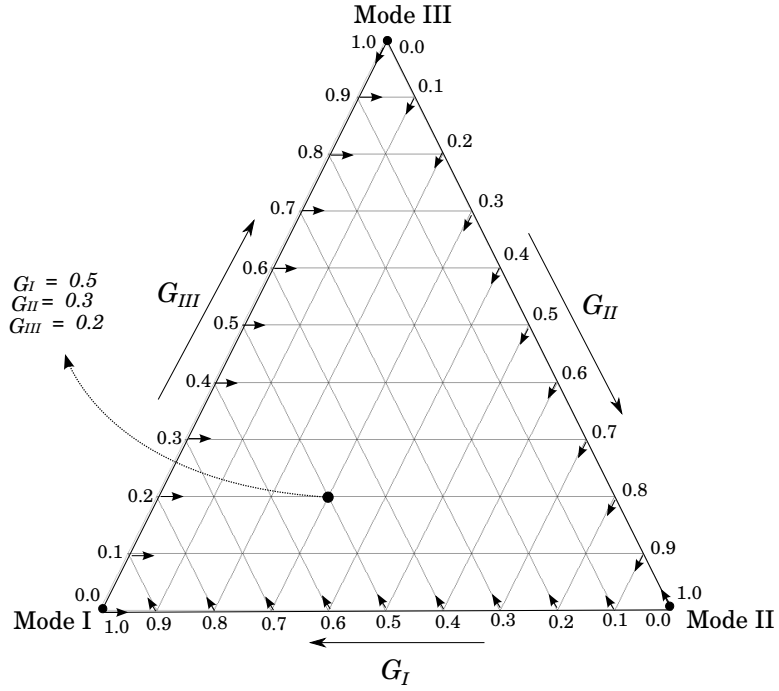

Figure 7.35: *Barycentric coordinate system for visualization of crack deflection angles.*

of energy release rate for Nuismer's criterion. Similar operations can be carried out for Hussain's equations, and a deflection angle surface can be computed as shown in Figure 7.36(b). Nuismer's and Hussain's criteria give similar results. When $\mathcal{G}_I = 0.0$, $\mathcal{G}_{II} = 1.0$ and $\mathcal{G}_{III} = 0.0$, the kinking angle has its maximum value of $\theta = 70.5^o$. An anamalous behavior is observed when Mode II and Mode III are combined. At pure Mode III the deflection angle is zero and it remains at that value while combining with low values of Mode II. Suddenly when Mode II increases, the deflection angle has a jump. This does not seem to be a good representation of the true physical behavior. In these criteria no twisting angle is computed.

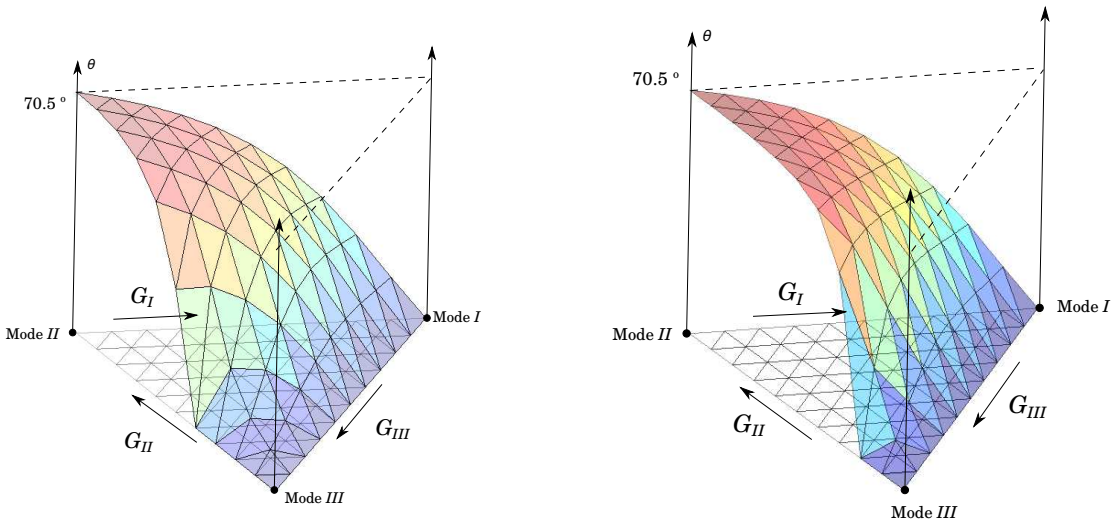

(a) Nuismer's criterion (b) Hussain's criterion

Figure 7.36: *Deflection angle* θ.

7.3.2 Zencrack Criterion

The criterion presented here is used in the commercial code Zencrack [184]. This tool is a 3-D fracture mechanics software that interfaces with other finite element codes. It allows calculation of fracture parameters such as energy release rate and stress intensity factors. The energy release rate is calculated using the J-integral method and the relationship with the stress intensity factors assuming plane strain is given by,

$$\begin{aligned} J_1 &= \frac{1-\nu^2}{E}\left(\mathcal{K}_I^2 + \mathcal{K}_{II}^2\right) + \frac{1+\nu}{E}\mathcal{K}_{III}^2 \\ J_2 &= \frac{-2\left(1-\nu^2\right)}{E}\left(\mathcal{K}_I * \mathcal{K}_{II}\right) \end{aligned}$$

This criterion also assumes that the crack propagates in the direction of maximum energy release rate and the equations used are [99]:

$$\begin{aligned} \mathcal{G}_{eq} &= \sqrt{J_1^2 + J_2^2} \\ \theta &= arctan\left(\frac{J_2}{J_1}\right) \end{aligned}$$

Figure 7.37 shows the variation of the deflection angle θ with respect to the stress intensity factor for this criterion.

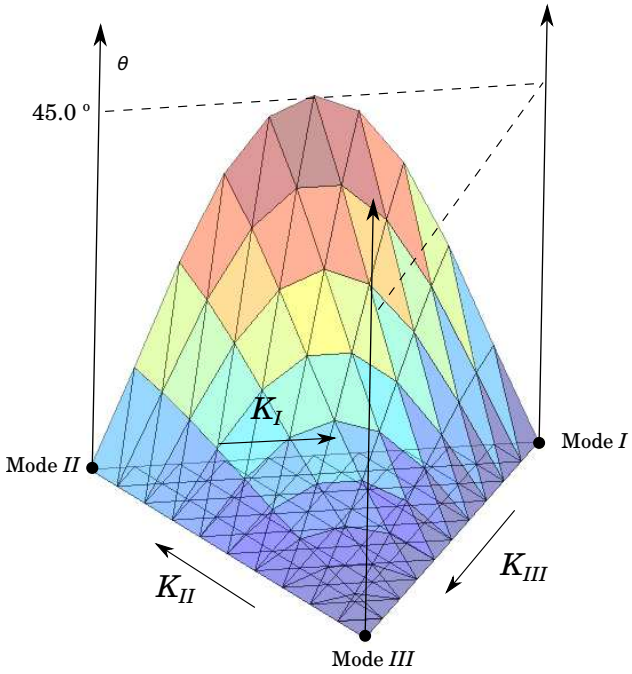

Figure 7.37: *Deflection angle Zencrack criterion.*

Note that in this cirterion, if $\mathcal{K}_I = 0$, then any combination of Modes *II* and *III* gives $\theta = 0$. Also, a combination of Modes *I* and *II* seems to increase the deflection angle similar to previous explained criteria, but eventually when Mode *II* becomes dominant the deflection angle drops to zero.

7.3.3 Shollmann's Criterion

Shollmann's criterion [151] for crack propagation is based on the fairly common assumption that crack growth develops perpendicularly to the direction of a maximum applied principal stress σ'_1. This is an extension of the Erdogan and Sih criterion [52] which includes Mode *III* effects. The principal stress is computed on a virtual cylindrical surface around the crack front and along a region of interest where the crack growth direction is then computed. The stress state on the cylindrical surface and the local coordinate system of the cylinder are shown in Figure 7.38. The

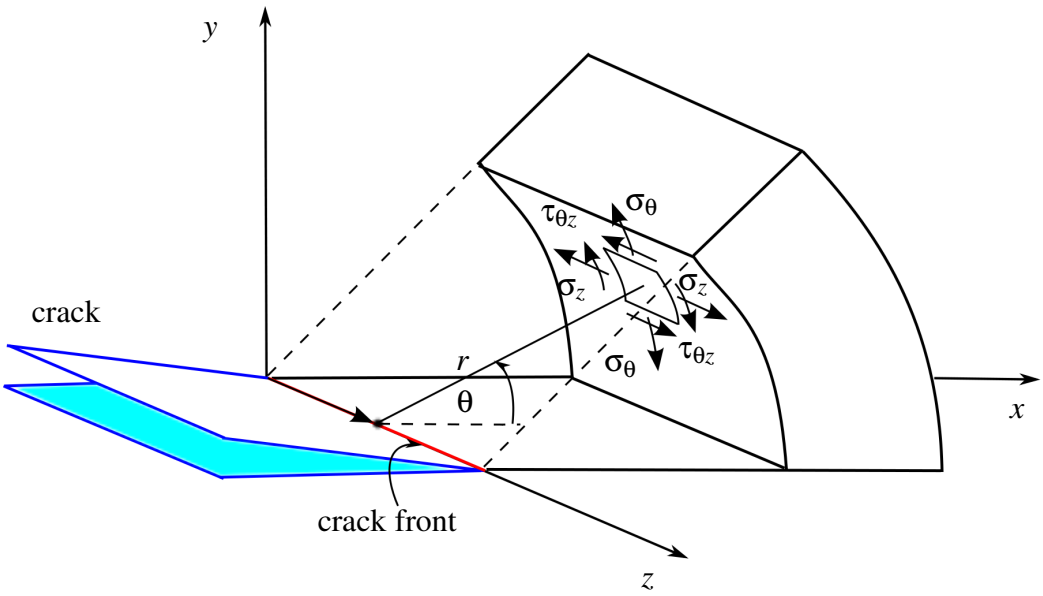

Figure 7.38: *Virtual cylindrical surface for the definition of the principal stress* σ_1'.

coordinate system is specific to the local crack configuration in which the z-axis is tangent to the crack front, the y-axis is normal and the x-axis is bi-normal to the crack plane. σ_1' is defined by the near field stresses σ_θ, σ_z and $\tau_{\theta z}$ as follows:

$$\sigma_1' = \frac{\sigma_\theta + \sigma_z}{2} + \frac{1}{2}\sqrt{(\sigma_\theta - \sigma_z)^2 + 4\tau_{\theta z}^2} \tag{7.20}$$

where σ_θ, σ_z and $\tau_{\theta z}$ are the components of the stress tensor obtained by the superposition of all three fracture modes. The stress components are described by the near-front solution in cylindrical coordinates r, θ, and z, computed as

$$\begin{aligned}
\sigma_\theta &= \frac{\mathcal{K}_I}{4\sqrt{2\pi r}}\left[3\cos\left(\frac{\theta}{2}\right) + \cos\left(\frac{3\theta}{2}\right)\right] - \frac{\mathcal{K}_{II}}{4\sqrt{2\pi r}}\left[3\sin\left(\frac{\theta}{2}\right) + 3\sin\left(\frac{3\theta}{2}\right)\right] \\
\tau_{\theta z} &= \frac{\mathcal{K}_{III}}{\sqrt{2\pi r}}\cos\left(\frac{\theta}{2}\right) \\
\sigma_z &= \frac{8\nu}{4\sqrt{2\pi r}}\left[\mathcal{K}_I\cos\left(\frac{\theta}{2}\right) - \mathcal{K}_{II}\sin\left(\frac{\theta}{2}\right)\right]
\end{aligned} \tag{7.21}$$

This criterion also makes the assumption that σ_z does not contribute to the kinking angle, and is therefore neglected. Using Equations (7.20) and (7.21), an equivalent $\mathcal{K}_{eq}$ can be computed as

follows:

$$\mathcal{K}_{eq} = \frac{1}{2} cos\left(\frac{\theta}{2}\right)\left\{\mathcal{K}_I\, cos^2\left(\frac{\theta}{2}\right) - \frac{3}{2}\,\mathcal{K}_{II}\, sin\left(\frac{\theta}{2}\right) + \sqrt{\left[\mathcal{K}_I\, cos^2\left(\frac{\theta}{2}\right) - \frac{3}{2}\,\mathcal{K}_{II}\, sin\left(\frac{\theta}{2}\right)\right]^2 + 4\,\mathcal{K}_{III}^2}\right\} \tag{7.22}$$

The relation between stress intensity factors and energy release rate is,

$$\mathcal{G}_{eq} = \frac{1-\nu^2}{E}\,(\mathcal{K}_{eq})^2 \tag{7.23}$$

and the equivalent energy release rate in terms of its components is given by,

$$\begin{aligned}\mathcal{G}_{eq} = \\ &\frac{1}{2} cos^2\left(\frac{\theta}{2}\right)\left[\mathcal{G}_I\, cos^4\left(\frac{\theta}{2}\right) + \frac{9}{4}\,\mathcal{G}_{II}\, sin^2(\theta) - 3\sqrt{\mathcal{G}_I\,\mathcal{G}_{II}}\, cos^2\left(\frac{\theta}{2}\right) sin(\theta) + 2\,\mathcal{G}_{III}\,(1-\nu)\right] \\ &+ \frac{1}{4} cos^2\left(\frac{\theta}{2}\right)\left[2\sqrt{\mathcal{G}_I}\, cos^2\left(\frac{\theta}{2}\right) - 3\sqrt{\mathcal{G}_{II}}\, sin(\theta)\right] \\ &* \left[\sqrt{\mathcal{G}_I\, cos^4\left(\frac{\theta}{2}\right) + \frac{9}{4}\,\mathcal{G}_{II}\, sin^2(\theta) - 3\sqrt{\mathcal{G}_I\,\mathcal{G}_{II}}\, cos^2\left(\frac{\theta}{2}\right) sin(\theta) + 4\,\mathcal{G}_{III}\,(1-\nu)}\right]\end{aligned} \tag{7.24}$$

According to this criterion the crack growth kinking angle θ is computed as

$$\frac{\partial \sigma_1'}{\partial \theta} = 0 \quad and \quad \frac{\partial^2 \sigma_1'}{\partial \theta^2} < 0 \tag{7.25}$$

There is no closed-form solution to the above equation. Therefore the deflection angle θ needs to be determined using a root finder algorithm. Figure 7.39 shows the variation of the deflection angle θ with respect to the components of energy release rate.

Note that the deflection angle surface exhibits a smooth behavior. For combinations of Modes *I* and *III* the deflection angle is zero, while other combinations involving Mode *II* yield a non-zero value with a maximum of 70.5^o. Experimental results are in close agreement yielding a maximum value of 70^o for pure Mode *II* [177].

All fracture modes are considered with this criterion making it well-suited for computational

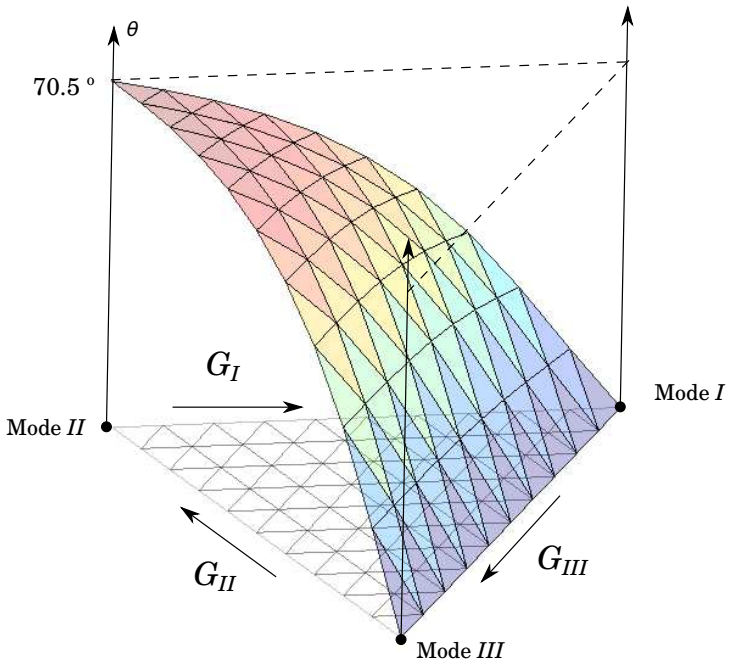

Figure 7.39: *Deflection angle* θ *(kinking) Schöllmann's criterion.*

implementations aimed at fully 3-D crack growth prediction. This criterion has been successfully implemented in FEM and GFEM research codes [130, 152].

Figure 7.40 shows a comparison of the deflection angle surfaces for the criteria presented here. It was found that the computation of the deflection angles gives the same result if using Equation (7.22) with SIFs or Equation (7.24) with ERR components. Furthermore, there is almost no influence of the value of ν in Equation (7.24) and it can be neglected.

It may be noted that Richard et al. [139] developed an approximate function to simplify the prediction of the crack growth under Schöllmanns criterion. In [139] the equivalent stress intensity factor is computed as

$$\mathcal{K}_{eq} = \frac{\mathcal{K}_I}{2} + \frac{1}{2}\sqrt{\mathcal{K}_I^2 + 4(\alpha_1 \mathcal{K}_{II})^2 + 4(\alpha_2 \mathcal{K}_{III})^2} \tag{7.26}$$

with $\alpha_1 = 1.155$ and $\alpha_2 = 1.0$. Previous equation is a good approximation of Equation (7.22).

The second defection angle under consideration (twisting ψ) is dependent upon the orientation

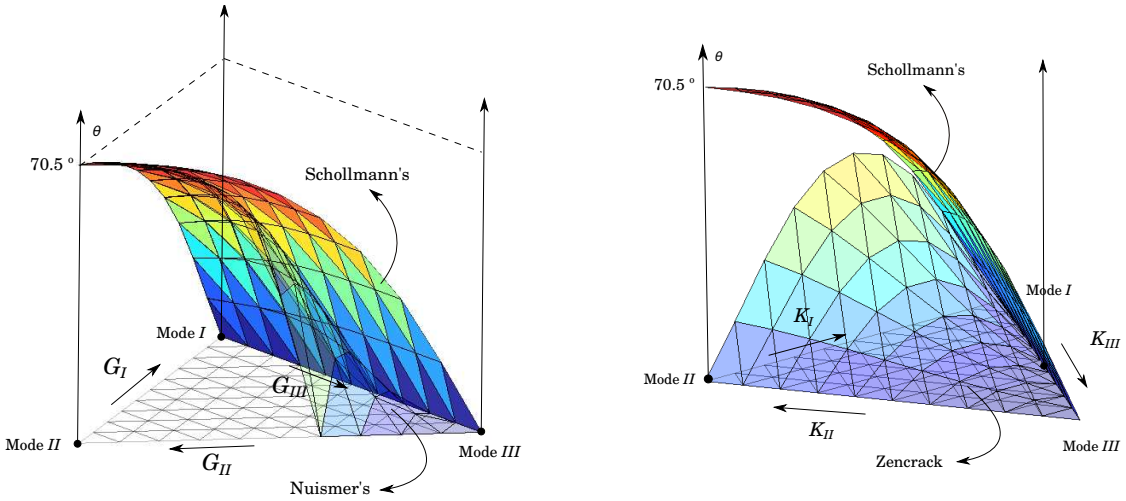

(a) Schollman's vs. Nuismer's

(b) Schollman's vs. Zencrack

Figure 7.40: *Deflection angle comparison.*

of the principal stress σ_1' and can be computed as

$$\psi = \frac{1}{2}\arctan\left[\frac{2\tau_{\theta z}(\theta)}{\sigma_\theta(\theta) - \sigma_z(\theta)}\right]. \tag{7.27}$$

Similar to the kinking angle (θ), the all possible combinations of Modes *I*, *II* and *III* on the value of ψ may be captured on a single plot. Figure 7.41 shows the computation of the twisting angle ψ in the barycentric coordinate system.

7.3.4 Crack Vertex Advancement

In this incremental algorithm for fatigue crack growth in linear elastic materials, the maximum crack front increment Δa_{max} is set at the beginning of each crack step. A characteristic variation of variation of energy release rate $\Delta\mathcal{G}_{eq}$ is computed as explained in Section 7.2. In a 3-D mixed-mode crack simulation, $\Delta\mathcal{G}_{eq}$ may vary along the crack front and therefore, the increments along the crack front must be scaled accordingly. This is a requirement to allow for (7.15) to remain valid, and thus subject each crack front vertex to the same number of loading cycles. As such, the

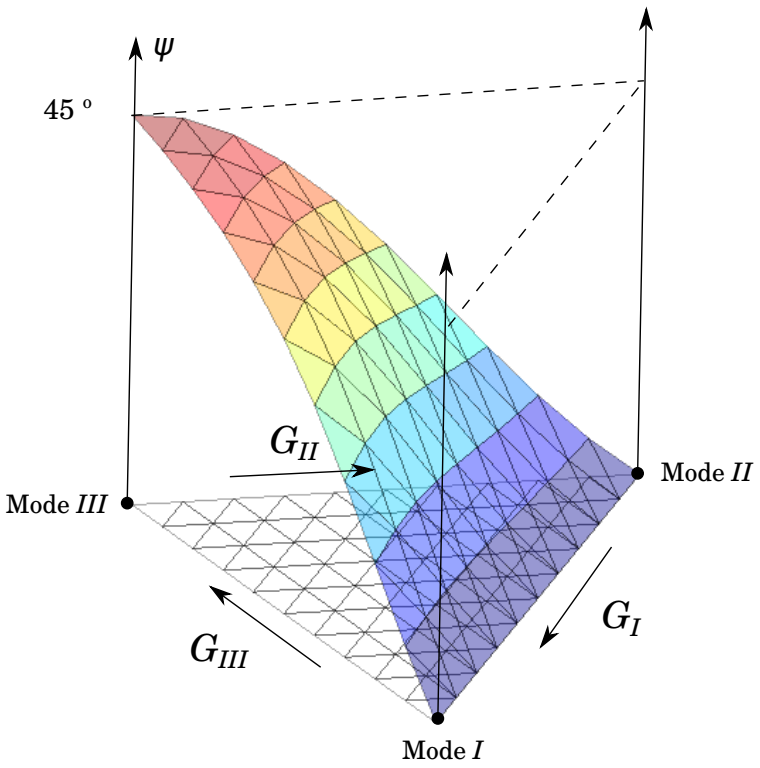

Figure 7.41: *Deflection angle* ψ *(twisting) Schöllmann's criterion.*

maximum crack increment size, Δa_{max}, is applied only to the crack front vertex that has maximum $\Delta \mathcal{G}_{eq_{max}}$, i.e., for which $\Delta \mathcal{G}_{eq} = \Delta \mathcal{G}_{eq_{max}}$. The crack growth increments for the other vertices are computed using the crack growth rate and the number of cycles of the current step. Thus, for a given crack front vertex j, we have, The crack growth increments for the other vertices are computed using the crack growth rate and the number of cycles of the current step. Thus, for a given crack front vertex j, we have,

$$\Delta a_j = A \left(\Delta \mathcal{G}_{eq_j}\right)^n \frac{\Delta a_{max}}{A \left(\Delta \mathcal{G}_{eq_{max}}\right)^n} = \Delta a_{max} \left(\frac{\Delta \mathcal{G}_{eq_j}}{\Delta \mathcal{G}_{eq_{max}}}\right)^n \tag{7.28}$$

where $\Delta \mathcal{G}_{eq_j}$ is the variation of the equivalent crack energy release rate for vertex j.

Fatigue life can be estimated in an incremental form of Equation (7.15),

$$N_i = N_{i-1} + \frac{\Delta a_{max}}{A \left(\Delta \mathcal{G}_{eq_{max}}\right)^n} \tag{7.29}$$

where N_i and N_{i-1} are the number of cycles in the current and previous steps, respectively. This is possible because crack advances are computed incrementally with a prescribed maximum increment, assumed to be relatively small with respect to the crack length and other characteristic dimensions of the analysis domain.

The time corresponding to given number of cycles and crack size can be computed by,

$$t_i = N_i * T = N_i * 2\,t_{peak} \tag{7.30}$$

with T as the period of the cyclic load function. This time must be larger than the time used to compute a stabilized solution t_s in Section 7.2.

As an example of the computation of these two different time quantities, take $\Delta\mathcal{G}$ from Figure 7.7. Consider the case for a temperature of 20^o C. and time period of 12.8 s. The stabilized solution is found after 12 cycles. The corresponding stabilized time may be computed as follows,

$$t_s = 12 * 12.8 = 153.60 \ \ seconds = 2.56 \ \ minutes.$$

Assume material properties for the modified Paris law, Equation (7.15), $A = 3.0 * 10^{-4}$ and $n = 1.6296$ from the paper [93]. These correspond to an asphalt mixture with 19 mm nominal maximum aggregate size and a PG64-22 asphalt binder used in a laboratory test. The number of cycles for a 3 percent increment in a 10 cm crack size is,

$$N_1 = \frac{30}{3.00 * 10^{-4}\,(63)^{1.6296}} \approx 117 \ \ cycles.$$

The time corresponding to this crack propagation is,

$$t_1 = 117 * 12.8 = 1498.60 \ \ seconds = 24.96 \ \ minutes.$$

Note that the time to find the stabilized solution is less than the propagation time ($t_s < t_i$). This

guaranties that the chosen $\Delta\mathcal{G}$ is a good representation for the current crack size.

Chapter 8

Reflective Cracking Simulation and Life Prediction

Based on the model and criteria for quasi-static crack propagation in fatigue presented in Chapter 7, a computational methodology for automated simulation using GFEM and $GFEM^{g\text{-}l}$ has been completed. This implementation together with all geometrical improvements for the crack surface representation including crack coalescence (see Chapter 6) allow a more realistic simulation of reflective cracking (RC) in airfield pavements.

In this Chapter, an accelerated reflective cracking test in progress at the Federal Aviation Administration (FAA) test facility is simulated. It consists of a section of overlayed pavement subject to an accelerated imposed opening and closing of the Portland cement concrete (PCC) joint. The goal is to accurately predict its fatigue life by simulating the propagation of many small cracks using all the proposed computational tools and research. Figure 8.1 shows some pictures of the reflective crack machine provided by the FAA.

Consider a model of a portion of the asphalt layer on the FAA testing machine as seen in Figure 8.2. The dimensions of this rectangular model domain are $t = 10.0$, $h = 5.0$, $b = 20$ and the crack has an assumed initial radius of $a = 1.0$. All dimensions are in inches. The material properties assumed here are from [32]. This report presents laboratory testing results for cores extracted from the asphalt layer on the RC machine at the FAA laboratory and shared by the FAA. Table 8.1 shows the mathematical representation of the viscoelastic material in the form of a Prony series. Coefficients $C_1 = 12.75$ and $C_2 = 78.00$ for a reference temperature of $T_0 = -24^o$C are used together with the William-Landell-Ferry (WLF) equation as explained in Section 2.4 to introduce temperature effects. The opening and closing of the PCC joint is modeled by imposing displacement boundary conditions $\delta\lambda(t)$ in the form of a sinusoidal function $\lambda(t) = |\sin(\frac{t\,\pi}{t_{peak}})|$.

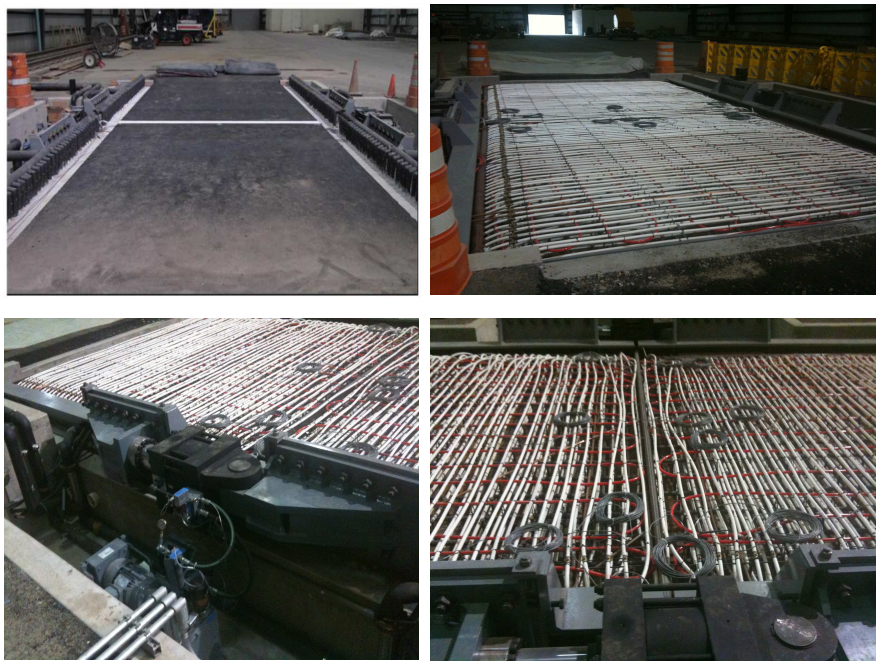

Figure 8.1: *Reflective crack machine at the FAA National Airport Pavement Test Facility, Atlantic City, New Jersey.*

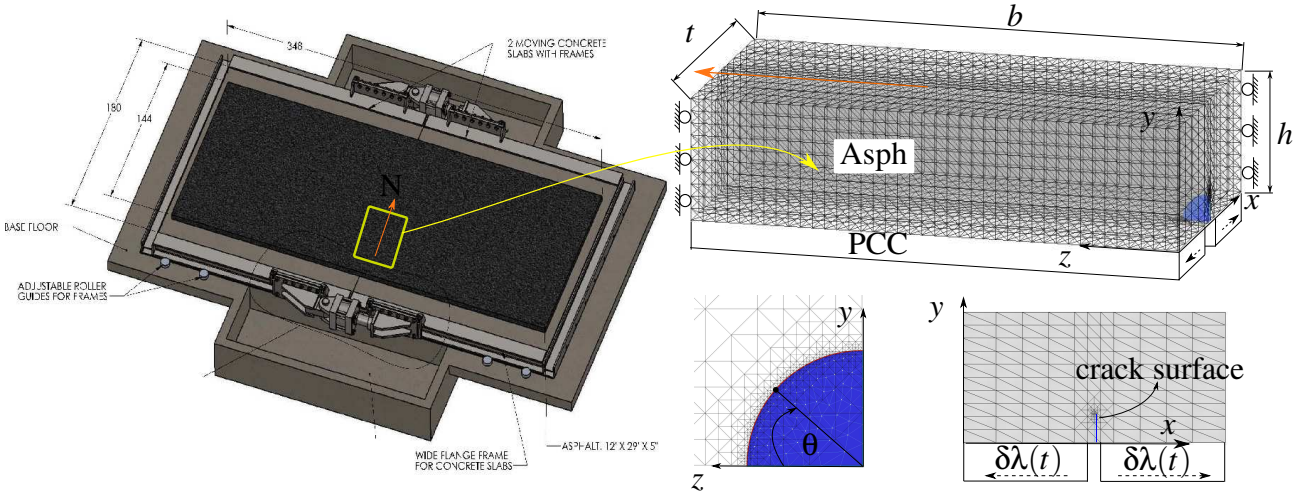

Figure 8.2: *Schematics of the reflective crack machine. Picture courtesy of the FAA.*

Table 8.1: *Mathematical representation of the viscoelastic material (Prony series).*

m	G_m (ksi)	K_m (ksi)	ρ_m (s)
1	72.463	157.00	6.298e-7
2	399.45	865.47	7.679
3	447.50	969.56	63.669
4	533.56	1156.0	1.9782e3
5	183.20	396.94	2.908e4
$G_0 = 1635.74$ and $K_0 = 3544.11$			

These are imposed at the bottom of the rectangular domain at each side of the joint. The maximum opening value is of $2\delta_{max} = 15$ mils.

8.1 Static Analysis

Consider a reference elastic model with the same mesh and crack surface as in the viscoelastic model (illustrated in Figure 8.2). The instantaneous *Go* and *Ko* are used as the linear elastic deviatoric and volumetric modulus, respectively. The imposed displacement at the bottom of the rectangular domain is $\delta = 7.5$ mils at each side of the PCC joint. GFEM shape functions of degree $p = 3$ are used for the continuous part of the problem. Furthermore, Heaviside and branch functions are used as enrichments to represent the discontinuity and singularity created by the presence of the crack (ref. Section 4.2).

The stress intensity factors extracted are shown in Figure 8.3. As seen in previous similar RC examples, this is a mode *I* dominated problem and the maximum value of $\mathcal{K}_I$ is at $\theta = 0$. This means that the crack surface would tend to propagate faster in the longitudinal direction (z-dir) of the asphalt layer than towards the surface.

Let us focus on the region of the crack where the highest value of $\mathcal{K}_I$ is found, that is at $\theta = 0$. The viscoelastic time-dependent ERR $\mathcal{G}(t)$ is obtained using Equation (3.32) and computing its inverse Laplace transform. Figure 8.4 shows the normalized viscoelastic energy release rate $\mathcal{G}$ for different frequencies at temperatures of $T = -10^o, 0^o$ and 10^o C. The maximum values of ERR

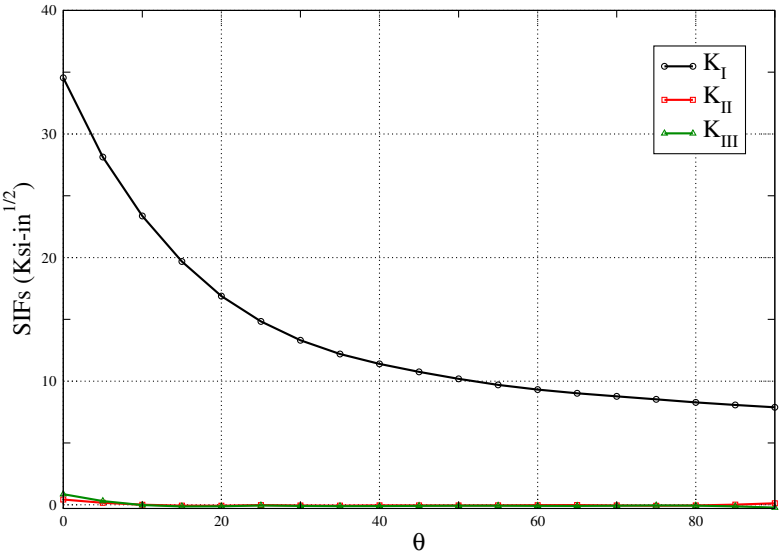

Figure 8.3: *Stress intensity factors for RC reference elastic problem along the crack front.*

when $t_{peak} = 150$s for each temperature are $\mathcal{G}_{max}^{-10^oC} = 122.00$, $\mathcal{G}_{max}^{0^oC} = 36.16$ and $\mathcal{G}_{max}^{10^oC} = 5.84$.

The variation of ERR ($\Delta\mathcal{G}$) stabilizes at different times depending on the temperature. At higher temperatures, lower stabilization times have been found for this material. Observe that after $t = 1500$ s, the values of $\Delta\mathcal{G}$ for all temperatures have stabilized. To assure a correct computation of a representative $\Delta\mathcal{G}$ at every crack growth step, the stabilization time $t_s = 3000$ s is adopted.

8.2 Crack Growth Analysis

In this section a quasi-static crack growth simulation of the previous RC model is presented. The imposed displacement boundary condition $\delta\lambda(t)$ is the sinusoidal function $\lambda(t) = |\sin(\frac{t\,\pi}{t_{peak}})|$, with $t_{peak} = 150$ s. Which is a similar rate used by the FAA in their Full-scale RC test performed in June, 2012.

At every propagation step, SIFs are computed using a reference elastic model and then a representative $\Delta\mathcal{G}$ is computed considering a stabilization time of $t_s = 3000$ s. Again, temperatures of $T = -10^o, 0^o$ and 10^o C are considered. Figure 8.5 shows the viscoelastic ERR for steps $0, 1, 2$ and 3 evaluated for a period of 3000 s at $\theta = 0$.

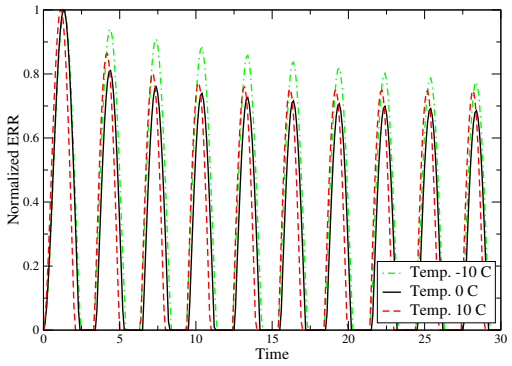

(a) $t_{peak} = 1.5$ s.

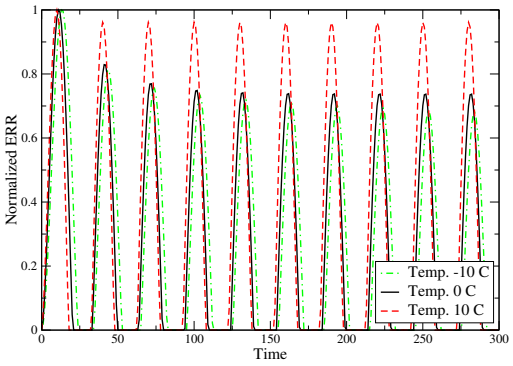

(b) $t_{peak} = 15$ s.

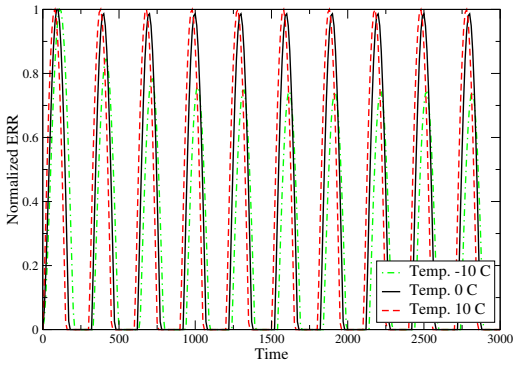

(c) $t_{peak} = 150$ s.

Figure 8.4: *Viscoelastic Energy Release Rate computed at* $\theta = 0$.

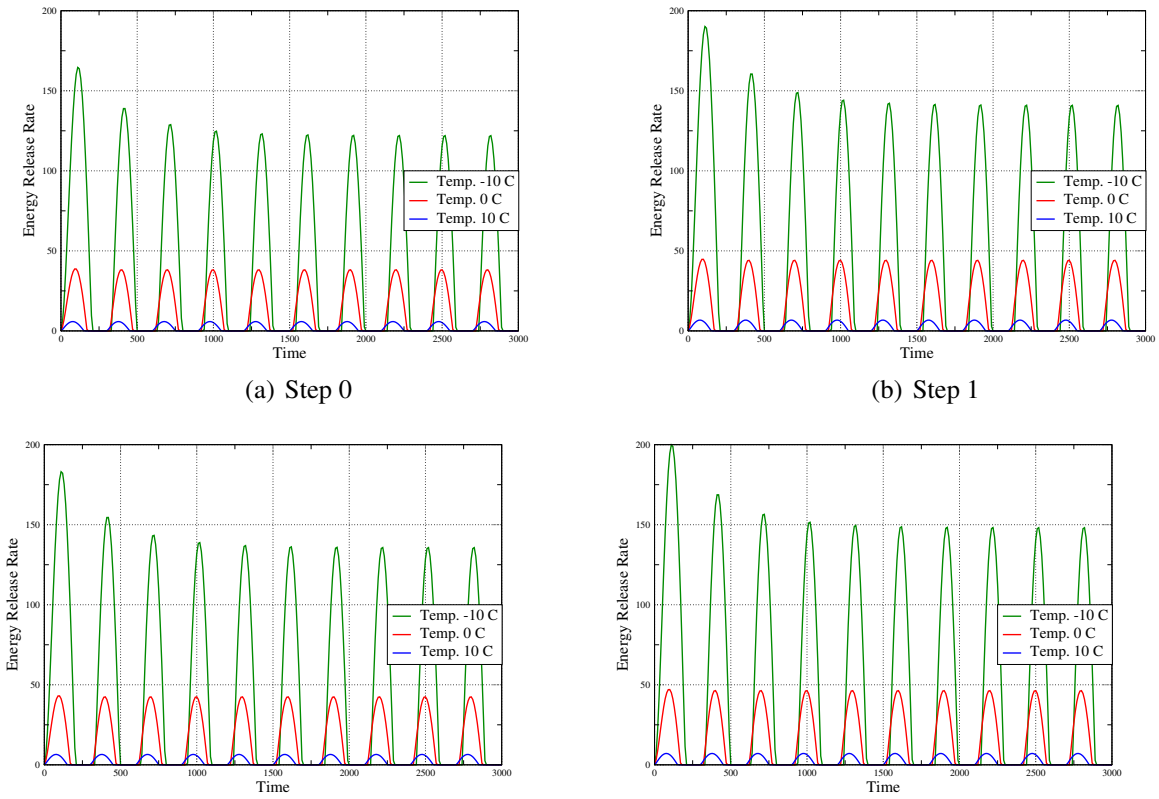

(a) Step 0 (b) Step 1

(c) Step 2 (d) Step 3

Figure 8.5: *Viscoelastic Energy Release Rate computed at* $\theta = 0$*, for different propagation steps.*

The SIFs of the reference elastic problem and the representative $\Delta\mathcal{G}$ are used to compute the direction and magnitude of propagation using the crack growth criteria presented in Section 7.3. Additionally, all techniques presented in Chapter 6 are used. Figures 8.6 and 8.7 show the evolution of the crack surface and the von Mises stress plotted on the deformed configuration, respectively, for several propagation steps. In order to observe with more clarity the evolution of the crack front, the localized refinement along the front is not shown in these figures.

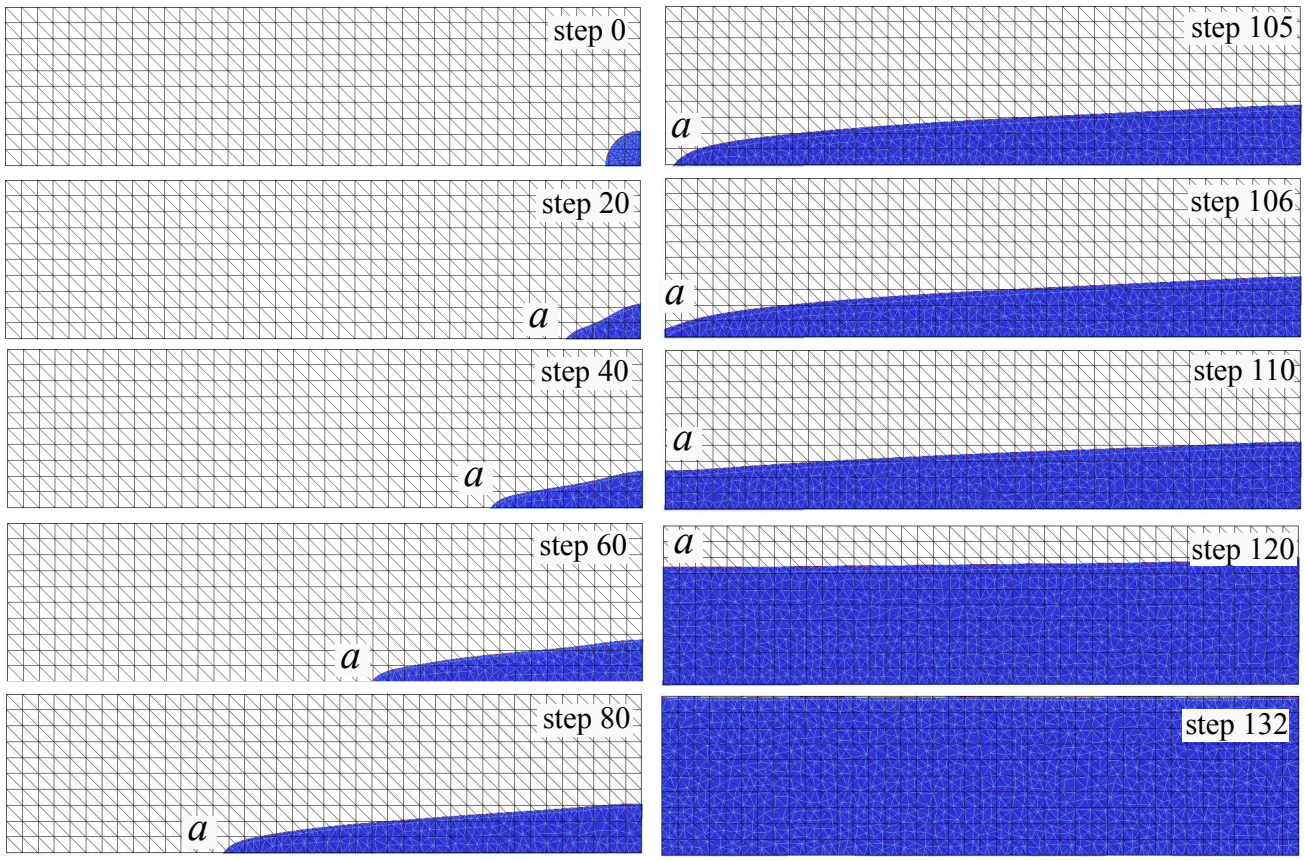

Figure 8.6: *Surface crack evolution.*

In order to make a life prediction, material properties for the modified Paris law (Equation (7.15)) A and n are needed. These can be obtained by experimentation as done by Kuai et al.[93]. The authors used specimens cut into a disk-shaped compact geometry with loading holes and a initial notch to perform a fatigue crack propagation test. The set-up of this test is similar to the disk-shaped compact tension (DC(T)) test developed by Wagner et al. [175, 176]. The main difference

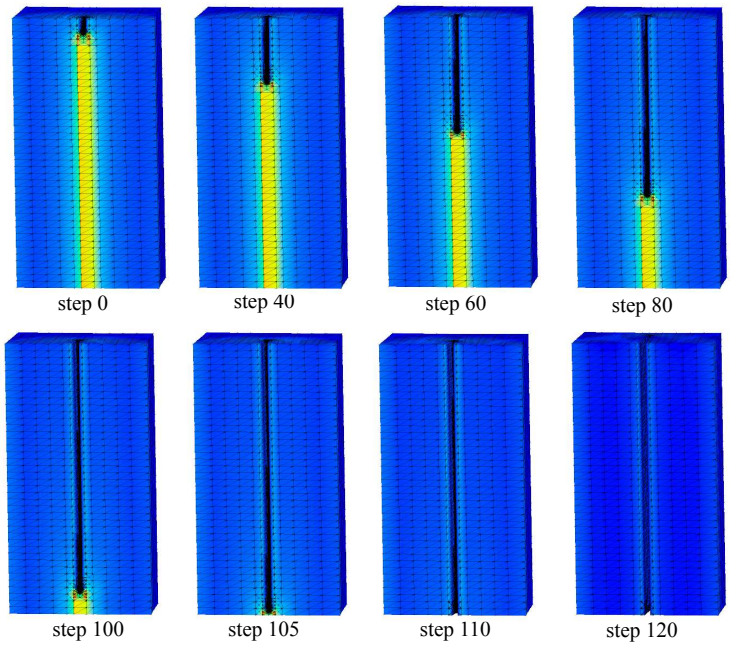

Figure 8.7: *Crack propagation: von Mises stress plotted on deformed configuration.*

is the loading fixtures which are frictionless and allow 2-directional loading to achieve opening and closing of the crack at different rates. Researchers at the University of Illinois (Dr. Buttlar research group) are currently working on a similar test in order to obtain fatigue parameters. Experimental results can be used to calibrate the computational model proposed in this dissertation. Figure 8.8 shows an example of crack propagation on a DC(T) specimen done with GFEM.

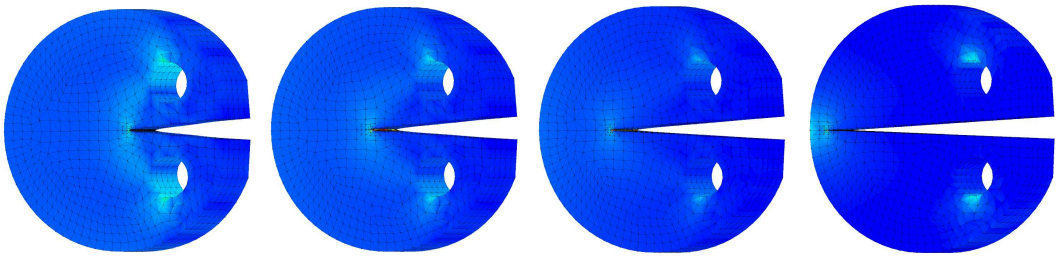

Figure 8.8: *Crack propagation on DC(T) specimen: von Mises stress plotted on deformed configuration.*

For now, adopt $A_{-10^o} = 7.0 * 10^{-5}$, $A_{0^o} = 1.7 * 10^{-4}$ and $A_{10^o} = 1.7 * 10^{-3}$ for temperatures -10^o C, 0^o C and 10^o C, respectively. The value for A_{0^o} assumed here is based on the propagation length and number of cycles observed in the the FAA laboratory tests (see Figure 8.9). Using Equation (7.29) and all the computed information for each crack step, a value for $A = A_{0^o}$ is

Table 8.2: *Number of cycles corresponding to crack step.*

Step	-10^o **C** (cycles)	0^o **C** (cycles)	10^o **C** (cycles)
0	0	0	0
20	9	24	46
40	29	74	142
60	59	152	290
80	98	251	480
105	164	421	805
106	173	444	849
110	277	710	1359
120	2807	7186	13763
132	10373	26553	50855

chosen so that for a crack length of 13.25 in. a corresponding number of 243 cycles is obtained. For other temperatures the value of A has been increased (10^o C) or decreased (-10^o C) by a factor close to 10 based on similar results found in [93]. Also, take a value of $n = 1.5725$, from the same reference, for all cases.

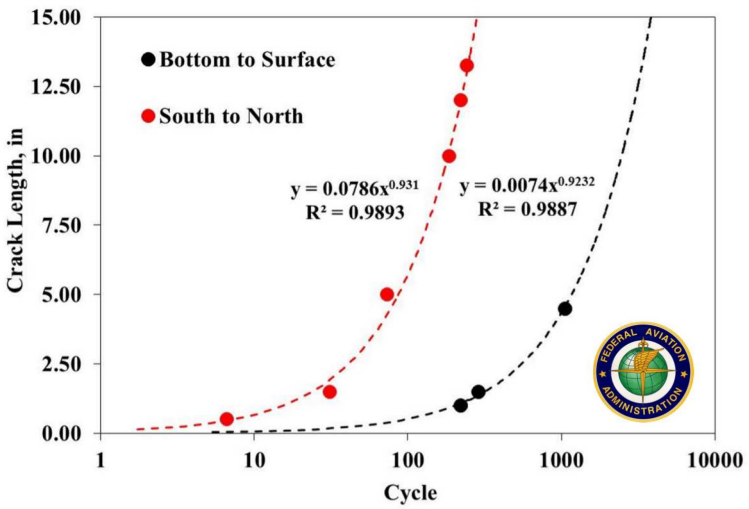

Figure 8.9: *Live prediction results provided by the FAA. Temperature* 0^o *C and loading rate* 0.1 *mil/s.*

Table 8.2 shows the number of cycles corresponding to the crack propagation step for all temperatures. Also, Figure 8.10 shows the life prediction. Note that for every temperature, there is a curve named "South to North" and "Bottom to Top". The first one corresponds to the horizontal advancement of the front through the specimen; while the other is the vertical advancement of the

front. Results are considered at $z = a$ in Figure 8.6.

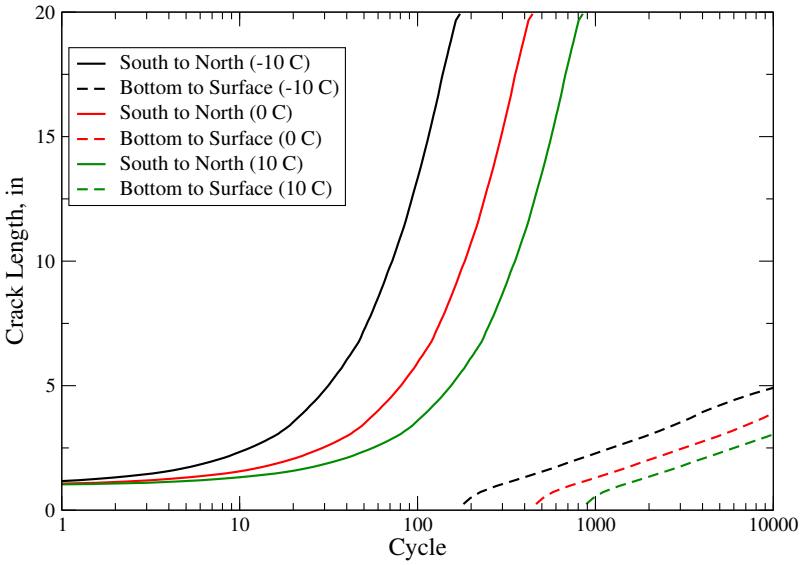

Figure 8.10: *Life prediction of the specimen for different temperatures.*

8.3 RC Multiple Cracks

Since symmetry BCs are used at the left and right faces of the domain, when the crack surface reaches the boundary, $z = a$, it is equivalent to meeting and coalescing with another crack. This other crack would be a mirror image of the simulated crack. Effectively, in this example, we have assumed that the asphalt layer on the testing machine has an initial flaw every $2 * b = 40$ inches. Only experimentation would allow us to determine a realistic distribution of initial cracks. Pending such a determination, we consider different distances between initial flaws and compute the life corresponding to each assumed distance. Three more cases with initial cracks at every $20, 10$ and 5 inches are simulated. Figure 8.11 shows the model description for each case.

Figures 8.12-8.14 and 8.15 show the evolution of the crack surfaces and the von Mises stress plotted on the deformed configuration for all cases. Tables 8.3-8.5 show the number of cycles corresponding to the crack step for all temperatures. Figure 8.16 shows the life prediction for all cases at temperatures -10^o, 0^o and 10^o C.

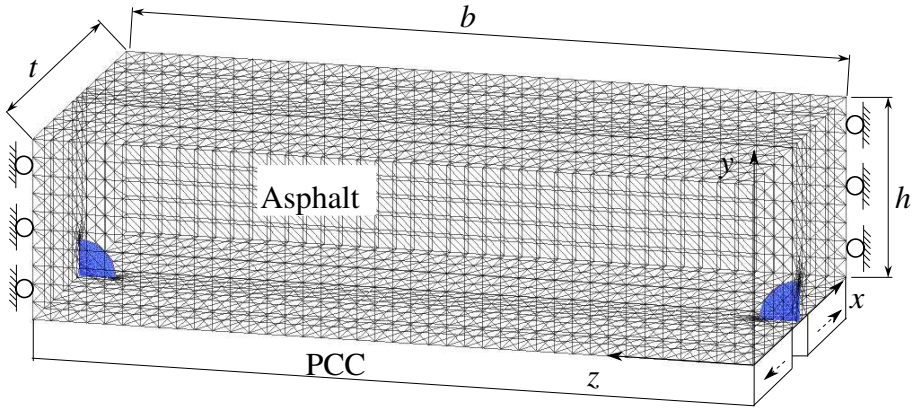

(a) A crack every 20 inches

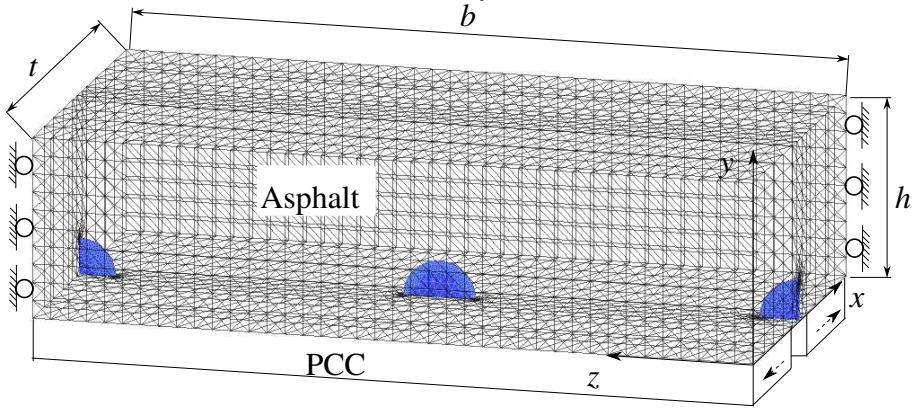

(b) A crack every 10 inches

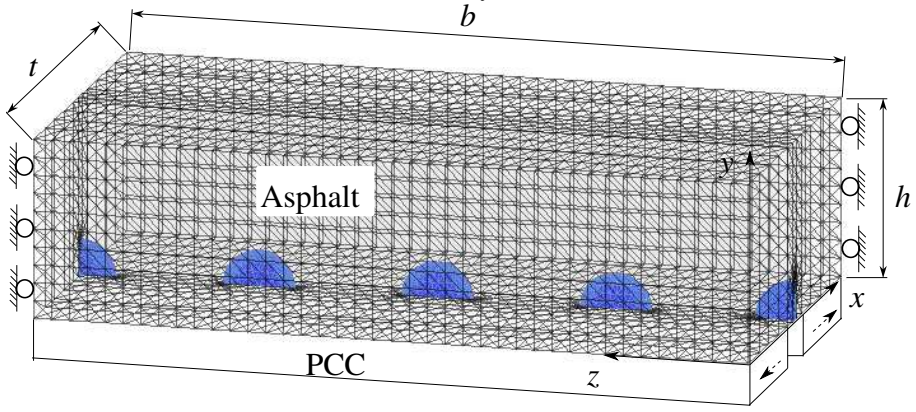

(c) A crack every 5 inches

Figure 8.11: *Model description.*

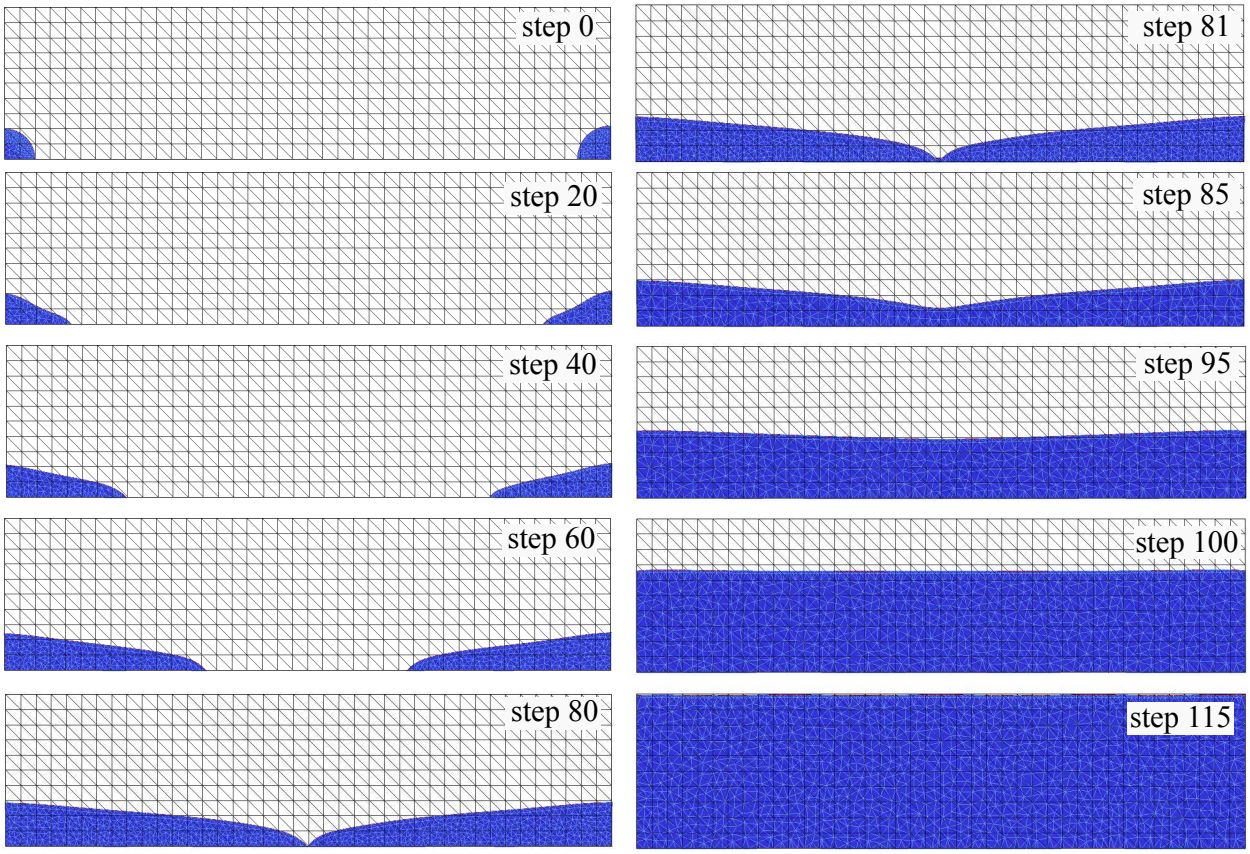

Figure 8.12: *Surface crack evolution. A crack every* 20 *inches.*

Table 8.3: *Number of cycles corresponding to crack step. A crack every* 20 *inches.*

Step	-10^o **C** (cycles)	0^o **C** (cycles)	10^o **C** (cycles)
0	0	0	0
20	8	20	38
40	22	56	107
60	44	112	214
80	77	197	378
81	78	200	384
85	104	267	512
95	589	1509	2889
100	1413	3616	6926
115	6274	16060	30759

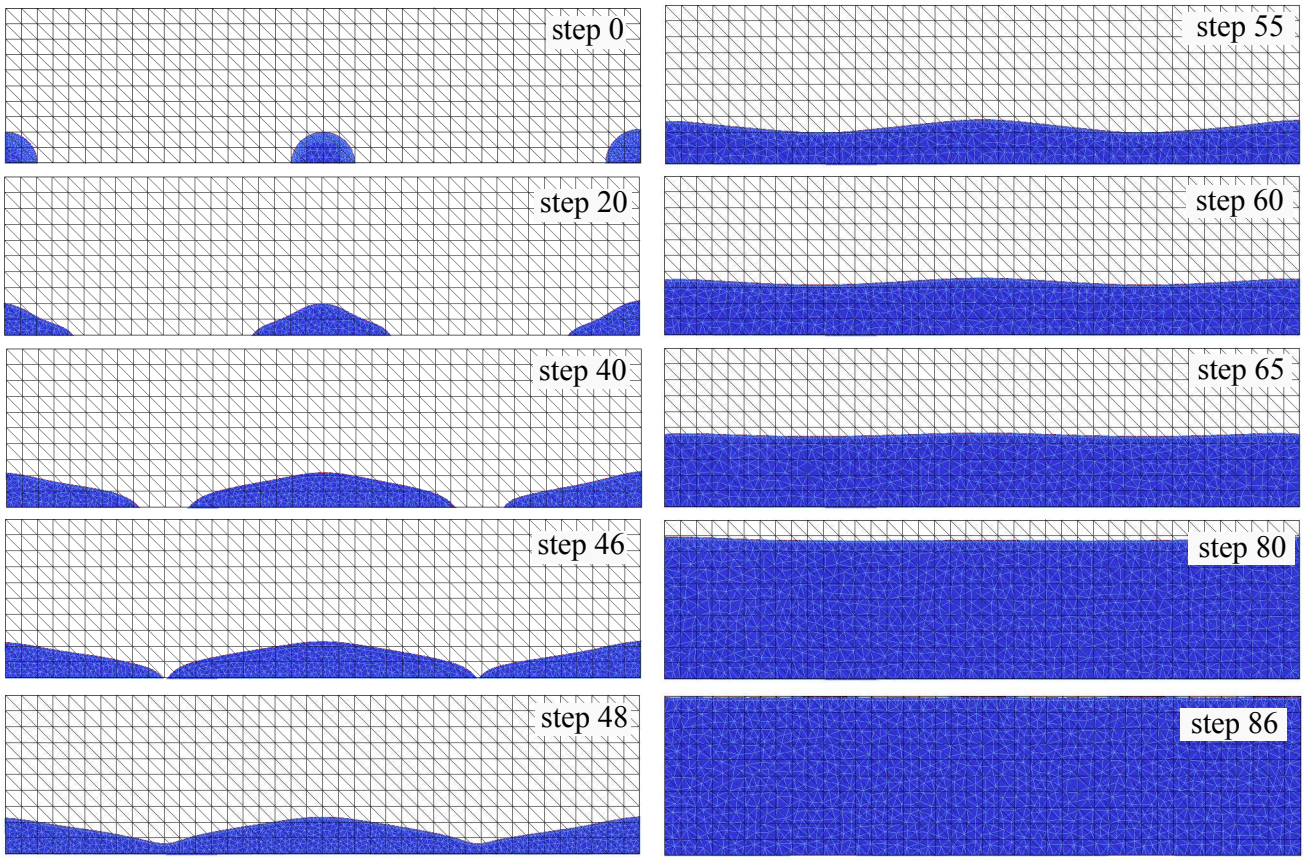

Figure 8.13: *Surface crack evolution. A crack every* 10 *inches.*

Table 8.4: *Number of cycles corresponding to crack step. A crack every* 10 *inches.*

Step	-10^o **C** (cycles)	0^o **C** (cycles)	10^o **C** (cycles)
0	0	0	0
20	8	20	38
40	24	61	116
46	30	76	145
48	34	86	164
55	123	316	605
60	331	846	1621
65	764	1957	3747
80	4851	12419	23784
86	6187	15837	30332

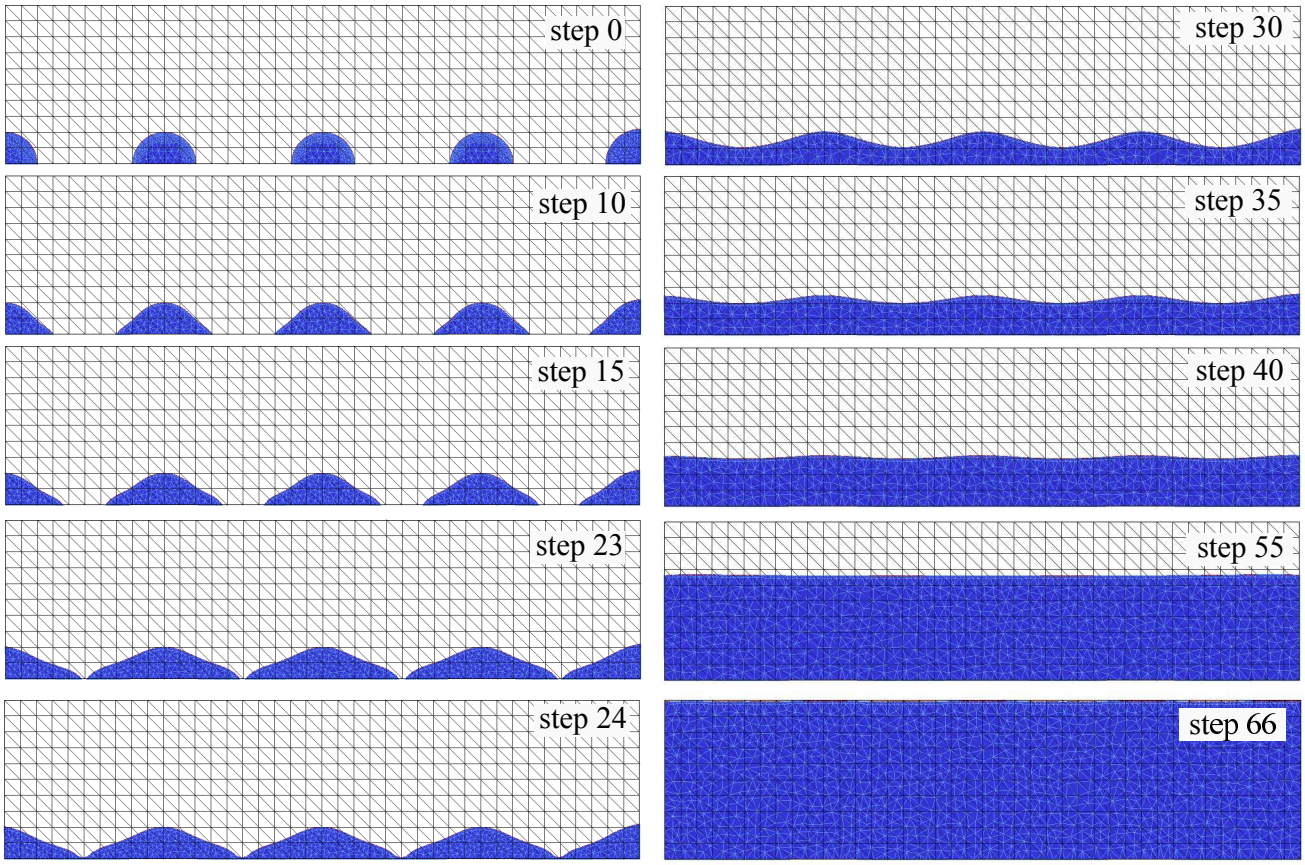

Figure 8.14: *Surface crack evolution. A crack every* 5 *inches.*

Table 8.5: *Number of cycles corresponding to crack step. A crack every* 5 *inches.*

Step	-10^o **C** (cycles)	0^o **C** (cycles)	10^o **C** (cycles)
0	0	0	0
10	3	8	15
15	5	13	26
23	9	24	46
24	10	26	50
30	33	84	160
35	104	266	509
40	267	683	1308
55	2224	5692	10904
66	5534	14165	27131

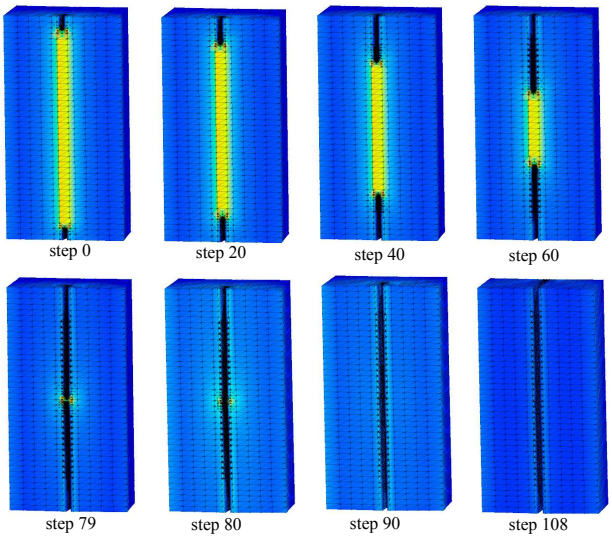

(a) A crack every 20 inches

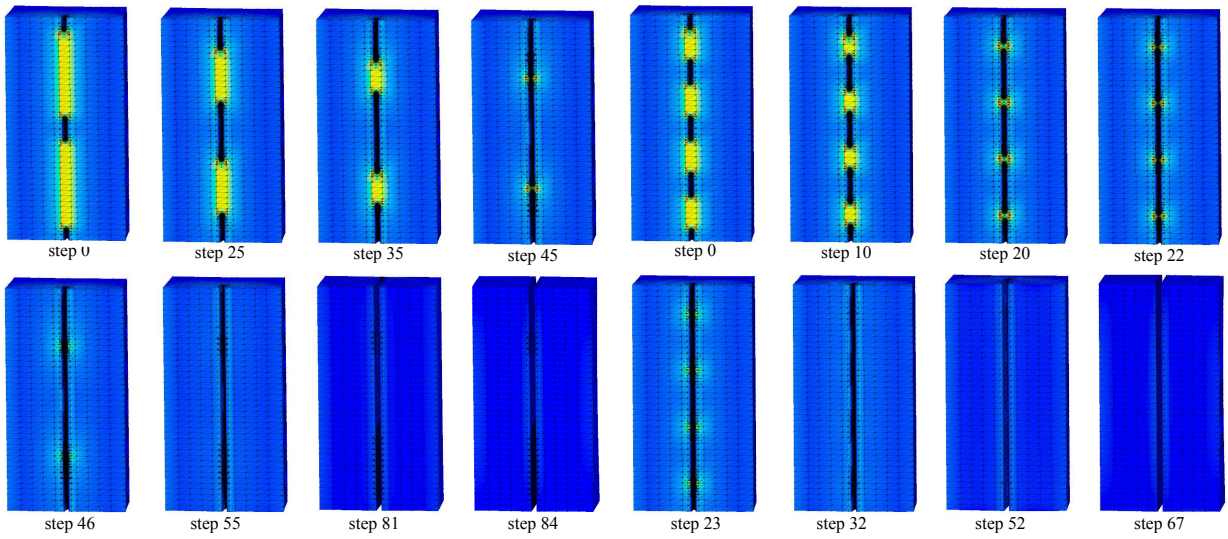

(b) A crack every 10 inches

(c) A crack every 5 inches

Figure 8.15: *Crack propagation: von Mises stress plotted on deformed configuration.*

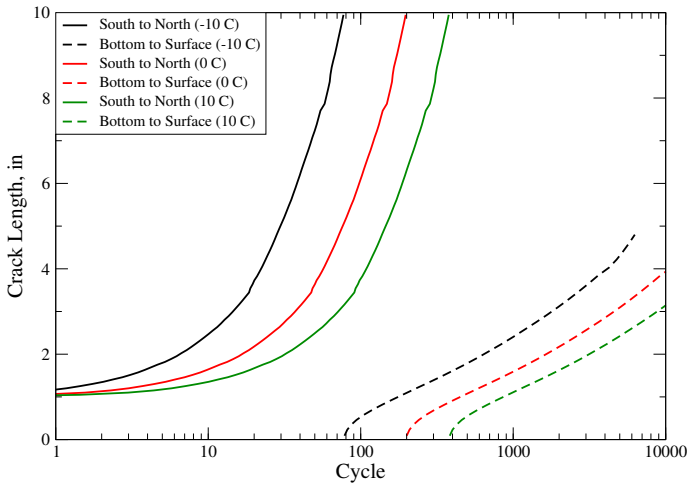

(a) A crack every 20 inches

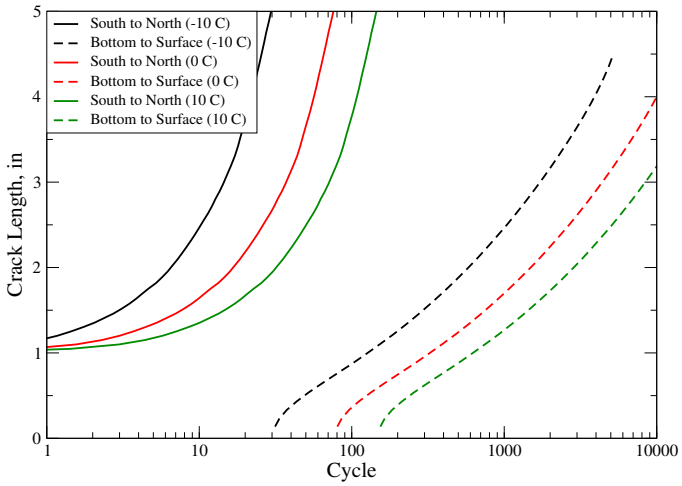

(b) A crack every 10 inches

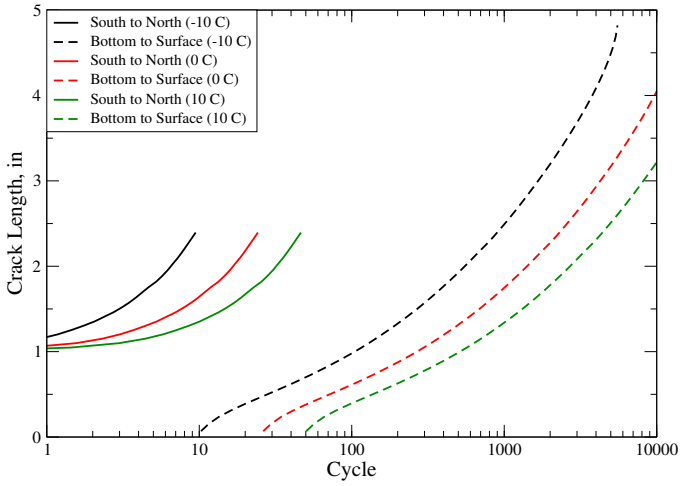

(c) A crack every 5 inches

Figure 8.16: *Life prediction of the specimen at different temperatures.*

8.4 RC Larger Domain

In this section a larger portion of the FAA testing machine is simulated. Figure 8.17 shows details of model. The dimensions of this rectangular domain are $t = 384$, $h = 5.0$, $b = 20$, and the crack assumed initial radius of $a = 1.0$. All dimensions are in inches. The material properties

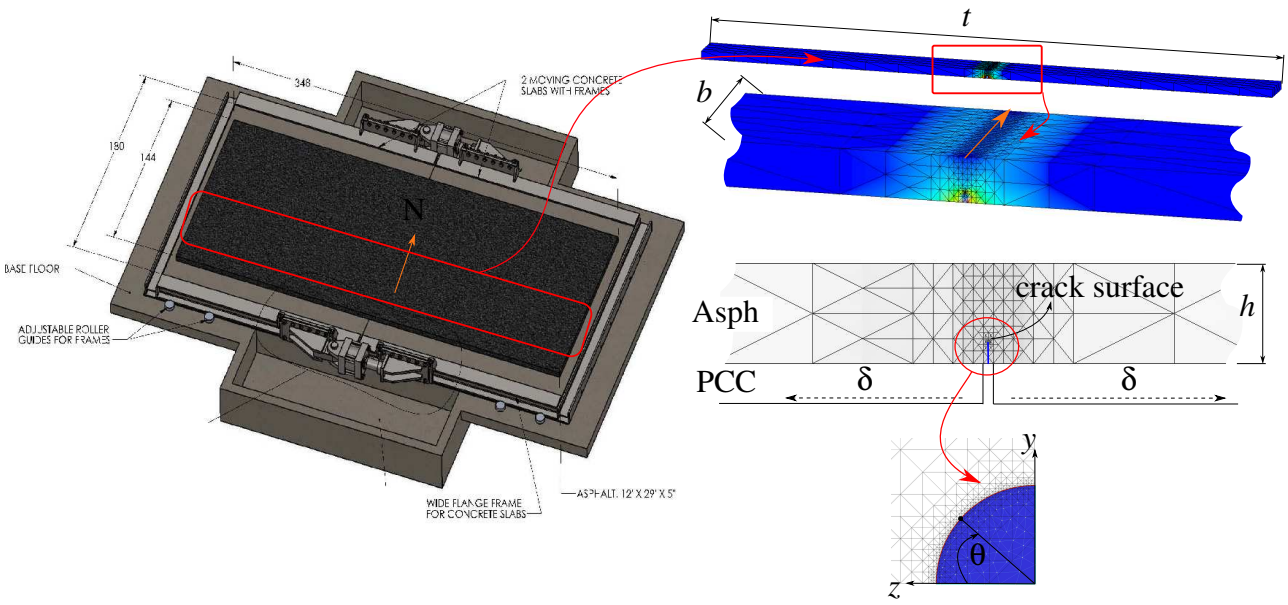

Figure 8.17: *Schematics of the Reflective crack machine. Picture courtesy of the FAA.*

and boundary conditions assumed here are the same as in previous section. Table 8.1 shows the mathematical representation of the viscoelastic material in the form of a Prony series. The imposed displacements at the bottom of the rectangular domain are $\delta = 7.5$ mils at each side of the PCC joint. GFEM shape functions of degree $p = 3$, Heaviside and branch functions are used as enrichments, as done in previous section. The SIFs of the reference elastic problem for step 0 are shown in Figure 8.18. These are compared to the SIFs obtained at the beginning of this Chapter.

A quasi-static crack growth simulation, as done before, is performed here. The imposed displacement boundary condition $\delta\lambda(t)$ is the sinusoidal function with $t_{peak} = 150$ s. At every propagation step, SIFs are computed using a reference elastic model and then a representative $\Delta\mathcal{G}$ is computed considering a stabilization time of $t_s = 3000$ s. Again, temperatures of $T = -10^o, 0^o$ and 10^o C are considered.

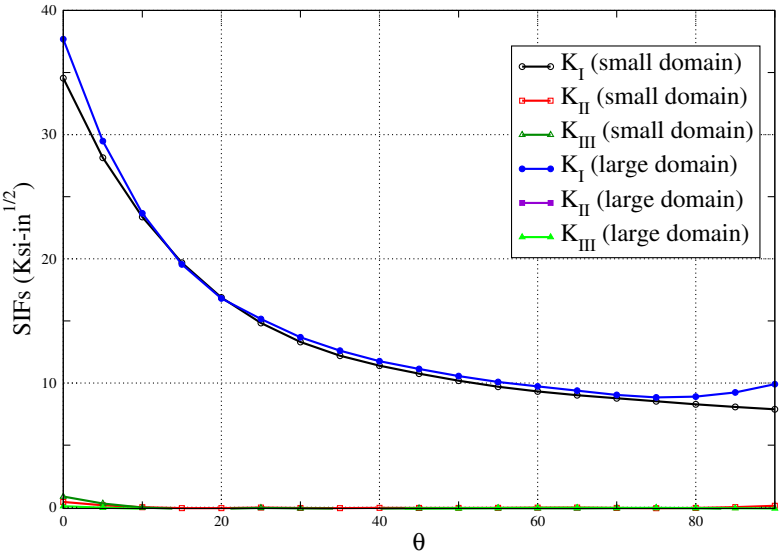

Figure 8.18: *Stress intensity factors for RC reference elastic problem along the crack front (step* 0*).*

Figures 8.19 and 8.20 show the evolution of the crack surface and the von Mises stress plotted on the deformed configuration, respectively, for several propagation steps. Table 8.6 shows the number of cycles corresponding to the crack step for all temperatures. The same constants assumed earlier, A and n, for the modified Paris law are used in this problem. Figure 8.21 shows the life prediction for all temperatures, compared to the results obtained at the beginning of this Chapter. The words "small" and "large" referrer to the size of the simulated domain.

Observe that life prediction curves "Bottom to Surface" of the larger domain are different than the curves corresponding to the small domain. This is because the value of dimension t in the small domain is only 10 in. and the movement of the underlaying PCC far from the position of the reflective crack is neglected. It appears that the size of dimension t has a direct influence on the vertical propagation towards the surface. On the other hand, this influence far from the reflective crack does not affect the propagation from "South to North".

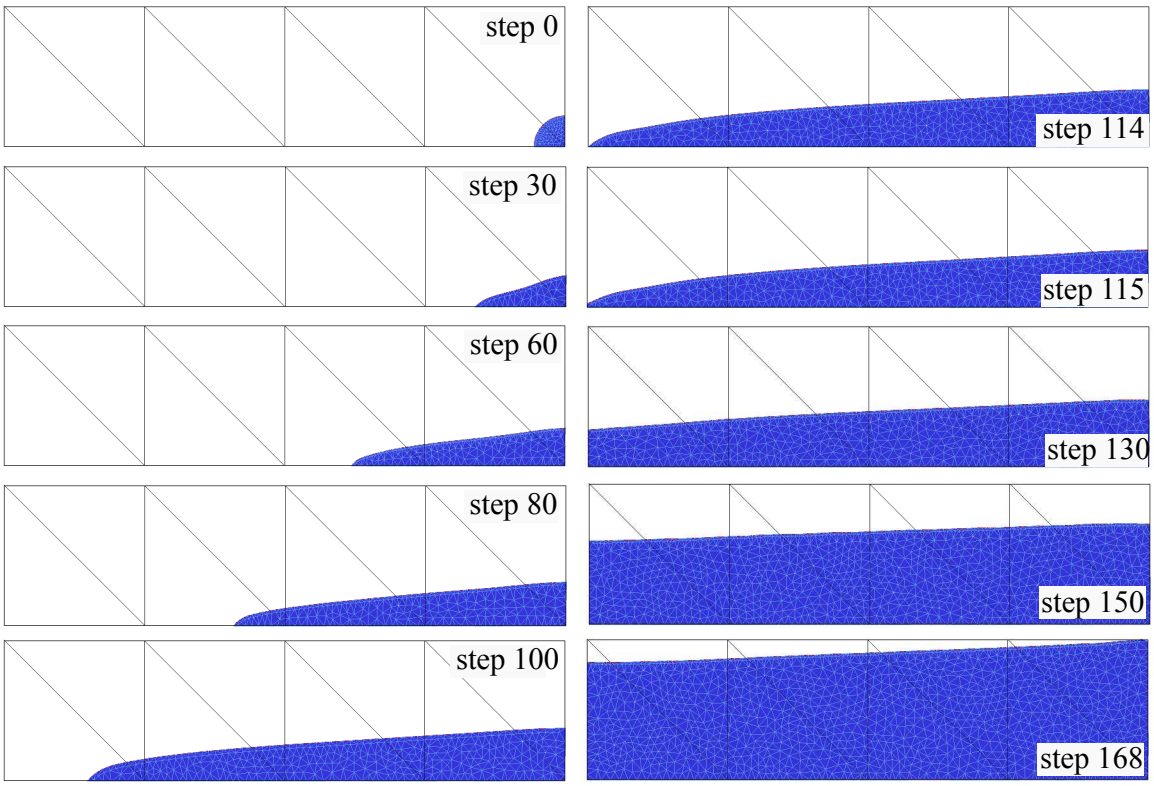

Figure 8.19: *Surface crack evolution.*

Table 8.6: *Number of cycles corresponding to crack step. A crack every* 40 *inches (large simulation domain).*

Step	-10^o **C** (cycles)	0^o **C** (cycles)	10^o **C** (cycles)
0	0	0	0
30	16	41	79
60	54	139	267
80	88	224	429
100	143	367	703
114	172	441	845
115	174	445	853
130	362	927	1776
150	1238	3169	6071
168	2169	5552	10638

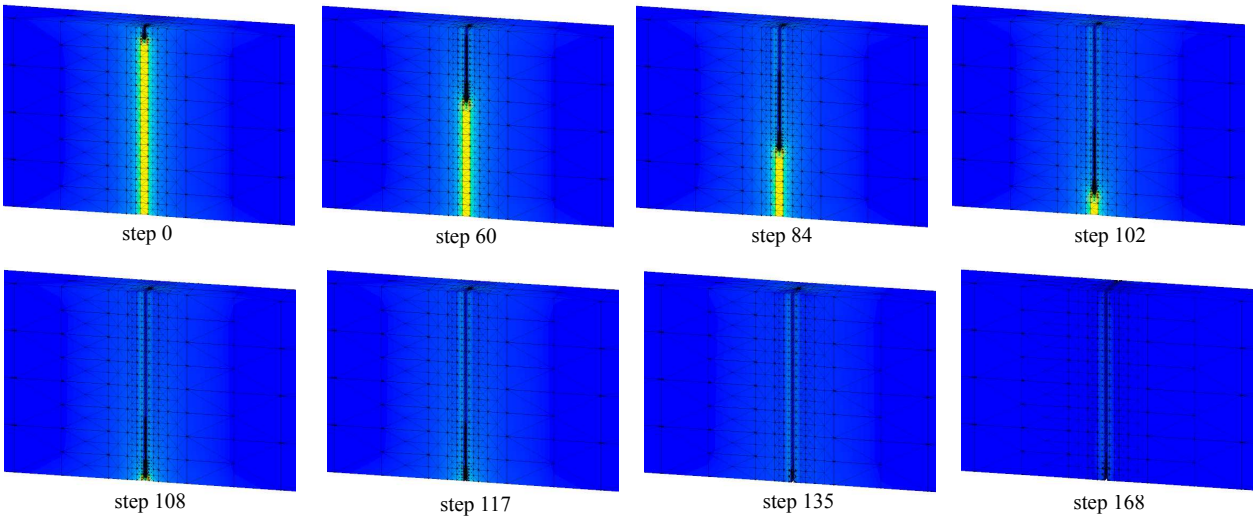

Figure 8.20: *Crack propagation: von Mises stress plotted on deformed configuration.*

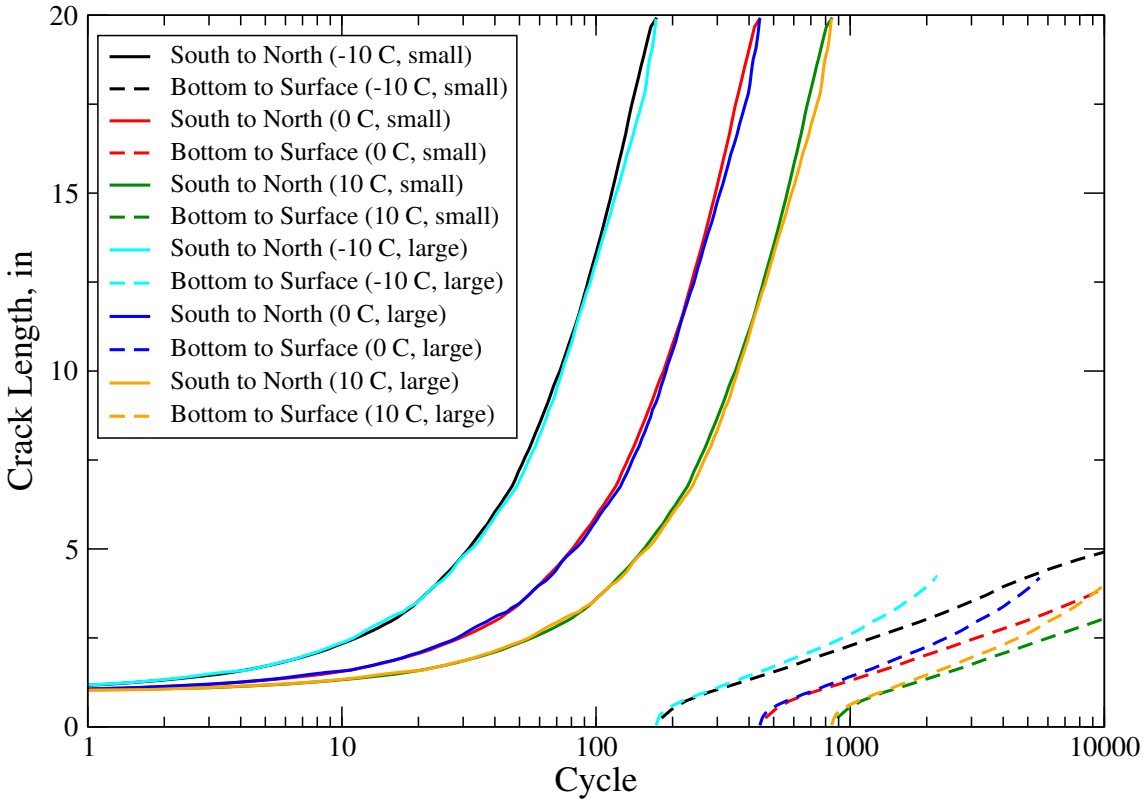

Figure 8.21: *Life prediction of the specimen for different temperatures.*

Chapter 9

Summary and Conclusions

Placing an asphalt concrete (AC) overlay on top of an existing deteriorated Portland Cement Concrete (PCC) is a very attractive option for the rehabilitation of airfield pavements, because the initial cost is low and the placement process is fast. However, the factor that controls the lifespan of overlays is often reflective cracking caused by stress concentrations in the vicinity of joints and cracks in the underlying pavement. Reflective cracking can reduce the life expectancy of the overlay because it leads to roughness, and moisture infiltration.

Reflective cracking is a three dimensional problem involving multiple spatial scales of interest. Thus, the analysis of this class of problem using available finite element methods leads to high computational costs in terms of CPU time and memory requirements.

The Generalized Finite Element Method (GFEM) is a promising technique to overcome the shortcomings of the standard FEM in 3-D crack growth simulations. In this method, singularities and discontinuities in the solution are represented using selected enrichment functions. Geometrical descriptions of crack surfaces, which *do not fit the FE mesh*, provide the necessary information to select the proper location and type of enrichment functions to be used. The *GFEM*$^{\text{g-l}}$ involves the use of numerically computed global-local enrichment functions to efficiently solve multi-scale problems such as reflective cracking. These two methods enable the analysis of reflective cracking in a 3-D setting while requiring significantly less user intervention in model preparation. Furthermore, the global-local enrichment functions allow users to solve this class of problems, efficiently, especially if multiple cracks are present.

The accuracy of the solution obtained with the *GFEM*$^{\text{g-l}}$ is comparable with that attained by Direct Numerical Simulations (DNS) with the GFEM, even though the *GFEM*$^{\text{g-l}}$ does not require

refinement of the global mesh. This enables, for example, the use of coarse meshes to represent large airfield pavement models with many slabs. The initial global problem in the *GFEM*$^{g\text{-}l}$ only needs to be solved once and the same global coarse mesh can be subsequently used for any crack configuration. This brings substantial computational savings to problems with many reflective cracks and to crack propagation simulations [131].

As seen in Section 5.4, the size of the local domain may significantly affect the solution of the standard global-local approach (GL-FEM). The larger the local problem, the better the accuracy of computed SIFs. The SIFs computed with the *GFEM*$^{g\text{-}l}$ on the other hand, are far less sensitive to the size of the local domain. The *GFEM*$^{g\text{-}l}$ was able to obtain very accurate results using a relatively small local domain as enrichment. The same size local domain in the GL-FEM proved to be far less accurate. The number of nodes enriched with global-local enrichments has an influence on the accuracy of the SIFs, especially if the initial global problem is approximated with linear shape functions. A suggestion for a future improvement is to develop a systematic approach for selecting the optimal size of the enrichment zone.

In Chapter 6, improvements to the capabilities of fully 3-D crack propagation within the GFEM have been presented. The techniques initially put forth in [130] are assessed in scenarios which pose difficulty in their ability to sufficiently represent a crack surface throughout the course of a lengthy crack propagation. In particular, reflective cracking proves to have a large discrepancy between effective energy release rate in different regions of its crack front, and associated discrepancy in the magnitude of the crack front increments. In these scenarios, the FOM techniques proposed in [130] do not perform satisfactorily.

The numerical examples in Chapter 6 show that in addition to the ability to simulate lengthy crack propagation, the approach also has the ability to handle crack front interactions with the domain boundary, as well as coalescence of multiple crack surfaces. The use of MLSM to redistribute crack front vertices after a propagation step allows the propagation of highly non-convex crack fronts, such as those arising in coalescence simulations, without interpenetration of the crack front edges. The use of a highly graded mesh [128] in crack front regions alleviates the issues as-

sociated with enrichment strategies for multiple cracks in close proximity arising from the use of a quasi-uniform mesh. In summary, the computational improvements to the explicit crack surface representation presented in this work are able to provide accurate results for large crack propagation analyses with multiple cracks as seen in the case of reflective cracking in Chapter 8. Crack surface features as well as crack front shape are able to be maintained throughout the entire simulation without the use of unnecessarily large numbers of small facets to represent the crack surface. The resulting methodology is less computationally demanding while actually producing higher quality crack surfaces when a large number of crack propagation steps are analyzed.

In this study a time-dependent energy release rate (ERR) $\mathcal{G}(t)$ has been taken as a crack front parameter to accurately describe the fracture behavior. It is computed along 3-D crack fronts by applying the elastic-viscoelastic correspondence principle to the associated GFEM elastic solution. The inversion from the Laplace domain to the physical domain is done numerically using the Fourier series method. Other methods were also studied, but Fourier series method proved to be the most robust. In contrast with other methods, the associated numerical problem is only solved once and is enough to compute the viscous solution in time. This significantly reduces the simulation time compared to any incremental formulation of viscoelastic fractured media. A detailed formulation has been presented in Chapter 3. Through this work many verification examples have been explored in order to validate the prosed methodology for static and propagating cracks.

The main contribution of this work is to provide a methodology to simulate and predict fatigue life of airfield pavements subject to reflective cracking. If low temperature, small crack increments and sufficient stabilization time are considered, the proposed methodology is able to simulate quasi-static crack propagation in linear viscoelastic materials. Any available propagation criteria can be adapted to this model. The current criteria used is a modification of the Paris Law based on the variation of ERR. Material constants are necessary for this criteria and can be obtained through experimentation.

Life prediction results presented in Chapter 8 are influenced by the material constants assumed by the author and therefore can not be taken as definitive. Researchers at the University of Illinois

(Dr. Buttlar research group) are working on an experimental set-up to obtain such constants. Even though this simulation does not give definitive quantitative results, it does show the capability of the method to solve different scenarios for reflective cracking. Propagation paths applicable to a single reflective crack and to multiple reflective cracks are seen *for the first time*. They are governed solely by the characteristic crack front parameter which in turn depends on the linear viscoelastic material properties, load, frequency and temperature. A realistic distribution of initial flaws is necessary for a correct life prediction, because it has a great influence in the pavement life. Figure 8.16 shows that the shortest life corresponds to the case where the most frequent spacing between initial cracks is considered.

The final result of all the work presented in this dissertation, is a very robust and accurate method for fully 3-D reflective cracking propagation simulations within the GFEM context. As such, it provides support for the development of mechanistic based design procedures for airfield overlays that incorporate reflective cracking as a failure mode.

Appendix A

Extraction of Stress Intensity Factors

In three-dimensional linear elastic fracture analysis, the stress state at the crack front is fully characterized by the Stress Intensity Factors (SIFs) $\mathcal{K}_I$, $\mathcal{K}_{II}$, and $\mathcal{K}_{III}$. They are basic parameters used, for example, to describe the fatigue crack growth behavior and assess the fatigue life of structural components.

Several extraction techniques have been proposed in the literature including: the displacement correlation method [28], the virtual crack extension method [29], the crack closure integral method [73], the J-integral method [137, 140] and its generalization the M-integral [91]. A review of methods for calculating energy release rates can be found in [98]. Most methods methods where developed with the FEM in mind and as such their implementation relies on a finite element mesh with rings of elements around the crack front. This type of implementation is in general not suitable for the GFEM since the generalized finite element mesh does not fit the crack front.

Babuška et al. [11, 169] proposed the Contour Integral Method (CIM) and the Cutoff Function Method (CFM) as super-convergent techniques for the extraction of stress intensity factors in the context of the p-version of the finite element method. The CIM has its origins in the works of Stern et al. [160]. This method and the CFM are based on the computation of functionals from a numerical solution and the so-called extraction functions. They are said to be super-convergent since the computed quantities converge to their exact values at least as fast as the strain energy. The CIM and the CFM can be used to extract Mode I, II and III SIFs from mixed mode problems, in contrast with the J-integral method and some methods based on it. A rigorous decomposition of the J-integral for 3-D mixed-mode problems is presented in [140]. A formulation of the CIM suitable for 2-D problems with loaded cracks is presented in [127]. Implementations of the CIM

and CFM tailored for meshfree methods and the GFEM are presented in [126]. A formulation of the CFM for 3-D problems was presented by Andersson et al. [6] in the context of the p-version of the FEM.

In this appendix, a three-dimensional formulation of the CIM and CFM for the extraction of Modes *I*, *II*, and *III* SIFs is presented. The case of crack faces loaded by prescribed tractions is also considered. This type of boundary condition appears, for example, in the simulation of hydraulic fracturing. Several material-dependent constants used in the CFM and CIM formulations are, also presented here.

The remainder of this appendix proceeds as follows: Section A.1 presents integral identities that form, together with the so-called extraction functions, the theoretical basis of the Contour Integral Method (CIM). The formulation of the CIM for cracks with tractions applied to their faces is presented in Section A.2, while the formulation of CFM is presented in Section A.3. The use of the Moving Least Squares Method (MLSM) [96] to provide a continuous and smooth approximation of SIFs extracted point-wise along a 3-D crack front is shortly discussed in Section A.4. Numerical examples including 3-D mixed-mode fatigue crack growth simulations, and the case of a pressurized crack, are presented in Section A.5.

A.1 Problem Description

Consider a cracked three dimensional elastic domain Ω as illustrated in Fig. A.1. A local Cartesian coordinate system (x_1, x_2, x_3) is defined at each point along the crack front Γ_c and oriented as illustrated in Fig. A.1. Let $\boldsymbol{u}(x_1, x_2, x_3)$ denote the displacement field in Ω written in terms of the local Cartesian coordinates

$$\boldsymbol{u}(x_1, x_2, x_3) = \left\{ \begin{array}{c} u_1(x_1, x_2, x_3) \\ u_2(x_1, x_2, x_3) \\ u_3(x_1, x_2, x_3) \end{array} \right\}$$

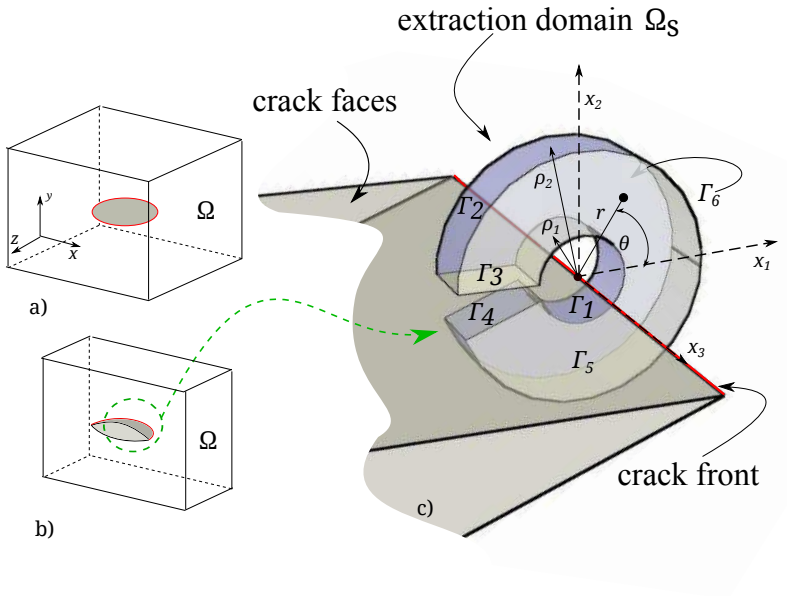

Figure A.1: *a) Cracked three dimensional domain Ω. b) Cutting plane view. c) Crack front coordinated systems, and neighborhood Ω_s around the crack front.*

The linear elasticity equilibrium equations in the domain Ω, in the absence of body forces, are given by

$$\sigma_{ij,j}^{(u)} = 0 \quad \text{in } \Omega$$

where

$$\begin{aligned} \sigma_{ij}^{(u)} &= D_{ijkl}\varepsilon_{kl}^{(u)} \\ \varepsilon_{ij}^{(u)} &= \frac{1}{2}(u_{i,j}+u_{j,i}) \end{aligned}$$

with D_{ijkl} being the tensor of elastic constants for a homogeneous isotropic material with Young's modulus E and Poisson's ratio ν.

The components of the traction vector at a point on the boundary $\partial\Omega$ are given by

$$T_i^{(u)} = \sigma_{ij}^{(u)} n_j \quad \text{on } \partial\Omega$$

where $\sigma_{ij}^{(\boldsymbol{u})}$ are the stress tensor components computed from the displacement field $\boldsymbol{u}$. The components of the outward normal vector to the boundary $\partial\Omega$ are denoted by n_j.

Let $\boldsymbol{v}$ define a virtual displacement field defined on Ω

$$\boldsymbol{v}(x_1,x_2,x_3) = \left\{ \begin{array}{c} v_1(x_1,x_2,x_3) \\ v_2(x_1,x_2,x_3) \\ v_3(x_1,x_2,x_3) \end{array} \right\}$$

Consider a hollow cylindrical sub-domain Ω_s with axis in the coordinate direction x_3, length t_z, internal radius ρ_1 and external radius ρ_2 as illustrated in Fig. A.1. The boundary of Ω_s is given by $\partial\Omega_s = \Gamma_1 \cup \Gamma_2 \cup \Gamma_3 \cup \Gamma_4 \cup \Gamma_5 \cup \Gamma_6$.

Following the derivation of Principle of Virtual Work (see, e.g. [168]), it can be shown that

$$\int_{\Omega_s} \sigma_{ij}^{(\boldsymbol{u})} \varepsilon_{ij}^{(\boldsymbol{v})} d\Omega = \int_{\partial\Omega_s} T_i^{(\boldsymbol{u})} v_i \, d\Gamma \tag{A.1}$$

with $\varepsilon_{ij}^{(\boldsymbol{v})}$ as the strain components computed from the virtual displacement field $\boldsymbol{v}$. Equation (A.1) holds for any virtual displacement field $\boldsymbol{v}$ with an associated finite strain energy in Ω_s.

Any type of boundary conditions on the boundary $\partial\Omega_s$ can be considered. Herein we assume that the crack faces, Γ_3 and Γ_4, are either stress free or loaded by prescribed tractions. We also assume that body forces are zero.

Since the tensor of elastic constants is symmetric we have that,

$$\sigma_{ij}^{(\boldsymbol{u})} \varepsilon_{ij}^{(\boldsymbol{v})} = D_{ijkl} \varepsilon_{kl}^{(\boldsymbol{u})} \varepsilon_{ij}^{(\boldsymbol{v})} = D_{klij} \varepsilon_{ij}^{(\boldsymbol{v})} \varepsilon_{kl}^{(\boldsymbol{u})} = \sigma_{kl}^{(\boldsymbol{v})} \varepsilon_{kl}^{(\boldsymbol{u})}$$

and therefore,

$$\int_{\Omega_s} \sigma_{kl}^{(\boldsymbol{v})} \varepsilon_{kl}^{(\boldsymbol{u})} d\Omega = \int_{\partial\Omega_s} T_i^{(\boldsymbol{u})} v_i \, d\Gamma \tag{A.2}$$

The symmetry of the stress tensor and the above definitions lead to

$$\begin{aligned}\sigma_{kl}^{(\boldsymbol{v})}\varepsilon_{kl}^{(\boldsymbol{u})} &= \sigma_{kl}^{(\boldsymbol{v})}\frac{1}{2}(u_{k,l}+u_{l,k}) = \frac{1}{2}\sigma_{kl}^{(\boldsymbol{v})}u_{k,l}+\frac{1}{2}\sigma_{lk}^{(\boldsymbol{v})}u_{k,l} \\ &= \frac{1}{2}\sigma_{kl}^{(\boldsymbol{v})}u_{k,l}+\frac{1}{2}\sigma_{kl}^{(\boldsymbol{v})}u_{k,l} = \sigma_{kl}^{(\boldsymbol{v})}u_{k,l}\end{aligned}$$

Using Green's theorem,

$$\begin{aligned}\int_{\Omega_s}\sigma_{kl}^{(\boldsymbol{v})}\varepsilon_{kl}^{(\boldsymbol{u})}\,d\Omega &= \int_{\Omega_s}\sigma_{kl}^{(\boldsymbol{v})}u_{k,l}\,d\Omega = \int_{\partial\Omega_s}\sigma_{kl}^{(\boldsymbol{v})}u_k n_l\,d\Gamma - \int_{\Omega_s}\sigma_{kl,l}^{(\boldsymbol{v})}u_k\,d\Omega \\ &= \int_{\partial\Omega_s}T_k^{(\boldsymbol{v})}u_k\,d\Gamma - \int_{\Omega_s}\sigma_{kl,l}^{(\boldsymbol{v})}u_k\,d\Omega\end{aligned}$$

Substituting the above in Eq. (A.2)

$$\int_{\partial\Omega_s}T_k^{(\boldsymbol{v})}u_k\,d\Gamma - \int_{\Omega_s}\sigma_{kl,l}^{(\boldsymbol{v})}u_k\,d\Omega = \int_{\partial\Omega_s}T_i^{(\boldsymbol{u})}v_i\,d\Gamma \tag{A.3}$$

If the displacement field $\boldsymbol{v}$ satisfies the equilibrium equations, we arrive at Betti's law

$$\int_{\partial\Omega_s}T_k^{(\boldsymbol{v})}u_k\,d\Gamma = \int_{\partial\Omega_s}T_i^{(\boldsymbol{u})}v_i\,d\Gamma \tag{A.4}$$

The integral Equations (A.4) and (A.3) are used in Sections A.2 and A.3 to derive the contour integral and the cutoff function methods, respectively.

Let $\bar{\boldsymbol{u}}$ denote the displacement field in Ω_s written in terms of the local cylindrical coordinates (r,θ,z).

$$\bar{\boldsymbol{u}}(r,\theta) = \left\{\begin{array}{c}\bar{u}_1(r,\theta)\\ \bar{u}_2(r,\theta)\\ \bar{u}_3(r,\theta)\end{array}\right\}$$

Herein, bar quantities, "$\bar{\ }$", are defined in terms of local cylindrical coordinates. If the internal radius, ρ_1, of the sub-domain Ω_s is sufficiently small and assuming that the extraction domain is

completely inside the material in a state of plane strain, the displacement field in the interior of sub-domain Ω_s can be approximated by

$$\begin{aligned}
\bar{\boldsymbol{u}}(r,\theta) = \left\{ \begin{array}{c} \bar{u}_1(r,\theta) \\ \bar{u}_2(r,\theta) \\ \bar{u}_3(r,\theta) \end{array} \right\} &= \frac{\mathcal{K}_I}{2G\sqrt{2\pi}}\sqrt{r}\left\{ \begin{array}{c} (\kappa-\frac{1}{2})\cos(\frac{\theta}{2}) - \frac{1}{2}\cos(\frac{3\theta}{2}) \\ (\kappa+\frac{1}{2})\sin(\frac{\theta}{2}) - \frac{1}{2}\sin(\frac{3\theta}{2}) \\ 0 \end{array} \right\} \\
&+ \frac{\mathcal{K}_{II}}{2G\sqrt{2\pi}}\sqrt{r}\left\{ \begin{array}{c} (\kappa-\frac{3}{2})\sin(\frac{\theta}{2}) + \frac{1}{2}\sin(\frac{3\theta}{2}) \\ -(\kappa-\frac{3}{2})\cos(\frac{\theta}{2}) - \frac{1}{2}\sin(\frac{3\theta}{2}) \\ 0 \end{array} \right\} \\
&+ \frac{\mathcal{K}_{III}}{G}\sqrt{\frac{2}{\pi}}\sqrt{r}\left\{ \begin{array}{c} 0 \\ 0 \\ \sin(\frac{\theta}{2}) \end{array} \right\}
\end{aligned} \tag{A.5}$$

where $\mathcal{K}_I$, $\mathcal{K}_{II}$ and $\mathcal{K}_{III}$ are SIFs corresponding to Modes *I*, *II* and *III*; G is the shear modulus and κ is the Kolosov's constant. Hereafter, $\bar{\boldsymbol{T}}^{(\bar{\boldsymbol{u}})}(r,\theta,z)$ defines the traction vector computed from the displacement field $\bar{\boldsymbol{u}}(r,\theta,z)$.

The so-called *extraction functions* are defined using the expressions of the asymptotic expansion of the elasticity solution near the crack front and using the negative of the eigenvalues associated with each mode. A detailed procedure to define these functions is found in [168]. For Modes *I*, *II* and *III* and based on the displacement field presented in Eq. (A.5) [168], the extraction functions are given by

$$\bar{\boldsymbol{v}}^{-I}(r,\theta) = \left[\begin{array}{c} \bar{v}_1^{-I}(r,\theta) \\ \bar{v}_2^{-I}(r,\theta) \\ \bar{v}_3^{-I}(r,\theta) \end{array} \right] = \frac{B^{-I}}{2G\sqrt{2\pi}}\frac{1}{\sqrt{r}}\left[\begin{array}{c} (\kappa-\frac{3}{2})\cos(\frac{\theta}{2}) + \frac{1}{2}\cos(\frac{5\theta}{2}) \\ -(\kappa+\frac{3}{2})\sin(\frac{\theta}{2}) + \frac{1}{2}\sin(\frac{5\theta}{2}) \\ 0 \end{array} \right] \tag{A.6}$$

$$\bar{\boldsymbol{v}}^{-II}(r,\theta) = \begin{bmatrix} \bar{v}_1^{-II}(r,\theta) \\ \bar{v}_2^{-II}(r,\theta) \\ \bar{v}_3^{-II}(r,\theta) \end{bmatrix} = \frac{B^{-II}}{2G\sqrt{2\pi}} \frac{1}{\sqrt{r}} \begin{bmatrix} -(\kappa+\frac{1}{2})\sin(\frac{\theta}{2}) - \frac{1}{2}\sin(\frac{5\theta}{2}) \\ -(\kappa-\frac{1}{2})\cos(\frac{\theta}{2}) + \frac{1}{2}\sin(\frac{5\theta}{2}) \\ 0 \end{bmatrix} \tag{A.7}$$

$$\bar{\boldsymbol{v}}^{-III}(r,\theta) = \begin{bmatrix} \bar{v}_1^{-III}(r,\theta) \\ \bar{v}_2^{-III}(r,\theta) \\ \bar{v}_3^{-III}(r,\theta) \end{bmatrix} = \frac{B^{-III}}{G} \sqrt{\frac{2}{\pi}} \frac{1}{\sqrt{r}} \begin{bmatrix} 0 \\ 0 \\ \sin(\frac{\theta}{2}) \end{bmatrix} \tag{A.8}$$

where B^{-I} , B^{-II} and B^{-III} are constants defined later. Eqs. (A.6),(A.7) and (A.8) are used in the following sections and are very important in the definition of extraction methods. These functions do not have finite strain energy in Ω. However, they have finite strain energy in Ω_s and satisfy the equilibrium equations.

Hereafter, $\bar{\boldsymbol{T}}^{(\bar{\boldsymbol{v}}^{-I})}$, $\bar{\boldsymbol{T}}^{(\bar{\boldsymbol{v}}^{-II})}$ and $\bar{\boldsymbol{T}}^{(\bar{\boldsymbol{v}}^{-III})}$ denote the traction vectors computed from $\bar{\boldsymbol{v}}^{-I}$, $\bar{\boldsymbol{v}}^{-II}$ and $\bar{\boldsymbol{v}}^{-III}$, respectively. It is not difficult to verify that these tractions are zero on the crack faces, i.e., on Γ_3 and Γ_4.

A.2 The Contour Integral Method

In this section, the Contour Integral Method (CIM) for cracks with tractions applied to their faces is derived using the integral identity (A.4).

The boundary $\partial\Omega_s$ of the 3-D cylindrical extraction domain is given by $\partial\Omega_s = \Gamma_1 \cup \Gamma_2 \cup \Gamma_3 \cup \Gamma_4 \cup \Gamma_5 \cup \Gamma_6$, as illustrated in Fig. A.1. In the CIM, the extraction domain Ω_s degenerates to a planar slice Ω_s^L of Ω_s, as illustrated in Fig. A.2.

The surface integrals on Γ_1, Γ_2, Γ_3 and Γ_4 degenerates to line integrals over Γ_1^L, Γ_2^L, Γ_3^L and Γ_4^L, respectively. The surface integrals of $T_k^{(\boldsymbol{v})} u_k$ and $T_i^{(\boldsymbol{u})} v_i$ over Γ_5 and Γ_6 cancel out since the

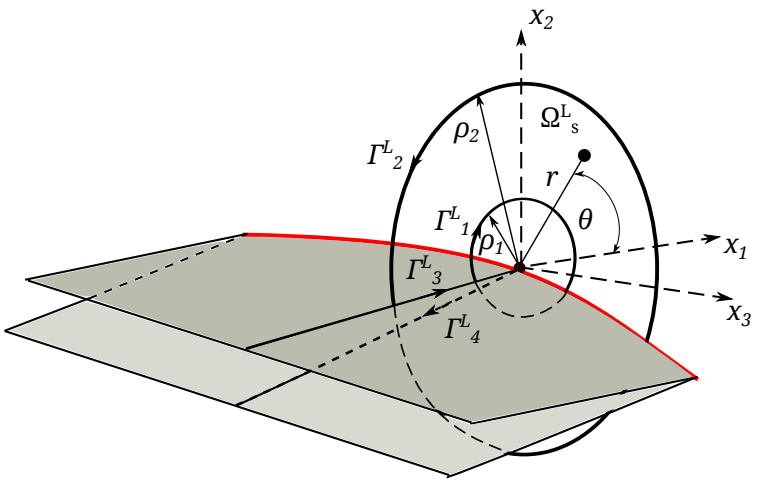

Figure A.2: *Extraction domain Ω_s^L and local coordinated system used in the CIM.*

traction vectors on these surfaces have the same magnitude and opposite directions. Thus, the CIM involves line integrals over Γ_1^L, Γ_2^L, Γ_3^L and Γ_4^L only.

Consider first the integral on the left hand side of Eq. (A.4) for extraction domain Ω_s^L

$$\int_{\partial\Omega_s^L} T_k^{(\boldsymbol{\nu})} u_k \, d\Gamma = \int_{\Gamma_1^L \cup \Gamma_2^L \cup \Gamma_3^L \cup \Gamma_4^L} T_k^{(\boldsymbol{\nu})} u_k \, d\Gamma = \int_{\Gamma_1^L \cup \Gamma_2^L \cup \Gamma_3^L \cup \Gamma_4^L} \bar{T}_k^{(\bar{\boldsymbol{\nu}})} \bar{u}_k \, d\Gamma$$

Let $\bar{\boldsymbol{\nu}}$ define the extraction function $\bar{\boldsymbol{\nu}}^{-I}$, $\bar{\boldsymbol{\nu}}^{-II}$ and $\bar{\boldsymbol{\nu}}^{-III}$. Then

$$\int_{\Gamma_3^L} T_k^{(\bar{\boldsymbol{\nu}})} \bar{u}_k \, d\Gamma = \int_{\Gamma_4^L} \bar{T}_k^{(\bar{\boldsymbol{\nu}})} \bar{u}_k \, d\Gamma = 0$$

since $\bar{\boldsymbol{T}}^{(\bar{\boldsymbol{\nu}}^{-I})}(r,\theta)$, $\bar{\boldsymbol{T}}^{(\bar{\boldsymbol{\nu}}^{-II})}(r,\theta)$, and $\bar{\boldsymbol{T}}^{(\bar{\nu}^{-III})}(r,\theta)$ are zero on the crack faces. Let $\bar{\boldsymbol{\nu}} = \bar{\boldsymbol{\nu}}^{-I}$. then it can be shown that, if contour Γ_1^L is in the K-dominant region of the elasticity solution, where Eq. (A.5) holds,

$$\int_{\Gamma_1^L} \bar{T}_k^{(\bar{\boldsymbol{\nu}}^{-I})} \bar{u}_k \, d\Gamma = C_l^{-I} B^{-I} \mathcal{K}_I \tag{A.9}$$

where

$$C_l^{-I} = -\frac{(3\kappa+1)}{8G}$$

Similarly, if $\bar{\boldsymbol{v}} = \bar{\boldsymbol{v}}^{-II}$, then,

$$\int_{\Gamma_1^L} \bar{T}_k^{(\bar{\boldsymbol{v}}^{-II})} \bar{u}_k \, d\Gamma = C_l^{-II} \, B^{-II} \, \mathcal{K}_{II} \tag{A.10}$$

where

$$C_l^{-II} = -\frac{(\kappa+3)}{8G}$$

and, finally if $\bar{\boldsymbol{v}} = \bar{\boldsymbol{v}}^{-III}$, then,

$$\int_{\Gamma_1^L} \bar{T}_k^{(\bar{\boldsymbol{v}}^{-III})} \bar{u}_k d\Gamma = C_l^{-III} \, B^{-III} \, \mathcal{K}_{III} \tag{A.11}$$

where

$$C_l^{-III} = -\frac{1}{G}$$

Consider now the integral on the right hand side of Eq. (A.4), i.e.,

$$\int_{\partial\Omega_s^L} T_i^{(\boldsymbol{u})} v_i \, d\Gamma = \int_{\Gamma_1^L \cup \Gamma_2^L \cup \Gamma_3^L \cup \Gamma_4^L} T_i^{(\boldsymbol{u})} v_i \, d\Gamma = \int_{\Gamma_1^L \cup \Gamma_2^L \cup \Gamma_3^L \cup \Gamma_4^L} \bar{T}_i^{(\bar{\boldsymbol{u}})} \bar{v}_i \, d\Gamma$$

Tractions are prescribed on the crack faces and are denoted by

$$\bar{\boldsymbol{T}}^{(\bar{\boldsymbol{u}})} = \begin{cases} \bar{\boldsymbol{p}}^3 & \text{on} \quad \Gamma_3^L \\ \bar{\boldsymbol{p}}^4 & \text{on} \quad \Gamma_4^L \end{cases}$$

Let $\bar{\boldsymbol{v}} = \bar{\boldsymbol{v}}^{-I}$, then

$$\int_{\Gamma_1^L} \bar{T}_i^{(\bar{\boldsymbol{u}})} \bar{v}_i^{-I} \, d\Gamma = C_r^{-I} \, B^{-I} \, \mathcal{K}_I \tag{A.12}$$

where

$$C_r^{-I} = \frac{\kappa+3}{8G}$$

Similarly, if $\bar{\boldsymbol{v}} = \bar{\boldsymbol{v}}^{-II}$, then,

$$\int_{\Gamma_1^L} \bar{T}_i^{(\bar{\boldsymbol{u}})} \bar{v}_i^{-II} \, d\Gamma = C_r^{-II} \, B^{-II} \, \mathcal{K}_{II} \tag{A.13}$$

where

$$C_r^{-II} = \frac{3\kappa+1}{8G}$$

and also, if $\bar{\boldsymbol{v}} = \bar{\boldsymbol{v}}^{-III}$, then,

$$\int_{\Gamma_1^L} \bar{T}_i^{(\bar{\boldsymbol{u}})} \bar{v}_i^{-III}\, d\Gamma = C_r^{-III} B^{-III}\, \mathcal{K}_{III} \tag{A.14}$$

where

$$C_r^{-III} = \frac{1}{G}$$

Using Eq. (A.4) and the above we have,

$$\begin{aligned} C_l^{-I} B^{-I}\, \mathcal{K}_I + \int_{\Gamma_2^L} \bar{T}_k^{(\bar{\boldsymbol{v}}^{-I})} \bar{u}_k\, d\Gamma &= C_r^{-I} B^{-I}\, \mathcal{K}_I + \int_{\Gamma_2^L} \bar{T}_i^{(\bar{\boldsymbol{u}})} \bar{v}_i^{-I}\, d\Gamma \\ &+ \int_{\Gamma_3^L} \bar{p}_i^3 \bar{v}_i^{-I}\, d\Gamma + \int_{\Gamma_4^L} \bar{p}_i^4 \bar{v}_i^{-I}\, d\Gamma \end{aligned}$$

Therefore, adopting

$$B^{-I} = \frac{1}{C_l^{-I} - C_r^{-I}} = -\frac{2G}{\kappa+1}$$

$$B^{-II} = \frac{1}{C_l^{-II} - C_r^{-II}} = -\frac{2G}{\kappa+1}$$

and

$$B^{-III} = \frac{1}{C_l^{-III} - C_r^{-III}} = -\frac{G}{2}$$

and using local Cartesian coordinates instead of polar coordinates, we have that

$$\mathcal{K}_I = \sum_{i=1}^{2} \left[\int_{\Gamma_2^L} T_i^{(\boldsymbol{u})} v_i^{-I}\, d\Gamma - \int_{\Gamma_2^L} T_i^{(\boldsymbol{v}^{-I})} u_i\, d\Gamma + \int_{\Gamma_3^L} p_i^3 v_i^{-I}\, d\Gamma + \int_{\Gamma_4^L} p_i^4 v_i^{-I}\, d\Gamma \right] \tag{A.15}$$

Similarly, $\mathcal{K}_{II}$ and $\mathcal{K}_{III}$ can be computed using

$$\mathcal{K}_{II} = \sum_{i=1}^{2} \left[\int_{\Gamma_2^L} T_i^{(\boldsymbol{u})} v_i^{-II}\, d\Gamma - \int_{\Gamma_2^L} T_i^{(\boldsymbol{v}^{-II})} u_i\, d\Gamma + \int_{\Gamma_3^L} p_i^3 v_i^{-II}\, d\Gamma + \int_{\Gamma_4^L} p_i^4 v_i^{-II}\, d\Gamma \right] \tag{A.16}$$

$$\mathcal{K}_{III} = \int_{\Gamma_2^L} T_3^{(\boldsymbol{u})} v_3^{-III}\, d\Gamma - \int_{\Gamma_2^L} T_3^{(\boldsymbol{v}^{-III})} u_3\, d\Gamma + \int_{\Gamma_3^L} p_3^3 v_3^{-III}\, d\Gamma + \int_{\Gamma_4^L} p_3^4 v_3^{-III}\, d\Gamma \tag{A.17}$$

Although Eqs. (A.15)-(A.17) are exact, neither the solution $\boldsymbol{u}$ nor the corresponding traction $\boldsymbol{T}^{(\boldsymbol{u})}$ are known. Any approximation method can be used to obtain a numerical solution; in this study the Generalized Finite Element Method is adopted. The contours Γ_2^L, Γ_3^L and Γ_4^L are independent of meshes used to compute GFEM solutions. Thus, it may cross element boundaries where the tractions $\boldsymbol{T}^{(\boldsymbol{u})}$ have jumps if the GFEM is not accurate. The quadrature rules used in the evaluation of the above integrals must take this into account. Details about the numerical implementation of the CIM in 2-D can be found in [126].

One of the advantages of the CIM is the flexibility in choosing the size for the contour Γ_2^L. It does not have to be close to the crack front. In fact, it should be chosen outside the first layer of elements at the crack front. This is important because numerical solution close to the crack front are in general of lesser quality. This freedom of choosing the size of the external radius ρ_2 is demonstrated in the numerical examples presented in Section A.5. On the other hand, the curvature of the crack surface within the extraction domain should be small since the extraction functions from Eqs. (A.6),(A.7) and (A.8) are for planar crack surfaces.

A.3 The Cutoff Function Method

In this section, the integral identity (A.3)

$$\int_{\partial\Omega_s} T_k^{(\boldsymbol{v})} u_k\, d\Gamma - \int_{\Omega_s} \sigma_{kl,l}^{(\boldsymbol{v})} u_k\, d\Omega = \int_{\partial\Omega_s} T_i^{(\boldsymbol{u})} v_i\, d\Gamma$$

is used to derive the Cutoff Function Method for 3-D cracks. In this method, the extraction functions are built from the product of those used in the CIM, Eqns. (A.6), (A.7) and (A.8), and a smooth function–The cutoff function [6]

$$\bar{\phi}(r,z) = \bar{\phi}_r(r)\bar{\phi}_z(z)$$

Function $\bar{\phi}_r(r)$ is 1 near the crack front and zero, together with its first derivative, for $r \geqslant \rho_2$ and therefore on the boundary Γ_2. It has the following form [168]

$$\bar{\phi}_r(r) = \begin{cases} 1 & r \leqslant \rho_1 \\ 1 - 3(\frac{r-\rho_1}{\rho_2-\rho_1})^2 + 2\left(\frac{r-\rho_1}{\rho_2-\rho_1}\right)^3 & \rho_1 < r < \rho_2 \\ 0 & r \geq \rho_2 \end{cases}$$

Figure A.3 shows a plot of function $\bar{\phi}_r(r)$.

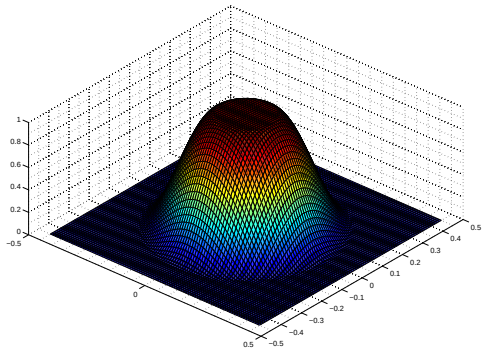

Figure A.3: *Function $\bar{\phi}_r(r)$ used in the definition of the cutoff function.*

Function $\bar{\phi}_z(z)$ is zero, together with its first derivative on the sub-domain boundaries Γ_5 and Γ_6. It is defined as follows [6]

$$\bar{\phi}_z(z) = \hat{\phi}_z[s(z)]$$

where

$$\hat{\phi}_z(s) = (1-s^2)^2$$

with s computed as follows,

$$s = \frac{2z - z_1 - z_2}{t}$$

where $t = z_2 - z_1$ is the thickness of the cylindrical extraction domain and z_1, z_2 are the z-coordinates of boundaries Γ_5 and Γ_6, respectively. A plot of this function is shown in Fig. A.4.

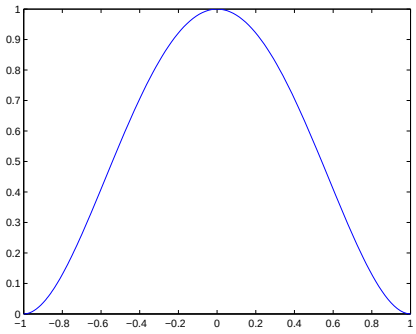

Figure A.4: *Function $\hat{\phi}_z(s)$ used in the definition of the cutoff function.*

The extraction functions used in the CFM are given by [168]

$$\bar{\boldsymbol{w}}^{-I}(r,\theta,z) = \bar{\boldsymbol{v}}^{-I}(r,\theta)\,\bar{\phi}_r(r)\,\bar{\phi}_z(z) \tag{A.18}$$

$$\bar{\boldsymbol{w}}^{-II}(r,\theta,z) = \bar{\boldsymbol{v}}^{-II}(r,\theta)\,\bar{\phi}_r(r)\,\bar{\phi}_z(z) \tag{A.19}$$

$$\bar{\boldsymbol{w}}^{-III}(r,\theta,z) = \bar{\boldsymbol{v}}^{-III}(r,\theta)\,\bar{\phi}_r(r)\,\bar{\phi}_z(z) \tag{A.20}$$

The extraction functions $\bar{\boldsymbol{w}}^{-I}$, $\bar{\boldsymbol{w}}^{-II}$ and $\bar{\boldsymbol{w}}^{-III}$ do not satisfy the equilibrium equations. In addition, the tractions corresponding to these functions are not zero on the crack faces. However, Identity (A.3) still holds for these functions. Let us consider first the boundary integrals from the left hand side of Eq. (A.3).

Let the tractions corresponding to $\bar{\boldsymbol{w}}^{-I}$, $\bar{\boldsymbol{w}}^{-II}$ and $\bar{\boldsymbol{w}}^{-III}$ be denoted by $\bar{\boldsymbol{T}}^{(\bar{\boldsymbol{w}}^{-I})}$, $\bar{\boldsymbol{T}}^{(\bar{\boldsymbol{w}}^{-II})}$ and $\bar{\boldsymbol{T}}^{(\bar{\boldsymbol{w}}^{-III})}$, respectively. On Γ_1, $\bar{\phi}(\rho_1,z) = \bar{\phi}_r(\rho_1)\bar{\phi}_z(z) = \bar{\phi}_z(z)$ and $d\bar{\phi}/dr(\rho_1,z) = 0$. Using this, it can be shown that on Γ_1,

$$\begin{aligned}
\bar{\boldsymbol{T}}^{(\bar{\boldsymbol{w}}^{-I})}|_{\Gamma_1} &= \bar{\phi}_z(z)\bar{\boldsymbol{T}}^{(\bar{\boldsymbol{v}}^{-I})}|_{\Gamma_1} \\
\bar{\boldsymbol{T}}^{(\bar{\boldsymbol{w}}^{-II})}|_{\Gamma_1} &= \bar{\phi}_z(z)\bar{\boldsymbol{T}}^{(\bar{\boldsymbol{v}}^{-II})}|_{\Gamma_1} \\
\bar{\boldsymbol{T}}^{(\bar{\boldsymbol{w}}^{-III})}|_{\Gamma_1} &= \bar{\phi}_z(z)\bar{\boldsymbol{T}}^{(\bar{\boldsymbol{v}}^{-III})}|_{\Gamma_1}
\end{aligned}$$

Thus, if contour Γ_1 is in the K-dominant region of the elasticity solution, where Eq. (A.5) holds,

$$\int_{\Gamma_1} \bar{T}_k^{(\bar{\boldsymbol{w}}^{-I})} \bar{u}_k \, d\Gamma = \int_{\Gamma_1} \bar{T}_k^{(\bar{\boldsymbol{w}}^{-I})} \bar{u}_k \, \rho_1 d\theta dz = \int_{\Gamma_1^L} \int_{z_1}^{z_2} \bar{T}_k^{(\bar{\boldsymbol{v}}^{-I})} \bar{\phi}_z(z) \bar{u}_k \, \rho_1 d\theta dz$$

$$= \int_{\Gamma_1^L} \bar{T}_k^{(\bar{\boldsymbol{v}}^{-I})} \bar{u}_k \, \rho_1 d\theta \int_{z_1}^{z_2} \bar{\phi}_z(z) dz$$

Let

$$\int_{z_1}^{z_2} \bar{\phi}_z(z) dz = \int_{-1}^{1} \hat{\phi}_z(s) \frac{t}{2} ds = \frac{t}{2} \int_{-1}^{1} (1-s^2)^2 \, ds = \frac{t}{2} \frac{16}{15} = C_z$$

From the above and Eqs. (A.9), (A.10) we then have that

$$\int_{\Gamma_1} \bar{T}_k^{(\bar{\boldsymbol{w}}^{-I})} \bar{u}_k \, d\Gamma = C_l^{-I} C_z B^{-I} \mathcal{K}_I \tag{A.21}$$

$$\int_{\Gamma_1} \bar{T}_k^{(\bar{\boldsymbol{w}}^{-II})} \bar{u}_k \, d\Gamma = C_l^{-II} C_z B^{-II} \mathcal{K}_{II} \tag{A.22}$$

$$\int_{\Gamma_1} \bar{T}_k^{(\bar{\boldsymbol{w}}^{-III})} \bar{u}_k \, d\Gamma = C_l^{-III} C_z B^{-III} \mathcal{K}_{III} \tag{A.23}$$

Also, from Eqs. (A.12), (A.13) and (A.14), we have that

$$\int_{\Gamma_1} \bar{T}_i^{(\bar{\boldsymbol{u}})} \bar{w}_i^{-I} \, d\Gamma = C_r^{-I} C_z B^{-I} \mathcal{K}_I \tag{A.24}$$

$$\int_{\Gamma_1} \bar{T}_i^{(\bar{\boldsymbol{u}})} \bar{w}_i^{-II} \, d\Gamma = C_r^{-II} C_z B^{-II} \mathcal{K}_{II} \tag{A.25}$$

$$\int_{\Gamma_1} \bar{T}_i^{(\bar{\boldsymbol{u}})} \bar{w}_i^{-III} \, d\Gamma = C_r^{-III} C_z B^{-III} \mathcal{K}_{III} \tag{A.26}$$

On Γ_2, $\bar{\phi}_r(\rho_2) = 0$ and $d\bar{\phi}/dr(\rho_2, z) = 0$. In addition, on Γ_5, $\bar{\phi}_z(1) = 0$ and $d\bar{\phi}_z/dz(1) = 0$; also on Γ_6, $\bar{\phi}_z(-1) = 0$; and $d\bar{\phi}_z/dz(-1) = 0$. Therefore, it can be shown that

$$\bar{T}^{(\bar{\boldsymbol{w}}^{-I})}|_{\Gamma_2} = \bar{T}^{(\bar{\boldsymbol{w}}^{-II})}|_{\Gamma_2} = \bar{T}^{(\bar{\boldsymbol{w}}^{-III})}|_{\Gamma_2} = 0$$

and

$$\bar{T}^{(\bar{\boldsymbol{w}}^{-I})}|_{\Gamma_{5\cup 6}} = \bar{T}^{(\bar{\boldsymbol{w}}^{-II})}|_{\Gamma_{5\cup 6}} = \bar{T}^{(\bar{\boldsymbol{w}}^{-III})}|_{\Gamma_{5\cup 6}} = 0$$

From Eq. (A.3) and the above, using local Cartesian coordinates instead for polar coordinates, and assuming stress-free crack faces

$$C_l^{-I} C_z B^{-I} \mathcal{K}_I + \int_{\Gamma_3} T_k^{(\boldsymbol{w}^{-I})} u_k \, d\Gamma + \int_{\Gamma_4} T_k^{(\boldsymbol{w}^{-I})} u_k \, d\Gamma - \int_{\Omega_s} \sigma_{kl,l}^{(\boldsymbol{w}^{-I})} u_k \, d\Omega = C_r^{-I} C_z B^{-I} \mathcal{K}_I$$

Taking,

$$B^{-I} = \frac{1}{C_l^{-I} - C_r^{-I}} * \frac{1}{C_z} = -\frac{2G}{\kappa+1} * \frac{2}{t} * \frac{15}{16}$$

$$B^{-II} = \frac{1}{C_l^{-II} - C_r^{-II}} * \frac{1}{C_z} = -\frac{2G}{\kappa+1} * \frac{2}{t} * \frac{15}{16}$$

$$B^{-III} = \frac{1}{C_l^{-III} - C_r^{-III}} \frac{1}{C_z} = -\frac{G}{2} * \frac{2}{t} * \frac{15}{16}$$

as before;

$$\mathcal{K}_I = \int_{\Omega_s} \sigma_{kl,l}^{(\boldsymbol{w}^{-I})} u_k \, d\Omega - \int_{\Gamma_3} T_k^{(\boldsymbol{w}^{-I})} u_k \, d\Gamma - \int_{\Gamma_4} T_k^{(\boldsymbol{w}^{-I})} u_k \, d\Gamma \tag{A.27}$$

Similarly, for $\mathcal{K}_{II}$ and $\mathcal{K}_{III}$, we have that

$$\mathcal{K}_{II} = \int_{\Omega_s} \sigma_{kl,l}^{(\boldsymbol{w}^{-II})} u_k \, d\Omega - \int_{\Gamma_3} T_k^{(\boldsymbol{w}^{-II})} u_k \, d\Gamma - \int_{\Gamma_4} T_k^{(\boldsymbol{w}^{-II})} u_k d\Gamma \tag{A.28}$$

$$\mathcal{K}_{III} = \int_{\Omega_s} \sigma_{kl,l}^{(\boldsymbol{w}^{-III})} u_k \, d\Omega - \int_{\Gamma_3} T_k^{(\boldsymbol{w}^{-III})} u_k \, d\Gamma - \int_{\Gamma_4} T_k^{(\boldsymbol{w}^{-III})} u_k \, d\Gamma \tag{A.29}$$

The idea of using the extraction functions (A.18), (A.19) and (A.20), instead of (A.6), (A.7) and (A.8), is to get rid of the integrals on Γ_2 that appear in the expressions for the contour integral method (Cf Eqs. (A.15), (A.16) and (A.17)). As a consequence, the expressions for $\mathcal{K}_I$, $\mathcal{K}_{II}$ and $\mathcal{K}_{III}$ given above do not contain terms related to the derivative of the solution $\boldsymbol{u}$.

A.4 Smoothing of 3-D SIFs

Errors in Stress Intensity Factors (SIFs) extracted along the crack front lead to perturbations in the predicted crack front geometry. Such perturbations, hereafter referred to as noise, can accumulate throughout a crack growth simulation resulting in an inaccurate approximation of the crack surface shape. The stress intensity factor for each mode in a 3-D analysis is a continuous and smooth function defined along the crack front. However, SIFs are typically extracted at discrete points along the crack front, namely at crack front vertices. These values are extracted independently at each vertex and may show some noise in their values. The intensity of the noise depends on the amount of mesh refinement along the front, enrichment functions adopted and the quality of the crack front representation. Numerical noise is common in problems with a dominant mode. The extracted SIFs for the other modes usually oscillate around zero and introduce perturbations in the predicted crack front geometry.

Noise in SIFs can be dealt with by extracting the SIFs *functions* directly instead of their discrete values as proposed in [122]. An alternative approach to control the noise of extracted SIFs is using the Moving Least Squares Method (MLSM) method similar to the one presented in Section 6.3.

Similarly as done in Section 6.3, consider a MLSM approximation of a SIF function defined along the crack front $K(s) : \Gamma_c \rightarrow \Re$. Let it be a continuous function that represents the stress intensity factor of Mode *I*, *II* or *III* along a crack front Γ_c. The stress intensity factor values $K^L \equiv K(s_L)$, $L = 1,...,N$, are assumed to be known at crack front vertices $s_L \in \Gamma_c$, where N is the number of vertices on the crack front and s is a parametric coordinate along the crack front.

With a similar derivation as the one presented in Section 6.3, a local and global approximations can be computed and are written as,

$$\begin{aligned} L_{\bar{s}}K(s) &= \sum_{k=1}^{n} a_k^*(\bar{s})\, P_k(s) \\ &= \sum_{L}^{N}\sum_{j}^{n}\sum_{k}^{n} P_k(s)\, A_{kj}^{-1}(\bar{s})\, B_{jL}(\bar{s})\, K^L \end{aligned}$$

$$GK(\bar{s}) = L_{\bar{s}}K(\bar{s}) = \sum_{k=1}^{n} a_k^*(\bar{s})\, P_k(\bar{s}) \quad \forall \bar{s} \in \Gamma_c$$
$$= \sum_{L}^{N}\sum_{j}^{n}\sum_{k}^{n} P_k(\bar{s})\, A_{kj}^{-1}(\bar{s})\, B_{jL}(\bar{s})\, K^L$$

with a weight functions, $W_L,\ L = 1, ldots, N$, and the basis, $\{P_k\}_{k=1}^{n}$, of the MLSM approximation.

This approach provides a continuous and smooth approximation of SIF functions for each fracture mode. It allows the evaluation of SIFs at any point along the crack front, including front vertices where the extraction is difficult. This is the case, for example, at the intersection between a crack front and a 3-D domain boundary.

A.5 Numerical Examples

A.5.1 Plate with Inclined Crack

Static Crack Analysis: This example consists of a rectangular plate with a through the thickness inclined crack. The geometry of the domain and boundary conditions for the problem are illustrated in Fig. A.5. The plate dimensions are $b = 2.0$, $h = 2.0$, $t = 0.25$ and crack size is $2a = 0.5$. Linear elastic material properties are assumed with Youngs modulus $E = 200,000$ and Poissons ratio $= 0.30$. The crack surface has an inclination $\alpha = \pi/4$ rad with respect to the lower edge of the plate. Boundary conditions consist of tractions of magnitude $\sigma = 1.0$ applied at the top and bottom edges of the plate. Stress intensity factors for all modes are extracted using the Contour Integral Method.

In order to study the convergence of SIFs values, the problem is solved four times using GFEM shape functions of degree $p = 1,2,3,4$. Furthermore, Heaviside and branch functions are used as enrichments to represent the discontinuity and singularity created by the presence of the crack. The same mesh is used in all cases. The smallest edge of elements along the crack front, l_{min}, is in the range $0.0039 < l_{min} < 0.0078$.

Figure A.6 shows extracted raw $\mathcal{K}_I$ values at crack front vertices using the CIM with extraction

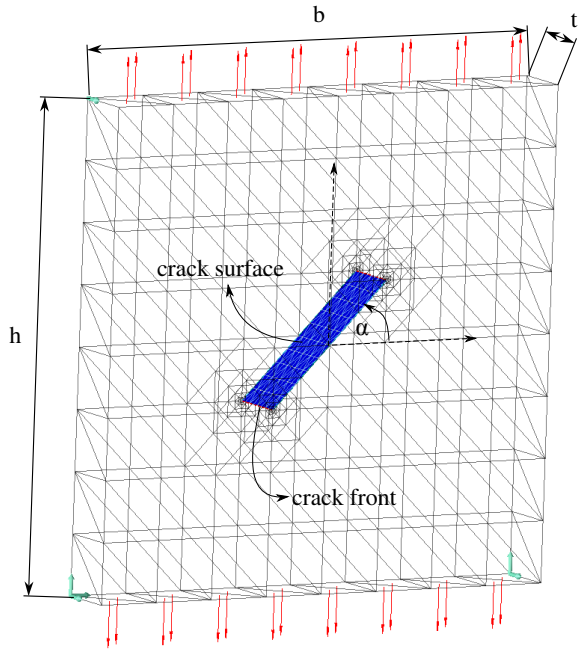

Figure A.5: *Problem description for the case of stress-free crack surface.*

radius $r = \rho = 0.019$ and GFEM shape functions of degree $p = 1,2,3,4$. The figure also shows MLSM approximations for all cases. The horizontal axis in the plot corresponds to the crack front position. to $t = 0.25$. Notice that there are no extracted values at crack front ends since it is difficult to guarantee that the extraction contour Γ_2^L shown in Fig. A.2 is inside the solution domain when extracting at crack front ends. The MLSM is used to obtain an approximation at these points. Another benefit of using the MLSM is to smooth out oscillatory values extracted from low order GFEM approximation, like the case $p = 1$ shown in the figure. Hereafter, all SIF plots are based on MLSM approximations. These approximations are also used in the computation of crack front propagation parameters as described later.

Figure A.7 shows the SIFs (after MLSM) for Modes *I* and *II* for all cases. Fast convergence can be observed. The extracted values for $p = 2,3,4$ are almost identical.

To investigate the robustness of the CIM method, the case with polynomial order $p = 3$ is solved again with different extraction radius r. Figure A.8 shows the SIFs results along the crack front. Only Modes *I* and *II* are plotted; Mode *III* its omitted because its not present in this problem.

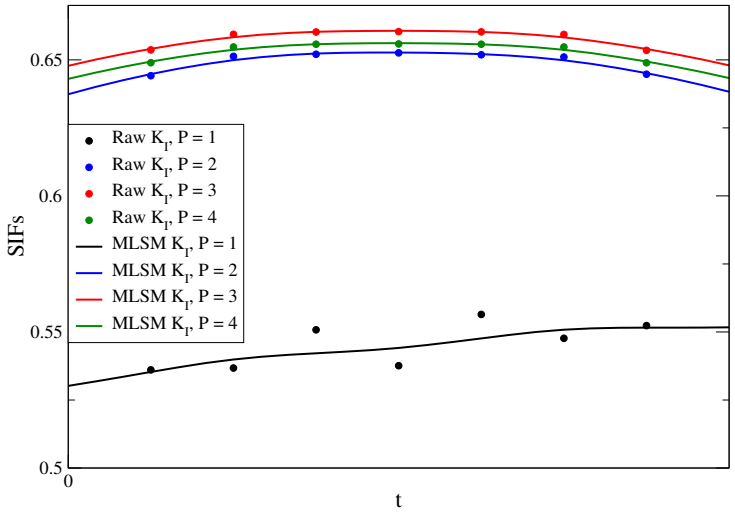

Figure A.6: *Extracted $\mathcal{K}_I$ values at crack vertices and MLSM approximation for different polynomial order of GFEM shape functions.*

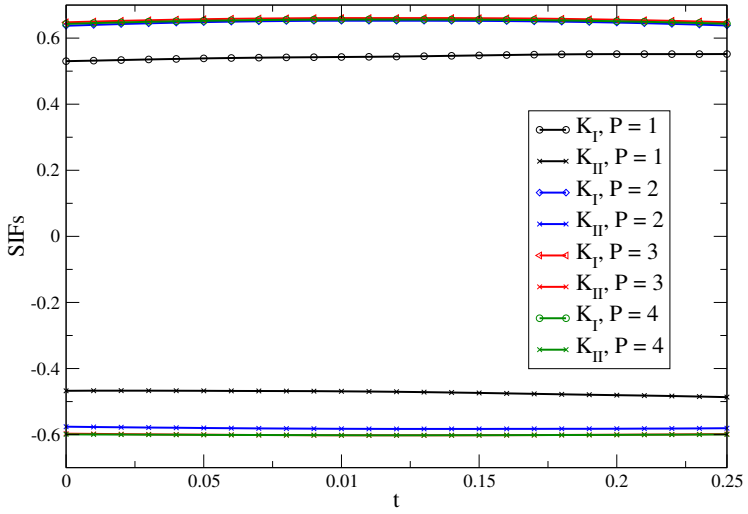

Figure A.7: *Stress intensity factors along the crack front for different polynomial order of GFEM shape functions.*

Because of the symmetry of the problem, only the upper crack front SIFs are presented. Extracted SIFs values using the CIM show a low dependence on r values (less than 2%).

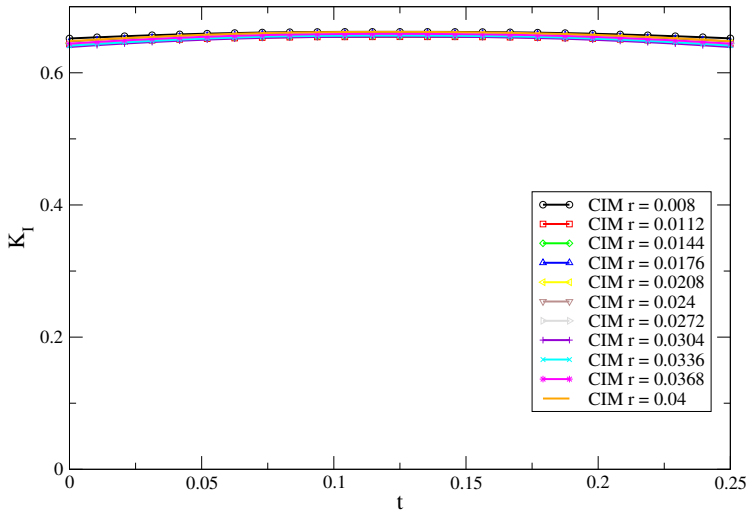

(a) $\mathcal{K}_I$

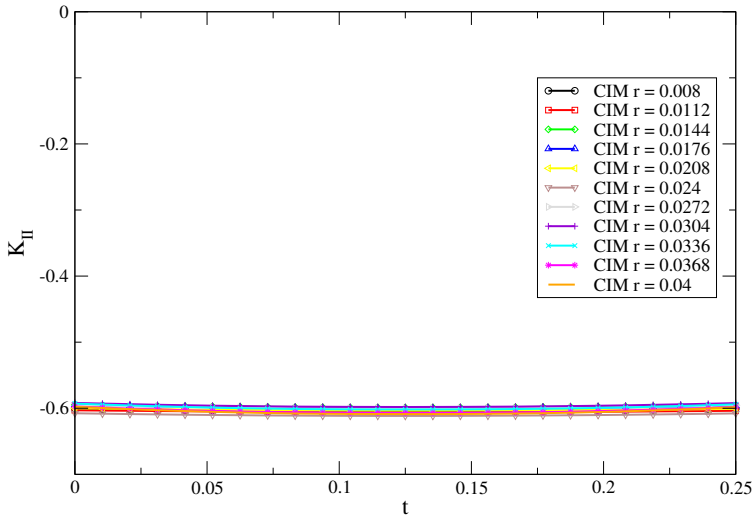

(b) $\mathcal{K}_{II}$

Figure A.8: *Stress intensity factors extracted using the CIM method. Variation of radius of extraction domain r.*

Fatigue Crack Propagation: The propagation of the crack shown in Fig. A.5 is considered in this section. The plate is subjected to a cyclic tensile load of maximum and minimum magnitudes $\sigma_{max} = 1.0$ and $\sigma_{min} = 0.0$, respectively, along the direction shown in Fig. A.5. The simulation consists of propagating the crack surface until it reaches the boundary of the domain. At every propagation step, extraction of SIFs is performed with the CIM and used for the prediction of the direction of crack front propagation using Shollmann's criterion [151]. In this problem, Modes *I* and *II* are present and therefore a non-planar propagation is expected. Figure A.9 shows the crack surface evolution while Fig. A.10 shows contour plots of von Mises stress. Figure A.11 shows the SIFs values for the initial and final crack propagation steps. The plots show that while $\mathcal{K}_I$ increases, $\mathcal{K}_{II}$ decreases until it becomes nearly zero.

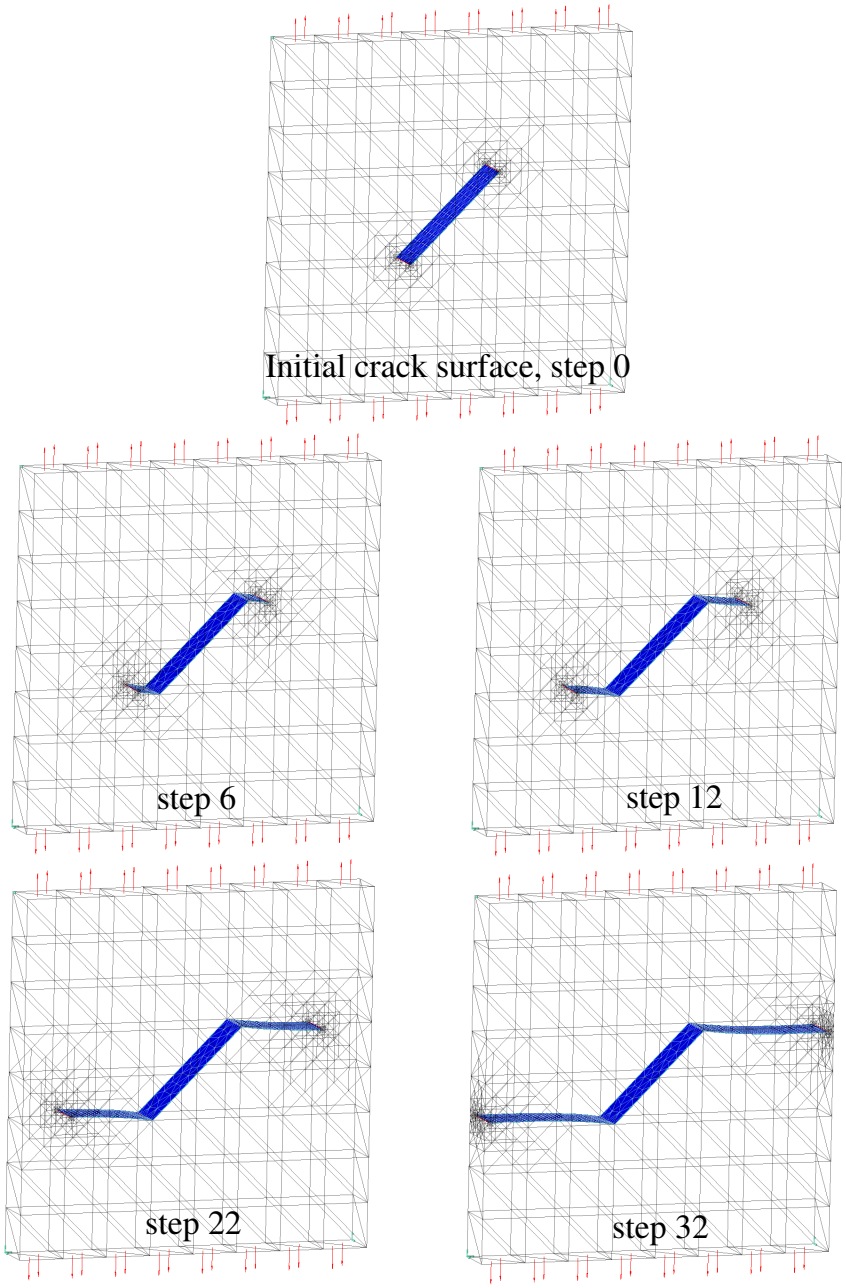

Figure A.9: *Evolution of the through-the-thickness crack surface.*

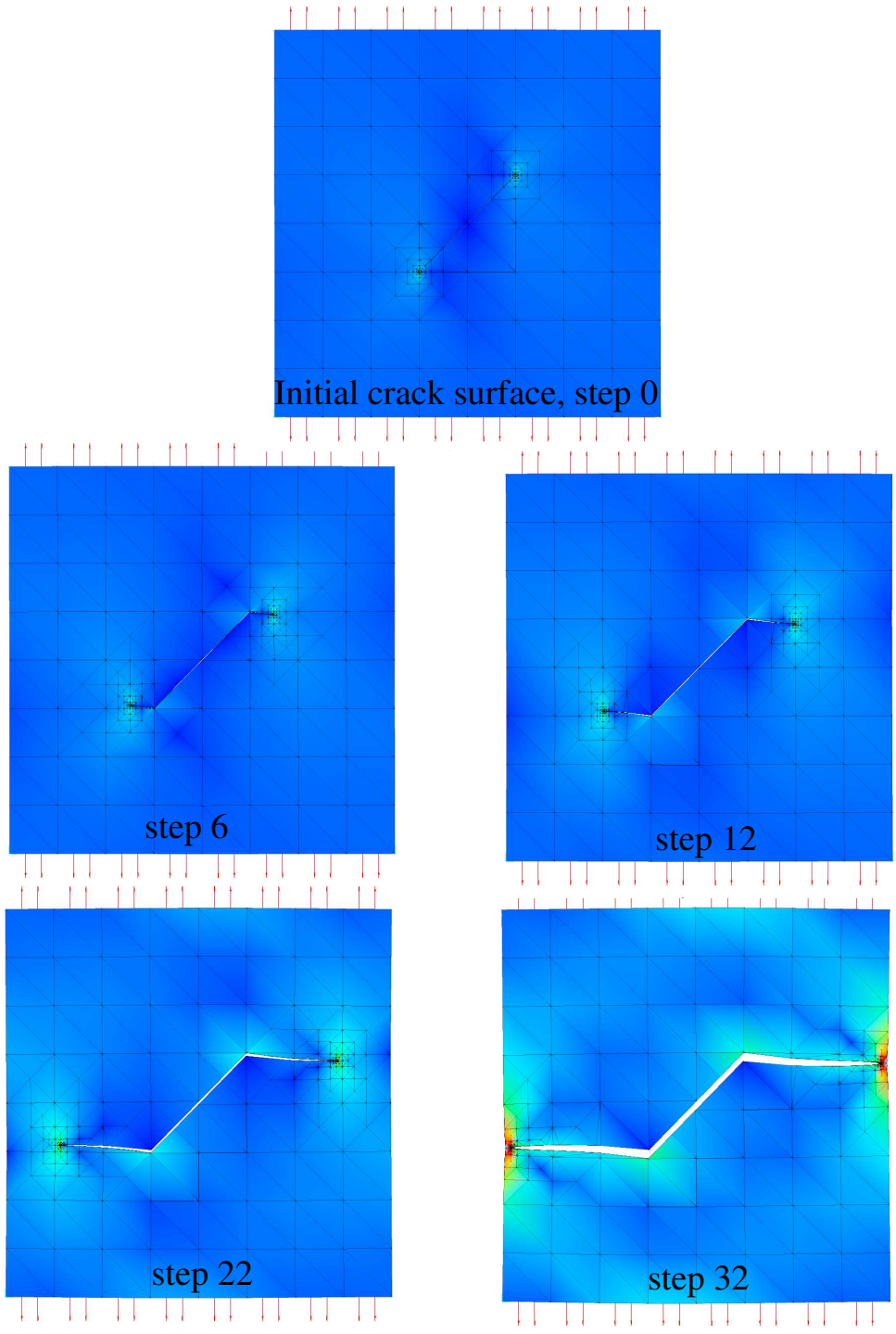

Figure A.10: *Contour plot of von Mises stress and deformed configuration at several crack propagation steps.*

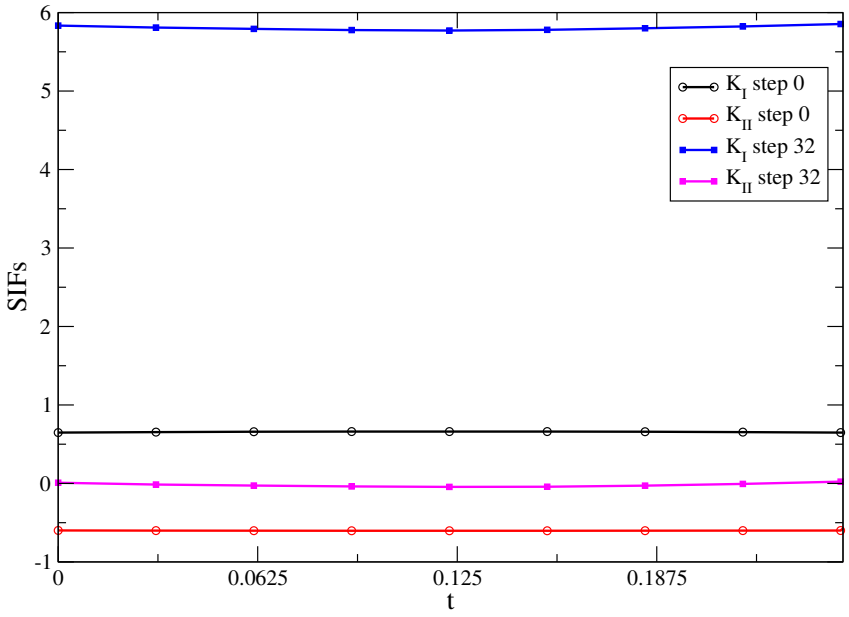

Figure A.11: *Stress intensity factors for initial and final crack steps.*

A.5.2 Pressurized Crack

Static Crack Analysis: In this section, the previous example is again considered but with a change in boundary conditions. No tractions are applied on the exterior faces of the plate. Instead, a pressure of magnitude $p = 0.5$ is applied on the crack faces. The GFEM mesh and boundary conditions are illustrated in Fig. A.12.

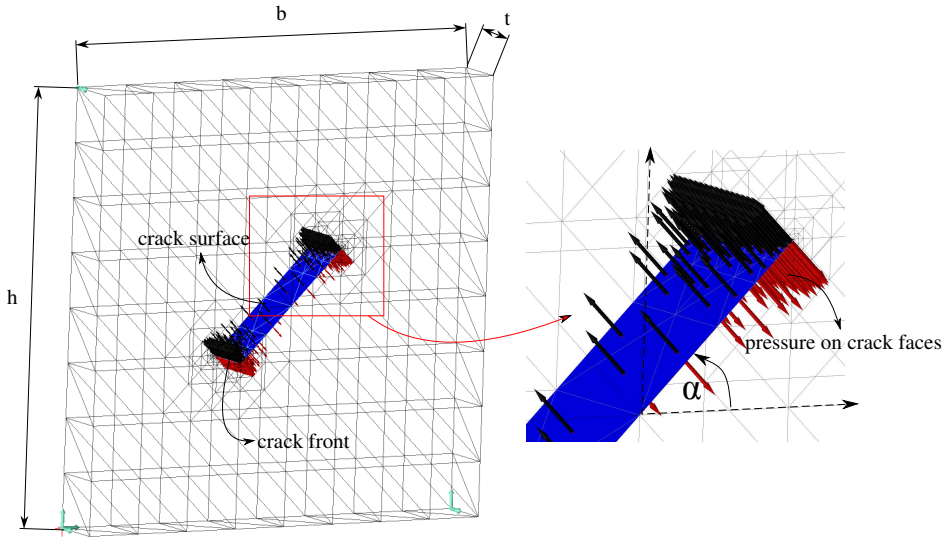

Figure A.12: *Problem description for the case of pressure on crack faces.*

A SIF convergence study similar to the one in previous section is performed for this problem. The same mesh and enrichments as in the previous example are adopted. Figure A.13 shows the Mode I and II SIFs extracted with the CIM for different polynomial orders of GFEM shape functions. Figure A.14 shows the values of $\mathcal{K}_I$ extracted at the center of the crack front for the discretizations with $p = 1,2,3,4$. The values of $\mathcal{K}_I$ from the previous example are also shown in the figure. A fast and nearly monotonic convergence is observed in both problems.

A robustness study for the CIM extraction method is again performed. Figure A.15 shows the SIFs for different values of extraction radius r. Only Mode I SIF is plotted; SIFs for Modes II and III are omitted because they are zero. As observed in the previous example, the SIF values extracted using the CIM show a very low dependence on the size of the extraction radius r (less

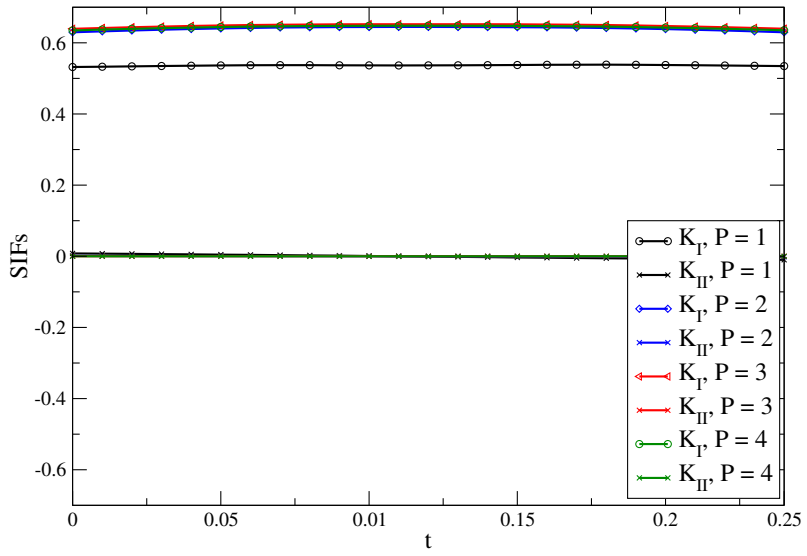

Figure A.13: *Stress intensity factors extracted along the crack front with the CIM for different polynomial orders of GFEM shape functions.*

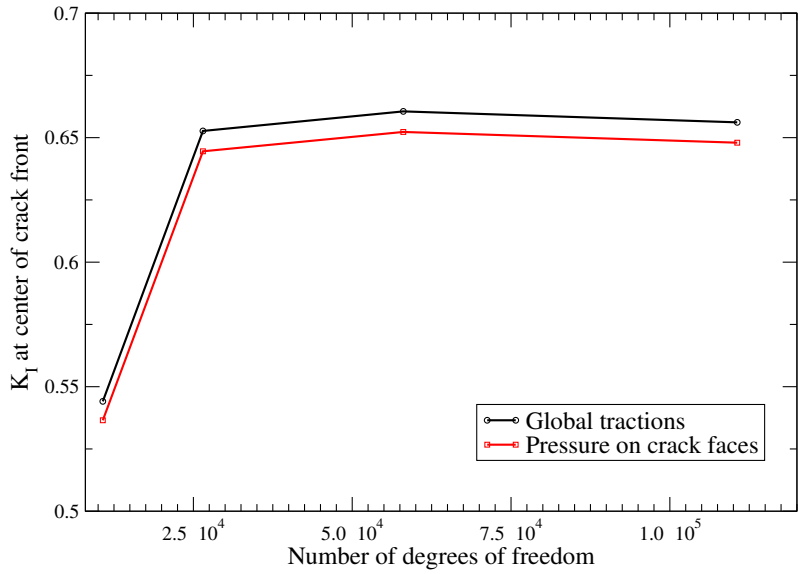

Figure A.14: *Convergence of $\mathcal{K}_I$ at the center of the crack front for the discretizations with $p = 1,2,3,4$. The values of $\mathcal{K}_I$ from the previous example are also shown in the figure.*

than 2%).

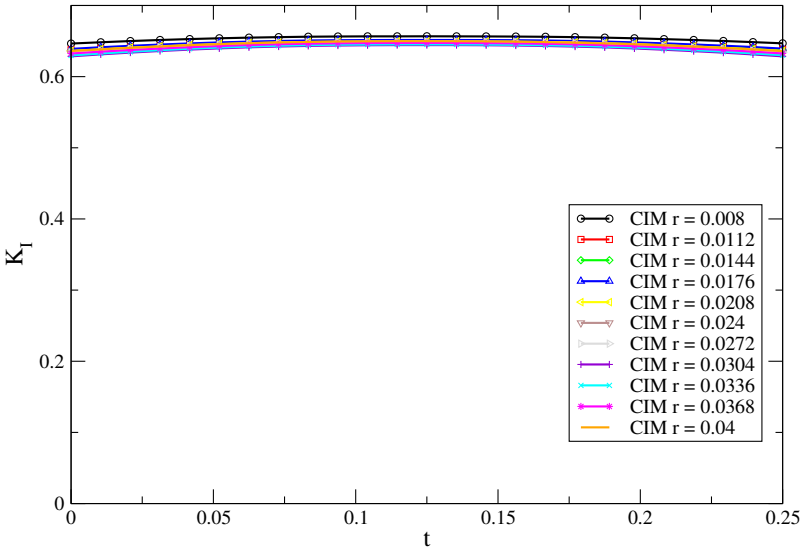

Figure A.15: *Stress intensity factor $\mathcal{K}_I$ extracted using the CIM method; Variation of radius of extraction domain r.*

Fatigue Crack Propagation: The crack faces are subjected to a uniform cyclic pressure load of maximum and minimum magnitudes $\sigma_{max} = 0.5$ and $\sigma_{min} = 0.0$, respectively, As done in the previous example, the crack propagation is carried out until the surface has reached the boundary of the domain. At every propagation step, extraction of SIFs is performed with the CIM and used for the prediction of the direction of crack front propagation using Shollmann's criterion [151]. Figures A.16 and A.17 show the crack surface evolution and contour plots of von Mises stress.

Different propagation paths are observed in these two last examples, due to the different boundary condition considered. The previous example starts as a mixed mode problem and the crack front quickly turns and grows toward a plane perpendicular to the applied tractions. At the end of the simulation it becomes a pure Mode *I* problem. On the other hand, this example is a Mode *I* problem from the start, because the pressure applied on the crack faces is perpendicular to the plane of the crack. Therefore the crack surface grows on the same plane the entire simulation.

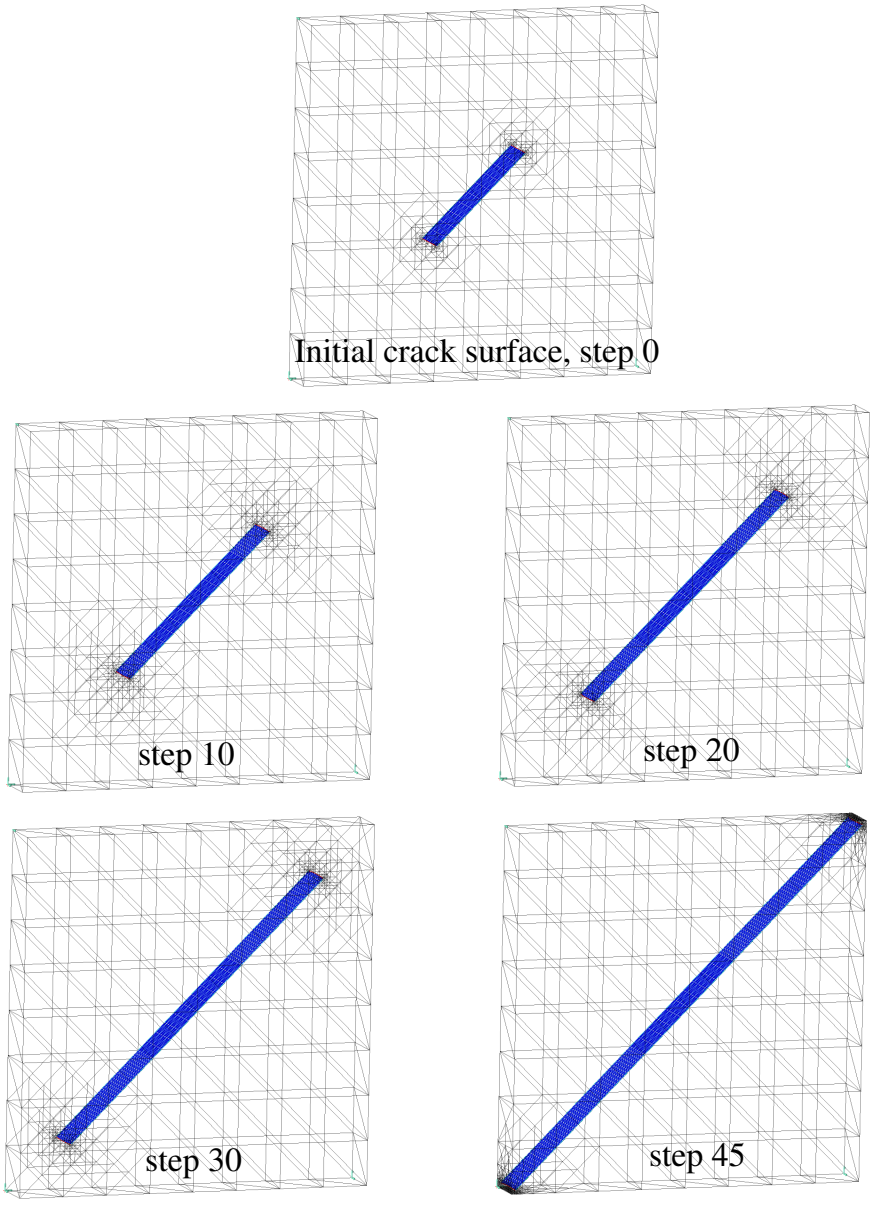

Figure A.16: *Evolution of pressurized crack surface.*

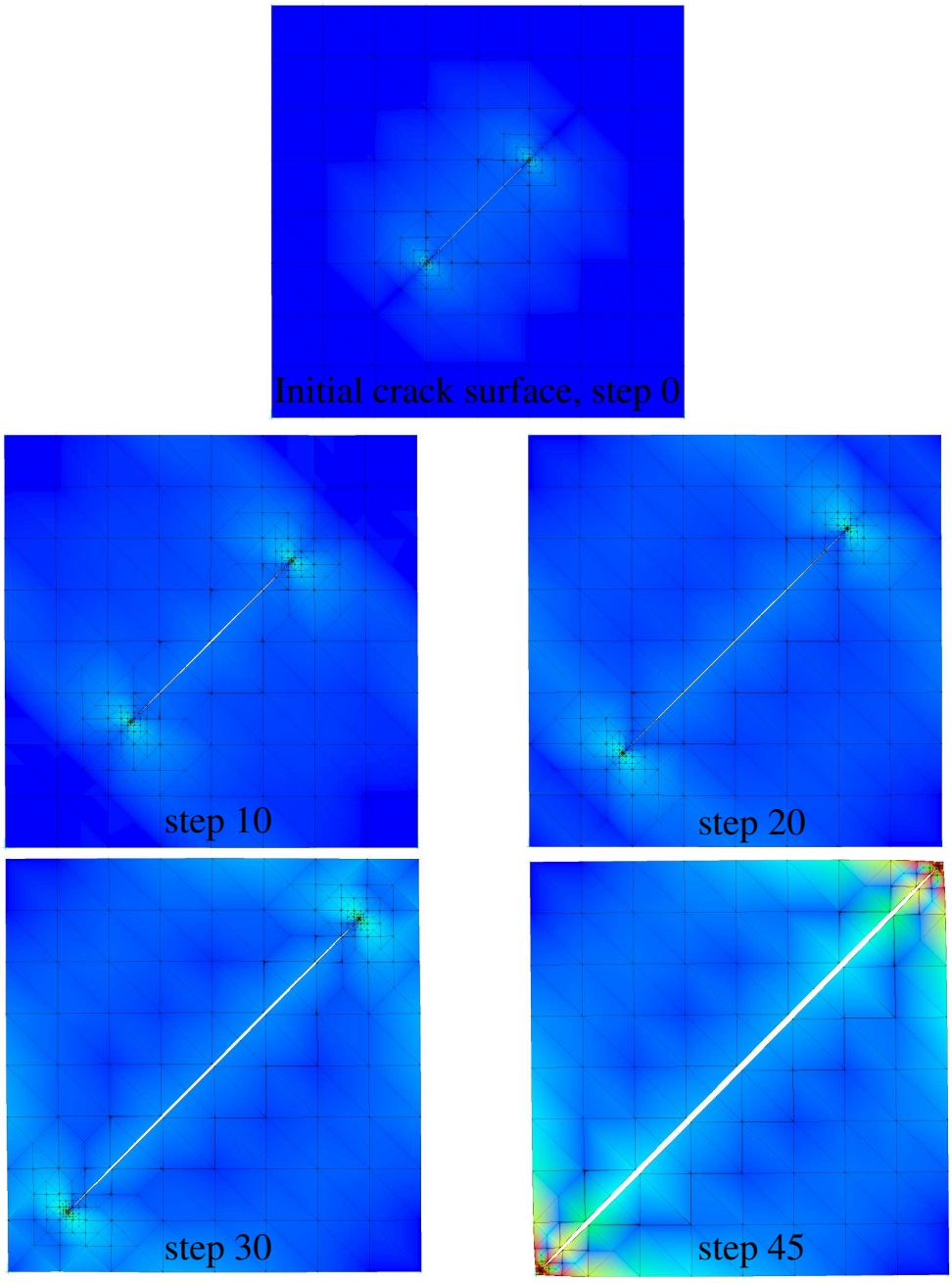

Figure A.17: *Contour plot of von Mises stress for the case of crack with pressure on crack faces.*

A.5.3 Inclined Elliptical Crack

Static Crack Analysis: This problem is presented in Section 4.3.3 and repeated here to show details of the extraction of SIFs. Consider an elliptical crack surface inserted into an elastic cube. The crack surface has an inclination of 30° with respect to the horizontal axis. The ratio between the minor and major axes of the crack surface is $\frac{a}{c} = \frac{9}{15}$. The cube dimension is taken as $\frac{b}{c} = \frac{40}{3}$. Details are shown in Fig. A.18.

The linear elastic material properties are taken as Young Modulus $E = 1.0$ and Poisson's ration $v = 0.25$. The cube is loaded by tractions of magnitude $\sigma = 1.0$ and normal to the top and bottom surfaces of the cube.

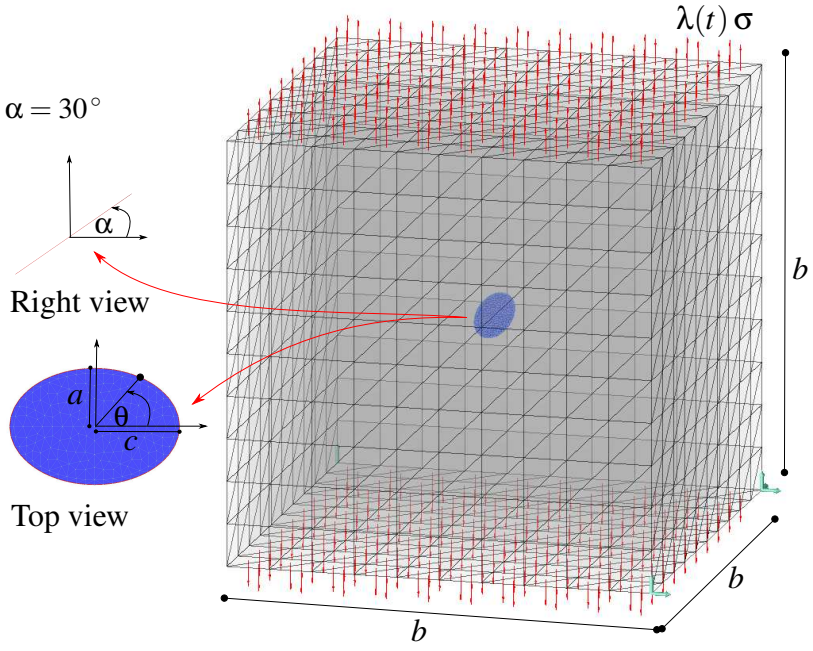

Figure A.18: *Geometrical details of elliptical crack problem.*

The SIFs for Modes I, II, and III are extracted using the CFM and CIM methods presented in previous sections. The Generalized Finite Element Method with second order polynomial enrichments is adopted. Additionally, Heaviside and branch functions are used as enrichments to represent the discontinuity and singularity created by the presence of the crack. Details about GFEM enrichments for 3-D fracture problems can be found in Section 4.2.1 Automatic local mesh refinement is performed such that the ratio between the smallest edge of elements along the crack

front, l_{min} and the semi-major axis of the crack surface, c, is in the range $0.018 < \frac{l_{min}}{c} < 0.030$. Figure A.19 shows details about the refinement close to the crack front.

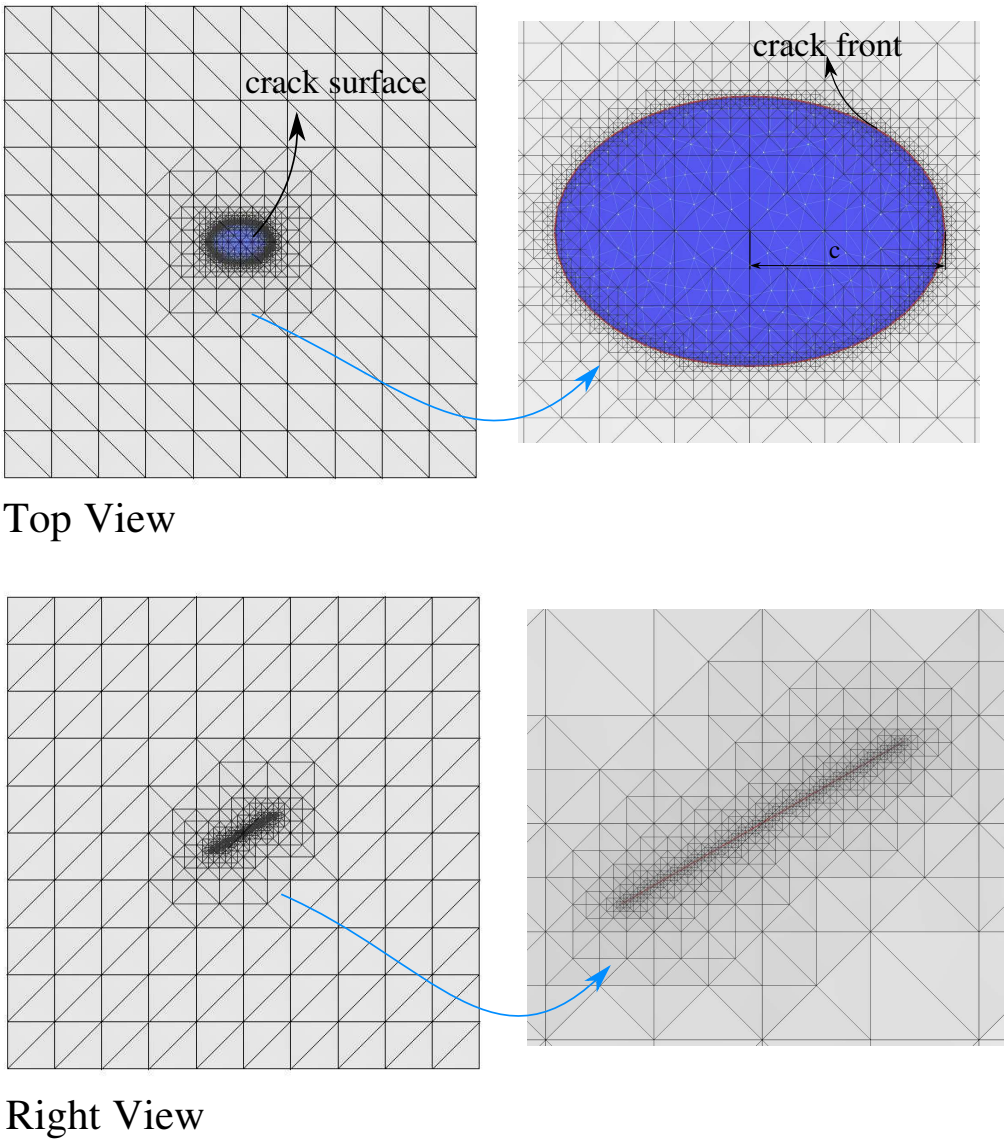

Figure A.19: *Details of local refinement along the crack front. The ratio between the smallest edge of elements along the crack front, l_{min}, and the semi-major axis of the crack surface, c, is in the range* $0.018 < \frac{l_{min}}{c} < 0.030$.

For the CFM method, two radii of extraction ($r_1 = \rho_1$ and $r2 = \rho_2$) are specified. r_1 defines the inner radius of the extraction domain. It should be within the K-dominant region of the elastic solution but should be large enough such that it is outside of the first layer of elements at the crack front. r_2 defines the outer radius of the extraction domain and it can be much larger than r_1 as

long as the crack surface is nearly planar within the extraction domain. It should also avoid the influence of other portions of a 3-D crack front within the extraction domain. Similar care must be taken when dealing with multiple interacting cracks. Figures A.20(a)-A.20(c) show the stress intensity factors extracted using the CFM for different values of r_1 while keeping r_2 constant. Figures A.21(a) - A.21(c) show SIFs extracted with the CFM for a constant r_1 and different values of r_2. The extracted values are compared to with the analytical solution for an infinite domain [170]. SIFs are normalized using Equation (4.38).

For the CIM method only one radius of extraction (r) is needed. As mentioned before, r can be large. Here, we choose it large enough such that it is outside the first layer of elements at the crack front. Figures A.22(a)-A.22(c) show the stress intensity factors extracted using the CIM for different values of r.

Excellent accuracy is observed for SIFs extracted with both the CIM and CFM. The methods show low sensitivity to the size of extraction radius provided some basic guidelines are observed. The inner radius used in the CFM, r_1, should be small enough such that the interior surface of the extraction domain, Γ_1, is in the K-dominant region of the elasticity solution. The outer radius, r_2, and the extraction radius used in the CIM may be much larger than r_1. However, the crack surface should be nearly planar within the extraction domain. Radius r_2 should be such that it avoids the influence of other portions of a 3-D crack front within the extraction domain. There is no constraint in the shape of the crack front. As with any extraction method in 3-D, performing the computations for several sizes of the extraction domain provides information on how the SIFs converge as the domain change.

The implementation and computational cost of the CIM is much simpler than the CFM since it involves 1-D integrals instead of the 3-D integrals required by the CFM. Based on this, the numerical results presented, and the requirement of selecting a single parameter for the extraction domain definition, we recommend the use of the CIM over the CFM. We have also shown that the CIM can handle without difficulties the case of crack faces loaded by prescribed tractions.

The use of the Moving Least Squares Method provides a continuous and smooth approximation

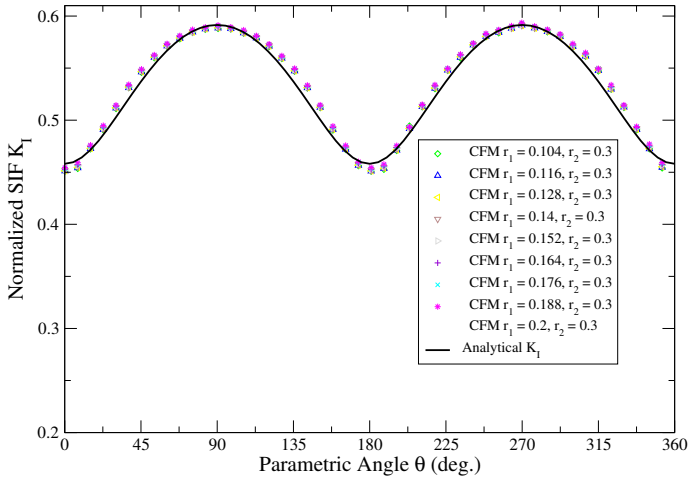

(a) $\mathcal{K}_I$

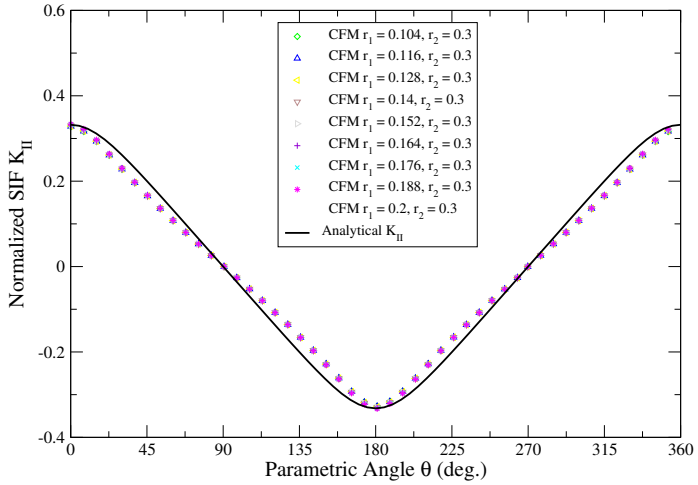

(b) $\mathcal{K}_{II}$

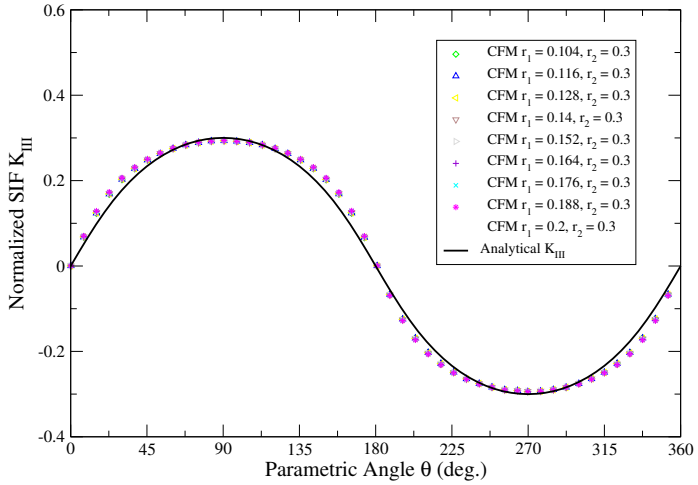

(c) $\mathcal{K}_{III}$

Figure A.20: *Stress intensity factors extracted using the CFM method. Variation of inner radius of extraction domain r_1. In all cases, r_1 is taken larger than the smallest edge of elements along the crack front, l_{min}, and $r_2 = 0.3$.*

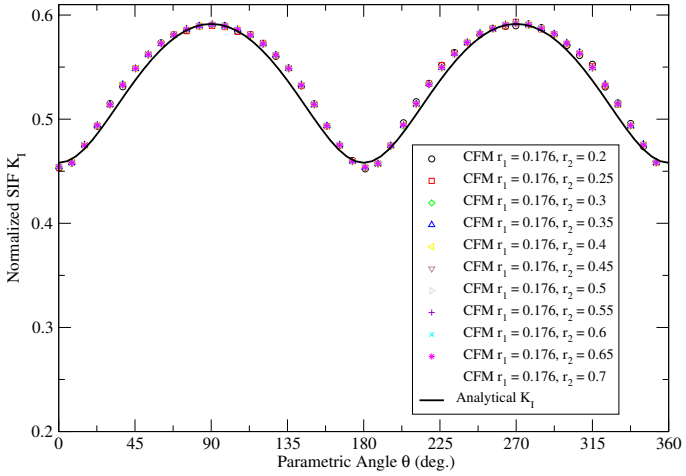

(a) $\mathcal{K}_I$

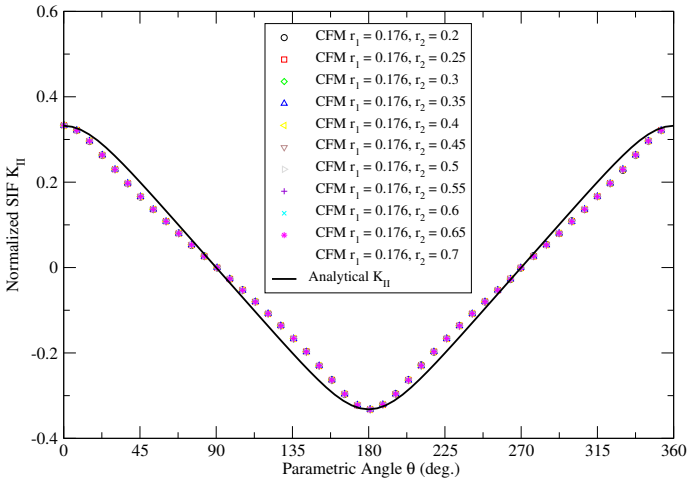

(b) $\mathcal{K}_{II}$

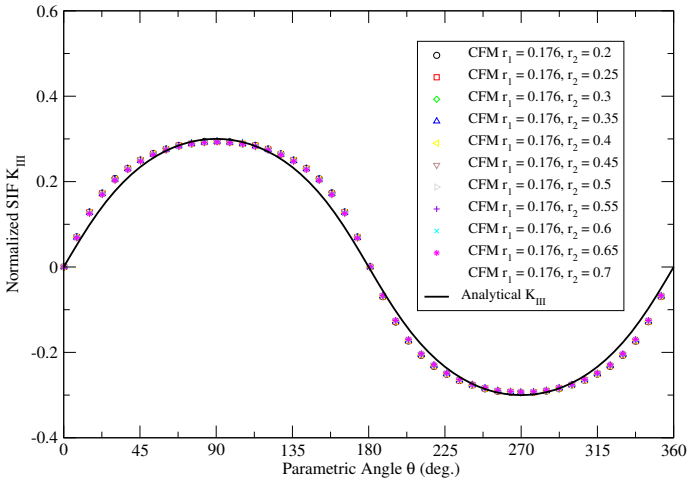

(c) $\mathcal{K}_{III}$

Figure A.21: *Stress intensity factors extracted using the CFM method. Variation of outer radius of extraction domain r_2. In all cases, $r_1 = 0.176$ is adopted.*

of 3-D SIF functions for each fracture mode. It can be used with any method that extracts SIFs point-wise along the crack front, instead of the SIF function directly as proposed in [122]. Its computational cost is low and our experience with this approach has shown that it is quite robust.

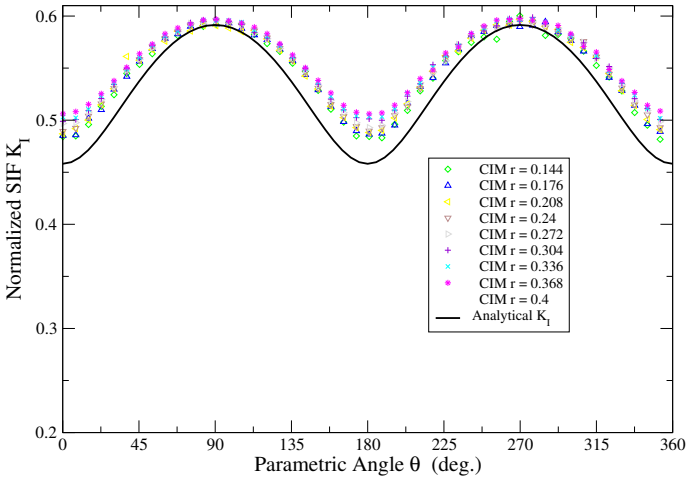

(a) $\mathcal{K}_I$

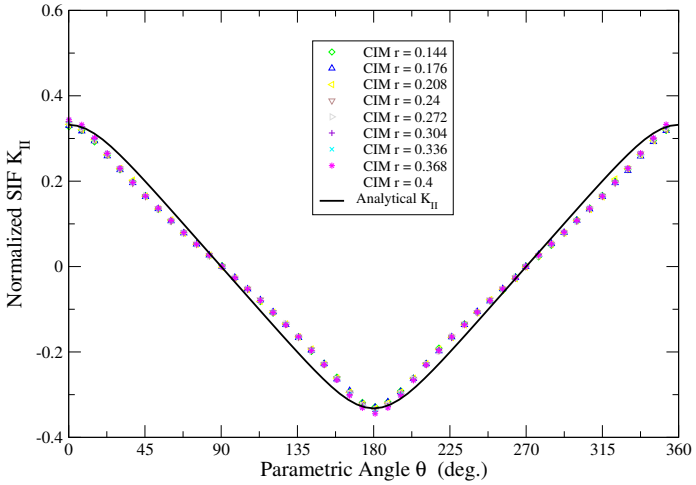

(b) $\mathcal{K}_{II}$

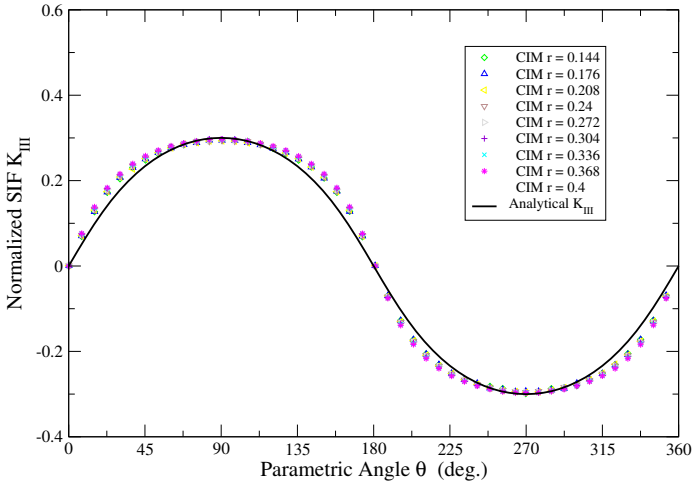

(c) $\mathcal{K}_{III}$

Figure A.22: *Stress intensity factors extracted using the CIM method. Variation of radius of extraction domain r. In all cases, r is taken larger than the smallest edge of elements along the crack front,* l_{min}.

References

[1] CGAL, Computational Geometry Algorithms Library. http://www.cgal.org.

[2] I. Abaqus. Abaqus user's manual. *ABAQUS Ine, Dassault Systèmes, Rhode Island, USA*, 2007.

[3] Federal Aviation Administration(FAA). Advisory circular: Airport pavement design for boeing 777 airplane. Technical Report AC No. 150/5320-16, Department of Transportation, Washington, DC, 1995.

[4] O. Ayhan Ali. Mixed mode stress intensity factors for deflected and inclined corner cracks in finite-thickness plates. *IJF*, 29:305–317, 2007.

[5] T.L. Anderson. *Fracture mechanics: fundamentals and applications*. CRC Press LLC, 1994.

[6] B. Andersson, I. Babuška, and U. Falsk. Accurate and reliable determination of edge and vertex stress intensity factors in three-dimensional elastomechanics. In *Proceedings 17th Congress of the International Council of the Aeronautical Sciences*, volume ICAS-90-4.9.2, pages 1730–1746, 1990.

[7] I. Ansys. Ansys user's manual. *ANSYS Inc., Southpointe, 275 Technology Drive, Canonsburg, PA, USA*, 2004.

[8] I. Babuska and B. Andersson. The splitting method as a tool for multiple damage analysis. *SIAM Journal on Scientific Computing*, 26(4):1114–1145, 2005.

[9] I. Babuška and J.M. Melenk. The partition of unity finite element method. Technical Report BN-1185, Inst. for Phys. Sc. and Tech., University of Maryland, June 1995.

[10] I. Babuška and J.M. Melenk. The partition of unity method. *IJNME*, 40:727–758, 1997.

[11] I. Babuška and A. Miller. The post-processing approach in the finite element method–part 2: The calculation of stress intensity factors. *IJNME*, 20:1111–1129, 1984.

[12] I. Babuška, G. Caloz, and J.E. Osborn. Special finite element methods for a class of second order elliptic problems with rough coefficients. *SIAM-JNA*, 31(4):945–981, 1994.

[13] R.E. Bank and L.R. Scott. On the conditioning of finite element equations with highly refined meshes. *SIAM Journal on Numerical Analysis*, 1989.

[14] F.M. Bayomy, M.A. Mull-Aglan, A.A. Abdo, and M.J. Santi. Evaluation of hot mix asphalt (hma) fracture resistance using critical strain energy release rate. *Presented at 85th Annual Meeting of the Transportation Research Board*, 2006.

[15] Z.P. Bazant and M. Jirsek. Nonlocal integral formulations of plasticity and damage: Survey of progress. *Journal of Engineering Meachanics ASCE*, 128:1119–1149, 2002.

[16] T. Belytschko and T. Black. Elastic crack growth in finite elements with minimal remeshing. *IJNME*, 45:601–620, 1999.

[17] T. Belytschko, R. Gracie, and G. Ventura. A review of extended/generalized finite element methods for material modeling. *MSMSE*, 17:24pp, 2009. http://dx.doi.org/10.1088/0965-0393/17/4/043001.

[18] A. Braham. *Fracture characteristics of asphalt concrete in Mode I, Mode II and mixed-mode*. PhD thesis, University of Illinois at Urbana-Champaign, 2008.

[19] A. Braham, W.G. Buttlar, and F. Ni. Laboratory mixed-mode craking of asphalt concrete using the single-edge notch beam. *Road Materials and Pavement Design*, pages 947–968, 2010.

[20] D.R. Brill. Calibration of FAARFIELD rigid pavement design procedure. Technical report, Federal Aviation Administration, 2010.

[21] S.F. Brown. Achievements and challenges in asphalt pavement engineering. *Keynote Lecture, Proceedings of the 8th International conference on asphalt pavements*, 3:19–41, 1997.

[22] Belgian Road Research Center BRRC. Design of overlaid cement concrete pavements reinforced with bitufor traffic loading. *Research report*, 1998.

[23] W.G. Buttlar, B. Dempsey, and D Bozkurt. Evaluation of reflective crack control policy. Technical report, Illinois Transportation Research Center, 1999.

[24] J.W. Button and R.L. Lytton. Guidelines for using geosynthetics with hot mix asphalt overlays to reduce reflective cracking. *Presented at the 86th Transportation Research Board Annual Meeting*, 2007.

[25] M.A. Castell, A.R. Ingraffea, and L.H. Irwin. Fatigue crack growth in pavements. *J. Transp. Eng.*, 126(4):283290, 2011.

[26] E. Chahine, P. Laborde, and Y.A. Renard. Spider-xfem, an extended finite element variant for partially unknown crack-tip displacement. *European Journal of Computational Mechanics*, 15(5-7):625–636, 2008.

[27] E. Chahine, P. Laborde, and Y.A. Renard. A reduced basis enrichment for the extended finite element method. *Mathematical Modelling of Natural Phenomena*, 4(1):88–105, 2009.

[28] K Chan, I.S. Tuba, and W.K. Wilson. On the finite element method in linear fracture mechanics. *Engineering Fracture Mechanics*, 2:1–17, 1970.

[29] K Chan, I.S. Tuba, and W.K. Wilson. On the finite element method in linear fracture mechanics. *Engineering Fracture Mechanics*, 2:1–17, 1970.

[30] H. S. Chang, R.L. Lytton, and S.H. Carpenter. Prediction of thermal reflection cracking in west texas. *Texas Transportation Institute. Research Report*, 18-3, 1976.

[31] H.J. Chen and D.A. Frederick. Interlayers on flexible pavements. *Transportation Research Record 1374, Transportation Research Board*, 1992.

[32] T. Chiawat and W.G. Buttlar. Laboratory evaluation of faa reflective cracking rig materials. Technical report, University of Illinois, 2012.

[33] D.L. Chopp and N. Sukumar. Fatigue crack propagation of multiple coplanar cracks with the coupled extended finite element/fast marching method. *IJES*, 41:845–869, 2003.

[34] G.S. Cleveland, J.W. Button, and R.L. Lytton. Geosynthetics in flexible and rigid pavement overlay systems to reduce reflection cracking. Technical report, Publication FHWA/TX-02/1777-1, FHWA, U.S. Department of Pavement, 2002.

[35] A.C. Collop, A.J. Sewell, and H. Thom. Laboratory assessment of the resistance to crack propagation in high-stiffness asphaltic materials. *J. Materials: Design and Applications*, 218:55–66, 2004.

[36] A.Th. Diamantoudis and G.N. Labeas. Stress intensity factors of semi-elliptical surface cracks in pressure vessels by global-local finite element methodology. *Engineering Fracture Mechanics*, 72:1299–1312, 2005.

[37] N.E. Dowling and J.A. Begley. Fatigue crack growth during gross plasticity and the J-integral. *ASTM STP 589. ASTM, West Conshohocken, Pa*, pages 82–103, 1988.

[38] Q. Duan, J.-H. Song, T. Menouillard, and T. Belytschko. Element-local level set method for three-dimensional dynamic crack growth. *IJNME*, 2009. In press. http://dx.doi.org/10.1002/nme.2665.

[39] C.A. Duarte. *The hp Cloud Method*. PhD dissertation, The University of Texas at Austin, December 1996. Austin, TX, USA.

[40] C.A. Duarte and D.-J. Kim. Analysis and applications of a generalized finite element method with global-local enrichment functions. *Computer Methods in Applied Mechanics and Engineering*, 197(6-8):487–504, 2008. doi: 10.1016/j.cma.2007.08.017.

[41] C.A. Duarte, I. Babuška, and J.T. Oden. Generalized finite element methods for three dimensional structural mechanics problems. *Computers and Structures*, 77:215–232, 2000. doi: 10.1016/S0045-7949(99)00211-4.

[42] C.A. Duarte, O.N. Hamzeh, T.J. Liszka, and W.W. Tworzydlo. A generalized finite element method for the simulation of three-dimensional dynamic crack propagation. *Computer Methods in Applied Mechanics and Engineering*, 190(15-17):2227–2262, 2001. doi: 10.1016/S0045-7825(00)00233-4.

[43] C.A. Duarte, D.-J. Kim, and I. Babuška. Chapter: A global-local approach for the construction of enrichment functions for the generalized fem and its application to three-dimensional cracks. In V.M.A. Leitão, C.J.S. Alves, and C.A. Duarte, editors, *Advances in Meshfree Techniques*, volume 5 of *Computational Methods in Applied Sciences*, The Netherlands, 2007. Springer. ISBN 978-1-4020-6094-6.

[44] C.A. Duarte, L.G. Reno, and A. Simone. A high-order generalized FEM for through-the-thickness branched cracks. *International Journal for Numerical Methods in Engineering*, 72(3):325–351, 2007. doi: 10.1002/nme.2012.

[45] C.A.M. Duarte and J.T. Oden. Hp clouds–A meshless method to solve boundary-value problems. Technical Report 95-05, TICAM, The University of Texas at Austin, May 1995.

[46] C.A.M. Duarte and J.T. Oden. *Hp* clouds – An *hp* meshless method. *Numerical Methods for Partial Differential Equations*, 12:673–705, 1996. doi: 10.1002/(SICI)1098-2426(199611)12:6¡673::AID-NUM3¿3.0.CO;2-P.

[47] C.A.M. Duarte and J.T. Oden. An *hp* adaptive method using clouds. *Computer Methods in Applied Mechanics and Engineering*, 139:237–262, 1996. doi: 10.1016/S0045-7825(96)01085-7.

[48] H. Dubner and J. Abate. Numerical inversion of laplace transforms and the finite fourier transform. *J. ACM*, 15:115–123, 1968.

[49] M. Duflot. A study of the representation of cracks with level sets. *IJNME*, 70:1261–1302, 2007.

[50] M. Duflot and S. Bordas. XFEM and mesh adaptation: A marriage of convenience. In *Eighth World Congress on Computational Mechanics*, Venice, Italy, July 2008.

[51] M. Elseifi and I.L. Al-Qadi. A simplified overlay design model against reflective cracking utilizing service life prediction.

[52] F. Erdogan and G.C. Sih. On the crack extension in plates under plane loading and transverse shear. *Journal of Basic Engineering*, 85:519–525, 1963.

[53] FEACrack Version 2.7. Quest Reliability, LLC. Boulder, Colorado. http://www.srt-boulder.com/feacrack.htm.

[54] C.A. Felippa. Introduction to finite element methods., 2004. Course Notes. Department of Aerospace Engineeing Sciences, University of Colorado at Boulder. Available at http://www.colorado.edu/engineering/Aerospace/CAS/courses.d/IFEM.d.

[55] J.D. Ferry. *Viscoelastic Properties of Polymers*, Ney York:3rd, 1980.

[56] W. Findley, J. Lai, and K. Onaran. *Creep and Relaxation of Nonlinear Viscoelastic Materials*. North-Holland Publishing Company, 1976.

[57] W. Flugge. *Viscoelasticity*. Blaisdell Publishing Company, 1967.

[58] L. Francken and A. Vanelstraete. Interface systems to prevent reflective cracking. *International Conference on Asphalt Pavements, International Society for Asphalt Pavements*, 7: 45–60, 1992.

[59] T.-P. Fries and T. Belytschko. The generalized/extended finite element method: An overview of the method and its applications. *IJNME*, pages 253–304, 2010.

[60] T.P. Fries and M. Baydoun. Crack propagation with the extended finite element method and a hybrid explicitimplicit crack description. *IJNME*, 89:1527–1558, 2012.

[61] J. Garzon, C.A. Duarte, and W. Buttlar. Analysis of reflective cracks in air field pavements using a 3-D generalized finite element method. *Road Materials and Pavement Design*, 11 (2):459–477, 2010. doi: 10.3166/rmpd.11.459-477.

[62] J. Garzon, D.-J. Kim, C.A. Duarte, and W. Buttlar. Two-scale three-dimensional analysis of reflective cracks in airfield pavements. *International Journal of Computational Methods*, 2011. Accepted for publication.

[63] A. Gravouil, N. Moës, and T. Belytschko. Non-planar 3d crack growth by the extended finite element and level sets – Part II: Level set update. *IJNME*, 53(11):2569–2586, 2002.

[64] V. Gupta, D.-J. Kim, and C.A. Duarte. Analysis and improvements of global-local enrichments for the generalized finite element method. *Computer Methods in Applied Mechanics and Engineering*, 245–246:47–62, 2012. doi: 10.1016/j.cma.2012.06.021.

[65] D.J. Halsted and D.E. Brown. Zakians technique for inverting Laplace transform. *Chem. Eng. J.*, 3:312–313, 1972.

[66] H. Hassanzadeh and M. Pooladi-Darvish. Comparison of different numerical laplace inversion methods for engineering applications. *Applied Mathematics and Computation*, 189: 1966–1981, 2007.

[67] H.H. Hilton. *Engineering Design for Plastics*. Polymer Science And Engineering Series, 1964.

[68] R.M. Hinterhoelzl and R.A. Schapey. Fem implementation of a three-dimensional viscoelastic constitutive model for particulate composites with damage growth. *Mechanics of Time-Dependent Materials*, 8:65–94, 2004.

[69] I. Hirai, B.P. Wang, and W.D. Pilkey. An efficient zooming method for finite element analysis. *IJNME*, 20:1671–1683, 1984.

[70] S. Hu, X. Hu, F. Zhou, and L. Walubita. SA-CrackPro: A new finite element analysis tool for pavement crack propagation. *Journal of Transportation Research Record*, 2068:10–19, 2008.

[71] Y.H. Huang. Pavement analysis and design, prentice hall. *Englewood Cliffs, New Jersey*, 1993.

[72] S. L. Hussain and J. Underwood. Strain energy release rate for a crack under combined mode i and mode ii. *ASTM STP*, 560:2–28, 1973.

[73] GR. Irwin. Analysis of stresses and strains near the end of a crack traversing a plate. *ASME J Appl Mech*, 24:361–364, 1957.

[74] GR. Irwin. Fracture I. *Handbuch der Physik*, 6:558–590, 1958.

[75] M.M. Jacobs, P.C. Hopman, and A.A.A. Molenaar. Application of fracture mechanics principles to analyze cracking in asphalt concrete. *Asphalt Paving Technol*, 65, 1996.

[76] P. Jäger, P. Steinmann, and E. Kuhl. Modeling three-dimensional crack propagation – A comparison of crack path tracking strategies. *IJNME*, 76:1328–1352, 2008.

[77] T.A. Jelmert. The effect of distributed block length function on double porosity transitions during linear flow. *J. Petrol. Sci. Eng.*, 12:277–293, 1995.

[78] X. Jiao. Face offsetting: A unified framework for explicit moving interfaces. *Journal of Computational Physics*, 220(2):612–625, 2007.

[79] R.A. Jiminez. Fatigue testing of asphaltic concrete slabs. *Fatigue of compacted bituminous aggregate mixtures, ASTM STP*, 508:3–17, 1972.

[80] D.D. Joseph. Change of type and loss of evolution in the flow of viscoelastic fluids. *Journal of Non-Newtonian Fluid Mechanics*, 20:117–141, 1986.

[81] Y. Jun, F. Guanhua, L. Qing, C. Rongsheng, and D. Xuejun. Deep analysis on interlayer restraining reflective cracks in asphalt overlay old concrete pavement. *Proceedings pro37: Cracking in Pavements: Mitigation, Risk Assessment and Prevention*, pages 223–230, 2004.

[82] A.A. Kaminski. *Soviet Applied Mechanics*, 16:741–836, 1980.

[83] D.-J. Kim, C.A. Duarte, and J.P. Pereira. Analysis of interacting cracks using the generalized finite element method with global-local enrichment functions. *Journal of Applied Mechanics*, 75(5):051107, 2008. doi: 10.1115/1.2936240.

[84] D.-J. Kim, J.P. Pereira, and C.A. Duarte. Analysis of three-dimensional fracture mechanics problems: A two-scale approach using coarse generalized FEM meshes. *International Journal for Numerical Methods in Engineering*, 81(3):335–365, 2010. doi: 10.1002/nme.2690.

[85] D.-J. Kim, C. Duarte, and S. Proenca. A generalized finite element method with global-local enrichment functions for confined plasticity problems. *Computational Mechanics*, pages 1–16, 2012. ISSN 0178-7675. doi: 10.1007/s00466-012-0689-7.

[86] H. Kim and W.G. Buttlar. Finite element cohesive fracture modeling of airport pavements at low temperatures. *Cold Regions Science and Technology*, 57:123–130, 2009.

[87] H. Kim and W.G. Buttlar. Discrete fracture modeling of asphalt concrete. *International Journal of Solids and Structures*, 46:2593–2604, 2009.

[88] J. Kim and W.G. Buttlar. Analysis of reflective crack control system involving reinforcing grid over base-isolating interlayer mixture. *ASCE Journal of Transportation Engineering*, 28(4):375–384, 2002.

[89] Y. Richard Kim. *Modeling of Asphalt Concrete*. McGraw-Hill, 2009.

[90] W.G. Knauss. *Applied Mechanics Reviews*, 26:1–17, 1973.

[91] J.K. Knowles and E. Sternberg. On a class of conservation laws in a linearized and finite elastostatics. *Arch. Rat. Mech. Anal.*, 44:187–211, 1978.

[92] P. Krysl and T. Belytschko. The element free Galerkin method for dynamic propagation of arbitrary 3-D cracks. *IJNME*, 44:767–800, 1999.

[93] H. Kuai, H.J. Lee, Z. Goangseup, and S. Mun. Application of generalized j -integral to crack propagation modeling of asphalt concrete under repeated loading. *Transportation Research Record: Journal of the Transportation Research Board*, 2127:72–81, 2009.

[94] R. Lakes. *Viscoelastic Materials*. Cambridge University Press, 2009.

[95] Y. Lambert, P. Saillard, and C. Bathias. Application of the J concept to fatigue crack growth in large-scale yielding. *ASTM STP 589. ASTM, West Conshohocken, Pa*, pages 318–329, 1988.

[96] P. Lancaster and K. Salkauskas. Surfaces generated by moving least squares methods. *Mathematics of Computation*, 37(155):141–158, 1981.

[97] S.S. Lee and Y.J. Kim. Time-domain boundary element analysis of cracked linear viscoelastic solids. *EFM*, 51(4):585–590, 1995.

[98] F.Z. Li, C.F. Shih, and A. Needleman. A comparison of methods for calculating energy release rates. *Engineering Fracture Mechanics*, 21(2):405–421, 1985.

[99] M. Lifeng, J. Tian, and A Korsunsky. Vector J-integral analysis of crack interaction with pre-existing singularities. *ASME*, 73:876–883, 2006.

[100] S. Loehnert and T. Belytschko. A multiscale projection method for macro/microcrack simulations. *IJNME*, 71(12):1466–1482, 2007.

[101] V.M. Lorenz. New mexico study of interlayers used in reflective crack control. *Transportation Research Record: Journal of the Transportation Research Board*, pages 94–103, 1987.

[102] L.G. Loria-Salazar. *Reflective Craking of Flexible Pavements: Literature Review, Analysis Models, and Testing Methods*. PhD thesis, University of Nevada, Reno, 2008.

[103] J Mackerle. Finite-element analysis and simulation of polymers: a bibliography. *Modelling and Simulation in Material Science and Engineering*, 5:15–50, 1997.

[104] K. Majidzadeh, E.M. Kauffmann, and D.V. Ramsamooj. Application of fracture mechanics in the analysis of pavement fatigue. *Proc Assoc. Asphalt Paving Technol.*, 40:227–246, 1971.

[105] U.M. Mayer, A. Gerstenberger, and W.A. Wall. Interface handling for three-dimensional higher-order XFEM-computations in fluid-structure interaction. *IJNME*, 2009. doi: 10.1002/nme.2600.

[106] J.M. Melenk and I. Babuška. The partition of unity finite element method: Basic theory and applications. *CMAME*, 139:289–314, 1996.

[107] A. Menk and P.A. Bordas. Numerically determined enrichment functions for the extended finite element method and applications to bi-material anisotropic fracture and polycrystals. *IJNME*, 83(7):805828, 2010.

[108] N. Moës, J. Dolbow, and T. Belytschko. A finite element method for crack growth without remeshing. *IJNME*, 46:131–150, 1999.

[109] N. Moës, A. Gravouil, and T. Belytschko. Non-planar 3D crack growth by the extended finite element and level sets – Part I: Mechanical model. *IJNME*, 53(11):2549–2568, 2002.

[110] N. Moës, M. Cloirec, P. Cartraud, and J.-F. Remacle. A computational approach to handle complex microstructure geometries. *CMAME*, 192:3163–3177, 2003.

[111] C.L. Monismith and N.F. Coetzee. Reflection cracking: Analysis, laboratory studies and design consideration. *Proceedings of Association of Asphalt Paving Technologists*, 49:268–313, 1980.

[112] S.E. Mousavi, E. Grinspun, and N. Sukumar. Harmonic enrichment functions: A unified treatment of multiple, intersecting and branched cracks in the extended finite element method. *International Journal for Numerical Methods in Engineering*, 85:13061322, 2011. doi: 10.1002/nme.3020.

[113] H.K. Mueller and W.G. Knauss. *Journal of Applied Mechanics*, 38:483–488, 1971.

[114] NASGRO/FLAGRO. Fatigue crack growth computer program NASGRO/FLAGRO version 2.0. Structures and Mechanics Division, NASA/Lyndon B. Johnson Space Center, Houston, TX, 1992.

[115] A.K. Noor. Global-local methodologies and their applications to nonlinear analysis. *fead*, 2:333–346, 1986.

[116] R. J. Nuismer. An energy release rate criterion for mixed mode fracture. *International Journal of Fracture*, 11:245–250, 1975.

[117] J.T. Oden and C.A. Duarte. Chapter: Clouds, Cracks and FEM's. In B.D. Reddy, editor, *Recent Developments in Computational and Applied Mechanics*, pages 302–321, Barcelona, Spain, 1997. International Center for Numerical Methods in Engineering, CIMNE. http://citeseer.ist.psu.edu/17994.html.

[118] J.T. Oden and C.A.M. Duarte. Chapter: Solution of singular problems using *hp* clouds. In J.R. Whiteman, editor, *The Mathematics of Finite Elements and Applications – Highlights 1996*, pages 35–54, New York, NY, 1997. John Wiley & Sons. http://citeseer.ist.psu.edu/170015.html.

[119] J.T. Oden, C.A. Duarte, and O.C. Zienkiewicz. A new cloud-based *hp* finite element method. *Computer Methods in Applied Mechanics and Engineering*, 153:117–126, 1998. doi: 10.1016/S0045-7825(97)00039-X.

[120] P. O'Hara, C.A. Duarte, and T. Eason. Generalized finite element analysis of three-dimensional heat transfer problems exhibiting sharp thermal gradients. *Computer Methods in Applied Mechanics and Engineering*, 198(21-26):1857–1871, 2009. doi: 10.1016/j.cma.2008.12.024.

[121] P. O'Hara, C.A. Duarte, and T. Eason. Transient analysis of sharp thermal gradients using coarse finite element meshes. *Computer Methods in Applied Mechanics and Engineering*, 200(5-8):812–829, 2011. doi: 10.1016/j.cma.2010.10.005.

[122] H. Ozer, C.A. Duarte, and I.L. Al-Qadi. Formulation and implementation of a high-order 3-d domain integral method for the extraction of energy release rates. *Computational Mechanics*, 49:459–476, 2012. doi: 10.1007/s00466-011-0651-0.

[123] A. Paris and F. Erdogan. A critical analysis of crack propagation laws. *Journal of Basic Engineering*, 85:528–534, 1963.

[124] Patran. MSC Software, http://www.mscsoftware.com/products/patran.cfm.

[125] P.S. Pell and K.E. Cooper. The effect of testing and mix variables on the fatigue performance of bituminous paving mixtures. *Asphalt Paving Technol*, 44:1–37, 1975.

[126] J.P. Pereira and C.A. Duarte. Extraction of stress intensity factors from generalized finite element solutions. *Engineering Analysis with Boundary Elements*, 29:397–413, 2005. doi: 10.1016/j.enganabound.2004.09.007.

[127] J.P. Pereira and C.A. Duarte. The contour integral method for loaded cracks. *Communications in Numerical Methods in Engineering*, 22(5):421–432, 2006. doi: 10.1002/cnm.824.

[128] J.P. Pereira, C.A. Duarte, D. Guoy, and X. Jiao. *Hp*-Generalized FEM and crack surface representation for non-planar 3-D cracks. *International Journal for Numerical Methods in Engineering*, 77(5):601–633, 2009. doi: 10.1002/nme.2419.

[129] J.P. Pereira, C.A. Duarte, X. Jiao, and D. Guoy. Generalized finite element method enrichment functions for curved singularities in 3D fracture mechanics problems. *Computational Mechanics*, 44(1):73–92, 2009. doi: 10.1007/s00466-008-0356-1.

[130] J.P. Pereira, C.A. Duarte, and X. Jiao. Three-dimensional crack growth with *hp*-generalized finite element and face offsetting methods. *Computational Mechanics*, 46(3):431–453, 2010. doi: 10.1007/s00466-010-0491-3.

[131] J.P. Pereira, D.-J. Kim, and C.A. Duarte. A two-scale approach for the analysis of propagating three-dimensional fractures. *Computational Mechanics*, 49(1):99–121, 2012. doi: 10.1007/s00466-011-0631-4.

[132] B. Prabel, A. Combescure, A. Gravouil, and S. Marie. Level set X-FEM non-matching meshes: Application to dynamic crack propagation in elastic-plastic media. *IJNME*, 69: 1553–1569, 2007.

[133] N.H. Predoehl. Evaluation of paving fabric test instalation in california. Technical report, California Department of Transportation, Translab, 1989.

[134] J. Qian and A. Fatemi. Mixed mode fatigue crack growth: A literature survey. *EFM*, 55(6): 969–990, 1996.

[135] T. Rabczuk, S. Bordas, and G. Zi. On three-dimensional modeling of crack growth using partition of unity methods. *CS*, 2009. In press. http://dx.doi.org/10.1016/j.compstruc.2008.08.010.

[136] J.C. Raju, I.S. Newman Jr. Finite-element analysis of corner cracks in rectangular bars. Technical report, NASA, 1987.

[137] J. R. Rice. A path independent integral and the approximate analysis of strain concentration by notches and cracks. *Journal of Applied Mechanics*, 35:379–386, 1968.

[138] H.A. Richard, M. Fulland, F.G. Buchholz, and M. Schöllmann. 3D. *Steel Research*, 74(8): 491–497, 2003.

[139] H.A. Richard, M. Fulland, and M. Sander. Theoretical crack path prediction. *Fatigue & Fracture of Engineering Materials & Structures*, 28:3–12, 2005. http://dx.doi.org/10.1111/j.1460-2695.2004.00855.x.

[140] R.H. Rigby and M.H. Aliabadi. Decomposition of the mixed-mode J-integral–revisited. *International Journal of Solids and Structures*, 35(17):2073 – 2099, 1998. doi: 10.1016/S0020-7683(97)00171-6.

[141] A. Scarpas, J. Blaauwendraad, A.H. de Bondt, and A.A. Molenaar. Capa: A modern tool for the analysis and design of pavements. *Proceedings of the 2nd International Conference on Reflective Crackingin Pavements*, pages 121–128, 1993.

[142] A. Scarpas, A.H. de Bondt, and Gaarkeuken. Reflective cracking control via reinforcing system: Fe modelling of reinforced overlays. *Proceedings of the 3rd International RILEM Conference*, page 344353, 1996.

[143] R.A. Schapery. Approximate methods of transform inversion for viscoelastic stress analysis. 1962.

[144] R.A. Schapery. Viscoelastic behavior and analysis of composite materials. *New York, Academic Press*, pages 85–168, 1974.

[145] R.A. Schapery. A theory of crack inititation and growth in viscoelastic media, part I. *International Journal of Fracture*, 11(1):141–159, 1975.

[146] R.A. Schapery. A theory of crack inititation and growth in viscoelastic media, part II. *International Journal of Fracture*, 11(3):369–388, 1975.

[147] R.A. Schapery. A theory of crack inititation and growth in viscoelastic media, part III. *International Journal of Fracture*, 11(4):549–562, 1975.

[148] R.A. Schapery. Correspondence principles and generalized J integral for large deformation and fracture analysis of viscoelastic media. *International Journal of Fracture*, 25:195–223, 1984.

[149] R.A. Schapery. On some path independent integrals and their use in fracture of nonlinear viscoelastic media. *International Journal of Fracture*, pages 189–207, 1990.

[150] J. Schijve. *Fatigue of structures and materials*. Kulver Academic, Boston, MA, USA, 2001.

[151] M. Schöllmann, H.A. Richard, G. Kullmer, and M. Fulland. A new criterion for the prediction of crack development in multiaxially loaded structures. *IJF*, 117:129–141, 2002.

[152] M. Schöllmann, M. Fulland, and H.A. Richard. Development of a new software for adaptive crack growth simulations in 3-D structures. *EFM*, 70:249–268, 2003.

[153] J.A. Sethian. *Level Set Methods and Fast Marching Methods Evolving Interfaces in Computational Geometry, Fluid Mechanics, Computer Vision, and Materials Science*. Cambridge Monograph on Applied and Computational Mathematics. Cambridge University Press, London, 1999.

[154] S. Shen, G.D. Airey, S.H Carpenter, and H. Huang. A dissipated energy approach to fatigue evaluation. *Road Materials and Pavement Design*, 7(1):47–69, 2006.

[155] H. Simon, T. Zacharia, and R. Stevens. Modeling and simulation at the exascale for energy and the environment. Technical report, Lawrence Berkeley National Laboratory, 2007.

[156] A. Simone. Partition of unity-based discontinuous elements for interface phenomena: Computational issues. *cnme*, 20:465–478, 2004.

[157] A. Simone, C.A. Duarte, and E. van der Giessen. A generalized finite element method for polycrystals with discontinuous grain boundaries. *International Journal for Numerical Methods in Engineering*, 67(8):1122–1145, 2006. doi: 10.1002/nme.1658.

[158] K. Sobczyk and B.F. Spencer. *Random Fatigue: From Data to Theory*. Academic Press, inc., San Diego, USA, 1992.

[159] S. H. Song, G. Paulino, and W.G. Buttlar. A bilinear cohesive zone model tailored for fracture of asphalt concrete considering viscoelastic bulk material. *Engineering Fracture Mechanics*, 73:2829–2848, 2006.

[160] M. Stern, E. B. Becker, and R. S. Dunham. A contour integral computation of mixed-mode stress intensity factors. *International Journal of Fracture*, 12:359–368, 1976.

[161] T. Strouboulis, K. Copps, and I. Babuška. The generalized finite element method. *CMAME*, 190:4081–4193, 2001.

[162] T. Strouboulis, L. Zhang, and I. Babuška. Generalized finite element method using mesh-based handbooks: Application to problems in domains with many voids. *CMAME*, 192: 3109–3161, 2003.

[163] N. Sukumar, N. Moës, B. Moran, and T. Belytschko. Extended finite element method for three-dimensional crack modelling. *IJNME*, 48(11):1549–1570, 2000.

[164] N. Sukumar, D.L. Chopp, and B. Moran. Extended finite element method and fast marching method for three-dimensional fatigue crack propagation. *EFM*, 70:29–48, 2003.

[165] J.W. Swegle, S.W. Attaway, M.W. Heinstein, F.J. Mello, and D.L. Hicks. An analysis of the smoothed particle hydrodynamics. Technical Report SAND93-2513 UC-705, Sandia National Laboratories, Albuquerque, NM, 1994.

[166] S. Syngellakis and J. Wu. Evaluation of various schemes for quasi-static boundary element analysis of polymers. *Engineering Analysis with Boundary Elements*, 28:733–745, 2004.

[167] S. Syngellakis and J. Wu. Evaluation of polymer fracture parameters by the boundary element method. *Engineering Fracture Mechanics*, 75:1251–1265, 2008.

[168] B. Szabo and I. Babuška. *Finite Element Analysis*. John Wiley and Sons, New York, 1991.

[169] B. A. Szabo and I. Babuška. Computation of the amplitude of stress singular terms for cracks and reentrant corners. In T.A. Cruse, editor, *Fracture Mechanics: Nineteenth Symposium, ASTM STP 969*, pages 101–124, Southwest Research Institute, San Antonio, TX, 1988.

[170] H. Tada, P. Paris, and G. Irwin. *The Stress Analysis of Cracks Handbook*. ASME Press, New York, 3rd edition, 2000.

[171] K. Tanaka. Mechanics and micromechanics of fatigue crack propagation. In R.P. Wei and R.P. Gangloff, editors, *Fracture Mechanics: Perspectives and Directions (Twentieth Symposium)*, ASTM STP 1020, pages 151–183, Philadelphia, 1989. American Society for Testing and Materials.

[172] M.R. Thompson and S.H. Carpenter. Fatigue design principles for long lasting hma pavements. *ISAP International Symposiun on Long-Lasting Asphalt Pavements*, 2004.

[173] A. Ural, G. Heber, P. Wawrzynek, A. Ingraffea, D. Lewicki, and J. Neto. Three-dimensional, parallel, finite element simulation of fatigue crack growth in a spiral bevel pinion gear. *EFM*, 72:1148–1170, 2005.

[174] D.A. Virkler, B.M. Hillberry, and P.K. Goel. The statistical nature of fatigue crack propagation. *Journal of Engineering Materials and Technology*, 101:148–153, 1979.

[175] M.P. Wagoner, W.G. Buttlar, and G.H. Paulino. Disk-shaped compact tension test for asphalt concrete fracture. *Experimental Mechanics*, 3:270–277, 2005.

[176] M.P. Wagoner, W.G. Buttlar, G.H. Paulino, and P. Blankenship. Investigation of the fracture resistance of hot-mix asphalt concrete using a disk-shaped compact tension test. *Transportation Research Record*, 1929:183–192, 2005.

[177] T.C. Wang. *Fracture 1977*, 4:135–154, University of Waterloo (1977).

[178] P.A. Wawrzynek, L.F. Martha, and A.R. Ingraffea. A computational environment for the simulation of fracture processes in three-dimensions. In A. J. Rosakis, editor, *Analytical, Numerical and Experimental Aspects of Three Dimensional Fracture Process*, volume 91, pages 321–327, New York, 1988. ASME AMD, ASME.

[179] G.N. Wells and L.J. Sluys. A new method for modeling cohesive cracks using finite elements. *IJNME*, 50:2667–2682, 2001.

[180] J.D. Whitcomb. Iterative global/local finite element analysis. *cs*, 40:1027–1031, 1991.

[181] M.P. Wnuk and W.G. Knauss. *International Journal of Solids and Structures*, 6:995–1009, 1970.

[182] P.E. Yongqi Li and J.B. Metcalf. Fatigue characteristics of asphalt concrete from asphalt slab tests. *Journal of Materials in Civil Engineering*, 16:306–314, 2004.

[183] T.T. YU and Q.W. REN. Modeling crack in viscoelastic media using the extended finite element method. *Science China: Technological Science*, 54:1599–1606, 2011.

[184] *ZENCRACK*. Zentech International Limited, http://www.zentech.co.uk/zencrack.htm, 2008.

[185] C.Y. Zhang. *Viscoleastic Fracture Mechanics*. Beijing:Science Press, 2006.

[186] M.A. Zocher, S.E. Groves, and D.H. Allen. A three dimensional finite element formulation for thermoviscoelastic orthotropic media. *International Journal of Numerical Methods and Engineering*, 40:2267–2288, 1997.